d^0 magnetism in oxides and alkaline-earth hexaborides

A thesis submitted to the University of Dublin, Trinity

College in partial fulfillment of the

requirements for the degree of

Doctor of Philosophy

by

Karl Ackland

School of Physics and CRANN

Trinity College Dublin

June 4th 2014

Declaration

This thesis is submitted by the undersigned for examination for the degree Doctor of Philosophy at the University of Dublin. I declare that this thesis has not been submitted as an exercise for a degree at this or any other University and that apart from the advice, assistance and joint effort mentioned in the acknowledgements and in the text is entirely my own work

I agree to deposit this thesis in the University's open access institutional repository or allow the library to do so on my behalf, subject to Irish Copyright Legislation and Trinity College Library conditions of use and acknowledgement. I agree that Trinity College Library may lend or copy this thesis upon request.

Karl Ackland

4th June 2014

To the common good of humanity

Summary

The term "d^0 ferromagnetism" is applied to a wide range of materials which exhibit a weak, anhysteretic ferromagnetic-like response to an applied magnetic field although they would not normally be expected to be magnetic since they contain none of the unpaired *d* or *f* electrons traditionally associated with magnetic order. A somewhat controversial area of research, it has been proposed that the magnetism may be intrinsic and related to defects, although in some reports the magnetism may be attributed to spurious magnetic signals associated with extrinsic ferromagnetic impurities. In chapter 1 of this thesis an introduction to d^0 magnetism is presented, together with an introduction to one of the potential practical applications of d^0 magnetism, namely spin electronics. Chapter 2 details the experimental methods and characterization tools used.

In this thesis, three d^0 candidate systems have been studied: the first two systems are wide bandgap oxides, namely HfO_2 micropowders (Chapter 3) and CeO_2 nanoparticles (Chapter 4), while the third system is divalent alkaline-earth hexaboride thin films (Chapter 5) of formula MB_6 (M = Ca, Sr, Ba). Necessary precautions were taken throughout in order to try to minimize any extrinsic ferromagnetic impurity contributions to the magnetic signals.

For HfO_2 commercial micropowders firstly, the effect of vacuum annealing and the associated creation of oxygen vacancies on the room temperature magnetic signal wasinvestigated. Upon vacuum annealing, a weak anhysteretic room temperature magnetic signal was measured within the annealing temperature range 600 – 750 °C, which reached a maximum value of 14 A m^{-1} at an annealing temperature of 700 °C. Upon re-annealing in air, the magnetic signal was significantly diminished, from which it was inferred that the magnetism may be linked to oxygen vacancies induced by vacuum annealing.

Secondly, CeO_2 nanoparticles of diameter 4-6 nm were synthesized by a wet chemical route via oxidation of $Ce(NO_3)_3.6H_2O$. Ferromagnetic samples exhibiting virtually anhysteretic, isotropic and temperature independent magnetism in the range 4 – 300 K were synthesized using a 99 % nominal purity cerium nitrate precursor, which contained ~ 1-2 wt% of La as the main impurity. M_s is of order 100 A m^{-1} and less than 0.1 % of the sample volume is really magnetically ordered, consistent with inhomogeneous defect magnetism associated with interfaces or surfaces. Non-ferromagnetic samples were synthesized using 99.999 % purity cerium nitrate. In addition it was found that the magnetic signal may be "turned on" by doping the non-magnetic samples with small quantities (|~ 1 wt %) of high purity non-magnetic elements such as La.

Lastly, amorphous MB_6 (M = Ca, Sr, Ba) films were grown by pulsed laser deposition (PLD) on Al_2O_3 substrates between 300 and 850 °C. Intrinsic, defect-related magnetism, with magnetic moments of order 3×10^{-8} Am^2, was measured for many of these films, particularly for several grown at 400 - 650 °C; the magnetism is virtually anhysteretic, isotropic, temperature independent from 4 – 300 K and saturates quickly (< 0.3 T) with applied field. It is shown that ferromagnetic impurities cannot account for the magnitude of the larger magnetic signals measured.

The magnetic signals correspond to an average film magnetization in the range ~ 10 - 100 kA m^{-1}, but from analysis of the variation of the magnetic moment with film thickness, it is shown that the magnetism originates mainly near the interface with the substrate.

Three models for interpretation of the results are discussed. The first model proposes that the magnetism is due to a defect-based impurity band, which can become spin split and result in high temperature Stoner ferromagnetism when the density of states at the Fermi level is sufficiently high. This is named Charge Transfer Ferromagnetism (CTF). Another model predicts the formation of a 2-D electron gas at the surface of nanoparticles of small diameter (≤ 10 nm) which can easily spin polarize and produce very large orbital moments, to which the term Giant Orbital Paramagnetism (GOP) is ascribed. For the third model, termed collective magnetism, the magnetic signals are proposed to be due to giant orbital moments which form in coherent domains of clumps (~ 100 nm) of nanoparticles at the mesoscale, with a theoretical basis in the resonant fluctuations of the electromagnetic field (zero-point energy).

A discussion of each model for d^0 magnetism in relation to each of the three experimental systems studied is presented in Chapter 6, followed by a summary of the main conclusions and a plan for future work in Chapter 7.

Acknowledgements

First of all I would like to thank Prof. Michael Coey for giving me the opportunity and support to work in his laboratory, for always pushing me in the right directions, and not least for allowing me to attend a fair share of conferences and summer schools! Secondly, I am very grateful to Venky (Munuswamy Venkatesan) for performing the magnetization measurements and for his readiness to offer his wide-ranging advice on all magnetism-related questions. His guidance has proved invaluable.

I want to thank Karsten Rode for guidance with XRD, PLD and for lots of help with both the measuring and analysis of XMCD data, the last of which necessitated a trip to the Paul Scherrer Institute in Switzerland. I thank Plamen Stamenov for general advice on magnetism, scientific discussion and for help with a plethora of experimental technical issues. I am grateful to Lorena Monzon for any questions I had relating to chemistry. Thanks to Huseyin Kurt for his advice about scientific careers, typically promulgated with a dash of his idiosyncratic humour!

I wish to acknowledge the help and support Bob Barklie gave me with EPR and for allowing me to make use of his EPR setup, as well as for the time he took to discuss the EPR results with me. I thank James Lunney for facilitating the use of his PLD system, and to his students, Gearóid, Inam and Mubarak for assistance with PLD experiments. Thanks to Trevor Woods, Mustafa Lotya and Marguerite Hughes for help with Raman, Photoluminescence and UV-Vis measurements respectively. At the AML, I would like to thank Markus Boese for help with TEM, Cathal MacCauley for help with SEM, and Colm Faulkner for lots of guidance with FIB work. At the CMA, I wish to thank Neal Leddy for help with TEM, Heath Bagshaw for help with FT-IR measurements, and Leona O'Connor for ICP-MS measurements. Thanks to Dr. Donald MacLaren at the University of Glasgow for TEM-EELS analysis of CeO_2 nanoparticles. At the Paul Scherrer Institute in Switzerland I would like to thank the beamline scientists Cinthia Piamonteze and Andreas Suter for help with XAS/XMCD and muon spin rotation measurements plus analysis respectively.

Back in the lab, I want to thank Peter Dunne for help and advice regarding Mössbauer spectroscopy, Jonathan Alaria for additional help with XRD, Hongjun Xu for transport measurements and Zhu Diao for teaching me AFM. And thank you to all of my other colleagues in the Coey group who helped enrich the PhD experience in their various ways, in alphabetical order: Ali, Amir, Anna (Majcher and Schuhl), Aoife, Arnaud, Arushi, Asra, Ciaran, Chris, Christian, Conor, Dalai, Damaris, Darragh, David, Davide, Eoin, Fiona, Franklyn, Gavin, Guoqiang, Huseyin Tokuc, Ishita, James, Jane, Jerome, Jiafeng, John (Campbell and Duffy), Juliette, Junyang, Kaan, Katie, Kiril, Lorcan, Lorenzo, Louise, Marina, Marita, Milena, Mohsen, Naganivetha, Nigel, Pelin, Rémy (Lasser-Ballier and Soucaille), Robert, Saba, Sarat, Séan, Simone, Stephen, Terry, Thiago, Tomohiko, Vatsal, Yash, Yongchang and Zsolt. Apologies to

anybody that I have forgotten.

In the physics workshop, I would like to express my thanks to Dave, Pat and Gordon for repairs and servicing of equipment, and in administration to Robbie, Ciara, Samantha, Jeanette, Gabriella and Sandra.

I also wish to thank and acknowledge all of my teachers from primary and secondary school, and my lecturers during my time as an undergraduate at Trinity College Dublin.

I want to acknowledge generous support from Science Foundation Ireland who funded me for the majority of the duration of the PhD (2009 – 2013) as part of the IRCSET EMBARK Initiative, and to Trinity College Dublin for funding me for the following few months thereafter during which the thesis was written up and completed. The IEEE Magnetics Society kindly provided funding for travel to the Intermagnetics Asia 2011 conference and also to their summer school that same year.

Lastly, I am thankful beyond words to my parents, Joan and Damon, for bringing me into the world and for their constant and loving support, and to my sisters, Gillian and Katie, for enriching my life. I am grateful to Eoghan for distracting me from my thesis when I needed to take a break, in order to delve into musical delights, and to Buddy for being a good companion while he was here.

Table of Contents

List of Figures

List of Tables

Chapter 1

Introduction

1.1 d^0 magnetism

The term "d^0 magnetism" [1], sometimes also variably termed d^0 ferromagnetism, phantom (ferro)magnetism or defect-magnetism, refers to a phenomenon found in a wide range of materials which exhibit a weak, anhysteretic ferromagnetic-like response to an applied magnetic field although they would not normally expected to be magnetic since they contain neither the *d* or *f* electrons traditionally associated with magnetic order. Whether this unconventional magnetism is really a completely new phenomenon and intrinsic or is simply an artefact due to ferromagnetic impurities has remained hotly debated since the outset of this new field of magnetism about ten years ago, perhaps fuelled by the fact that the weak magnetic signals are often only of similar magnitudes to that due to 100's of parts per million (ppm), in some cases less, of ferromagnetic contaminants. Hence care with sample preparation and comprehensive quantification of impurity content by sensitive techniques such as inductively coupled plasma mass spectroscopy (ICP-MS) is of paramount importance in order to lay a convincing claim that the magnetic signal may not be entirely ascribed to ferromagnetic impurities and/or contamination.

d^0 magnetism has been reported to occur in a wide variety of materials, such as zinc oxide (ZnO) nanoparticles [2-4], cerium dioxide nanoparticles [5, 6] and electrodeposited thin films [7], hafnium dioxide thin films [8], alkaline earth hexaboride films [9], gold, silver and copper nanoparticles capped with dodecaenthiol [10], graphene [11] and even for severed Teflon tape [12], to name but a few. The materials are either undoped or contain a small quantity (typically a few weight % at most) of non-magnetic dopant. While the range of materials purported to display d^0 magnetism is undoubtedly diverse, common features include the necessary absence of unpaired *d* or *f* electrons and the presence of defects. It is important to firmly establish that the defect free bulk is never found to display d^0 magnetism; instead, materials which are rich in defects, often in thin film and nanoparticulate form, exhibit the phenomenon, which may suggest that nanoscale interfaces and surfaces may play an important role in mediating the magnetism. For thin films, the saturation magnetization values, often of order 1-100 kA m^{-1}, are typically several orders of magnitude larger than that for nanoparticles or powders, which rarely exceed 1 kA m^{-1}, and are more commonly found to lie within the range 1-100 A m^{-1}.

Other characteristics of d^0 magnetism include a magnetic signal that is virtually temperature independent from ~ 4 K to several hundred degrees above room temperature (ruling out superparamagnetism), often anisotropic magnetic signals for thin films, and the inhomogeneous or non-uniform distribution of ferromagnetic regions within d^0 materials. Possible locations for d^0 magnetism at defect-rich sites within nanostructures are schematically shown in Figure 1.1, such as at random point defects, substrate-thin film interfaces, grain boundaries etc. Some magnetization curves measured for nanoparticles exhibiting d^0 magnetism are shown in Figure 1.2. While high T_c is advantageous for potential use of these materials in spin electronics devices, irreproducibility and weak signals are the major disadvantages which need to be overcome in order to derive any practical application. In spite of this, d^0 magnetism may be of interest from a theoretical point of view, a novel addition to the known types of magnetic order. The need for a theory to explain d^0 magnetism is pressing, since it appears to contradict the '*m-J*' paradigm of magnetism, which has established through decades of research that high-temperature magnetic order requires materials with a high concentration of magnetic atoms or ions possessing a moment *m*, and strong exchange coupling between them. Dilute magnetic systems generally order at low temperature, if at all.

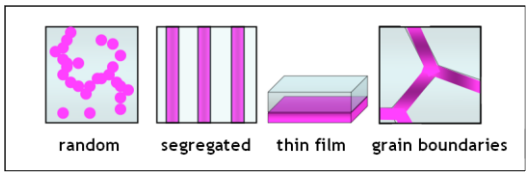

Figure 1.1. Some examples of inhomogeneous defect-rich sites within nanostructures with which d^0 magnetism may be associated.

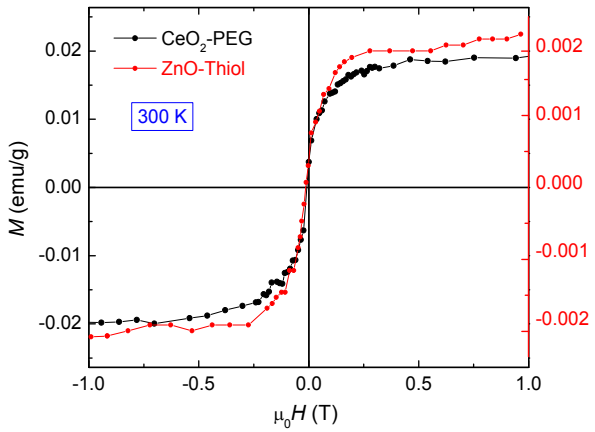

Figure 1.2. Some representative room temperature magnetization curves measured for undoped nanoparticles, CeO_2 [13] and ZnO [14], with surfactant used during synthesis indicated (note: for cgs to SI unit conversion, 1 emu/g = 1 Am^2/kg).

The field of d^0 magnetism research, originating when the term was first coined in 2005, emerged from that of dilute magnetic semiconductors (DMS) and dilute magnetic oxides (DMO), for which partial ferromagnetic order below 7.5 K was first measured for Mn doped (1.3 at. %)

InAs in 1992 [15] (DMS) and for which room temperature magnetism was first predicted in 2000 for *p*-type ZnO with 5 at. % Mn [16] (DMO). For the latter, a 320 K Curie temperature (T_c) was predicted due to a long-range exchange mediated by holes in the 2*p* valence band. Note that oxides which also happen to be semiconducting are still named dilute magnetic oxides (or sometimes dilute magnetic semiconducting oxides), and should not be confused with dilute magnetic semiconductors (DMS), which denote a different class of materials including GaAs and InAs for example. A DMS is a uniform semiconductor where the magnetic dopants order ferromagnetically, interacting via spin-polarized electrons or holes in the conduction or valence band, for example 5-8 at. % Mn substitution for Ga in GaAs in 1998 [17]. For DMS, the magnetic dopants are homogenously dispersed, unlike for DMOs where the dopants are typically inhomogenously distributed throughout the sample volume. One major drawback of DMS however is that T_c is limited to about 180 K [18]. For DMOs (and indeed for d^0 magnetism also), there is no such constraint on T_c. A comprehensive overview of ferromagnetism in DMS materials is given in recent views [19,20], the latter of which also includes DMOs.

Dilute magnetic oxides meanwhile are transparent, wide-bandgap materials that behave ferromagnetically when doped with a few percent of *magnetic* 3*d* cations (in contrast to d^0 magnetic materials which as mentioned previously are either doped with *non-magnetic* cations or are *undoped*). The magnetism, which appears well below the cation percolation threshold, cannot be understood in terms of the conventional theory of magnetism in insulators; nor can a carrier-mediated ferromagnetic exchange mechanism account for the magnitude of the high T_c, often far in excess of room temperature. Other common traits are that the magnetism (when it is not attributed to impurity phases or experimental artefacts) is closely associated with defects in the material, is inhomogeneously distributed throughout the sample volume, and the magnetization curves are essentially anhysteretic and show very little temperature dependence between room temperature and liquid helium temperatures (~ 4 K). The first *experimental* report for ferromagnetism in a dilute magnetic oxide was published in 2001 concerning Co doped TiO_2 thin films grown by molecular beam epitaxy [21], for which the maximum magnetic moment was measured for 7 % doping (0.32 μ_B/Co at 300 K). Following this initial report there was an explosion of interest in the field, with reports of room temperature ferromagnetism in a wide variety of transition metal (TM) doped oxides such as of TiO_2, Cu_2O, SnO_2, In_2O_3, CeO_2 and ZnO to name but a few, the last of which alone has more than 10^3 publications attributed to it. Common TM dopants include Fe, Ni, Co, V, Mn, Al and Cr. Some typical magnetization curves for DMO thin films are shown in Figure 1.3. Ferromagnetic exchange mediated by shallow donor electrons that form bound magnetic polarons, which overlap to create a spin-split impurity band, was proposed as a general explanation for the DMO phenomenon [22]. As DMOs are not the main subject of this thesis, and in order not to be exhaustive, the reader is directed towards reviews of DMOs for further details [20,23], the latter of which is particularly comprehensive.

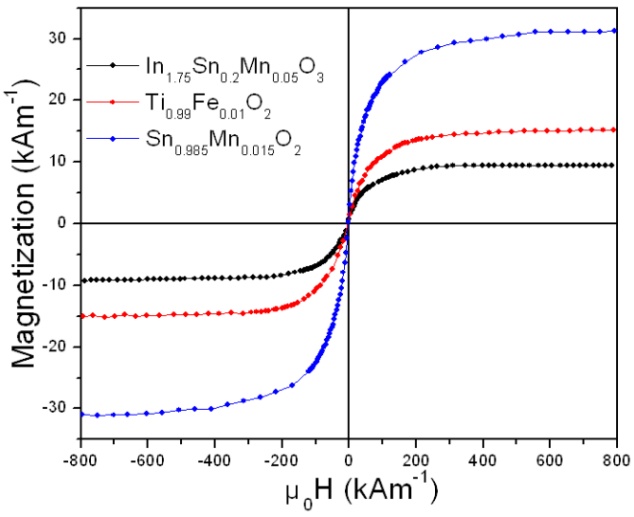

Figure 1.3. Some representative room temperature magnetization curves measured for thin films of dilute magnetic oxides.

Returning to d^0 magnetism, the phenomenon reinforces the idea that defects are necessary, but that 3*d* dopants (as in the case of DMOs) are not essential. In terms of a theoretical explanation for the d^0 magnetism phenomenon, two distinct approaches to explain room temperature magnetism in d^0 systems have been proposed. One is charge transfer ferromagnetism (CTF) [24, 25], where electrons from defects, impurity dopants or adsorbate molecules populate the extended defect band, as shown schematically in Figure 1.4. Note that in part (a) of the figure, the defect band need not necessarily be located equidistant between the conduction and valence bands, as its location will depend on the precise band structure of the material in question; the schematic is for illustrative purposes only.

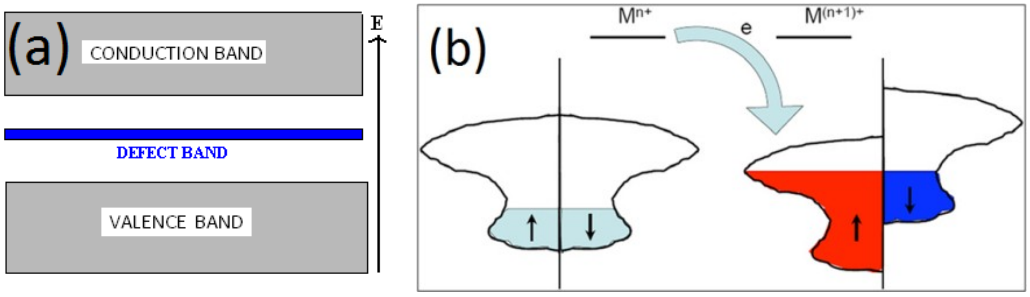

Figure 1.4. (a) Simplified schematic of impurity-band ferromagnetism in insulators and semiconductors. A defect band provides a charge reservoir for electron transfer, for which Stoner's criterion for ferromagnetism may be satisfied if the defect band coincides with a sufficiently high density of states (DOS) at the Fermi level; this may result in spontaneous spin-splitting (b) shown in terms of the DOS of the donor and acceptor bands.

The defects may be associated with grain boundaries in a thin film, or with surfaces in nanoparticles and nanoporous films. If the density of states in the impurity band formed by the defects near the Fermi level is sufficiently great, spontaneous spin-splitting according to the Stoner criterion $D(E_F)I > 1$ may occur, where $D(E_F)$ is the density of states at the Fermi level for both spins and I is the Stoner exchange parameter. Such a scenario can give rise to ferromagnetism since the energy gain from exchange splitting the defect band can compensate not only the kinetic energy cost of splitting of the band, as in the standard Stoner model, but also the energy cost of transferring the electrons from the charge reservoir. The T_c of a half-metallic defect band can be substantially greater than room temperature [26], which may explain the high T_c measured for d^0 materials.

A feature of the high-temperature Stoner magnetism in d^0 materials is expected to be an anhysteretic magnetization curve, which is practically temperature independent below room temperature. Magnetocrystalline anisotropy is expected to be negligibly small in the defect band for two reasons: (i) the spin–orbit coupling is typically small, or absent for *s* or *p* electrons trapped at oxygen vacancies (F-centres) or grain boundaries and (ii) if there is a local direction for the crystal field determined by the local symmetry created by the defects, this direction will vary from site to site, and the anisotropy averages to zero provided it is small to begin with. The resulting coercivity should be negligibly small. The magnetization process in these materials is hence unrelated to magnetocrystalline anisotropy, but may be controlled by dipolar fields; the dipolar field may be written as $H_d = -\mathcal{N}M_0$ where $\mathcal{N}$ is a local demagnetizing factor. The micromagnetic state governed by the magnetic dipole interactions will consequently depend on the shape of the percolating magnetic regions where the unpaired spins are to be found which may be related to a wandering ferromagnetic axis for example for the case of grain boundaries. The ground state here will not be strictly ferromagnetic because the local ferromagnetic axis wanders over a macroscopic sample in response to the competition between the local dipole field and the exchange stiffness. There is no tendency to form collinear ferromagnetic domains separated by domain walls when the anisotropy is negligible. For example, if the ferromagnetic regions with the spin-polarized electrons are the grain boundaries, the magnetization will tend to lie in the plane of the grain boundary, provided the grain size is greater than the exchange length. The magnetization process involves straightening out the ferromagnetic order, which means overcoming the local dipole fields. This process will scale with the saturation magnetization, which is practically independent of temperature well below T_c. Any residual coercivity originating from the dipole interactions will also be temperature-independent; temperature-independent saturation magnetization and coercivity together rule out superparamagnetism as an origin of the magnetic signals.

A simple calculation for macrospins subject to a local dipole field with random direction gives the fit to the magnetization curve. The approach to saturation is determined by the value of the saturation magnetization M_s of the ferromagnetic regions. It may be fitted closely to a simple tanh function of the form $M/M_s = \tanh(H/H_0)$, with $H_0 = \mathcal{N} M_0$ [27] where H_0 is a constant effective field that impedes saturation, $\mathcal{N}$ is an effective demagnetising factor, and M_0 is the magnetization of the ferromagnetic regions. H_0 may be readily estimated by extrapolating the slope at the origin, as

shown in Figure 1.5, which reaches the saturation magnetization when $H = H_0$. $\mathcal{N}$ may take values of 1/3 for isotropic magnetism (spheres), ~ 1/6-1/7 for a grain boundary foam [27], or 1 for thin films (out-of-plane magnetization) for example. The ratio M_s/M_0 thus corresponds to the ferromagnetic volume fraction of the sample *f*, a measure of the volume of the sample that is magnetically ordered.

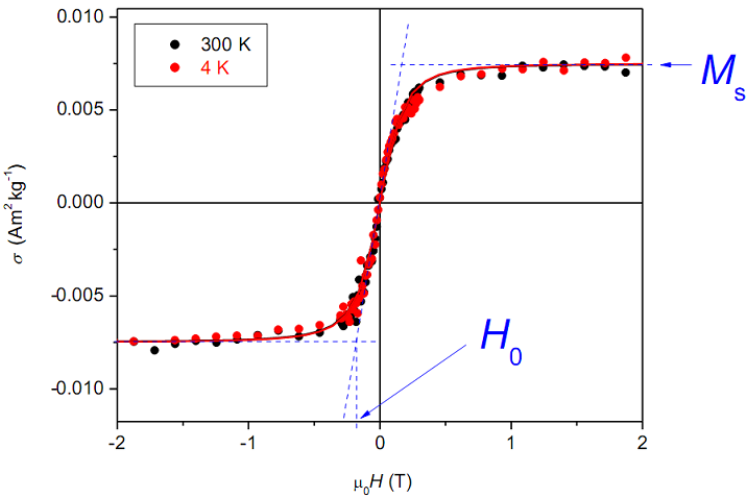

Figure 1.5. Illustration of how the parameters M_s and H_0 are extracted from the magnetization curve.

Another approach to try to explain room temperature magnetism in d^0 systems is that of giant orbital paramagnetism (GOP) [28-30]. Here the coulomb correlation among electrons in a two-dimensional electron gas at the surface of a nanoparticle is proposed to lead to the formation of a giant orbital moment *m*, of order 10^3 μ_B or more, which saturates easily, typically at 0.1–0.01 μ_B per nanoparticle atom, in modest fields (1-2 T) at room temperature. It is not a typical itinerant magnetism caused by electrons pumped to energy levels above the Fermi energy. It is the electrons at the generally unfilled Fermi level that generate the magnetic moment. There is no magnetic order and no permanent moment in zero applied field according to this model. It has been shown that nanoparticles with radii below 10 nm, even materials which are diamagnetic in bulk form, can exhibit giant paramagnetism when capped with molecules that act as donors or acceptors of surface electrons [28-30]. The same effect may also be observed in uncapped nanoparticles which contain impurities, which can also induce a 2-D confinement of electrons (or holes) in previously empty surface states resulting in the creation of a magnetic moment. The GOP model may help to explain why magnetism is only measured for the smallest nanoparticles, since upon increasing the particle size, the magnetic contribution from the much smaller fraction of surface atoms is masked by the core diamagnetism; for nanoparticles, the surface to volume ratio decreases exponentially as the particle size increases, as shown in Figure 1.6. In addition, since the atomic moment is so small, it can be detected only for very small particle sizes, when the diamagnetic contribution of the interior is negligible. The theory could also be extended from that pertaining to the surfaces of small

nanoparticles only to other general sources of broken symmetry which can create orbital states of large radius, for instance, twin boundaries, film-substrate interfaces or groups of defects induced by irradiation. Magnetization curves for different moments calculated from the Langevin function for paramagnetism, $M/M_s = \coth(x) - 1/(x)$, are plotted in Figure 1.7. It can be seen from the figure that only "giant" moments of order 10^3 μ_B or more fit the model.

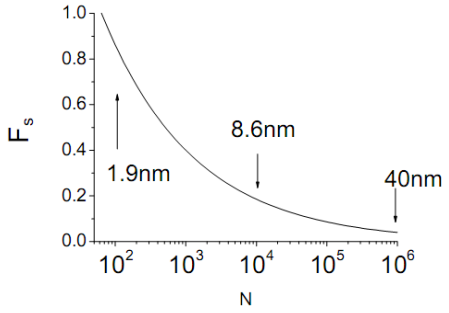

Figure 1.6. General trend for the increase of the fraction of surface atoms (F_s) with decreasing number of atoms (N) for smaller sized nanoparticles.

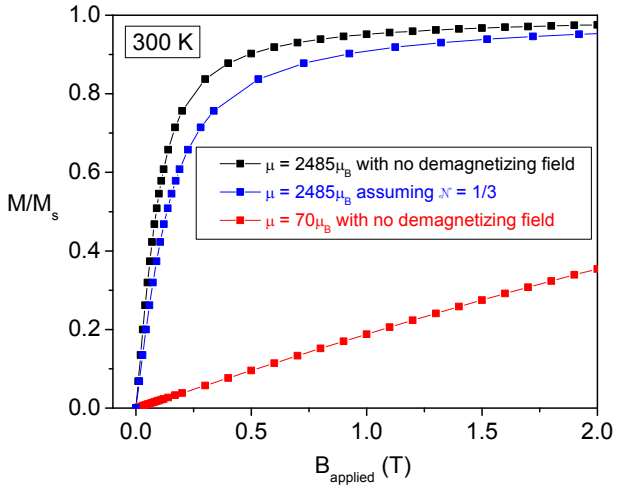

Figure 1.7. Magnetization curves calculated from the Langevin function, corresponding to two different magnetic moments at room temperature. The effect of the demagnetizing field (assuming a demagnetizing factor $\mathcal{N}$ = 1/3 for spherical nanoparticles) is to shift the applied field to higher values for a given magnetization.

Finally, it is important to mention that parasitic ferromagnetic impurity phases are not a general explanation for d^0 magnetism. However, the experimental picture is confused by the difficulty in reproducing many of the results, the often ephemeral nature and weakness of the ferromagnetic signal and the problem of characterizing defects. The poor reproducibility of the experimental data may be due to the difficulty in precisely recapturing the process conditions which lead to a specific defect distribution and density. The as-prepared samples are typically not in equilibrium and they often evolve with time and temperature. Stringent precautions must always be

taken when synthesizing samples in order to minimize contamination and to ensure that the ferromagnetism does not come from *extrinsic* sources, such as trace ferromagnetic impurities of Fe, Ni, Co and their respective oxides. For example, 50 ppm of iron corresponds to a magnetization of at most 85 A m^{-1}, a value of similar magnitude to many of the saturation magnetizations reported for d^0 materials, especially for nanoparticles, while ferromagnetic magnetite (Fe_3O_4) is also ubiquitous in the environment. However, the assumption that a set quantity of ferromagnetic impurities will produce a corresponding ferromagnetic signal is open to scrutiny, since it assumes that all iron impurities form metallic clusters and that all clusters are large enough to behave ferro- or ferri-magnetically; in addition, the simple addition of transition metals does not lead to ferromagnetic properties, as no interaction pathway is provided [31]. In the absence of a better method to determine the magnetization due to ferromagnetic impurities however, this assumption shall henceforth be followed. The use of high purity reagents, non-magnetic tweezers to handle samples, and thorough cleaning of reaction vessels must be routinely practiced. Adequate controls must also be run and the magnetic properties of such control samples thoroughly analyzed.

In this thesis, three different d^0 materials have been studied, for which magnetic signals attributed to d^0 magnetism (and not trivial ferromagnetic contamination) may be reproduced time and again with a certain degree of reproducibility. A chapter is devoted to each of the three materials, which in order of appearance are;

(1) HfO_2 vacuum annealed (reduced) micropowders
(2) polycrystalline CeO_2 nanoparticles synthesized by chemical precipitation
(3) MB_6 (M = Ca, Sr, Ba) amorphous thin films grown by pulsed laser deposition on (mostly) Al_2O_3 single crystalline substrates.

1.2. References

[1] J. M. D. Coey, Solid State Sciences **7**, 660 (2005).

[2] A. Sundaresan, R. Bhargavi, N. Rangarajan, U. Siddesh, and C. Rao, Physical Review B **74**, 161306 (2006).

[3] B. Straumal, A. Mazilkin, S. Protasova, A. Myatiev, P. Straumal, G. Schütz, P. van Aken, E. Goering, and B. Baretzky, Physical Review B **79**, 205206 (2009).

[4] J. Chaboy, et al., Physical Review B **82**, 064411 (2010).

[5] Q. Y. Wen, H. W. Zhang, Y. Q. Song, Q. H. Yang, H. Zhu, and J. Q. Xiao, J Phys Condens Matter **19**, 246205 (2007).

[6] M. Y. Ge, H. Wang, E. Z. Liu, J. F. Liu, J. Z. Jiang, Y. K. Li, Z. A. Xu, and H. Y. Li, Applied Physics Letters **93**, 062505 (2008).

[7] V. Fernandes, et al., Physical Review B **80**, 035202 (2009).

[8] M. Venkatesan, C. B. Fitzgerald, and J. M. D. Coey, Nature **430**, 630 (2004).

[9] L. S. Dorneles, M. Venkatesan, M. Moliner, J. G. Lunney, and J. M. D. Coey, Applied Physics Letters **85**, 6377 (2004).

[10] J. S. Garitaonandia, et al., Nano Letters **8**, 661 (2008).

[11] Y. Wang, Y. Huang, Y. Song, X. Zhang, Y. Ma, J. Liang, and Y. Chen, Nano Letters **9**, 220 (2009).

[12] Y. W. Ma, et al., Nature Communications **3**, 727 (2012).

[13] K. Ackland, L. M. A. Monzon, M. Venkatesan, and J. M. D. Coey, IEEE Transactions on Magnetics **47**, 3509 (2011).

[14] M. A. Garcia, et al., Nano Letters **7**, 1489 (2007).

[15] H. Ohno, H. Munekata, T. Penney, S. Vonmolnar, and L. L. Chang, Physical Review Letters **68**, 2664 (1992).

[16] T. Dietl, H. Ohno, F. Matsukura, J. Cibert, and D. Ferrand, Science **287**, 1019 (2000).

[17] H. Ohno, Science **281**, 951 (1998).

[18] T. Jungwirth, et al., Physical Review B **72**, 165204 (2005).

[19] A. Bonanni and T. Dietl, Chem Soc Rev **39**, 528 (2010).

[20] T. Dietl, Nature Materials **9**, 965 (2010).

[21] Y. Matsumoto, Science **291**, 854 (2001).

[22] J. M. D. Coey, M. Venkatesan, and C. B. Fitzgerald, Nature Materials **4**, 173 (2005).

[23] S. B. Ogale, Adv Mater **22**, 3125 (2010).

[24] J. M. D. Coey, K. Wongsaprom, J. Alaria, and M. Venkatesan, Journal of Physics D: Applied Physics **41**, 134012 (2008).

[25] J. M. D. Coey, P. Stamenov, R. D. Gunning, M. Venkatesan, and K. Paul, New Journal of Physics **12**, 053025 (2010).

[26] D. M. Edwards and M. I. Katsnelson, Journal of Physics: Condensed Matter **18**, 7209 (2006).

[27] J. M. D. Coey, J. T. Mlack, M. Venkatesan, and P. Stamenov, IEEE Transactions on Magnetics **46**, 2501 (2010).

[28] A. Hernando, P. Crespo, and M. García, Physical Review Letters **96**, 057206 (2006).

[29] A. Hernando and M. A. García, Journal of Nanoparticle Research **13**, 5595 (2011).

[30] A. Hernando, P. Crespo, M. Angel Garcia, M. Coey, A. Ayuela, and P. Miguel Echenique, Physica Status Solidi B-Basic Solid State Physics **248**, 2352 (2011).

[31] K. D. Sattler, *Handbook of Nanophysics: Principles and Methods* (25-19, 25-20, CRC Press, Boca Raton, USA, 2011).

Chapter 2

Experimental Methods

This chapter describes the experimental methods used for the synthesis and characterization of HfO_2 microparticles, CeO_2 nanoparticles and alkaline-earth hexaboride MB_6 (M = Ca, Sr, Ba) thin films. HfO_2 commercial microparticles were annealed in oxygen and air. CeO_2 nanoparticles were synthesized by a wet chemical method termed homogeneous precipitation. MB_6 thin films were grown by pulsed laser deposition.

2.1. HfO_2 micropowder annealing

High-purity commercial HfO_2 powders (Sigma Aldrich 99.95% and Alfa Aesar 99.995%) were placed in acid-cleaned ceramic boats and annealed in vacuum (10^{-5} mbar) for 1 hour in an Indfur temperature controlled furnace located in our laboratory at various maximum temperatures in the range 550-850 ºC, using rapid heating and cooling rates (10 ºC/min). The vacuum pressure is achieved by use of an oil diffusion pump which is backed by a standard roughing pump. Approximately 150 mg of sample was used in each separate batch, i.e. separate anneals of discrete powders were performed rather than cumulative anneals of the same powder. The same furnace was also used for anneals which were carried out at atmospheric pressure.

2.2. CeO_2 nanoparticle synthesis

Polycrystalline CeO_2 nanoparticles were synthesized by a sol-gel precipitation process in which a solution of $Ce(NO_3)_3.6H_2O$ and the polymer polyethylene glycol (PEG) of molecular weight 1500 was oxidized to CeO_2 by adding small volumes of concentrated NaOH [1,2]. The sol-gel method involves the formation of an oxide network through polycondensation reactions of a molecular precursor in a liquid. The sol is defined as a stable dispersion of colloidal particles or polymers in a solvent, while the gel (PEG) consists of a three dimensional continuous network which encloses the liquid phase. The PEG acts as a surfactant and facilitates the gelation process by keeping the particles seperated by binding to their surfaces. The degree of binding of PEG to the particle surface then determines the surface potential. Counter-ions in the solution will cover this layer, shielding the rest of the solution from the surface charges. For hydroxides, the surface potential will be determined by reactions with the ions H^+ and OH^-. Thus, the surface potential is pH dependent. The pH where the particle is neutral is called the point of zero charge (PZC), which depends somewhat on the size of the particle and the degree of condensation. For CeO_2 nanoparticles, some reported values for the PZC include a pH of 8.1 for particles synthesized by thermal decomposition of $CeCl_3.7H_2O$ [3], or up to 10.5 for those obtain by precipitation of $Ce^{4+}(NO_3^-)_4$ [4], the latter higher value being attributed to the hydrous oxide which may superficially retain anions. Hence by adding a base (NaOH here) dropwise to a solution of cerium precursor (cerium nitrate) and PEG, the CeO_2 will begin to precipitate out of solution once the pH of PZC is reached. The sol-gel method prevents the problems with co-precipitation, which may be inhomogeneous, hence it is sometimes termed “homogeneous precipitation”. The reaction is particularly suited to the production of many oxide nanoparticles, since it enables mixing at an atomic level and results in the formation of crystalline monodisperse small particles, which are easily sinterable.

In the sol-gel process used, NaOH solution was added dropwise to a stirred solution of cerium nitrate and PEG until the pH stabilized at ~ 11. At this stage the solution was pink in colour. The solution was then heated to 60 ºC, with continuous stirring. Gradually the solution began to turn yellow in colour, indicating the formation of CeO_2. After 1 h of heating/stirring, the CeO_2 powder was extracted from solution by either vacuum filtration or centrifugation, washed with pure ethanol and deionised water, and dried at 50 ºC for about 24 h. Two different grades of $Ce(NO_3)_3.6H_2O$ were used in separate syntheses, 99 % and 99.999 % nominal purity (Sigma Aldrich). The main impurity in the 99 % precursor is La (~ 1-2 wt %). The purity of the NaOH was 99.99% and the PEG was an ultrapure grade for molecular biology. As mentioned above, the PEG acts as both a surfactant and facilitates the gelation process by keeping the particles seperated during precipitation.

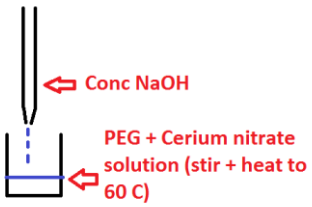

Figure 2.1. Simplified schematic of CeO_2 nanoparticle synthesis by homogeneous precipitation.

For the synthesis of *ferromagnetic* CeO_2 nanopowders, the following precise reagent concentrations and volumes were used: 4.5 ml 10 mM $Ce(NO_3)_3.6H_2O$ 99 % (Sigma) + 0.5 ml 0.5 M PEG-1500 (Sigma) solutions added to a 40 ml glass beaker. The 0.5 M PEG-1500 solution was made by dissolving 1.3 ml of PEG-1500 in 1 ml of water. All water used was deionised. Then 4 ml of a 0.1 M NaOH (99.99% Sigma) solution was added slowly dropwise (about 1 drop per second) from a burette into the mixed cerium nitrate/PEG solution. The rest of the procedure follows that described in the previous paragraph. The total mass of the batch was about 4 mg. The exact same concentrations and volumes were used to synthesize the nonmagnetic CeO_2 nanopowders, the *only single difference* being that 99.999 % purity $Ce(NO_3)_3.6H_2O$ (Sigma) was used instead of 99 % purity $Ce(NO_3)_3.6H_2O$ (Sigma).

2.3. MB_6 (M = Ca, Sr, Ba) thin film deposition

MB_6 thin films were grown by pulsed laser deposition, a versatile thin film growth technique, especially for multi-component materials whose stoichiometry cannot be easily maintained by sputtering. A pulsed laser beam, produced by an excimer laser with wavelength 248 nm, is focused onto the surface of a solid rotating target, as shown in Figures 2.2 & 2.3. The strong absorption of the pulsed radiation by the solid surface leads to rapid heating (10^8 K/s) and subsequent evaporation of the target materials. The evaporated materials consist of highly excited and ionized species which form a glowing, congruent plasma plume in front of the target surface. Experimental variables include the deposition pressure, temperature and atmosphere (ambient, oxygen, argon etc.), laser pulse repetition rate, spot size and energy density, and target to substrate distance. In effect, the mean free path of the ablated species and hence the plume size and subsequent film growth rate / morphology can be modified by changing the pressure in the vacuum chamber through introduction of oxygen gas for example. The most important feature of PLD, due to the rapid heating of the target materials, is that the stoichiometry of the target can be retained in the deposited films, irrespective of the evaporating point of the constituent elements or compounds of the target. One of the main disadvantages of PLD however is the “splashing” or deposition of

particulates on the films, some of which may be as large as a few micrometers, induced by sub-surface boiling and ablation induced recoil pressure, both of which present more of a problem at high laser energy densities. Such particulates will greatly affect the growth of the subsequent layers as well as the electrical properties of the films. It is noted however that the MB_6 films grown here are amorphous, and the effect of splashing is not a major issue. The other main limitation of PLD, which limits production of large area uniform thin films, is the narrow angular distribution of the ablated species generated by the adiabatic expansion of the laser-produced plasma plume.

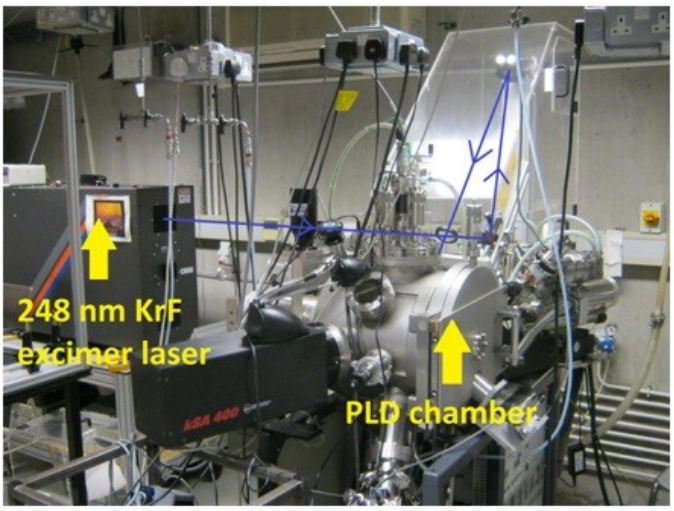

Figure 2.2. Photograph of PLD setup used, which is located in Prof. James Lunney's laboratory, SNIAM Building, Trinity College Dublin; blue arrows indicate the laser path.

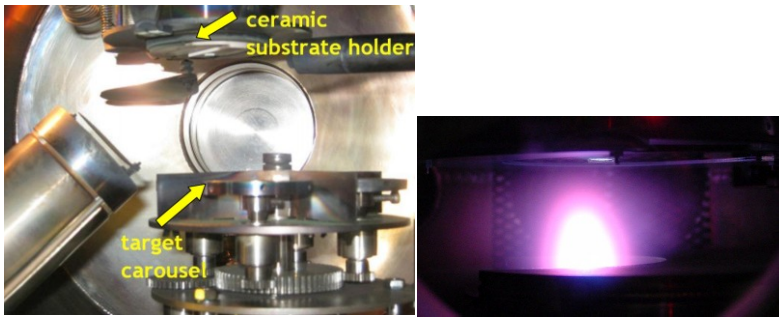

Figure 2.3. Left: Photograph showing inside of vacuum chamber used for PLD; the laser enters the chamber through a port from the upper right side; Right: an example of a plasma plume (© Helsinki University of Technology).

MB_6 films were usually deposited on single crystal Al_2O_3 (0001) 99.99% nominal purity substrates (MTIXTL) of dimensions 5×5 mm (0.5 mm thick), which were affixed with non-magnetic silver paint (Agar Scientific) to a ceramic substrate holder. Targets were produced from MB_6 powders in the following way: MB_6 (M = Ca, Sr, Ba) powders were synthesized from high-purity elemental powders by solid state reaction at 1000 °C in evacuated sealed quartz tubes (10^{-5} mbar) using a temperature controlled box furnace (Indfur, Chennai). The nominal purity of

the Ca used was 99.5% while the Ba and Sr were of 99.9% nominal purity. The nominal purity of boron used was 99.7%. The hexaboride powders were subsequently ground, pressed in 13 mm dies using a 10 ton press, and sintered under vacuum in acid-cleaned ceramic boats placed inside clean quartz tubes using the box furnace maintained at 10^{-5} mbar for 12 hours at 950 °C. Slow (1-2 °C/min) heating/cooling rates were used. The target densities were typically 60% of the theoretical values.

For a typical thin film deposition, the sapphire substrate was first heated to 800 °C in 0.3 mbar of O_2 in order to outgas any impurities before film deposition. The targets were pre-ablated at high laser repetition rates (20 Hz) for 5 minutes immediately prior to deposition in order to avoid any possible contamination from the surface of the target, thus presenting the pristine material beneath for ablation and film growth. Typical deposition parameters used were an energy density of 6 J cm^{-2} (well above the ablation threshold), a laser repetition rate of 6 Hz, and a deposition pressure of 10^{-6} mbar in order to grow thermodynamically stable MB_6 films within the experimental range of substrate temperatures [5]. The target to substrate distance was fixed at 70 mm.

Figure 2.4. High resolution optical image of a BaB_6 target used for PLD; pitting due to the impact of the of the focused laser beam on the surface can be seen.

In addition to MB_6, some CeO_2 thin films were also grown by PLD using the same setup, although the main focus in this thesis is on CeO_2 in nanoparticular form. Further details of the precise film deposition conditions used are given in Chapter 4 (section 4.3.15), concerning experimental results for CeO_2 films.

2.4. Structural characterization

2.4.1. X-ray diffraction

The atoms in a crystal are a periodic array of coherent scatterers and thus can diffract electromagnetic radiation. Diffraction occurs when each object in a periodic array scatters radiation coherently, producing concerted constructive (and destructive) interference at specific angles. Since the wavelength of X-Rays is similar to the distance between atoms, diffraction from different atomic planes produces a diffraction pattern containing information about the atomic arrangement within the crystal. Diffraction of X-rays occurs within the sample according to Bragg's Law,

$$m\lambda = 2\mathrm{d}\sin\theta \tag{2.1}$$

where λ is the X-ray wavelength, d is the atomic layer separation, m is the diffraction order and θ is the angle of incidence of the X-Ray to the sample surface.

The interference of the waves diffracted from crystal planes is constructive when the phase shift is a multiple of 2π. Depending on the intensity, the position and the width of the diffraction peaks, the type and the quality of the crystal structure may be determined. The positions of the peaks are given by the unit cell (lattice) parameters and the intensity depends on the structure factor, which depends on the structure and contents of the unit cell. A comparison of the position and the intensity of the observed peaks with known systems (from an available powder diffraction database containing around 100,000 different phases) enable a determination of the crystal structure of most unknown samples. Peak width varies inversely with crystallite size (for crystallite sizes below approximately 100 nm), according to the Scherrer equation,

$$B = (K\,\lambda)/(L\cos\theta) \tag{2.2}$$

where B is the mean size of the ordered (crystalline) domains, K is the shape factor (typically ~ 0.9 for spherical approximation to particle morphology), λ is the x-ray wavelength, L is the line broadening at half the maximum intensity (FWHM) in radians, and θ is the Bragg angle. This formula provides a lower bound on the particle size as inhomogeneous strain and instrumental effects also serve to broaden the peaks. Instrumental broadening can be determined by measuring the diffraction pattern of a powder with micron-sized crystallites and subsequently plotting the FWHM for each peak vs. 2θ angle.

X-Ray powder diffraction was carried out using a PANalytical X'pert Pro diffractometer located in the CRANN institute at TCD, with an operational wavelength of 1.5405 Å (Cu anode). In order to accurately determine the crystal structure of some of the samples, the Rietveld refinement method [6, 7] was used, using the FullProf program [8], which is freely available online at

http://www.ill.eu/sites/fullprof/index.html. The Rietveld refinement method uses a least squares minimization procedure in which a crystal (and/or magnetic) structure is refined by minimizing the weighted squared difference between the measured and the calculated pattern against a parameter vector. The program FullProf has been mainly developed to perform Rietveld analysis of neutron or X-ray powder diffraction data collected at constant or variable steps in scattering angle 2θ or collected using the neutron time-of-flight (TOF) technique. Single crystal refinements can also be performed alone or in combination with powder data.

2.4.2. X-ray reflectivity

X-ray reflectivity (XRR) is a technique used to measure the thickness and roughness of thin films of order 100 nm thickness or less. When X-rays are incident onto a material's flat surface at grazing angles of incidence, total internal reflection may occur in which reflected X-rays from the interface between the substrate and the thin film as well as from the free surface of the film will interfere with each other either constructively or destructively The result is the oscillation in reflected intensity as a function of incident angle as shown in Figure 2.5.

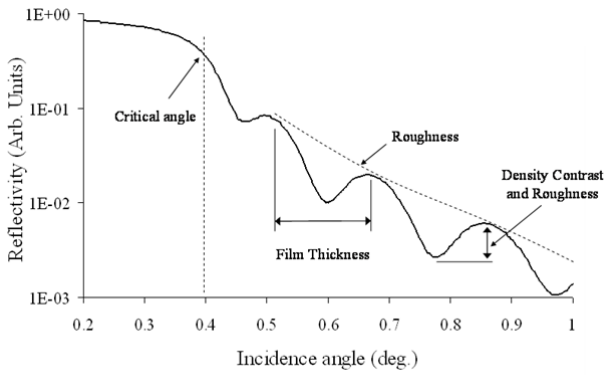

Figure 2.5. Parameters which may be deduced from an X-Ray reflectivity measurement.

The positions of the maxima of reflected intensity are related to the thickness of the film according to the modified Braggs' law

$$m\lambda = 2t\sin^2\theta - 2\delta \qquad (2.3)$$

where t is the film thickness, m = 1, 2, 3 and δ is the dispersive part of the refractive index of the sample. The higher the incident X-ray angle relative to the critical angle, the deeper the X-rays penetrate into the material. If the surface is rough it can cause a more drastic decrease in

reflectivity. Simple fitting of the oscillations results in a quick estimation of the thickness of the film while surface roughness can be deduced by fitting the amplitude and slope. Density contrast between the film and substrate or between multilayers may also be deduced from fitting of the oscillation amplitude and from the position at which the interference fringes first appear at low angles.

For high-angle diffraction experiments, a Phillips X'cellerator detector was used. For XRR measurements, a PRS/PASS detector was used which is equipped with a beam attenuator for $0.2° < 2\theta < 6°$. Measured XRR curves were fitted using the Phillips WinGixa software. WinGixa allows, starting from an assumed sample model, the calculation of the reflectivity. Within the fitting part of WinGixa, parameters such as thickness, roughness, density and absorption coefficient of the layer together with several instrumental parameters can be obtained from the measured spectra. A useful manual for how to use the WinGixa program may be freely obtained from the following website: http://www.stanford.edu/group/glam/xlab/PhilipsLit/WinGIXA.pdf

2.4.3. Scanning electron and focused ion beam microscopy

Scanning electron microscopy (SEM), in which an electron beam is rastered across the region of interest, may be used to obtain images of sample morphology down to a practical resolution of ~ 5 nm. The types of signals produced by a scanning electron microscope include secondary electrons (SE), back-scattered electrons (BSE), characteristic X-rays and a specimen current. Secondary electrons are generated as ionization products of their interaction with atoms at or near the surface of the sample and are typically used for high resolution imaging. Back-scattered electrons (as the name implies) are elastically back-scattered electrons which provide information about the distribution of different elements in the sample since the fraction of electrons backscattered in this way varies strongly with the atomic number Z of the scattering atoms and hence BSE images provide Z contrast. Energy dispersive X-ray (EDX) measurements are performed to analyze the chemical composition of the specimen by analysis of the characteristic X-rays emitted during the transition / relaxation of electrons from excited states back to their ground states; in effect this is X-Ray fluorescence (XRF). In energy dispersive analysis, the fluorescent X-rays emitted by the sample are directed into a solid-state detector which produces a continuous distribution of pulses, the voltages of which are proportional to the incoming X-Ray energies. This signal is processed by a multichannel analyzer (MCA) which produces an accumulating digital spectrum that can be processed to obtain analytical data.

Specimens must be electrically conductive, at least at the surface, and electrically grounded to prevent the accumulation of electrostatic charge at the surface. Dispersions of powder samples may be deposited on sticky carbon tabs, while thin films grown on substrates may be affixed using silver paint to the stainless steel specimen stub. SEM analysis was carried out at the

Advanced Microscopy Laboratory (AML), Trinity College Dublin, using a Zeiss Ultra plus microscope possessing an Oxford instruments X-Max EDX silicon drift detector with a detection level of ~ 0.2 wt % for Z > 5 under normal operating conditions.

Cross-sectioning and milling/irradiation of samples may be performed using focused ion beam (FIB) microscopy which uses a focused beam of Ga^+ ions to remove (etch) material. FIB-SEM was performed using either the FEI Strata SEM or the Zeiss Supra SEM, both of which are dedicated FIB-SEM tools also located at the AML.

2.4.4. Transmission electron microscopy

Transmission electron microscopy (TEM) may be used to obtain sub-nanometre resolution images of particles and thin film cross-sections in real space together with structure determination from the diffraction patterns acquired in reciprocal space. In contrast to SEM, a high energy beam of electrons is primarily transmitted *through* an ultra-thin specimen, typically less than 100 nm thick, and the electrons which are scattered by the specimen may be used for imaging and diffraction from specific areas.

In terms of sample preparation, for powder samples, a suitable dilute dispersion may be prepared, such as CeO_2 in distilled water, a single droplet of which is placed on a holey or lacey carbon grid and left to dry. In order to prepare thin film cross-sections, FIB-SEM must first be performed in order to cut and etch a thin lamella using a focused beam of Ga^+ ions, which is then excised using a micro-manipulator.

An FEI Titan field emission TEM operating at an accelerating voltage of 300 kV, located in the AML was used. The system also has detectors for elemental analysis: energy dispersive X-ray (EDX) and Gatan Tridiem Energy Filtering (EFTEM) for Electron Energy Loss Spectroscopy (EELS). EELS measures the inelastic scattering of the electron beam transmitted through the specimen, and is the electron analogue of X-Ray absorption spectroscopy (XAS). EELS may be considered complementary to EDX, since EELS is more sensitive for the detection of low Z elements (except for hydrogen) while EDX is more sensitive for the detection of high Z elements.

Some additional TEM and TEM-EELS analysis was conducted at the University of Glasgow with the help of Dr. Donald MacLaren, using a Technai G2 aberration corrected instrument operating at 200 kV (the FEI Titan TEM at the AML is not aberration corrected), equipped with a similar EELS detection system to that used at the AML.

2.4.5. Inductively coupled plasma mass spectrometry

Sample purity was checked by inductively-coupled plasma mass spectroscopy (ICP-MS) at the Centre for Microscopy and Analysis (CMA) at TCD, using an Agilent 7700 spectrometer with a MARS microwave digester. This is a highly sensitive quantitative analytical tool (typically ≤ 1 ppm sensitivity) for trace elemental analysis in which samples are weighed, digested in strong acid (HNO_3) using a microwave digester, and then decomposed to their neutral elements in a high temperature argon plasma and analyzed based on their mass to charge ratios. ICP-MS allows identification of most elements of atomic mass 7 - 250 simultaneously. The setup also contains a helium neutralizer, through which the plasma passes before entering the mass spectrometer, which is essential since argon may combine with oxygen to give a mass of 56, the same as the most abundant isotope of iron (otherwise the minor Fe^{57} isotope would have to be measured, whose abundance is only ~ 2 % that of Fe^{56}). This is crucial since ICP-MS is often used to quantify the abundance of iron (as well as other ferromagnetic impurities) in d^0 samples.

2.4.6. Raman spectroscopy

Raman spectroscopy measures the vibrational, rotational, and other low-frequency modes in a system. It relies on inelastic scattering of monochromatic laser light. A change in the molecular polarization potential with respect to the vibrational coordinate is required for a molecule to exhibit a Raman effect and the pattern of shifted frequencies is determined by the rotational and vibrational states of the sample. This dependence on the polarizability differs from Infrared (IR) spectroscopy where the interaction between the molecule and light is determined by the dipole moment. Generally modes that are not IR active are Raman active and vice versa, since changes in both polarization (Raman active) and net dipole moment (IR active) do not usually mutually occur for most molecules, except for molecules which possess no symmetry.

Unpolarized micro-Raman back-scattered spectra of powders and films were measured to a resolution of ~ 1 cm^{-1} using a LabRAM HR (Horiba) spectrometer equipped with a 633 nm He-Ne ion laser, focused to a spot size of order 10 μm, located in the SNIAM building (group of Professors Coleman and Blau), TCD. Energy calibration was performed using the measured Raman peak position of a silicon standard.

2.4.7. Ultra-violet – Visible spectroscopy

Ultra-violet visible (UV-Vis) spectroscopy is one of the most common methods of determining the molecular structure of compounds by measuring the absorption associated with transitions from the ground state to the excited state, typically within the range 300-700 nm. The Beer-Lambert law states that the absorbance of a solution is directly proportional to the concentration of the absorbing species in the solution and the path length, hence for a fixed path length, UV-Vis spectroscopy can be used to determine the concentration of the absorber in a solution. The wavelengths of the absorption peaks may be correlated with the types of bonds/functional groups in a given molecule.

The optical absorption coefficient (α) may be evaluated using the following relation [9];

$$\alpha = (2.3\times10^{-6}\, A\, \rho) / (l\, c) \qquad (2.4)$$

where A is the absorbance measured, ρ is the density of the powder (g cm^{-3}), l is the path length of the UV-Vis cell (1 cm usually), and c is the concentration of the powder in solution (g L^{-1}).

In the bandgap region (high absorption) or above the fundamental absorption edge, the absorption follows a power law of the following form [10];

$$(\alpha h\nu) = B(h\nu - E_g)^n \qquad (2.5)$$

where $h\nu$ is the energy of the incident photon, B is a constant (related to the absorption edge width) and E_g is the bandgap. The exponent n takes values of ½ and 2 for direct and indirect-allowed transitions respectively. The optical bandgap may thus be estimated by plotting $(\alpha h\nu)^{1/2}$ (or $(\alpha h\nu)^2$) versus photon energy and determining the x-axis intercept of the slope for indirect (or direct) bandgaps.

UV-Vis measurements were performed at room temperature using a Varian Cary 6000i spectrometer located in the SNIAMS building, TCD (group of Professors Coleman and Blau), capable of scanning from 190-1000 nm.

2.4.8. Photoluminescence spectroscopy

Photoluminescence (PL) spectroscopy, specifically photoluminescence excitation (PLE), is a spectroscopic technique in which the frequency of the excitation light is varied and the resultant emission of light or luminescence of the sample being excited is monitored over a range of typical emission frequencies. PLE spectroscopy is essentially the reverse of UV-Vis spectroscopy, since in PLE the transition from excited states to lower energy states is measured.

There are three main forms of PL, the first of which is resonant radiation, in which a photon of a particular wavelength is absorbed and an equivalent photon is immediately emitted with little or no net energy transfer occurring over a timescale of order 10 ns. A second form is fluorescence, in which a net energy transfer occurs resulting in the emitted light photons possessing a lower energy than those absorbed. The lifetime of this process ranges from 10^{-8} to 10^{-4} s. The third type of PL is phosphorescence in which the absorbed energy undergoes intersystem crossing into a state with a different spin multiplicity. The lifetime of phosphorescence is typically the longest of the three PL processes, 10^{-4}-10^{-2} s, but is rarer than fluorescence, since a molecule in the triplet state has a high probability of undergoing intersystem crossing to the ground state before phosphorescence can occur.

Photoluminescence measurements were performed using a Perkin Elmer IS55 luminescence spectrometer using a scanning/excitation range of 200-800 cm^{-1} (equivalent to 50-12.5 μm) at room temperature. The spectrometer was located in the SNIAMS building, TCD (group of Professors Coleman and Blau).

2.5. Magnetic characterization

2.5.1. SQUID magnetometry

The Quantum Design Magnetic Property Measurement System (MPMS XL5) located in the SNIAM building was used to characterize the macroscopic magnetic properties of samples to an ultra-high sensitivity (absolute limit of order 10^{-11} Am^2), ideal for the detection of the weak ferromagnetic-like signals characteristic of d^0 magnetism. The MPMS XL5 system consists of a superconducting quantum interference device (SQUID) detection system which is integrated with a temperature control unit, a high field superconducting magnet and a computer processer. A closed cycle helium refrigerator is used for cooling the superconducting components as well as for low temperature measurements. Measurements can be made between 1.9 and 400 K in a field of up to 5 T. For measurement of powder samples, typically 1-50 mg (depending on the density) of powder is placed in a small gelatin capsule (gelcap), of 4.5 mm diameter, which was then secured in position by sliding and pressing another small gelcap into the first gelcap containing the powder. Thus the powder is sandwiched between the two gelcaps and should not move, which is important since movement of the powder inside the gelcap can contribute to signal noise during the magnetization measurement. The powder within the gelcaps is then securely inserted into the middle of a 4 mm plastic drinking straw and the magnetization as a function of applied magnetic field (or temperature in constant field if required) is measured in the SQUID. An empty gelcap within a long drinking straw gives a diamagnetic contribution to the

measured signal, which must be subtracted from the net signal in order to deduce the signal due to the powder only. The use of a diamagnetic sample holder ensures that an effective subtraction is possible, since diamagnetism is temperature independent, linear, and has a negative value with increasing field. For thin films, 5 × 5 mm^2 pieces were mounted directly inside the plastic straw enabling perpendicular or parallel magnetic fields to be applied. Data were collected at the maximum gradient point of the second derivative curve, with no auto-tracking. All data was corrected for the linear diamagnetic background due to the gelcap. The thin film samples, which were all deposited by PLD, were stored in a desiccator after deposition and magnetization data was measured shortly afterwards. Plastic tweezers were used to handle the thin film samples throughout; it has been reported that stainless steel tweezers may produce magnetic signals due to impregnated iron impurities [11].

A typical room temperature field scan measured for two empty gelcaps mounted in a long plastic drinking straw are shown in Fig. 2.6, both before and after correction of the high field susceptibility (diamagnetic background) due to the geclap (the long drinking straw does not contribute any signal due to symmetry). The dimensionless diamagnetic susceptibility χ at 2 T is -3.23×10^{-7}. A very weak signal with a saturation moment of ~ 1-2$\times10^{-9}$ Am^2 is measured for the empty gelcaps, which may be attributed to an artefact induced by the pickup coils of the SQUID when the applied magnetic field switches polarity at 0 T, and hence may be regarded as the *practical* detection limit for powder samples. In Figures 2.7 & 2.8 typical room temperature magnetization curves measured for two d^0 powder systems analyzed in this thesis, reduced HfO_2 micropowders and ferromagnetic CeO_2 nanoparticles, are displayed. For both systems the corrected saturation moment is always > 1×10^{-8} Am^2, which is an order of magnitude greater than that due to the empty gelcaps alone; hence the d^0 magnetic signals cannot be accounted for by measurement artefacts.

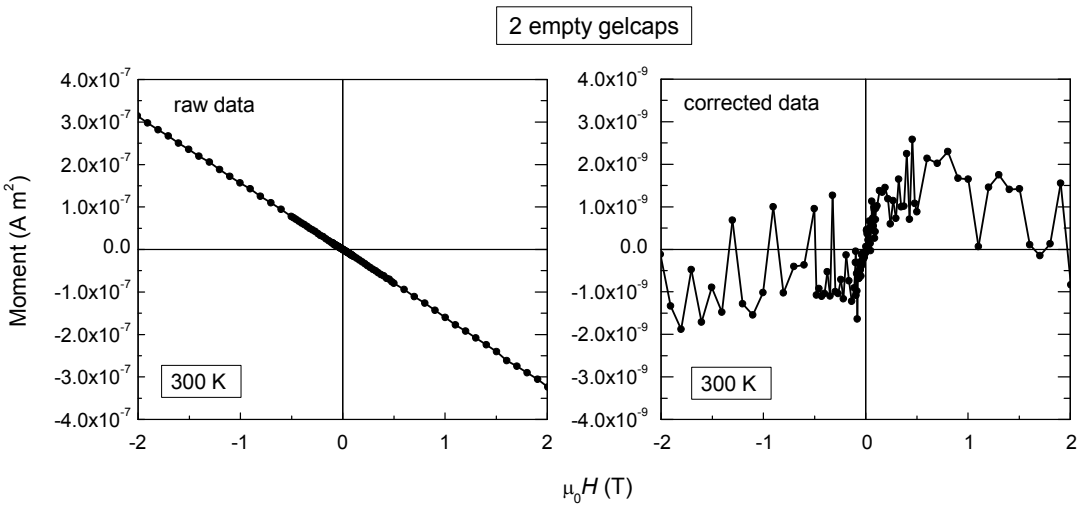

Figure 2.6. Room temperature magnetization data measured for two empty gelcaps mounted in a long plastic drinking straw.

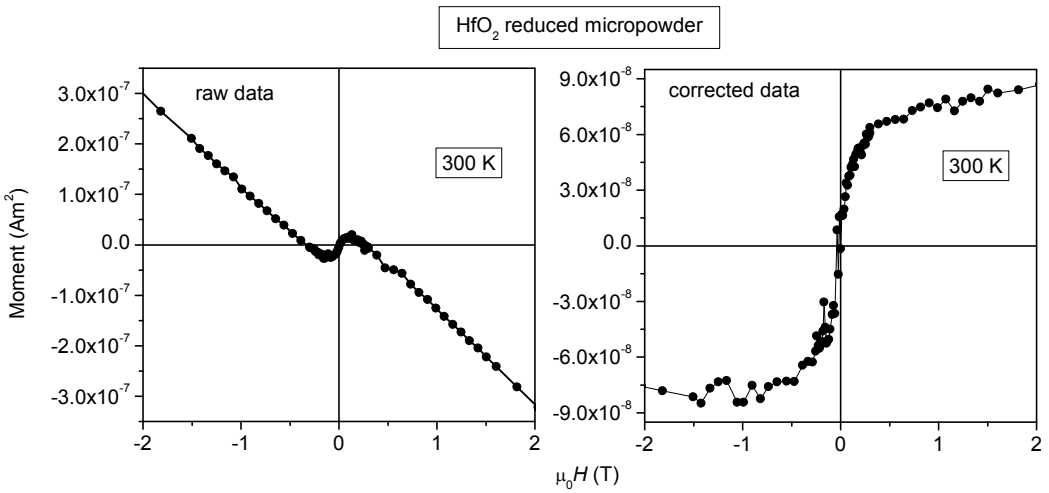

Figure 2.7. Room temperature magnetization data measured for reduced HfO_2 micropowder (Sigma ≥ 99.95%, 700 °C).

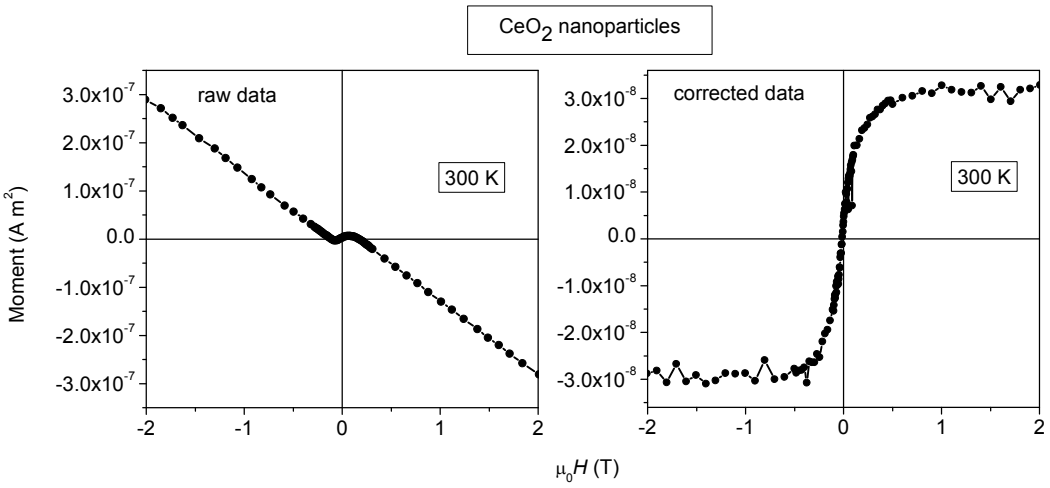

Figure 2.8. Room temperature magnetization data measured for CeO_2 nanoparticles (synthesized using 99% cerium nitrate).

For thin films deposited on substrates, the substrate contribution to the magnetic signal must be first subtracted from the total net signal in order to elucidate the magnetic signal due to the film alone. Since the mass of the substrate is typically several orders of magnitude larger than that of the thin film (of order 10^3 times larger for a typical 100 nm thick thin film deposited on a 5×5×0.5 mm substrate), the high field susceptibility may be considered to be that due to the substrate since the film contribution is negligible in comparison. Room temperature magnetization data measured for bare c-cut Al_2O_3 (0001) and MgO (100) single crystalline substrates (> 99.99% purity), both of dimension 5×5×0.5 mm (purchased from MTIXTL) are shown in Figs. 2.9 & 2.10 below. Both substrates are virtually purely diamagnetic with no trace of any ferromagnetic-like

signal detected, apart from a tiny switch of magnitude of order 10^{-10} Am^2 at 0 T as the polarity of the magnet changes, and which may be considered a measurement artefact. For Al_2O_3 the signal measured at 4 K is identical to that measured at 300 K, indicating temperature-independent diamagnetism from 300-4 K, whereas a paramagnetic signal is measured at 4 K for MgO, most likely due to paramagnetic impurities in the substrate, for which the typical impurity concentration (ppm) is given by the supplier as Fe ≤ 50, Ca ≤ 40, Al ≤ 15, Si ≤ 10, C ≤ 10, Cr ≤ 10 and B ≤ 5.

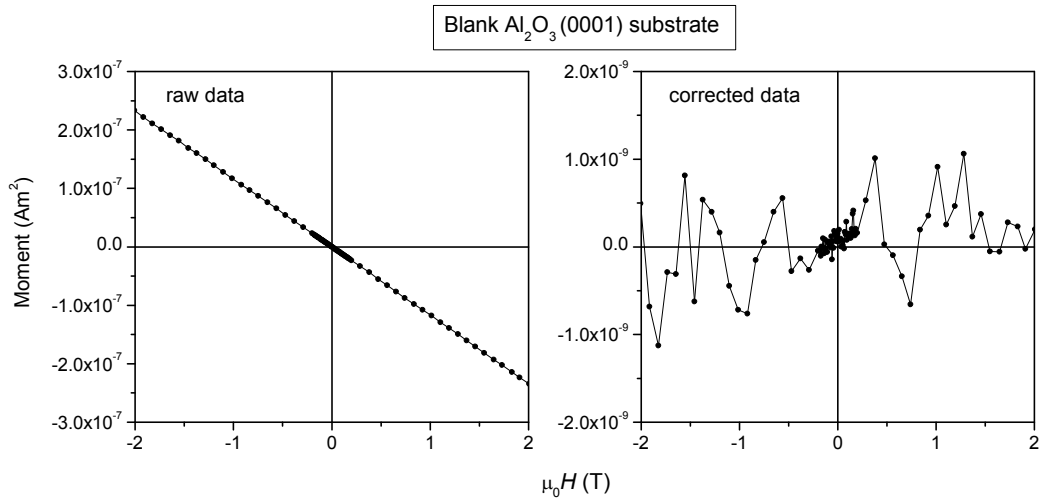

Figure 2.9. Room temperature magnetization data measured for a bare c-cut Al_2O_3 (0001) single crystalline substrate of dimension 5×5×0.5 mm (purchased from MTIXTL).

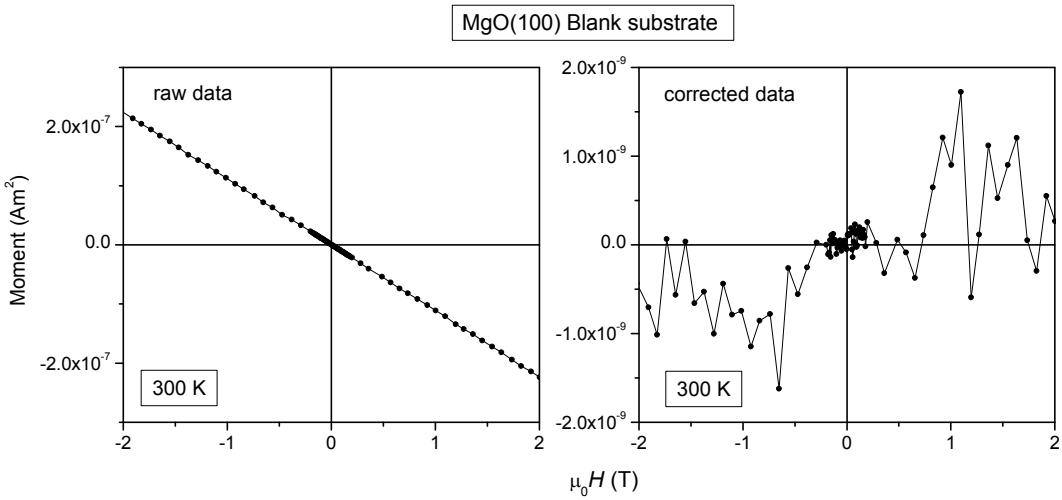

Figure 2.10. Room temperature magnetization data measured for a bare MgO (100) single crystalline substrate of dimension 5×5×0.5 mm (purchased from MTIXTL).

As a test, blank Al_2O_3 substrates were subjected to identical heating conditions used to deposit the MB_6 films; a small ferromagnetic-like signature in addition to diamagnetism was measured for some samples as shown in Fig. 2.11, but it was never more than 0.3×10^{-8} Am^2, about an order of magnitude smaller than that measured for many of the MB_6 films. Similar results were found for blank MgO substrates subjected to PLD processing conditions. Separate control films of ZnO and Al_2O_3 grown by ablation of targets made from 99.99 % nominal purity ZnO and Al_2O_3 powders respectively and deposited on Al_2O_3 (0001) substrates using similar conditions to those used for MB_6 films that produced the larger moments exhibited maximum moments of no more than 0.2×10^{-8} Am^2 at room temperature. These controls indicate that ferromagnetic contamination from the deposition chamber is not the source of hexaborides' magnetic signals when they exceed 0.3×10^{-8} Am^2. Furthermore, the silver paint (source: Agar scientific) used to affix the substrates to the substrate holder did not exhibit any ferromagnetic-like signature when measured at room temperature; additional confirmation arose from the measurement of the room temperature magnetization of a blank Al_2O_3 (0001) substrate subject to typical PLD processing conditions to which several mg of silver paint was clearly adhered to the backside, but for which no appreciable room temperature magnetic signal was measured, i.e. $< 0.3\times10^{-8}$ Am^2. A typical room temperature magnetization curve measured for a MB_6 film (100 nm thick BaB_6 deposited on Al_2O_3 (0001) at 500 °C) is shown in Fig. 2.12. The saturation moment is an order of magnitude greater than that due to the Al_2O_3 substrate alone subject to similar PLD processing conditions as for the film, after subtraction of the Al_2O_3 contribution to the ferromagnetic-like signal (0.3×10^{-8} Am^2). For the other deposited MB_6 film systems (CaB_6 and SrB_6) the largest moments of $\approx 3\times10^{-8}$ Am^2 are also about an order of magnitude greater than that due to the Al_2O_3 substrate alone on which they were deposited.

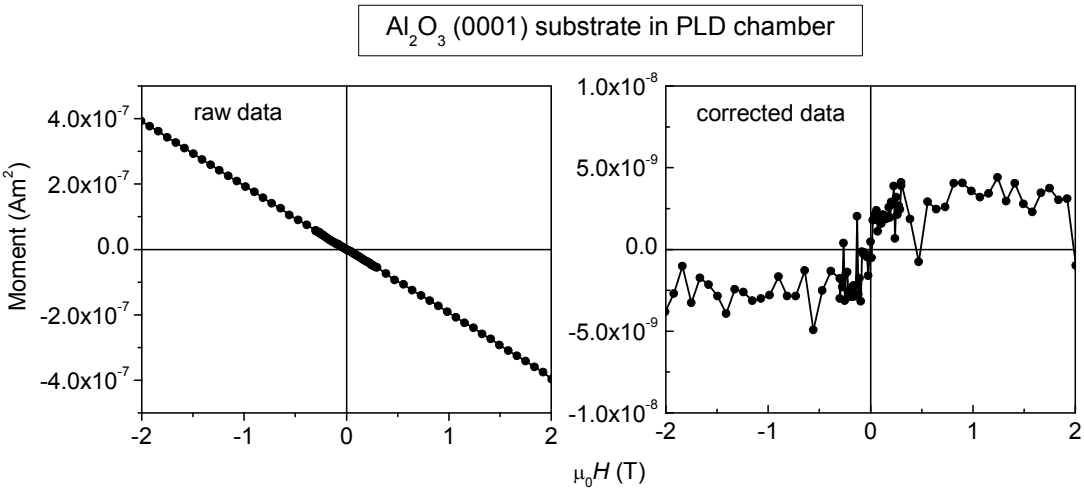

Figure 2.11. Room temperature magnetization data measured for a bare c-cut Al_2O_3 (0001) single crystalline substrate of dimension 5×5×0.5 mm (purchased from MTIXTL) subject to typical PLD processing conditions for MB_6 films.

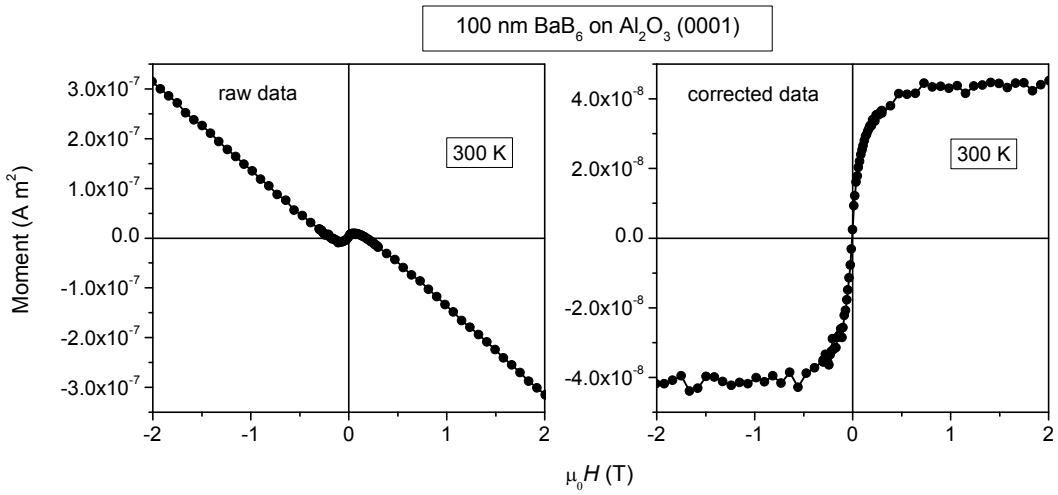

Figure 2.12. Room temperature magnetization data measured for a 100 nm thick BaB_6 film deposited on 5×5×0.5 mm Al_2O_3 (0001) at 500 °C.

It is important to distinguish d^0 ferromagnetic-like signals from those which may be attributed to ferromagnetic contamination, most likely in the form of iron impurities. Typical room temperature magnetization curves measured for iron (Fe) microparticles and magnetite (Fe_3O_4) nanoparticles are shown in Fig. 2.13. The iron microparticles have a saturation magnetization of 1.5 MA m^{-1}, slightly smaller than that of bulk iron (1.71 MA m^{-1}). Metallic iron may generally be ruled out as a source of the ferromagnetism in d^0 systems however since the value of H_0, the field obtained by extrapolating the initial susceptibility to saturation, for iron is significantly larger, generally 250-400 kA m^{-1}, than that measured for d^0 samples, for which H_0 is typically ≤ 100 kA m^{-1}. For magnetite nanoparticles (of ~ 40 nm size) the saturation magnetization is 0.3 MA m^{-1}, slightly smaller than that of bulk magnetite (0.478 MA m^{-1}), while H_0 is 80 kA m^{-1}, which is significantly less than that of metallic iron but in a similar range to that typically measured for d^0 samples. H_0 values for about 50 magnetic nanoparticles (~ 20-80 nm size) are found to lie within the range 50-100 kA m^{-1}, with M_s typically 0.3 ± 0.05 MA m^{-1}. Hence for MB_6 d^0 thin films studied in this thesis, for which M_s is typically of order 10-100 kA m^{-1}, the ferromagnetic-like signals may be accounted for ~ 3 – 33% magnetite impurities in the form of nanoparticles 20-80 nm in size. For d^0 samples in powder form, for which M_s is typically ≤ 100 A m^{-1}, the quantity of nanoparticulate magnetite required to account entirely for the almost anhysteretic ferromagnetic-like d^0 signals would be much less, ≤ 330 ppm. It is noted that careful impurity analysis carried out for each d^0 system investigated in this thesis can confidently rule out ferromagnetic contamination as an explanation for the magnitudes of the d^0 signals measured.

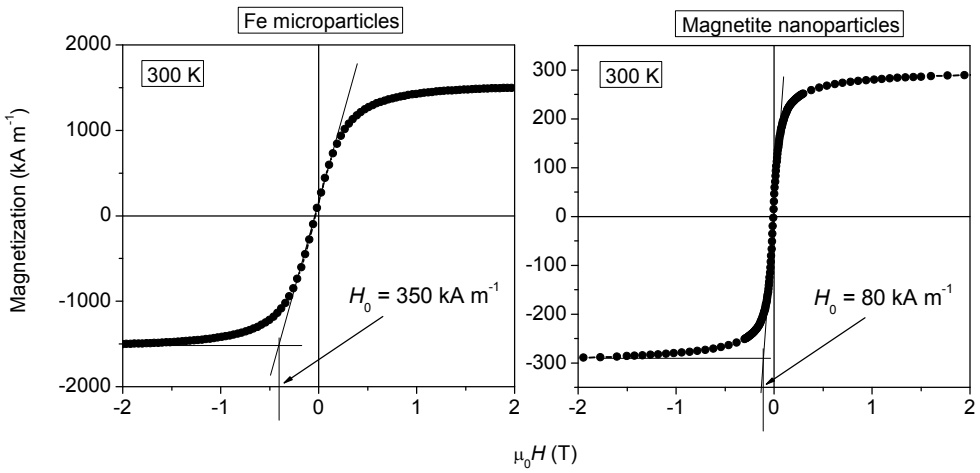

Figure 2.13. Room temperature magnetization data measured for iron microparticles and magnetite nanoparticles.

It is also important to distinguish d^0 ferromagnetic-like signals from those which could be attributed to superparamagnetism (SPM), since at room temperature the shape of the magnetization curves are similar for both. The definition of a SPM material matches at least two requirements; firstly, above the blocking temperature, the system must not show any hysteresis, which is not a thermal equilibrium property, while secondly, the magnetization curve must be temperature dependent to the extent that curves taken at different temperatures should superpose when being plotted against H/T, provided the initial susceptibility does not exceed the demagnetizing limit, $1/\mathcal{N}$. Single domain SPM NPs should show appreciable H_c at liquid He temperatures below the blocking temperature T_b, while above T_b irrespective of the orientations of the easy axes, the magnetization curves for should fit the Langevin function and should show no hysteresis. In the superparamagnetic region $T_b < T < T_c$, the particle behaves like a Langevin paramagnet with a giant, classical moment m. Hence the practical test for superparamagnetism is the superposition of anhysteretic magnetization curves as a function of H/T over a wide range of temperature between T_b and T_c, as shown in Fig. 2.14 for example for superparamagnetic iron nanoparticles (2.2 nm diameter) measured at 70 K and 200 K. The magnitude and shape of typical d^0 signals are virtually identical from liquid He temperatures up to room temperature (with no evidence of any upturns attributable to SPM in thermal magnetization scans) however, and the anhysteretic magnetization curves certainly do not superpose as a function of H/T, as shown for CeO_2 nanoparticles for example in Fig. 2.15. Similar results are found for the other d^0 systems studied in this thesis.

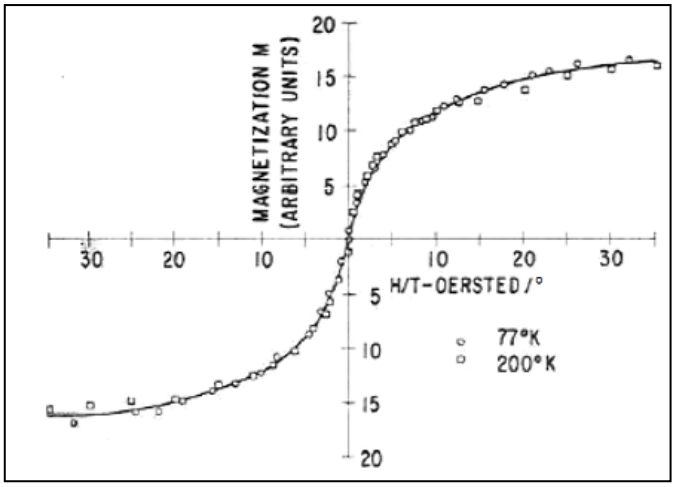

Figure 2.14. Magnetization M as a function of H/T at T = 77 and 200 K of 2.2 nm superparamagnetic iron nanoparticles suspended in mercury; from Bean and Jacobs, J. Appl. Phys. 27 1448 (1956).

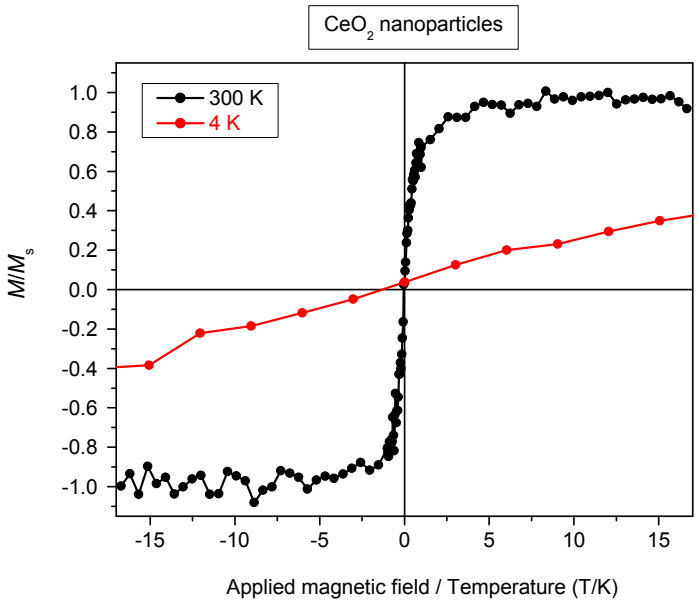

Figure 2.15. Magnetization as a function of *H*/T at T = 4 and 300 K for 4 nm CeO_2 nanoparticles.

2.5.2. Electron paramagnetic resonance spectroscopy

Electron paramagnetic resonance (EPR) spectroscopy can be a useful experimental tool in helping to elucidate the magnetic properties of certain materials by detecting unpaired spins to a sensitivity of less than 1 part per billion. The simplest case to consider is that of an isolated, localised unpaired electron with spin only angular momentum, which is quantised as $m_s = \pm ½$; an externally applied magnetic field will split the energy levels; transitions between the levels may then be induced by an appropriately polarised electromagnetic field of frequency ν, giving the resonance condition

$$\Delta E = h\nu = g\mu_B B_0 \tag{2.6}$$

where g = 2.002319, μ_B is the Bohr magneton unit and B_0 is the applied magnetic field.

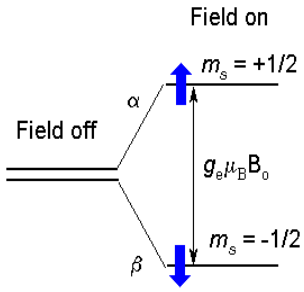

Figure 2.16. Splitting of the energy levels of an unpaired spin in an applied field.

For a free atom or ion with total orbital angular moment quantum number L (in addition to total spin angular momentum quantum number S) the g-value becomes

$$g = 1 + \frac{S(S+1) - L(L+1) + J(J+1)}{2J(J+1)} \tag{2.7}$$

where J = L + S. In thermal equilibrium, the number of spins in the lower energy state will be greater than the number of spins in the higher energy state and resonance will therefore lead to a net absorption of energy. In an EPR experiment, the frequency is typically fixed and the field is swept at a constant rate. Hyperfine interactions between the nucleus and the unpaired electron will result in a splitting of the signal; If the spin of the nucleus has quantum number I, each of the electronic levels, a and b, will split into 2I + 1 sublevels resulting in 2I + 1 observed lines of almost equal intensity under normal conditions. The main components of an EPR system are shown in Figure 2.17 below; these include a monochromatic water-cooled microwave source (klystron or Gunn diode), a waveguide for guiding the microwave power to the sample, and a resonant cavity designed to set up a microwave standing wave and to increase sensitivity by focusing or

concentrating the microwave power at the sample and storing the microwave energy, as well as various other components which are labelled in the figure. To minimize the noise from all of the electrical components for steady state measurements, a magnetic field modulation scheme with phase sensitive detection (using a lock in amplifier) was typically employed, which converts the absorption signal to its first derivative. To further improve the sensitivity, a time constant is used to filter out additional noise and the EPR signal is transformed into an output signal of amplitude proportional to the slope of the absorption signal.

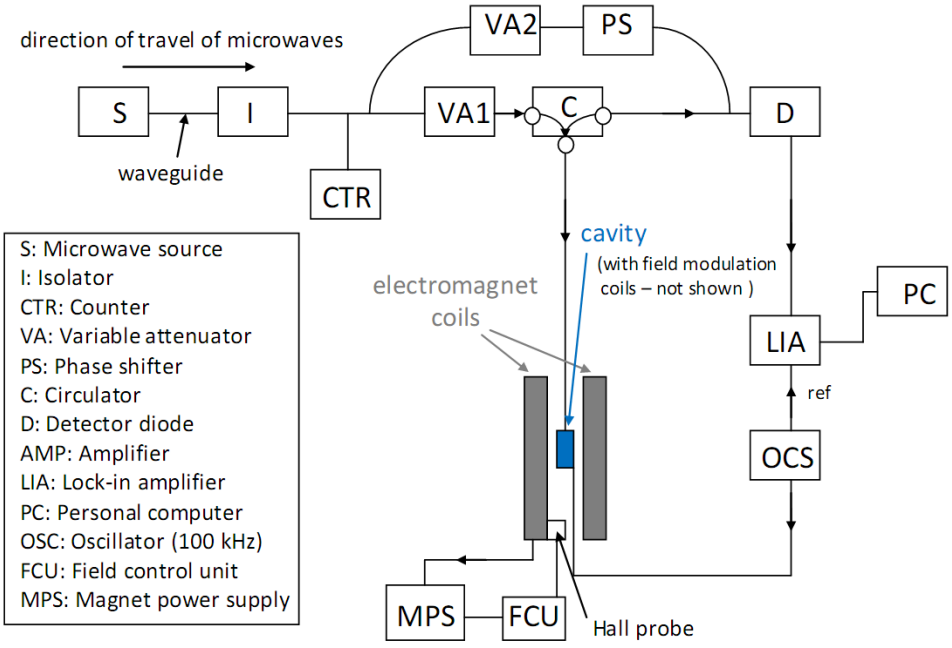

Figure 2.17. Schematic of the main components of an EPR measurement system.

EPR measurements were carried out using a Bruker EMX X-Band spectrometer located in Dr. Robert Barklie's laboratory in the SNIAM building, TCD, operating at a frequency in the region of 9.8 GHz (microwave regime). The microwave source was a Gunn diode (rather than a klystron), while a rectangular shaped (TM_{110} mode) microwave cavity was used. Powder samples were contained within spin free quartz tubes of inner (outer) diameter 4 mm (6 mm). Thin film samples were affixed to the bottom of the tubes using sellotape (which did not display an EPR signal when measured alone) and orientated relative to the field as required. The spectrometer was operated in standard absorption mode under slow passage conditions with a 100 kHz field modulation. The magnetic field sweep range was calibrated using an NMR probe; a check on the absolute value was made using an EPR signal of F^+ centres in MgO of known g value (2.0023). Spin populations were found by comparing the integrated area of the signal to that of a Varian standard sample of pitch in KCl. The absolute spin populations (and spin concentrations) are estimated to be correct to at least within a factor of two but relative values are correct to about ± 20

%. Care was taken to ensure that non-saturating power levels were used and that the signals were not distorted by over-modulation.

2.5.3. X-Ray absorption spectroscopy and X-Ray magnetic circular dichroism

2.5.3.1 XAS

In order to obtain further information about the stoichiometry and magnetism of the ceria nanopowders and bulk, X-Ray absorption spectroscopy (XAS) and X-Ray magnetic circular dichroism (XMCD) measurements were performed on the following samples at the Xtreme Beamline at the Swiss Light Source (SLS) synchrotron located in the Paul Scherrer Institute, near Zurich, Switzerland: CeO_2 nanopowders (both ferromagnetic, FM, and ~ non-magnetic, NM, synthesized using 99% and 99.999% purity cerium nitrate respectively), ~ 1 wt % La-doped high purity nanopowder (synthesized using 99.999 % cerium nitrate), and finally a bulk micropowder reference sample (99.999 % Sigma).

X-Ray absorption spectroscopy (XAS) is the fundamentally the excitation of electrons from their core levels using synchrotron X-Rays as the excitation source, which is sensitive to elemental oxidation state and coordination number of the sample being measured. The energy range of interest for the study of CeO_2 in this thesis is in the soft X-Ray (400 eV – 3000 eV) regime, at the X-ray absorption near-edge structure (XANES) region, which is typically defined to occur within ~ 50 eV of the absorption edge, sometimes also termed the *near* X-ray absorption fine structure (NEXAFS). At higher energies (> 100 eV) above the absorption edge one may find the *extended* X-ray absorption fine structure (EXAFS), characteristic of delocalized electrons and the extended electronic band structure.

The most intense features in an XAS (XANES) spectrum are due to electric-dipole allowed transitions ($\Delta l = \pm 1$) to unfilled orbitals, and hence is a probe of the density of unoccupied states. The characteristic absorption edges of the elements Ce and O (plus La and Fe to check for these impurities) were measured. For the Ce *M* edge probed, the main features in the XAS spectrum (M_4 and M_5 peaks) are related to transitions from $3d$ core states to $4f$ states [12], specifically $3d_{3/2} \rightarrow 4f_{5/2}$ (M_4) and $3d_{5/2} \rightarrow 4f_{7/2}$ (M_5), and are a probe of the $4f$ excited state occupancy, and are characterized by sharp white lines at 890 eV and 882 eV respectively for metallic cerium [13]. For Ce^{4+}, the excited $4f^1$ state is probed, corresponding to the electronic transition $3d^{10}4f^0 \rightarrow 3d^9 4f^1$, whereas for Ce^{3+}, the excited $4f^2$ state is probed, corresponding to the transition $3d^{10}4f^1 \rightarrow 3d^9 4f^2$. The post-edge features meanwhile, at ~ 5 eV higher energy than those of the *M* edge maxima intensity, originate from transitions to the $4f$ admixture in the

conduction states, indicative of empty localized $4f^1$ states within the band gap [14,15]; the pre-edge features (at ~1-5 eV lower energy than those of the *M* edge maxima) are indicative of Ce^{3+}. The analogous M_4 and M_5 edges were also measured for La. For the Oxygen *K* edge probed, which is detected over the energy range ~ 525-540 eV, information is provided about the O 2*p* valence and Ce conduction states. The XAS of stoichiometric CeO_2 has 3 peaks, related to electronic transitions from O 1*s* core levels to empty O 2*p* hole states hybridized with Ce dominated 4*f*, 5*d*-e_g and 5*d*-t_{2g} levels respectively in order of increasing energy [16]. Hence the lowest energy peak may be considered as a measure of Ce-O bonding or hybridization [17], while the higher energy peaks are more characteristic of the band structure due to delocalized electrons extending into the EXAFS regime. A typical XAS measured for the O *K*-edge of CeO_2 nanopowders synthesized during this study is shown in Figure 2.18, which illustrates the typical features of X-Ray absorption spectra.

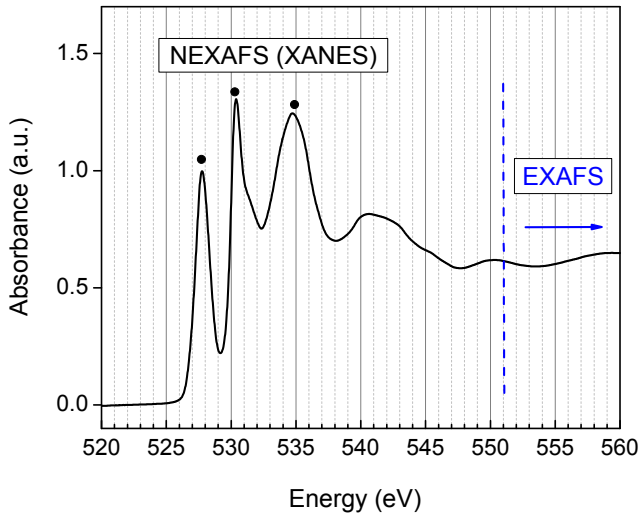

Figure 2.18. X-Ray absorption spectrum measured for the O *K* edge of a CeO_2 nanopowder at 300 K. The spectrum can be generally separated into two components, the near-edge X-Ray absorption fine structure (NEXAFS, or XANES), and the extended X-Ray absorption fine structure (EXAFS) at higher energies. The three characteristic absorption peaks of the O *K* edge for CeO_2 (further details of which are given in the text) are marked by the black dots.

In terms of XAS signal detection, total electron yield (TEY) mode was used (~ 2-5 nm penetration depth), which consists of all electrons (mostly inelastically scattered) escaping from the specimen as a result of the cascade process initiated by the initial absorption of each synchrotron photon. TEY detection is the most commonly used method to detect the X-Ray absorption signal because of the large signal available and the ease of measuring the signal via the drain current from the sample. The main disadvantages of TEY are the range of mechanisms giving rise to escaping electrons and the relatively small depth probed in the sample. Close to the actual threshold of an absorption edge, the signal is dominated by the cascade process initiated by the ejected Auger

electron as the photoelectron has little energy. However, the underlying background also has contributions arising from high-energy photoelectrons ejected from much less tightly bound atomic states, the Auger electrons from which can have much lower energy. Approximating for Auger dominated electron emission at ~ 1 keV energy in TEY detection mode, the mean escape depth (or inelastic mean free path) of the ejected photoelectrons are of order ~ 5 nm (characteristic of *all* photoelectrons collected at energies lower than the X-Ray excitation energy) as estimated from the universal curve for the energy dependent mean free path of electrons in matter [18]. Hence for the nanopowders, generally the whole particle volume is probed, since the diameters of the FM and NM nanopowders are about 4 nm and 6 nm respectively. The mean free path is defined as the depth at which the probability that 1/e (~ 37 %) of the photoelectrons escape without energy loss. XAS may also be performed by detecting the fluorescence yield (~ 50 - 100 nm penetration depth), whose yield is typically of order 1 % that of TEY for soft X-Rays and detects the photoelectrons that are emitted after electrons of lower binding energy fill the core holes which are created by the X-Ray excitation. TEY mode was used in our measurements simply due to its much higher yield compared to fluorescence. Whereas fluorescence yield has a large probing depth advantage over electron yield, it is often unsuitable for concentrated samples due to self absorption effects. In addition, core levels below 2 keV have a higher Auger electron yield than fluorescence yield per absorption event, making TEY detection more practical for measurements in most of the soft X-Ray energy range. Lighter elements generally have higher Auger electron yields than heavier elements. A third mode of detection is that of transmission, in which the X-Rays transmitted through the sample are detected.

For measurement of XAS, ~ 1 mg of each CeO_2 powder was first pressed on Indium foil (99.99 % nominal purity) and mounted in an ultra high vacuum (10^{-9} mbar) for measurement. The only known absorption edges for Indium at any energy are the $N_{4,5}$ edges at ~ 17 eV, which are much lower in energy than those measured in the soft X-Ray range for Ce, O, La and Fe (typically 100s of eV). The total area irradiated was about 30 × 230 μm. The photon flux within the energy range measured (500 – 1000 eV) in TEY mode was 10^{15}/s. Data was collected at an incident angle of 28° to the normal in order to minimise the incident X-Ray flux, as ceria in particular has a tendency towards reduction under irradiation, while also serving to increase the area of the sample surface scanned. The data for each Ce and O edge was typically acquired for a duration of ~ 100 scans lasting about 8 hours (in both positive and negative applied field with right and left circular light polarization for each scan, as detailed further in the next sub-section).

2.5.3.2 XMCD

An XMCD spectrum is the difference spectrum of two X-Ray absorption spectra (XAS) measured in both positive and negative applied magnetic field with both left and right circularly polarized light. In the electric dipole approximation, changing the polarization from left to right or

reversing the magnetic field are equivalent actions. Analysis of the XMCD spectrum can yield information on the magnetic properties of the atom of a specific element, such as its spin and orbital magnetic moment. The XMCD signal is in fact directly proportional to the magnetic moment on the absorber atom [19], and with the development of sum rules applied to the total absorption and XMCD spectra [20,21], enables the calculation of direct values for the orbital and spin moment of the probed atom from the measured XMCD data. In addition, the sign of the XMCD signal reveals the net spin orientation for a given element or ion. Element selectivity is a significant advantage of this technique over conventional magnetometry. One disadvantage is that only limited focusing is possible when using X-rays on a typical synchrotron beamline, which sets a limit on the lateral spatial resolution, typically of order 10s of microns at best (contrast with TEM-EELS where nanometric resolution is obtained), however conversely the spectral resolution obtained by XAS is typically superior to that obtained by TEM-EELS.

The XMCD signal is defined as

$$XMCD = (XMCD_{H^-} - XMCD_{H^+}) / 2$$
$$XMCD_{H^-} = H^-c^+ - H^-c^-, \quad XMCD_{H^+} = H^+c^+ - H^+c^- \qquad (2.8)$$

where H denotes the applied magnetic field (+ for positive applied field, – for negative applied field) and c denotes the circular polarization (+ for clockwise/right, – for anticlockwise/left).

For the XMCD measurements of CeO_2 performed in conjunction with XAS, at 300 K (2 K) the circular polarization was measured in fields of +/– 2T (+/– 7 T), with the magnetic field applied parallel to the X-ray beam.

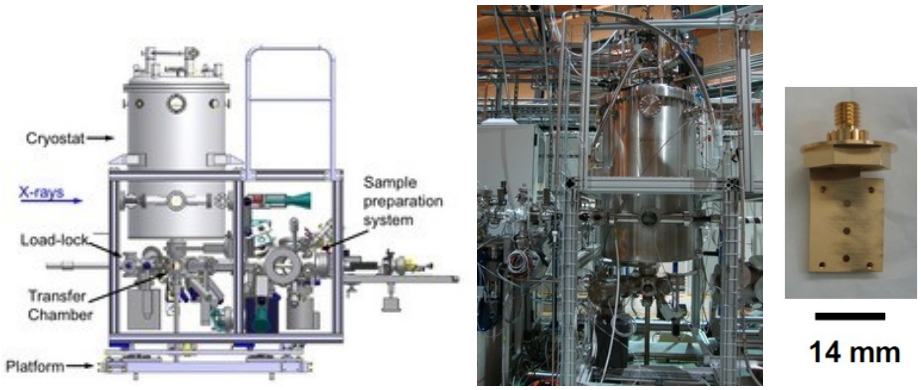

Figure 2.19. The endstation of the Xtreme Beamline (at the Swiss Light Source) used for XAS/XMCD measurements is shown schematically (left) together with an actual photograph (centre); the sample holder is also shown (right).

In terms of data processing, the raw XAS signals were first normalised using an energy range well below the lowest energy absorption edge to a background signal intensity of 1, after which an intensity value of 1 was subtracted from the resultant XAS signals in order to give a common zero background baseline intensity at the lowest energies. The corresponding

XMCD signals were then deduced as described in the experimental section. For clarity of display only, the XAS signals were subsequently all normalised (divided by a certain number) to an absolute intensity magnitude of 1 at the lowest energy absorption peak, which hence gives a step edge of intensity 1 at this peak; the XMCD signal was then divided by the same factor used to divide the XAS signal by above, in order to show and compare all of the XMCD signal magnitudes corresponding to a common XAS signal step edge intensity of 1 at the lowest energy absorption edge. In an final extra step, a total value of 1 was then added to the XAS intensity scale, in order to shift up the XAS signals to facilitate plotting of the XMCD signal directly underneath the XAS, which is in effect what is displayed here for the combined XAS/XMCD result plots. The corresponding XMCD signals were additionally smoothed using a 7 point Savitzky-Golay adjacent averaging in order to optimally display the results without showing at one extreme unphysically sharp features (no smoothing at all), or at the other over-averaged signals (too much smoothing).

2.5.4. Muon spin rotation spectroscopy

Muon spin rotation (μSR) spectroscopy measurements of MB_6 thin films and powders were undertaken at the laboratory for muon spin spectroscopy at the Paul Scherrer Institute, near Zurich, Switzerland. μSR is an experimental technique based on the implantation of spin-polarized muons in matter and on the detection of the influence of the atomic, molecular or crystalline surroundings on their spin motion. The motion of the muon spin is due to the local magnetic field experienced by the particle.

In order to create muons, charged pions (π^+) are first produced in a cyclotron from collisions of high-energy protons (> 500 MeV) with the nuclei of an intermediate light element target such as carbon. The charged pions that are produced live for only 26 billionths of a second and then decay via the weak interaction into a muon (μ^+) and muon neutrino (ν_μ). Thanks to maximal parity violation during pion decay, the muons are almost perfectly spin polarized opposite to their momenta, i.e. they are nearly ~ 100 % spin-polarized. The muons then in turn decay according to the following characteristic decay scheme;

$$\mu^+ \xrightarrow{\sim 2\ \mu s} e^+ + \overline{\nu}_\mu + \nu_e \qquad (2.9)$$

where the three decay products in the order they are listed from left to right represent a positron, a muon anti-neutrino and an electron neutrino respectively. While the lifetimes of a free μ^+ and a μ^- are the same (2.197 μs), the measured mean lifetime in matter is considerably shorter for the μ^- because of capture by the nuclei. Hence positively charged muons μ^+ are typically used as an experimental probe. In a solid, μ^+ generally comes to rest at an interstitial site of high symmetry between the lattice ions, where it exists in a diamagnetic state as a "quasi-free" probe of the

magnetic field at the interstitial site, with its precession frequency determined by its gyromagnetic ratio of 851.615 MHz/T. In the decay scheme shown in (2.9) above, only the fast positron emitted preferentially along the direction of its spin due to the parity violating decay is detected. By measuring the anisotropic distribution of the decay positrons the statistical average direction of the spin polarization of the muon ensemble may be determined. The polarization as a function of time, an example of which is shown in Figure 2.20, is characterized by precession and/or relaxation and contains information about both static and dynamic properties of the local environment. The time evolution of the muon spin polarization depends sensitively on the spatial distribution and dynamical fluctuations of the muons' magnetic environment. Magnetic and non-magnetic regions co-existing in the same specimen result in distinct μSR signals whose amplitudes are proportional to the volume of the sample occupied by the particular phase. Thus the μSR technique recognizes and provides quantitative information on coexisting phases in a material.

Several properties of polarized muons make them suitable for probing magnetism: Spin ½, almost 100 % polarization, a magnetic moment of 3.18 μ_{proton} (sensitive to 10^{-3} – 10^{-4} μ_B) and low mass (about 207 electron masses). The small moment allows the detection of fields with nuclear and electronic origins. In systems with very small and/or dilute and/or random ordered moments, μSR is often the only method available for clear detection of such phenomena. Thin film sensitive (< 100 nm) low energy muons (keV) may be obtained by moderating the high energy muons (MeV) used for bulk investigation. The most successful approach has been simple moderation in a thin degrader consisting of a condensed Van der Waals gas (Ar or N_2). Fortunately, the moderated muons remain highly polarized.

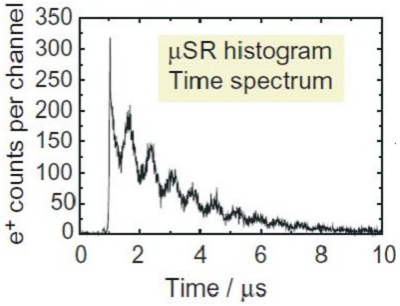

Figure 2.20. Example of the time evolution of the muon polarization. The amplitude of the oscillations is related to the magnetic volume fraction, their frequency is a measure of the magnitude of the local field and the size of magnetic moments, while the damping reveals the inhomogeneity of the magnetic regions. In practice, the oscillations are often smeared out, most commonly due to inhomogeneous magnetic field distributions.

Two different configurations can be used when using muons to study matter, either transverse or longitudinal field μSR, which involves the application of an external magnetic field either perpendicular (transverse) or parallel to the initial direction of the muon spin polarization respectively. In the first case, the muon spin precesses about the transverse field with a frequency that is proportional to the size of the field at the muon site in the material. In the second case one

measures the time evolution of the muon polarization along its original direction. Alternatively, such measurements may be performed in the absence of an external field, called zero field μSR, which is a very sensitive method of detecting weak internal magnetism that arises due to ordered magnetic moments, or random fields that are static or fluctuating with time. The capability of studying materials in zero external fields is a tremendous advantage over other magnetic resonance techniques.

At the Paul Scherrer Institute there is a continuous (as opposed to a pulsed) source of muons. Both MB_6 thin films / bulk powders and CeO_2 nanopowders / bulk were measured there. For measurements in zero field, a muon spin rotation of -10° was used, while for measurements in transverse applied field (in order to decouple the muon spin from internal magnetic fields), +/– 90° was used as the term implies. For measurements of MB_6 thin films, the films (deposited on 10×10 mm area substrates) were mounted on a circular Al_2O_3 plate using silver paint; the muon beam also irradiates some of the Al_2O_3 plate as well as the film, contributing to the background noise in the polarization vs. time signal. The aim was to probe both magnetic and ~ non-magnetic MB_6 films in regions near the surface and near the film-substrate interface (by selecting appropriately tuned implantation energies) from room temperature down to low temperatures (~ 5 K).

MB_6 bulk powders and CeO_2 bulk/nanopowders were measured on the bulk muon instrument (GPS, General Purpose Surface muon instrument) by tightly encasing a batch of ~ 50-100 mg of compacted powder in aluminized mylar coated superinsulation tape (sticky on the outside, i.e. not in contact with the powder sample), with the sample mounted on a fork-like sample holder in order to reduce the background contribution; thin films were measured on the low energy muon instrument (LEM), shown in Figure 2.21 below.

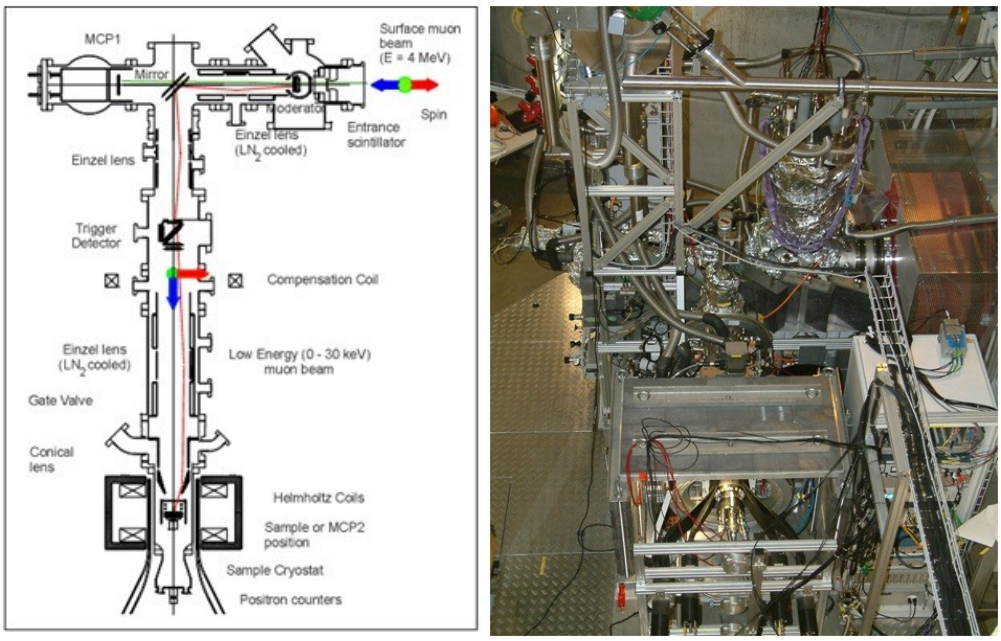

Figure 2.21. The low energy muon (LEM) end-station at the Laboratory for Muon Spin Spectroscopy, PSI, is shown both schematically (left) together with a photograph of the setup (right)

2.6. References

[1] Y. Liu, Z. Lockman, A. Aziz, and J. MacManus-Driscoll, Journal of Physics: Condensed Matter **20**, 165201 (2008).

[2] K. Ackland, L. M. A. Monzon, M. Venkatesan, and J. M. D. Coey, IEEE Transactions on Magnetics **47**, 3509 (2011).

[3] L. A. Defaria and S. Trasatti, Journal of Colloid and Interface Science **167**, 352 (1994).

[4] M. Nabavi, O. Spalla, and B. Cabane, Journal of Colloid and Interface Science **160**, 459 (1993).

[5] S. Shang and Z.-K. Liu, Applied Physics Letters **90**, 091914 (2007).

[6] H. M. Rietveld, Acta Crystallographica **22**, 151 (1967).

[7] H. M. Rietveld, Journal of Applied Crystallography **2**, 65 (1969).

[8] J. Rodriguez-Carvajal, Physica B **192**, 55 (1993).

[9] W. N. Delgass, G. L. Haller, R. Kellerman, and J. H. Lunsford, *Spectroscopy in Heterogeneous Catalysis* (p. 128, Academic Press, New York, 1979).

[10] E. Ziegler, A. Heinrich, H. Oppermann, and G. Stover, Physica Status Solidi a-Applied Research **66**, 635 (1981).

[11] D. W. Abraham, M. M. Frank, and S. Guha, Applied Physics Letters **87**, 252502 (2005).

[12] J. C. Fuggle, F. U. Hillebrecht, J. M. Esteva, R. C. Karnatak, O. Gunnarsson, and K. Schonhammer, Physical Review B **27**, 4637 (1983).

[13] B. T. Thole, G. Vanderlaan, J. C. Fuggle, G. A. Sawatzky, R. C. Karnatak, and J. M. Esteva, Physical Review B **32**, 5107 (1985).

[14] E. Wuilloud, B. Delley, W. Schneider, and Y. Baer, Physical Review Letters **53**, 202 (1984).

[15] R. C. Karnatak, J. M. Esteva, and H. Dexpert, Physical Review B **36**, 1745 (1987).

[16] D. R. Mullins, S. H. Overbury, and D. R. Huntley, Surface Science **409**, 307 (1998).

[17] Z. Hu, et al., Physical Review B **60**, 1460 (1999).

[18] M. P. Seah and W. A. Dench, Surface and Interface Analysis **1**, 2 (1979).

[19] J. L. Erskine and E. A. Stern, Physical Review B **12**, 5016 (1975).

[20] B. T. Thole, P. Carra, F. Sette, and G. Vanderlaan, Physical Review Letters **68**, 1943 (1992).

[21] P. Carra, B. T. Thole, M. Altarelli, and X. D. Wang, Physical Review Letters **70**, 694 (1993).

Chapter 3

HfO_2

This chapter presents experimental results on d^0 magnetism in HfO_2, the first d^0 material studied as part of this thesis. Specifically, the effect of vacuum annealing on the magnetic properties of pure HfO_2 micropowders was investigated. Firstly, a brief introduction to HfO_2 is presented, followed by an overview of literature reports pertaining to magnetism in HfO_2, both experimental and theoretical. Experimental results follow before a summary of the results is finally presented.

3.1. Introduction

HfO_2 (hafnia) is a wide band gap insulator, with an electronic band gap of ~ 5.7 eV and a high dielectric constant of 25 [1], which is about six times higher than that of SiO_2 (3.9). Stoichiometric HfO_2, which has no unpaired electrons since the Hf^{4+} ion has a closed shell [Xe]$4f^{14}$ configuration, presents no evidence of any magnetic order, and as such is a valid candidate for investigating d^0 magnetism. At room temperature and pressure, HfO_2 exists in the monoclinic phase (*P21/a* space group); the crystal structure is shown in Figure 3.1.

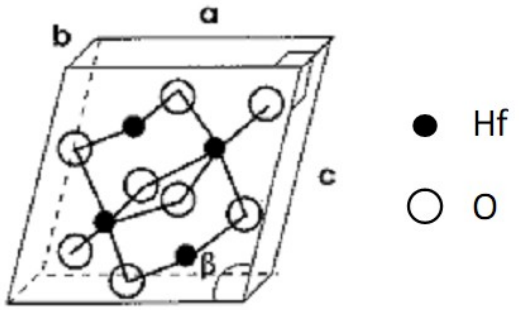

Figure 3.1. Monoclinic crystal structure for HfO_2 under ambient conditions.

Because of its high dielectric constant and large band-gap (good insulating properties), plus its good compatibility with polysilicon, hafnium-based oxides are leading candidates to replace SiO_2 as a gate insulator in field-effect transistors. The reason a new gate insulator is required is due the downscaling of advanced metal oxide semiconductor field-effect transistors (MOSFETs), and the fact that the SiO_2 gate oxide becomes too thin (< 2 nm) to prevent leakage currents due to tunnel effects [1], whereas HfO_2 can be grown 3-5 nm thick while maintaining standard device parameters. In addition, a resistive switching effect as a function of applied voltage has been found for non-stoichiometric polycrystalline HfO_x films [2], in which the switching is thought to be due to the defects that are generated by the applied bias; this could have potential applications in non-volatile memories. If resistive switching could be combined with d^0 room temperature ferromagnetism, it would significantly boost the importance of hafnium oxide for microelectronics, since it can already be integrated with CMOS processing technology.

Oxygen vacancy defects may readily form in monoclinic HfO_2 and can account for trap assisted conduction, direct electron injection, and optical absorption phenomena as calculated by Broqvist *et al* [3]. Figure 3.2 below provides a schematic of the bandstructure for stoichiometric and oxygen deficient HfO_2 films from Hildebrandt *et al.* [4]. The general effect of the oxygen vacancy formation is to introduce mid-gap defect states; bandgap reduction may be due to hybridization of defect states with the conduction band.

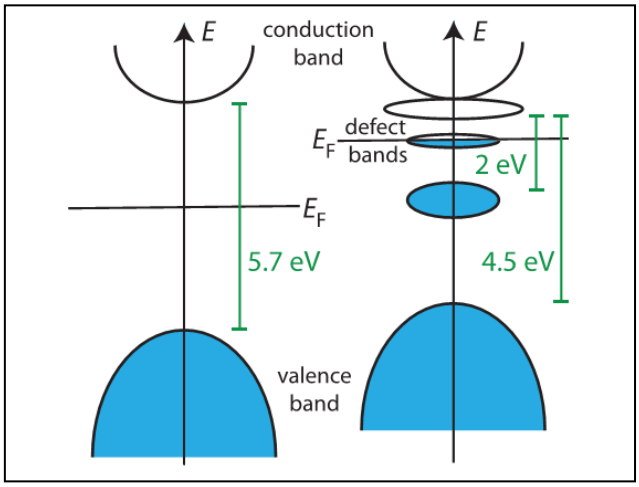

Figure 3.2. Band model of stoichiometric HfO_2 (left) and simplified band model of oxygen deficient HfO_{2-x} (right) – Figure from Hildebrandt *et al* [4]. This schematic serves as a *general* illustration only of the band-structure of HfO_{2-x}, since the precise position of the Fermi level, and the position, size and number of defect bands sensitively depend on sample growth and deposition conditions.

In the next section a detailed discussion of the literature reports which measure and/or calculate magnetism for HfO_2, the key property of interest in this thesis, is presented.

3.2. Literature summary

The first report for room temperature ferromagnetism (RTFM) in undoped HfO_2 was for thin crystalline films grown by our research group at Trinity College Dublin, grown by PLD at 750 °C in an oxygen atmosphere (10^{-4} – 1 mbar) on Al_2O_3 r-cut (11-02) crystalline substrates by Venkatesan *et al.* [5] in the year 2004. A 99.95 % purity HfO_2 target was used. 80 nm thick films displayed large room temperature magnetizations, 12.5 kA m^{-1} and 50 kA m^{-1} for in-plane and out of plane respectively, the magnitude of which was virtually constant from 5-400 K, with very little hysteresis (H_c ~ 5 mT). The magnetization curves which were published are shown in Figure 3.3 below. Lattice defects were invoked in order to explain the measured magnetic signals. More specifically, the formation of an impurity band due to lattice vacancies was proposed. It was further suggested that by allowing the impurity band to mix with the empty 5*d* states of hafnium and to transfer a fraction of an electron for each vacancy, the 5*d* states would in turn polarize the impurity band and provide the necessary ferromagnetic coupling. The impurity band scenario was further elucidated by Coey [6] in which lattice defects were proposed as the common source of magnetism in not just HfO_2 but also carbon structures such as C_{60} and graphite, alkaline earth hexaboride films (MB_6, M = Ca, Sr, Ba) and various dilute magnetic oxides and nitrides such as 5 at. % Sc doped ZnO and Fe, Mn and Co doped SnO_2. It was proposed that if the density of states of an impurity band is sufficiently great, spontaneous spin splitting based on the Stoner criterion $D(E_F)\ I > 1$ may occur. Another idea proposed was that defect states themselves give rise to magnetic moments associated with molecular orbitals localized in the vicinity of the defects.

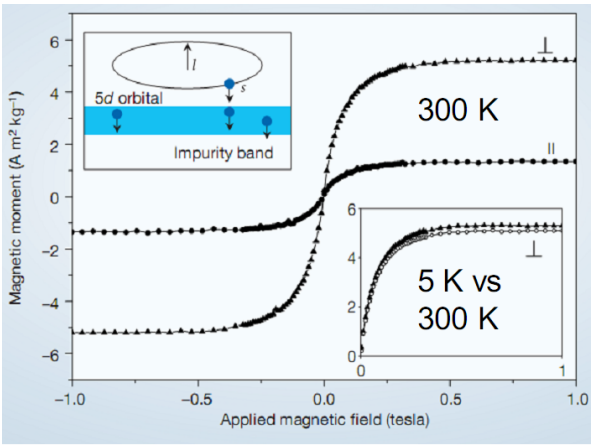

Figure 3.3. Magnetization curves from the first experimental report of RTFM in HfO_2, for thin films, ~ 80 nm thick, grown by PLD on Al_2O_3 (11-02) substrates, published by Venkatesan *et al.* [5]. An impurity band defect-mediated magnetism was proposed as the origin of the magnetic signals (further details given in the text).

A further report by Coey *et al.* [7] for RTFM in HfO_2 films (all (poly)crystalline for all publications mentioned henceforth unless stated otherwise) deposited by PLD on not only Al_2O_3 but also on Yttrium-stabilized zirconia (YSZ) (100) and silicon (100) substrates soon followed their initial paper. For 13 nm thick films the magnetization was as high as 250 kA m^{-1}, although there was found to be no correlation between the absolute magnetic moment and film thickness. In addition, RTFM was measured for a HfO_2 commercial micropowder annealed under vacuum, although M_s was several orders of magnitude smaller than that for films at 18 A m^{-1}. Due to the findings that there was no trace of ferromagnetism in the pristine powder and that the ferromagnetism disappeared after re-heating the ferromagnetic sample in air, it was suggested that oxygen vacancies created during vacuum annealing may play a role in mediating the magnetism; this suggestion is also supported by the finding that the magnetism decays rapidly over time (only 10 % of its initial magnitude after 6 months), consistent with re-oxidation of ferromagnetic oxygen vacancy-rich non-stoichiometric HfO_{2-x} to non-ferromagnetic stoichiometric HfO_2. The type of oxygen vacancy responsible was not specified however; in hafnia, oxygen vacancies can be doubly or singly positively charged (V_O^{++}, V_O^{+}), neutral (V_O^{0}) or singly or doubly negatively charged (V_O^{-}, V_O^{--}) depending on the number of trapped electrons. Furthermore, the oxygen vacancies may be either three-fold or four-fold coordinated (a hafnium vacancy meanwhile is seven-fold coordinated). It is noted that while oxygen vacancies appear to be correlated with the magnetism, the results are open to interpretation since one cannot assume that it is a straightforward cause (oxygen vacancies) and effect (RTFM) relationship.

In terms of theory, preceding the initial experimental reports of magnetism in HfO_2, calculations [8] using density functional theory (DFT) within the generalized gradient approximation (GGA) type II (Perdew and Wang) found that atomic oxygen incorporation is energetically favoured over molecular incorporation in hafnia, and that charged defect species are more stable than neutral species when electrons are available from the hafnia conduction band. Subsequently, and shortly after the initial reports of magnetism in HfO_2 were published, a DFT calculation [9] within the local density approximation (LDA) suggested that Hf vacancies mediate the magnetism in the monoclinic phase, to which moments of up to 3.5 μ_B /vacancy were attributed; it is noted however that if oxygen vacancies are present there should also be Hf vacancies present for charge compensation, in corroboration with the previous experimental reports. The above result was also supported by [10], who calculated 4 μ_B/Hf vacancy, while in contrast another DFT calculation suggested that the formation of Hf vacancies results in the creation of holes in the oxygen 2*p* valence band and magnetic moments on the surrounding *oxygen* atoms (max. 0.79 μ_B/O) [11]. Another DFT study finds that the O rich non-stoichiometric surfaces are ferromagnetic for the cubic phase (4 μ_B /vacancy) [12], while in contrast to all of the above calculations, *no evidence* for any magnetic defects or ferromagnetism in HfO_2 was found by [13]. Using other methods of calculation, vacancy- or substitutional-induced ferromagnetism of the oxygen holes is reported using the unrestricted Hartree-Fock (UHF) approximation (3 μ_B /unit cell) [14]. Thus it can be seen that there is still no consensus among theoreticians as to whether Hf or O vacancies mediate the magnetism; it is likely that the disagreement is due in part to the sensitivity of the theoretical results to the initial

conditions used in the calculations.

In a further experimental report, the magnetic signals ($M_s \sim 0.1$ kA m^{-1}) for both undoped and Gd doped (3 at. %) 200 nm thick HfO_2 films grown by PLD on Si(100), Al_2O_3 (11-02) and $LaAlO_3$ (001) substrates are attributed to impurities from the PLD target and/or due to signals from the substrates [15]. However these films were deposited at the base vacuum pressure (10^{-7} mbar), and not in an oxygen ambient as reported before [5,7], which may be a possible explanation for the discrepancy in the sizes of the measured magnetic signals. Hong *et al.* show in several reports [16-18] that 200 nm thick films of undoped HfO_2 grown by PLD on YSZ (100) substrates at 800 °C give a room temperature magnetization of ~ 28 kA m^{-1} , slightly larger than the ~ 16 kA m^{-1} signal measured for films of similar thickness grown at 750 °C by our group [7]; note that RFTM for TiO_2 and In_2O_3 films is also included in [16,17]. For 10 nm thick films the magnetization reaches much larger values of up to 500 kA m^{-1} [18]. Since the numbers of defects (most likely oxygen vacancies) in the film are independent of its thickness, the enhanced magnetization may therefore be due to defects mostly localized near the interface between the film and the substrate, and not distributed throughout the bulk of the film. In addition a room temperature bulk magnetization of ~ 10 A m^{-1} is measured for the HfO_2 PLD target from which the films were grown in [16,18]. Another report gives room temperature M_s values of order ~ 30 kA m^{-1} for nanoparticulate HfO_2 films of ~ 50 nm thickness grown by PLD at 750 °C on Al_2O_3 (0001) substrates [19]. The grain size is modified by varying the number of laser shots used to grown the film. In particular, the authors show that the magnetic moments of the individual nanoparticles of which the films are composed exhibit a maximum signal of order 1000 μ_B/particle for a particle diameter of 8 nm, with the moment per particle decreasing for either smaller or larger particle diameters. Furthermore, the authors more generally propose that up and down spins in ultrafine diamagnetic systems are spatially separated and form asymmetric spin-singlet pairs (with a correlation length of about 4 nm in HfO_2), and that net magnetic moments within these systems arise from the imbalance between the spatial spin density distributions, which may also explain the anisotropic and virtual temperature independent (from ~ 4 – 300 K) characteristics of the magnetism.

In contrast to those initial reports which measured ferromagnetism for HfO_2 films, several subsequent reports did not measure any ferromagnetism. For example, no evidence of any ferromagnetism is measured for undoped films grown on (100) YSZ substrates by PLD [20] ($t \approx 50$ nm) using a range of growth conditions, including nominally similar conditions to those used in a previous study [7]. Another report [21] does not find any evidence for ferromagnetism in 50 nm thick films grown by PLD at various oxygen pressures on c-cut sapphire (0001) substrates using a Nd:YAG laser (λ=355 nm) with an energy density of 10 J cm^{-2}. Elsewhere, an X-Ray absorption study (which probes unoccupied electronic states) of a 2 nm thick oxygen deficient $HfO_{1.8}$ film grown by PLD on a Si(100) substrate reveals nonzero Hf 5*d* state occupation in the presence of oxygen vacancies [22]; the absence of any magnetic circular dichroism (MCD) signal measured on the Hf N_3 X-Ray absorption edge (at ~ 370-400 eV) however shows that there is no intrinsic ferromagnetic spin order present in the sample. Meanwhile, the contribution of ferromagnetic contamination to the magnetic signal due the use of stainless steel tweezers to handle film

substrates is highlighted by [23], to which magnetizations of up to approximately 4.2 kA m^{-1} for the thinnest films grown (for t = 30 nm) are attributed. The same report also finds no ferromagnetism in undoped films grown by either atomic layer deposition (ALD) or metal organic chemical vapour deposition (MOCVD) on SiON coated Si(100) n-type substrates. Hildebrandt *et al.* [4] find that for both oxygen deficient and oxygen rich $HfO_{2\pm x}$ films, 50-200 nm thick and grown by molecular beam epitaxy (MBE) on Al_2O_3 (0001) substrates, no measurable trace of ferromagnetism is found for any of the films grown under a wide range of oxygen partial pressures. Hence it is evident that the appearance of ferromagnetism in HfO_2 films may be sensitively linked not only to the specific growth method but also the precise deposition conditions used, which may explain why some researchers do not measure any ferromagnetism; it is possible that their specific growth methods and/or deposition conditions do not generate the optimum concentration of defects within the films needed to create the magnetic signal, if the magnetism is indeed linked to defects.

In further support of intrinsic ferromagnetism however, magnetizations of up to 0.12 kA m^{-1} are measured for 220 nm thick undoped films [24] (albeit significantly smaller than many of the values of order 10-100 of kA m^{-1} reported previously) for magnetron sputtered oxygen-deficient samples grown on Al_2O_3 (0001) at 800 °C. A later report [25] measures magnetizations of ~ 10 kA m^{-1} for 90 nm thick films grown by a similar method but using a lower deposition temperature of 300 °C.

Glinchuk *et al.* [26] have very recently developed a theory of oxygen vacancy ferromagnetism for thin films of non-magnetic oxides (including HfO_2) in which oxygen vacancies may become magnetic at the film–substrate interface with the appearance of long-range ferromagnetic order to >> 300 K. The ferromagnetic magnetization is proposed to be uniformly oriented perpendicular to the film surface, while the vacancy accumulation is proposed to be highly substrate-dependent. In addition, an explanation is proposed for the much smaller magnetization values typically measured for nanoparticles compared to thin films; for every nanoparticle the local c-axis (ferromagnetic direction) is directed radially, hence for an ensemble of randomly oriented spherical nanoparticles there is a concomitant reduction in the average value of the spontaneous magnetization.

A summary of some representative magnetization signals measured at room temperature for the undoped HfO_2 films just discussed are summarized in Table 3.1. The data confirm that the largest magnetization values are measured for the thinnest (~ 10 nm thick) films, regardless of substrate used. The anisotropy of the magnetic signals is also evident from the data, with the perpendicular value exceeding the parallel value in the majority of reports. For those reports that attribute the magnetic signals to ferromagnetic impurities, the magnetization values are nevertheless orders of magnitude smaller than the largest reported values attributed to intrinsic defect magnetism.

Table 3.1. Representative room temperature magnetization signals measured for undoped HfO_2 films.

Growth method	Thickness (nm)	M_s (kA/m)	Ref
PLD on r-Al_2O_3 (11-02)	80	12.5 ∥ [i] 50.3 ⊥ [i]	5
PLD on YSZ (100)	192	15.8 ∥ 13.3 ⊥	7
PLD on c-Al_2O_3 (0001)	13	215 ∥ 255 ⊥	7
PLD on YSZ (100)	200	28 ∥ [ii] 3.3 ⊥	16
PLD on YSZ (100)	10	500 ∥	18
PLD on c-Al_2O_3 (0001)	50	30 ∥	19
ALD on SiON coated Si (100)	30	4.2 ⊥ *	23
Magnetron sputtering (300 °C) in Ar/O_2 on c-Al_2O_3 (0001)	90	10 ∥	25
Magnetron sputtering (800 °C) in Ar/O_2 on c-Al_2O_3 (0001) + vacuum annealed	220	0.12 ∥	24
PLD on Si (100) or r-Al_2O_3 (11-02) or $LaAlO_3$ (001)	200	0.1 ∥ **	15

[i] 1st report; similar data presented in [6,7] [ii] similar data also presented in [18]
* attributed to ferromagnetic impurities due to handling with stainless steel tweezers
** attributed to impurities from PLD target and/or substrate

For other nanostructures, RTFM is reported for nanorods and nanocrystals, although the magnetization values are several orders of magnitude smaller than those typically measured for films. Nanorods grown by sol-gel syntheses have been found to exhibit room temperature magnetizations of 125 A m^{-1} (10.6 nm length, 2.3 nm diameter) [27] and 95 A m^{-1} (33 nm length, 9 nm diameter) [28]. The magnetism appears to depend sensitively on the type of surfactant / solvent and processing conditions used in each case. For example, in the former report, while ferromagnetism is measured for samples synthesized using 1-octadecene (solvent) and oleylamine (surfactant), when TOPO (trioctyl phosphine oxide) is employed as both solvent and surfactant paramagnetism alone is measured. In the latter report, only those samples which were annealed at 200 °C for 5 h and subsequently at 400 °C for 5 h in a reducing atmosphere (5% H_2, 95% Ar) exhibited RTFM; samples annealed in the reducing environment at 200 °C for 5 h only were superparamagnetic; the pristine sample (not annealed) was paramagnetic. Elsewhere, for spherical HfO_2 nanoclusters of size 7-12 nm grown by plasma-gas-condensation cluster beam deposition, paramagnetism only was measured at 5 K both for the as-prepared samples and for those which were annealed at temperatures of up to 800 °C in reducing environments [29]; no room temperature magnetization measurements were performed however.

Figure 3.4 displays TEM images obtained from the literature for some undoped hafnia samples which exhibit RTFM.

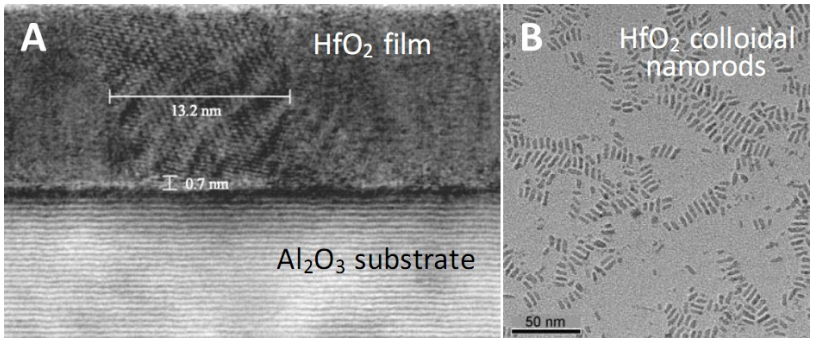

Figure 3.4. TEM images of some undoped hafnia nanostructures from the literature which exhibit RTFM; A = polycrystalline thin film [7], B = colloidal nanorods [27].

Up until this point, a summary of the literature for mainly *undoped* HfO_2 samples, mostly in thin film form grown by PLD, has been presented. However it is also prudent to mention those reports in which magnetism of *doped* HfO_2 samples are presented, typically where the dopant is a transition metal and the doping level is only several atomic %. Experimental evidence is presented in the most of the reports that the transition metal ions do not in fact contribute to the magnetism, which means that the phenomenon is that of dilute magnetic oxides or even d^0 magnetism, since it would appear that the magnetism does not arise from the unpaired *d* or *f* electrons of the dopants. The magnetism for doped films possesses many of the characteristics measured for undoped films, namely a noticeable lack of hysteresis, often a significant anisotropy, and virtual temperature independence of the magnetic signal from low temperatures to several hundred degrees above room temperature. The first experimental report for RFTM in transition metal doped HfO_2 may be found in the paper by Coey *et al.* [7] which focused mainly on undoped HfO_2 films grown by PLD. They find that for doping with various transition metals, the magnetic signals are reduced compared to undoped films. For example, for 80-90 nm thick films grown on either r-cut Al_2O_3 (11-02) or YSZ (100) substrates and doped with 2 % Fe, 2 % Co or 3 % Ti, the in (out) of plane magnetizations are 8.2 (11.6), 4.4 (5.9) and 5.2 kA m^{-1} respectively; in comparison, the corresponding in (out) of plane magnetization for an 80 nm thick undoped film grown on r-cut Al_2O_3 is 12.5 (50.3) kA m^{-1}. A subsequent publication presented RTFM data for ~ 200 nm thick films grown by PLD on YSZ (100) at 750-850 °C in vacuum (10^{-4} - 10^{-6} mbar) doped with 5 at. % Ni [30]. The film with the largest measured magnetization in this report has values of 30 kA m^{-1} (in plane) and 17 kA m^{-1} (out of plane). It is argued that the measured magnetic moments are too large to be due to any precipitation of grains of pure Ni, so that it more likely comes from the doped matrix. The same authors later report RTFM in similarly grown Fe doped films [31], for which M_s = 20 kA m^{-1} for a 130-140 nm thick film. As before, the magnetism is not attributed to the transition metal dopant; here oxygen vacancies are suggested as playing a role, as evidenced by the reduction (in some cases disappearance) of the magnetic signal upon air annealing. Similar results are presented by the same authors in [18]. In contrast, the same group of authors who find no evidence for ferromagnetism in undoped PLD grown HfO_2 films [20], attribute the ferromagnetism of Co doped films (3-5 at. %) to

Co in the same paper, using experimental identification of Co phases from secondary ion mass spectrometry (SIMS), and from energy electron loss spectroscopy (EELS) performed in a transmission electron microscope. The largest magnetization measured is ~ 4.2 kA m^{-1} at room temperature for a 40 nm thick film doped with 5 at. % Co.

Room temperature magnetization values of up to 37 kA m^{-1} for both 30 nm and 60 nm thick amorphous films of $HfAlO_x$ (a mixture of HfO_2 and Al_2O_3 compounds) grown by PLD at 600 °C on Al_2O_3 (0001) substrates are reported by [32]. Smaller magnetizations were measured for similarly thick films grown on Si (100) and MgO (001) substrates. Polycrystalline HfO_2 films, 110 nm thick and doped with 4.7 at. % Co, grown by MBE at 100 C on YSZ (100), have been found to exhibit room temperature magnetization values of up to 5 kA m^{-1} [33]; the magnetism is not ascribed to Co clusters, but to oxygen vacancies; M_s and the shape of the magnetization curve are very similar at 10 K also. In another report, the same authors report a value for M_s of ~ 3.5 kA m^{-1} (at 10 K only) for similarly grown films doped with 10 at. % Co [34]. In further support of their hypothesis for oxygen vacancy mediated magnetism, a structural study of their 10 at. % Co doped films (120 nm thick) by the extended X-Ray absorption fine structure (EXAFS) method finds no evidence for Co clustering [35]. Meanwhile oxygen deficient Co doped films (at. % not given), 220 nm thick, grown by magnetron sputtering at 800 °C on Al_2O_3 (0001) substrates and vacuum annealed, give magnetizations of up to 20 kA m^{-1}, which is ~ 130 % higher than that measured for the as-deposited films before vacuum annealing [24]; the authors are unsure however whether the magnetism is intrinsic or due to metallic Co. In contrast, for thinner films (125 nm thick) grown by the same method but at lower temperature (25 °C) on Si (100) and doped with 1 at. % Ni [36], the largest magnetization of 2.1 kA m^{-1} is proposed to be intrinsic and oxygen vacancy related; upon irradiation with 120 MeV Ni^{9+} ions, the magnetization increases by up to 150 % for a 5×10^{12} ions/cm^2 dose. It is emphasized here that the Ni irradiation does not implant any additional Ni, but only creates structural disorder. Elsewhere, films doped with 6 at. % Y_2O_3, 10 nm thick and grown by PLD on Si at 350 °C in vacuum, exhibit strong anisotropy, with a room temperature saturation magnetization of 12 kA m^{-1} and 55 kA m^{-1} for in and out of plane measurements respectively [37]; the latter signal is the largest reported magnetization for doped HfO_2 films to date.

A summary of some representative magnetization signals measured at room temperature for the doped HfO_2 films just discussed is presented in Table 3.2 in order of the size of the signal measured. The magnetization quoted is for the in-plane measurement unless otherwise stated. The data suggest that the magnetic signal does not sensitively depend on the film thickness. The anisotropy of the magnetic signals is also evident from the data.

Table 3.2. Representative room temperature magnetization signals measured for doped HfO_2 films.

Growth method	thickness (nm)	Dopant (at. %)	M_s (kA/m)	Ref
PLD on Si	10	6 % Y_2O_3	12.5 ∥ 55 ⊥	37
PLD on c-Al_2O_3 (0001)	30, 60	$HfO_2 + Al_2O_3 = HfAlO_{x\ (x=3)}$	37	32
PLD on YSZ (100)	200	5 % Ni	30 ∥ 17 ⊥	30
PLD on YSZ (100)	135	5 % Fe	20	31
Magnetron sputtering on Al_2O_3 (0001) + vacuum anneal	220	Co (% not given)	20 *	24
PLD on YSZ (100)	200	5 % Ni	12	18
PLD on YSZ (100)	90	2 % Fe	8.2 ∥ 11.6 ⊥	7
PLD on YSZ (100)	135	1 % Fe	6	18
PLD on YSZ (100)	80	2 % Co	4.4 ∥ 5.9 ⊥	7
PLD on r-Al_2O_3 (11-02)	90	3 % Ti	5.2	7
PLD on r-Al_2O_3 (11-02)	90	6 % Sc	4.8	7
PLD on r-Al_2O_3 (11-02)	90	20 % Ta	4.3	7
MBE on YSZ (100)	110	4.7 % Co	5	33
PLD on YSZ (100)	40	5 % Co	4.2 **	20
Magnetron sputtering on Si (100) + irradiated with 120 MeV Ni^{9+} ($5x10^{12}$ ions/cm^2)	125	1 % Ni	3.2	36
PLD on Si (100) or r-Al_2O_3 (11-02) or $LaAlO_3$ (001)	200	3 % Gd	0.14 ***	15

* (very) tentatively attributed to Co ** attributed to Co (from SIMS and EELS measurements)
*** attributed to impurities from PLD target and/or magnetic signals from substrate

Some theoretical calculations using DFT have also predicted magnetic moments for doped HfO_2. Hole-doping of hafnia by K, Sr or Al substitution is calculated to give a magnetic moment [38]. It is proposed that the doped holes distribute mainly on the *p* orbitals of the O3 atoms (an O atom surrounded by three Hf atoms, possessing a near trigonal planar structure) near to the dopant. The magnitudes of the magnetic moments calculated are 1, 2, 3, 4 μ_B/monoclinic supercell (2x2x2) for Al, Sr, K and Hf vacancies respectively. In other words, the total number of μ_B/supercell equates to the number of doped holes. In another DFT paper, half-metallic ferromagnetism is calculated for $Hf_{1-x}Mn_xO_{2-\delta}$ when $x_{Mn} > 0.2$ and $\delta < 0.125$ [39]. A maximal moment of $4\mu_B$/Mn is calculated. Lastly, it is calculated that ferromagnetism in Co doped HfO_2 may be mediated by 3-fold co-ordinate O atoms in the monoclinic phase [40], somewhat similar to the scenario proposed by [38]. A maximum magnetic moment of 4.95 μ_B/unit cell is calculated for electron-rich conditions.

Apart from films, there are much fewer experimental reports of magnetism in other doped HfO_2 structures, similar to the case for undoped HfO_2. Low temperature ferromagnetism, with $M_s \approx$

100 kA m^{-1} at 2 K (T_c = 43 K), is reported for 16 at. % Mn doped HfO_2 nanocrystals of ~ 6 nm diameter, synthesized by the sol-gel process in benzyl alcohol and subsequently annealed in air [41]; however the magnetism here is attributed to the formation of ferromagnetic Mn_3O_4 clusters; none of the pristine nanocrystals (nor Cr doped samples) exhibited any ferromagnetism. Elsewhere, Ni doped HfO_2 nanoparticles of ~ 13-14 nm size, synthesized by wet chemical methods, exhibit rather large room temperature magnetizations of 19 kA m^{-1} and 58 kA m^{-1} for 2 at. % and 5 at. % doping levels respectively [42]. No ferromagnetism is measured for undoped, pristine nanopowders. Although the X-Ray photoelectron (XPS) studies within this report also show the presence of a small fraction of Ni metal (most likely Ni nanoclusters) for lightly doped samples, suggesting that the observed room temperature ferromagnetism is at least partly due to Ni nanoclusters, it is argued that the larger magnetization values cannot be entirely attributed to Ni metal clusters. It is further proposed that oxygen vacancies, which mediate the ferromagnetic interactions, are created to retain charge neutrality within the HfO_2 matrix upon replacement of Hf ions by Ni.

3.3. Experimental results

Ferromagnetic-like signals have been measured in vacuum annealed HfO_2 micropowders. The procedure for annealing the samples is briefly summarized, followed by presentation of the results for the magnetic and structural measurements performed.

3.3.1 Vacuum annealing procedure for HfO_2 micropowders

As previously outlined in the experimental methods section (Chapter 2, section 2.1), high-purity commercial HfO_2 powders (Sigma Aldrich 99.95% and Alfa Aesar 99.995%) were placed in acid-cleaned ceramic boats and annealed in vacuum (10^{-5} mbar) for 1 hour in the Indfur temperature controlled furnace at various maximum temperatures in the range 550-850 ºC, using rapid heating and cooling rates (10 ºC/min), in order to further investigate the initial reports of d^0 magnetism in these powders [7]. Approximately 150 mg of sample was used in each separate batch, i.e. separate anneals of discrete powders were performed rather than cumulative anneals of the same powder (unless explicitly stated otherwise). Whereas the as-received powders were white in appearance, upon vacuum annealing the powders turned grey, indicating loss of oxygen (as well as an increase in conductivity) [43,44]. In addition to the magnetization, XRD and electron microscopy characterisation that was previously performed for similarly prepared samples in our laboratory, Raman, photoluminescence, UV-Vis and EPR characterization were also performed for the first time.

3.3.2 Magnetization data

Magnetization measurements were conducted by SQUID magnetometry; typically 40-60 mg of powder was mounted in gelcaps which were placed in long drinking straws. For the vacuum-annealed powders, the measurements were carried out within 1 hour after the time the powders were removed from vacuum (since the powders must be exposed to air before performing the magnetization measurement as it is not possible to transfer the sample under vacuum from the furnace directly to the SQUID). The measured magnetic signals were corrected for the linear diamagnetic background contribution due to the gelcap and powder.

Untreated powders were measured to be diamagnetic, with dimensionless susceptibilities χ of -1.6×10^{-5} and -0.8×10^{-5} for 99.95% and 99.995% nominal purity powders respectively at 300 K. It is noted that the diamagnetic susceptibility is smaller for the higher purity powder. Some of the vacuum annealed samples exhibited ferromagnetic-like signals at room temperature. For all of the annealed powders, after correction of the linear diamagnetic background due to the gelcap, a small diamagnetic signal remained, with a dimensionless susceptibility of typically less than -0.5×10^{-5}, which may be attributed to the powders themselves. Corrected magnetization curves for the 99.95% purity powder subject to various vacuum annealing temperatures and after re-annealing in air (at 650 °C for 1 h) are shown in Figure 3.5. The largest magnetic moment at room temperature, ~ 9×10^{-8} Am^2, was found for the 99.95% purity powder annealed at 700 ºC. Its mass magnetisation of 1.5×10^{-3} Am^2 kg^{-1} corroborates approximately with that found by [7] (1.9×10^{-3} Am^2 kg^{-1}). The virign powder (before annealing), when corrected for the diamagnetic slope, exhibits a barely detectable moment of 1×10^{-9} Am^2, virtually indistinguishable from the background noise level, which may be attributed to an artefact arising from the tiny magnetic moment induced by the pickup coils of the SQUID when the applied magnetic field switches polarity at 0 T, and may be regarded as the practical detection limit for these powders; this is supported by the finding that a signal of ~ $1\text{-}2\times10^{-9}$ Am^2 is also measured for the empty gelcap, and is hence likely due to the pickup coils. The magnetization curves are almost anhysteretic. For the powders exhibiting the largest magnetic signals, it may be estimated that only 10-50 ppm of the sample volume is actually magnetically ordered from analysis of the magnetization curves, assuming $\mathcal{N}$=1/3, which is the case for random isotropic magnetism of spherical particles. By air-annealing the powder which was initially vacuum annealed at 650 ºC, the magnetic signal is significantly diminished.

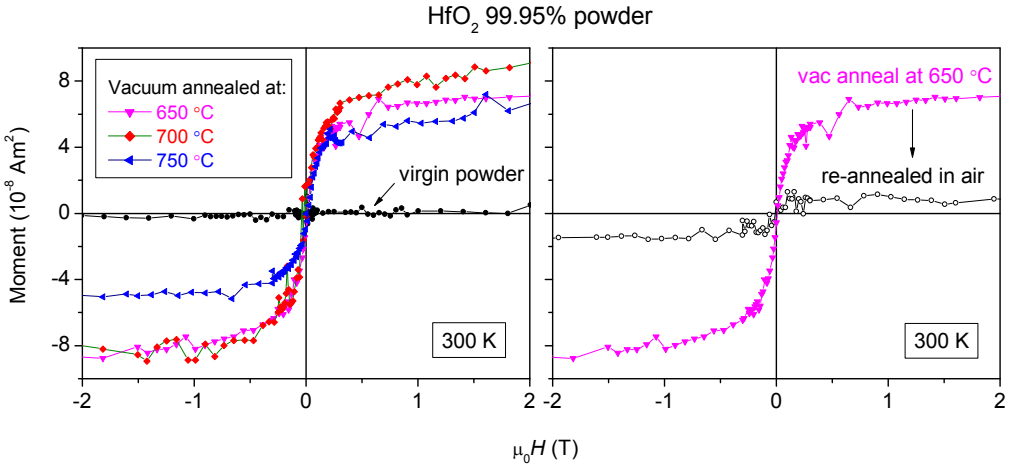

Figure 3.5. Room temperature magnetization curves for HfO_2 99.95% powder, before and after vacuum annealing at various temperatures (left) and after re-annealing in air at 650 °C for 1 h (right). All data has been corrected for the linear diamagnetic background due to the gelcap + powder.

Since vacuum annealing creates oxygen vacancies, transforming the stoichiometric HfO_2 virgin powder into HfO_{2-x}, it is proposed that the RTFM may be related to their presence, which could explain why the ferromagnetism diminishes upon re-annealing in air, since the oxygen vacancies will tend to be re-filled by oxygen; the fact that the magnetic signal does not disappear completely upon re-annealing in air suggest that a small percentage of oxygen vacancies are still retained which help to mediate the ferromagnetism. It is noted however that the largest and most distinct RTFM signals were measured for powders vacuum annealed in the range 650-750 °C only, and not for those which were vacuum annealed at either lower temperatures (500, 550, 600 °C) or higher temperatures (800, 850 °C). *All* of the vacuum annealed powders should be oxygen deficient, and hence *all* should exhibit RTFM according to the previous proposal; hence it is additionally postulated that there must be a certain *optimum concentration* of oxygen vacancy defects required to mediate the magnetism, and that this optimum defect concentration occurs within the vacuum annealing temperature window of 650-750 °C only. It is stated that the magnetism is *mediated* by oxygen vacancies, but it cannot be concluded whether the magnetism is specifically associated with the oxygen vacancies, with hafnium (in the form of Hf^{3+} formed to charge compensate for the oxygen vacancies), or possibly with both. Corrected magnetization curves for the higher purity powder (99.995%) are shown in Figure 3.6. The magnetic moments (and magnetizations) are smaller for the 99.995% vacuum annealed samples than for the 99.95% samples. Figure 3.7 summarizes the variation of magnetic moment and magnetization with vacuum annealing temperature. It was noted that the vacuum annealed sample, upon re-annealing in air at 650 °C for 1 h, changed colour from grey back to white, the same colour as for the virgin powder.

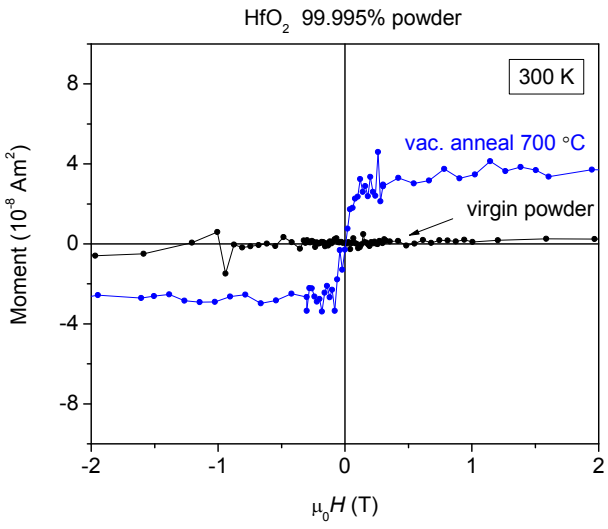

Figure 3.6. Room temperature magnetization curves for HfO_2 99.995% powder, before and after vacuum annealing. All data has been corrected for the linear diamagnetic background due to the gelcap + powder.

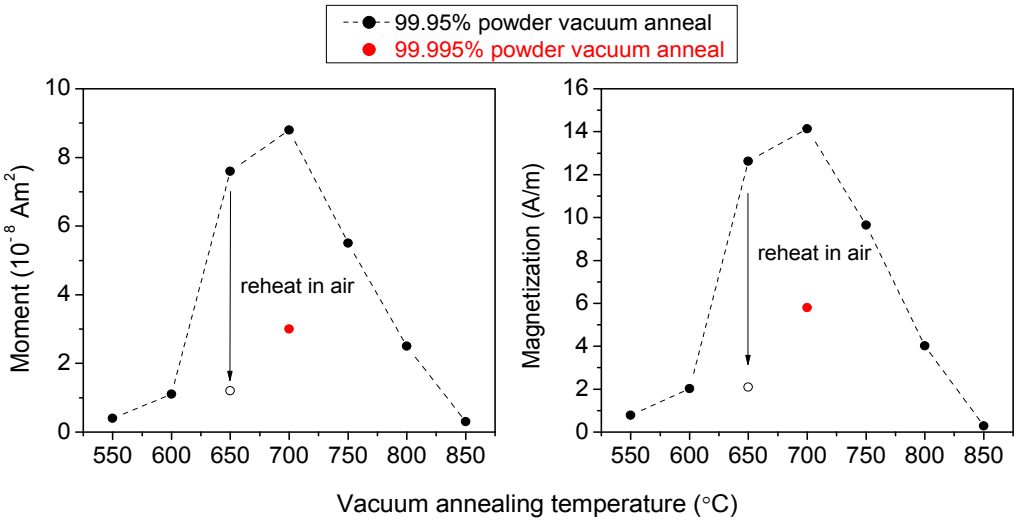

Figure 3.7. Magnetic moment and magnetization as function of vacuum annealing temperature for all HfO_2 powders.

The largest magnetization (14 A m^{-1}) could be explained by ~ 8 ppm of Fe impurities, taking the bulk magnetization of iron as 1.7 kA m^{-1} (1 ppm = 1.7 A m^{-1}). However, ICP-MS analyses confirmed that less than ≤ 1 ppm of Fe, Ni or Co was present in the 99.95% purity powder, and since the virgin powder showed no trace of ferromagnetism at 300 K, it indicates that the trace ferromagnetic impurities are not ferromagnetically ordered at this temperature. In addition, the values of H_0 for the vacuum annealed powders, obtained by extrapolating the initial susceptibility to saturation, lie within the range 100-160 kA m^{-1}; these values are considerably smaller than those typically due to Fe, about 300 kA m^{-1}, as shown in Figure 3.8 on the next page. The dashed lines show where the ferromagnetic volume fraction f, defined as the ratio of the saturation magnetization M_s to the magnetization of the ferromagnetic regions M_0, reaches 100 % for different demagnetizing factors $\mathcal{N}$, where $H_0 = \mathcal{N}M_0$ by definition. For powders, $\mathcal{N}$=1/3 may be used (isotropic approximation for spherical-like morphology). While the magnetic signals may be explained by tens of ppm of magnetite (Fe_3O_4) impurities which have H_0 values of 50-100 kA m^{-1}, more similar to that for reduced HfO_2, this is unlikely from the ICP-MS results. Low temperature magnetization data for the 99.995% purity powder shows no evidence of ferromagnetic impurity phases down to 100 K in applied field (Figure 3.9). It is inferred from the aforementioned evidence that ferromagnetic impurities cannot explain the magnitudes of the magnetic signals measured.

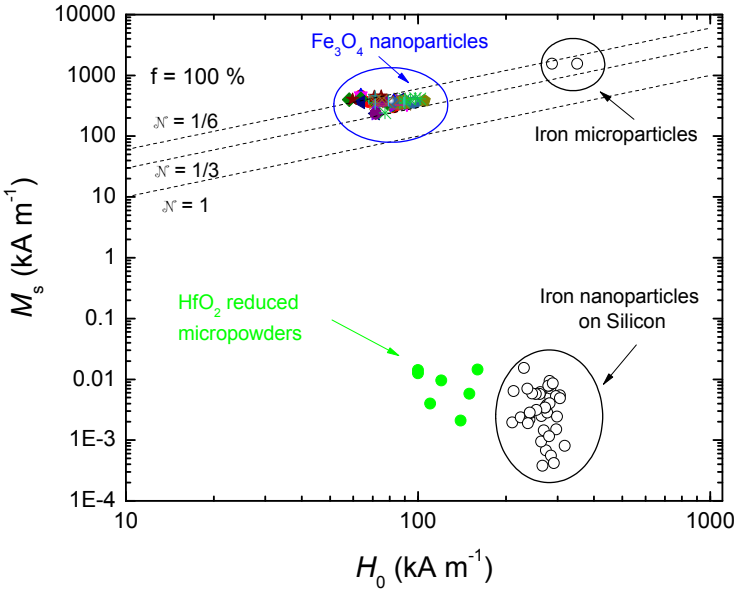

Figure 3.8. Saturation magnetization M_s plotted as a function of H_0 obtained by extrapolation of the initial susceptibility to saturation for reduced HfO_2 micropowders together with values for some ferromagnetic impurities. Only a few ppm of the volume of the HfO_2 samples are magnetically ordered.

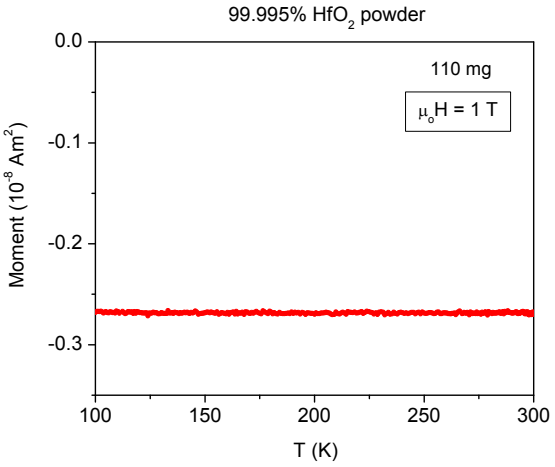

Figure 3.9. Thermal magnetization data measured for 99.995% purity HfO_2 powder in an applied field of 1 T; only diamagnetism (negative moment) is measured down to 100 K.

It is also useful at this point when analyzing the M_s and H_0 values measured here for the reduced HfO_2 micropowders, to compare with data from the literature. By analysis of the magnetization curves presented in published papers, values for the parameters M_s and H_0 may be extracted. Firstly, M_s vs. H_0 data for magnetism measured for undoped HfO_2 samples obtained from the literature are displayed in Figure 3.10. Data for iron samples (microparticles, nanoparticles) are included, while magnetite has been excluded for clarity, but its location on the plot may be deduced by referral to Fig. 3.8, i.e. $M_s \approx$ 300-400 kA m^{-1}, $H_0 \approx$ 50-100 kA m^{-1}.

Data for the reduced micropowders measured in this thesis are denoted and marked in green, while other systems from the literature are colour coded by sample type (films, micropowder, nanorods, bulk). For some of the data points it can be seen that the signals are attributed to ferromagnetic impurities [15,23]. It is evident that all of the H_0 values for undoped HfO_2 samples from the literature are less than that of iron, but some are similar to those of nanoparticular magnetite. It is also clear that M_s for films is typically several orders of magnitude higher than that for micropowders or the bulk. The films shown in Figure 3.10 are generally of order 100 nm thick or greater, but thinner films of order 10 nm thick, encircled in by the solid red line, have the highest M_s values. For the latter films, it can be seen that the ferromagnetic volume fraction f is around 100 %, which means that the samples are virtually completely magnetically ordered throughout their volume.

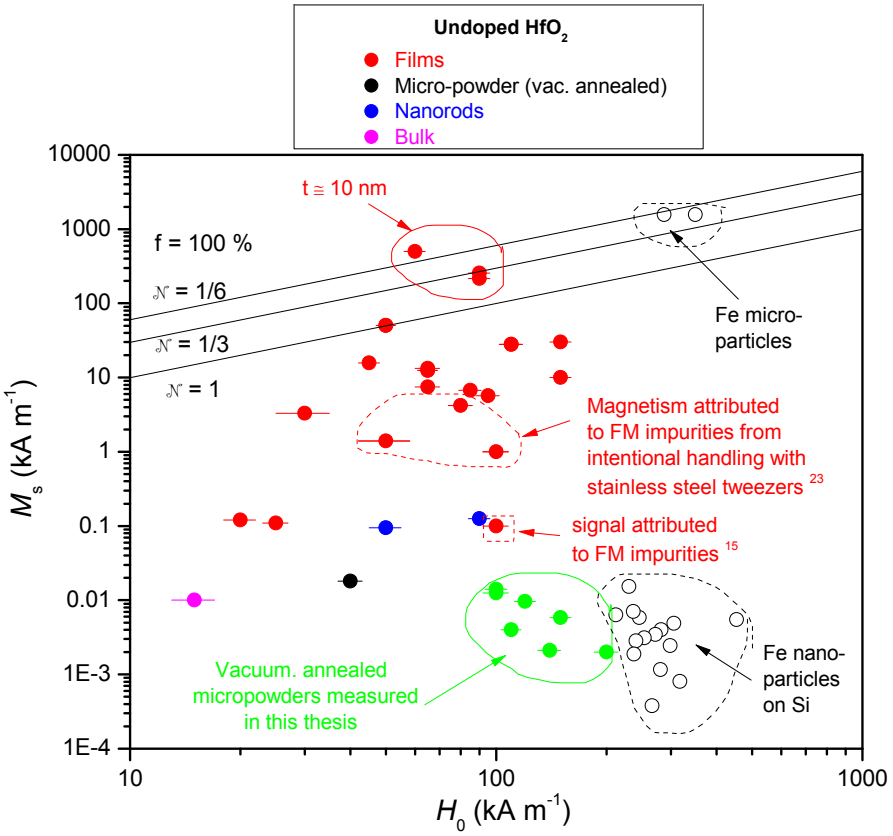

Figure 3.10. M_s and H_0 values for undoped HfO_2 samples from literature reports.

Similar data for M_s and H_0 for doped HfO_2 samples from the literature are shown in Figure 3.11. The majority of the films are of order 100 nm thick. The region where data for magnetite (in nanoparticle form) lies is also shown. Similar to the undoped samples, the values of H_0 are less than that of iron samples, and similar to magnetite. As an illustration, for a HfO_2 sample with M_s = 1 kA m^{-1} and $H_0 \approx$ 80 kA m^{-1}, the latter of which is similar to magnetite, the sample would have to contain about 1 part in 350 (or about 2850 ppm) of magnetite if the magnetic signal was to be entirely accounted for by magnetite impurities, a quantity which

should be readily detected, by SEM-EDX or ICP-MS for example. While the majority of the reports show that the magnetism cannot be attributed to such impurities by performing impurity analyses, the magnetism for some of the data points (for films) is attributed to iron containing impurities by the authors [15,20,24], and are denoted in the figure below.

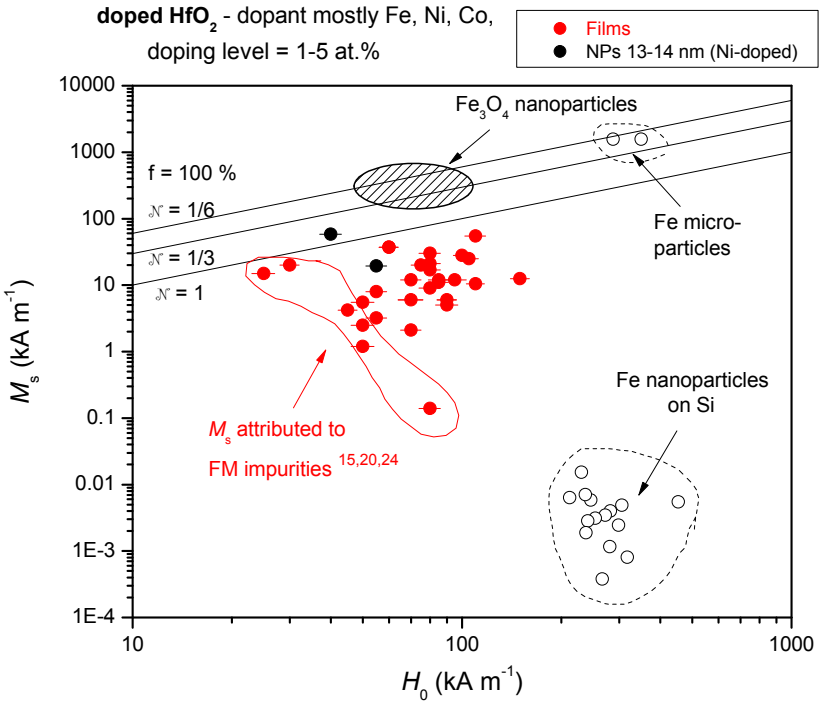

Figure 3.11. M_s and H_0 values for doped HfO_2 samples from literature reports.

Finally, to complete the analysis of M_s and H_0 values, Figure 3.12 on the next page summarizes data for all of the undoped (red dots) and doped (black dots) samples from the literature, together with lots of unpublished data points for films (blue dots) grown by PLD by previous researchers in our group. The films are mostly of order 100 nm thick unless stated otherwise and are typically vacuum annealed and/or doped with a few wt. % of transition metals. The reports which attribute the data points to ferromagnetic impurities may be deduced by referral back to Figs. 3.10 & 3.11. The plot highlights once again that it is again unlikely that ferromagnetic impurities are solely responsible for the magnitude of the magnetic signals, especially for the thinner films, for which 1000s of ppm (in some cases much more) of magnetite or iron would be required to account for these magnetic signals.

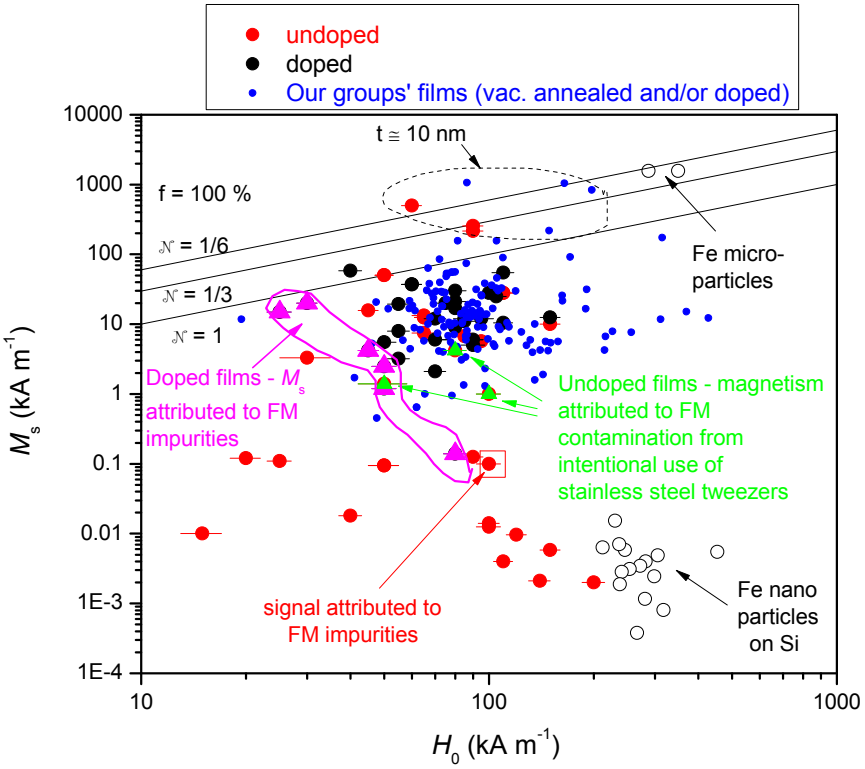

Figure 3.12. ***M_s*** **and** ***H_0*** **values for all HfO_2 samples (both doped and undoped) from literature reports, including unpublished data for films grown by previous researchers in our group.**

3.3.3 X-Ray powder diffraction

Following the magnetization data summarized thus far, some structural data for HfO_2 is now presented. X-Ray powder diffraction data was collected for powders before and after vacuum annealing. Hafnia has three polymorphs with monoclinic, tetragonal and cubic structure at atmospheric pressure. Under ambient conditions, pure HfO_2 tends to appear in the monoclinic phase, which transforms to the tetragonal phase upon heating at 1510-2000 °C, whereas the cubic phase crystallises at temperatures higher than 2700 °C [45]. It was confirmed that all powders here were single phase and monoclinic (space group *P21/a*). The diffractogram for the 99.95% purity powder before annealing is displayed in Figure 3.13. There are approximately 125 indexed peaks for the monoclinic phase in the range 17-120° 2θ. No significant change in lattice parameter upon vacuum annealing, air annealing, or between 99.95% and 99.995% purity powders was measured. A variation in peak position of ± 0.01° was measured between samples; such small deviations of peak position are typically indistinguishable from instrumental shifts however.

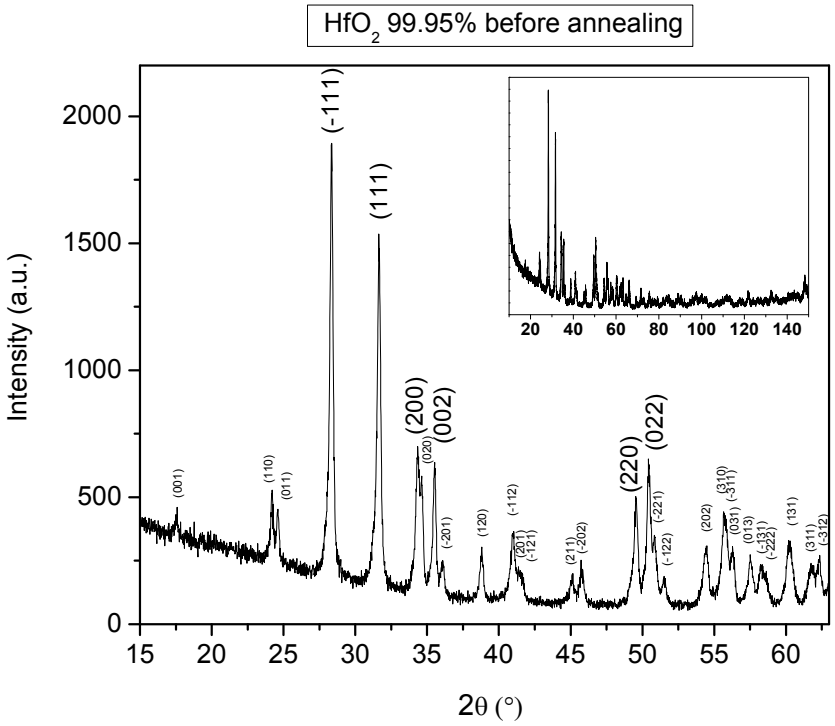

Figure 3.13. XRD data for 99.95% purity HfO_2 virgin powder before annealing. The most intense peaks are indexed in larger font. All peaks are indexed to the monoclinic phase (*P21/a*) of HfO_2. The inset displays the full diffractogram.

The crystallite sizes of the powders, calculated using the Scherrer relation, are shown in Figure 3.14. The crystallite sizes of the 99.95% and 99.995% powders before vacuum annealing are about 65 nm and 100 nm respectively. Vacuum annealing appears to generally increase the crystallite size compared that of the virgin powders. In addition, there is little change in crystallite size when the 99.95% powder which has already been vacuum annealed at 650 °C is then subsequently re-annealed in air.

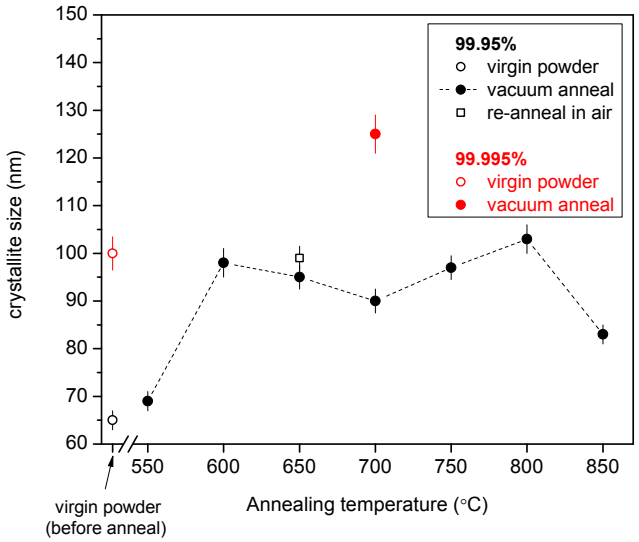

Figure 3.14. Crystallite size for HfO_2 powders calculated from XRD data.

3.3.4 Electron microscopy analysis

An SEM image together with elemental maps determined by EDX of large clumps of the 99.95% purity powder is shown in Figure 3.15. The carbon contribution is due to the carbon tab background in addition to a smaller contribution from carbon deposited during imaging (artifact). No other traces of elements were detected. The hafnium oxide is slightly reduced, although this is likely due to reduction of the oxide in the electron beam – this effect, together with dependence of the oxide stoichiometry on precise acquisition conditions (such as acquiring a spot versus an area scan, focusing on large versus small clumps, tuning electron energy to probe the surface versus the bulk) means that a comparative study of stoichiometry of powders before and after annealing is rather complex, and was not undertaken here.

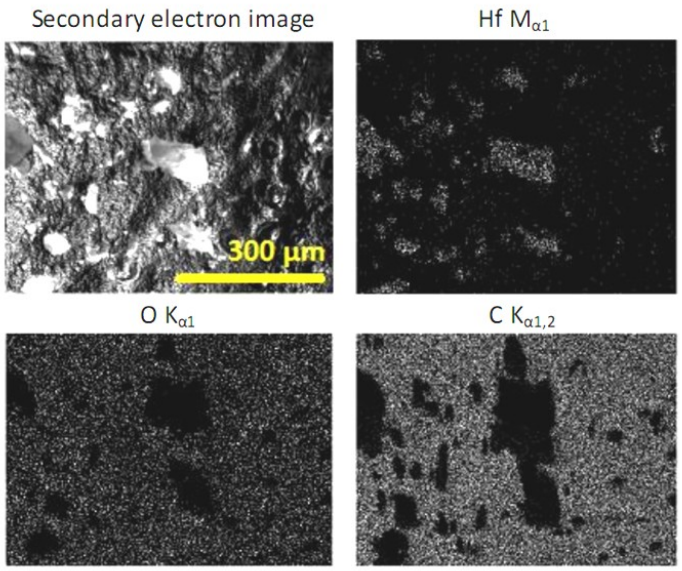

Element	Weight %	Atomic %
C_K	4.67	9.65
Hf_M	76.73	24.39
O_K	18.60	65.96

Figure 3.15. SEM-EDX elemental maps of HfO_2 99.95% virgin powder; the stoichiometry is $HfO_{1.97}$.

SEM images of 99.95% HfO_2 powder dispersed in ethanol, both before and after vacuum annealing, are shown in Figure 3.16. The in-lens detector was used to acquire the images, which provides good depth resolution. The low magnification images show that clumps of particles are of order 1 µm size, and that the clumps are composed of many aggregated crystallites of ~ 60-90 nm size, in approximate agreement with the sizes estimated from the XRD peak broadening. Very similar images were obtained of dispersions of 99.995% HfO_2 powder.

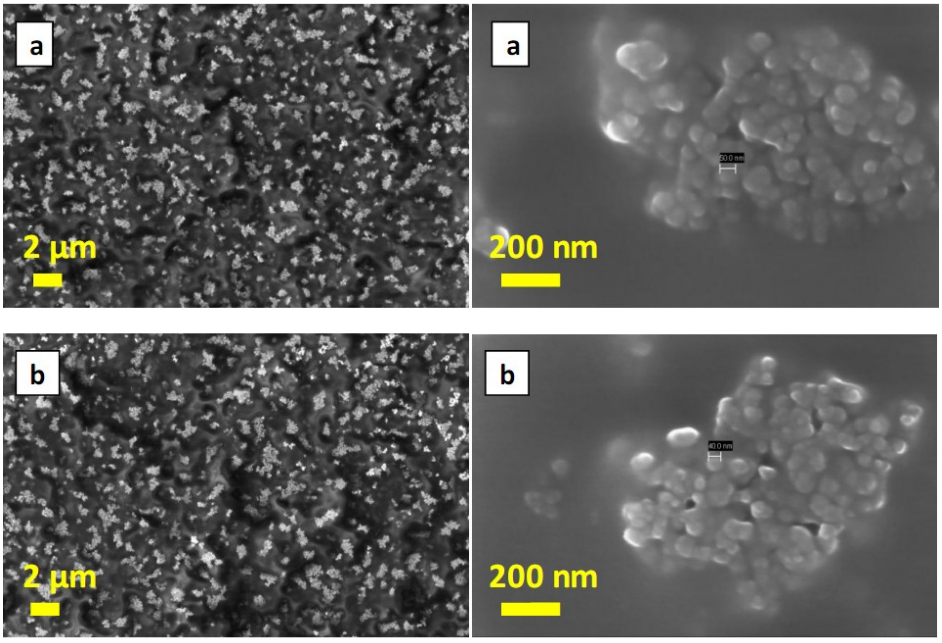

Figure 3.16. SEM images of HfO_2 99.95% powder (a) before and (b) after vacuum annealing at 750 °C.

In order to obtain higher resolution images of the nanostructure of the powders, TEM was performed. Powders were dispersed in ethanol and dropped onto lacey carbon TEM grids for imaging. Representative electron images of the 99.95% powder are shown in Figure 3.17. Many of the particles appear to be fused, especially when viewed at higher magnifications, and some appear faceted. Images of the particles in reciprocal (diffraction) space revealed many spots, indicating a large crystalline component.

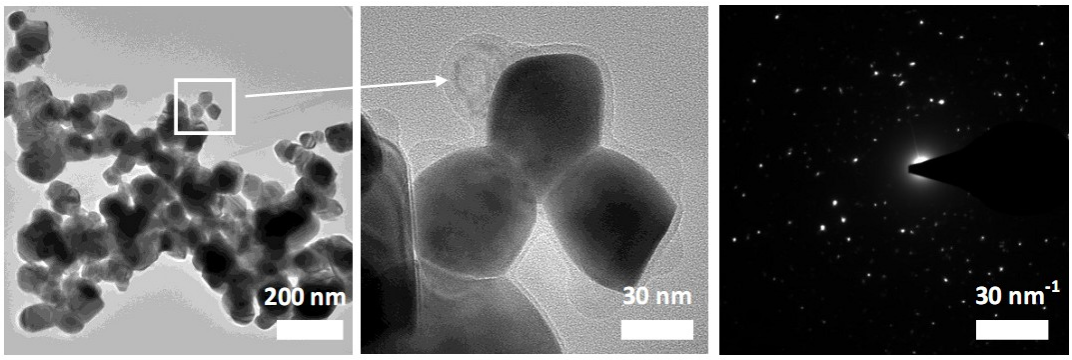

Figure 3.17. TEM images (left and centre) and electron diffractogram (right) of HfO_2 99.95% virgin powder.

3.3.5 Raman spectroscopy

Further structural information concerning the powders was obtained by Raman spectroscopy measurements. Raman spectra measured for the 99.95% purity powder before and after vacuum annealing are displayed in Figure 3.18. The Raman peaks for the powder before annealing may be attributed to the monoclinic phase (marked in Fig. 3.18) as have been reported experimentally elsewhere [46].

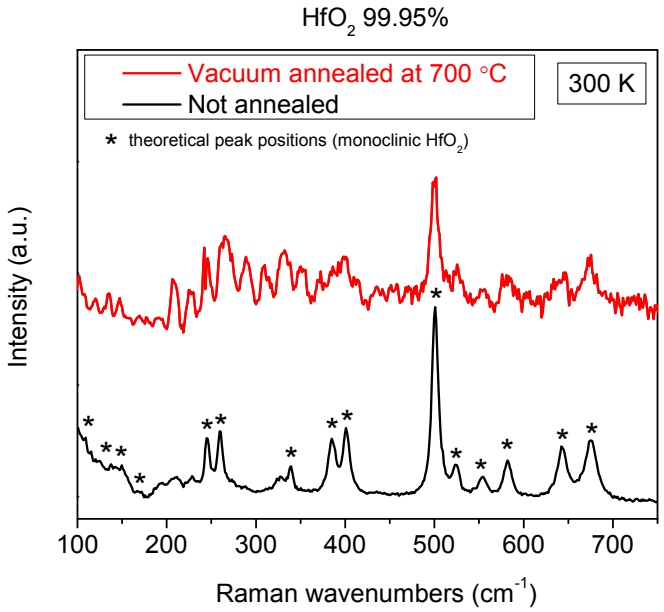

Figure 3.18. Raman spectra measured for 99.95% purity HfO_2 powder before and after vacuum annealing.

It has also been calculated from first principles [47] that the monoclinic structure of HfO_2 possesses 36 phonon modes, 18 of which are Raman-active ($9A_g + 9B_g$), 15 of which are IR-active ($8A_u + 7B_u$), with the remaining 3 corresponding to zero-frequency translations. The cubic and tetragonal phases may be distinguished from the monoclinic phase by the presence of strong peaks at 620 cm^{-1} [48] and 276 cm^{-1} [49] respectively. Since the aforementioned peaks are not found here, only the monoclinic crystalline phase must be present, as found previously by XRD. For the vacuum annealed powder, the peaks are less intense and exhibit some additional peaks compared to the virgin powder; the reduction in peak intensity in addition to the presence of some extra peaks may reflect loss of symmetry due to defects such as vacancies induced by vacuum annealing. In addition, the background intensity contribution, due to fluorescence, is enhanced for the vacuum annealed powder. No systematic variations were measured however between spectra measured for powders vacuum annealed at different temperatures (550 – 850 °C).

3.3.6 Photoluminescence spectroscopy

Photoluminescence (PL) emission spectra for 99.95% purity HfO_2 powders were acquired at room temperature within the visible range (500-700 nm) for excitation at a wavelength of 488 nm, which corresponds to an energy of 2.54 eV. Measurements were performed for powders both before and after vacuum annealing; the PL spectra are shown in Figure 3.19 below.

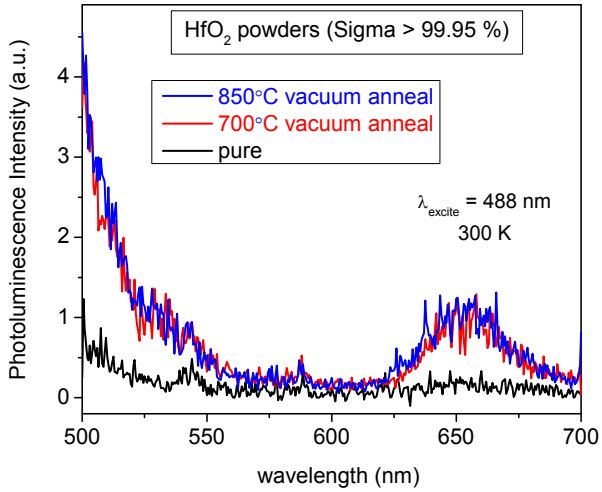

Figure 3.19. Photoluminescence emission spectra measured for 99.95% purity HfO_2 powder before and after vacuum annealing at the indicated temperatures.

The increased PL signal intensity at 650 nm (1.9 eV) for the vacuum annealed powders may be attributed to oxygen vacancies, which have also been measured for 120 nm thick e-beam deposited HfO_2 films [50], which may decrease the effective band-gap from the theoretical value of ~ 5.7 eV. No such feature is measured for the pure 99.95% powder before annealing. The appearance of the oxygen vacancy feature at 650 nm within the visible spectrum for the vacuum annealed powders may possibly be correlated with the transition in colour of the powders from white to grey upon vacuum annealing. Note that the intensity of the oxygen vacancy related feature is the same for both ferromagnetic (700 °C) and non-ferromagnetic (850 °C) vacuum annealed powders, which indicates that the presence of oxygen vacancies alone is not sufficient to explain the existence of ferromagnetism in vacuum annealed HfO_2 powders. The large increase in PL intensity at 500 nm is an artifact from the excitation wavelength used (488 nm). Elsewhere, a report for HfO_2 rice-like nanostructures (of particle width 15-75 nm) measures a green emission (548 nm) in the PL spectrum [51], while another report for HfO_2 thin films grown by chemical vapour deposition (CVD) attributes a PL feature measured at 4 eV (~ 300 nm) to an OH^- radical species [52].

3.3.7 Ultraviolet-Visible spectroscopy

Ultraviolet-Visible (UV-Vis) absorbance spectra were acquired at room temperature for 99.95% purity HfO_2 powders, both before and after vacuum annealing, and are shown in Figure 3.20 (a). The optical bandgap of monoclinic HfO_2 is indirect [53], and may be estimated by plotting $(\alpha h\nu)^{1/2}$ versus photon energy and determining the x-axis intercept of the slope. Such plots are shown in Figure 3.20 (b) and yield similar values of 5.21 eV and 5.19 eV for the indirect bandgap for pure and vacuum annealed powders respectively, which are smaller than the theoretical (bulk) value of ~ 5.7 eV. No systematic variations were measured between spectra measured for powders vacuum annealed at different temperatures (550 – 850 °C) however.

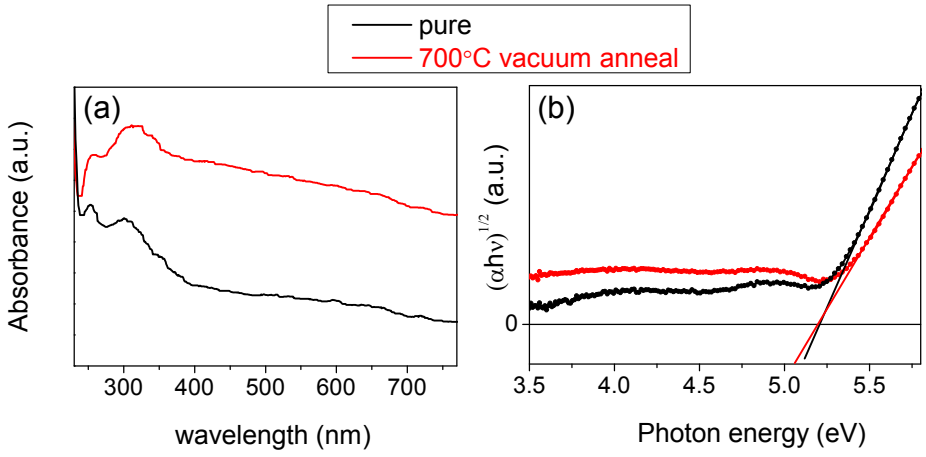

Figure 3.20. (a) UV-Vis spectra measured for 99.95% purity HfO_2 powder before and after vacuum annealing at 700 °C; (b) Corresponding indirect bandgap estimate from UV-Vis data.

In comparison to other literature reports which also deduce the bandgap from UV-Vis measurements, an indirect optical bandgap of 5.54 eV is measured for monoclinic HfO_2 films [54], while direct bandgaps in the range 5.92 – 6.08 eV are measured for films with different ratios of cubic to monoclinic phases [55]. A much smaller value of 3.31 eV is measured for the indirect bandgap of HfO_2 rice-like nanostructures [51]. For EELS measurements, which probe both the direct and indirect bandgaps, a value of 5.3±0.5 eV is measured for HfO_2 thin films for example [56]. All of the bandgaps quoted above were primarily as part of optical studies of HfO_2 only, and as such, their magnetic properties were not measured or mentioned in those publications. Meanwhile for magnetic HfO_2 nanorods, the bandgap is reported to be slightly

reduced (by up to ~ 1 eV) from the bulk value [27]; the bandgap reduction is proposed to be due to the formation of impurity bands associated with oxygen vacancies in the defect-rich HfO_2 lattice.

3.3.8 Electron paramagnetic resonance spectroscopy

Electron paramagnetic resonance (EPR) spectroscopy measurements at room temperature and pressure were performed in order to search for possible ferromagnetic phases, in addition to any paramagnetic centres, for the vacuum annealed HfO_2 99.95% and 99.995% powders, since vacuum annealing of the powders is found to produce distinct ferromagnetic-like signals (as measured by SQUID magnetometry) for those which were vacuum annealed at 650-750 °C in particular. EPR measurements were conducted at ambient pressure within several hours of the magnetization measurements finishing; as mentioned previously, in order to perform the initial magnetization measurements, the vacuum must be broken, after which the EPR measurements were then performed, which means that the powders have typically been exposed to air for several hours by the time the EPR measurement is conducted. Typically 15-20 mg of powder was used in each measurement; the exception was the 99.995% purity powder, for which 40 mg was used (in order to detect the relatively weaker EPR signal). All signals were subsequently normalized for mass. Powders were inserted into spin-free quartz tubes (4 mm inner diameter); the tubes were first pre-cleaned with de-ionized water, ethanol and finally acetone, and dried for several hours in a drying cabinet at 50 °C. The empty tubes were also scanned alone prior to adding the powders in order to make sure that there were no impurities residing within the tubes that would give EPR or FMR (ferromagnetic resonance) signals. None of the powders, either as-received or after vacuum annealing (and subsequent air exposure for several hours in order to measure the magnetization measurement first before the EPR measurement) produced any reduction in the EPR cavity Q-factor upon insertion, which indicates that the samples are not conductive.

EPR spectra for the 99.95% powder annealed under vacuum at various temperatures (and subsequently exposed to atmospheric pressure for several hours) are shown in Figure 3.21. Wider field ranges than those shown of 0.1-0.6 T were also scanned, but no evidence of any ferromagnetic resonance signals (with centres far from 0.35 T or $g \approx 2$ due to the expected additional internal magnetic field contribution) were detected after subtraction of the small background contribution due to the cavity (no contribution to the signal from the EPR tubes alone were detected).

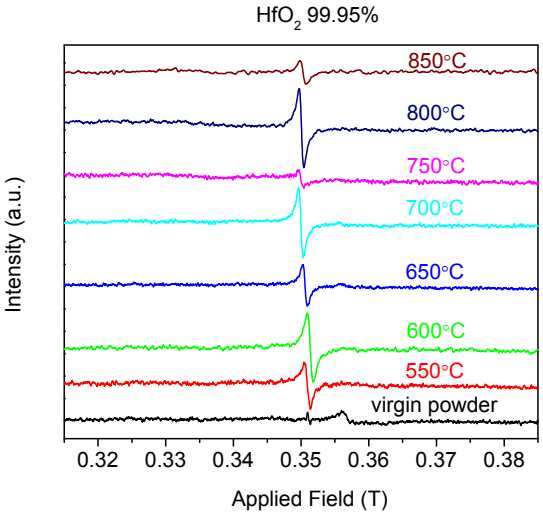

Figure 3.21. EPR spectra measured at room temperature for individual 99.95% purity HfO_2 powder samples after vacuum anneals at 1 hr at the indicated temperatures. The virgin (not annealed) powder spectrum is also shown. The vacuum annealed samples were exposed to atmospheric pressure for several hours before the EPR measurement, in order to first perform the magnetization measurements which necessitated a breaking of the vacuum in order to mount the sample.

All of the spectra for the vacuum annealed samples exhibit symmetrical signals with peak to peak widths in the range 0.7-0.95 mT, contain ~ 2-6×10^{15} spins per gram, and possess g values in the range 2.0017-2.0023. The g value for the free electron, g_e, is 2.0023. Here, a g value of 2 corresponds to an applied field of ~ 0.351 T under the typical acquisition conditions used for each measurement. Since 1 mole of HfO_2 (210.6 grams) contains 6×10^{23} atoms, or 2.8×10^{21} atoms/gram, 2×10^{15} spins/gram is equivalent to a paramagnetic concentration of ~ 1 ppm. Figure 3.22 below displays the values for the numbers of spins per gram and peak to peak widths ΔB_{pp} for the spectra shown previously in Fig. 3.21.

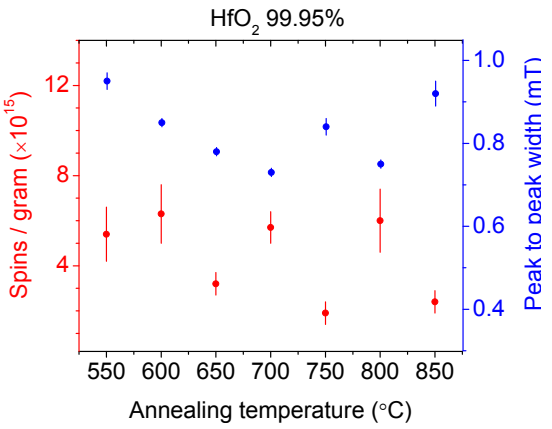

Figure 3.22. Numbers of spins per gram and peak to peak widths of EPR signals for vacuum annealed 99.95% purity HfO_2 powders shown in previous figure (Fig. 3.21).

Similar signals to those shown in Figure 3.21 have been measured before for 99.995% purity (Alfa Aesar) vacuum annealed powders (monoclinic phase) [57], henceforth referred to as the publication of Wright *et al.*, which they denote HfAA, for which they measure single isotropic lines of Lorentzian shape with g values of 2.0025±0.0003 for powders vacuum annealed at 300-750 °C. It is important to emphasize however that Wright *et al.* [57] measure the EPR spectra of their powders *in vacuum*, and do not break the vacuum between the vacuum anneal and subsequent EPR measurements, whereas our powders are *exposed to air for several hours* (in order to perform the magnetization measurement first) and subsequently the EPR spectra are measured at atmospheric pressure rather than in vacuum. Wright *et al.* [57] denote the signal for HfAA with g ≈ 2.0025 as H4 and consider many possibilities as to its origin such as F centres (an electron trapped in an oxygen vacancy) at the surface or conduction electron spin resonance (CESR) from precipitated Hf metal. It is interesting to note that the powders change colour from colourless (white) to grey upon vacuum annealing, and that signal H4 only appears upon vacuum annealing. It has also been recently postulated that the H4 signal may be due to unpaired electrons from carbon, due to contamination from the air (almost every surface exposed to air has carbon present) or from the vacuum pump oil (from the pump used in the vacuum annealing process) or arising from acetone used to clean the EPR tubes and ceramic boats in which the HfO_2 powders are vacuum annealed [58]. In reducing conditions at high temperature any carbon containing compounds or oxides will be reduced to elemental carbon. In order to test this hypothesis, an EPR tube was liberally rinsed with acetone, left it to dry in a drying cabinet at 60 °C for 2 h, after which the tube was subjected to an EPR measurement at ambient conditions; no EPR signal was resolved. Thereafter, the tube was vacuum annealed for 1 h in a separate furnace at 700 °C using rapid heating/cooling rates of about 10 °C/min and an EPR measurement was performed again under ambient conditions as the vacuum must be broken in order to transfer the tube from the furnace to the EPR spectrometer. There was a visible blackish residue along the length of the inside of the tube, and a symmetric signal similar to H4 was measured, with a g value of 2.0023(1), ΔB_{pp} of 0.8 mT, and containing of order 10^{17} spins/gram. Hence an additional explanation for signal H4 is that the vacuum annealed HfO_2 powders are contaminated with carbon. It is also noted that the g values, EPR linewidth variation and relaxation behaviour of the H4 signal measured by Wright *et al.* [57] are similar to those measured for carbon radicals in amorphous hydrogenated carbon by Barklie *et al.* [59,60] previously.

Wright *et al.* [57] also show that 99.95% purity powder (Sigma Aldrich), denoted HfA1, exhibits similar EPR spectra to higher purity 99.995% powder, HfAA. At a vacuum annealing temperature of 750 °C they measure a maximum spin concentration of $(1.0\pm0.2)\times10^{17}$ cm^{-3}, equivalent to ~ $(1.0\pm0.2)\times10^{16}$ spins/gram, or approximately twice as large as the largest signals that we measured. The higher spin concentrations measured by Wright *et al.* [57] are due to the fact that they measured the EPR signals of their powders under vacuum annealing in-situ, whereas our powders were exposed to air for several hours between the vacuum annealing and subsequent EPR measurements as previously mentioned. During this time the number of oxygen vacancies created by vacuum annealing will have decreased due to oxidation. We note that for the pure 99.95% powder before annealing, two distinct signals are measured, denoted H2 and H1 in Figure 3.23

below, following the labeling convention of Wright *et al.* [57]. In contrast to their measurement, where they measure only $(2\pm1)\times10^{13}$ spins/gram for H1 for both the 99.95% and 99.995% as-received (virgin) powders, we measure a value of $(3\pm1)\times10^{15}$ spins/gram for the 99.95% as-received virgin powder, about 2 orders of magnitude higher than that measured by Wright *et al.* [57]. The number of spins/gram for H2 that we measure, $(5\pm2)\times10^{13}$, is of a similar magnitude however to that measured by Wright *et al.* [57], who measure $(8\pm2)\times10^{13}$ spins/gram. The authors do however measure larger H1 signals for powders of 99.9% purity or less. They attribute signal H1 to Hf^{3+} in coordinatively unsaturated sites at or near the surface of the powder particles, while signal H2 is due to centres with S=1/2 and orthorhombic symmetry; these centres are suggested by Wright *et al.* [57] to be trapped electron centres due to the fact that their principal g values are just less than or equal to the free electron value. Meanwhile recent DFT calculations have indicated that H1 could be a V^+ centre [61]. For our measurements, upon vacuum annealing of the 99.95 % purity HfO_2 powder at 650 °C, there is a decrease in H1 signal intensity (from 3×10^{15} to 3×10^{14} spins/gram) accompanied by the appearance of the H4 signal, as shown in Figure 3.23. As for all of the vacuum annealed powders, it is re-emphasized that by the time the EPR measurement is conducted they have been exposed to air (ambient conditions) for several hours. Upon re-annealing in air at 650 °C for 1 h, H4 disappears and H1 increases in intensity to $(1\pm0.5)\times10^{15}$ spins/gram, although the intensity of H1 does not quite recover to its value in the virgin state; Wright *et al.* [57] actually measure an *increase* in intensity for H1 for their air-annealed sample as compared to the virgin powder. It is observed that the powder recovers its original white colour upon re-annealing in air for 1 h at 650 °C, consistent with the elimination of possible F centres associated with signal H4. For the 99.95% powder we do not measure the weak signal denoted H3 by Wright *et al.* [57] which they attribute to holes trapped on oxygen. If H1, H2, H3 are not uniformly distributed then their local concentrations will be different, which may partly explain some of the discrepancies in the values of the absolute spin concentrations between our measurements and those of Wright *et al.* [57].

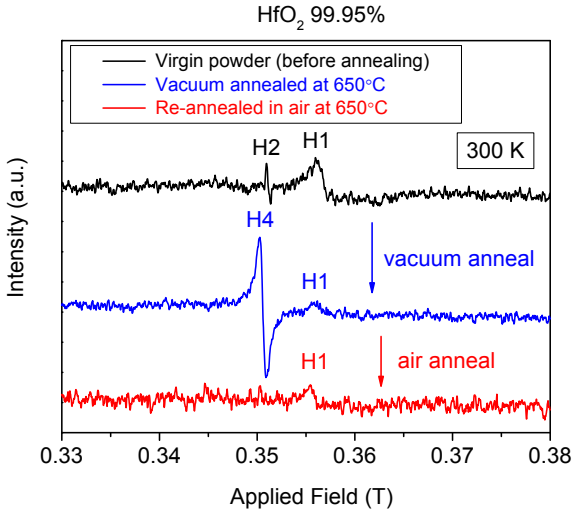

Figure 3.23. EPR spectra measured at room temperature for 99.95% purity HfO_2 powder before and after vacuum annealing (+ subsequent air exposure at room temperature for several hours) and after re-annealing in air at 650 °C for 1 h.

EPR spectra measured under ambient conditions for the 99.995% purity powder both before and after vacuum annealing (with a delay time between the vacuum anneal and EPR measurements of several hours during which the powder was exposed to air in order to mount it for the magnetization measurements at 300 K, similar to the 99.95% purity powders) are shown in Figure 3.24. Weak signals H2 and H1 are measured for the virgin powder, which contain $(5\pm3)\times10^{13}$ and $\leq10^{13}$ spins/gram respectively. Wright *et al.* [57] measure $(8\pm2)\times10^{13}$ and $(5\pm2)\times10^{13}$ spins/gram for H2 and H1 respectively in the same powder. Upon vacuum annealing at 700 °C, signal H4 appears (similar to the 99.95% powder) containing $(8\pm2)\times10^{15}$ spins/gram, which is accompanied by a weak H1 contribution containing only $(3\pm2)\times10^{13}$ spins/gram. In comparison, Wright *et al.* [57] measure $(1\pm0.2)\times10^{16}$ spins/gram for H4, but for the powder vacuum annealed at a slightly higher temperature of 750 °C, and they do not resolve signal H1. Once again, it is reminded that Wright *et al.* [57] measure the EPR spectra of their powders in vacuum, and do not break the vacuum between their vacuum annealing and EPR measurement steps, whereas our powders are exposed to air for several hours before measurement of the EPR spectra at air under ambient conditions.

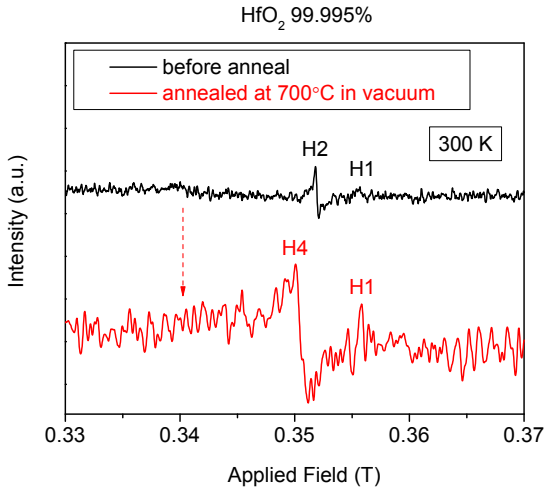

Figure 3.24. EPR spectra measured at 300 K for 99.995% purity HfO_2 powder before and after vacuum annealing (+ subsequent air exposure at room temperature for several hours).

Wright *et al.* [57] also conduct some structural measurements not performed here which provide some extra useful information pertaining to the 99.95% and 99.995% purity powders. By measuring the surface area per unit mass of their powders using the Brunauer–Emmett–Teller (BET) method of gas adsorption, they measure 1.3 and 3.3 m^2/g for the 99.95% and 99.995% purity powders respectively. The authors also estimate particle diameters of 0.46 and 0.18 μm for the 99.95% and 99.995% purity powders respectively assuming spherical particles, and that the ratio of bulk to surface atoms is typically greater than about 100:1. They also note that grinding has no effect on the EPR signal for the 99.95% powder. Here the powders were not ground. Interestingly they measure 10 ppm of iron in their 99.95% powder by ICP-MS, whereas we measured ≤ 1 ppm.

Nevertheless, no iron impurities (in the form of Fe^{3+}) were detected by wide-field EPR scans at 300 K (a more sensitive detection method than ICP-MS) by either Wright *et al.* [57] or during our measurements. For the 99.995% purity powder Wright *et al.* [57] measure ≤ 1 ppm of iron. Finally it is noted that some of the results in the definitive paper by Wright *et al.* [57] have been published previously by the same authors in less detail in shorter conference papers [62-65].

In summary, several paramagnetic features are measured for high purity vacuum annealed HfO_2 powders; signal H1 attributed to Hf^{3+} in coordinatively unsaturated sites at or near the surface of the powder particles and/or a V^+ centre, and H4 which may correspond to F centres, precipitated Hf metal and/or carbon impurities. For the virgin powder, signal H1 is measured in addition to H2, the latter of which corresponds to orthorhombic centres with S=1/2. Upon air annealing, only signal H1 remains. No evidence of any broad ferromagnetic resonance signals were detected for any of the powders, including the 99.95% powders which were vacuum annealed at 650-750 °C and which displayed the largest room temperature ferromagnetic properties from magnetometry measurements; this does not conclusively rule out their presence however, since it is possible that the ferromagnetic-like signal is broadened out so much at 300 K that it could elude detection.

3.4. Summary

Weak room temperature ferromagnetism was measured by SQUID magnetometry for high purity HfO_2 micropowders which were vacuum annealed at 650-750 °C. The largest magnetic signal measured was 9×10^{-8} Am^2, corresponding to 14 A m^{-1}. The samples were exposed to air after vacuum annealing for a short duration (< 1 h) prior to the magnetization measurement in order to mount the samples for the measurement. No ferromagnetism was measured for the virgin powders, while the magnetic signal for the ferromagnetic vacuum annealed powders was diminished upon re-annealing in air for 1 h at 650 °C. The magnetism is virtually anhysteretic, and from analysis of the magnetization curve it may be estimated that only a small fraction (10s of ppm) of the samples are magnetically ordered. Ferromagnetic contamination is ruled out as a source of the magnetic signals from ICP-MS and SEM-EDX analyses. It is hence proposed that the magnetism is likely related to defects, primarily oxygen vacancies, induced by vacuum annealing, which occupy a defect-based impurity band, which can become spin-split and result in high temperature Stoner ferromagnetism when the density of states at the Fermi level is sufficiently high. The appearance of magnetism within a narrow range of annealing temperatures only suggests that there is an optimum concentration of oxygen vacancies for mediating the magnetism.

Lastly it is also noted here that in addition to HfO_2, vacuum annealing experiments were also conducted for commercial tungsten trioxide (WO_3) powder of 99.9% nominal purity, for which RTFM was measured, although the maximum magnetization of ~ 1.4 A m^{-1} was about an *order of magnitude smaller* than that measured for the largest of the HfO_2 signals. The results are briefly summarized in Appendix A.1. It is also important to note that previous experiments (pre-2009) conducted by other researchers in our group *did not measure any RTFM* for vacuum annealed commercial TiO_2, CeO_2 or ZrO_2 powders, and no RFTM for any of the oxide powders (HfO_2, WO_3, TiO_2, CeO_2 or ZrO_2) which were annealed in an Ar/H atmosphere.

3.5. References

[1] G. D. Wilk, R. M. Wallace, and J. M. Anthony, Journal of Applied Physics **89**, 5243 (2001).

[2] H.-Y. Lee, P.-S. Chen, C.-C. Wang, S. Maikap, P.-J. Tzeng, C.-H. Lin, L.-S. Lee, and M.-J. Tsai, Japanese Journal of Applied Physics Part 1-Regular Papers Brief Communications & Review Papers **46**, 2175 (2007).

[3] P. Broqvist and A. Pasquarello, Applied Physics Letters **89**, 262904 (2006).

[4] E. Hildebrandt, J. Kurian, and L. Alff, Journal of Applied Physics **112**, 114112 (2012).

[5] M. Venkatesan, C. B. Fitzgerald, and J. M. D. Coey, Nature **430**, 630 (2004).

[6] J. M. D. Coey, Solid State Sciences **7**, 660 (2005).

[7] J. Coey, M. Venkatesan, P. Stamenov, C. Fitzgerald, and L. Dorneles, Physical Review B **72**, 024450 (2005).

[8] A. Foster, F. Lopez Gejo, A. Shluger, and R. Nieminen, Physical Review B **65**, 174117 (2002).

[9] C. Das Pemmaraju and S. Sanvito, Physical Review Letters **94**, 217205 (2005).

[10] J. Osorio-Guillén, S. Lany, S. Barabash, and A. Zunger, Physical Review B **75**, 184421 (2007).

[11] J. I. Beltrán, M. C. Muñoz, and J. Hafner, New Journal of Physics **10**, 063031 (2008).

[12] G. Chen, Q. Zhang, X. Gong, and S. Yunoki, Journal of Physics: Conference Series **400**, 032008 (2012).

[13] J. Zheng, G. Ceder, T. Maxisch, W. Chim, and W. Choi, Physical Review B **75**, 104112 (2007).

[14] G. Bouzerar and T. Ziman, Physical Review Letters **96**, 207602 (2006).

[15] W. Wang, Y. Hong, M. Yu, B. Rout, G. A. Glass, and J. Tang, Journal of Applied Physics **99**, 08M117 (2006).

[16] N. Hong, J. Sakai, N. Poirot, and V. Brizé, Physical Review B **73**, 132404 (2006).

[17] N. H. Hong, J. Sakai, and F. Gervais, Journal of Magnetism and Magnetic Materials **316**, 214 (2007).

[18] N. H. Hong, physica status solidi (c) **4**, 1270 (2007).

[19] J. Y. Yang, Y. Sun, L. He, C. M. Xiong, R. F. Dou, and J. C. Nie, Journal of Applied Physics **109**, 123908 (2011).

[20] M. S. Ramachandra Rao, et al., Applied Physics Letters **88**, 142505 (2006).

[21] N. Hadacek, A. Nosov, L. Ranno, P. Strobel, and R. M. Galéra, Journal of Physics: Condensed Matter **19**, 486206 (2007).

[22] D. Y. Cho, J. M. Lee, S. J. Oh, H. Jang, J. Y. Kim, J. H. Park, and A. Tanaka, Physical Review B **76**, 165411 (2007).

[23] D. W. Abraham, M. M. Frank, and S. Guha, Applied Physics Letters **87**, 252502 (2005).

[24] J. Ran and Z. Yan, Journal of Semiconductors **30**, 102002 (2009).

[25] K. K. Bharathi, S. Venkatesh, G. Prathiba, N. H. Kumar, and C. V. Ramana, Journal of Applied Physics **109**, 07C318 (2011).

[26] M. D. Glinchuk, E. A. Eliseev, V. V. Khist, and A. N. Morozovska, Thin Solid Films **534**, 685 (2013).

[27] E. Tirosh and G. Markovich, Advanced Materials **19**, 2608 (2007).

[28] X. Liu, Y. Chen, L. Wang, and D.-L. Peng, Journal of Applied Physics **113**, 076102 (2013).

[29] K.-Q. Lin, L.-S. Wang, Z.-W. Wang, R.-T. Wen, Y. Chen, and D.-L. Peng, European Physical Journal D **67**, 42 (2013).

[30] N. H. Hong, J. Sakai, N. Poirot, and A. Ruyter, Applied Physics Letters **86**, 242505 (2005).

[31] N. H. Hong, N. Poirot, and J. Sakai, Applied Physics Letters **89**, 042503 (2006).

[32] X. Y. Qiu, Q. M. Liu, F. Gao, L. Y. Lu, and J. M. Liu, Applied Physics Letters **89**, 242504 (2006).

[33] Y. H. Chang, et al., Applied Physics Letters **91**, 082504 (2007).

[34] C. N. Wu, T. S. Wu, S. Y. Huang, W. C. Lee, Y. H. Chang, Y. L. Soo, M. Hong, and J. Kwo, Journal of Applied Physics **113**, 17C309 (2013).

[35] Y. Soo, et al., Physical Review B **76**, 132404 (2007).

[36] M. K. Sharma, A. Kanjilal, M. Voelskow, D. Kanjilal, and R. Chatterjee, Journal of Physics D: Applied Physics **43**, 305003 (2010).

[37] L. Shi, Y. Zhou, J. Yin, and Z. Liu, Journal of Applied Physics **107**, 014104 (2010).

[38] H. Weng and J. Dong, Physical Review B **73**, 132410 (2006).

[39] I. V. Maznichenko, S. Ostanin, A. Ernst, and I. Mertig, Journal of Magnetism and Magnetic Materials **321**, 913 (2009).

[40] C. Han, S.-S. Yan, X.-L. Lin, S.-J. Hu, M.-W. Zhao, X.-X. Yao, Y.-X. Chen, G.-L. Liu, and L.-M. Mei, Journal of Computational Chemistry **32**, 1298 (2011).

[41] A. Pucci, G. Clavel, M.-G. Willinger, D. Zitoun, and N. Pinna, Journal of Physical Chemistry C **113**, 12048 (2009).

[42] M. Kumar Sharma, D. Kumar Mishra, S. Ghosh, D. Kanjilal, P. Srivastava, and R. Chatterjee, Journal of Applied Physics **110**, 063902 (2011).

[43] A. Zenkevich, Y. Lebedinskii, M. Pushkin, and V. Nevolin, Applied Physics Letters **89**, 172903 (2006).

[44] K. Yamamura, K. Kita, A. Toriumi, and K. Kyuno, Applied Physics Letters **89**, 222101 (2006).

[45] M. Yashima, H. Takahashi, K. Ohtake, T. Hirose, M. Kakihana, H. Arashi, Y. Ikuma, Y. Suzuki, and M. Yoshimura, Journal of Physics and Chemistry of Solids **57**, 289 (1996).

[46] A. Jayaraman, S. Y. Wang, S. K. Sharma, and L. C. Ming, Physical Review B **48**, 9205 (1993).

[47] X. Y. Zhao and D. Vanderbilt, Physical Review B **65**, 233106 (2002).

[48] H. Fujimori, M. Yashima, S. Sasaki, M. Kakihana, T. Mori, M. Tanaka, and M. Yoshimura, Chemical Physics Letters **346**, 217 (2001).

[49] J. Tang, J. Fabbri, R. D. Robinson, Y. M. Zhu, I. P. Herman, M. L. Steigerwald, and L. E. Brus, Chemistry of Materials **16**, 1336 (2004).

[50] J. Ni, Q. Zhou, Z. Li, and Z. Zhang, Applied Physics Letters **93**, 011905 (2008).

[51] S. A. Eliziario, L. S. Cavalcante, J. C. Sczancoski, P. S. Pizani, J. A. Varela, J. W. M. Espinosa, and E. Longo, Nanoscale Research Letters **4**, 1371 (2009).

[52] A. A. Rastorguev, V. I. Belyi, T. P. Smirnova, L. V. Yakovkina, M. V. Zamoryanskaya, V. A. Gritsenko, and H. Wong, Physical Review B **76**, 235315 (2007).

[53] D. M. Ramo, J. L. Gavartin, A. L. Shluger, and G. Bersuker, Physical Review B **75**, 205336 (2007).

[54] F. L. Martinez, M. Toledano-Luque, J. J. Gandia, J. Carabe, W. Bohne, J. Roehrich, E. Strub, and I. Martil, Journal of Physics D-Applied Physics **40**, 5256 (2007).

[55] Y. Xie, et al., Journal of Materials Research **26**, 50 (2011).

[56] M. C. Cheynet, S. Pokrant, F. D. Tichelaar, and J.-L. Rouviere, Journal of Applied Physics **101**, 054101 (2007).

[57] S. Wright and R. C. Barklie, Journal of Applied Physics **106**, 103917 (2009).

[58] R. C. Barklie, (Private Communication, 2013).

[59] R. C. Barklie, M. Collins, and S. R. P. Silva, Physical Review B **61**, 3546 (2000).

[60] R. C. Barklie, Diamond and Related Materials **10**, 174 (2001).

[61] R. Gillen, J. Robertson, and S. J. Clark, Applied Physics Letters **101**, 102904 (2012).

[62] S. Wright and R. C. Barklie, Materials Science in Semiconductor Processing **9**, 892 (2006).

[63] S. Wright and R. C. Barklie, Journal of Materials Science-Materials in Electronics **18**, 743 (2007).

[64] S. Wright, S. Feeney, and R. C. Barklie, Microelectronic Engineering **84**, 2378 (2007).

[65] R. C. Barklie and S. Wright, Journal of Vacuum Science & Technology B **27**, 317 (2009).

Chapter 4

CeO_2

Experimental results for d^0 magnetism in chemically synthesized CeO_2 nanoparticles, the oxide most intensively studied in this thesis, are presented in this chapter. Some structural information about CeO_2 is first presented, followed by an overview of the current state of the literature. The experimental characterization / results and a summary of the results then follow.

4.1. Introduction

Pure stoichiometric CeO_2 (ceria) is an insulating yellow-white rare earth oxide powder, which is slightly hygroscopic and can absorb CO_2 from the atmosphere. One of the main applications for ceria is in catalysis, such as in automotive catalytic converters, due to the ability of ceria to readily release or take in oxygen depending on the ambient partial pressure of oxygen, with the catalytic activity directly related to the number of oxygen vacancy defects in the crystal. As well as promoting increased catalytic activity, enhanced oxygen diffusion in ceria also serves to increase the ionic conductivity, which is related to polaron defects (electrons localized on cerium cations), making ceria interesting for use as a fuel cell electrolyte in solid-oxide fuel cells. Doped ceria has an extended ionic conductivity range compared to that of undoped ceria, with the addition of dopants such as gadolinium or samarium introducing additional oxygen vacancies in the crystal which can further enhance the ionic conductivity.

Ceria is a wide band-gap insulator with an electronic band-gap (O 2*p* – Ce 5*d*) of ~ 6 eV calculated from an early electronic structure calculation [1]. The compound possesses the fluorite structure with each Ce^{4+} surrounded by eight equivalent nearest O_2^- ions forming the corners of a cube with each O_2^- ion coordinated to four Ce^{4+} ions. The experimental lattice constant is 0.541 nm [2]. A schematic of the crystal structure of ceria is shown in Figure 4.1 (a). A recent theoretical report by Gillen *et al.* [3] provides a summary of the electronic band-gaps for both CeO_2

and Ce_2O_3 (among other rare earth oxides) obtained using various electronic structure calculations, with the (minimum) bandgap of ceria ranging from 5.5 - 8 eV for the O 2*p* – Ce 5*d* transition, and 1.5 - 4.2 eV for the O 2*p* – Ce 4*f* transition. A schematic of the bandstructure of ceria is shown in Figure 4.1 (b).

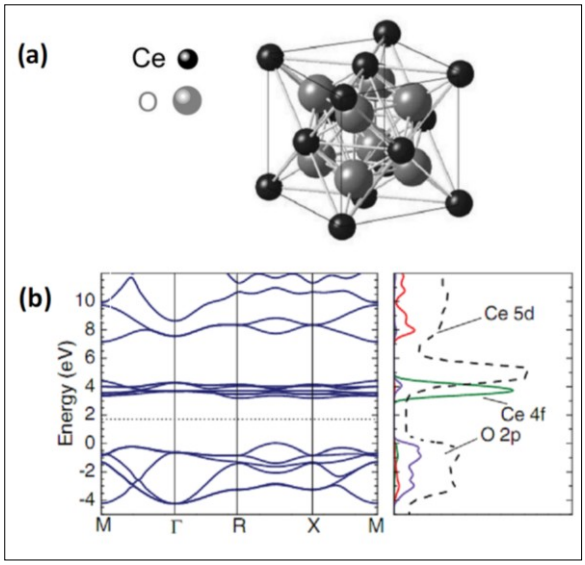

Figure 4.1 Schematic of (a) Crystal structure of CeO_2, and (b) typical bandstructure for CeO_2 from report of Gillen *et al.* [3] calculated using the HSE06 hybrid exchange-correlation functional. The dashed line corresponds to experimental data.

Calculations of defect formation energies at ceria surfaces using atomistic simulations based on the Mott-Littleton approach indicate that the surface energies corresponding to the relaxed structures are lower than those for unrelaxed structures [4]; the authors calculate that the relaxed energy is 30 % lower than the unrelaxed energy for the (111) surface and 56 % lower for the (110) surface. Secondly, they calculate that the (111) surface is more stable than the (110) surface both before and after relaxation. The same authors later report however that in terms of oxygen vacancy formation, the (110) and (310) surfaces preferentially form oxygen vacancies compared to (111) [5]. An experimental report on the structure of ceria in the vicinity of oxygen vacancies by scanning tunneling microscopy (STM) find that the relaxation of the surface structure around single vacancies is mainly controlled by the positive electrostatic field centered on the vacancy which repels the nearest neighbour Ce cations and attracts, to a lesser extent, the second nearest neighbour O anions [6]; these findings are also confirmed by their first-principles calculations (DFT). First principles band structure calculations by Skorodumova *et al.* [7] using DFT-LMTO (Linear Muffin Tin Orbital method) for the Ce^{3+} and Ce^{4+} oxides conclude that the 4*f* electron does not contribute to the bonding in Ce_2O_3, while for CeO_2 the calculated density of states, optical transitions, and electron localization function indicate that the unoccupied 4*f* states of Ce can be considered as essentially equivalent to an empty atomic like 4*f* level, and that the nature of bonding in CeO_2 and

Ce_2O_3 may be described as polarized ionic. The same authors also present an insight into the theory of oxygen-vacancy formation in ceria, in which the formation of reduced oxides can be viewed upon as a formation, migration, and ordering of virtual Ce^{3+}-vacancy complexes [8]. Specifically, they calculate (by DFT-LMTO) that it requires 4.55 eV to form an oxygen vacancy in pure CeO_2, but only 0.26 eV next to a pair of Ce^{3+} atoms embedded into the CeO_2 matrix.

Nanometric ceria is known to undergo lattice expansion with decreasing nanoparticle size as first evidenced by TEM studies [9], and subsequently corroborated by XRD/TEM [10,11]. The surface/volume ratio of nanoparticles increases with decreasing nanoparticle size, which results in a greater Ce^{3+} contribution (associated with unsaturated Ce-O bonds at the surface); since Ce^{3+} has a larger ionic radius (115 pm) than that of Ce^{4+} (101 pm), and due to the incorporation of oxygen vacancies to charge compensate for Ce^{3+}, the lattice parameter increases. X-Ray Photoelectron Spectroscopy (XPS) measurements have confirmed that the Ce^{3+} content increases with decreasing nanoparticle size, from 17 % (30 nm diameter) to 29 % (6 nm) to 44 % (3 nm) for example [12].

While in theory the stoichiometric CeO_2 phase (bulk) would be expected to be diamagnetic since it nominally contains no unpaired electrons, in practice CeO_2 is experimentally known to be weakly paramagnetic [13], due to the presence of residual Ce^{3+} at ambient pressure and temperature; i.e. ceria is always slightly reduced. The metastable sesquioxide of Ce, Ce_2O_3, is antiferromagnetic with a very low Neel temperature (T_N ~ 9 K) as deduced by experiment [2], with a lattice constant of 0.372 – 0.396 nm as deduced by DFT calculations [7]; just to clarify, there are in fact *no experimental reports* for the lattice parameter of Ce_2O_3, in contrast to the erroneous experimental reference number 16 given in [7] (which actually only pertains to the rare earth sesquioxides La_2O_3, Pr_2O_3 and Nd_2O_3).

4.2. Literature summary

The first experimental report for intrinsic room temperature ferromagnetism (RTFM) in undoped CeO_2 was published in 2006 by Sundaresan *et al.* [14] (similar data also presented in a later paper [15]) for nanoparticles (NPs) synthesized by the reaction of solutions of cerium nitrate and hexamethylenetetramine (HMTA). It was reported that NPs of diameter 7 and 15 nm had room temperature saturation magnetization values of 7 A m^{-1} and 11 A m^{-1} respectively, while particles of larger diameter were paramagnetic, as shown in Figure 4.2. RTFM was also measured for Al_2O_3, ZnO, In_2O_3 and SnO_2 NPs of diameter 7 – 30 nm. A noticeable feature of the ferromagnetism is the marked lack of hysteresis, with typical coercive fields of only several mT. Bulk samples obtained by sintering the NPs at high temperatures in air or oxygen were measured to be diamagnetic. As there were no magnetic impurities present, the authors suggest that the origin of ferromagnetism

may be due to exchange interactions between localized electron spin moments resulting from oxygen vacancies at the surfaces of NPs.

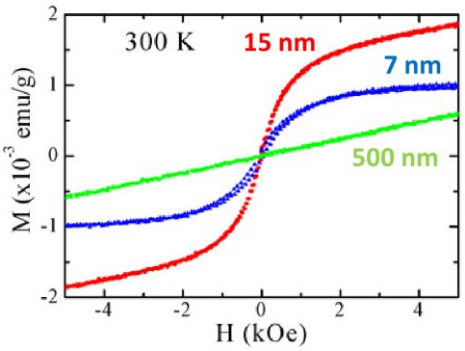

Figure 4.2 Room temperature magnetization curves from first report for RTFM in undoped CeO_2 nanoparticles by Sundaresan *et al.* [14]. The particle diameter is indicated. Note that 1 emu/g = 1 Am^2/kg, while 1 kOe is equivalent to 0.1 T.

The next experimental report for RTFM in CeO_2 was for micropowders (1 – 3 μm size), obtained by the grinding down of a single crystal piece, for which a magnetization of 35 A m^{-1} was obtained at room temperature [16] (the authors also report RTFM in Co-doped CeO_2; this shall be discussed further later). Upon oxygen annealing, the ferromagnetic CeO_2 powder became paramagnetic, so the authors suggested an oxygen vacancy meditated ferromagnetic ordering, similar to the explanation given in the initial report of Sundaresan *et al*.

A subsequent experimental report presented RTFM in polycrystalline CeO_2 nanosheets and nanoporous structures synthesized by electrodeposition on copper substrates [17]. The sheets were 60 nm thick and several μm long, while the pores were 2 μm in size with 600 nm thick walls. The morphology was modified by changing the concentration of the cerium nitrate precursor used during electrodeposition. The magnetization values were quite small however, with saturation magnetizations of 5 A m^{-1} for pores and 6 A m^{-1} for sheets at 300 K, which increased in magnitude by about three orders of magnitude when measured at 4 K. The magnetism was attributed to oxygen vacancies induced by the presence of Ce^{3+}, the latter of which was detected by XPS (% not given).

In contrast to the above reports, a subsequent report by Liu *et al.* [18] for RTFM in CeO_2 nanostructures did not find any correlation between oxygen vacancies and ferromagnetism. The authors reported a room temperature magnetization value of ~ 550 A m^{-1} for nano-needles (length 5 nm, diameter 1 nm) synthesized by a sol-gel process involving the reduction of cerium nitrate by NaOH in a solution of polyethyleneglycol (PEG) and water. When ethanol or pure water was employed as the solvent instead, spheres of size 5-20 nm or 200-500 nm were obtained respectively, and neither exhibited any RFTM. Upon annealing the ferromagnetic sample in oxygen (should remove oxygen vacancies) or a reducing atmosphere (should create oxygen vacancies), the RTFM vanishes, from which the authors deduce that oxygen vacancies do not mediate the magnetism. It is noted that whereas needles were synthesized from the cerium nitrate/PEG-water

mixture, in a subsequent report by our research group, 4 nm diameter nanoparticles with a maximum room temperature M_s of 150 A m^{-1} were produced by a similar synthesis [19]; the difference in morphology between the two reports may be due to different cerium nitrate concentrations [20] and/or different NaOH concentrations [21] used which have been shown elsewhere [20,21] to produce ceria nanostructures of different morphology varying from spherical to rod-like.

A subsequent publication to that of Liu *et al.* reverted back to the oxygen vacancy explanation for RTFM in NPs however, in which the samples were synthesized by another sol-gel process using citric acid as a complexing agent [22]. Magnetization values of 8 A m^{-1} were measured for the as-prepared NPs (10 nm diameter), which increase to 11 A m^{-1} upon annealing in forming gas (creates oxygen vacancies). Cyclical oxidation/reduction anneals are shown to repeatedly reduce/enhance the magnetization.

Subsequently, there was a rapid increase in the number of experimental reports for RTFM in undoped CeO_2. For nanoparticles, those synthesized by solution combustion using L-glutamic acid (8 nm diameter) exhibit a magnetization of ~ 1.5 A m^{-1} (undoped) [23]. Undoped NPs synthesized by the self-propagating room temperature (SPRT) synthesis method, which involves continually mixing the cerium nitrate and NaOH precursors, followed by exposure of the mixture to air, suspension of the mixture in water and extraction of the CeO_2 nanopowder by centrifugation and washing with water/ethanol, have magnetizations of 45 A m^{-1} (10 nm diameter) [24], 40 A m^{-1} (3 nm) [25] and 140 A m^{-1} (6 nm) [26].

For other undoped NPs synthesized by sol-gel precipitation, one of the most common synthesis methods used to grow small CeO_2 nanoparticles of narrow size distribution, the measured magnetization values are 15 A m^{-1} (7 nm) [27] and 0.7 A m^{-1} (5.7 nm) [28], for which the former sample was synthesized using by reduction of cerium nitrate in an inorganic solvent, and the latter using NaOH/cerium nitrate/PEG. For the latter sample however, the authors ascribe the small magnetization of their undoped NPs to ferromagnetic impurities (~ 20 ppm of Fe measured by ICP-OES). Other undoped NPs synthesized by similar co-precipitation processes (without use of surfactant) have room temperature magnetization values of 25 A m^{-1} (5.4 nm) [29], 15 A m^{-1} (2-3 nm) [30], 12 A m^{-1} (8 nm) [31], 10 A m^{-1} (9.2 nm) [32] , 3 A m^{-1} (4 nm) [33] and 30 A m^{-1} (10 nm) [34], the last of which increased to 45 A m^{-1} (22 nm) upon annealing at 700 °C in a reducing atmosphere.

Undoped NPs synthesized by yet other methods have maximum magnetization values of 20 A m^{-1} (20 nm) [35] and 120 A m^{-1} (9.2 nm) [36] for those synthesized using a polyvinylpyrrolidone (PVP) assisted hydrothermal method (mix PVP with H_2O, then add cerium nitrate solution and heat in an autoclave at 160 - 200 °C for 12 h), and 760 A m^{-1} (3.5 nm) [37] for nanoparticles synthesized by a thermal decomposition method. The thermal decomposition process involves heating a mixed solution of cerium(III) acetylacetonate hydrate, 1,2-dodecandiol (stabilizer), and octyl-ether to 100 °C, followed by the addition of surfactants (oleic acid and oleylamine) and further heating to reflux at 300 °C before the final separation of the precipitate by centrifugation; for the nanoparticles synthesized by this method the magnetic signals are attributed to enhanced Ce^{3+} content (40 %) at the surface of the nanoparticles (and correlated with oxygen vacancies, which create more Ce^{3+}), as measured by X-Ray absorption near edge spectroscopy (XANES) at the Ce $M_{4,5}$ absorption edge.

The authors [37] also deduce however that excess Ce^{3+} content (48 %) at the surface, i.e. too many oxygen vacancies, may suppress the magnetic signal. Note that the maximum measured room temperature magnetization value for this report, 760 A m^{-1}, is larger than that typical reported (~ 10 -100 A m^{-1}), and is comparable in size to the largest previously reported value of 550 A m^{-1} for the nano-needles synthesized by Liu *et al.* [18]. Elsewhere, nanostructures of different morphology (cubes) are found to exhibit size dependent magnetism, 5 A m^{-1} for 100 nm size cubes compared to 43 A m^{-1} for 5.3 nm [38]. Similar to many previous reports, oxygen vacancies and enhanced Ce^{3+} character at surfaces of samples of smaller dimension are suggested as mediating the magnetism.

The largest room temperature magnetization values reported to date for undoped CeO_2 nanoparticles, however, are for nanocrystals synthesized by the thermal decomposition method (as reported in [37]) and subsequently annealed under various conditions by Chen *et al.* [39]. The as-prepared nanoparticles are actually paramagnetic; they only exhibit RTFM once annealed. The largest magnetization measured is ~ 1800 A m^{-1} for 9.5 nm sized nanoparticles which were subsequently annealed at 500 °C for 2 h in an oxygen partial pressure (P_{O2}) of 20 %. The use of higher oxygen partial pressures (50 %) and/or lower annealing temperatures (300 °C) results in smaller magnetizations, ~ 750-1700 A m^{-1}, although these magnitudes are still larger than any of those reported in the previously mentioned experimental publications. The authors attribute the large magnetization to a narrow range of Ce^{3+} content at the *surface* as measured by XANES at the Ce *L* absorption edge ($0.40 < Ce^{3+}_{surface}/Ce_{surface} < 0.45$), similar to the explanation given in an earlier report by the same authors [37], and further suggest that electrons in Ce (and not O) bear the magnetic moments from X-ray magnetic circular dichroism (XMCD) measurements.

RTFM has also been recently measured for CeO_2 nanostructures in the form of nanopoles of length 0.5-1 μm and diameter 20–30 nm where M_s = 1280 A m^{-1} [40], bundles of nanowires of length 0.5-1 μm and bundle (individual) diameter ~ 200 (~ 20) nm where M_s = 580 A m^{-1} [41], and for nanocolumns of length 60-120 nm and diameter 30–60 nm where M_s = 230 A m^{-1} [42]. The nanopoles are grown by a hydrothermal synthesis route in which an aqueous solution of NaOH is added gradually to a cerium chloride aqueous solution after which ethylenediamine (which acts as a complexing agent) is added dropwise; the solution is then heated in an autoclave at 180 °C for 100 h, after which the precipitate is separated, washed and dried. The nanocolumns are synthesized in a similar way, except that an ethanol/H_2O solution is used instead of H_2O alone, $N_2H_4.H_2O$ (aq. hydrazine) is used as a base instead of NaOH, and the duration of heating in the autoclave is for 8 h only. The nanowire bundles are also grown in a similar fashion to the nanocolumns, where $NaH_2PO_4 \cdot 2H_2O$ is used instead of NaOH. It is interesting to observe that the nanopoles, which have an aspect ratio of ~ 17-50, have a magnetization more than 5 times that of the nanocolumns, which have an aspect ratio of 1-4. Furthermore, the nanoneedles synthesized by Liu *et al.* [18], which have an average aspect ratio of ~ 5 from inspection of their TEM images, which is intermediate between that of poles (17-50) and columns (1-4), have a value of M_s (550 A m^{-1}) which is also intermediate between those measured for poles (1280 A m^{-1}) and columns (230 A m^{-1}). For the nanowire bundles, which have an aspect ratio of ~ 2.5-5, M_s (580 A m^{-1}) is rather similar to that of the needles (550 A m^{-1}) which have a generally similar aspect ratio of ~ 5. Hence it is possible that M_s

may be somehow linked to the aspect ratio of these nanostructures which are prepared by similar syntheses; it seems that those nanostructures with higher aspect ratios have larger room temperature saturation magnetizations. The enhanced M_s values may also be related to the *larger surface areas* for CeO_2 nanostructures with higher aspect ratios; for example, it has been measured using nitrogen gas adsorption that ceria rods and spindles have larger surface areas than for spheres with an equivalent fundamental crystallite size (~ 8 nm) [20]. Larger surfaces areas may have more structural defects/oxygen vacancies associated with them, in agreement with the oxygen vacancy-mediated d^0 magnetism hypothesis.

Figure 4.3 displays TEM images of a selection of different undoped ceria nanostructures which exhibit RTFM from some of the aforementioned literature reports.

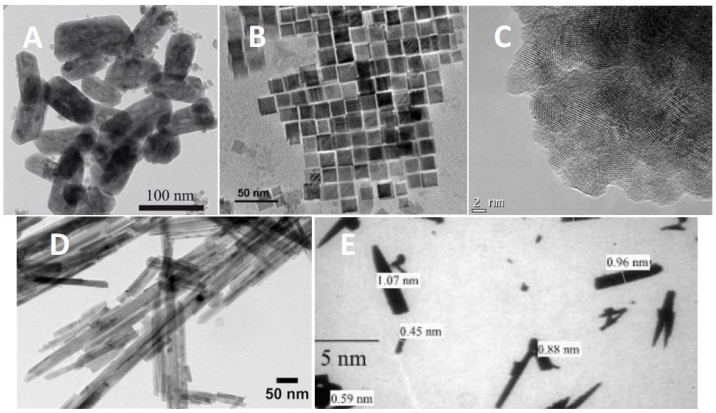

Figure 4.3 Selection of TEM images of undoped CeO_2 nanostructures from the literature which exhibit RTFM; A = nanocolumns [42], B = nanocubes [38], C = nanoparticles [39], D = nanowire bundles [41], E = nanoneedles [18]. Their respective maximally measured M_s values may be found in Table 4.1.

Table 4.1 below provides a brief summary of all the literature reports to date which measure RTFM for undoped CeO_2 nanostructures, most of which are nanoparticles, in order of the maximum magnetization measured per report. It is noted that there does not appear to be any clear correlation between nanoparticle diameter and M_s. In addition, whereas some nanoparticles exhibit RTFM when measured after synthesis, others do not exhibit RTFM unless post-treated in some way, typically by a reducing anneal.

Table 4.1. Maximum room temperature magnetization per publication for undoped CeO_2 nanostructures. Samples are in the form of nanoparticles unless stated otherwise.

Synthesis	Diameter (nm)	M_s (A/m)	Ref
Thermal decomposition method + annealed in air (20% P_{O2})	9.5	1800	[39]
Hydrothermal synthesis	750×25 [i]	1280	[40]
Thermal decomposition method	3.5	760	[37]
Hydrothermal synthesis	750×200 [ii]	580	[41]
Sol-gel (PEG)	5×1 [iii]	550	[18]
Hydrothermal synthesis	90×45 [iv]	230	[42]
Sol-gel (PEG)	4	150	[19]
Self-propagating room temperature synthesis (SPRT)	6	140	[26]
PVP assisted hydrothermal method	9.2	120	[36]
co-precipitation + annealed in H_2/Ar	22	45	[34]
SPRT	10	45	[24]
Cerium nitrate + Oleic acid /*tert*-butylamine / toluene	5.3 [v]	43	[38]
SPRT	3	40	[25]
co-precipitation	5.4	25	[29]
PVP assisted hydrothermal method	20	20	[35]
Sol-gel (using inorganic solvent)	7	15	[27]
co-precipitation	2-3	15	[30]
co-precipitation	8	12	[31]
cerium nitrate/HMTA	15	11	[14,15]
Sol-gel (citric acid) + anneal in H_2/N_2	14	11	[22]
co-precipitation	9.2	10	[32]
Electrodeposited on Cu	10000 x 60 [vi]	6	[17]
Electrodeposited on Cu	2000 [vii]	5	[17]
co-precipitation	4	3 [viii]	[33]
Solution combustion using L-glutamic acid	8	1.5	[23]
Sol-gel (PEG) + annealed in air	5.7	0.7*	[28]

[i] poles (average length × diameter) [ii] wire bundles (average length × diameter)
[iii] needles (average length × diameter) [iv] columns (average length × diameter) [v] cubes
[vi] sheets (average length × diameter) [vii] pores (diameter)
[viii] synthesized using either cerium nitrate or chloride; M_s = 1 A m^{-1} for NPs synthesized using cerium ammonium nitrate
* attributed to Fe impurities

Up to this point, a literature summary of experimental reports for RTFM in undoped CeO_2 mostly in nanoparticle/nanostructured form has been presented, which forms the majority of the literature. In addition there are a few reports however for RTFM in undoped CeO_2 microparticles and microcrystals, representative of the bulk. The first report for RTFM in undoped CeO_2 micropowders (1 – 3 μm size), obtained by the grinding down of a single crystal piece (the unground crystal does not show any RTFM), for which a magnetization of 35 A m^{-1} was obtained at room temperature [16], has been presented already near the beginning of this section, since this was one of the earliest reports for RTFM in any form of undoped CeO_2, second only to Sundaresan *et al.* in order of earliest publication date. The magnetism is suggested to arise due to grinding which may induce oxygen vacancies. Elsewhere, RTFM is measured for undoped CeO_2 microparticles of ~ 0.5-1.0 μm size, which have a magnetization of ~ 20 A m^{-1} [43]; the weak magnetism is attributed to limited surface defects of the micron-sized particles. Another report measures a small

magnetization of 6 A m^{-1} at room temperature for 99.99% nominal purity finely ground commercial powder [44]; upon annealing in O_2 the powder becomes paramagnetic, from which the authors deduce the oxygen vacancies induced by grinding are a possible explanation for the ferromagnetism. For 99.99% purity commercial powder annealed in vacuum or a hydrogen (reducing) atmosphere, room temperature magnetizations of 300 A m^{-1} [45] or 18 A m^{-1} [46] are measured respectively; for both cases, the as-received powder is paramagnetic before any treatment, and re-annealing the ferromagnetic powder in air destroys the ferromagnetism and recovers the original paramagnetism. Oxygen vacancies are suggested in both cases to mediate the magnetism. In addition, for higher purity 99.999% commercial powder, RTFM with a magnetization of 15 A m^{-1} is measured upon annealing in a hydrogen atmosphere [47].

It has also recently been reported that bulk CeO_2 pellets which are weakly paramagnetic at 320 K, prepared by sintering the powder at 1400 °C, when irradiated with 200 MeV swift heavy Xe ions exhibit a maximum room temperature magnetization of 380 A m^{-1} for an irradiation fluence of 2×10^{13} ions/cm^2 [48]. The RTFM vanishes when the irradiated samples are annealed in air, and the magnetization curves virtually superimpose at both 320 K and 20 K. Upon irradiation at successively higher doses the value of M_s decreases. Since the measured lattice constant of CeO_2 increases with increasing ion fluence (by about 0.2 %), which is correlated with an enhanced Ce^{3+} content previously measured by both XAS (~ 14 % for 2×10^{13} ions/cm^2) [49] and XPS [50], and due to the finding that the RTFM vanishes upon annealing in air (removes oxygen vacancies), the ion-irradiation is proposed to induce oxygen vacancies and the ferromagnetic behaviour of the ion-irradiated CeO_2 is attributed to the magnetic moments of localized 4*f* electrons on Ce^{3+} atoms (elsewhere, irradiation of CeO_2 films with 2 MeV He^+ ions of varying flux density is also shown to create oxygen vacancies and to enhance the Ce^{3+} content [51], by up to ~ 20 %). First principles calculations using the DFT-GGA (Generalized Gradient approximation) + U method [52] by some of the same authors of the aforementioned experimental irradiation paper [48] have calculated that for defective CeO_2, the Ce^{3+} ion originates not only from the oxygen vacancy but also from the oxygen Frenkel (interstitial–vacancy) pairs; hence reduction is not the only means of producing Ce^{3+} ions but that displacement of oxygen from the sublattice position to the interstitial region can also produce Ce^{3+} ions. Furthermore, an interstitial oxygen atom that moves from the lattice position and an oxygen atom on the lattice are calculated to form a dimer that may behave as an oxygen molecule of negative di-valence, a bonding state which can also produce excess electrons and the tri-valent cerium state in cerium dioxide, all of which may help to explain the experimental irradiation results. In addition, irradiation with Xe ions is shown by earlier TEM analysis to introduce structural disorder in the form of numerous ion tracks of diameter 5-7 nm in CeO_2 [53], which may help produce the off-stoichiometry required for Ce^{3+} and oxygen vacancy formation; upon irradiation at higher doses of $\geq 10^{13}$ ions/cm^2, the measured overlapping of these damaged tracks may hence enhance the lattice disordering and help to destroy the ferromagnetic interactions, which could explain the reduction in M_s upon further irradiation at higher fluences.

Table 4.2 summarizes the above results by listing the maximum magnetization reported in each paper for RTFM in undoped CeO_2 bulk samples. The sample purity is denoted where reported.

It is evident that the bulk does not typically exhibit significant RTFM unless it is treated in some way, such as by ion irradiation, grinding or annealing.

Table 4.2. Maximum room temperature magnetization per publication for undoped CeO_2 bulk samples.

Sample + treatment	M_s (A/m)	Ref
Bulk pellet (pressed from sintered powder) – irradiated (200 MeV Xe ions @ 2×10^{13} ions/cm^2)	380 [i]	48
99.99% powder - vacuum annealed	300 [ii]	45
Powder ground from single crystal	35	16
Bulk powder (no treatment)	20	43
99.99% powder - H_2 annealed	18	46
99.999% powder - H_2 annealed	15	47
99.99% powder finely ground	6	44

[i] Pellet is paramagnetic before irradiation [ii] As received powder paramagnetic; re-annealing ferromagnetic powder in air (8 h) recovers paramagnetism (ferromagnetism disappears)

The largest magnetic signals reported for undoped CeO_2 are measured for films. Magnetization values given are for in-plane measurements unless stated otherwise. For relatively thick (~ 0.5 μm) nanoporous films (pore size ~ 200 nm) electrodeposited by our research group (mostly the work of Lorena M.A. Monzon) using a stationary three-electrode cell with a commercial galvanostat/potentiostat on silicon (111) substrates possessing their native oxide layer [19], room temperature magnetization values of ~150-600 A m^{-1} were reported for some of the films after subtraction of a linear diamagnetic background due to the silicon substrate; some typical room temperature magnetization curves measured are shown in Figure 4.4. 99 % purity cerium nitrate (main impurity ~ 1-2 % La) was used as the cerium precursor, 99.999% purity KOH as the base and ultrapure PEG-200 molecular weight as a surfactant. The size of the ferromagnetic signal seems to depend on the overpotential used during electrodeposition which in turn alters the degree of porosity of the electrodeposits; some ferromagnetic films can be made virtually non-ferromagnetic simply by varying the overpotential, in which it is found that both the size of the ferromagnetic signal and the degree of porosity increase with decreased applied overpotential. The fact that some films were not ferromagnetic provides evidence that the ferromagnetic-like signals are not due to systematic impurities in the silicon substrate. The RTFM signals were tentatively associated with grain boundaries/surfaces of nanopores and/or small quantities of non-magnetic impurities in the cerium nitrate precursor (mainly La). For films electrodeposited using a higher purity cerium nitrate precursor (99.999% Sigma), *no* RTFM was measured whatever the deposition conditions used. It is noted that the pores for the magnetic films have a similar morphology to those grown previously elsewhere [17], however our pores are about 10 times smaller in size with M_s values for our films of about 30-120 times larger. It is somewhat open to debate whether these nanoporous structures are strictly films, but for the purposes of classification we have grouped them with films here. If grouped with the nanostructures listed in Table 4.1, it is evident that our nanoporous "films" will be

positioned near the top of the table with their relatively large magnetization values.

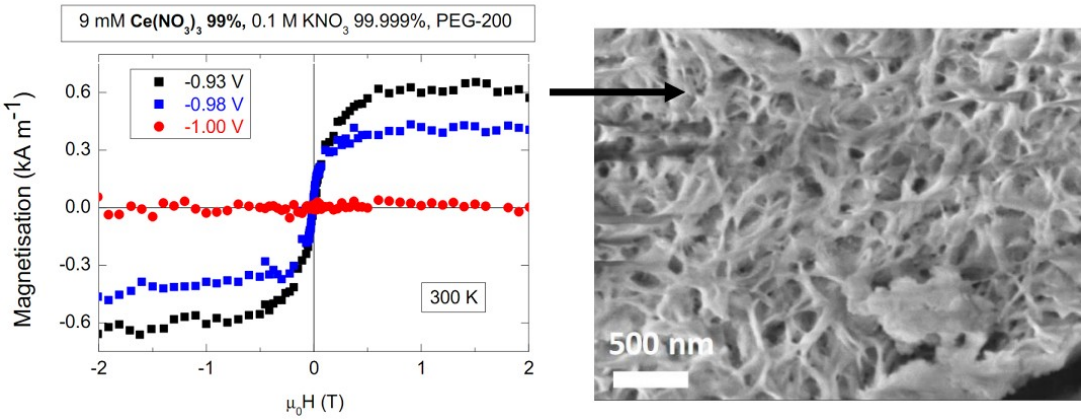

Figure 4.4. Selected room temperature magnetization curves measured for undoped nanoporous electrodeposited CeO_2 films on silicon [19]. The charge used during electrodeposition was constant at 0.7 C. A typical SEM image of the surface of the film with the largest magnetization is also shown on the right.

Much larger magnetizations than those measured for nanoporous films have been measured for thin compact nanocrystalline films in a series of papers by Fernandes *et al.* [54-58], the first of which reported very large room temperature magnetization values of up to ~ 120 kA m^{-1} for ~ 30 nm thick oxygen-deficient films electrodeposited on Si (001) (*p*-type) substrates [54]. Hydrogen peroxide (H_2O_2) additive is sometimes used during electrodeposition to modify the oxidizing conditions and hence the Ce^{3+} content of the films, with more stoichiometric-like (i.e. less Ce^{3+}) films obtained for higher H_2O_2 concentrations used. The electrodeposition does not occur in the dark but only when the electrolyte/Si interface is illuminated with bright light, the source of which is a halogen lamp (near UV-visible wavelength range). Further details of the experimental procedure are reported by the same authors elsewhere [55]. The cerium precursor used in all of the syntheses is 99.8 % $CeCl_3.7H_2O$ (Merck). The Ce^{3+} concentration is estimated to be 22.7% as measured by XPS measurements for the films exhibiting the largest magnetic signals. Thicker films (250 nm) also display a large magnetization of ~ 100 kA m^{-1}. Despite an exponential-like reduction in M_s from 100 to 7 kA m^{-1} after two years, this sample stabilizes in a ferromagnetic state at room temperature. The authors suggest that the magnetic signals are mostly associated with point defects (Ce and O vacancies) in the structure. They report even larger magnetizations, ~ 160 kA m^{-1}, for similar thinner films, 20 nm thick, the magnitude of which further increases up to a maximum of ~ 450 kA m^{-1} upon irradiation with 30 keV Ne^+ ions at a fluence of 2×10^{16} ions/cm^2 [56]. The effect of ion irradiation is to create more vacancies, and hence to enhance the Ce^{3+} content of the films, from 22.7% before irradiation to 47.2% after irradiation for the oxygen-deficient film exhibiting the maximum magnetization mentioned above; it is found that the saturation magnetization continuously increases with Ce^{3+} concentration, despite the significant amorphization of the films

upon irradiation. The largest magnetization of all is reported for similar 20 nm thick oxygen-deficient nanocrystalline films in a subsequent paper by the same research group [57]. In this case the films are deposited on SiO_2/Si substrates, since the native oxide layer is not removed by hydrofluoric (HF) acid etching, in contrast to their previous reports. While the in-plane magnetization for the films are 280 kA m^{-1}, the out-of-plane magnetization is giant at 1.15 M Am^{-1}, which also illustrates the huge anisotropy of the magnetization. The films are synthesized without H_2O_2 additive and contain 24.2% Ce^{3+}. Smaller magnetization values of 90 and 120 kA m^{-1} for in-plane and out of plane measurements respectively are measured for close to stoichiometric films (3.8% Ce^{3+}). The large magnetic signals and anisotropy are attributed to oxygen vacancy pairs lying along the (111) axes of the fluorite structure. Table 4.3 briefly summarizes the above results for undoped films.

Table 4.3. Representative magnetization values measured for undoped CeO_2 films which exhibit room temperature ferromagnetism.

Synthesis	thickness (nm)	M_s (kA/m)	Ref
Electrodeposited on Si (22.7% Ce^{3+})	250	100 ∥	[54]
Electrodeposited on Si (22.7% Ce^{3+})	30	119 ∥	[54]
Electrodeposited on Si (22.7% Ce^{3+})	20	245 ∥	[56]
Electrodeposited on Si (3.3% Ce^{3+})	20	159 ∥	[56]
Electrodeposited on Si (22.7% Ce^{3+}) + irradiated with 30 keV Ne^+ (2×10^{16} ions/cm^2) (Ce^{3+} content increases to 47.2%)	20	450 ∥	[56]
Electrodeposited on SiO_2/Si (3.8% Ce^{3+})	20	91 ∥ 117 ⊥	[57]
Electrodeposited on SiO_2/Si (24.2% Ce^{3+})	20	280 ∥ [i] 1150 ⊥	[57]
Electrodeposited on Si (111) [ii]	~ 500	0.6 ∥	[19]

[i] same sample presented in [58] [ii] cerium nitrate precursor used contains ~1-2 wt % La
- For the Fernandes *et al.* reports [54,56,57] the Ce^{3+} content is measured by XPS, while H_2O_2 is added in order to create more stoichiometric films (i.e. less Ce^{3+} content); their films are compact and have a nanocrystalline texture, whereas those of Ackland *et al.* [19] are nanoporous

In response to the reports of the extraordinarily large magnetization values measured for some of the undoped CeO_2 films of Fernandes *et al.*, by following their reported electrodeposition methods [55] an attempt was made to reproduce the results in our laboratory (Asra S. Razavian, unpublished) using a stationary three-electrode cell with a commercial galvanostat/potentiostat, and using a UV lamp (50 W power) as the bright-light irradiation source in order to facilitate the electrodeposition process. Magnetization measurements for a large number of electrodeposited films (~ 30) on silicon substrates synthesized using a range of conditions similar to those of Fernandes *et al.* [55] revealed that the largest room temperature saturation moment was $1x10^{-8}$ Am^2 (and typically ~ $0.2x10^{-8}$ Am^2), corresponding to a saturation magnetization M_s of at most 8 kA m^{-1} (the estimated film thickness is ~ 50-100 nm); although significant, this signal is still *several orders*

of magnitude smaller than the 100s of kA m^{-1} typically measured by Fernandes *et al.* in their publications for similar undoped electrodeposited CeO_2 films where they measured RTFM [54,56,57].

RTFM has also been reported for a host of doped CeO_2 samples, where the dopant is a transition metal in the majority of reports. While some of the transition metal dopants used are ferromagnetic (Fe, Co, Ni), in many of the publications it is found that the magnetism is not entirely attributable to the ferromagnetism of the dopants themselves, and that the magnetization curves are typically anhysteretic and saturate easily in applied field; hence the scenario may be somewhat similar to d^0 magnetism, where the dopants, when present, are strictly non-magnetic. The phenomenon may even be similar in both cases, doped and undoped, regardless of whether the impurities are magnetic or non-magnetic. The first report for RTFM in doped CeO_2, and also the first report for RTFM in any form of CeO_2, either doped or undoped (actually slightly predating the first publication for RTFM in undoped CeO_2 by Sundaresan *et al.*) was by Tiwari *et al.* [59] for Co doped CeO_2 films. Crystalline films doped with 3 at. % Co were grown by pulsed laser deposition (PLD) on $LaAlO_3$ (LAO) (001) substrates. The magnetization curves are virtually anhysteretic, shown in Figure 4.5, with a room temperature magnetization of ~ 45 kA m^{-1}, equivalent to a magnetic moment of 6 μ_B/Co. It was argued that the magnetism cannot be entirely due to cobalt, since the maximum moment of 8.2 μ_B/Co at 725 K is larger than the maximum value that cobalt can contribute in which the orbital moments are unquenched (6.7 μ_B/Co). In addition, the magnitude of the magnetic moment measured was virtually identical from 300 K down to 5 K, which rules out superparamagnetism as an explanation due to its characteristic temperature dependence. An F-centre mediated exchange mechanism was proposed as a plausible mechanism in order to explain the ferromagnetic ordering. An F center consists of an electron trapped in an oxygen vacancy; earlier EPR studies showed that at liquid He temperature, electrons are trapped in oxygen vacancy sites forming F centers rather than occupying 4*f* band states [60]. Following this initial report of RTFM, a large number of publications followed, the next of which reported RFTM signals of very similar magnitude for films also doped with 3 at. % Co and grown by PLD but on Si (111) and glass substrates instead of on LAO [61]. A similar F-centre mechanism was proposed. A subsequent report measured somewhat smaller magnetizations of up to ~ 16 kA m^{-1} for 4.5 at. % Co doped PLD grown films on either Si or $SrTiO_3$ (STO) substrates [62]. The authors report that the presence of oxygen during the growth or annealing reduces the ferromagnetism drastically, and suggest that oxygen vacancies play a key role in the magnetic coupling between Co ions, although they do not elaborate on the mechanism responsible.

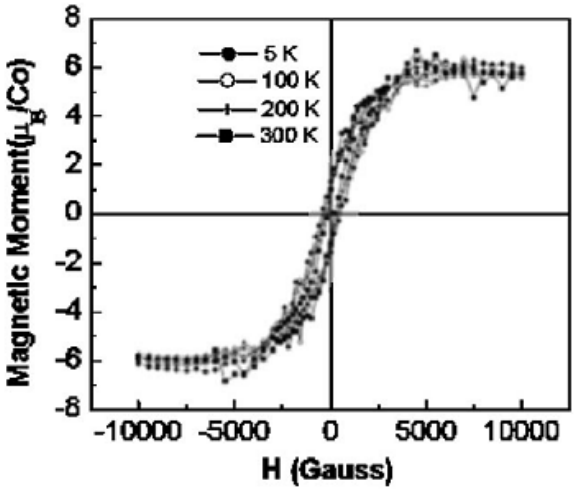

Figure 4.5. Magetization curves from the first report for RTFM in doped CeO_2 (films) by Tiwari *et al.* [59]; 10^4 G is equivalent to 1 T.

It has also been shown in our laboratory (Lorena M.A. Monzon, unpublished) that by intentionally doping nanoporous films of ~ 0.5 μm thickness synthesized in a similar way to those electrodeposited previously [19], but using a higher purity (99.999%) cerium nitrate precursor and *non-magnetic* dopants such as Mg, Zn and Bi (obtained from their respective nitrate salts), a ferromagnetic-like signal may be produced, which supports the previous suggestion that the non-magnetic impurities may "turn on" or create the ferromagnetic-like signals [19]. All of the salts are of high purity (≥ 99.99%) except for that of Zn. It is noted that films synthesized using the higher purity (99.999%) cerium nitrate precursor *do not exhibit any RTFM when undoped*. Some representative magnetization curves are shown in Figure 4.6. The magnitudes of the magnetic signals are varied here by changing the electrodeposition current at constant overpotential. The magnetic signals are not as large as those measured for some of the CeO_2 films grown using the 99 % cerium nitrate precursor shown previously in Figure 4.4.

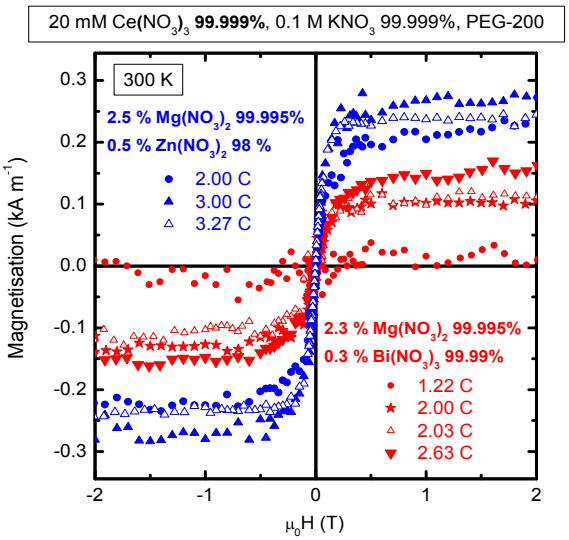

Figure 4.6. Typical room temperature magnetization curves measured for nanoporous CeO_2 films electrodeposited on silicon, doped with a few wt % of different non-magnetic elements obtained from their respective nitrate salts (Lorena M.A. Monzon, unpublished). The charge used during electrodeposition (at constant overpotential) is indicated.

A summary of literature reports for RTFM in doped CeO_2 films is given in Table 4.4. The majority of the dopants are (ferromagnetic) transition elements. Similar to undoped CeO_2, the largest magnetizations for doped CeO_2 are measured for films. The maximum magnetization value reported is displayed for each reference. The magnetic measurements are performed in-plane unless stated otherwise. All films are (poly)crystalline unless stated otherwise. The first three listed samples correspond to the first three reports in order of date of publication which have been previously discussed, after which the rest of the listed films are broadly grouped according to their method of fabrication. It appears that the magnitudes of the magnetic moments are not correlated with either film thickness or substrate used. Interestingly, some of the largest magnetizations (and also moments per dopant atom), up to 220 kA m^{-1} for 3 % Fe doped electrodeposited CeO_2 films, are reported by Fernandes *et al.* [58], the same authors that report the largest RTFM values for undoped CeO_2, although the M_s values for the doped films are not as large as the maximum values reported for undoped films. Since the calculated moments per dopant atom are unphysically large, for example 29 μ_B/Fe and 13 μ_B/Co, it implies that the magnetism cannot be partly or wholly attributed to the ferromagnetic dopants themselves. The authors measure smaller magnetizations compared to pure CeO_2 films upon doping with different transition metal elements, and they attribute the loss of magnetization as due to sharing of the excess electrons left behind by oxygen atoms in the vacancies with dopant species, i.e. the magnetization is no longer correlated with the number of oxygen vacancies. Similarly large magnetizations of 230 kA m^{-1}, equivalent to 7.2 μ_B/Co, are measured elsewhere for 12 % Co doped films [63], which are attributed to the combined contributions of spin polarized Co, Ce, and O atoms with the enhancement of O vacancies from first principles calculations. Other notably large magnetizations of ~ 100 kA m^{-1} are also reported for Co doped films [64,65], however for the former report the magnetism is attributed to Co clusters.

Table 4.4. Maximum room temperature magnetization values per dopant reported for doped CeO_2 films.

Growth method	thickness (nm)	Dopant (at. %)	M_s (kA/m)	Moment (μ_B/dopant)	Ref
PLD on LAO (001)	Not given, estimate ≥ 60 nm	3 % Co	45	6 μ_B/Co	59
PLD on Si (111) or glass	Not given, estimate 100 nm	3 % Co	45	6 μ_B/Co	61
PLD on STO (001)	400-500	4.5 % Co	16 ⊥/∥ [i]	1.4 μ_B/Co	62
Electrodeposited on Si (001)	Not given, est. 20 nm	13.2 % Co	35 ∥	1 μ_B/Co	66
Electrodeposited on SiO_2/Si (001)	20	3 % Fe	220 [ii]	29 μ_B/Fe	58
Electrodeposited on SiO_2/Si (001)	20	3.2 % Mn	140 [ii]	17 μ_B/Mn	58
Electrodeposited on SiO_2/Si (001)	20	2.7 % Co	90 [ii]	13 μ_B/Co	58
Electrodeposited on SiO_2/Si (001)	20	3.4 % Cu	50 [ii]	5.8 μ_B/Cu	58
Electrodeposited on Si (111)	~ 500	2.5 % Mg 0.5 % Zn	0.28	~ 0.04 μ_B/Mg	x
Electrodeposited on Si (111)	~ 500	2.3 % Mg 0.3 % Bi	0.16	~ 0.02 μ_B/Mg	x
PLD on LAO (001)	Not given, est. 100 nm	3 % Cu	8.3	1.1 μ_B/Cu	67
PLD on Si (111)	≥ 100	12 % Co	230	7.2 μ_B/Co	63
PLD on STO (001)	≥ 150	15 % Co	≈ 100 * (est.) ⊥	2.5 μ_B/Co	64
PLD on MgO (100)	953	25 % Co	105 ⊥	1.5 μ_B/Co	65
PLD on Al_2O_3 (0001)	1000	3 % Co	14.3 ∥	1.9 μ_B/Co	68
PLD on Al_2O_3 (0001)	1000	3 % Co	12 ⊥	1.6 μ_B/Co	68
PLD on LAO (001)	200	1 % Fe	0.38	0.15 μ_B/Fe	69
PLD on LAO (001)	200	5 % Co	0.5*	0.04 μ_B/Co	70
Magnetron sputtering on Al_2O_3 (0001) + Ar^+ sputtered for 10 min	1000	3 % Co	24.2 [iii]	3.2 μ_B/Co	71
Magnetron sputtering on Al_2O_3 (0001) [iv]	1000	3 % Co	38	5 μ_B/Co	72

[i] same data presented in [73] [ii] undoped film has M_s = 280 kA m^{-1}
[iii] before Ar^+ sputtering, M_s = 7.5 kA m^{-1} (1μ_B/Co)
[iv] sputtered in vacuum (oxygen deficient films formed) vs. sputtered in oxygen [71] (stoichiometric films)
[x] Lorena M.A. Monzon (unpublished); films are nanoporous rather than compact
*Magnetism attributed to Co clusters
- There is also a report without magnetization curves for which XPS measurements show that Ce ions are in a mixed valence state in Fe doped (2, 6 wt %) films (PLD grown at 550 °C on Si (100), t = 200 nm, (111) oriented films), with Fe ions in the ionic state, the latter result from which the authors rule out the possibility of ferromagnetic metallic clusters [74]

A summary of the literature reports for RTFM in doped CeO_2 nanostructures (mostly nanoparticles) is given in Table 4.5. The maximum magnetization value reported for each reference is listed in order, starting with the largest magnetization. For the co-precipitation syntheses, nitrates of cerium and cobalt were used in each case unless stated otherwise. From the data it appears that the magnetization values are not correlated with either the particle size or specific dopant used. While the majority of the reports attribute the enhanced magnetization to oxygen vacancies created by doping, another possible contribution is RFTM due to free-electron interactions provided by transition metal dopants with a 3+ charge state for example [33].

Table 4.5. Maximum room temperature magnetization values per dopant reported for doped CeO_2 nanostructures (nanoparticles unless stated).

Synthesis	Diameter (nm)	Dopant (at. %)	M_s (A/m)	Ref
Electrodeposited on Cu at 1 mA/cm^2	250-400 [i]	5 % Fe	65000	[75]
Electrodeposited on Cu at 3 mA/cm^2	27 [ii]	10 % Fe	50000	[75]
Gel-combustion (glycine + nitrates)	10	15 % Fe	14500	[76]
co-precipitation + vacuum anneal	7	9 % Co	6100	[77]
co-precipitation + vacuum anneal	17	5 % Co	3000	[78]
co-precipitation + VSM activated anneal in N_2 atmosphere at 450 °C	8	8 % Ni	2100	[79]
Sol-gel using coconut water	45	1 % Fe	840	[80]
Self-propagating room temp. synthesis (SPRT)	10	12 % Fe^{3+}	150 [iii]	[24]
Composite Hydroxide Mediated (CHM) synthesis	55, length = 3-7 μm [iv]	Mn (% not given)	150	[43]
co-precipitation	6	7 % Ni	125	[32]
co-precipitation	7.5	7 % Fe	100	[81]
co-precipitation	11	1 % Fe	90	[82]
SPRT	4	1 % Pr	75	[26]
co-precipitation	8	3 % Co	75	[83]
co-precipitation	7.2	3 % Co	65	[31]
co-precipitation	2-3	11 % Cr	60	[30]
Sol-gel with citric acid	10	3 % Cr	45	[84]
Sol-gel with PVP	15	3 % Co	45	[35]
Sol-gel (PVA) + calcined at 600 °C	25	3 % Fe	45	[85]
co-precipitation	4	20 % Fe	11 [v]	[33]
co-precipitation	7	4 % Ni	9	[86]
Sol-gel (PEG) + calcined at 400 °C	6.6	10 % Cu	5.5	[28]
Solution combustion using L-glutamic acid	4	10 % Ca	1.7	[23]

[i] grain size is actually much smaller (16 nm) [ii] nanopores (pore size given)
[iii] the same authors report a similar magnetization value for 3 nm diameter particles elsewhere [25]
[iv] rods; CHM synthesis involves adding $CeO_2/MnCl_2$ to a basic solution (KOH + NaOH) and heating to 200 °C for 72 h [v] synthesized using cerium chloride; M_s = 5 (3) A m^{-1} for similar NPs doped with 10 % Fe synthesized using cerium nitrate (ammonium nitrate)

It is evident from Table 4.5 that most of the M_s values for doped nanoparticles are much smaller than for doped films. In comparison to undoped nanoparticles though, M_s for their doped

counterparts above are typically larger. The largest room temperature magnetization values are measured for Fe doped nanospheres and nanopores electrodeposited on a 99.99 % purity copper plate [75]. The nanospheres are of diameter 250-400 nm but are polycrystalline and are actually composed of 16 nm grains, while the nanoporous structures have pore diameters of 27 nm. The authors do not state the thickness of the deposits, but the samples may actually be considered as quasi-films rather than true free-standing nanostructures since they are deposited on a substrate. The morphology of the nanostructures is varied by changing the applied current density during electrodeposition. The largest values of M_s measured are 65 and 50 kA m^{-1} for the nanospheres and nanopores respectively, magnitudes which are more similar to those typically measured for films rather than for nanoparticles, where the magnetization is measured perpendicular to the Cu substrate plane. The coercivities of these samples (~ 330-660 mT) are markedly larger than those typically measured for d^0 or dilute magnetic oxides (usually several mT), however the authors argue that all of the iron is incorporated by substitution into the ceria lattice as inferred from XRD and XPS measurements, and that the magnetic signal may be attributed to oxygen vacancies.

The next largest magnetization reported is 14.5 kA m^{-1} for 10 nm nanoparticles doped with 15 at. % Fe and synthesized by a gel-combustion reaction [76]. The coercivities measured are ≤ 50 mT, and the authors deduce (from magnetization, XRD, TEM and Raman data) that for ≤ 15 at. % doping their samples are free of iron/iron oxide clusters and that the magnetism may be attributed to defects and/or oxygen vacancies. For 20 at. % doping they measure a magnetization of 18 kA m^{-1}, but they also detect an Fe_2O_3 phase in XRD for this sample, and hence the source of the magnetism for this particular sample may be different than for the other more lightly doped samples. They also note that their undoped nanoparticles are diamagnetic. Elsewhere, it is reported that the iron solubility limit in the ceria lattice is between 10 and 20 mol % for doped nanoparticles synthesized by the co-precipitation method [87]. Interestingly, all of the remaining reports for nanoparticles with magnetizations > 1 kA m^{-1} in Table 4.5 are for samples subject to reducing anneals, which suggests that those samples which are richer in oxygen vacancies may have enhanced magnetization values compared to those which are not additionally vacuum annealed after synthesis. In the report for Pr doped nanoparticles [26], the authors find that Pr doping actually suppresses the ferromagnetic-like signal that they measure compared to their undoped CeO_2 sample, which is somewhat similar to the scenario that Fernandes *et al.* previously reported for their transitional metal doped films [58]. Meanwhile, a recent XAS study of Fe doped CeO_2 nanoparticles performed in transmission mode on the O *K*, Fe *L* and Ce *M* edges reveals that the relative Ce^{3+} content does not vary monotonically with Fe doping concentration [88]. At lower doping concentrations (< 5-7 at. % Fe) it is proposed that the defect structure is Fe^{3+}–V_O–Ce^{3+} which allows charge transfer between the Ce and Fe and RTFM, while for higher doping levels of up to 11 at. % Fe the defect structure is Fe^{3+}–V_O–Fe^{3+}, and that the paired ion structure is antiferromagnetic which acts to negate (reduce) the RTFM signal.

In order to complete the literature summary for doped CeO_2, experimental reports for RTFM in the last remaining sample form, the bulk or micropowders/crystals, are listed in Table 4.6. As before, the maximum magnetization value reported for each reference is listed in order, starting with the largest magnetization.

Table 4.6. Maximum room temperature magnetization values per dopant reported for doped CeO_2 bulk samples (micropowders).

Synthesis	Dopant (at. %)	M_s (kA/m)	Ref
Solid state reaction (SSR) + H_2 anneal	5 % Fe	11.5	[47]
SSR + H_2/Ar anneal	3 % Co	8.5	[89]
SSR + H_2/N_2 anneal	3 % Co	8.4	[90]
SSR	2.7 % Fe	7.6	[91]
SSR	5 % Co	7.5	[92]
SSR	3 % Co	4.7*	[93]
SSR + H_2/Ar anneal	3 % Co	3.7	[94]
SSR	2.1% Co	3.6	[16]
SSR	2 % Co	3.0	[95]
SSR	3 % Co + 10 % Y	2.7	[96]
Chemical solution method (with citric acid) + calcined in air	20 % Nd	0.38	[97]
SSR	3 % Fe	0.3	[44]
Sol-gel (coconut water) + calcined in air	10 % Zn	0.23	[98]
Sol-gel (coconut water) + calcined in air	10 % Co +10 % Zn	0.007**	[99]

* Attributed to Co clusters ** Attributed to Co_3O_4 clusters

From Table 4.6 it can be seen that most of the room temperature magnetization values for doped CeO_2 bulk samples are several kA m^{-1}. The three highest magnetizations values are all for samples subject to reducing anneals, again indicating that oxygen vacancy rich samples give larger magnetization values. Samples not subject to vacuum annealing mostly have intermediate magnetizations, while those calcined in air (which will reduce the oxygen vacancy concentration) have the lowest magnetizations; nevertheless, the magnetization values for doped bulk samples are still typically larger than for undoped bulk samples (shown previously in Table 4.2). Note that for two of the reports listed in Table 4.6, the indicated magnetization is attributed to additional cobalt metal/oxide phases.

In terms of a band structure explanation for magnetism in CeO_2, several density functional theory calculations have been performed for ceria. It is first noted that DFT+U (where U is Hubbard-like, localised term) must be implemented in the calculation in order to capture the full electron localization on Ce 4*f* states and to more accurately model the ground state [100]; standard DFT calculations cannot account accurately for the strong on-site Coulomb repulsion between the electrons in the localized Ce 4*f* orbitals. One of the earlier calculations for magnetism in ceria attributes the ferromagnetism for the Co doped case to the combined contributions of spin polarized Co, Ce, and O atoms as well as O vacancies (V_O) where the concentration of both the Co and V_O is 12.5% [63]. The magnitudes of the moments are 2.681 μ_B for Co *d* electrons, 1.476 μ_B for Ce and 0.168 μ_B for spin polarized O. For undoped ceria, they find that while an oxygen vacancy can cause exchange splitting in nonmagnetic oxides, an oxygen vacancy itself cannot induce an obvious ferromagnetic signal in ceria; the authors suggest that this result may explain the existence of weak paramagnetism only (no ferromagnetism detected) measured for their pure CeO_2 films in the same report. The same authors report similar findings for Co doped ceria in a later paper, where the U parameter is

fixed at 5.3 eV, in which they further propose that V_O defects may lead to strong ferromagnetic exchange coupling between nearest neighboring Co ions, mainly attributed to spin-splitting of Co 3*d* states, via electrons trapped in V_O (F-center mediated exchange) [101]. Again, no ferromagnetism is calculated for V_O for undoped ceria. In contrast, another early calculation for undoped ceria finds thst V_O defects *do* produce magnetic signals which are enhanced at the surface compared to in the bulk [38]. They calculate moments of 1.41 μ_B, 1.87 μ_B and 1.98 μ_B per (2×2×2) supercell for 1 V_O in the bulk, 1 V_O at the surface and for 2 V_O at the surface respectively, although they do not state what value of U they use in their calculation. These calculations may support some of the experimental reports for ferromagnetism in undoped ceria nanoparticles and thin films, where the surface to volume ratio is greatly enhanced compared to the bulk and where surfaces can accommodate oxygen vacancies most readily. No moment is measured for the bulk without oxygen vacancies, which corroborates with the experimental reports that measure ferromagnetism in undoped ceria bulk upon grinding, irradiation or vacuum annealing (creates defects and oxygen vacancies) only, and not in the pristine, defect-free, stoichiometric phase.

Another calculation, performed within the local spin density approximation (LSDA) + U scheme, using U = 8 eV, calculates that with increasing oxygen deficiency, the electrons left behind by oxygen removal localize not only on the Ce 4*f* orbitals but also on the vacancy sites, leading to ferromagnetism with both superexchange and polarization in the cases of heavy doping [102]. However, soon afterwards a paper was published by another group in direct response to the above calculations which they hotly debated [103], finding that V_O concentrations of up to 12.5% *do not* cause localization in the vacancy site, and thus are *not responsible* for any enhanced ferromagnetism on any of (111), (110) or (100) ceria surfaces. The authors use a U value of 5 eV, and note that the value of U utilized in [102] could have been too large, as U values > 6 eV have been shown to return to a delocalized solution, similar to smaller values of U, which could explain the appearance of an erroneous density of states in the vacancy position. Furthermore, the authors note that the absence of density in the vacancy position is not a surprise, as ceria is known *not* to behave like a strongly ionic oxide where an F centre forms upon vacancy formation. Instead, the authors emphasize that the localization of the excess electrons on neighbouring Ce sites is well characterized [104], but despite this, note that F centre coupling mechanisms due to oxygen vacancy formation are still being proposed as the reason for reported enhanced ferromagnetic behaviour in undoped CeO_2 samples.

However, in contrast to the above, subsequent calculations concerning undoped ceria by Fernandes *et al.* [54] reveal that both Ce and O vacancies are consistent with a ferromagnetic state for 3-25% V_O concentrations, with calculated maximum moments 4 μ_B/Ce vacancy (associated with O 2*p* states) and 2 μ_B/O vacancy (related to Ce 4*f* states). The authors use a U value of 5 eV, which should not return a delocalized solution. In a later calculation the same authors report paramagnetism for V_O–V_O pairs located along the (110) directions and ferromagnetism for V_O–V_O pairs along the (100) (0.04 μ_B/V_O) and (111) (2.67 μ_B/V_O) directions [57]. For both of their reports, the authors use the LMTO method. A more recent

calculation finds that Ce vacancies can induce a magnetic moment in undoped ceria which arises mainly from the 2*p* hole state of the nearest neighbouring O atom to the Ce vacancy [105].

It is thus evident from the aforementioned calculations that whether oxygen vacancies mediate ferromagnetism in *undoped* ceria is still hotly debated among theoreticians using DFT calculations to elucidate the band structure, and it would appear that the contradicting results may be in part due to the sensitivity of the band structure results to both the DFT method used and the U parameter implemented.

In a continuation of the literature summary of calculations for *doped* ceria, further to the two reports mentioned previously which calculate oxygen vacancy mediated magnetism in Co doped ceria (and none in undoped ceria) [63,101], another calculation using DFT-GGA calculates that Co polarizes the neighbouring Ce and O atoms with a maximum moment of ~ 4 μ_B/supercell or 2.82 μ_B/Co for 6.5% Co doping and a 6.25% V_O concentration [90]. Similar to the previous reports, they calculate no ferromagnetism in pure CeO_2 due to oxygen vacancies, whereas for Co doped ceria, the oxygen vacancies help enhance the ferromagnetic coupling of the Ce, as well as those of the doped magnetic impurity spins. For the ferromagnetic ground state the F-centre ferromagnetic exchange mechanism (involving a spin-polarized electron trapped at an oxygen vacancy) is suggested. A subsequent calculation for the same material reports a transition from antiferromagnetic to ferromagnetic coupling as the V_O concentration increases, with maximum calculated moments of 5 μ_B per (2×2×2) supercell for 2 V_O with both 6.5 and 12.5% Co doping, corresponding to ~2.5 μ_B/Co and ~0.95 μ_B/Ce [106]. The authors note that the calculated magnetic moments per cell depend on the degree of reduction, which they suggest could explain the widespread magnetization values measured by experiments. Hence for the case of Co doped ceria, there is a general agreement among theoreticians that oxygen vacancies do mediate the magnetism.

Elsewhere, calculations have been performed for ceria doped with other elements. Using the LSDA + U method (U = 5.3 eV), for ceria doped with carbon, a moment of 2 μ_B/supercell has been calculated with 1 carbon atom/supercell, equivalent to 0.65 μ_B/C [107] (and where 1 supercell is equivalent to 4 unit cells in this case). The magnetism is attributed to hole-mediated long-range magnetic coupling (double exchange) between local magnetic moments attributed to the collective effects of the *p-p*, *p-d*, and *p-f* hybridizations between C and neighbouring O or Ce atoms. In addition, the authors calculate that an oxygen vacancy makes the ferromagnetism in C-doped CeO_2 disappear, since the two electrons that are left behind by removing one O atom are believed to compensate for the two holes provided by the C dopant, thus wiping out the ferromagnetism according to the physical picture that additional hole-doping is needed to stabilize the ferromagnetic ground state. For nitrogen (N) doped ceria, a half-metallic ground state with ~ 1.0 μ_B/N impurity is calculated (0.4 μ_B associated directly with the N atom itself, ~ 0.25 μ_B due to next-nearest neighbouring O atoms) using either DFT-GGA or DFT-LSDA, both with and without U, where U = 5.3 eV, for N doping levels of either 3 % or 6 % [108]. The ferromagnetism is attributed to a hole-mediated long-range exchange mechanism similar to that proposed for the previously mentioned carbon doped ceria

calculations [107]. A DFT calculation for Cu doped ceria calculates a moment of 1.0 μ_B per Cu_{Ce}-V_O complex (or 0.5 μ_B/Cu), where U = 8 eV is chosen [109]. It is proposed that the defect complex formed by substitution of a Cu atom for a Ce atom (Cu_{Ce}) and a nearest neighbour oxygen vacancy (V_O) has a low formation energy, and that strong ferromagnetic coupling between the defect complexes may be attributed to a magnetic coupling chain formed by the strong *p-d* interactions between the Cu and O atoms.

A DFT-GGA+U calculation (U = 5.3 eV) for Fe doped ceria predicts the emergence of ferromagnetism with/without oxygen vacancies, attributable to an F-centre/double exchange mechanism respectively [110]; a large calculated moment of ~ 4.0 μ_B/Fe dopant is almost entirely associated directly with the Fe atom, with or without V_O and for both 6 % and 12.5 % Fe doping levels. The result of this calculation is hence different to those mentioned previously for other ferromagnetically doped ceria systems, namely with Co [63,90,101,106] for which oxygen vacancies *are* proposed to mediate the ferromagnetism in the Co doped samples.

Finally it is noted that the magnitudes of the magnetic moments per dopant atom which are calculated for doped CeO_2, typically ~1-5 μ_B/dopant, correspond to many of the moments experimentally measured for several at. % doped films, such as those listed in Table 4.4; however, some of the higher moments per dopant atom experimentally measured for films exceed those values which are calculated, suggesting that magnetism may not be due to the dopant atom alone, as was mentioned earlier. For the majority of nanoparticles in contrast, it can be readily calculated that the moments per dopant atom are generally much lower than those for films, typically << 1 μ_B per dopant, and thus rarely exceed the values obtained by calculation.

4.3. Experimental results

4.3.1 Nanoparticle synthesis

CeO_2 nanoparticles were synthesized in powder form by homogeneous precipitation, a wet chemical synthesis in which the precipitating agent (NaOH in this case) is synthesized in the solution with the cerium nitrate reagant by slow addition such as by dropwise titration from a burette. More detailed information about the synthesis is given in Chapter 2, experimental methods (section 2.2). CeO_2 nanoparticles start to precipitate from the solution when the pH reaches a certain level, followed by gentle heating (60 °C) and stirring for about 1 hour in order to promote further precipitation and nanoparticle formation. Some surfactant, such as polyethylene glycol (PEG), is added to the solution in order to reduce particle aggregation and to facilitate the homogeneous precipitation of the ceria from solution.

Cerium nitrate ($Ce(NO_3)_3.6H_2O$) precursors of nominal purity 99 % and 99.999 % (Sigma Aldrich) were used to synthesize ferromagnetic and ~ non-ferromagnetic nanoparticles respectively; the NaOH was 99.99 % nominal purity (Sigma), while the PEG (also purchased from Sigma) was ultrapure grade 1500 molecular weight for molecular biology (≤ 5 ppm of ferromagnetic impurities according to the manufacturer, < 1 ppm actually measured by ICP-MS). Both the PEG-1500 and NaOH were measured to be purely diamagnetic at room temperature, with $\chi = -8.3\times10^{-6}$ and -1.3×10^{-5} respectively, with no trace of any ferromagnetic-like signals measured for either reagent. ICP-MS analysis of the $Ce(NO_3)_3.6H_2O$ 99 % purity precursor revealed < 1 ppm of ferromagnetic impurities, while magnetization measurements at room temperature revealed that the precursor was purely paramagnetic ($\chi = +2.8\times10^{-4}$) with no trace of a ferromagnetic-like signal. The main impurity in $Ce(NO_3)_3.6H_2O$ 99 % is lanthanum (~ 1-2 wt %), present due to the difficulty in fully separating lanthanum from cerium in the lower purity grade cerium compounds. In addition, no sharp upturns (due to ferromagnetic clustering) in the magnetic moment measured as a function of temperature from 300 - 4 K in an applied field of 1 T were measured for the same precursor. All glassware was cleaned with strong acid, followed by ethanol and deionised water. For a typical synthesis, 0.1 M NaOH (99.99% nominal purity) was slowly added dropwise from a burette into a stirred solution of 4.5 mL 10 mM cerium nitrate and 0.5 mL 0.5 M PEG-1500 until the pH of the solution stabilized > 11, which could be observed by a visible colour change of the solution from colourless to pink. The total NaOH volume added was typically 4 mL. After gentle heating (60 °C) and gentle stirring for 1 h, the solution turned a pale yellow colour, after which the powder was washed with deionised water and high purity ethanol, extracted from solution by vacuum

filtration (or centrifugation) and dried in a drying cabinet at ~50 °C for 24 h, after which about 4 mg of dry yellow CeO_2 powder was typically finally recovered. Distinct room temperature magnetic signals were measured for nanopowders synthesized using the 99% cerium nitrate, but not for those synthesized using the 99.999% cerium nitrate. For the syntheses where additional dopants were intentionally added, lanthanum nitrate, magnesium nitrate, and zinc nitrate (all 99.999 % nominal purity) were used as sources of La, Mg and Zn respectively and were made up with the cerium nitrate solution. In addition, it is noted that a marked reduction in the magnetic signal of the ferromagnetic nanopowders was measured for larger batches (> 10 mg) where the volume of the reagents used were scaled up. Hence the ferromagnetic nanopowders were typically synthesized in 4 mg batches as outlined above. For characterization experiments where larger masses of ferromagnetic nanopowder were required for analysis, multiple 4 mg ferromagnetic nanopowder batches were synthesized and their masses combined.

4.3.2 X-Ray powder diffraction

A typical X-Ray powder diffractogram measured for a ferromagnetic CeO_2 powder is shown in Figure 4.7. The reflections are indexed to the face centred cubic crystal structure of ceria, which has the *Fm-3m* space group.

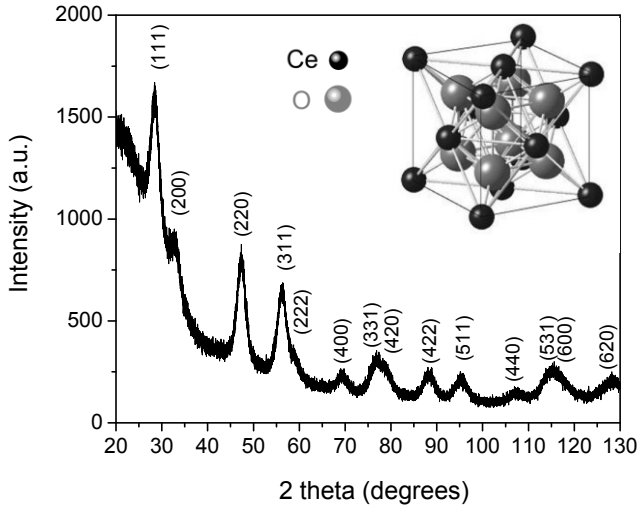

Figure 4.7. XRD spectrum for a ferromagnetic CeO_2 nanopowder together with an illustration of its crystal structure.

The ferromagnetic nanopowder is single phase within the detection limits of the measurement, with no evidence of any other possible phases such as Ce, Ce_2O_3, La, La_2O_3, or $Ce(OH)_3$ intermediates formed during the synthesis for example. The broad background intensity contribution to the signal at low angles (< 35° 2θ) is due the amorphous quartz micro-slide upon which the powders were mounted for measurement. The reflection peaks are significantly broadened due to the small crystallite size. Using the Scherrer equation, the crystallite size was estimated to be 4.2 ± 0.3 nm, with 1.5 ± 0.1 % lattice strain.

Refinement of the XRD pattern was performed using the Rietveld method, in order to more accurately calculate the lattice parameter, and is shown in Figure 4.8, together with the powder profile for a reference micropowder. The lattice parameter for the ferromagnetic nanopowder is calculated to be 5.4168 Å, which represents an expansion of ~ 0.1% compared to the bulk value of 5.4113 Å. Such a lattice expansion is consistent with enhanced Ce^{3+} character with decreasing crystallite size for nanoceria, since the ionic radius of Ce^{3+} is larger (115 pm) than that of Ce^{4+} (101 pm), and is also correlated with the formation of charge compensating oxygen vacancies. Note that for the micropowder, no broadening of the XRD peaks is evident due to the large size (≥ 1 μm) of the crystallites, to which Scherrer broadening does not apply. Very similar results were obtained for the non-ferromagnetic nanopowder, except that its crystallite size was typically slightly larger, ~ 6 nm, than that measured for the ferromagnetic nanopowder.

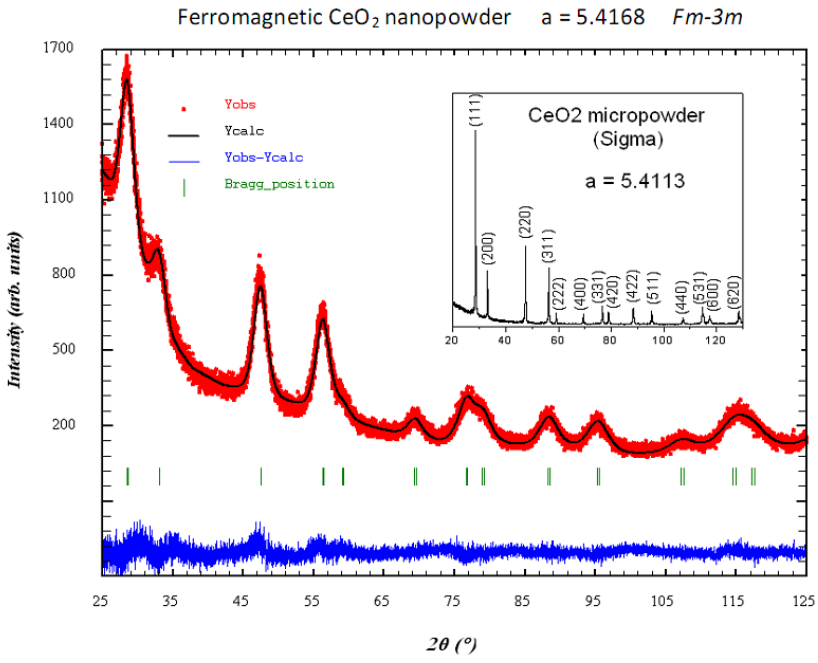

Figure 4.8. Rietveld refinement of X-Ray powder diffraction data for a ferromagnetic CeO_2 nanopowder; the inset displays the measured diffractogram for a bulk micropowder (Sigma Aldrich 99.999% nominal purity).

4.3.3 Electron Microscopy analysis

Electron microscopy analysis was performed using scanning and transmission electron microscopy (SEM and TEM respectively) in order to elucidate the microstructure and nanostructure respectively of CeO_2.

SEM images of the ferromagnetic nanopowder synthesized using 99% cerium nitrate are shown in Figure 4.9. The powder was dispersed in ethanol, sonicated, and a droplet of solution was dropped onto a carbon sticky tab, which was then affixed to an SEM stub for imaging. The nanoparticles are largely aggregated in clumps of several hundred nanometers in size. Since the nanoparticles are very small and also due to clumping, it is difficult to resolve discrete particles, although some smaller particles (< 20 nm) may be resolved in Fig. 4.9 (c). Similar images were obtained for all other nanopowders, ferromagnetic and non-ferromagnetic, and for those dispersed in H_2O as well as in ethanol. For dry powders dispersed directly onto the carbon tabs for analysis (and not suspended in solvent) the agglomerate sizes are typically about an order of magnitude larger than those shown in Fig. 4.9. An SEM image for the dry Sigma 99.999 % micropowder (i.e. not dispersed in solvent) is shown also in Figure 4.10. The contrast is not so high due to the tendency of bulk ceria to retain electrostatic charge under the electron beam as it is a poor conductor.

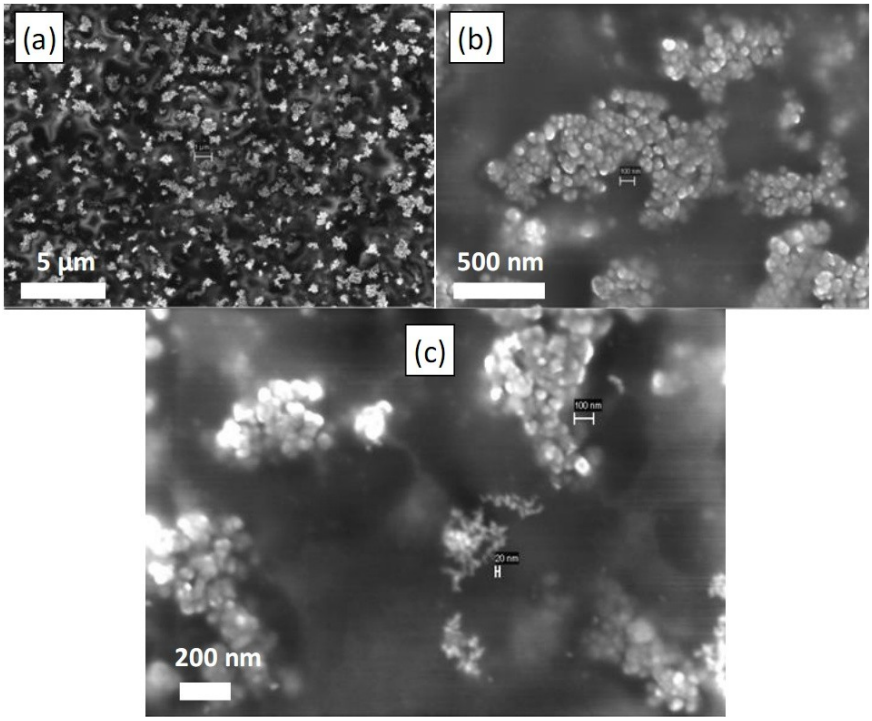

Figure 4.9. SEM images for a ferromagnetic CeO_2 nanopowder synthesized using 99% cerium nitrate.

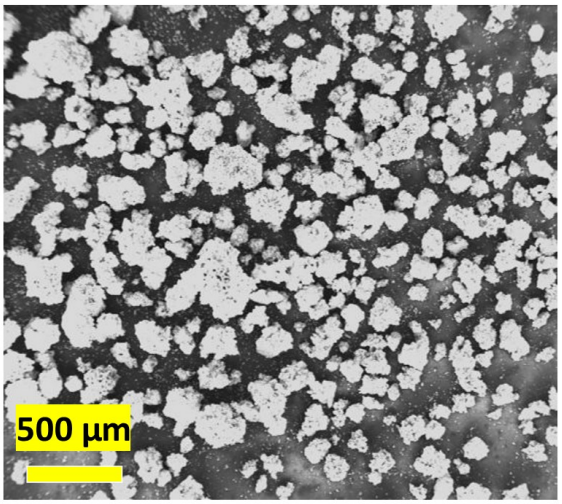

Figure 4.10. SEM image of bulk CeO_2 micropowder purchased from Sigma Aldrich (99.999 % nominal purity).

In order to obtain higher magnification images of the nanoparticles than possible by SEM, TEM analysis was also performed. High resolution TEM images of the ferromagnetic nanopowder, denoted FM, synthesized using 99% cerium nitrate, and the non-(ferro)magnetic nanopowder, denoted NM, synthesized using 99.999% cerium nitrate, are shown in Figure 4.11, together with a typical TEM selected area electron diffractogram (SAED) for the nanopowder.

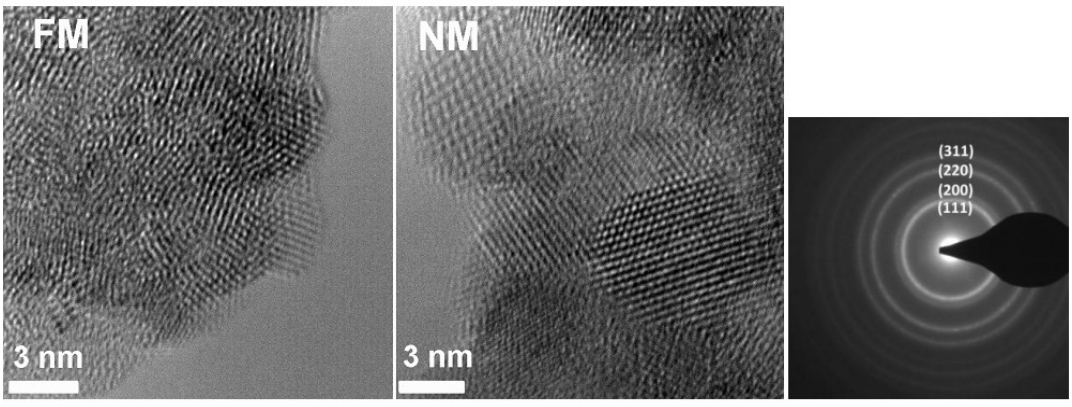

Figure 4.11. HRTEM images in real space for (left) ferromagnetic and (middle) non-magnetic nanoparticles, and (right) in diffraction space for the ferromagnetic sample.

It may be estimated from Fig. 4.12 that the crystallite size for the ferromagnetic nanopowder is ~ 4 nm, in agreement with that calculated from the XRD peak broadening. The crystallite size for the non-magnetic nanopowder is slightly larger at ~ 6 nm. The ferromagnetic nanopowder shows evidence of enhanced polycrystallinity compared to the non-

magnetic nanopowder. For both powders however the SAED pattern is similar, exhibiting diffraction rings indicative of polycrystalline nanoceria, which correspond to the reflections measured by XRD. The nanoparticles are not completely spherical but are somewhat faceted; the predominant lattice reflection in real space is from the (111) family of lattice planes. Although it is possible to crudely estimate the lattice parameter by determining the spacing of the lattice fringes in the real space TEM image, this was not performed here due to the lack of aberration correction for the instrument together with other approximations; the value obtained from Rietveld refinement of the XRD pattern is more definitive. Figure 4.12 compares real space images of the same two nanopowders at a lower magnification. It is again evident that the crystallite size is slightly larger and the overall crystallinity is slightly enhanced for the non-magnetic (NM) powder synthesized using 99.999% cerium nitrate compared to the ferromagnetic (FM) one synthesized using 99% cerium nitrate. Powders were typically aggregated, regardless of dispersion in H_2O or ethanol or by preparing different concentrated dispersions or by using different concentrations of surfactants during synthesis; the driving force for aggregation is likely due to electrostatic attraction between the nanoparticles.

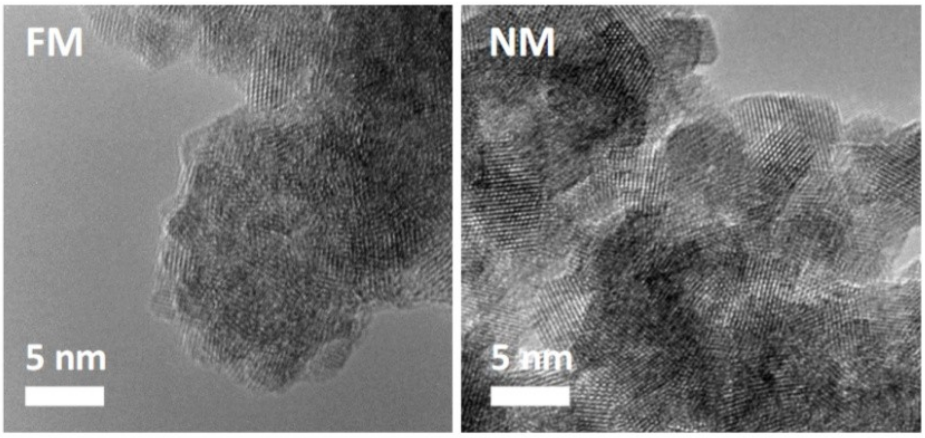

Figure 4.12. TEM real space images comparing the morphologies of ferromagnetic and non-magnetic nanoparticles.

Figure 4.13 displays the aggregation exhibited at the mesoscale for a ferromagnetic nanopowder at low magnification. The aggregate sizes are typically ~ 100 nm or larger in size, with a minority of clumps of smaller size, although the figure preferentially focuses on some of the smaller clumps since it is easier to show discrete nanoparticles this way.

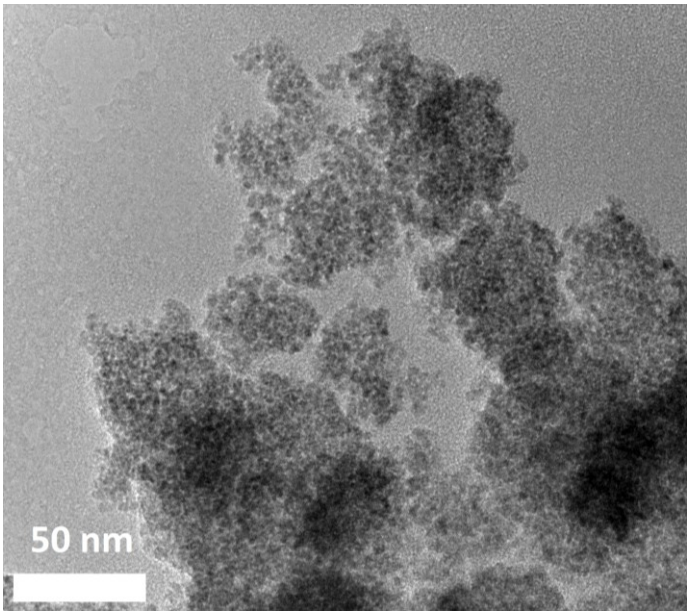

Figure 4.13. Low resolution real space TEM image of ferromagnetic nanoparticles which illustrates the degree of particle aggregation at the mesoscale.

4.3.4 Inductively Coupled Plasma Mass Spectrometry

Sample purity was sensitively checked by Inductively Coupled Plasma Mass Spectrometry (ICP-MS). As mentioned previously the 99% purity $Ce(NO_3)_3.6H_2O$ and ultrapure PEG-1500 reagents each had < 1 ppm by weight of each of Fe, Ni and Co present when tested. The main impurity in the 99 % purity $Ce(NO_3)_3.6H_2O$ reagent is non-magnetic La (~1-2 wt %). La is incorporated substitutionally in CeO_2 forming the solid solution $Ce_{1-x}La_xO_{2-\delta}$, with the fluorite crystal structure maintained even up to 55 at. % La doping for bulk CeO_2 [111], demonstrative of the high stability of the ceria lattice, and also indicative of why ceria is an efficient catalyst allowing facile oxygen incorporation/removal. ICP-MS analysis was also performed on the CeO_2 nanopowders synthesized using the 99% and 99.999% $Ce(NO_3)_3.6H_2O$ precursors, the results of which are displayed in Table 4.7, with ferromagnetic elements denoted in bold. CeO_2 nanopowders synthesized using 99% cerium nitrate displayed less than 1 ppm of trace ferromagnetic impurities whereas nanopowders synthesized using 99.999% cerium nitrate contained 8 ppm of Ni, which nevertheless could contribute at most 4 A m^{-1} (M_s bulk Ni = 488 kA/m) to the magnetization at room temperature. The other impurities detected may come from the general laboratory environment in which the synthesis was performed, as well as from the precursors. In comparison, for a magnetization of order 100 A m^{-1}, which is typically measured for ferromagnetic CeO_2, about 60 ppm of iron metal (M_s bulk Fe = 1710 kA/m) or 210 ppm of magnetite (M_s bulk Fe_3O_4 = 478 kA/m) for example would be required to

produce a magnetization value of similar magnitude; in light of the ICP-MS results, it therefore seems unlikely that ferromagnetic impurities can account wholly (or even partly) for the ferromagnetism of CeO_2 nanopowders.

Table 4.7. ICP-MS results for CeO_2 nanopowders synthesised using 99 % and 99.999 % nominal purity cerium nitrate reagents; quantities are given in units of ppm (parts per million).

Element	CeO_2 (99 %)	CeO_2 (99.999 %)
Boron	57.9	25.3
Aluminium	35.1	14.5
Vanadium	< 0.4	29.8
Manganese	4.3	< 0.4
Iron	**< 0.4**	**< 0.4**
Cobalt	**< 0.4**	**< 0.4**
Nickel	**< 0.4**	**8.1**
Copper	25.1	41.3
Zinc	51.6	4.3

It is noted in addition to the impurities listed above, there may likely be for example H, C, O and N impurities from the precursors used during the synthesis, but these elements are not detectable by ICP because their atomic weight is too small and/or they are gaseous.

4.3.5 Magnetization data

Room temperature magnetization data measured by SQUID magnetometry for CeO_2 nanoparticles synthesized using both low (99%) and high (99.999%) purity cerium nitrate are shown in Figure 4.14. In each case the concentration of cerium nitrate used was 10 mM and the total batch size was ~ 4 mg. It is evident that for these 4 mg batches, nanopowders synthesized using the lower purity precursor are ferromagnetic-like, whereas those synthesized using the higher purity precursor are almost non-magnetic, after correction for the diamagnetic background due to the gelatin capsule in which the samples were mounted for the magnetization measurement in addition to the small paramagnetic background due to CeO_2.

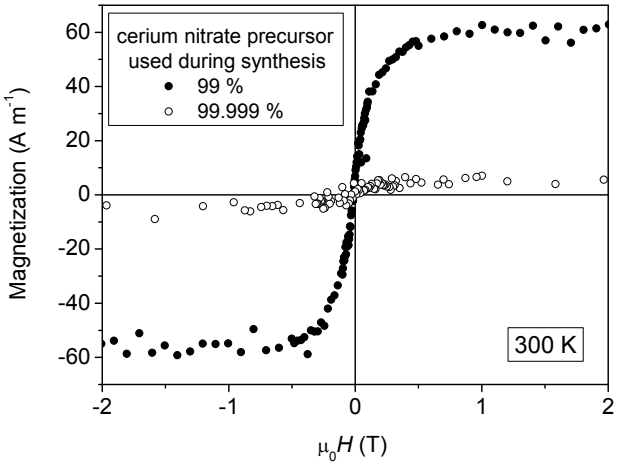

Figure 4.14. Room temperature magnetization curves (corrected for the diamagnetic background of the gelcap plus a small paramagnetic CeO_2 contribution) for CeO_2 nanopowders synthesized using different purity 10 mM cerium nitrate precursors. The measured batch size is ~ 4 mg for each sample.

The fact that no distinct ferromagnetism is measured for nanopowders synthesized using the higher purity precursor proves that the ferromagnetic-like signals do not arise from impurities due to the glassware or from ferromagnetic contamination during synthesis. The 99% cerium nitrate precursor was previously measured to be purely paramagnetic at room temperature while ICP-MS revealed that it contained < 1 ppm of ferromagnetic impurities; hence it is unlikely that impurities in this precursor can account for the magnitude of the magnetization values measured. In addition, a thermal magnetization scan of the 99% cerium nitrate precursor in a field of 2 T revealed a low temperature Curie law paramagnetic upturn only, with no trace of ferromagnetic impurity phases; the Ce^{3+} content was estimated to be ~ 40% from the paramagnetic upturn, which suggests that the sample does not have purely Ce^{3+} character. ICP-MS analysis of the nanopowder synthesized using the 99% cerium nitrate precursor was previously shown to contain < 0.4 ppm of any ferromagnetic impurity, providing further evidence that the magnetic signal cannot be due to ferromagnetic impurities. The magnetization curve for the magnetic nanopowder is almost anhysteretic (H_c = 10 mT) and saturates readily (< 0.5 T) in applied magnetic field. Only one half of the hysteresis loop is shown for clarity of display (as are all subsequently displayed magnetization curves for CeO_2). The saturation magnetization for the magnetic nanopowder is ~ 60 A m^{-1} (magnetic moment ~ 3×10^{-8} Am^2) as shown for a typical 4 mg batch, but was generally measured to fall within the range 40 – 180 A m^{-1}, with the largest magnetizations actually measured for smaller batches of order 1 mg in size. The nanopowder synthesized using the 99.999 % purity precursor has a value for M_s of at most 5 A m^{-1}, although the data is quite noisy; the saturation magnetization for this sample was never measured to be more than this value. One possibility is that this small magnetization arises due to a few ppm of total ferromagnetic impurities in the precursor

materials (PEG, NaOH, cerium nitrate); ICP-MS revealed 8 ppm of nickel measured for the CeO_2 nanopowder synthesized using the higher purity cerium nitrate precursor, which corresponds to a magnetization of ~ 4 A m^{-1}.

The magnitude of the saturation magnetization of the nanopowders synthesized using 99% cerium nitrate appears to depend on the batch size synthesized and measured by SQUID magnetometry. Figure 4.15 illustrates the effect of batch size on the saturation magnetization M_s for a variety of batches of different masses prepared using the 99% cerium nitrate precursor (10 mM). For the syntheses of larger batches, the NaOH concentration was adjusted (increased) accordingly so that the same rate of addition of NaOH to the cerium nitrate/PEG solution for each batch size was maintained. In the majority of cases, the batch size is equal to the mass measured by SQUID magnetometry, i.e. the whole batch mass was measured. The exceptions are the two blue data points, where sub-parts of the total batch were measured. Most of the batches measured are about 4 mg in size, for which M_s ~ 60 A m^{-1}, whereas for batches < 2 mg in size M_s > 100 A m^{-1}. For larger batches with masses > 15 mg, the magnetization is greatly diminished, with $M_s \leq 10$ A m^{-1}. It is noted here also that TEM analysis showed little difference in crystallite size or morphology for batches of different size (mass), so that the reduction in M_s for larger batches does not seem to be a size-dependent magnetism effect. For nanopowders synthesized using 99.999 % cerium nitrate, for batch sizes of ~ 4 mg they are almost non-ferromagnetic ($M_s \leq 5$ A m^{-1}) as is evident from Fig. 4.14 for example, while M_s almost vanishes for larger batches of 20-30 mg size.

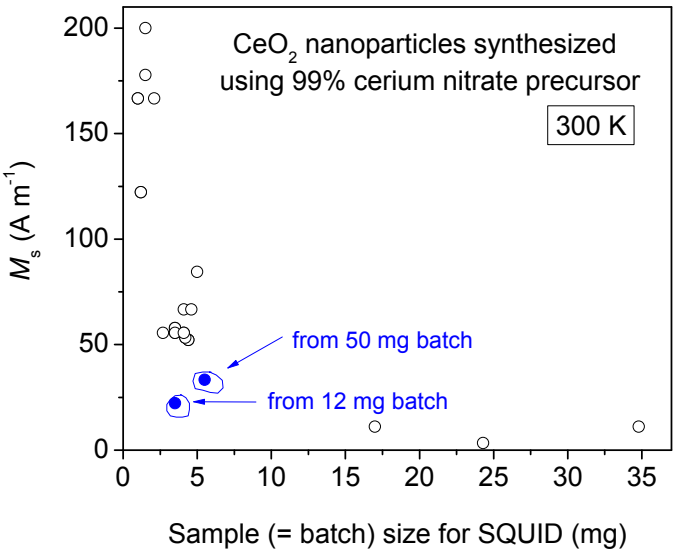

Figure 4.15. M_s measured at 300 K for different batch sizes of ferromagnetic CeO_2 nanopowders synthesized using 99 % cerium nitrate.

By fitting the magnetization curves to a tanh function of the form $M/M_s = \tanh(H/H_0)$, the value of H_0, which is a constant effective field that impedes saturation, may be obtained by

extrapolating the slope of the magnetization curve at the origin to where it intersects the saturation magnetization M_s. From the relation $H_0 = \mathcal{N}M_0$ and by using a demagnetizing factor of $\mathcal{N} = 1/3$ for a spherical isotropic approximation, the ferromagnetic volume fraction $f = M_s/M_0$ may be estimated, where M_0 is the magnetization of the ferromagnetic regions only, while M_s is the saturation magnetization of the total sample volume. The data for M_s plotted as a function of H_0 is shown in Figure 4.16, together with data deduced by analysis of the magnetization curves presented for other undoped CeO_2 samples in the literature, in addition to data for some iron metal and iron oxide samples. The black lines on the data plot illustrate where the data points would lie if the samples were 100 % magnetically ordered, when $f = 100$ %, for different values of the demagnetizing factor $\mathcal{N}$. Several key points may be inferred from the data. Firstly, it may be deduced that for the ferromagnetic nanoparticles synthesized in this study using the 99 % cerium nitrate precursor, denoted by the large blue open circles, approximately 1×10^{-3} – 1×10^{-4} of the sample volume is magnetically ordered, which may be estimated by comparing M_s for these samples with the values of M_s corresponding to $f = 100$ % and $\mathcal{N} = 1/3$. Hence only a small fraction of the sample volume is really magnetically ordered. Secondly, the values of H_0 for the same nanoparticles are distinctly less than that due to iron, either micron or nano-sized, but some values are similar to those of magnetite nanoparticles. If the ferromagnetic-like signals measured for the CeO_2 nanoparticles synthesized here are indeed due to magnetite nano-impurities, of order 10^{-4} – 10^{-3} or 100–1000 ppm of magnetite would be required, which is unlikely from the impurity analysis previously performed (ICP-MS). Thirdly, comparison of data for the nanoparticles synthesized here with other magnetic nanostructures (most of which are nanoparticles) from the literature, reveals that while the M_s values are broadly similar for both datasets, the H_0 values for nanostructures from the literature are generally lower, either comparable to or lower than that of magnetite. Magnetic microparticles from the literature fall within a similar region to nanoparticles on the plot. Lastly, for films, it is evident that thinner (20-30 nm) compact nanocrystalline films electrodeposited by Fernandes *et al.* [54,56,57], have M_s values which are several orders of magnitude larger than those which were synthesized in a similar way but were slightly thicker (50-100 nm) and were electrodeposited by Asra S. Razavian (unpublished) in our laboratory, or those which are nanoporous and ~ 500 nm thick electrodeposited by Ackland *et al.* [19]. The M_s values of some of the films of Fernandes *et al.* even approach those of pure magnetite or bulk iron; on average, the majority of all of the films (20-500 nm thick, denoted by red dots) have larger M_s values than those measured for the majority of either the microparticles (magenta triangles) or nanostructures (black dots), the latter of which are mostly in nanoparticle form.

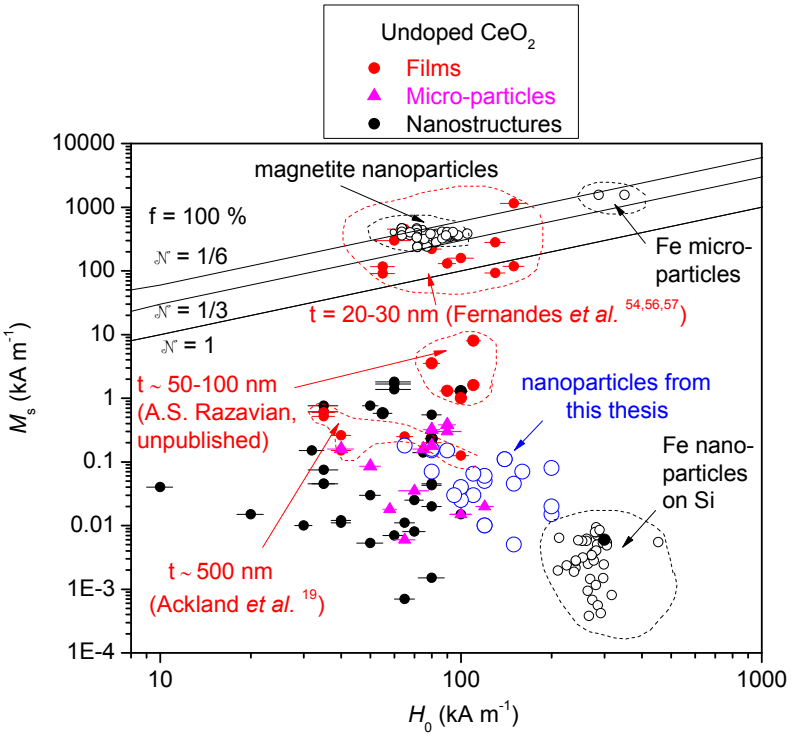

Figure 4.16. Room temperature saturation magnetization M_s plotted as a function of the field H_0 for undoped CeO_2 nanoparticles synthesized in this study together with data deduced for other magnetic undoped samples (films, microparticles, nanostructures) from literature reports. The majority of the nanostructures are in the form of nanoparticles. Data for some metallic iron and iron oxide samples is also included.

Figure 4.17 shows a similar plot of M_s vs. H_0 to that presented in the previous figure, but for undoped nanostructures only (excluding films), separated by morphology. It is evident that nanostructures of high aspect ratio such as wires, columns, poles and needles have higher M_s values (and consequently higher ferromagnetic volume fractions f) than those measured for the majority of spherical or near-spherical nanoparticles; an exception are the sheets/pores [17], but H_0 is also much larger for these latter samples than for the rest of the nanostructures, similar to that of metallic iron, which casts doubt on the purity of the samples (in addition at 5 K for these samples, H_c ~ 600 mT, whereas d^0 samples typically have negligible coercivity, of order 10 mT or less).

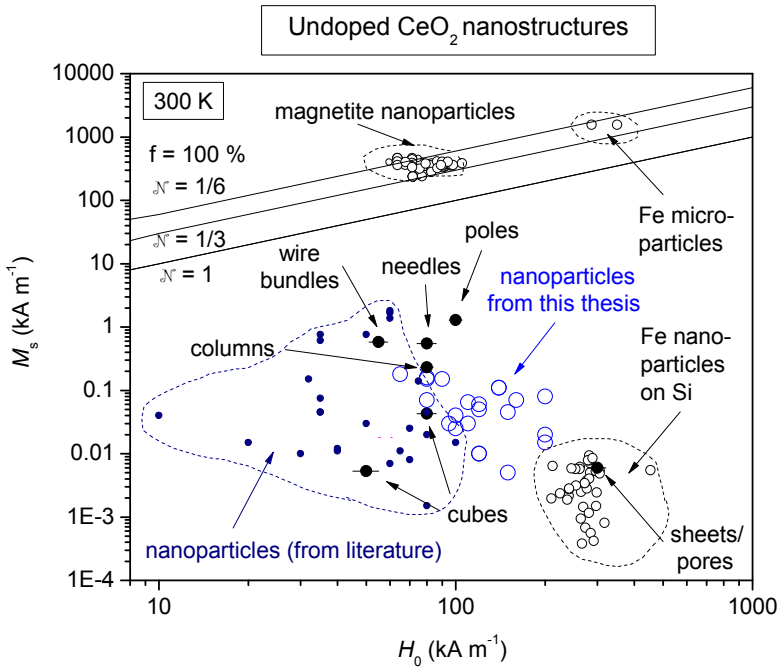

Figure 4.17. Room temperature M_s vs. H_0 values for undoped CeO_2 nanostructures (black dots) from literature reports categorized by their morphology. The dimensions of the nanostructures are listed in Table 4.1 in the literature review section. Nanoparticles from this study (orange dots) are clearly differentiated from the rest of the nanoparticles from the literature (purple dots).

Figure 4.18 shows a similar plot of M_s vs. H_0 to that presented in Fig. 4.17, but for *doped* CeO_2 samples from the literature, most of the dopants of which consist of several at. % of ferromagnetic elements. For clarity of display, the error bars have not been included. As per the previous figure, the black open circles denote iron in both metallic (H_0 ~ 300 kA m^{-1}) and oxide (H_0 ~ 60-100 kA m^{-1}) form (magnetite). It is evident firstly that nanoparticles have the lowest M_s values (generally 10-100 A m^{-1}), microparticles have intermediate M_s values (~ 0.1 – 10 kA m^{-1}) and the majority of the generally compact (poly)crystalline films have the largest M_s values (~ 10 – 100 kA m^{-1}); the minority of the films with M_s values of ~ 0.1 – 1 kA m^{-1} are nanoporous (rather than compact) and ~ 500 nm thick (Lorena M.A. Monzon, unpublished). Secondly, there is quite a broad spread of H_0 values for all of the samples, although most values are less than that of metallic iron. Several of the nanoparticle samples have H_0 values which are noticeably less (≤ 30 kA m^{-1}) than those of either microparticles or films. Thirdly, the groups of large open triangles marked A, B and C denote samples in which the authors explicitly ascribe the magnetic signals to magnetic impurities; A denotes nanoparticles for which M_s is attributed to Fe_2O_3 impurities [76], B denotes films for which M_s is attributed to Co clusters [64,70], while C denotes micro-crystals for which M_s is attributed to Co_3O_4 clusters [99]. Finally, it is noted that for Fe doped CeO_2 nanospheres and nanoporous structures electrodeposited on Cu [75] (blue circles), the values of H_0 are larger (similar to or greater than that of metallic iron) than those measured for the vast majority of the other doped CeO_2 samples.

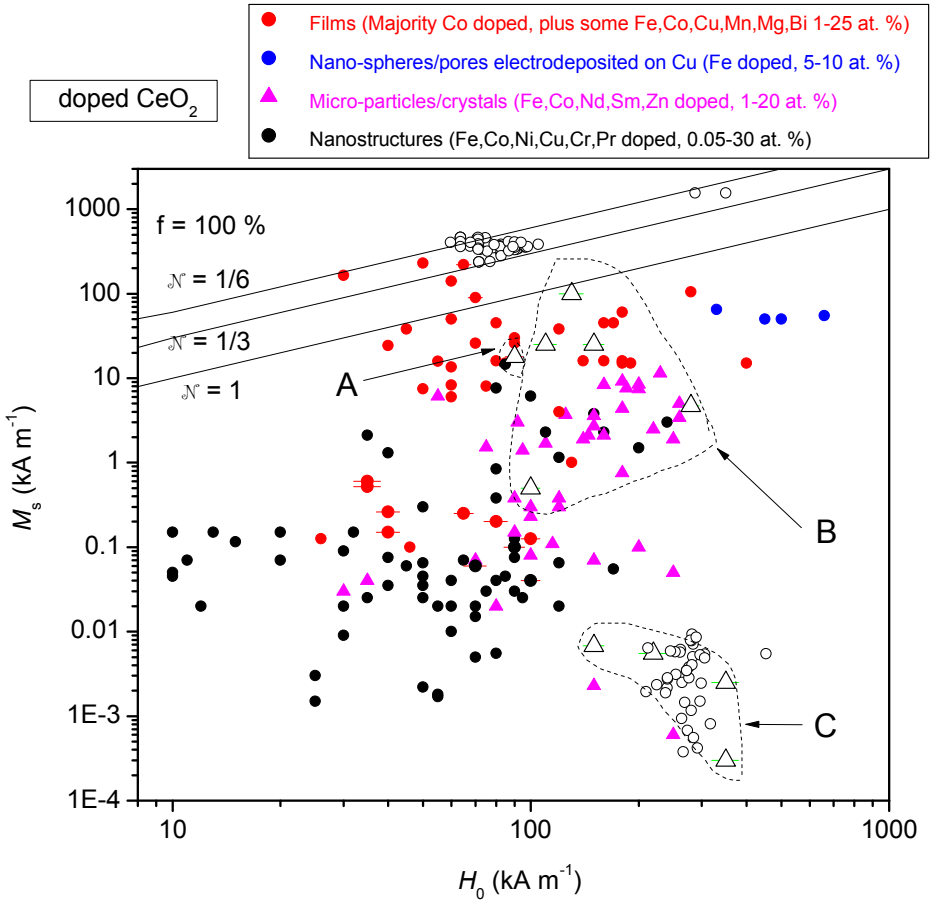

Figure 4.18. Room temperature M_s vs. H_0 values deduced for doped CeO_2 samples from literature reports. All of the nanostructures are in the form of nanoparticles except for one rod-shaped sample for which M_s = 0.15 kA m^{-1} (H_0 = 10 kA m^{-1}). Open circles denote metallic iron and iron oxide samples (as denoted previously in Fig. 4.17 for example). Data points (large open triangles) encircled A, B and C are explained in the preceding paragraph.

Figure 4.19 combines data for M_s and H_0 shown in the two preceding figures, in order to compare all of the data for doped and undoped samples in all forms. No distinction is made between sample type (film, micro-sized or nano-sized. From the previous two figures it may be deduced however that data points for nano/micro-particles generally lie near regions towards the bottom of the plot, while those for films usually lie near the middle to top.

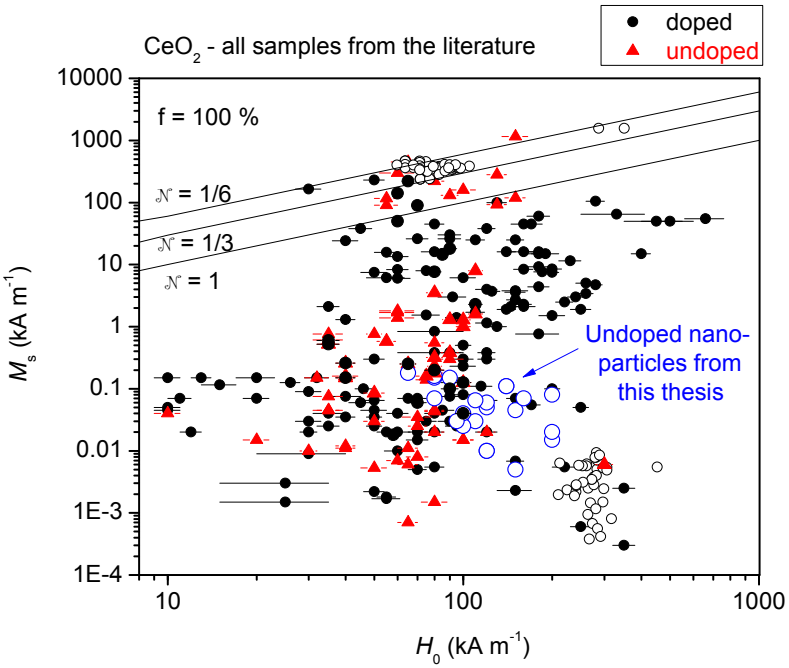

Figure 4.19. Room temperature M_s vs. H_0 values deduced for all CeO_2 samples from literature reports. Open black circles denote metallic iron and magnetite samples (as denoted previously in Fig. 4.17).

Magnetization data measured at low temperature (4 K) for CeO_2 nanoparticles synthesized using 99% cerium nitrate is shown in Figure 4.20. The signal magnitude and shape is virtually identical at both room temperature and 4 K, from which it may be inferred that the Curie temperature is much greater than room temperature. The data has been fitted to a function which physically represents collective orbital magnetism and is of the form

$$m(H) = m(0)\ x/(1 + x^2)^{1/2} \qquad (4.1)$$

where $x = cH$ and H is the magnetic field. The collective orbital magnetism model is discussed further later in this chapter (in section 4.3.13) and in Chapter 6 (Discussion), while an overview of the theoretical and mathematical basis for this equation is given in Appendix A.2. A Langevin function fits equally well, or a tanh function may also be used. The parameter c relates the energy scale to the length scale of the effect, and is virtually the same (5.18 – 5.15 T^{-1}) for the data at 4 K and 300 K since the fits are very similar. The insensitivity of the magnetization to thermal excitations at 300 K is evidence that an unusually large energy scale, > 0.1 eV, is involved. The inset shows a thermal magnetization scan in applied field, which has been corrected for the diamagnetic gelcap contribution. There is a clear paramagnetic upturn at low temperature (< 25 K), which when fitted to the Curie Law may be used to estimate that the Ce^{3+} content is ~ 0.5 %, assuming J = 5/2 for a $4f^1$ electronic configuration. There is no evidence of any secondary ferromagnetic phases or clusters below 300 K, which would be expected to produce extra peaks/features in the thermal magnetization data. In an applied field of 2 T at room temperature,

the nanoparticles possess a weak paramagnetic character with $\chi = +4.5\times10^{-6}$ in addition to their ferromagnetic-like signature.

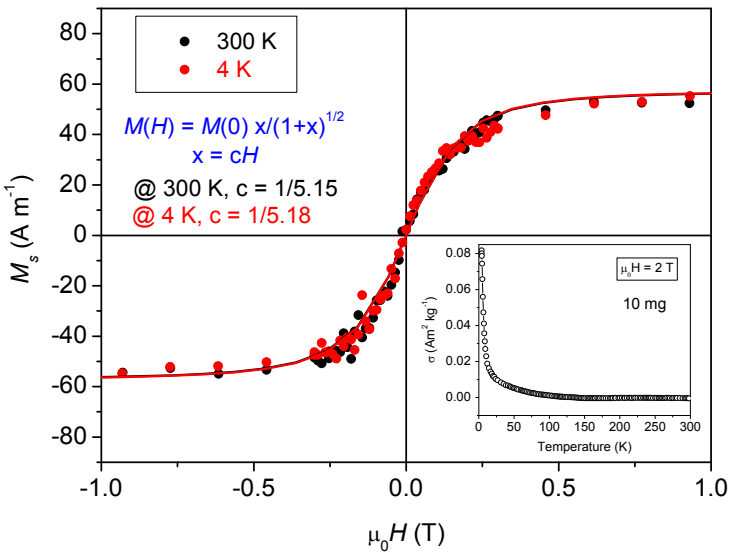

Figure 4.20. Magnetization data (corrected for diamagnetic gelcap + paramagnetic CeO_2 background) for 4 mg batches of CeO_2 nanopowders synthesized using 99% cerium nitrate measured at 300 K and 4 K. The data has been fitted to the function indicated in blue font. The inset shows a thermal magnetization scan in an applied field of 2 T, corrected for the high-field diamagnetic susceptibility due to the gelcap.

Thermal magnetization scans of the ~ non-ferromagnetic CeO_2 nanopowder synthesized using 99.999% cerium nitrate as well as a high nominal purity 99.999% CeO_2 micropowder purchased from Sigma Aldrich were also performed. The data is shown in Figure 4.21. Firstly, for the nanopowder synthesized using 99.999% cerium nitrate, shown in part (a), the thermal magnetization scan does not show any evidence of sharp upturns due to ferromagnetic impurities. From the Curie law upturn at the lowest temperatures, the Ce^{3+} content is estimated to be ~ 0.1 % (assuming J = 5/2), lower than that estimated for the ferromagnetic nanopowder synthesized using 99% cerium nitrate (~ 0.5 % Ce^{3+}). The higher Ce^{3+} content estimated for the low purity nanopowder compared to the higher purity nanopowder may be due to greater quantities of additional impurity phases which may favour Ce^{3+} formation by inducing off-stoichiometry and charge imbalance in the ceria lattice in order to try to accommodate the extra impurities (especially La^{3+} substitution for Ce^{4+} in the lower purity nanopowders). At room temperature, the high purity nanopowder is weakly paramagnetic with $\chi = +3.9\times10^{-6}$ (compared to $+4.5\times10^{-6}$ for the low purity nanopowder), while at 4 K χ has increased by more than order of magnitude to $+5.0\times10^{-5}$, as measured by the respective magnetization/field scans at 300 K and 4 K. Importantly, no trace of any ferromagnetism is measured for the field scans at 4 K for any of the nanopowders. By plotting the inverse susceptibility against temperature from the thermal magnetization data, the extrapolated

intersection of the data with the temperature (x) axis is approximately – 5 K for both nanopowders (high and low purity), which indicates a possible *antiferromagnetic* character for both; if ferromagnetic (paramagnetic) the x-axis intersection should be positive (zero). One of the limitations of SQUID magnetometery is that it is rather insensitive to antiferromagnetic order (it only measures the total net macroscopic magnetic moment), which may manifest itself as a weak paramagnetic-like and/or ferromagnetic-signal signal instead which is what is measured for the nanopowders. Further possible evidence for antiferromagnetism is provided by the muon polarisation results, presented later on in section 4.3.7, in which the possibility of antiferromagnetic order is discussed further.

Meanwhile, the reference Sigma micropowder is also weakly paramagnetic at room temperature, although slightly less so than the nanopowder synthesized using 99.999% cerium nitrate, with $\chi = +3.5\times10^{-6}$. This residual paramagnetism is likely due to some unpaired Ce^{3+} ions in the sample. The thermal magnetization data shown in part (b) of Figure 4.21 presents no evidence of ferromagnetic impurity phases below room temperature for high purity bulk CeO_2. The paramagnetic Ce^{3+} content for the micropowder estimated from the low temperature Curie upturn (assuming J = 5/2) is ~ 0.01 %, at least an order of magnitude smaller than that estimated for the nanopowders. Hence it is evident that even high purity CeO_2 micropowder may have a small residual Ce^{3+} content. By plotting the inverse susceptibility against temperature, the extrapolated data intersects the origin (temperature = 0 K) indicating pure paramagnetic behaviour. It is noted that while in theory even traces of *any* paramagnetic impurity may produce the low temperature upturn in the susceptibility, it is most likely to be Ce^{3+} for CeO_2.

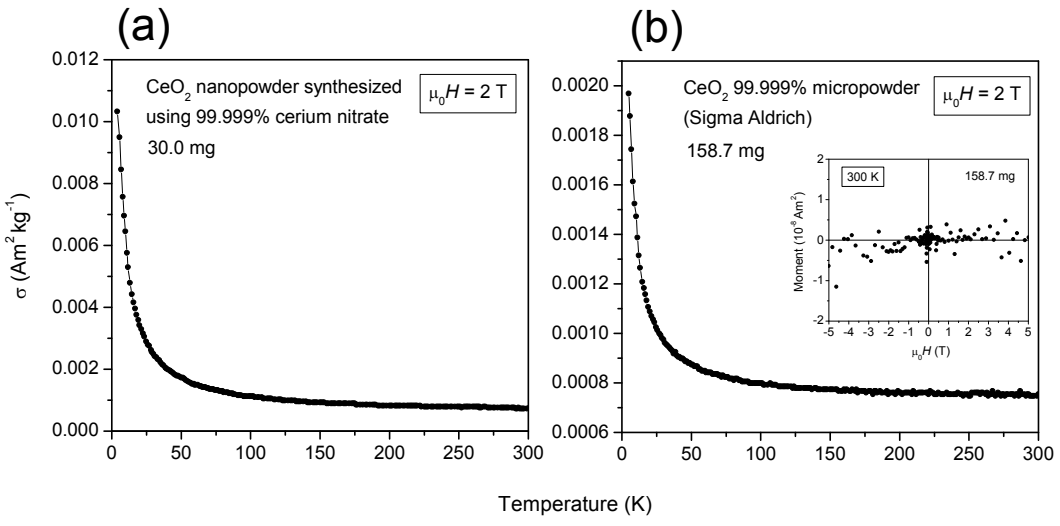

Figure 4.21. Thermal magnetization data (corrected for diamagnetic gelcap background) for (a) CeO_2 nanopowder synthesized using 99.999% cerium nitrate, and (b) bulk CeO_2 micropowder, for which the corrected room temperature magnetization curve (for both the diamagnetism of the gelcap and the weak paramagnetism of CeO_2) is displayed in the inset.

The magnetic moment measured for the CeO_2 nanopowders synthesized using 99% cerium nitrate was determined to be quite stable over a period of 24 months, with a decay in moment magnitude of a single batch (4 mg) of ~ 20 % only during this period. The time-dependent magnetization curves are shown in Figure 4.22. It is also evident that the magnetization curve shapes are virtually unchanged when re-measured after 24 months.

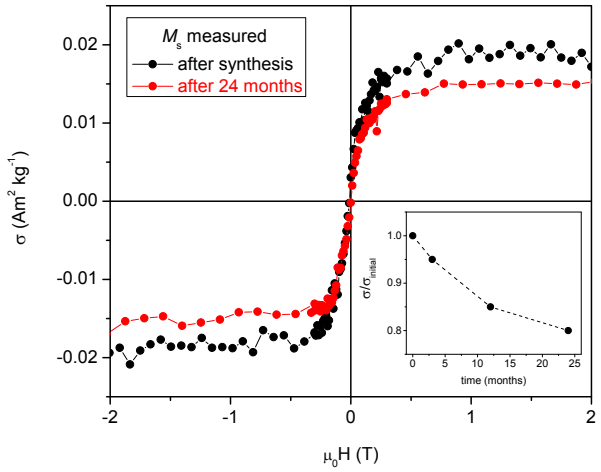

Figure 4.22. Background-corrected magnetization curves for a single batch of CeO_2 nanopowders synthesized using 99% cerium nitrate, showing the decay of the magnetic signal with time.

Many experimental reports attribute the magnetism of nanostructured CeO_{2-x} to oxygen vacancies. The number of oxygen vacancies would be expected to rapidly decay over time in ambient conditions, as the samples become oxidised. In such a case, the magnitude of the magnetic moments should also decay rapidly over time if the magnetism is indeed correlated with oxygen vacancies. Due to the existence of some cerium sesquioxide Ce_2O_3 phase however, it is possible that not all of the cerium oxide is actually re-oxidised to CeO_2 over time since some Ce_2O_3 phase remains, and hence many oxygen vacancies and much Ce^{3+} character may be retained; this may explain why a magnetic moment due to oxygen vacancies and Ce^{3+} does not decay rapidly over time. In addition, it is possible that the presence of small amounts of other phases such as cerium hydroxide ($Ce(OH)_3$) for example, an intermediate formed during nanoparticle synthesis during which Ce^{3+} is oxidized to Ce^{4+}, may help to retain Ce^{3+} character/oxygen vacancies and to prevent full oxidation to CeO. It is noted however that $Ce(OH)_3$ was not detected in XRD measurements of the nanopowders. However, the phase detection limit of X-Ray powder diffraction is not so low, typically ~ 0.1-1 wt %, and coupled with the large peak broadening and rather small peak intensities measured for the nanopowders, means that the actual detection limit here is higher, possibly several wt %, and hence it is possible that impurities present at these concentrations could elude detection. Another possibility is that surfactants (PEG here) used during nanoparticle synthesis may protect the

nanoparticles from oxidation, and hence assist in Ce^{3+} retention.

Some of the ferromagnetic CeO_2 nanopowder (synthesized using 99% purity cerium nitrate) was post-annealed after synthesis at atmospheric pressure (i.e. in air) at selected temperatures in order to determine the effect of air-annealing on the magnetic signals. Initially the magnetic moment of a ferromagnetic nanopowder was measured, after which the powder was subsequently placed in a clean ceramic boat and heated to 200 °C at atmospheric pressure for 2 hours in a furnace. Heating/cooling rates of 5 °C/min per used. The magnetic moment was then re-measured, followed by further sequential air anneals at 400 °C, 600 °C and 800 °C (5 °C/min heating/cooling rate, temperature held for 2 h at the maximum temperature), with the magnetization re-measured after each successive anneal. The resultant magnetization curves measured are shown in Figure 4.23. It is evident that while air annealing the nanopowder at 200 °C does not have a significant effect on the magnitude of the magnetic signal or particle size (~ 4 nm), further cumulative air anneals at higher temperatures are accompanied by an exponential-like decrease in signal magnitude, as well as a marked increase in particle size. For the nanopowder which has been air annealed at 800 °C following prior anneals at the lower temperatures indicated, the magnetization value has fallen to about 40 % of its initial value, while the particle size has increased from 4 – 40 nm, as estimated by Scherrer peak broadening of the XRD peaks.

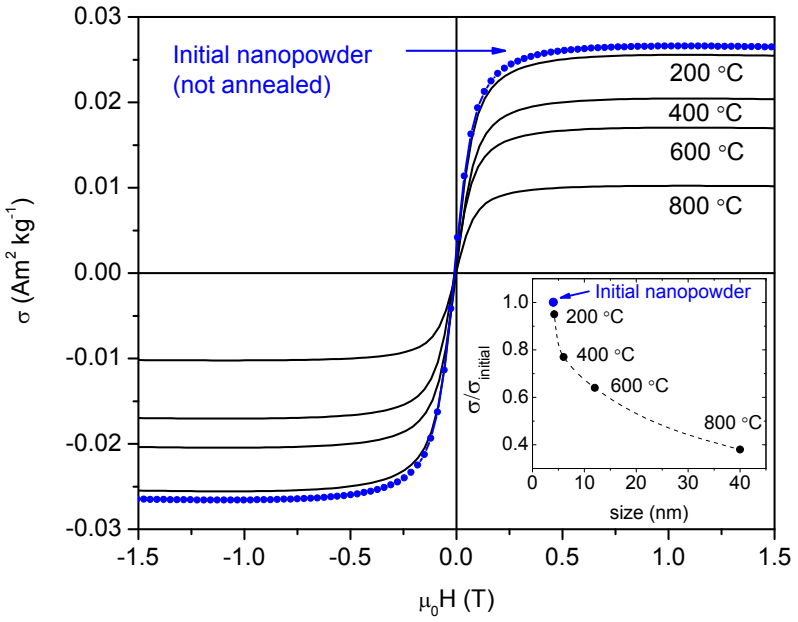

Figure 4.23. Room temperature magnetization curves, background corrected and fitted to a tanh function, for ferromagnetic CeO_2 nanopowder air-annealed at various temperatures. The inset plots the normalized mass magnetization against particle size upon air-annealing at various temperatures (ramp rate = 5 °C / min, dwell time at T_{max} = 2 h).

The relative decrease in magnetization may be related to the increase in particle size. Samples which are not ferromagnetic in the bulk often exhibit ferromagnetism when in nanoparticulate form, and it has been reported that the ferromagnetism in CeO_2 nanostructures may be size dependent for example [14,18,38], for which the onset of ferromagnetism at small nanoparticle size may be related to an increase in the surface to volume ratio with decreasing particle size (and possibly also to an increased amount of oxygen vacancies associated with Ce^{3+}); the nanoparticle surface acts in effect like a defect due to the unsaturation of chemical bonds there compared to saturated bonds within the interior of the nanoparticle. The fraction of surface atoms increases almost exponentially with decreasing number of atoms in the nanoparticle as shown in Figure 4.24 (previously shown in the introduction in Chapter 1). As the CeO_2 nanoparticles decrease in size, due to the increase in unsaturated bonds at the surface, the Ce^{3+} content increases rapidly, while the nanoparticle core remains Ce^{4+}-rich. The increased Ce^{3+} content results in elevated strain and lattice expansion, since the radius of the Ce^{3+} ion (115 pm) is greater than that of Ce^{4+} (101 pm), which in turn favours the formation of charge compensating oxygen vacancies at the surface. Hence the decrease in magnetization with increasing particle size induced by air annealing at successively higher temperatures may be proposed to be due to the relative decrease in Ce^{3+} and oxygen vacancy content as the particle size increases; in addition, by annealing in air, CeO_2 will become more oxidized, which will further reduce the oxygen vacancy content of the nanoparticles. As an aside, it is noted that previous unpublished annealing studies performed by previous researchers in our laboratory did not find any evidence for magnetism in *vacuum* annealed high purity (99.999 %) *bulk* CeO_2 powders (nor in vacuum annealed ZrO_2 or TiO_2 high purity bulk powders), for anneals performed at either 600 °C, 700 °C or 800 °C. Hence for our bulk powders it seems that oxygen vacancies created by vacuum annealing may not be sufficient alone to induce ferromagnetic-like signals. For nanopowders however, the physical structure is very different due to the large surface/volume ratios and significant inherent Ce^{3+}/oxygen vacancy character due to the nanostructure and the increased surface to volume ratio as discussed above. If the ferromagnetism is purely size-dependent however, this does not explain why the nanoparticles synthesized using 99.999% cerium nitrate are not ferromagnetic (despite having a similarly small size to the ferromagnetic nanoparticles); it is possible that another requisite for ferromagnetism in our nanoparticles is the presence of impurities such as La in the 99% cerium nitrate used to synthesize the ferromagnetic nanoparticles, which is discussed next.

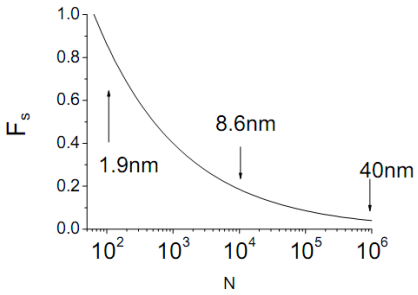

Figure 4.24. General trend for the increase of the fraction of surface atoms (F_s) with decreasing number of atoms (N) for nanoparticles of small size.

In order to further investigate the possible influence of La on the ferromagnetism of CeO_2, nanoparticles were synthesized using the higher purity cerium nitrate precursor (99.999 %) and intentionally doped with various weight percent of lanthanum nitrate (hexahydrate) of purity 99.999 %. For La doped CeO_2, to convert between weight % and atomic % doping levels, the conversion is 1 wt % ≈ 1.2 at %. By making up a solution of cerium and lanthanum nitrate and following the same synthesis procedure as for the ferromagnetic CeO_2 nanoparticles before, La will tend to dope substitutionally for Ce in the ceria crystal lattice. Since the magnetization of nanoparticles synthesized using the 99.999 % cerium nitrate precursor is very small (at most 5 A m^{-1}), the effect of lanthanum doping should be readily measurable as long as the magnetization is clearly > 5 A m^{-1}. Selected magnetization curves for CeO_2 nanoparticles synthesized using 99.999% cerium nitrate doped with various quantities of La are shown in Figure 4.25 below.

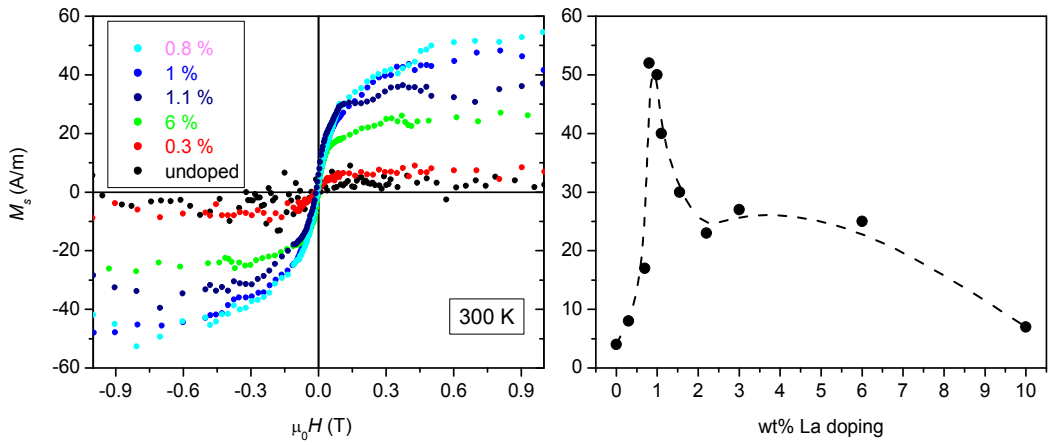

Figure 4.25. Room temperature magnetization curves (corrected for high-field background slope) for CeO_2 nanoparticles synthesized using 99.999% cerium nitrate and doped with various wt % La (1 wt % ≈ 1.2 at % for this sample). The mass of each sample is about 3 mg. The correlation between M_s and the quantity of La doping is shown on the right.

It is evident from Fig. 4.25 that doping with La serves to increase the magnetization value from ~ 5 A m^{-1} for the undoped case to ~ 50 A m^{-1} for 0.8 wt % La doping. Values of M_s > 30 A m^{-1} are measured for a rather narrow range of doping levels only, ~ 1.0 ± 0.2 wt % (equivalent to ~ 1.2 at. %) The maximum magnetization does not reach quite as large a value as that typically measured for the ferromagnetic nanoparticles synthesized using the lower purity cerium nitrate precursor however, for which M_s is typically > 50 A m^{-1} for 3 mg batches. It is noted that the maximum M_s measured here occurs for a similar wt % La to that already present in the 99 % cerium nitrate precursor (~1-2 %). Thus it may be deduced that La may indeed play a role in mediating the magnetism in CeO_2 nanoparticles, since ferromagnetic-like signals are measured for both nanoparticles intentionally doped with La synthesized using 99.999% cerium nitrate, and also in nanoparticles synthesized using 99% cerium nitrate in which the La dopant is already present in the cerium nitrate precursor. In the *absence* of La, it has been shown that *no distinct ferromagnetism* is measured for nanoparticles, such as for those synthesized using 99.999% cerium nitrate. Substitutional La within the ceria lattice may induce lattice strain and favour defect formation due both to the larger size of the La^{3+} ion (117 pm ionic radius) compared to that of Ce^{4+} (101 pm) for which La^{3+} substitutes, and due to the fact that oxygen holes must be created in order to maintain overall charge neutrality upon replacement of Ce^{4+} with La^{3+}; it may be these extra defects that induce magnetism in these small (~ 4 nm diameter) CeO_2 nanoparticles. This same explanation for the appearance of magnetism may also apply for ferromagnetic CeO_2 nanoparticles synthesized using the lower purity 99% cerium nitrate containing La impurities. La only forms the La^{3+} ion when bonding as there is no La^{4+} valence state unlike for cerium. The Ce^{3+} ion meanwhile has a similar ionic radius (115 pm) to that of La^{3+} (117 pm), whereas that of O_2^- is slightly larger (126 pm) than those of either La or Ce ions. The defects induced by La doping may be in the form of extra Ce^{3+} ions accompanied by the formation of charge compensating oxygen vacancies.

A comparison of the XRD spectra (included here rather than in the previous XRD section for the sake of continuity) measured for CeO_2 nanoparticles synthesized using 99.999% cerium nitrate, both undoped and 1 wt % La doped, are displayed in Figure 4.26. All reflections may be indexed to the ceria face-centred cubic crystal lattice (*Fm-3m*), as per the nanoparticles synthesized using 99% cerium nitrate shown previously in Fig. 4.8. Equal masses of powders were measured for each spectrum, which were mounted with the same geometry and scanned under identical conditions. It is evident that the peak intensity is higher for the undoped nanoparticles compared to those doped with La, from which it may be inferred that doping with La reduces the overall crystallinity of CeO_2. A subtle shift in peak positions to lower 2θ angles is also measured for the La doped sample compared to the undoped sample, which the inset in Figure 4.26 more clearly shows, indicative of lattice expansion upon doping pure CeO_2 with La.

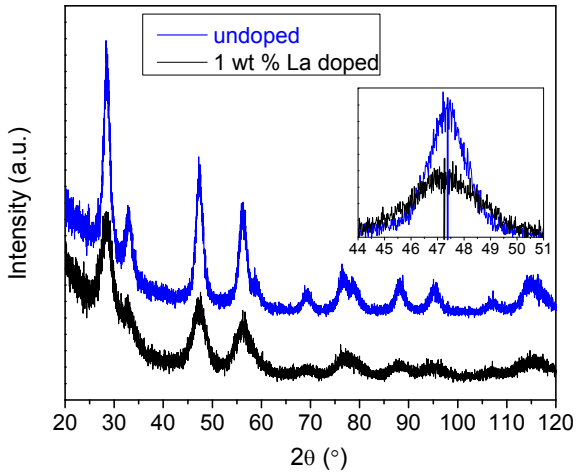

Figure 4.26. XRD spectra measured for CeO_2 nanopowders synthesized using 99.999% cerium nitrate.

XRD did not resolve the presence of either La_2O_3 or metallic La, even for the most heavily doped sample with 10 wt % La. A reason for the difficulty in resolving La_2O_3 (in addition to the relatively small concentration of dopant used) may be due to the fact that several of the reflection angles for La_2O_3 (hexagonal) occur at similar positions to those of CeO_2. For small nanopowders, in which the peaks are already significantly broadened due to the small crystallite size, this makes it more difficult to distinguish the La_2O_3 hexagonal phase from that of CeO_2 face-centred cubic. The absence of reflections for metallic La (hexagonal phase at room temperature) suggests that the La dopant has been incorporated into the ceria lattice, most likely substituting for Ce in the fluorite lattice as mentioned already.

Further to the La doping experiments, an investigation of the effect on the magnetic signal of doping CeO_2 nanoparticles synthesized using the high purity 99.999% cerium nitrate precursor with other non-magnetic impurities apart from La was carried out. Here, high purity (99.999 %) magnesium nitrate and zinc nitrate precursors were added to the cerium nitrate solution in order to dope CeO_2 with Mg and Zn respectively. 1 wt % of each of magnesium nitrate and zinc nitrate was used, and the resultant magnetization curves are shown in Figure 4.27. It is apparent that doping with 1 wt % of each of Mg and Zn produces a ferromagnetic-like signal, or "turns on" the magnetic signal compared to the undoped case, with an M_s value of ~ 50 A m^{-1} measured at room temperature upon doping. Hence doping with Mg and Zn at a level of 1 wt % produces an M_s value of similar size to that measured for doping with a similar wt % of La. It is also possible that doping with Mg and Zn create the defects necessary to induce magnetism, although it is noted that in contrast to La^{3+}, the ionic radii of Mg^{2+} (86 pm) and Zn^{2+} (88 pm) are significantly smaller than that of either Ce^{3+} (115 pm) or Ce^{4+} (101 pm). The results are rather similar to those measured for the doped nanoporous films shown previously in Figure 4.6 (Lorena M.A. Monzon, unpublished), which were synthesized by electrodeposition using the

same 99.999% cerium nitrate precursor. For the nanoporous films it was found that a ferromagnetic-like signal could be "turned on" by the addition of a few wt % of non-magnetic dopants to the electrodepostion solution, similar to the case for nanoparticles here, and that for the undoped case in which 99.999% cerium nitrate was used as the cerium precursor, no ferromagnetism was measured.

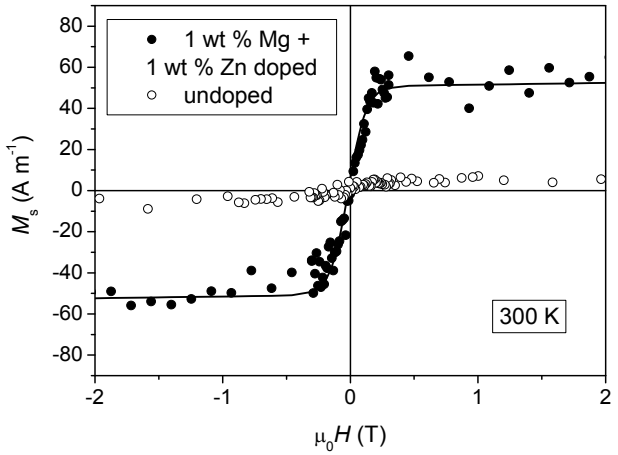

Figure 4.27. Corrected room temperature magnetization curves for CeO_2 nanoparticles synthesized using 99.999% cerium nitrate. The data for the doped nanoparticles (black dots) has been fitted to a tanh function (black line). The mass of each sample is ~ 3 mg.

4.3.6 X-Ray absorption spectroscopy (XAS) and X-Ray Magnetic Circular Dichroism (XMCD)

In order to obtain further information about the magnetism and stoichiometry of the ceria nanopowders, X-Ray absorption spectroscopy (XAS) and X-Ray magnetic circular dichroism (XMCD) measurements were performed on the following samples: CeO_2 nanopowders (both ferromagnetic and ~ non-ferromagnetic synthesized using 99% and 99.999% purity cerium nitrate respectively), ~ 1 wt % La-doped high purity nanopowder (synthesized using 99.999 % cerium nitrate), and finally a bulk micropowder reference sample (99.999 % Sigma). Approximately 1 mg of each powder was pressed onto Indium foil (99.99 % nominal purity) for measurement, the total area irradiated was typically 30 × 230 μm, and total electron yield (TEY) mode was used to detect the X-Ray absorption signal, where the escape depth is ~ 5 nm. Hence for the CeO_2 nanopowders, generally the whole particle volume is probed. XAS data were collected at the Ce $M_{4,5}$, La $M_{4,5}$, O K and Fe $L_{2,3}$ absorption edges, which all lie in the soft X-Ray energy regime. For the simultaneous XMCD measurements, at

300 K (2 K) the circular polarization was measured in fields of +/- 2T (7 T), with the magnetic field applied parallel to the X-ray beam. Data were collected at an incident angle of 28° to the normal.

Prior to presenting data measured for the Ce $M_{4,5}$ edge, a reminder of the main features in the XAS spectrum are first given. The most intense features in an XAS (XANES) spectrum are due to electric-dipole allowed transitions ($\Delta\ l = \pm\ 1$) to unfilled orbitals, and hence is a probe of the density of unoccupied states.The M_4 and M_5 absorption edges are related to transitions from 3*d* core states to 4*f* states, for which the excited core *d* states for example may be represented by the Russell-Saunders term symbols (spectroscopic notation) $^2D_{5/2}$ (M_4) and $^2D_{7/2}$ (M_5). For the Ce *M* edge probed, the main features in the XAS spectrum (M_4 and M_5 peaks) are related to transitions from 3*d* core states to 4*f* states and are a probe of the 4*f* excited state occupancy. For Ce^{4+}, the excited $4f^1$ state is probed, corresponding to the electronic transition $3d^{10}4f^0 \rightarrow 3d^9 4f^1$, whereas for Ce^{3+}, the excited $4f^2$ state is probed, corresponding to the transition $3d^{10}4f^1 \rightarrow 3d^9 4f^2$. The post-edge features at ~ 5 eV higher energy than those of the *M* edge maxima intensity originate from transitions to the 4*f* admixture in the conduction states, indicative of empty localized $4f^1$ states within the band gap, whereas the pre-edge features (at ~1-5 eV lower energy than those of the *M* edge maxima) are indicative of Ce^{3+}. For the Oxygen *K* edge probed, the features in the XAS spectrum strongly depend on the oxidation state; the O *K* edge gives information about the O 2*p* and Ce conduction states. Stoichiometric CeO_2 has 3 peaks in XAS, related to electronic transitions from O 1*s* core levels to empty O 2*p* hole states hybridized with Ce dominated 4*f*, 5*d*-e_g and 5*d*-t_{2g} levels respectively. Hence the lowest energy peak is a measure of Ce-O bonding or hybridization, while the higher energy peaks are more characteristic of the band structure (i.e. delocalized electrons) extending into the EXAFS regime.

Figure 4.28 displays XAS/XMCD data measured for the Ce $M_{4,5}$ edge of the ferromagnetic CeO_2 nanopowder (denoted FM) at both 300 K (at ± 2 T) and at 2 K (at ± 7 T). The XAS spectra have been normalised to an intensity of 1 at the M_5 step edge according to the procedure detailed in the experimental section (2.5.3).

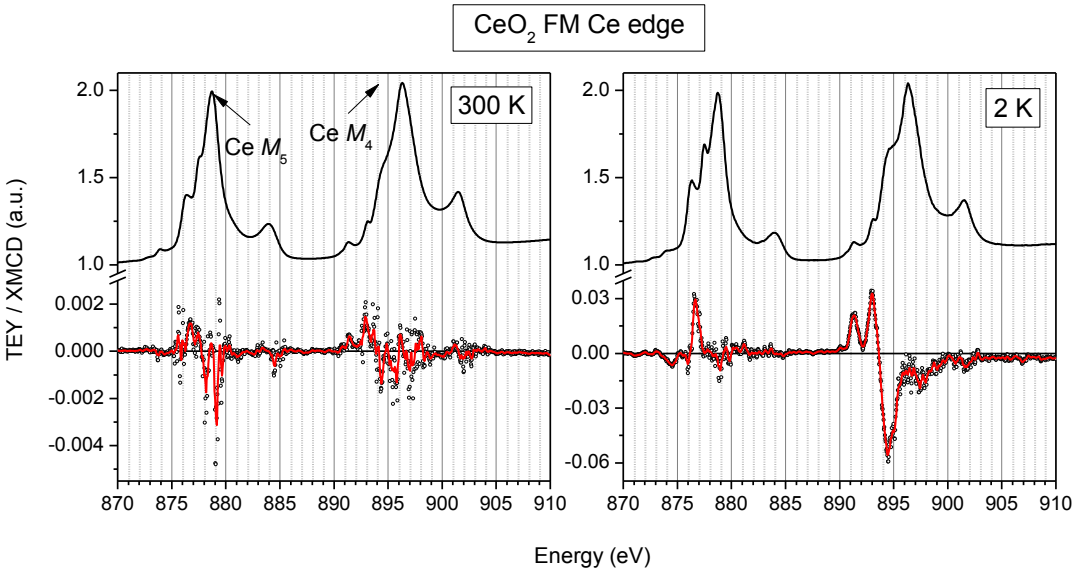

Figure 4.28. XAS and XMCD data for the Ce $M_{4,5}$ edge of the ferromagnetic (FM) CeO_2 nanopowder at 300 K and 2 K.

It is evident from the previous figure that the pre-edge features in the XAS, due to Ce^{3+}, are more prominent in the low temperature spectrum due to less temperature broadening of the spectral lines, while the XMCD amplitude is more than an order of magnitude larger than for that measured at room temperature. A magnetic moment of 1 μ_B/CeO_2 corresponds to ~ 230 kA m^{-1}, hence for 60 A m^{-1} (which is measured for this particular ferromagnetic nanopowder at 300 K) the magnetic moment is ~ 2.5×10^{-4} μ_B/CeO_2, or 2×10^{-4} μ_B/Ce (if all of the moment is assumed to be due to Ce only). A magnetic fraction of order 10^{-4} agrees with that deduced previously from analysis of the magnetization curves for the ferromagnetic nanoparticles, where *f* was estimated to be of order 10^{-4} – 10^{-3}. At 2 K, it may be reasonably assumed that the paramagnetic-dominated XMCD signal is almost entirely due to Ce^{3+}, as would be expected. It is also evident from Fig. 4.28 that the most intense XMCD signals at 2 K match the corresponding Ce^{3+} pre-edge XAS features in energy, rather than the Ce^{4+} features which are associated with the M_4 and M_5 edge maxima in XAS.

The XAS at the rare-earth $M_{4,5}$ and the 3*d* transition metal $L_{2,3}$ absorption edges are highly sensitive to the valence state and the distribution of valence electrons between the metal ion and the ligand orbitals, which allows the experimental spectral structures to be well reproduced by atomic multiplet calculations. Figure 4.29 compares the experimental XMCD data measured at 2 K with the Ce^{3+} contribution obtained by such a multiplet calculation, based on the calculations of Kotani *et al.* [112]; in these calculations, the 3*d* (and 4*d*) XAS for Ce^{3+} and Ce^{4+} are interpreted based on a simplified version of the Anderson Model combined with interactions described by the Slater Integrals and spin-orbit interactions which assumes 100 % polarization of cerium. Here we have used a fixed exchange parameter of 0.01 in our multiplet calculations which corresponds to an arbitrarily chosen 0.01 eV energy splitting of

the J-J mulitplet levels, the splitting magnitude of which may be denoted as $|E(m_j=n) - E(m_j=n\pm1)|$, and with no crystal field splitting (CFS). The XMCD signals, experimental and calculated, have been normalized. In order to scale the magnitude of the calculated XMCD signal to match that of the experimentally measured XMCD signal, a scaling factor of 0.14 was used (both here and for all subsequent spectra) to multiply the calculated XMCD signal by; this scaling factor implicitly assumes that all of the Ce^{3+} at 2 K for the FM nanopowder is paramagnetic and that its spins are free to orientate with respect to the applied magnetic field. In addition, the scaling factor of 0.14 shows that the realistic exchange parameter is much smaller at 0.0014 eV rather than the initial estimate of 0.01 eV.

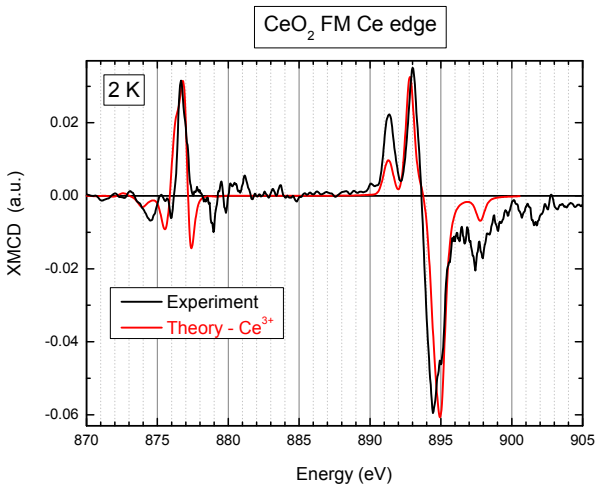

Figure 4.29. Normalised XMCD data for the Ce $M_{4,5}$ edge of the ferromagnetic (FM) CeO_2 nanopowder at 2 K compared to that calculated by multiplet calculations for fully polarized Ce^{3+}.

It is important to note that the multiplet calculations do *not* infer anything about the magnetic order in the system. In Fig. 4.29 shown previously the calculated signal (red line) has had to be shifted relative to the experimental data (black line) in order to achieve the best match between them, due to the inability of the calculation to accurately model the spherical part of the ground state energy of cerium. In addition, the relative energy between the ion valences often comes wrong in the simulations, and must also be corrected manually by inspection of the experimental and calculated signals. The experimental and theoretical spectra in Fig. 4.32 match quite well indicating that the XMCD spectrum at 2 K is almost completely due to paramagnetic Ce^{3+} only.

By appropriate scaling of the XMCD signal magnitude measured for ferromagnetic CeO_2 at 2 K and using the Langevin function for paramagnetism, the purely paramagnetic contribution to the XMCD signal at 300 K may be estimated, since at 2 K the XMCD signal is assumed to be entirely due to paramagnetic Ce^{3+} only. At 2 K in 7 T the magnetization of Ce^{3+} reaches 80 % of saturation, while at 300 K in 2 T it reaches just 0.32 % of saturation. Hence Ce^{3+} at 2 K and 7 T is still not quite completely polarized and the values of 0.8 and 0.0032 are the "Langevin scaling

factors" at 2 K and 300 K respectively. The resultant paramagnetic contribution to the XMCD signal at 300 K for the FM sample is displayed in Figure 4.30; the paramagnetic contribution is rather small (in agreement with SQUID magnetometry), of order 10 % of the experimentally measured signal magnitude only, with the remaining contribution most likely due to ferromagnetic and/or antiferromagnetic order.

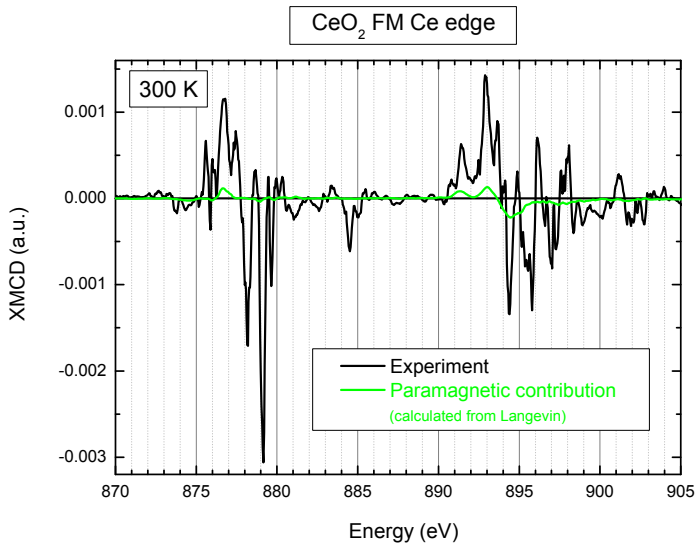

Figure 4.30. Paramagnetic contribution to the XMCD signal at 300 K for the Ce $M_{4,5}$ edge of ferromagnetic CeO_2.

In addition to calculating the Ce^{3+} contribution, the Ce^{4+} contribution to the XAS/XMCD signals may also be calculated. The following optimum parameters were used which were found to correspond best with the experimental data: exchange parameter = 0.01 (as per Ce^{3+}), charge transfer mixing parameter = 0.8, no CFS, Δ=0.5, 55% f0 and 45% f1L (where f0 + f1L = 100%). Δ defines the energy difference between the f0 and the f1L configurations, while the mixing parameter defines how much these configurations intermix. Both parameters modify the amount of charge transfer. Figure 4.31 shows which ratio of Ce^{3+}:Ce^{4+} obtained from the multiplet calculations fits most closely to the experimental data for the XAS of the Ce $M_{4,5}$ edge of the ferromagnetic CeO_2 nanopowder at 2 K. Since there are no background signals included in the calculated XAS, the background signal for the experimental XAS has been subtracted appropriately (which in effect alters the M_5:M_4 edge intensity ratio) using an edge step subtraction of magnitude 3/5 for the background due to the M_5 edge and 2/5 for the background due to the M_4 edge (these magnitudes correspond to the standard branching ratios for the $M_{4,5}$ edges) in order to give the best comparison between experiment and theory. The main contributions to the background signal are high-energy quasi-elastically scattered photoelectrons ejected from much less tightly bound atomic states than that due to Ce 3*d* states, the Auger electrons from which can have much lower energies. For all subsequent XAS spectra which

are compared to the theoretical Ce^{3+} and Ce^{4+} contributions, the plural background has similarly been subtracted.

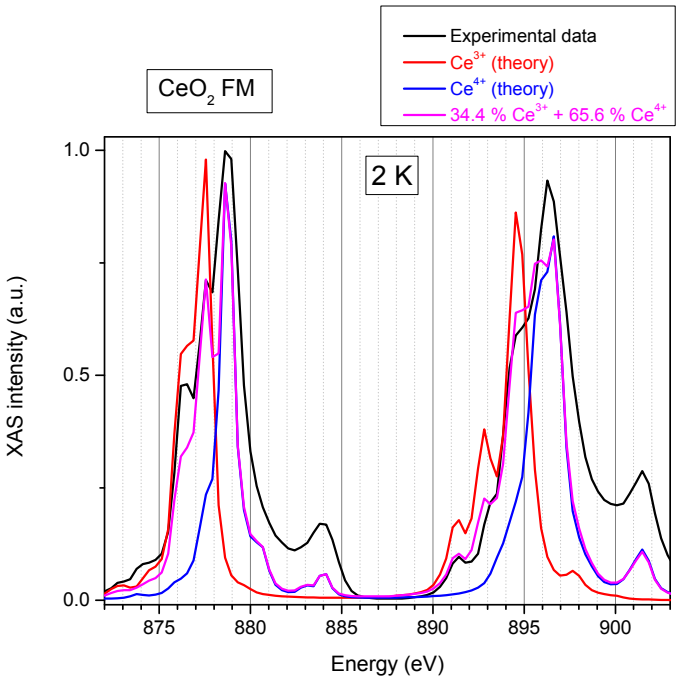

Figure 4.31. Relative contributions of Ce^{3+} and Ce^{4+} to the XAS (corrected for background) measured for the Ce $M_{4,5}$ edge of ferromagnetic CeO_2 at 2 K; the sample contains 34.4±1.5 % Ce^{3+}.

Fitting the multiplet calculations (theory) to the experimental spectra in Fig. 4.31 above reveals that the ferromagnetic nanopowder contains ~ 34.4 % Ce^{3+} at 2 K, the rest of cerium existing in Ce^{4+} form. The error in the above number (and similarly for subsequently calculated Ce fractions) is ± ~1.5 %, since it is not possible to get an excellent match between the experimental and theoretical XAS signals. Stoichiometric bulk CeO_2 would be expected to contain Ce^{4+} only; for nanoparticles however, the Ce^{3+} content is typically significant due its presence at the nanoparticle surface which is charge compensated for by the formation of oxygen vacancies which manifests itself in an expansion of the lattice parameter [9-11]. For example, the quantity of Ce^{3+} measured for ceria nanoparticles of 3.5 nm diameter measured elsewhere by XANES on the Ce $M_{4,5}$ edge is 40 % at maximum M_s [37], and generally > 20 % for several nanoparticles of ~ 3 nm diameter within the same report. Here, the Ce^{4+} contribution is not easily resolved in the XMCD spectra at 2 K since the spectrum is dominated by the paramagnetic Ce^{3+} contribution as demonstrated by the data previously displayed in Fig. 4.29, but the multiplet calculations show that the sample does in fact contain 65.6 % Ce^{4+}. According to the multiplet calculations the Ce^{4+} contribution to the XMCD signal at 2 K is more than two orders of magnitude smaller than the contribution due to Ce^{3+}. As mentioned before but noted again for clarity, a scaling factor of 0.14 was used (both here and for all subsequent spectra) to multiply the calculated XMCD signal by in order to match the intensity of the experimental and

calculated XMCD spectra. It is evident that the XAS post edge features of the *M* edge for Ce^{4+} in Fig. 4.31 cannot be accounted for very well by the multiplet calculations; the optimum parameters were found to be those mentioned in the previous paragraph.

At 300 K, the ratio of Ce^{3+} to Ce^{4+} for the FM sample should be the same as that at 2 K (since it is physically the same sample and only the measurement temperature has changed). It is arbitrarily approximated (in the absence of a better way of estimating) that the Langevin scaling factor (from 2 to 300 K) for the Ce^{4+} ion is the *same* as that calculated for the Ce^{3+} ion. In addition to the applied Langevin scaling factor of 0.0032 (in order to scale the magnitude of the calculated XMCD signals from 2 K to 300 K as discussed before), the other scaling factor of 0.14 also previously mentioned (in order to match the calculated and experimental XMCD signal intensity at 2 K in order to accurately represent the magnitude of the exchange splitting of the J-J levels in the samples) has also been applied to the calculated XMCD signals. A third and final step is to scale the calculated XAS signals to an absorption step edge of intensity = 1 and to scale the corresponding calculated XMCD signals by the same scaling factor, in order to compare the magnitudes with the experimentally measured data. Hence the final calculated XMCD signals which are subsequently shown have been scaled by three different successive values in order to account for the magnitudes of the Langevin, exchange and normalization (of XAS to 1) corrections. A comparison of the experimental data for XAS/XMCD and the calculated Ce^{3+} and Ce^{4+} contributions from the multiplet calculations performed are shown in Figure 4.32. In this figure, the Ce^{4+} contribution to the XMCD signal is displayed as it may be more easily resolved at 300 K (unlike at 2 K); it is approximately an order of magnitude smaller than the Ce^{3+} contribution.

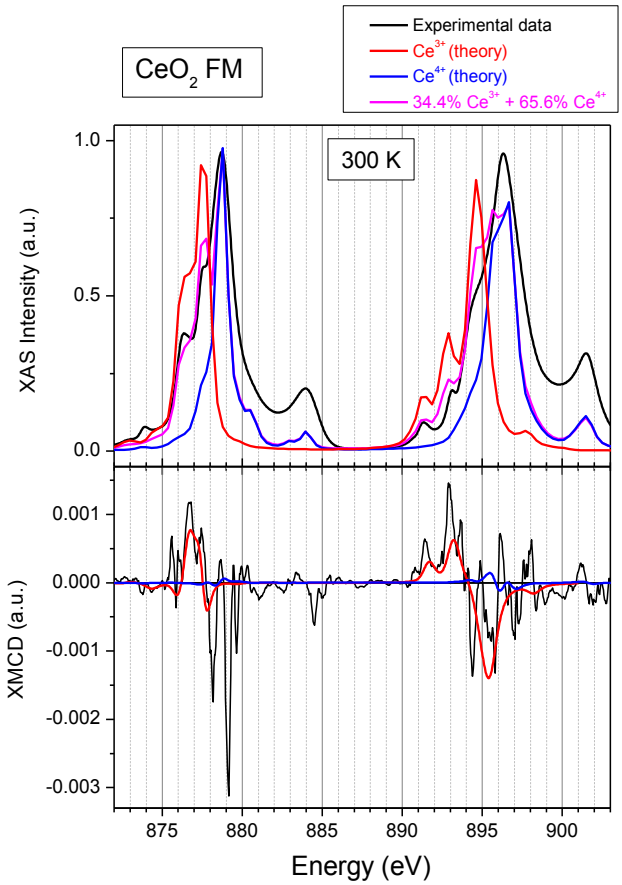

Figure 4.32. Relative contributions of Ce^{3+} and Ce^{4+} to the XAS/XMCD spectra measured for the Ce $M_{4,5}$ edge of ferromagnetic CeO_2 at 300 K.

A better correspondence between the experimental and calculated XMCD signal to that shown in the lower panel in Fig. 4.32 above may be obtained by suitable weighting of the magnitudes (as well as the signs and hence relative orientations) of the calculated Ce^{3+} and Ce^{4+} contributions. In Figure 4.33 shown on the next page, the Ce^{3+} contribution has been scaled up by a factor of 1.5, while that due to Ce^{4+} has been scaled up by a factor of 4, which is found to give the closest match between the experimental and calculated XMCD signals. It is evident that the net calculated and experimental XMCD signals generally match quite well within experimental error, except for a noticeable narrow (in energy) XMCD contribution of negative sign for the experimental signal between ~ 878 and 880 eV which is not accounted for by the multiplet calculations. For all subsequent data plots which compare the calculated and experimental XMCD signals, only the net calculated XMCD signal (denoted in magenta) after suitable weighting of the magnitudes (and signs) of the calculated Ce^{3+} and Ce^{4+} contributions such as that illustrated in Fig. 4.33, is presented.

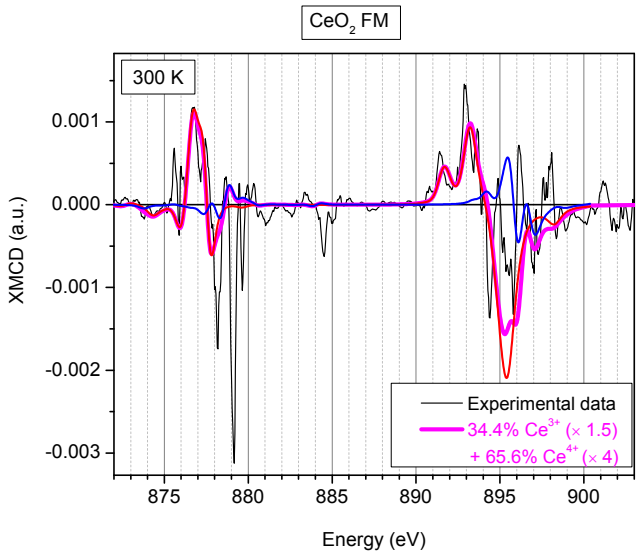

Figure 4.33. Comparison of the net calculated XMCD contribution (magenta), using suitable weighting of the Ce^{3+} (red) and Ce^{4+} (blue) calculated contributions, to that measured experimentally (black line) for the Ce $M_{4,5}$ edge of ferromagnetic CeO_2 at 300 K.

XAS and XMCD data measured for the oxygen *K* edge of ferromagnetic CeO_2 are shown in Figure 4.34; due to the more delocalised nature of this edge compared to the cerium *M* edge, it is more difficult to make quantitative predictions based on multiplet calculations. Relative to the absorbance for the Ce edge, that of O was typically ~ 30 %, reflecting both its lower concentration as measured by the incident synchrotron radiation and its specific cross section. The data have been normalised to an edge step of 1 for the first (lowest energy) peak in the XAS, as detailed previously in the second paragraph of this sub-section. Three characteristic peaks in the XAS due to CeO_2 are measured, which correspond to the transitions from O 1*s* core levels to empty O 2*p* hole states hybridized with Ce dominated 4*f*, 5*d*-e_g and 5*d*-t_{2g} levels respectively in order of increasing energy. The XAS are very similar at 300 K and 2 K with no discernible energy shifts; the only difference between the XAS is a more pronounced post-edge shoulder at 2 K for the XAS peak at 530.5 eV, corresponding to the O 1*s*-2*p* → Ce 5*d*-e_g transition (marked by an arrow in the figure); this extra shoulder may be indicative of enhanced Ce^{3+} content [113]. For XMCD, the signal measured at 2 K is more than an order of magnitude larger than that measured at 300 K, however the former signal is noisier. At 300 K there is no pronounced XMCD signal above ~ 531 eV, with some rather sharp features evident below this energy.

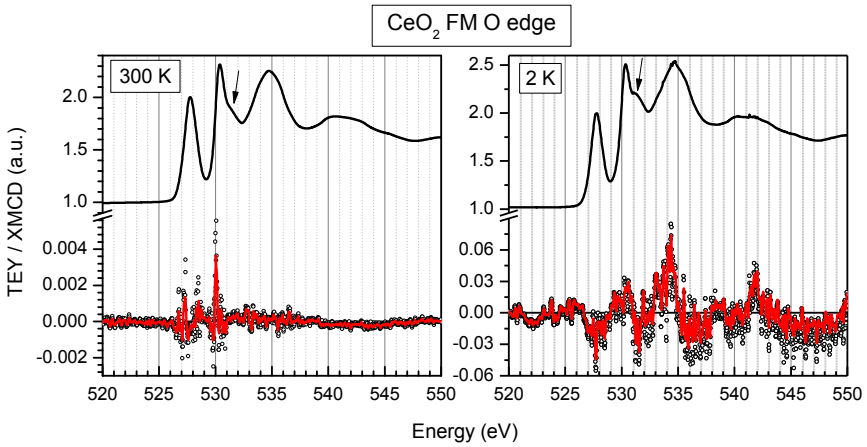

Figure 4.34. XAS and XMCD data for the O *K* edge of the ferromagnetic (FM) CeO_2 nanopowder at 300 K and 2 K. The black arrows point to the post-edge shoulder of the middle peak.

It is important to check for artefacts in the form of energy shifts in the XAS due the long timescale (up to 8 h) taken to acquire data for the absorption edges (particularly for data acquired at the Ce $M_{4,5}$ and O *K* edges). Over several hours it is possible that instrumental drift in the detection system may occur. Energy shifts were ruled out as a source of the sharp features measured for the XMCD signals however as energy shifts of up to 0.1 eV (even large instrumental drifts should typically not exceed this value) did not change the XMCD *shapes* significantly for either the Ce $M_{4,5}$ or O *K* edges measured, but only small changes in overall XMCD *intensity* were measured.

XAS/XMCD data were also measured at the La $M_{4,5}$ and Fe $L_{2,3}$ edges of the ferromagnetic CeO_2 nanopowder at 300 K, shown in Figure 4.35, whose features are described in more detail in the subsequent paragraph.

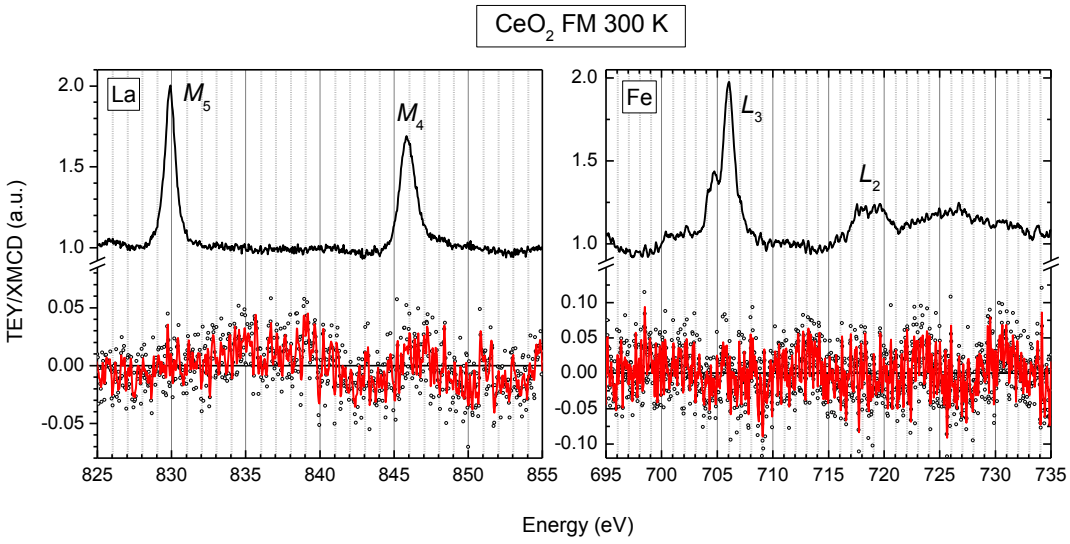

Figure 4.35. XAS/XMCD data for the La $M_{4,5}$ and Fe $L_{2,3}$ edges of the ferromagnetic (FM) CeO_2 nanopowder measured at 300 K.

The maximum absorption magnitudes due to La and Fe were typically ~ 0.3 % that of Ce. The transition metal $L_{2,3}$ XAS edges generally correspond to transitions from core *p* to excited *d* states, and as such are a probe of the *d* state occupancy. 32 scans of the La edge were acquired (~ 2 hour duration), while 8 scans of the Fe edge were acquired. From Fig. 4.35 shown on the previous page, for the La edge of the FM nanopowder no clear XMCD signal was resolved above the noise floor. For the Fe edge, no discernible XMCD signal was measured either; for pure iron the XMCD signal intensity should be about 1/3 – 1/2 that of the absorption edge jump in XAS and hence should be readily resolved, while here no signal is resolved at the 10 % level. Hence despite the fact that an XAS signal for iron is resolved (possibly an oxidised form of iron, although it is difficult to quantify the stoichiometry from XAS), it is not ferromagnetically ordered at 300 K since there is no clear XMCD signal. Whereas ICP-MS results show that the ferromagnetic nanopowder contains < 1 ppm of iron metal, the detection of an Fe XAS signal suggests that the concentration of Fe is actually at least of order 100 ppm, which is typically around the elemental detection limit of XAS. It is possible that the iron may have been implanted during sample mounting by pressing with metal (stainless steel) spatulas or is due to some other source of contamination.

XAS/XMCD data measured at 300 K at the Ce $M_{4,5}$ and O *K* edges of the ~ non-magnetic (NM) CeO_2 nanopowder synthesized using high purity 99.999% cerium nitrate are displayed in Figure 4.36 below.

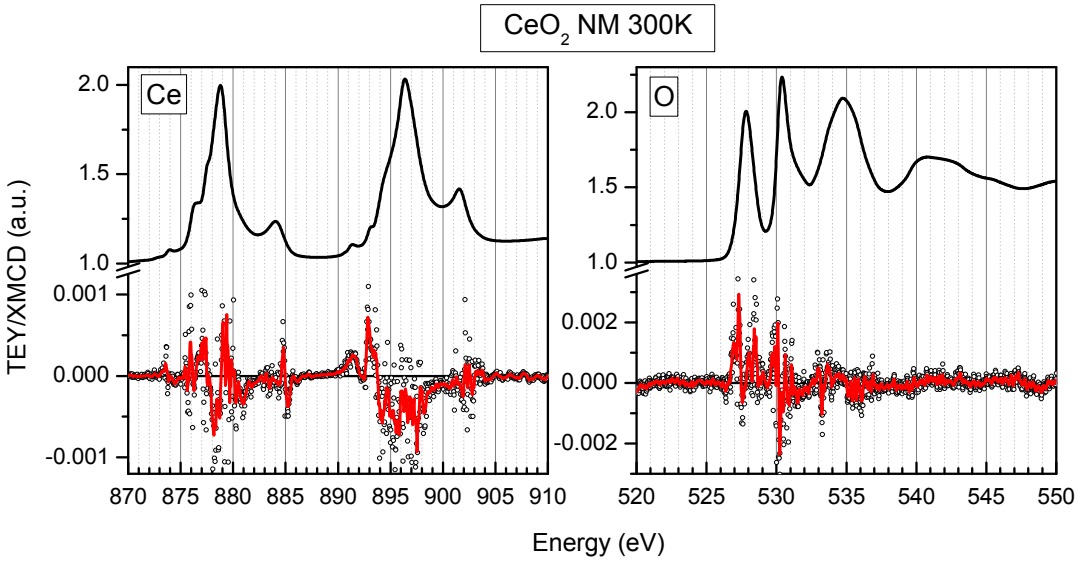

Figure 4.36. XAS/XMCD data measured at 300 K for the non-magnetic (NM) CeO_2 nanopowder.

A comparison of the above Ce $M_{4,5}$ and O *K* edge XAS data and the Ce $M_{4,5}$ edge XMCD data for the NM nanopowder with that measured previously for the ferromagnetic (FM) nanopowder highlights the main spectral differences between FM and NM and is shown subsequently in Figure 4.37. For the Ce $M_{4,5}$ edge XAS comparison shown in Fig. 4.37 (a), there

are enhanced pre-edge features due to Ce^{3+} for FM compared to NM. For the O *K* edge XAS comparison shown in Fig. 4.37 (b), both of which have been normalised to intensity = 1 at 550 eV after first performing the data reduction detailed in the second paragraph, there is some extra post-edge intensity for the 530.5 eV (middle energy) peak for FM compared to NM, while the overall intensity of the two lower energy peaks are smaller for FM versus NM, indicative of enhanced Ce-O hybridization, and also enhanced Ce^{3+} character, for the former sample. It is noted that there are no discernible energy shifts between the XAS of either edge for both samples. A comparison of smoothed XMCD signal amplitudes shown in Fig. 4.37 (c) reveals that both the FM and NM signal shapes are generally rather similar except for some extra sharp negative intensity at ~ 878-880 eV for FM.

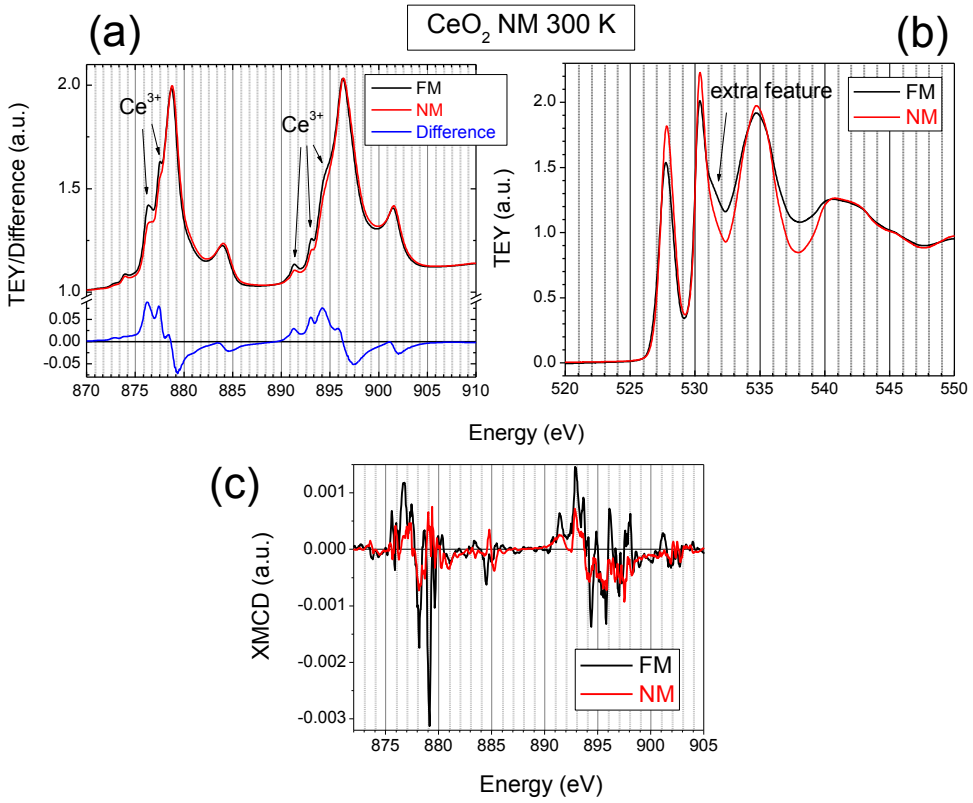

Figure 4.37. Comparison of normalized (a) Ce $M_{4,5}$ edge and (b) O *K* edge XAS spectra for FM and NM nanopowders (c) Corresponding comparison of the amplitudes of the Ce $M_{4,5}$ edge XMCD (smoothed) spectra.

Similar to the data presented previously in Figure 4.32 which displayed the relative Ce^{3+} and Ce^{4+} contributions at 300 K to the XAS/XMCD for the Ce $M_{4,5}$ edge of the ferromagnetic (FM) CeO_2 nanopowder deduced by multiplet calculations, Figure 4.38 shows the results of the multiplet calculations applied to the Ce $M_{4,5}$ edge of the non-ferromagnetic (NM) CeO_2 nanopowder. It is clear that the calculated proportion of Ce^{3+} for NM at 27.6 % (± ~1.5 %) is less than that for FM calculated previously at 34.4 %. By scaling the Ce^{3+} XMCD

contribution by 0.8, and that of Ce^{4+} by 2, the closest match between the experimental and calculated XMCD spectra is obtained; in contrast, for the FM sample, the Ce^{3+} and Ce^{4+} XMCD contributions were scaled by 1.5 and 4 respectively. The experimental and calculated XMCD data appear to match more closely for NM in Fig. 4.38 below than for FM shown previously in Fig. 4.33.

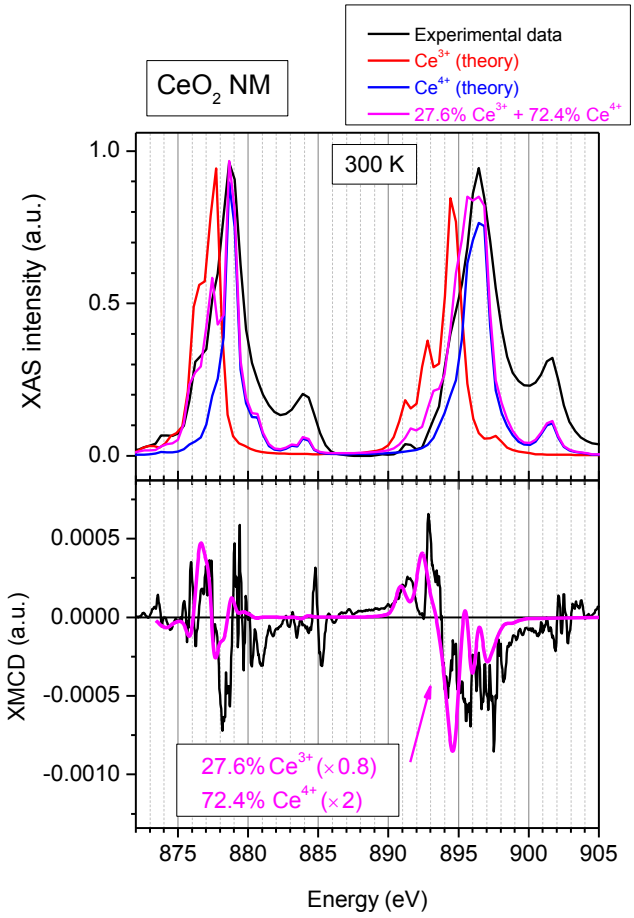

Figure 4.38. Relative contributions of Ce^{3+} and Ce^{4+} to the XAS/XMCD spectra measured for the Ce $M_{4,5}$ edge of non-magnetic (NM) CeO_2 at 300 K.

XAS/XMCD data measured at 300 K for the 1 wt % La-doped high purity CeO_2 nanopowder (synthesized using 99.999 % cerium nitrate) is shown in Figure 4.39. The XAS measured for the Ce $M_{4,5}$ edge is very similar to that measured for the ferromagnetic sample (no relative energy shifts) with pronounced pre-edge features due to Ce^{3+}. The XAS measured for the O *K* edge is also very similar to that measured for the ferromagnetic nanopowder (no relative energy shifts either), with a post-feature evident for the 530.5 eV peak which has previously been measured to be not as prominent in the non-magnetic (NM) high purity nanopowder. In terms of the XMCD data, for the O *K* edge firstly, the signal is rather complex and difficult to interpret. For the Ce $M_{4,5}$ edge, the data is somewhat similar to that measured for the FM nanopowder at 300 K, the main difference being extra negative intensity at ~ 895-900

eV for the La doped sample, as compared in Figure 4.40 (a). The XMCD signal for the Ce $M_{4,5}$ edge of the La-doped sample is also similar in *shape* to that measured for the FM nanopowder measured at 2 K as highlighted in Figure 4.40 (b), which suggests that the moment on Ce in the La-doped nanopowder at 300 K may be predominantly associated with Ce^{3+} since at 2 K for the FM nanopowder it is reasonably assumed that the signal is almost entirely due to (paramagnetic) Ce^{3+}.

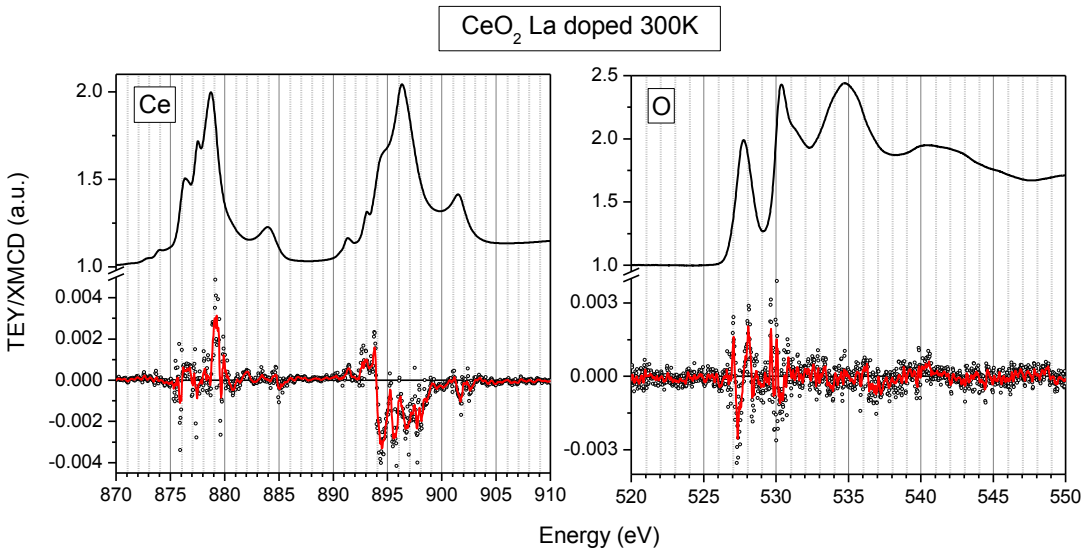

Figure 4.39. XAS/XMCD data measured at 300 K for the 1 wt% La-doped high purity CeO_2 nanopowder.

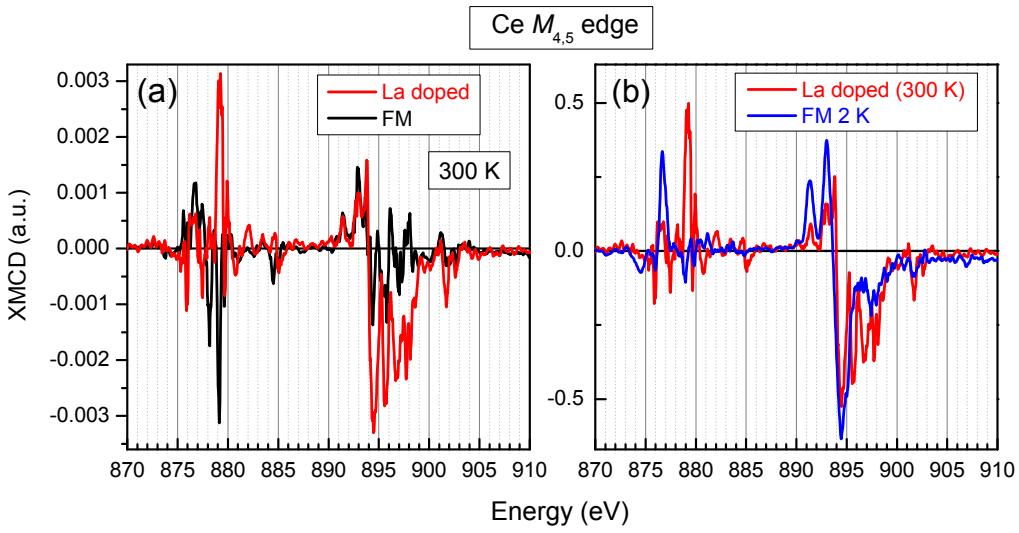

Figure 4.40. (a) Comparison of amplitudes of the smoothed XMCD data measured at 300 K at the Ce $M_{4,5}$ edge for the La-doped and FM nanopowders (b) Comparison of normalized smoothed XMCD data for the La-doped nanopowder (measured at 300 K) with the FM nanopowder measured at 2 K.

Fitting of the experimental and theoretical (multiplet calculated) XAS spectra for the La-doped nanopowder yields a Ce^{3+} contribution of 29.6 % (± ~1.5 %), which is less than that of FM (34.4 %), but slightly more than that of NM (27.6 %); the best fits to the experimental data are shown in Figure 4.41 below. The optimum scaling used for the calculated XMCD signals for Ce^{3+} and Ce^{4+} are found to be 2 and ~ 15 respectively.

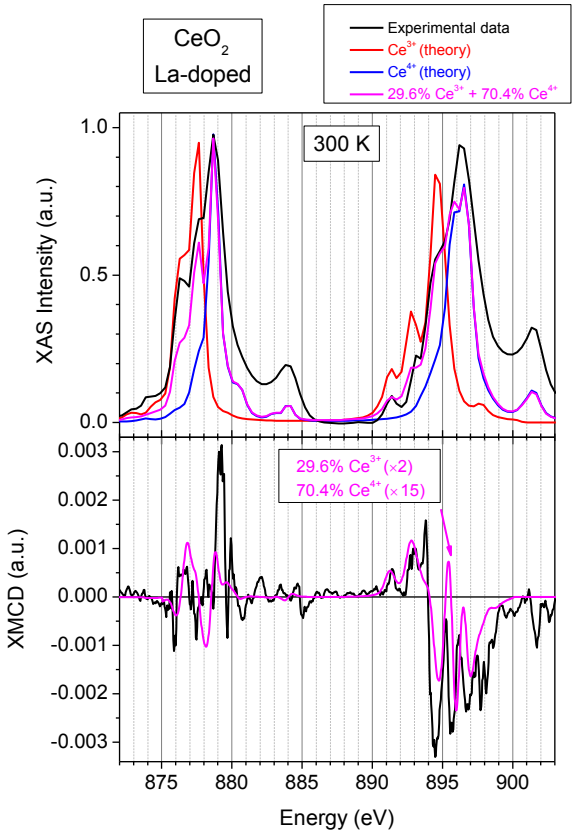

Figure 4.41. Relative contributions of Ce^{3+} and Ce^{4+} to the XAS/XMCD spectra measured at 300 K for the Ce $M_{4,5}$ edge of the 1 wt % La-doped high purity (99.999%) CeO_2 nanopowder.

Data measured for the La *M* edge of the La-doped CeO_2 nanopowder is shown in Figure 4.42. Similar to the La *M* edge of the FM nanopowder, no distinct XMCD signal is resolved from the noise. The XAS has an extra feature at ~848 eV in addition to the La *M* edges, which corresponds most closely to an oxidised form of Ni (L_3 edge). The absence of any distinct XMCD signal indicates that the oxidised form of nickel is not actually ferromagnetically ordered at room temperature. It is possible that the nickel has been implanted during sample mounting when the powders were pressed onto Indium foils (of 99.99% nominal purity) using the metal spatula, since the nickel content measured by ICP-MS was < 1 ppm which is too small a concentration to be detected by XAS. No such signal was measured for CeO_2 FM however, which was mounted in a similar way.

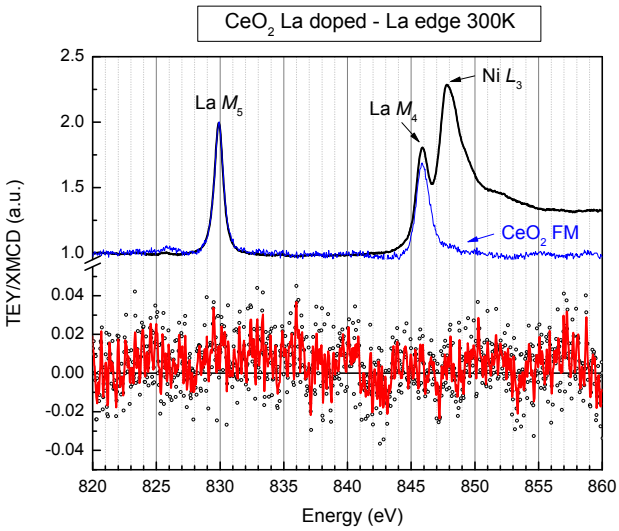

Figure 4.42. XAS/XMCD measured at 300 K for the La $M_{4,5}$ edge of the 1 wt % La doped high purity (99.999%) CeO_2 nanopowder. The XAS measured for the same edge for CeO_2 FM (blue line) is also shown for comparison.

The final sample measured was a bulk reference high purity (99.999%) CeO_2 micropowder purchased from Sigma Aldrich. Room temperature XAS/XCMD data are shown in Figure 4.43. For the Ce *M* edge, the XAS displays little evidence of pre-edge features due to Ce^{3+}, similar to NM as compared subsequently in Figure 4.44, but in contrast to the FM and La-doped nanopowders. The Ce $M_{4,5}$ edge XMCD signal is quite different in shape to all of the previous samples, most notably at the M_4 (higher energy) edge. For the O *K* edge, there is no evidence of any post-edge feature for the 530.5 eV peak, again similar to that for NM and in contrast to those measured for both FM and the La doped sample.

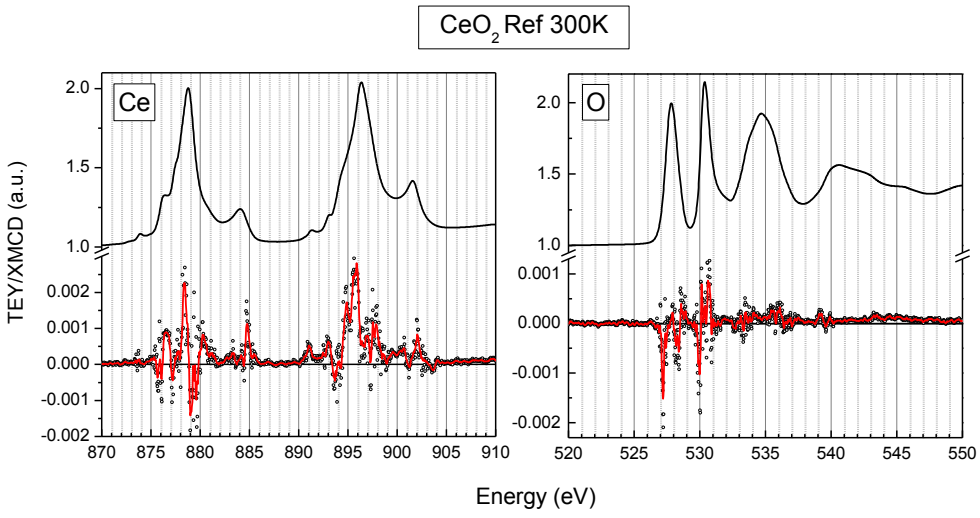

Figure 4.43. XAS/XMCD data measured at 300 K for bulk reference CeO_2 micropowder (99.999%).

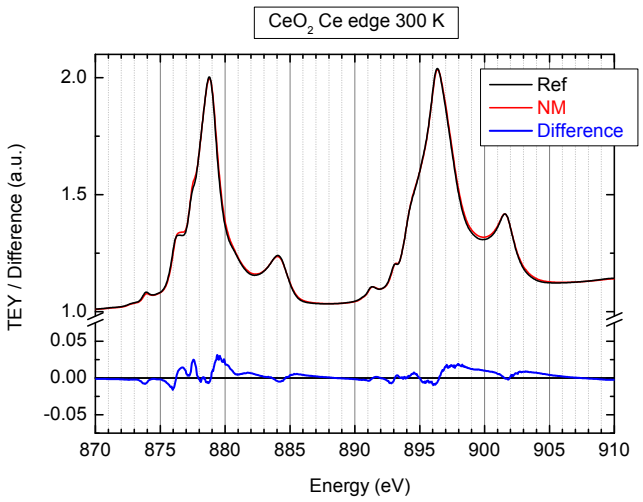

Figure 4.44. Comparison of XAS data measured at 300 K at the Ce $M_{4,5}$ edge for the bulk CeO_2 reference and the non-magnetic (NM) nanopowder; the difference is displayed on the same vertical scale as shown previously in Fig. 4.40 (a) which compared FM and NM.

Mulitplet calculations for the bulk CeO_2 powder yield a Ce^{3+} contribution of ~20 ± 1.5 %, the lowest proportion out of all of the samples measured; the fitted XAS/XMCD spectra are displayed in Figure 4.45 below.

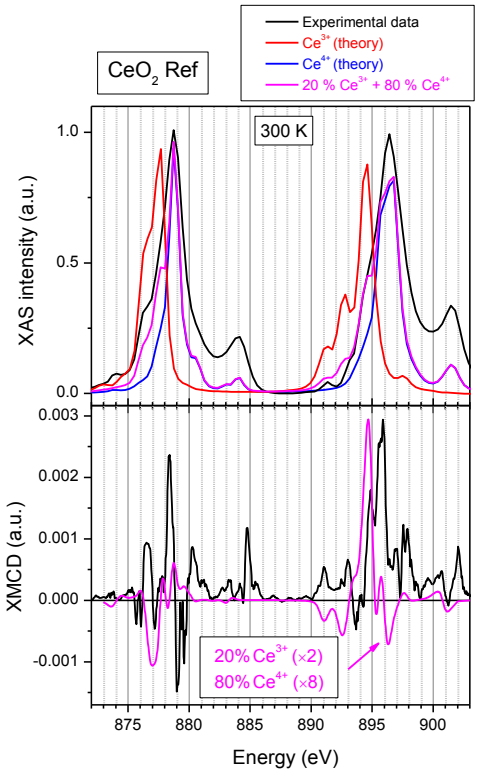

Figure 4.45. Relative contributions of Ce^{3+} and Ce^{4+} to the XAS/XMCD spectra measured at 300 K for the Ce $M_{4,5}$ edge of the bulk CeO_2 (99.999%) micropowder reference.

It is noted that elsewhere, XAS measurements of high purity bulk CeO_2 micropowder (Cerac 99.99 %) on the L_3 edge in transmission (rather than total electron yield) mode yielded at least 5% Ce^{3+} impurities [114], a value more representative of the whole sample volume due to transmission of X-Rays through the sample (instead of surface detection only in total electron yield mode as was performed here), indicating that it is not uncommon for the bulk micropowder to exhibit a significant Ce^{3+} contribution (i.e. several %) when measured by XAS. In terms of the weighted Ce^{3+} and Ce^{4+} calculated contributions to the XMCD signal measured here for the reference micropowder shown in the bottom panel of Fig. 4.48, the optimum scaling factors are found to be 2 and 8 respectively; a key difference from the other samples is that for the reference micropowder the Ce^{3+} orientation has been rotated by 180° (i.e. its contribution multiplied by -1) relative to that in the previous samples (all nanopowders), while the Ce^{4+} orientation is still the same as per the other samples. Whereas for the nanopowders the Ce^{3+} and Ce^{4+} polarized spins are orientated in the same sense with respect to each other, for the bulk micropowder reference their polarized spins are oriented in *opposite* directions relative to each other. An alignment of Ce^{3+} antiparallel to the Ce^{4+} contribution in effect results in a better match between the experimental and calculated XMCD signals for the bulk micropowder, although the optimum match is still not as close/good as for the other (nanopowder) samples.

Table 4.8 summarizes how the optimally scaled Ce^{3+} and Ce^{4+} calculated contributions to the XMCD signal are achieved for each sample in order to best match the experimental and calculated data. The Ce^{4+} scaling factor is multipled by 0.1 since its magnitude at 300 K is about an order of magnitude smaller than that due to Ce^{3+} before any scaling is performed (see Fig. 4.35 lower panel for example). It is evident that while the relative Ce^{3+} to Ce^{4+} scaling ratios are similar for the FM and NM samples, for the La doped sample, the relative Ce^{4+} contribution to the calculated XMCD signal is ~ 3 times more significant compared to that of Ce^{4+} for either FM or NM (or equivalently, it may be stated that the relative Ce^{3+} contribution is ~ 3 times *less* significant). For the reference powder, the relative Ce^{4+} contribution to the calculated XMCD signal is intermediate between that deduced for the FM/NM and the La doped samples. It is emphasized again that both Ce^{3+} and Ce^{4+} are aligned parallel with respect to each other for the FM, NM and La doped nanopowders; for the reference micropowder meanwhile, the alignment of Ce^{3+} has been rotated by 180° (multiplied by -1) so that it is antiparallel to Ce^{4+}.

Table 4.8. Optimally scaled Ce^{3+} and Ce^{4+} contributions to the calculated XMCD signal at 300 K for each CeO_2 sample in order to best match the experimental and calculated data. The Ce^{3+} and Ce^{4+} contributions are oriented parallel with respect each other, except for the reference micropowder (Ref) where the Ce^{3+} orientation only has been rotated by 180° (multiplied by -1).

Sample	Ce^{3+} scaling	Ce^{4+} scaling × 0.1*	Relative Ce^{3+}:Ce^{4+} scaling ratio
FM	1.5	0.4	3.7
NM	0.8	0.2	4.0
La doped	2	1.5	1.3
Ref	-2	0.8	2.5

* the magnitude of the Ce^{4+} contribution is about an order of magnitude (hence ≈ 0.1 times) smaller than that due to Ce^{3+} according to the multiplet calculations

Table 4.9 summarizes the values obtained for the Ce^{3+} and Ce^{4+} content of each CeO_2 sample deduced by multiplet calculations from the XAS data. The Ce^{3+} content is quite high, even for the bulk reference, which is only weakly paramagnetic with a room temperature susceptibility of $\chi = +3.5\times10^{-6}$; the enhanced Ce^{3+} content may be attributable to the X-Ray absorption measurement performed in surface sensitive total electron yield mode, in which the penetration depth is only typically several nanometres, thus measuring a larger quantity of surface Ce^{3+} for each sample. Another possible Ce^{3+} contribution is due to the high vacuum conditions (10^{-9} mbar) at which the X-Ray absorbance measurements were performed, which may reduce CeO_2 slightly and serve to increase the Ce^{3+} content of the samples. Another possibility is that some reduction of ceria in the synchrotron X-Ray beam occurred, i.e. radiation damage artefacts.

Table 4.9. Ce^{3+} and Ce^{4+} content calculated for CeO_2 powders from XAS data using multiplet calculations (exchange parameter = 0.01); the error is ≈ ± 1.5 %.

Sample	Ce^{3+} %	Ce^{4+} %
FM	34.4	65.6
NM	27.6	72.4
La doped	29.6	70.4
Ref	20.0	80.0

The Ce^{3+} content measured by XAS for CeO_2 seems anomalously high compared to that inferred from SQUID magnetometry, the latter of can be used to estimate a Ce^{3+} content of ≤ 0.5 % for all samples from the paramagnetic upturn of the susceptibility at low temperatures, assuming J = L - S = 5/2. This discrepancy in the Ce^{3+} content deduced from these two different measurements may be explained if the Ce^{3+} electrons are mostly delocalized in the Ce 4*f* band, although it is shown shortly that at 2 K and in a magnetic field of 7 T, the sum rules [115] indicate that Ce^{3+} is carrying ~ $1\mu_B/Ce^{3+}$, consistent with a *localised* moment on a spin 1/2 atom with g = 2.

Before application of the sum rules, it is first noted that another report for XAS/XMCD of CeO_2 nanoparticles by Chen *et al.* [39] reveals that (4*f*) electrons in cerium atoms bear magnetic moments (XMCD signal detected) while the oxygen atoms do not respond magnetically (no XMCD signal detected), in contrast to this study where an XMCD signal is also detected for the oxygen edges for the samples measured. There are several differences however between the experimental conditions used by Chen *et al.* and those used in this study here since Chen *et al.* measure XAS/XMCD in fluorescent yield mode on the Ce L_3 edge at ~ 5700 eV (instead of total electron yield on the $M_{4,5}$ edges at ~ 870-910 eV as was performed here) in an applied field of ±1 T. They estimate by fitting the Ce XAS spectra that their as-prepared (paramagnetic) nanoparticles contain 28 % Ce^{3+}, and that those annealed at 300 °C in air, N_2 and O_2 contain 17%, 35% and 10% Ce^{3+} respectively. As the electron escape depth in fluorescent yield mode exceeds their range of nanoparticle diameters (3-10 nm), the estimated Ce^{3+} content corresponds

to their entire nanoparticle volume. Although they measure no clear correlation between M_s and the total Ce^{3+} content, by considering the effect of particle size and by calculating the *surface* Ce^{3+} content only, M_s is actually found to reach a maximum for 40–45 % surface Ce^{3+}. Due to the weak XMCD signal and cited difficulties with the background subtraction, no attempt was made by the authors to obtain quantitative information about the orbital and spin moments. Apart from this and our study, there are no other reports of XMCD in undoped CeO_2 to date.

Meanwhile, for Cr doped CeO_2 nanoparticles of 2-3 nm diameter [30], an article published by many of the same authors of the undoped CeO_2 XMCD study [39] and using similar measurement conditions, an XMCD signal is measured for the Ce *L* edge, but not on the Cr *K* edge; hence the magnetism is associated with Ce^{3+} rather than the Cr dopant. Furthermore, it is postulated that the effect of Cr^{3+} doping reduces the distance between magnetic Ce^{3+} by increasing the density of defects, which could promote the formation of magnetism. For Fe doped (1-3 at. %) CeO_2 polycrystalline thin films, ~ 200 nm thick, grown by PLD on LAO (001) substrates [69], XMCD measurements of the Fe $L_{2,3}$ edge performed in fluorescence yield mode reveal enhanced Fe^{2+} character in a mixed valence Fe^{2+}/Fe^{3+} environment with increased Fe doping concentration. The authors propose that the reason why the absolute value of the magnetic moment of the system is reduced with increased Fe doping concentration is due to the fact that the Fe^{3+} contribution proposed to mediate the magnetism is diminished by the relative increase in Fe^{2+} character with increased Fe doping levels.

Later is this chapter, another estimation of the Ce^{3+} content in CeO_2 is obtained by energy electron loss spectroscopy (EELS) using TEM; generally a higher Ce^{3+} content is measured by TEM-EELS for the nanopowders, but a slightly lower Ce^{3+} content for the bulk reference; a key difference is that TEM-EELS is a nanoscale probe of valence state, whereas XMCD is a microscale probe, and hence TEM-EELS can monitor valence changes over nanoscale distances unlike XMCD. A comparison between the XMCD and EELS results are discussed further later on in the TEM-EELS section (4.3.9).

Finally, preliminary results are presented stemming from the application of the sum rules for the $M_{4,5}$ absorption edges of the rare earth elements to CeO_2 measured here, following the method of Carra *et al.* [115], which attempts to discriminate the orbital and spin contributions to the total magnetic moment. Table 4.10 on the next page lists the expectation values deduced for the spin and orbital moments upon application of the sum rules to the experimentally measured XAS and XMCD data for all of the CeO_2 samples. For the first listed sample, CeO_2 FM at 2 K (and 7 T), the spin contribution to the moment, the expectation value of which is denoted $\langle S_z \rangle$, deduced from the experimental spectrum upon application of the sum rules is 0.49, giving $2\langle S_z \rangle = 0.98\ \mu_B$ per Ce^{3+}, in close agreement with the theoretical value of 1 μ_B per Ce^{3+} (g = 2, spin ½). The expectation value of the orbital contribution, $\langle L_z \rangle$, meanwhile gives an orbital moment of -1.3 μ_B per Ce^{3+}, and is thus oppositely orientated with respect to the spin moment, in agreement with less a less than half full 4*f* band. This value is much less than that predicted from theory for an *f* state (L = 3), hence the orbital moment appears to be significantly quenched. It was estimated previously that the Ce^{3+} content inferred from the

paramagnetic upturn of the magnetic susceptibility at low temperatures, assuming J = L – S = 5/2, was ≤ 0.5 %; if the orbital moment is significantly quenched however, perhaps S = 1/2 is a better quantum number to use instead of J (normally the good quantum number used for the rare-earths), but using S = 1/2 instead the Ce^{3+} content inferred from the paramagnetic upturn of the magnetic susceptibility at low temperatures is still only ~ 1 %, i.e. approximately double what is was before using J = 5/2, but still significantly less than the 34 % measured by XAS.

Table 4.10. Expectation values for the spin and orbital moments deduced from sum rule calculations applied to the experimental XAS/XCMD data measured for CeO_2.

Sample	Spin moment $2\langle S_z\rangle$	Orbital moment $\langle L_z\rangle$	$\langle L_z\rangle/\langle S_z\rangle$
FM 2 K*	+ 0.98	- 1.30	- 2.65
FM 300 K	+ 0.003	- 0.004	- 2.67
NM **	+ 0.008	- 0.011	- 2.75
La doped **	+ 0.022	- 0.029	- 2.63
Ref **	- 0.037	+ 0.05	- 2.70

* at 2K is assumed that the XMCD signal is due to (paramagnetic) Ce^{3+} only
** all measured at 300 K

For the FM nanopowder at 300 K the expectation values of the spin and orbital moments listed in Table 4.10 are about three orders of magnitude smaller than those at 2 K, but with the same relative orientations as at 2 K. The spin moment $2\langle S_z\rangle$ at 300 K for FM is 0.003 μ_B per Ce as deduced from the sum rules, which is about an order of magnitude larger than that estimated previously from the room temperature magnetization data measured for CeO_2 FM, assuming that the moment is on Ce, for which a value of ~ 2×10^{-4} μ_B/Ce was estimated. The finding the that non-magnetic reference powder exhibits values for $2\langle S_z\rangle$ and $\langle L_z\rangle$ of - 0.037 and +0.05 respectively, values which are larger than those calculated for all of the nanopowders (FM, NM, La-doped) at 300 K, indicates that no reasonable physical meaning can be attached to calculated moments here of order this size or smaller (i.e. ~ 10^{-2} μ_B per formula unit or less) since the FM and La doped FM nanopowders are known to be weakly ferromagnetic while the reference is non-ferromagnetic, yet the latter exhibits larger expectation values for $2\langle S_z\rangle$ and $\langle L_z\rangle$ than for the former samples; this finding also illustrates that moments of magnitude ~ 10^{-2} μ_B per formula unit or less are typically at or below the noise level/detection limit of conventional XAS/XMCD measurements. It is also noted from Table 4.10 that the estimated spin and orbital moments for all of the nanopowders are aligned antiparallel with respect to each other; the same is true for the bulk reference micropowder, except that the orientations of both the spin and orbital moments are at 180° (i.e. multipled by -1) with respect to their orientations in the nanopowders. The ratio of the expectation values of the orbital to spin moments, $\langle L_z\rangle/\langle S_z\rangle$, are similar for all samples at ~ 2.6-2.7, the values of which indicate that the orbital moment contribution is consistently greater than the spin moment contribution for all samples. The analysis of the sum rule data is currently ongoing.

4.3.7 Muon spin rotation spectroscopy

In order to further elucidate the local magnetic properties of CeO_2 nanopowders, muon spin rotation (μSR) spectroscopy measurements were performed at the Swiss Muon source (SμS) at the Paul Scherer Institute. The General Purpose Surface muon instrument (GPS) was used to collect the data. Both ferromagnetic (FM) and non-ferromagnetic (NM) CeO_2 nanopowders, synthesized using 99 % and 99.999 % cerium nitrate respectively, were measured, in addition to a bulk reference CeO_2 micropowder (Sigma 99.999 %). The powders were prepared for measurement by tightly encasing the compacted powder in aluminized mylar coated superinsulation tape (sticky on one side, with the sticky side located on the outside, i.e. not in contact with the powder sample) to form a little "bag", which was then sealed using further tape. The sealed bag was then subsequently mounted on a fork-like sample holder for measurement in order to reduce the background contribution. The tape was first degreased by cleaning it with a tissue dabbed in benzene before making the bags. The aim is to use enough compacted powder so that the muons will stop within the depth of sample material, which for CeO_2 is ~ 0.17 mm (the muon range is approximately 130 mg per cm^2 of material as a rough guide). For the nanopowders, ~ 50 mg of powder was used, which gives a bag of approximate dimensions 5×5×0.3 mm (width × height × thickness). For the reference micropowder, several times more mass of powder was available, hence the bag prepared was larger and thicker for this measurement. The muon beam spot size (FWHM) incident on the sample is 5.3 mm (5.8 mm) for the horizontal (vertical) directions.

To re-cap briefly, μSR involves the implantation of positively charged ~ 100 % spin-polarized muons (μ^+) in matter, which have S=1/2, a moment of 3.18 μ_{proton} (sensitive to 10^{-3} – 10^{-4} μ_B) and a lifetime of 2.197 μs in vacuum. μSR is analogous to NMR (nuclear magnetic resonance) and EPR and measures the muon spin direction with time via the unique signature of the parity violating decay of the muon, in which its decay positron is emitted preferentially along the muon spin direction. The time evolution of the muon spin polarization depends sensitively both on the spatial distribution and dynamical fluctuations of the muons' magnetic environment. Specifically, the amplitude of the polarization signal corresponds to the magnetic volume fraction, the frequency to the local field (magnitude of magnetic moments), and the damping to the inhomogeneity of the magnetic regions. The muon can easily distinguish between paramagnetism and ordered magnetism. In the paramagnetic case, the electronic moments are fluctuating very fast which is typically averaged to zero during the muon precession hence only weak (or no) damping is measured, whereas magnetically ordered states can lead to zero-field precession signals or to strong damping if the magnetic state is very much disordered; the muon cannot readily *distinguish* between different types of long-range magnetic order however, such as whether it is ferromagnetic, antiferromagnetic or ferrimagnetic in character for example.

In the literature, the magnetic properties of CeO_2 are almost exclusively measured by SQUID magnetometry, the main advantage of which is detection of even the smallest ferromagnetic

contribution (~ 10^{-11} Am^2). Some disadvantages however are that SQUID is prone to measurement errors and sample contamination and measures only the *total* (macroscopic) magnetic moment. Unique advantages of (bulk) μSR for measuring the magnetic properties include the fact that it is a microscopic local probe and that the ground state in *zero* applied magnetic field is probed (unlike SQUID, XMCD for example). CeO_2 exhibits almost no nuclear damping since all Ce isotopes are spin 0 while for oxygen only ^{17}O has spin 5/2 with 0.038 % natural abundance. Hence μSR will be very sensitive for any coupled *electronic* moments (ferromagnetic, giant paramagnetic) in CeO_2. Cox. *et al.* [116] have previously shown that there is no muonium (isotopic analogue of a Hydrogen atom in which a μ^+ captures an electron) present for T > 30 K, neither shallow, nor atomic like in polycrystalline (bulk) CeO_2, which makes interpretation of the results easier. However, one advantage of probing materials with muoniums rather than muons is that the muonium is even more sensitive than the muon (of order 100 times) to the presence of local magnetic fields.

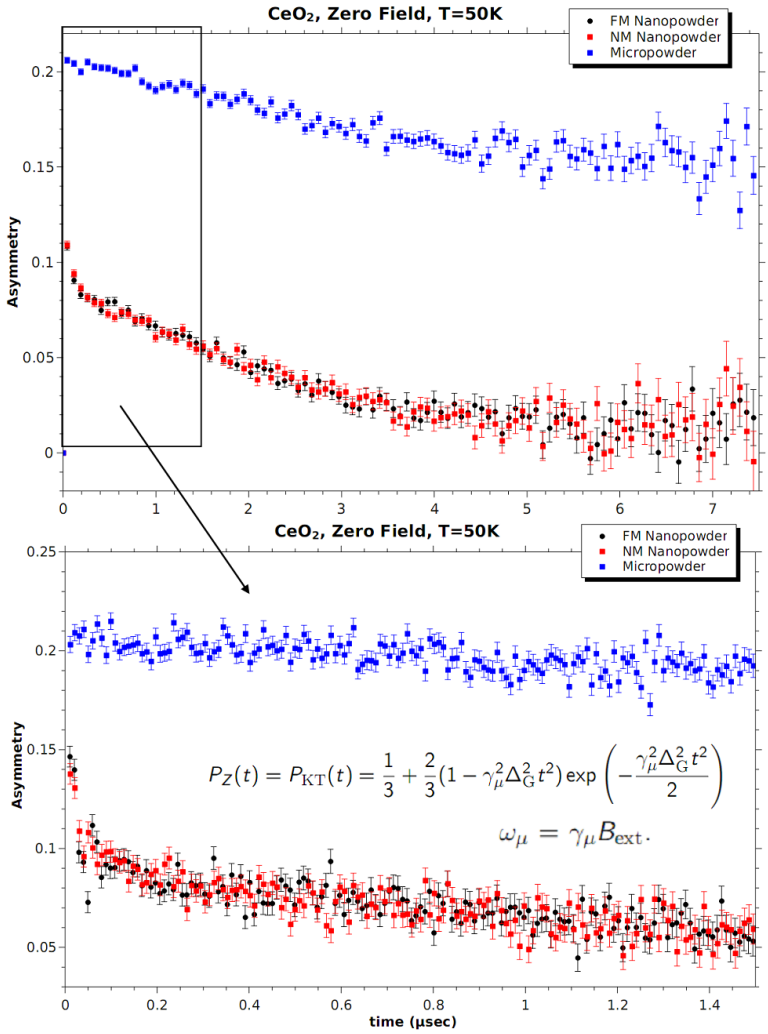

Figure 4.46. Temporal muon asymmetry measured for CeO_2 nanopowders (FM and NM) and bulk micropowder at 50 K in zero applied magnetic field. The lower graph displays the asymmetry at shorter timescales as well as the general form of the zero-field Kubo-Tobaye fit function.

Some preliminary results from the recent beamtime at the Paul Scherrer Institute are shown in Figure 4.46 on the previous page, which displays the muon asymmetry as a function of time in zero field for the FM and NM nanopowders plus the bulk micropowder, all measured at 50 K. It is immediately clear that the signals for the nanopowders are virtually identical and that the muon undergoes a significant reduction in asymmetry over its lifetime (large damping, in particular initially at ≤ 0.2 μs) which indicates that both nanopowders are magnetically ordered, especially at short muon timescales. For the CeO_2 bulk micropowder in contrast, there is much less damping of the muon asymmetry with time, which indicates that the muons sense much less magnetic order; the weak damping measured for the micropowder (theoretically a non-magnetic sample should display *no* damping at all) may be due to spin-exchange scattering, in which a muonium can form and decay again for a very short time. For the nanopowders, the value of the asymmetry is generally much lower than that measured for the micropowder, which may be due to muonium depolarization in the presence of internal magnetic fields for the nanopowders; as mentioned before, the muonium is of order 100 times more sensitive to the presence of local magnetic fields. While Cox *et al.* [116] report no muonium formation in the bulk above 30 K, they do not measure nanopowders in their study, so it is plausible that at 50 K here for the nanopowders there are still some muoniums present; since the muonium is ~ 100 times more sensitive than the muon to magnetic fields, this only needs to be a very small muonium fraction. The data may be fitted with the zero-field Kubo-Tobaye (KT) function [117], whose form is shown in Fig. 4.46 (lower graph), from which the magnetic field width Δ_G may be extracted. For the nanopowders, the magnetic field sensed by the muon as deduced from the KT fit function may be separated into two parts, the field experienced on a short time scale, indicative of the more immediate magnetic surroundings of the muon, for which $\Delta_G \approx 0.28$ T, and the field experienced by the muon on a longer time scale, indicative of the longer-range stray magnetic field, for which $\Delta_G \approx 0.003$ T. In addition, for the nanopowder, it is estimated that 38(3) % of the muons are sensitive to their immediate magnetic surroundings (short timescale component), with the remainder sensing the stray field only (long timescale component).

The reason that the asymmetry measurements were not performed at a higher temperature is due to the fact that muon diffusion (instead of hopping) typically occurs above 150 K which can *also* produce a decay in asymmetry over time, which greatly complicates the analysis and makes it difficult to separate the signal correlated with muon diffusion from that due to true magnetic order. Another possible complication is a decay in muon polarization produced by its interaction with protons (Hydrogen); for example, during the nanoparticle syntheses, proton-rich polyethylene glycol (PEG) is used both to mediate the nanoparticle growth and as a surfactant. The large transverse fields (> 0.5 T) necessary to decouple the muon spin from the internal magnetic fields (i.e. helps to separate the individual depolarization contributions originating from the muon spin and internal fields) indicates that protons are not in fact solely responsible for the sharp initial polarization decay for the nanopowders.

From the SQUID magnetometry data, the CeO_2 nanoparticles show weak paramagnetism ($\chi \leq 4.5\times10^{-6}$) apart from at the lowest temperatures (< 10 K), hence a strong paramagnetic component influencing the muon spin is unlikely. Likewise, the ferromagnetic contribution as

measured by SQUID magnetometry (typically of order 100 A m^{-1}) for FM is rather small, and the fact that the muon polarization is very similar for FM and NM suggests that the weak ferromagnetic character of FM does not influence the muon very strongly compared to NM. This leaves *antiferromagnetic* order as a remaining possibility; such an explanation can be reconciled with the magnetization data since SQUID magnetometry is not sensitive to antiferromagnetism, and will likely only measure a residual paramagnetism (and/or a small ferromagnetic-like signal) instead. In such a scenario, for the NM nanopowder, the net moment averaged over the two sublattices of the antiferromagnet may average to zero, whereas for the FM nanopowder the moment may be slightly higher on one of the sublattices compared to the other, giving rise to a small net moment overall, which may manifest itself as a small ferromagnetic-like signal measured by SQUID magnetometery, but which may in fact be representative of *ferri*-magnetic rather than *ferro*-magnetic order. For XMCD, the fixed exchange parameter of 0.01 (eV) applied to the multiplet calculations (which assumes full polarization) for Ce^{3+} and Ce^{4+} at the $M_{4,5}$ absorption edges was found to be much too large, and had to be reduced to 0.0014 in order to best match of the experimental and calculated XMCD signal magnitudes, which may also indicate an antiferromagnetic contribution since the XMCD signal due to one of the two sublattices will tend to cancel out the XMCD signal from the other sublattice.

4.3.8 Electron paramagnetic resonance spectroscopy

Electron paramagnetic resonance (EPR) spectroscopy measurements at room temperature and pressure were performed in order to search for possible ferromagnetic phases and/or paramagnetic centres in CeO_2 nanopowders (both ferromagnetic and ~ non-magnetic as measured by SQUID magnetometry) and bulk micropowder (Sigma 99.999 %). Typically ~ 10 mg of powder was measured for each scan (note: for the typical 4 mg ferromagnetic CeO_2 nanoparticle batches which were synthesized, several batches were synthesized and their masses combined to give the 10 mg net mass for measurement, since scaling up of the batch size *per synthesis* by using larger volumes of reagents is found to reduce the magnetic signal per batch (as demonstrated previously in Fig. 4.15 for example). For the bulk micropowder, no reduction in the EPR cavity Q-factor upon insertion of the powder sample was measured, indicating that the bulk powder was not conductive. For the non-ferromagnetic nanopowder, synthesized using 99.999% cerium nitrate, the relative reduction in the cavity Q-factor upon sample insertion was about 15 %, while the reduction upon insertion of the ferromagnetic nanopowder, synthesized using 99% cerium nitrate, was about 20 %, indicative of slightly enhanced conductivity for the latter.

Firstly, an EPR spectrum of a high purity CeO_2 micropowder (Sigma 99.999 %) was measured, which is shown in Figure 4.47. Since the quadrivalent cerium ion has the electronic

configuration $Xe\,4f^0 5d^0 6s^0$, the spectrum is not due to Ce^{4+}. Although Ce^{3+} does indeed exhibit an EPR signal due to its unpaired spin (S = 1/2), because of the fast spin-lattice relaxation at room temperature, a signal can be observed only at temperatures ≤ 20 K [118]. At room temperature the paramagnetic signal due to Ce^{3+} is hence completely broadened out. The six narrow lines measured in Fig. 4.50 may be due to a trace of Mn^{2+} impurities (I = 5/2) in this particular batch of high purity bulk ceria; the six (2I + 1) lines are characteristic of a hyperfine splitting in an applied magnetic field with similar line intensities and relative separations. The summed integral area of the signal corresponds to ~ 10^{15} spins per gram or ~ 0.4 ppm of Mn, illustrating the sensitivity of EPR to the presence of unpaired spins. No other signals were measured at higher or lower applied fields in the range 0.1-0.6 T.

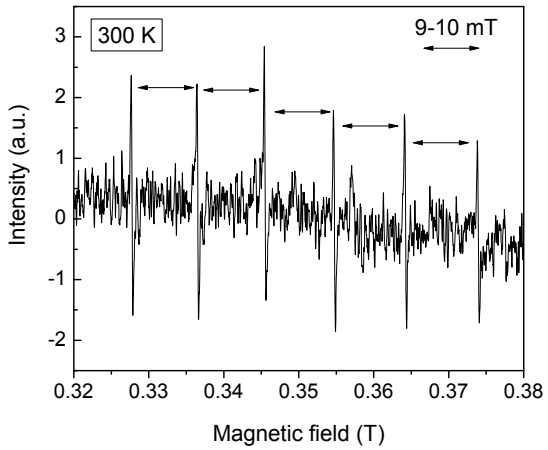

Figure 4.47. EPR spectrum measured at 300 K for CeO_2 99.999 % purity micropowder.

An EPR spectrum measured for ferromagnetic CeO_2 nanoparticles synthesized using 99 % cerium nitrate (from 4 mg batches) is shown in Figure 4.48. There appear to be two contributions to signal, a complex paramagnetic-like multiplet contribution near g = 2 (~ 0.35 T) which was measured for all of the ferromagnetic nanopowders, and a broad contribution at lower applied field which was measured for some of the ferromagnetic nanopowders, the latter of which may possibly be due to ferromagnetic resonance. The total number of spins per gram is of order 10^{20}, or of order 1 % of the sample volume. The number of spins per gram for the paramagnetic feature near g = 2 only is of order 10^{16}. Note that the paramagnetic feature appears slightly different in shape and intensity for wide and narrow magnetic field scans; this is a measurement artefact related to the scan time and time constant due to the fact that the wider scan does not capture the very sharp paramagnetic features as accurately as the narrow scan does. It was initially suspected that the broad signal may possibly be due to absorbed H_2O in the nanopowder sample, which has a broad resonance range and is very highly absorbing of microwaves. In order to test this hypothesis, a blank EPR tube was rinsed with H_2O and an EPR spectrum acquired using the same conditions as those used for the ferromagnetic nanopowder scan; no broad signal, or any EPR signal for that matter, was detected, despite the fact the some

water droplets were still visible inside the tube. Hence it is unlikely that the broad signal is due to absorbed H_2O in the sample and confirms that although the polar H_2O molecule is widely known to exhibit strong microwave *electric* resonance (which is incidentally the mechanism by which microwave ovens heat food), it does not exhibit any measurable *magnetic* resonance at room temperature. It is noted however that the response of free water in an EPR tube may be different to that of bound water in a compound. The paramagnetic-like signal meanwhile is probably due to some paramagnetic impurities or more likely point defects in the nanopowder, likely arising from the ~ 1-2 wt % La in the 99% cerium nitrate precursor used during synthesis. The La dopant serves to create both a charge imbalance (La^{3+} substitutes for Ce^{4+}) and lattice distortion (117 pm ionic radius for La^{3+} compared to 101 pm for Ce^{4+}) in CeO_2 which induces extra Ce^{3+} content (as found by SQUID, XAS and TEM-EELS for example) which in turn drives oxygen vacancy formation to charge compensate. Hence the ferromagnetic CeO_2 nanopowders are likely to be defect-rich, and the presence of a complex paramagnetic multiplet indicates that there are several different contributions to the paramagnetic signal, possibly from multiple defect sites. It is further postulated that these defect sites may be F centres (an electron trapped at an oxygen vacancy).

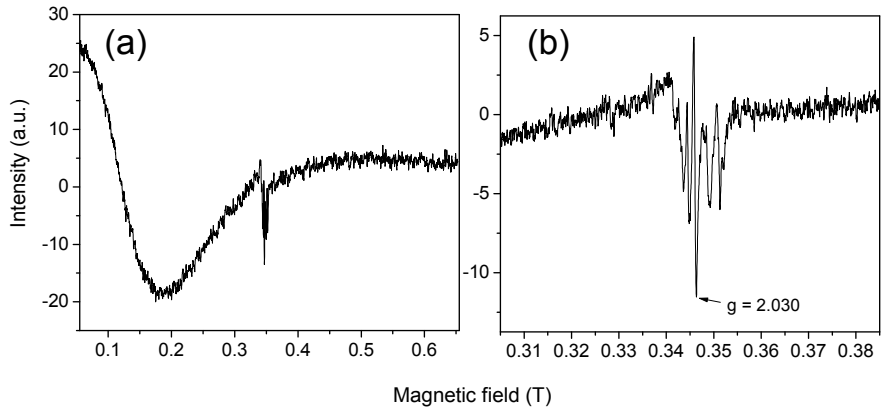

Figure 4.48. (a) EPR spectrum measured at 300 K for a typical ferromagnetic CeO_2 nanopowder synthesized using 99 % cerium nitrate; (b) A narrower magnetic field scan centred at the paramagnetic feature.

An EPR spectrum for CeO_2 nanoparticles synthesized using 99 % cerium nitrate but synthesized using scaled up reagent volumes (×10 compared to the regular 4 mg batch synthesis) is shown in Figure 4.49. The spectrum contains a similar paramagnetic-like feature to that measured previously for the corresponding ferromagnetic nanopowder synthesized using the same cerium nitrate precursor shown in Fig. 4.48. However, no broad signal was measured here in contrast to the ferromagnetic nanopowder; it has previously been shown that scaling up the reagent volume of the nanoparticle synthesis greatly reduces the magnitude of the ferromagnetic signal (Fig. 4.15). Hence it may be deduced that the complex paramagnetic signal is common to the nanopowders synthesized using 99 % cerium nitrate, regardless of whether the

nanopowders are actually ferromagnetic or ~ non-ferromagnetic, whereas additionally the broad signal, which is similar to a ferromagnetic resonance signal with a g value << 2 due to an internal field contribution, appears *only* for the ferromagnetic nanopowder.

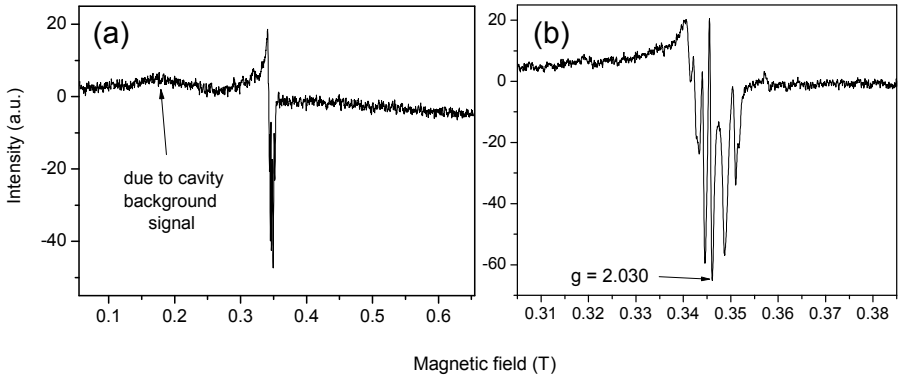

Figure 4.49. (a) EPR spectrum measured at 300 K for a ~non-ferromagnetic CeO_2 nanopowder synthesized using 99 % cerium nitrate in which the reagent volumes were scaled up by 10 times compared to those used for the regular ferromagnetic CeO_2 nanopowder syntheses; (b) A narrower magnetic field scan centred at the paramagnetic feature.

A room temperature EPR spectrum measured for the non-ferromagnetic CeO_2 nanopowder synthesized using the 99.999% cerium nitrate precursor (it is re-emphasized that *all* nanopowders synthesized using the 99.999% cerium nitrate precursor were non-ferromagnetic) is shown in Figure 4.50; no distinct EPR signals were detected between 0.1 and 0.6 T apart from a weak paramagnetic signal near g=2. Hence the concentrations of paramagnetic impurity phases and/or defect centres for this higher purity nanopowder are much lower than for the lower purity nanopowders synthesized using 99% cerium nitrate presented shown previously.

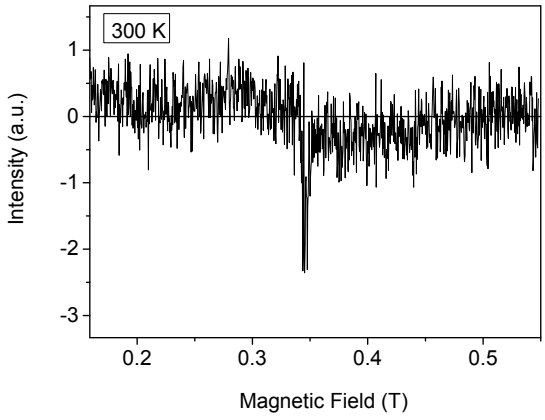

Figure 4.50. EPR spectrum measured at 300 K for the non-magnetic CeO_2 nanopowder synthesized using 99.999 % cerium nitrate.

In summary, whereas no EPR signals are detected for the non-ferromagnetic CeO_2 nanopowder synthesized using 99.999% cerium nitrate, signals indicative of paramagnetism and ferromagnetic resonance, the former due to point defects and/or paramagnetic impurities, are detected for the ferromagnetic CeO_2 nanopowder synthesized using 99% cerium nitrate (for 4 mg batches); scaling up the reagent volumes for CeO_2 nanopowders synthesized using 99% cerium nitrate results in a disappearance of the ferromagnetic resonance feature which is likely associated with the disappearance of ferromagnetism measured by magnetometery for these scaled up samples.

4.3.9 Energy Electron Loss Spectroscopy

Energy electron loss spectroscopy (EELS) measurements were also performed using TEM, in order to provide spatially local (~ 1 nm minimum) information about the oxidation state of cerium in the CeO_2 nanopowders, further to that obtained by XAS shown previously in section 4.3.6. In EELS, the basic principle is that incident electrons of sufficient energy can eject bound atomic electrons, giving rise to characteristic ionization edges (energies). Here, measurements in the vicinity of the cerium *M* edge and oxygen *K* edge were performed. EELS spectra and x-ray absorption spectra (XAS) or x-ray photoelectron spectroscopy (XPS) in the *M*-edge region of rare-earth elements carry information on the 4*f* state occupancy. The spectra are characterized by sharp white lines corresponding to general $3d_{3/2} \rightarrow 4f_{5/2}$ (M_4) and $3d_{5/2} \rightarrow 4f_{7/2}$ (M_5) transitions respectively, associated with the spin-orbit splitting of the core-hole. The spectral features are analogous to those for XAS discussed previously. Since the relative intensities of the white lines are associated with the 4*f* shell occupancy of the rare-earth elements, for cerium compounds the white line ratio may be used to determine the valence of cerium ions. The oxidation state of cerium may be estimated by twice differentiating the EELS spectrum, and comparing the resultant maximum amplitudes of the signal for the M_5 and M_4 edges, or by comparing the ratio of the areas of M_5 and M_4 peaks. Values for the M_5:M_4 white line ratio used to characterise the valence of cerium obtained from the literature are listed in Table 4.11 as a reference guide. In some reports where the M_4:M_5 ratio is given, the reciprocal has been listed below in order to compare all of the M_5:M_4 ratios together. The method of calculating this ratio is also listed.

Table 4.11. Typical M_5/M_4 edge ratios measured for the EELS spectra of cerium.

M_5/M_4 white line ratio			
100 % Ce^{3+}	**100 % Ce^{4+}**	**Measurement method [a]**	**Ref**
1.31	0.91	SD	119
1.28	0.91	SD	120
1.18	0.90	Direct	121

[a] SD = second derivative of EELS spectrum, ratio of resultant amplitudes, Direct = peak intensity ratio obtained directly from EELS spectrum

TEM-EELS spectra of the cerium $M_{4,5}$ edge for a ferromagnetic CeO_2 nanopowder synthesized using 99 % cerium nitrate are shown in Figure 4.51, with the background subtracted and normalised to the M_5 edge, together with an STEM image of the nanoparticles. The characteristic M_5 and M_4 edges of cerium are clearly resolved. EELS signals were acquired from areas of the sample located both at the interior where the particles are agglomerated and at the edge of the agglomeration. The results are further interpreted in the following paragraph.

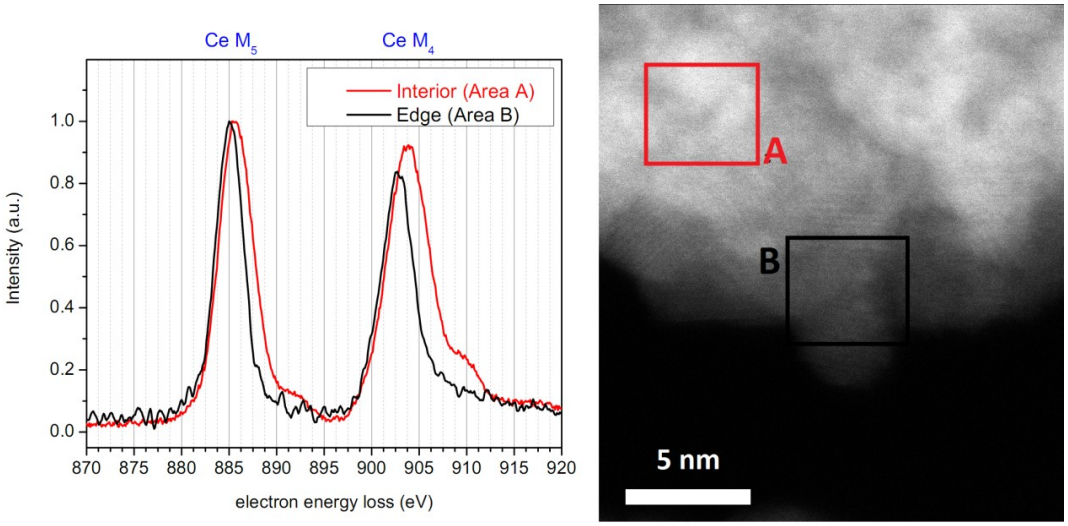

Figure 4.51. TEM-EELS spectrum of the cerium $M_{4,5}$ edge for a ferromagnetic (FM) CeO_2 nanopowder for both interior and edge areas of the sample acquired from the regions marked in the STEM image.

Because electron beam irradiation for extended periods risks damage with a resulting change of the valence of Ce ions from 4+ to 3+ accompanied by loss of oxygen [122], short EELS acquisition times of (≤ 5 s) were used to acquire the spectra shown in Fig. 4.51, which is possible using the parallel EELS (PEELS) detection system used here. The signal will mostly come from the surface of the nanoparticles when the beam is focused at the edge, while it will mainly come from the centre or bulk of the nanoparticles when the beam is focused at the interior of the agglomeration. For the interior scan shown above in Fig. 4.51, the ratio of the M_5 to M_4 signal amplitude from the double differentiated EELS signal (henceforth referred to

as the M_5:M_4 ratio for brevity) is 1.08, while for the edge scan the ratio rises to 1.19. From Table 4.11, the ratio for Ce^{3+} should be ~ 1.295±0.015 (taking the average result for the second derivative method of calculation), while that for Ce^{4+} is 0.91. Hence the Ce^{3+} fraction for the interior scan may be estimated to be (1.08-0.91)/(1.295-0.91) or 44 %. By a similar calculation, the Ce^{3+} fraction for the edge scan may be estimated to be 72 %. In addition, the disappearance of the high energy shoulders for the edge scan suggests that the strong covalent hybridization between the Ce 4*f* and O 2*p* states is diminished compared to the interior, indicating an enhanced Ce^{3+} content. The ~ 1 eV lower edge onset (binding energy) for the edge scan EELS spectrum is also indicative of enhanced Ce^{3+} character [122], since the characteristic Ce^{3+} low energy pre-edge features (located a few eV lower than the edge maximum) shift the centre of gravity of the edge to lower energy. These pre-edge features due to Ce^{3+} are not resolved due to the resolution limit of TEM-EELS, in contrast to XAS whose higher spectral resolution enables the Ce^{3+} pre-edge features to be distinguished. It is noted that neither La M_4 (~ 853 eV), La M_5 (~ 836 eV) nor Fe *L* (~ 845, 720, 707 eV) edges were detected by additional EELS scans for this powder (or for any of the other powders measured).

Figure 4.52 shows background corrected normalised EELS spectra acquired from the corresponding oxygen *K* edge in the region ~ 530-540 eV for same sample shown previously in Fig. 4.51. The EELS spectrum for this edge strongly depends on the oxidation state (is for XAS also), giving information about the O 2*p* and Ce conduction states. Stoichiometric CeO_2 contains three characteristic peaks spaced 3-4 eV apart with the lowest energy peak at ~ 531 eV. These three peaks, in order of increasing electron energy loss, are related to electronic transitions from O 1*s* core levels to empty O 2*p* hole states hybridized with Ce dominated 4*f*, 5*d*-e_g and 5*d*-t_{2g} levels respectively.

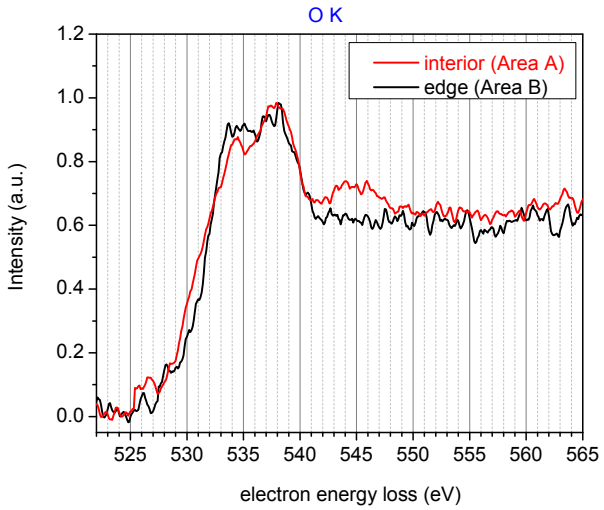

Figure 4.52. Oxygen *K* edge EELS spectra measured for a ferromagnetic CeO_2 nanopowder for both interior and edge areas of the sample acquired from the regions marked in the STEM image shown in Fig. 4.51 previously.

The lowest energy peak for the O *K* edge of CeO_2 is a measure of Ce-O bonding or Ce 4*f* / O 2*p* hybridization, corresponding to the unoccupied Ce 4*f* band; degradation of the Ce $4f^0$ state, caused by reduction of tetravalent Ce to trivalent Ce, manifests itself in a reduction of this lowest peak (~ 531 eV) intensity. The two higher energy peaks are due to higher energy Ce 5*d* / O 2*p* hybridizations. In Fig. 4.52 no peak is resolved at ~ 531 eV for either the interior or edge EELS scans, indicative of Ce^{3+} (rather than Ce^{4+}) associated with occupied localized core-like 4*f* states, which is also likely to be correlated with increased oxygen vacancy content. The spectra are rather similar, with only two peaks resolved at ~ 534 eV and 538 eV corresponding to the O 2*p* / Ce 5*d*-e_g and O 2*p* / Ce 5*d*-t_{2g} hybridized levels respectively.

Figure 4.53 (a) displays an STEM image of the ferromagnetic CeO_2 nanopowder for which an EELS spectrum along the marked line scan was acquired, corresponding to the edge of an agglomeration. Part (b) illustrates the resultant M_5:M_4 intensity ratio across the line scan. The ratio is ~ 1.20 at the start (~ 75 % Ce^{3+}), then falls to about 1.15 (~ 62 % Ce^{3+}) after a distance of 10 nm, before rising again to ~ 1.20 at around 20 nm, and lastly begins to decrease rapidly after a distance of 20 nm.

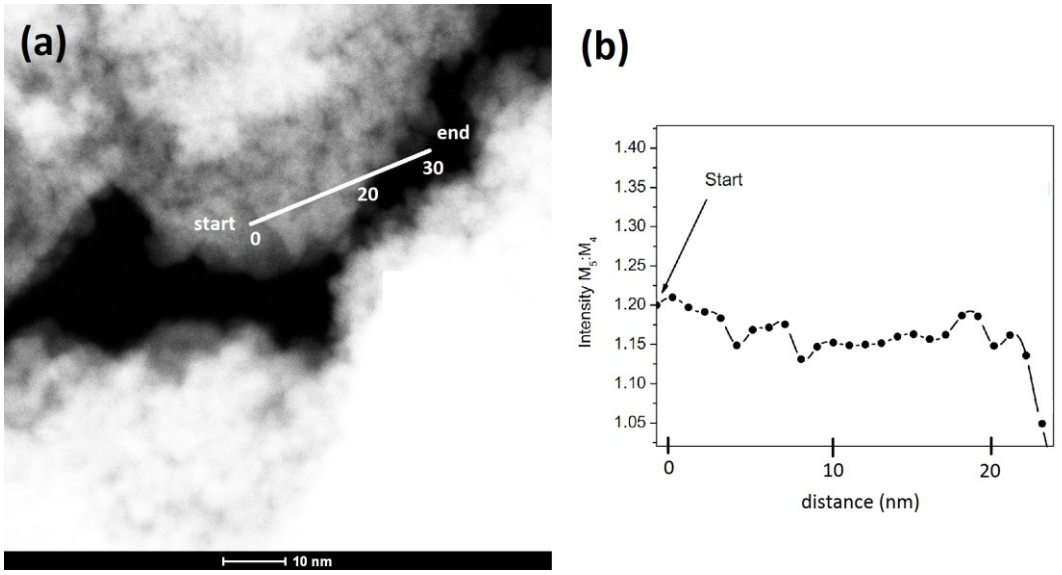

Figure 4.53. (a) STEM image of a ferromagnetic CeO_2 nanopowder with an EELS line scan marked; (b) corresponding M_5:M_4 intensity along the EELS line scan.

The data shown for the EELS line scan in Fig. 4.53 above may be interpreted as follows; firstly, the M_5:M_4 ratios are generally closer to that measured previously for an edge scan (1.19) rather than for the interior scan (1.08), as expected, since the region is generally more edge-like than interior-like. Secondly, since a higher ratio corresponds to enhanced Ce^{3+} character, it is apparent that the nanoparticles contain more Ce^{3+} content at 0 nm (start) and at around 20 nm, and less (by ~ 13 %) in between. From the STEM image, at the start position of

the line scan, the contrast is quite dark indicating that the particle agglomeration is thinner, and hence more edge-like, and hence may contain more Ce^{3+} character, while at the 10 nm position on the line scan the particle agglomeration is thicker (brighter contrast), and hence is more representative of the interior with less Ce^{3+} content. The Ce^{3+} content would then be expected to increase slightly again at around the 20 nm position (which it does), as the beam reaches the extreme edge of the agglomeration and then moves off into free space. The intensity ratio subsequently falls off rapidly after 20 nm since the beam is then probing the vacuum only.

Figure 4.54 (a) compares the background corrected normalised EELS spectra of the Ce $M_{4,5}$ edge for the ferromagnetic (FM) and non-magnetic (NM) CeO_2 nanopowders synthesized using 99% and 99.999% cerium nitrate respectively. For FM, an EELS spectrum from the interior was acquired (specifically area A shown before in Fig. 4.51), and likewise for NM. Whereas the M_5:M_4 ratio for FM is 1.08 (~ 44 % Ce^{3+}), for NM the ratio falls to 1.03 (~ 31 % Ce^{3+}), indicating less Ce^{3+} content for the latter, which may also be inferred from the subtle (~ 0.3 eV) shift in the $M_{4,5}$ peak positions to higher energy for the latter. Figure 4.54 (b) compares the Ce M edge EELS spectra for the same ferromagnetic nanopowder shown in (a) with a CeO_2 micropowder bulk reference (99.999% Sigma). For the micropowder, the M_5:M_4 ratio is inverted (0.93), indicative of enhanced Ce^{4+} content [122]. In this case, normalisation of spectra to the most intense edge of each was performed. For the micropowder, it may be estimated from the above ratio that the Ce^{3+} content is about 7 %. In addition, the small (~ 1 eV) shift in the $M_{4,5}$ peak positions to higher energy for the micropowder compared to the ferromagnetic nanopowder indicates a higher binding energy associated with enhanced Ce^{4+} content.

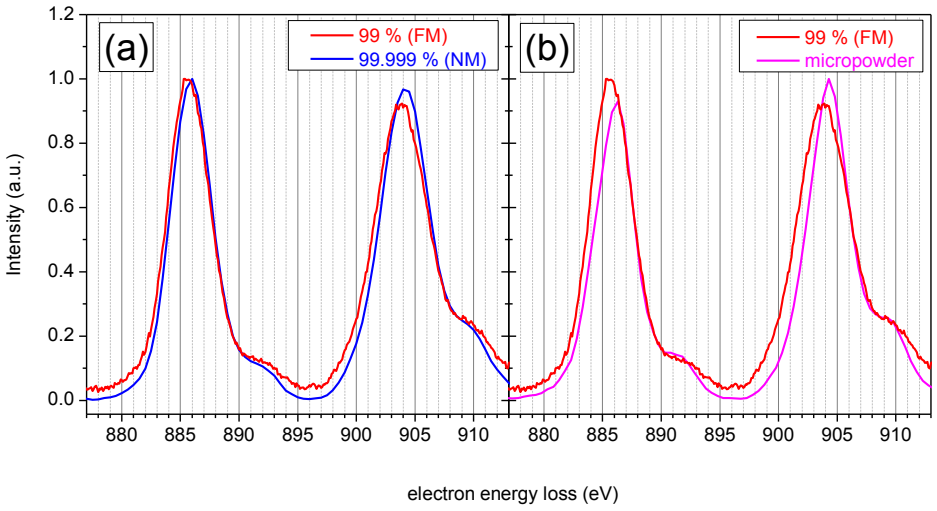

Figure 4.54. Ce $M_{4,5}$ edge EELS spectra for (a) ferromagnetic (FM) and non-magnetic (NM) CeO_2 nanopowders synthesized using 99% and 99.999% cerium nitrate respectively, and (b) for ferromagnetic (FM) nanopowder and CeO_2 micropowder (99.999% Sigma).

Figure 4.55 shows the background subtracted Oxygen *K* edge EELS spectra measured for CeO_2 nanopowders, both ferromagnetic (FM) and non-magnetic (NM), and for the reference micropowder. All spectra were acquired from interior-like (rather than edge-like) regions of the samples. Whereas the spectra for the nanopowders are rather similar, for the micropowder, the main difference compared to the nanopowders is the enhanced intensity of the peak at 531 eV and the shift of the middle peak from ~ 534.5 eV down to 533 eV. Since the lowest energy peak corresponds to the unoccupied Ce 4*f* band, its presence denotes enhanced Ce^{4+} character (hence less Ce^{3+} and corresponding oxygen vacancies) associated with unoccupied extended Ce 4*f* states, in general agreement with the estimation for enhanced Ce^{4+} content for the micropowder compared to the nanopowders from the Ce $M_{4,5}$ edge spectra. The reduction in energy of the middle (533 eV) peak for the micropowder, which is a measure of O 2*p* / 5*d*-e_g hybridization, may be also associated with enhanced Ce^{4+} content, while the "bump" at ~ 543 eV above the main *K* edge measured for all samples may be associated with occupation of the Ce 6*d* band [113].

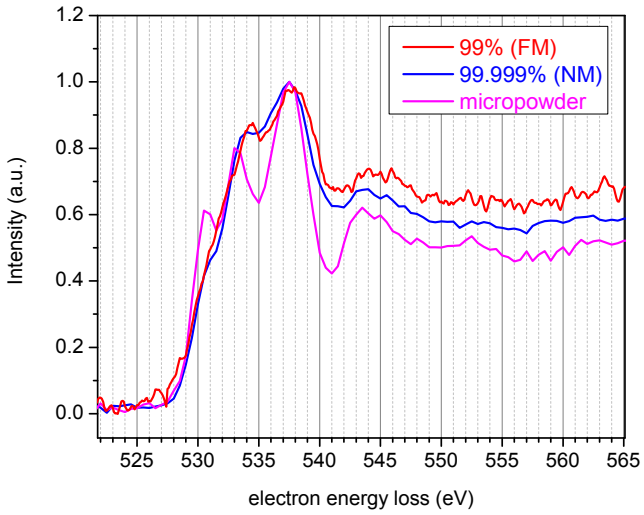

Figure 4.55. Oxygen *K* edge EELS spectra for ferromagnetic (FM) and non-magnetic (NM) CeO_2 nanopowders (cerium nitrate purity used in synthesis given in brackets), plus a reference CeO_2 micropowder (99.999% Sigma).

In summary, the TEM-EELS results reveal that the Ce^{3+} content measured for interior-like regions of the ceria agglomerates was 44 %, 31 % and 7 % for FM, NM and the reference micropowder (Ref) respectively. For edge-like regions of the FM ceria agglomerates, the Ce^{3+} content was as high as 75 %. A comparison is now made with the earlier XAS results, where the Ce^{3+} content was measured to be 35 %, 28 % and 20 % for FM, NM and Ref respectively (rounding to the nearest whole number). Hence the Ce^{3+} content measured for the nanopowders by TEM-EELS is slightly *higher* than that measured by XAS, whereas the Ce^{3+} content of the reference micropowder is actually *lower* when measured by TEM-EELS compared to the result of XAS. It is noted also that XAS can resolve the Ce^{3+} pre-edge features due to its higher

spectral resolution compared to that of TEM-EELS, the latter for which the Ce^{3+} features were not resolved explicitly; instead, the Ce^{3+} contribution in EELS manifests itself in a net shift of the Ce $M_{4,5}$ absorption edge maxima to lower energies, which means that clear differences in the Ce $M_{4,5}$ line peak positions are measured in TEM-EELS, but not in XAS. For the O *K* edge, TEM-EELS revealed significant differences between the spectra for the reference powder compared to the others, namely the presence of the lowest energy O 2*p* – Ce 4*f* hybridization peak for the micropowder *only*, accompanied by a shift of the O 2*p* – Ce 5*d*-e_g peak to lower energy, both of which are indicative of enhanced Ce^{4+} content in the micropowder. For XAS in contrast, the O *K* edge spectra were all rather similar for each powder measured, with the three characteristic O 2*p* – Ce 4*f*, 5*d*-e_g and 5*d*-t_{2g} peaks detected; the only discernible difference between spectra was a slightly enhanced O 2*p* – Ce 5*d*-e_g high energy shoulder for some samples indicative of less Ce^{4+} (more Ce^{3+}) character.

4.3.10 SEM-EDX analysis

Further to the ICP-MS analysis for which results were presented earlier, SEM-EDX analysis was also performed in order to determine the elemental composition of the CeO_2 powders and to also check for ferromagnetic impurities.

Firstly, EDX spectra of two high purity reference micropowders, CeO_2 99.999% and La_2O_3 99.99%, were acquired. Spot scans of each powder were acquired at an excitation energy of 15 keV, the EDX spectra for which are displayed in Figure 4.56 below. As a general rule of thumb, the excitation energy should be at least twice that of the emission energy of the element to be resolved. The characteristic emission energies for the rare earth elements are resolved, in addition to that of oxygen. Carbon was also resolved at a lower energy of 0.27 keV, but is not shown; carbon is a ubiquitous element in the SEM vacuum chamber, formed from the breakdown of hydrocarbons in the electron beam (and as such can make it challenging to quantitatively discern carbon artefacts from carboniferous samples).

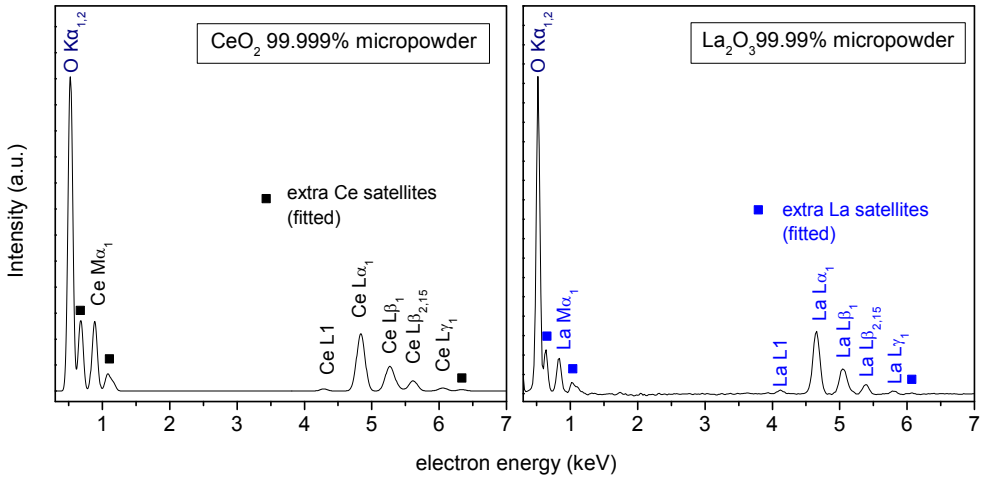

Figure 4.56. SEM-EDX spot spectra, fitted to the detected elemental emission peaks, for high purity CeO_2 and La_2O_3 micropowders.

Whereas the CeO_2 micropowder, whose EDX spectrum was just shown in Fig. 4.56, was measured to be close to stoichiometric, the La_2O_3 micropowder was actually measured to be closer to La_2O_5 in stoichiometry (i.e. oxidised); La_2O_3 is known to readily absorb CO_2 from the air, which may explain its enhanced oxidation versus CeO_2. No traces of any other elements were resolved, both for area scans (which measured smaller relative rare earth element contributions to the net signal) in addition to further spot scans. It is noted that for the detection of ferromagnetic elements, the most intense X-Ray emission energy for iron metal is the

$K\alpha_1$ line at 6.40 keV; at lower energy the less intense secondary emission $L\alpha_{1,2}$ at 0.705 keV may also be used to identify the element. For Co and Ni, the most intense $K\alpha_1$ X-Ray emissions occur at energies of 6.93 keV and 7.47 keV respectively, with less intense $L\alpha_{1,2}$ emissions at the lower energies of 0.77 keV and 0.85 keV respectively.

An SEM-EDX spot spectrum of the CeO_2 99.999% micropowder, undoped and doped with 2 wt % La_2O_3, is shown in Fig. 4.57 (a). The spectra are very similar, except for a small feature at 4.65 keV for the 2 wt % La_2O_3 doped sample, corresponding to the most intense X-Ray emission of La, $L\alpha_1$. Part (b) of the same figure compares EDX spot spectra for a ferromagnetic CeO_2 nanopowder, synthesized using 99% cerium nitrate, with the high purity CeO_2 micropowder. The spectra are also very similar, with a very slightly enhanced shoulder at 4.65 keV for the nanopowder, indicative of La (1.7 wt % quantified), which is present in the 99% cerium nitrate precursor used to synthesize the nanopowder at a level of 1-2 wt % according to the chemical supplier (Sigma Aldrich).

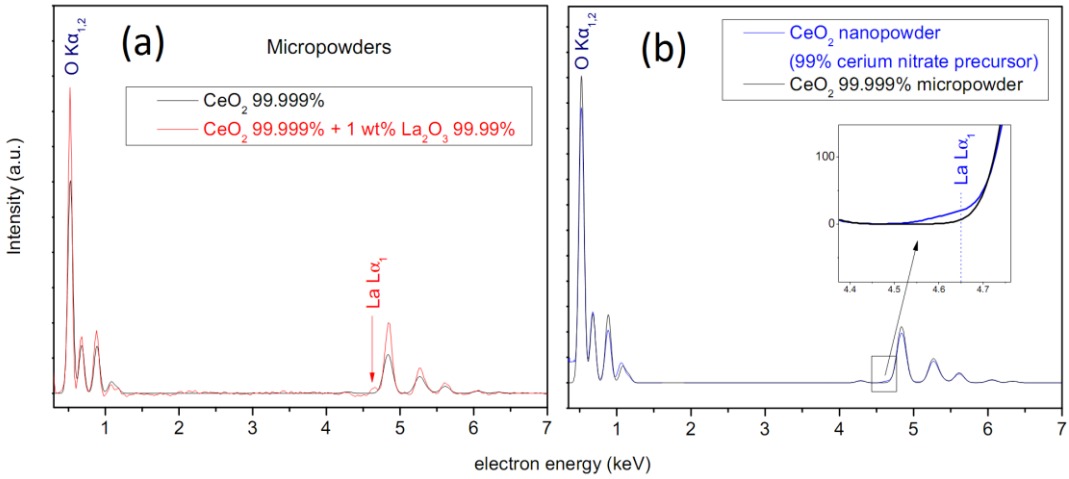

Fig. 4.57. SEM-EDX spot spectra, fitted to the detected elemental emission peaks, for (a) high purity CeO_2 micropowder, undoped and doped with 2 wt % La_2O_3 micropowder, (b) CeO_2 nanopowder with comparison to undoped micropowder. All peaks correspond to cerium unless labelled otherwise.

Two additional spot scans quantified the amount of La in the nanopowder whose EDX spectrum is shown in Fig. 4.57 (b) above at 2.1 wt % and 4.3 wt %, the latter of which is evidently slightly La rich (the initial spot scan gave 1.7 wt %). It is clear by comparing Figs. 4.57 (a) and (b) that the La contribution detected by the EDX spot spectrum for the nanopowder is less than that for the micropowder doped with a similar wt % of La, for which a 7.1 wt % La abundance was quantified for the latter. However, for a large area (400 µm × 400 µm) EDX scan of the micropowder doped with a La, the La abundance was measured to be less than for the spot scan, at 2.3 wt %, which is similar to the quantity intentionally doped with (~ 2 wt %). Therefore it is possible that the spot scan may have acquired data from a region that is

slightly La-rich compared to the rest of the sample, similar to one of the spot scans for the nanopowder. Finally, it is noted that the nanopowder exhibited no trace of ferromagnetic impurities detectable by EDX.

An SEM-EDX spectrum was also acquired for the 99% purity cerium nitrate precursor, in order to determine its composition and to check for ferromagnetic contamination. An SEM image of a large cerium nitrate chunk together with its elemental composition is shown in Figure 4.58 below. Apart from the expected composition of Ce, O, N and C, there are also small quantities (≤ 0.5 wt %) of P, Na, La and S, with no evidence of Fe, Ni or Co. The quantity of La detected (0.3 wt %) is less than that stated by the manufacturer (1-2 wt %). One explanation for this discrepancy may be that a La deficient piece was analysed. The variation in La content of the cerium nitrate precursor may also provide a clue as to why the magnitude of the magnetic signal of the CeO_2 nanopowders synthesized using this precursor are so variable, if the magnetism is related to the quantity of La in the nanopowders.

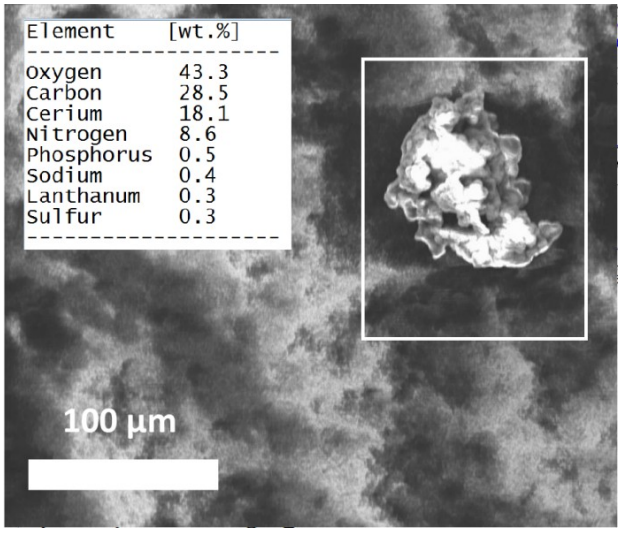

Fig. 4.58. SEM image of $Ce(NO_3)_3.6H_2O$ 99% nominal purity powder. An EDX spectrum was acquired from the rectangular area marked, the quantification results of which are listed.

4.3.11 Ultraviolet-Visible spectroscopy

Ultraviolet-Visible (UV-Vis) spectra were measured at room temperature for both the ferromagnetic CeO_2 powder as well as for a reference CeO_2 micropowder (Sigma Aldrich 99.999% nominal purity) and are shown in Figure 4.59.

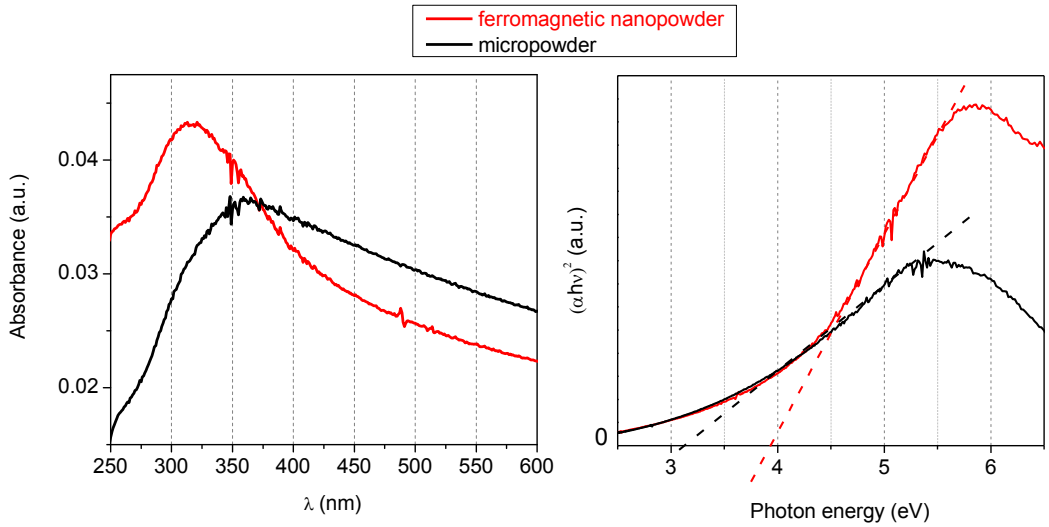

Figure 4.59. UV-Vis spectra measured at 300 K for ferromagnetic CeO_2 nanopowder and a bulk reference CeO_2 micropowder.

The UV-Vis absorption features in ceria may be attributed to charge transfer transitions between O 2*p* and Ce 4*f* bands, which predominate over $4f^1$ to $5d^1$ transitions from any Ce^{3+} species residing within ceria [123]. Both powders exhibited significant absorbance below 400 nm with a maximum absorbance at 362 nm and 317 nm for the reference micropowder and ferromagnetic nanopowder respectively. Hence the nanopowder absorbance is blue-shifted compared to the bulk, indicative of a decrease in particle size and related to the quantum confinement effect in nanomaterials [124], as has also been measured for other CeO_2 nanoparticles [123, 125-127] and nanoparticulate thin films [128]. It is also noted that in contrast to the blue-shifts typically measured for nanoparticles with decreasing particle size, red-shifts have been measured for nanorods and needles [129,130], which may be explained due to a shape dependent electron-phonon coupling effect, which may predominate over the quantum size effect in nanomaterials with high aspect ratios such as nanoneedles and rods. Since CeO_2 is a predominantly a direct bandgap semiconductor, the bandgap may be calculated by using the direct-bandgap absorbance equation, in which $(\alpha h\nu)^2$ is plotted versus photon energy as shown in the right panel of Fig. 4.59 above, with the x-axis intercept of the slope giving the direct

band-gap value. Using this method, the band-gaps for the bulk and ferromagnetic nanopowders are 3.1 eV and 3.9 eV respectively, with an increase in direct energy band-gap E for the nanopowder consistent with its blueshift in absorbance wavelength λ compared to the bulk ($E = hc/\lambda$). The bulk band-gap measured here (3.1 eV) is similar those measured elsewhere by UV-Vis spectroscopy, for example 3.19 eV [129, 131] and 3.20 eV [125]. The nanopowder direct band-gap measured here (3.9 eV) is slightly higher than those measured elsewhere for nanoparticles of similar diameter, for example, 3.61 eV (3-5 nm) [127], 3.60 eV (3.2 nm) [123], 3.68 eV (3.3 nm) [132] and 3.38 eV (4.1 nm) [133]. Although it may be suggested that the effect of increasing Ce^{3+} content in small ceria nanoparticles and the associated increase in defect concentration should be manifested in a decrease of band-gap due to the presence of extra localised defects levels, it appears that the quantum size effect and resultant blue-shift (increase of band-gap) strongly predominates here.

4.3.12 Raman spectroscopy

Room temperature Raman spectra measured for a ferromagnetic nanopowder and a bulk micropowder (99.999% Sigma) are shown in Figure 4.60.

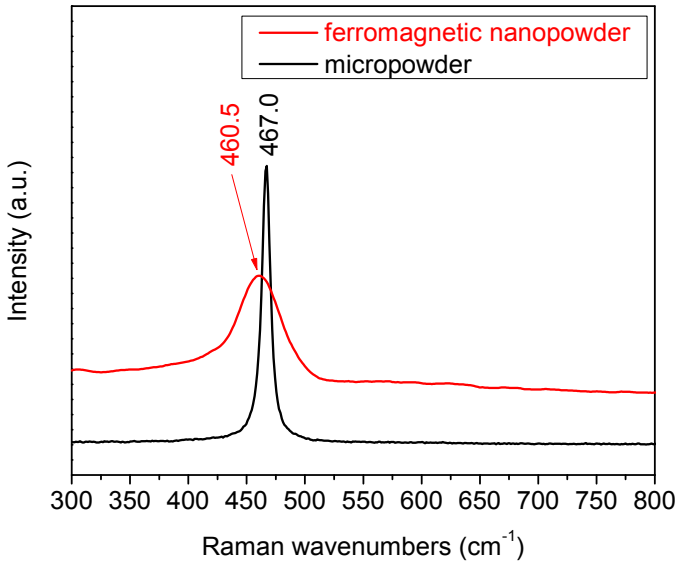

Figure 4.60. Room temperature Raman spectra measured for a ferromagnetic CeO_2 nanopowder and a bulk reference micropowder.

The micropowder displays an intense sharp peak at 467.0 cm^{-1}, whereas the ferromagnetic nanopowder exhibits a broader less intense peak at 460.5 cm^{-1}. These Raman active modes are attributed to an intense first-order symmetrical stretching mode (F_{2g} symmetry) of the Ce-8O vibrational unit and therefore are very sensitive to any disorder in the oxygen sublattice. The broadening (especially on the low energy shoulder) and increase in asymmetry of Raman peak shape for the nanopowder are attributed to the reduction of the phonon lifetime in the nanocrystalline regime [134], and may be also correlated with inhomogeneous strain and defects. Additional weak Raman peaks measured at 600 cm^{-1} and 1177 cm^{-1} for both the micropowder and nanopowder may be attributed to second order Raman modes (primarily A_{1g} symmetry with additional small contributions from E_g and F_{2g}); similar weak second order peaks have been measured for bulk CeO_2 elsewhere [135,136], with values of 464 cm^{-1} [135], 465 cm^{-1} [136] and 466 cm^{-1} [137] for example measured for the most intense first order F_{2g} mode, in comparison with 467.0 cm^{-1} measured for the bulk micropowder here. For other small diameter CeO_2 nanoparticles, values of 458 cm^{-1} (7.3 nm) [36], 460 cm^{-1} (6.1 nm) [135] and 462 cm^{-1} (3-5 nm) [127] for example have been measured for the F_{2g} mode, in comparison to 460.5 cm^{-1} measured here for CeO_2 nanopowder. The Raman line broadening (Γ) of CeO_2 can be described by the dependence of its half width upon the inverse grain size [136], and is given by the relation

$$\Gamma\ (cm^{-1}) = 10 + 124.7/d_g \qquad (4.2)$$

where d_g is the grain size (nm). This yields a grain size of 4.2 nm for the ferromagnetic nanopowder, in agreement with XRD and TEM results, and 1.24 μm for the micropowder, the latter of which was ground in a pestle and mortar prior to the measurement.

4.3.13 Solid dilution of CeO_2

In a further study, for the ferromagnetic CeO_2 nanoparticles synthesized using the 99 % cerium nitrate precursor, a series of experiments were conducted in which these nanopowders were mixed (diluted) with various quantities of other powders, namely Al_2O_3, icing sugar, polystyrene latex beads, and lycopodium. The data has been collated in this separate section. Results for mixing CeO_2 with γ-Al_2O_3 will be presented first.

Al_2O_3 γ-phase nanopowder of particle size ~ 15 nm and of high purity used for polishing (BDH chemicals), was measured by SQUID magnetometry at room temperature and was revealed to be purely diamagnetic ($\chi = -1.4\times10^{-5}$), with no trace of any ferromagnetic-like contribution to the signal. Meanwhile, a paramagnetic-like signal is measured at 4 K in ± 5 T. A thermal magnetization scan from 300 – 4 K in an applied field of 1 T for the Al_2O_3 powder

revealed a paramagnetic-like upturn at low temperature, with net paramagnetism (rather than diamagnetism otherwise) emerging only at < 10 K. Magnetization data measured for the γ-Al_2O_3 nanopowder is displayed in Figure 4.61. ICP-MS analysis of the same powder revealed trace ferromagnetic impurities consisting of 17 ppm of Fe, together with 27 ppm of Co and < 1 ppm of Ni.

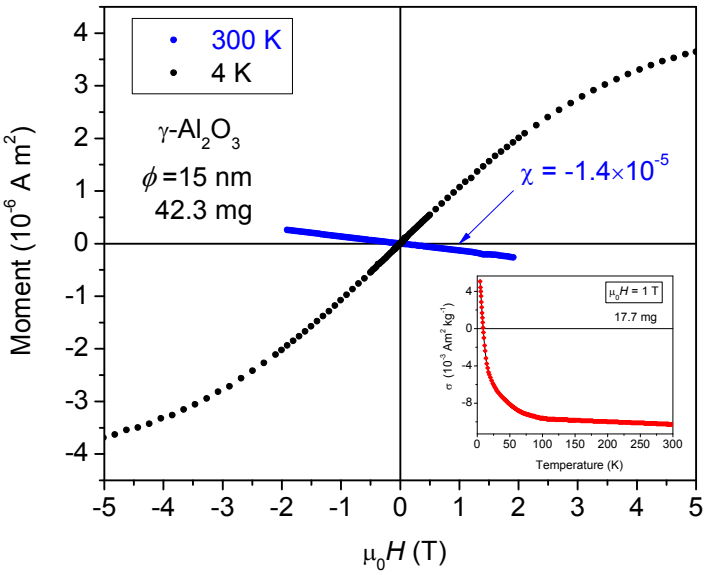

Figure 4.61. Magnetization curves (corrected for diamagnetic gelcap background) measured for γ-Al_2O_3 nanopowder at 300 K and 4 K (42.3 mg sample); the inset shows a thermal magnetization scan measured in 1 T (17.7 mg sample).

Various quantities of γ-Al_2O_3 nanopowder were then mixed in a pestle and mortar with the ferromagnetic CeO_2 nanopowder (synthesized from 99 % cerium nitrate) and the magnetization re-measured. Magnetization data are shown in Figure 4.62. The ferromagnetic-like signal due to CeO_2 is reduced upon mixing with Al_2O_3, with a noticeable change in the shape of the magnetization curve upon mixing with 4 mg of Al_2O_3, as shown in part (a) of the figure. The change in shape of the magnetization curve near the origin indicates that the demagnetizing factor $\mathcal{N}$ has changed. The decay in the magnetic signal of CeO_2 with increasing quantities of Al_2O_3 mixing follows an exponential-like trend, as shown in part (b) of the figure. The results for two separate mixing batches are displayed in order to show that the trend is reproducible.

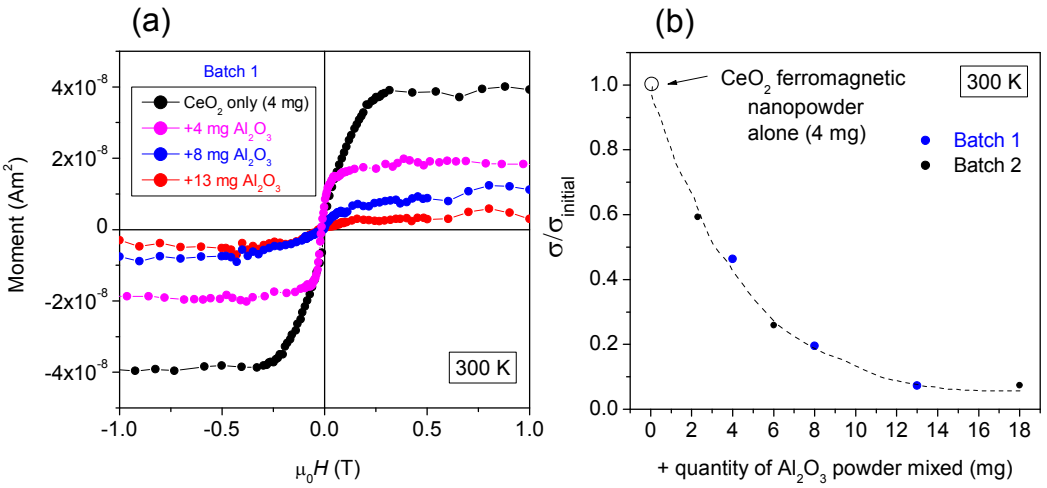

Figure 4.62. (a) Room temperature magnetization curves (corrected for diamagnetic background) for ferromagnetic CeO_2 nanoparticles (synthesized using 99 % cerium nitrate) mixed with γ-Al_2O_3 nanopowder; results for batch 1 are shown (b) Normalized mass magnetization of CeO_2/Al_2O_3 mixtures vs. quantity of Al_2O_3 nanopowder for both batches measured.

It is noted that the thermal magnetization data measured in 1 T from 300 – 4 K for CeO_2 well-diluted with 18 mg Al_2O_3 virtually superposed the data measured for a similar scan for 17.7 mg Al_2O_3 alone shown previously in the inset of Fig. 4.61, while measurements conducted at 4 K in a field of ± 5 T for the CeO_2 well-diluted with 18 mg Al_2O_3 revealed a very similar paramagnetic-like-signal to that measured for Al_2O_3 alone also shown previously in Fig. 4.61; hence it may be inferred that the low temperature magnetic behaviour of the mixture may be attributed to Al_2O_3 rather than to CeO_2.

TEM images for some of the 4 mg batch of CeO_2 nanopowder before and after intermediate dilution with 8 mg of γ-Al_2O_3 are shown in Figure 4.63. CeO_2 nanoparticles (~ 4 nm diameter) may be readily distinguished from γ-Al_2O_3 nanoparticles (~ 15 nm diameter). The effect of mixing CeO_2 with γ-Al_2O_3 is to break up and disperse the larger clumps of CeO_2 nanoparticles. Figure 4.64 displays some higher resolution TEM images of the mixture.

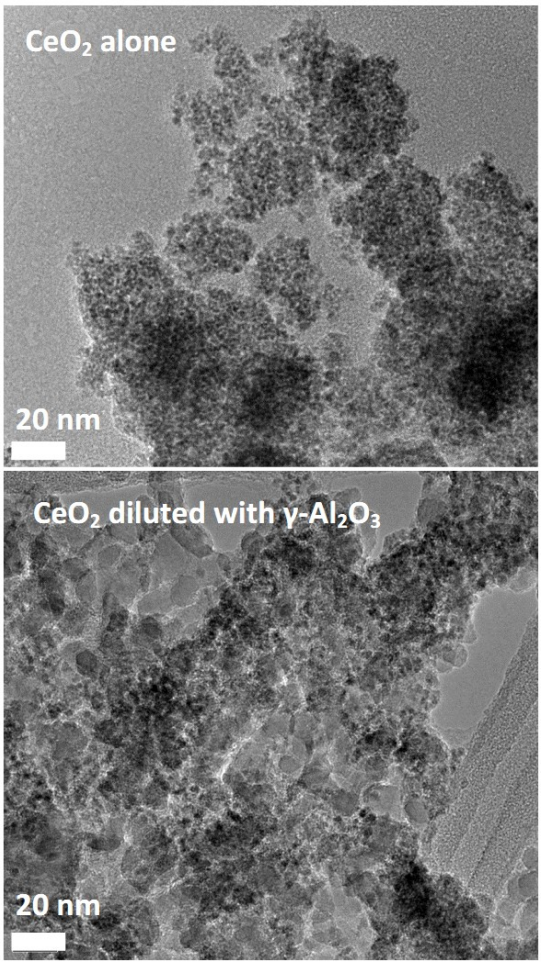

Figure 4.63. TEM images of ferromagnetic CeO_2 nanoparticles (4 mg batch) before and after dilution with 8 mg of γ-Al_2O_3 nanopowder.

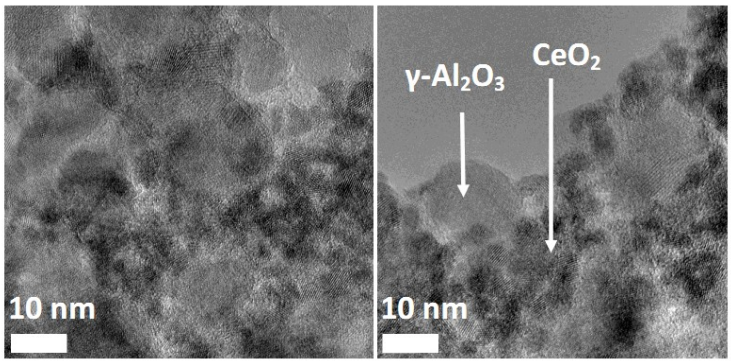

Figure 4.64. Higher resolution TEM images of ferromagnetic CeO_2 nanoparticles (4 mg batch) after dilution with 8 mg of γ-Al_2O_3 nanopowder.

For the second mixing experiment, icing sugar microparticles (Silver Spoon brand, UK) were first measured alone by SQUID magnetometry at room temperature, and were revealed to be purely diamagnetic ($\chi = -1.2\times10^{-5}$) with no trace of any ferromagnetic-like signal.

Various quantities of sugar were then mixed in a pestle and mortar with the ferromagnetic CeO_2 nanopowder (synthesized from 99 % cerium nitrate) and the magnetization re-measured. Magnetization data are shown in Figure 4.65. Similar to the experiment where Al_2O_3 was mixed with CeO_2, the magnetic moment decreases for mixtures containing successively larger quantities of sugar, however in contrast to the Al_2O_3/CeO_2 mixtures, the relative decrease in the size of the magnetic moment is not as large here, nor is the reproducibility of the results between different batches quite as good. When the CeO_2/sugar mixtures are dissolved in water (in order to dissolve the sugar) and the CeO_2 nanopowder recovered, the magnetic moment is still ~ 22±8% of its initial magnitude before mixing, despite the fact that only 0.4 – 0.5 mg of CeO_2 is recovered (by either vacuum filtration or centrifuging). However, since the mass of CeO_2 recovered is only ~ 10 %, the corresponding magnetic moment for 4 mg would be 220±80% of its initial value, i.e. around 2 times *greater* on average. It seems to be the case that the CeO_2 powder extracted from dissolving the CeO_2/sugar mixture has become magnetically concentrated.

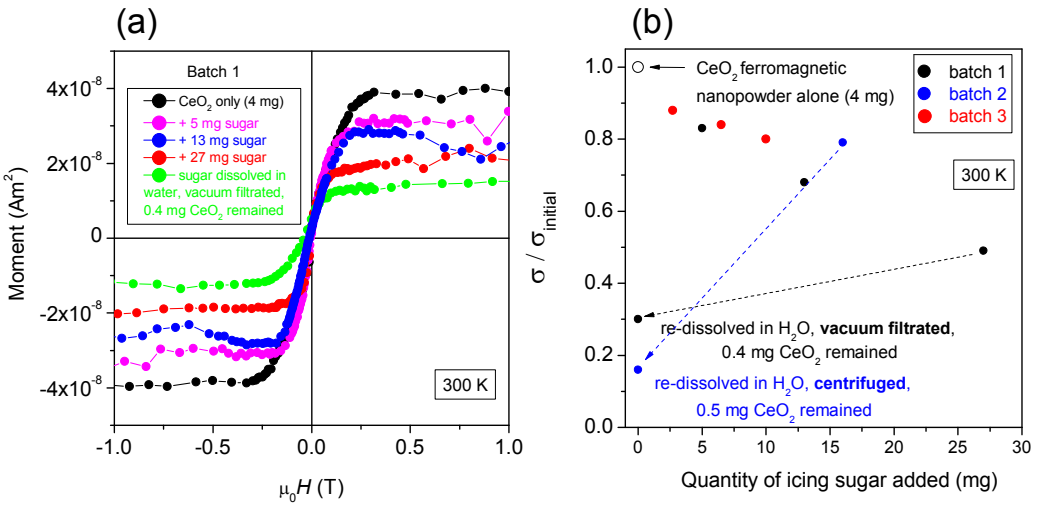

Figure 4.65. (a) Room temperature magnetization curves (corrected for diamagnetic background) for ferromagnetic CeO_2 nanoparticles (synthesized using 99 % cerium nitrate) mixed with icing sugar; results for batch 1 are shown; (b) Normalized mass magnetization of CeO_2/sugar mixtures vs. quantity of sugar for each batch measured.

Some representative SEM images of the magnetic CeO_2 nanopowder diluted with icing sugar (mass ratio of CeO_2 to sugar is ~1:2) are shown in Figure 4.66. The icing sugar powder is composed of large microcrystals of order 10 μm size or greater, while clumps of CeO_2 nanopowder mostly of size ≤ 1 μm appear to partially cover or adhere to the surface or the larger sugar microcystals. The background of each image is representative of the morphology of the CeO_2 clumps on their own (denoted by white arrows).

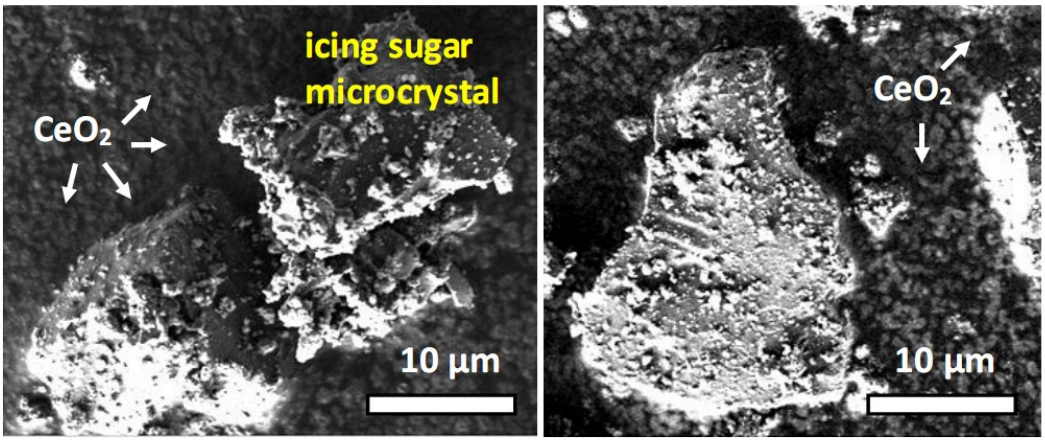

Figure 4.66. SEM images of ferromagnetic CeO_2 nanopowder diluted with icing sugar in the mass ratio 1:2; the large sugar microcystals are partially coated with clumps of CeO_2 nanopowder mostly of size ≤ 1 µm.

For the third mixing experiment, polystyrene-latex beads were mixed with the ferromagnetic CeO_2 nanopowder. Polystyrene is a long chain hydrocarbon wherein alternating carbon centers are attached to phenyl groups (aromatic ring benzene), with the chemical formula $(C_8H_8)_n$. Polystyrene microparticles are negative charge-stabilized colloidal particles produced by polymerization of styrene under conditions that induce spontaneous coalescent bead formation, termed latex beads when dispersed in an aqueous suspension, and are used in a variety of applications such as contrast agents for fluorescent imaging, as particles for flow tracking, or as biological carriers. Latex beads typically contain ~ 69 % water, ~ 30 % polymer, with the remainder composed of surfactant and inorganic salts. For this study, the polystyrene-latex beads were extracted in dry powder form from aqueous solution by drying in a drying cabinet for several days at 50 °C. Successively larger masses of the polystyrene-latex bead powder were then mixed with ferromagnetic CeO_2 nanopowders and the effect of mixing on the room temperature magnetic signal was measured, as shown in Figure 4.67. The figure shows the effect on the net magnetic signal of mixing CeO_2 with two different batches of dried polystyrene-latex beads of different particle diameter purchased from two different suppliers.

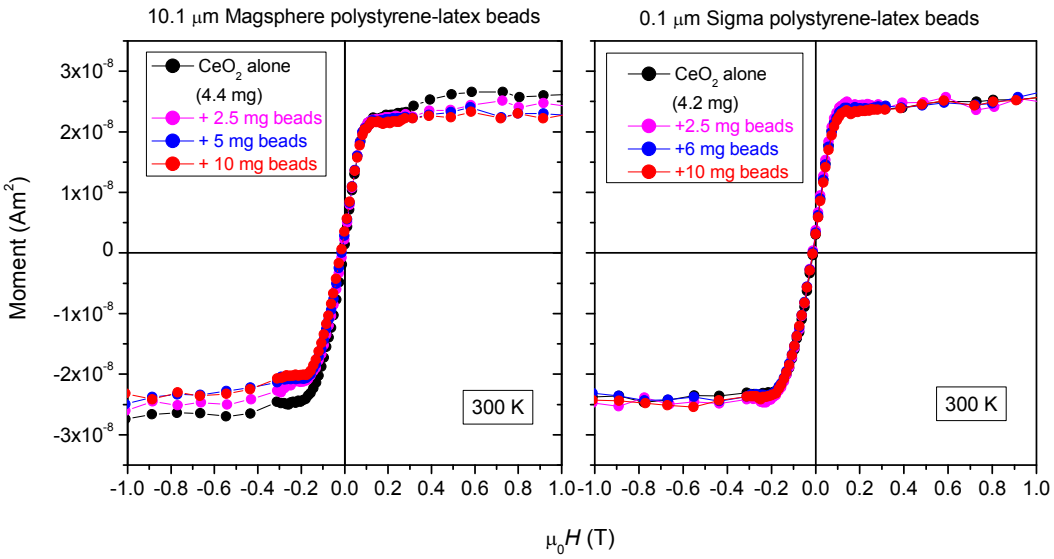

Figure 4.67. Room temperature magnetization curves (corrected for diamagnetic background) for ferromagnetic CeO_2 nanoparticles (synthesized using 99 % cerium nitrate) mixed with polystyrene-latex beads of (left) 10.1 μm size (supplier: Magsphere) and (right) 0.1 μm size (Sigma).

It is apparent that mixing CeO_2 with either batch of polystyrene-latex beads has little effect on the size of the magnetic signal. As a further test, 20 mg of beads were mixed with ~ 4 mg of CeO_2 ferromagnetic nanopowder, and the magnetic signal virtually superposes that measured for the 4 mg CeO_2 + 10 mg beads mixtures shown in Fig. 4.67 above.

Both batches of beads when measured alone at 300 K were diamagnetic, with $\chi = -9 \times 10^{-6}$; while the Sigma 0.1 μm beads contained an additional very weak trace of a ferromagnetic-like signal (at most 1×10^{-9} Am^2 for 30 mg of beads, but equivalent to the noise level), a similar mass of the Magsphere 10.1 μm beads had an additional ferromagnetic-like contribution whose magnitude was about ten times greater than that measured for the Sigma 0.1 μm beads (i.e. 1×10^{-8} Am^2), and could be due to trace ferromagnetic impurities.

SEM analyses of the mixtures of beads and CeO_2 nanopowders (4 mg CeO_2 + 10 mg beads mixtures), which are summarised in Figure 4.68 on the following page, revealed that the majority of the surfaces of many of the 10.1 μm beads were coated with clumps of CeO_2 nanoparticles > 100 nm in size, while the 0.1 μm beads were completely enveloped by the CeO_2 nanoparticles.

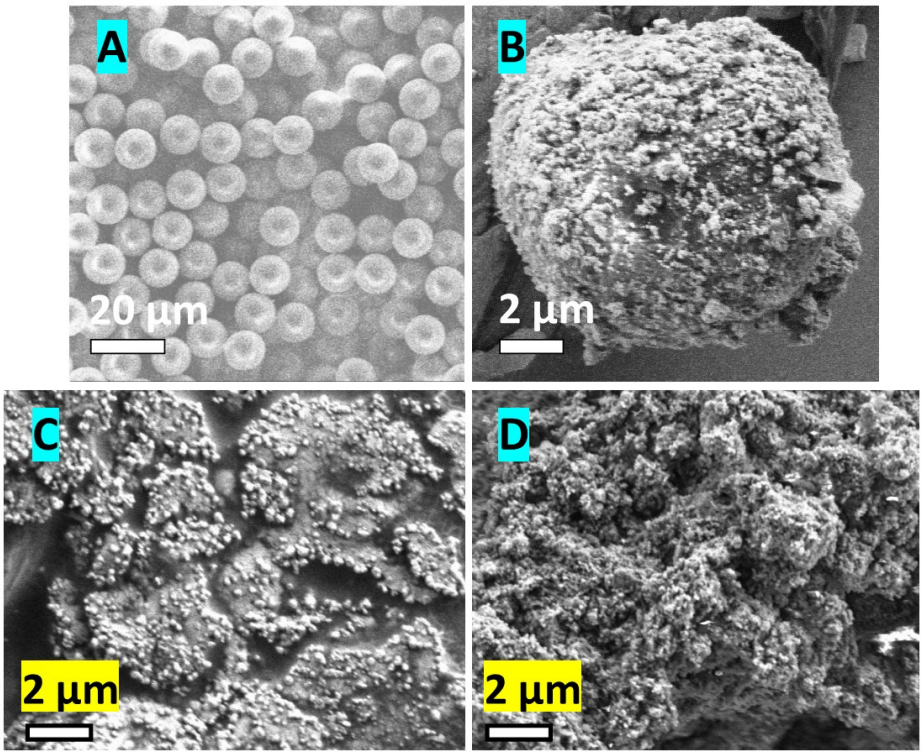

Figure 4.68. SEM images for 4 mg of ferromagnetic CeO_2 nanoparticles (synthesized using 99 % cerium nitrate) mixed with 10 mg of polystyrene-latex beads; (a) 10.1 µm beads alone (Magsphere), (b) A single 10.1 µm bead coated with CeO_2 nanoparticles (c) 0.1 µm beads alone (Sigma), (d) 0.1 µm beads enveloped with CeO_2 nanoparticles.

In the fourth and final mixing experiment, lycopodium powder from two suppliers (Sigma and Illusion Craft, the latter of which is marketed as "Dragon's Breath", hereafter denoted DB) was mixed with the ferromagnetic CeO_2 nanopowder. Lycopodium powder is a natural product composed of ~ 30 µm diameter unicellular spores from the common clubmoss (fern) family *Lycopodiaceae*, from which the dried spores were much used in the early days of flash photography, due to their tendency to readily ignite when in dust form due to their high fat content, and are also commonly used to demonstrate Brownian motion since the spores disperse well on the surface of water. Upon room temperature measurement of the magnetic properties of the lycopodium powders alone however, they were found to possess a small ferromagnetic-like signal after correction of the diamagnetic background signal, as shown in Figure 4.69, for which the ferromagnetic-like signal was found to scale linearly with the mass. Hysteresis is also clearly resolved. XRD showed that the dried spores were amorphous. In order to determine the ferromagnetic impurities present in each powder, they were ignited to 900 °C in air in order to burn off the organic matter and the remaining ash was recovered; typically about 1 % of the initial mass was recovered after this step. From XRD measurements the main phase detected after ignition was potassium phosphate, $K_3P_3O_9$. ICP-MS analysis of the ash was then performed, which revealed that 7200 ppm of iron metal was present in the Sigma lycopodium ash, and 4060 ppm of iron metal in the DB lycopodium ash, with the

quantities of nickel and cobalt < 10 ppm in both. Hence the quantity of iron in the powders before ignition may be estimated to be ~ 72 ppm and 41 ppm for Sigma and DB respectively (i.e. divide by 100). In terms of magnetite impurities for example, the maximum impurity levels would be 100 ppm and 57 ppm for the Sigma and DB lycopodium powders respectively. From Figure 4.69, the magnitudes of the magnetic signals for Sigma and DB lycopodium may be accounted for by 20 ppm and 8 pm of magnetite respectively; since these values are less than the measured iron or magnetite contents of the lycopodium powder by ICP-MS, it is concluded that the most likely source of the hysteretic ferromagnetic signal is magnetite.

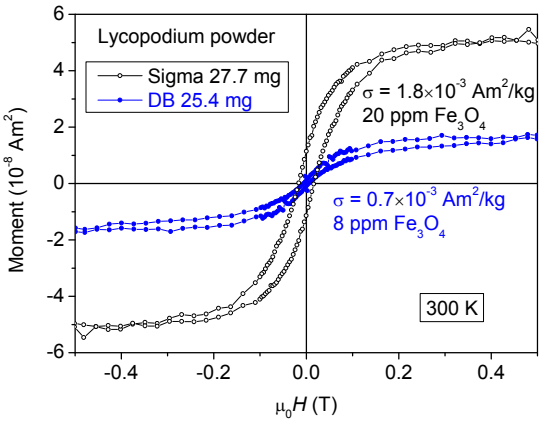

Figure 4.69. Room temperature magnetization curves (corrected for diamagnetic background) for lycopodium powder purchased from two different suppliers. The quantity of magnetite (Fe_3O_4) impurities required to re-produce the magnetic signals are displayed.

After characterization of the magnetic properties of the lycopodium powder alone and establishing that they most likely contain magnetite impurities, they were then mixed with the ferromagnetic CeO_2 nanopowder (synthesized using 99 % cerium nitrate). Results for the CeO_2/Sigma lycopodium mixture are presented first. Magnetization data for the CeO_2/Sigma lycopodium mixture is displayed in Figure 4.70 on the next page.

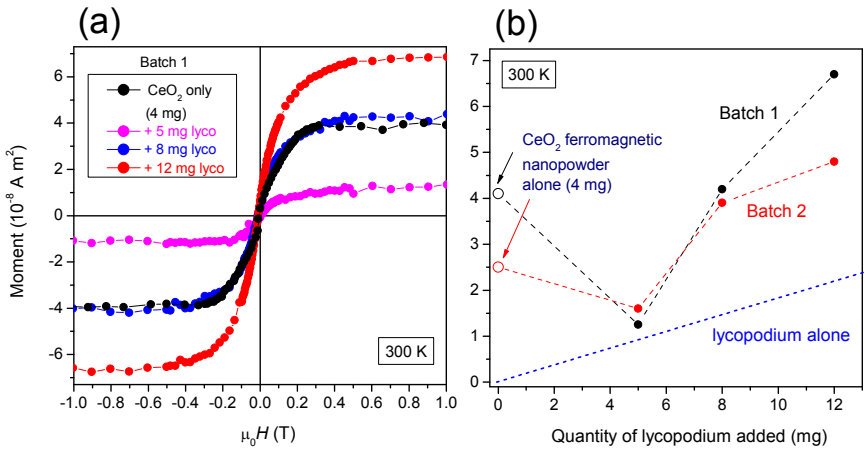

Figure 4.70. (a) Room temperature magnetization curves (corrected for diamagnetic background) for ferromagnetic CeO_2 nanoparticles (synthesized using 99 % cerium nitrate) mixed with Sigma lycopodium powder; results for batch 1 are shown; (b) Total magnetic moment for CeO_2/lycopodium mixtures vs. quantity of lycopodium for each batch measured. Note that the initial moment for each batch (CeO_2 alone) was different. The contribution of lycopodium powder alone to the magnetic signal is also marked (dashed blue line).

It is evident from Fig. 4.70 that the effect of mixing lycopodium with CeO_2 on the magnetism of the mixture is more complicated than for the previous dilution experiments of CeO_2 with non-magnetic powders, since the net magnetic signal for lycopodium/CeO_2 initially decreases but subsequently *increases* upon further dilution with lycopodium.

In order to try to separate the contribution of lycopodium to the magnetic signal from that due to CeO_2, the signal due to lycopodium was first subtracted and the resultant magnetic signal was normalized to that of CeO_2 alone measured initially for each batch; the results are displayed in Figure 4.71. After an initial decrease in the magnetic signal of CeO_2 upon mixing with lycopodium, the signal subsequently increases, and eventually upon further dilution with lycopodium the magnitude of the initial signal due to CeO_2 alone is actually recovered, or even slightly exceeded.

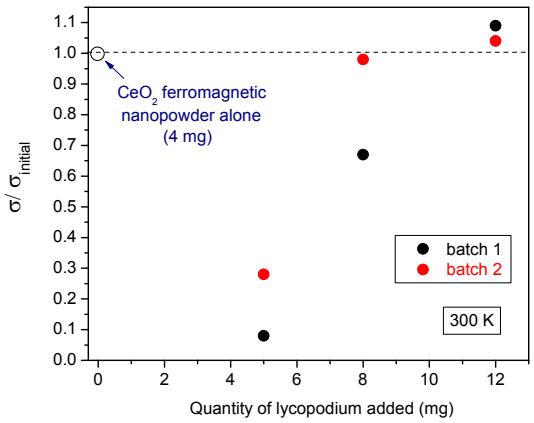

Figure 4.71. Normalized magnetic signal (to that of CeO_2 alone initially measured) for each batch of CeO_2/Sigma lycopodium mixtures vs. quantity of lycopodium mixed. The magnetic contribution due to lycopodium alone was subtracted before normalization.

In terms of the morphology of the CeO_2/lycopodium mixtures, Figure 4.72 below displays SEM images of the lycopodium powder (Sigma) before and after mixing with CeO_2 nanopowder; the effect of mixing is to coat the majority of the lycopodium spores (some remained uncoated) with CeO_2 nanoparticles. It is noted that for lycopodium powders before and after mixing with CeO_2, the spore sizes measured by SEM and optical microscopy were similar, hence mixing does not seem to break up the spores or to reduce their characteristic size.

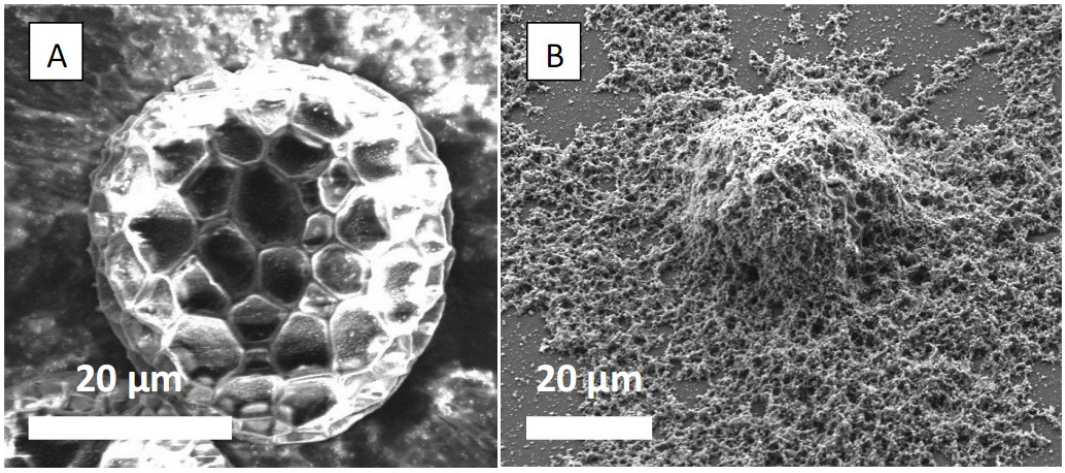

Figure 4.72. SEM images of (a) A bare (uncoated) lycopodium (Sigma) spore (b) A spore covered in ferromagnetic CeO_2 nanoparticles (4 mg CeO_2 + 12 mg lycopodium mixture); the image is tilted at 52° in order to show more perspective.

Magnetization data for the second lycopodium powder, "Dragon's Breath" (DB), mixed with the ferromagnetic CeO_2 nanopowder is shown in Figure 4.73. The total magnetic signal reaches a minimum when 5 mg of DB lycopodium is mixed with CeO_2, after which the signal increases upon further mixing with larger quantities of lycopodium. The size of the ferromagnetic signal due to the DB lycopodium powder alone scales with its mass, similar to the trend previously measured for the Sigma lycopodium powder alone, although the signal is smaller in magnitude than for the Sigma lycopodium, consistent with the lower ferromagnetic impurity content measured by ICP-MS for the DB lycopodium.

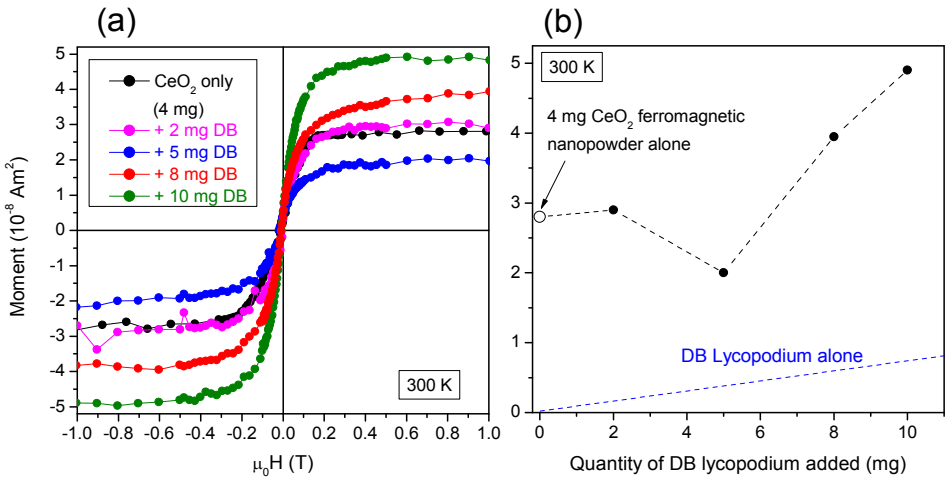

Figure 4.73. (a) Room temperature magnetization curves (corrected for diamagnetic background) for ferromagnetic CeO_2 nanoparticles (synthesized using 99 % cerium nitrate) mixed with "Dragon's Breath" (DB) lycopodium powder; (b) Total magnetic moment for CeO_2/lycopodium mixtures vs. quantity of lycopodium for each batch measured. The contribution of lycopodium powder alone to the magnetic signal is also marked (dashed blue line).

Figure 4.74 displays similar data to that shown previously in Fig. 4.73 (b) except that the lycopodium contribution has been subtracted and the signal normalized to that initially measured for CeO_2 alone prior to mixing with lycopodium. The normalized magnetic signal decreases to a minimum of ~ 60 % for 5 mg of DB lycopodium mixing, after which the signal increases, and actually starts to exceed the magnitude of CeO_2 alone when ~ 7-8 mg or more of lycopodium has been mixed. The trend is roughly similar to that measured previously for the CeO_2/Sigma lycopodium mixtures, except for the fact that both the minimum and maximum values of the normalized magnetic signal for the same mass of lycopodium mixed are larger for the CeO_2/DB lycopodium mixture than for the CeO_2/Sigma lycopodium mixture. SEM analysis of the DB lycopodium alone and mixed with CeO_2 nanoparticles revealed very similar morphologies to those measured previously for the Sigma lycopodium and its mixtures with CeO_2 (Fig. 4.72).

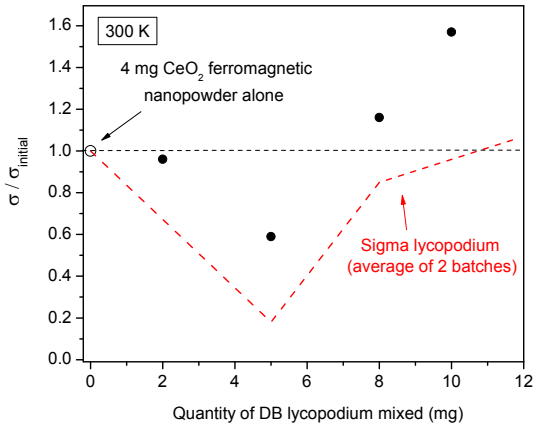

Figure 4.74. Normalized magnetic signal (to that initially measured for CeO_2 alone) for CeO_2/DB lycopodium mixtures vs. quantity of lycopodium mixed (black dots). The magnetic contribution due to the DB lycopodium alone was subtracted before normalization. The dashed red line shows the corresponding averaged data measured for the CeO_2/Sigma lycopodium mixtures (2 batches) shown previously in Fig. 4.71.

In summary, dilution of the ferromagnetic CeO_2 nanopowder with other non-magnetic powders such as γ-Al_2O_3 nanopowder and icing sugar microparticles produced a net reduction in the magnetic signal, the reduction being much more pronounced for the former. It is proposed that the reduction in the magnitude of the magnetic signal may be related to the breaking up the CeO_2 into clumps < 100 nm in size upon dilution, especially so for dilution with γ-Al_2O_3, and that the magnetism is associated with the collective coherent orbits of CeO_2 agglomerates. This theory is elucidated in Chapter 6 (Discussion) and an introductory mathematical basis given in Chapter 7 (Appendix A.2), in which a length of order 100 nm is calculated to be the characteristic length scale for the magnetic effect to appear (with clumps smaller than this size are proposed to be much less magnetic). For dilution of ferromagnetic CeO_2 nanopowder with polystyrene-latex beads meanwhile, the net magnetic signal is hardly diminished upon dilution, which may be due to the fact that the CeO_2 nanoparticle clumps are *not* broken up into clumps < 100 nm in size. Finally, for dilution of ferromagnetic CeO_2 nanopowder with lycopodium powder, the net magnetic signal initially decreases but subsequently increases upon dilution with increasing quantities of lycopodium, for which the latter effect is most probably due to the ferromagnetic contribution from the lycopodium powder itself. These results are preliminary, and warrant further investigation and experimentation in order to try to develop an understanding of the underlying magnetic phenomena.

4.4. Summary

Reproducible room temperature ferromagnetic-like signals are measured for 4 mg batches of polycrystalline CeO_{2-x} nanoparticles of ~ 4 nm diameter synthesized by homogeneous precipitation using a 99% purity (10 mM) cerium nitrate cerium precursor. The magnetism is relatively weak (M_s typically $\leq$ 100 A m^{-1}), virtually anhysteretic and temperature independent from 300 – 4 K. It is shown that ferromagnetic impurities alone cannot account for the magnitude of the ferromagnetic-like signals. No RTFM is measured for nanoparticles synthesized by homogeneous precipitation using a higher purity 99.999% cerium nitrate precursor (also 10 mM concentration), but by doping these nanoparticles with small quantities of non-magnetic dopants (~ 1 wt %), a RTFM signal is once again measured. A similar effect is measured for nanoporous films synthesized by electrodeposition. It is hence proposed that the magnetism may be related to structural defects, primarily Ce^{3+} and associated charge compensating oxygen vacancies, induced by intentionally doping pure nanometric ceria with non-magnetic dopants; the main impurity in the 99% purity cerium nitrate precursor is ~ 1-2 wt % La. It is shown from analysis of the magnetization curves that only a small fraction of the volume of the magnetic nanopowders are ferromagnetically ordered, at most 0.1 %, consistent with inhomogeneous defect-related magnetism associated with grain boundaries or surfaces for example. The Ce^{3+} content in the nanopowders is small, < 1 % as deduced from SQUID magnetometery, but much larger (of order 30 % or more) as measured by XAS and TEM-EELS; an explanation for this discrepancy may be that the Ce^{3+} is mainly delocalized at the bottom of the Ce 4*f* band, although XMCD of the ferromagnetic nanopowder CeO_2 at 2 K suggests that Ce^{3+} is actually carrying ~ $1\mu_B/Ce^{3+}$, consistent with a localised moment on a spin 1/2 atom with g = 2.

One possible origin of d^0 magnetism in nanometric ceria is the proposed existence of a defect impurity band which can become spin-split and result in high temperature Stoner ferromagnetism when the density of states at the Fermi level is sufficiently high. Another possible explanation is Giant Orbital Paramagnetism due to surface currents associated with a 2-D electron gas at the surface of small (< 10 nm) spherical particles. A related third possible explanation is that of collective magnetism, in which the magnetism is proposed to be due to giant orbital moments which form in coherent domains of clumps ($\geq$ 100 nm) of nanoparticles, with a theoretical basis in the resonant fluctuations of the electromagnetic field (zero-point energy). The last explanation is supported by magnetization and preliminary electron microscopy measurements for CeO_2 nanoparticles dispersed in either γ-Al_2O_3 nanopowder, icing sugar or latex beads, in which the magnetic signal is rapidly diminished when the clumps of CeO_2 appear to be broken up into < 100 nm sized aggregates.

4.5. References

[1] D. D. Koelling, A. M. Boring, and J. H. Wood, Solid State Communications **47**, 227 (1983).

[2] L. Eyring, *Handbook on the Physics and Chemistry of Rare Earths,* Vol. 3, Chapter 27 (North-Holland, Amsterdam 1979).

[3] R. Gillen, S. J. Clark, and J. Robertson, Physical Review B **87**, 125116 (2013).

[4] T. X. T. Sayle, S. C. Parker, and C. R. A. Catlow, Journal of the Chemical Society-Chemical Communications **14**, 977 (1992).

[5] T. X. T. Sayle, S. C. Parker, and C. R. A. Catlow, Surface Science **316**, 329 (1994).

[6] F. Esch, S. Fabris, L. Zhou, T. Montini, C. Africh, P. Fornasiero, G. Comelli, and R. Rosei, Science **309**, 752 (2005).

[7] N. Skorodumova, R. Ahuja, S. Simak, I. Abrikosov, B. Johansson, and B. Lundqvist, Physical Review B **64**, 115108 (2001).

[8] N. V. Skorodumova, S. I. Simak, B. I. Lundqvist, I. A. Abrikosov, and B. Johansson, Physical Review Letters **89**, 166601 (2002).

[9] S. Tsunekawa, K. Ishikawa, Z. Q. Li, Y. Kawazoe, and A. Kasuya, Physical Review Letters **85**, 3440 (2000).

[10] X. D. Zhou and W. Huebner, Applied Physics Letters **79**, 3512 (2001).

[11] F. Zhang, S.-W. Chan, J. E. Spanier, E. Apak, Q. Jin, R. D. Robinson, and I. P. Herman, Applied Physics Letters **80**, 127 (2002).

[12] S. Deshpande, S. Patil, S. Kuchibhatla, and S. Seal, Applied Physics Letters **87**, 133113 (2005).

[13] P. Wachter, *Valence Instabilities,* p. 145 (North-Holland, Amsterdam, 1982).

[14] A. Sundaresan, R. Bhargavi, N. Rangarajan, U. Siddesh, and C. Rao, Physical Review B **74**, 161306 (2006).

[15] A. Sundaresan and C. N. R. Rao, Nano Today **4**, 96 (2009).

[16] Q. Y. Wen, H. W. Zhang, Y. Q. Song, Q. H. Yang, H. Zhu, and J. Q. Xiao, J Phys Condens Matter **19**, 246205 (2007).

[17] G.-R. Li, D.-L. Qu, X.-L. Yu, and Y.-X. Tong, Langmuir **24**, 4254 (2008).

[18] Y. Liu, Z. Lockman, A. Aziz, and J. MacManus-Driscoll, Journal of Physics: Condensed Matter **20**, 165201 (2008).

[19] K. Ackland, L. M. A. Monzon, M. Venkatesan, and J. M. D. Coey, IEEE Transactions on Magnetics **47**, 3509 (2011).

[20] C. M. Ho, J. C. Yu, T. Kwong, A. C. Mak, and S. Y. Lai, Chemistry of Materials **17**, 4514 (2005).

[21] H. X. Mai, L. D. Sun, Y. W. Zhang, R. Si, W. Feng, H. P. Zhang, H. C. Liu, and C. H. Yan, Journal of Physical Chemistry B **109**, 24380 (2005).

[22] M. Li, S. Ge, Y. Zuo, L. Zhang, X. Zhou, and S. Yan, IEEE Transactions on Magnetics **44**, 2708 (2008).

[23] X. Chen, G. Li, Y. Su, X. Qiu, L. Li, and Z. Zou, Nanotechnology **20**, 115606 (2009).

[24] M. Radovic, Z. Dohcevic-Mitrovic, N. Paunovic, M. Scepanovic, B. Matovic, and Z. V. Popovic, Acta Physica Polonica A **116**, 84 (2009).

[25] Z. D. Dohčević-Mitrović, N. Paunović, M. Radović, Z. V. Popović, B. Matović, B. Cekić, and V. Ivanovski, Applied Physics Letters **96**, 203104 (2010).

[26] N. Paunovic, Z. Dohcevic-Mitrovic, R. Scurtu, S. Askrabic, M. Prekajski, B. Matovic, and Z. V. Popovic, Nanoscale **4**, 5469 (2012).

[27] M. Sakara, S. Arumugam, S. Tripathy, and S. Balakumar, AIP Conference Proceedings **1447**, 355 (2012).

[28] M. S. Seehra, S. Suri, and V. Singh, Journal of Applied Physics **111**, 07B516 (2012).

[29] M. Li, S. Ge, W. Qiao, L. Zhang, Y. Zuo, and S. Yan, Applied Physics Letters **94**, 152511 (2009).

[30] S.-Y. Chen, K.-W. Fong, T.-T. Peng, C.-L. Dong, A. Gloter, D.-C. Yan, C.-L. Chen, H.-J. Lin, and C.-T. Chen, The Journal of Physical Chemistry C **116**, 26570 (2012).

[31] S. Kumar, B. H. Koo, S. K. Sharma, M. Knobel, and C. G. Lee, Nano **05**, 349 (2010).

[32] S. Kumar, Y. J. Kim, B. H. Koo, and C. G. Lee, Journal of Nanoscience and Nanotechnology **10**, 7204 (2010).

[33] G. L. Beausoleil, II, A. Thurber, S. S. Rao, G. Alanko, C. B. Hanna, and A. Punnoose, Journal of Applied Physics **111**, 07B546 (2012).

[34] M. Li, R. Zhang, H. Zhang, W. Feng, and X. Liu, Micro & Nano Letters **5**, 95 (2010).

[35] S. Phokha, S. Pinitsoontorn, and S. Maensiri, Journal of Applied Physics **112**, 113904 (2012).

[36] S. Phokha, S. Pinitsoontorn, P. Chirawatkul, Y. Poo-arporn, and S. Maensiri, Nanoscale Research Letters **7**, 425 (2012).

[37] S.-Y. Chen, Y.-H. Lu, T.-W. Huang, D.-C. Yan, and C.-L. Dong, Journal of Physical Chemistry C **114**, 19576 (2010).

[38] M. Y. Ge, H. Wang, E. Z. Liu, J. F. Liu, J. Z. Jiang, Y. K. Li, Z. A. Xu, and H. Y. Li, Applied Physics Letters **93**, 062505 (2008).

[39] S.-Y. Chen, et al., The Journal of Physical Chemistry C **116**, 8707 (2012).

[40] F. Meng and L. Wang, Materials Letters **100**, 86 (2013).

[41] M. S. Anwar, S. Kumar, F. Ahmed, N. Arshi, G.-S. Kil, D.-W. Park, J. Chang, and B. H. Koo, Materials Letters **65**, 3098 (2011).

[42] F. Meng, C. Zhang, Q. Bo, and Q. Zhang, Materials Letters **99**, 5 (2013).

[43] C. Xia, C. Hu, P. Chen, B. Wan, X. He, and Y. Tian, Materials Research Bulletin **45**, 794 (2010).

[44] S. K. Sharma, M. Knobel, C. T. Meneses, S. Kumar, Y. J. Kim, B. H. Koo, C. G. Lee, D. K. Shukla, and R. Kumar, Journal of the Korean Physical Society **55**, 1018 (2009).

[45] R. K. Singhal, P. Kumari, A. Samariya, S. Kumar, S. C. Sharma, Y. T. Xing, and E. B. Saitovitch, Applied Physics Letters **97**, 172503 (2010).

[46] R. K. Singhal, S. Kumar, A. Samariya, M. Dhawan, S. C. Sharma, and Y. T. Xing, Materials Chemistry and Physics **132**, 534 (2012).

[47] R. K. Singhal, P. Kumari, S. Kumar, S. N. Dolia, Y. T. Xing, M. Alzamora, U. P. Deshpande, T. Shripathi, and E. Saitovitch, Journal of Physics D: Applied Physics **44**, 165002 (2011).

[48] K. Shimizu, S. Kosugi, Y. Tahara, K. Yasunaga, Y. Kaneta, N. Ishikawa, F. Hori, T. Matsui, and A. Iwase, Nuclear Instruments & Methods in Physics Research Section B-Beam Interactions with Materials and Atoms **286**, 291 (2012).

[49] H. Ohno, et al., Nuclear Instruments & Methods in Physics Research Section B-Beam Interactions with Materials and Atoms **266**, 3013 (2008).

[50] A. Iwase, H. Ohno, N. Ishikawa, Y. Baba, N. Hirao, T. Sonoda, and M. Kinoshita, Nuclear Instruments & Methods in Physics Research Section B-Beam Interactions with Materials and Atoms **267**, 969 (2009).

[51] A. Kumar, R. Devanathan, V. Shutthanandan, S. V. N. T. Kuchibhata, A. S. Karakoti, Y. Yong, S. Thevuthasan, and S. Seal, Journal of Physical Chemistry C **116**, 361 (2012).

[52] M. Iwasawa, T. Ohnuma, Y. Chen, Y. Kaneta, H.-Y. Geng, A. Iwase, and M. Kinoshita, Journal of Nuclear Materials **393**, 321 (2009).

[53] T. Sonoda, M. Kinoshita, Y. Chimi, N. Ishikawa, M. Sataka, and A. Iwase, Nuclear Instruments & Methods in Physics Research Section B-Beam Interactions with Materials and Atoms **250**, 254 (2006).

[54] V. Fernandes, et al., Physical Review B **80**, 035202 (2009).

[55] V. Fernandes, J. J. Klein, W. H. Schreiner, N. Mattoso, and D. H. Mosca, Journal of The Electrochemical Society **156**, E199 (2009).

[56] V. Fernandes, et al., J Phys Condens Matter **22**, 216004 (2010).

[57] V. Fernandes, et al., Electrochemical and Solid-State Letters **14**, P9 (2011).

[58] V. Fernandes, P. Schio, A. J. A. de Oliveira, W. H. Schreiner, J. Varalda, and D. H. Mosca, Journal of Applied Physics **110**, 113902 (2011).

[59] A. Tiwari, V. M. Bhosle, S. Ramachandran, N. Sudhakar, J. Narayan, S. Budak, and A. Gupta, Applied Physics Letters **88**, 142511 (2006).

[60] I. Vinokurov, Z. Zonn, and V. Ioffe, *Sov. Phys.-Solid State* **9** 2659 (1968).

[61] Y.-Q. Song, H.-W. Zhang, Q.-Y. Wen, Y.-X. Li, and J. Q. Xiao, Chinese Physics Letters **24**, 218 (2007).

[62] B. Vodungbo, Y. Zheng, F. Vidal, D. Demaille, V. H. Etgens, and D. H. Mosca, Applied Physics Letters **90**, 062510 (2007).

[63] Y. Q. Song, H. W. Zhang, Q. Y. Wen, H. Zhu, and J. Q. Xiao, Journal of Applied Physics **102**, 043912 (2007).

[64] F. Vidal, Y. Zheng, J. Milano, D. Demaille, P. Schio, E. Fonda, and B. Vodungbo, Applied Physics Letters **95**, 152510 (2009).

[65] L. Bi, H.-S. Kim, G. F. Dionne, S. A. Speakman, D. Bono, and C. A. Ross, Journal of Applied Physics **103**, 07D138 (2008).

[66] V. Fernandes, J. Klein, N. Mattoso, D. Mosca, E. Silveira, E. Ribeiro, W. Schreiner, J. Varalda, and A. de Oliveira, Physical Review B **75**, 121304 (2007).

[67] P. Slusser, D. Kumar, and A. Tiwari, Applied Physics Letters **96**, 142506 (2010).

[68] Y. Q. Song, C. H. Mu, W. R. Huo, A. F. Liu, B. Zhang, and Y. Xiang, Physica B-Condensed Matter **413**, 92 (2013).

[69] S. K. Sharma, P. Thakur, S. Kumar, D. K. Shukla, N. B. Brookes, C. G. Lee, K. R. Pirota, B. H. Koo, and M. Knobel, Thin Solid Films **519**, 410 (2010).

[70] S. Colis, A. Bouaine, R. Moubah, G. Schmerber, C. Ulhaq-Bouillet, A. Dinia, L. Dahéron, J. Petersen, and C. Becker, Journal of Applied Physics **108**, 053910 (2010).

[71] Y.-Q. Song, H.-W. Zhang, Q.-Y. Wen, L. Peng, and J. Q. Xiao, Journal of Physics: Condensed Matter **20**, 339803 (2008).

[72] Y. Q. Song, Q. H. Yang, H. W. Zhang, L. Peng, and L. R. Shah, Journal of Physics: Conference Series **152**, 012038 (2009).

[73] B. Vodungbo, et al., Journal of Physics: Condensed Matter **20**, 125222 (2008).

[74] A. Khare, R. J. Choudhary, D. M. Phase, and S. P. Sanyal, Journal of Applied Physics **109**, 123706 (2011).

[75] Z. L. Wang, G. R. Li, J. H. Liang, and Y. X. Tong, Chemphyschem **12**, 166 (2011).

[76] O. D. Jayakumar, A. Vinu, K. V. Guduru, T. Sakuntala, and A. K. Tyagi, Journal of Nanoscience and Nanotechnology **10**, 2299 (2010).

[77] J. Sacanell, M. A. Paulin, V. Ferrari, G. Garbarino, and A. G. Leyva, Applied Physics Letters **100**, 172405 (2012).

[78] S. Colis, A. Bouaine, G. Schmerber, C. Ulhaq-Bouillet, A. Dinia, S. Choua, and P. Turek, Phys Chem Chem Phys **14**, 7256 (2012).

[79] A. Thurber, K. M. Reddy, and A. Punnoose, Journal of Applied Physics **101**, 09N506 (2007).

[80] P. C. A. Brito, D. A. A. Santos, J. G. S. Duque, and M. A. Macêdo, Physica B: Condensed Matter **405**, 1821 (2010).

[81] S. Kumar, G. W. Kim, B. H. Koo, S. K. Sharma, M. Knobel, H. Chung, and C. G. Lee, Journal of Nanoscience and Nanotechnology **11**, 555 (2011).

[82] J. M. A. Almeida, P. E. C. Santos, L. P. Cardoso, and C. T. Meneses, Journal of Magnetism and Magnetic Materials **327**, 185 (2013).

[83] S. Kumar, Y. J. Kim, B. H. Koo, H. Choi, and C. G. Lee, IEEE Transactions on Magnetics **45**, 2439 (2009).

[84] N. S. Ferreira, L. G. Abraçado, and M. A. Macêdo, Journal of Superconductivity and Novel Magnetism **26**, 2549 (2012).

[85] S. Maensiri, S. Phokha, P. Laokul, and S. Seraphin, Journal of Nanoscience and Nanotechnology **9**, 6415 (2009).

[86] A. Thurber, K. M. Reddy, V. Shutthanandan, M. H. Engelhard, C. Wang, J. Hays, and A. Punnoose, Physical Review B **76**, 165206 (2007).

[87] L. Truffault, Q. W. Yao, D. Wexler, I. P. Nevirkovets, K. Konstantinov, T. Devers, and S. Nightingale, Journal of Nanoscience and Nanotechnology **11**, 4019 (2011).

[88] W.-C. Wang, et al., Physical chemistry chemical physics **15**, 14701 (2013).

[89] L. R. Shah, W. Wang, H. Zhu, B. Ali, Y. Q. Song, H. W. Zhang, S. I. Shah, and J. Q. Xiao, Journal of Applied Physics **105**, 07C515 (2009).

[90] L. R. Shah, B. Ali, H. Zhu, W. G. Wang, Y. Q. Song, H. W. Zhang, S. I. Shah, and J. Q. Xiao, J Phys Condens Matter **21**, 486004 (2009).

[91] Q.-Y. Wen, H.-W. Zhang, Q.-H. Yang, Y.-Q. Song, and J. Q. Xiao, Journal of Applied Physics **107**, 09C307 (2010).

[92] B. Ali, L. R. Shah, C. Ni, J. Q. Xiao, and S. I. Shah, J Phys Condens Matter **21**, 456005 (2009).

[93] A. Bouaine, R. J. Green, S. Colis, P. Bazylewski, G. S. Chang, A. Moewes, E. Z. Kurmaev, and A. Dinia, The Journal of Physical Chemistry C **115**, 1556 (2011).

[94] Y. Q. Song, H. W. Zhang, Y. L. Liu, Y. X. Li, L. R. Shah, and J. Q. Xiao, Physica B: Condensed Matter **405**, 2530 (2010).

[95] Q.-Y. Wen, H.-W. Zhang, Q.-H. Yang, Y.-Q. Song, and M.-G. Han, IEEE Transactions on Magnetics **44**, 2704 (2008).

[96] Y.-Q. Song, H.-W. Zhang, Q.-Y. Wen, H. Zhu, and J. Q. Xiao, Chinese Physics Letters **25**, 1106 (2008).

[97] M. C. Dimri, H. Khanduri, H. Kooskora, J. Subbi, I. Heinmaa, A. Mere, J. Krustok, and R. Stern, physica status solidi (a) **209**, 353 (2012).

[98] T. S. Santos and M. A. Macêdo, Journal of Superconductivity and Novel Magnetism **26**, 2541 (2012).

[99] T. S. Santos, W. S. D. Folly, and M. A. Macêdo, Physica B: Condensed Matter **407**, 3233 (2012).

[100] S. Fabris, S. de Gironcoli, S. Baroni, G. Vicario, and G. Balducci, Physical Review B **71**, 041102 (2005).

[101] Y. Q. Song, H. W. Zhang, Q. H. Yang, Y. L. Liu, Y. X. Li, L. R. Shah, H. Zhu, and J. Q. Xiao, J Phys Condens Matter **21**, 125504 (2009).

[102] X. Han, J. Lee, and H.-I. Yoo, Physical Review B **79**, 100403 (2009).

[103] P. R. Keating, D. O. Scanlon, and G. W. Watson, J Phys Condens Matter **21**, 405502 (2009).

[104] M. V. Ganduglia-Pirovano, A. Hofmann, and J. Sauer, Surface Science Reports **62**, 219 (2007).

[105] Z.-S. Lu, D.-W. Ma, J. Zhang, G.-L. Xu, and Z.-X. Yang, Chinese Physics B **21**, 047505 (2012).

[106] V. Ferrari, A. M. Llois, and V. Vildosola, Journal of Physics-Condensed Matter **22**, 276002 (2010).

[107] W.-Z. Xiao, L.-L. Wang, L. Xu, Q. Wan, and A.-L. Pan, Solid State Communications **150**, 923 (2010).

[108] W.-Z. Xiao, L.-L. Wang, L. Xu, Q. Wan, A.-L. Pan, and H.-Q. Deng, Physica B-Condensed Matter **405**, 4858 (2010).

[109] F. Li, C.-w. Zhang, and M. Zhao, Journal of Applied Physics **112**, 083702 (2012).

[110] H. S. Saini, M. Singh, A. H. Reshak, and M. K. Kashyap, Computational Materials Science **74**, 114 (2013).

[111] E. Zintl and U. Croatto, Z. Anorg. Allg. Chem. **242**, 79 (1939).

[112] T. Jo and A. Kotani, Physical Review B **38**, 830 (1988).

[113] D. R. Mullins, S. H. Overbury, and D. R. Huntley, Surface Science **409**, 307 (1998).

[114] P. Nachimuthu, W. C. Shih, R. S. Liu, L. Y. Jang, and J. M. Chen, Journal of Solid State Chemistry **149**, 408 (2000).

[115] P. Carra, B. T. Thole, M. Altarelli, and X. D. Wang, Physical Review Letters **70**, 694 (1993).

[116] S. F. J. Cox, et al., Journal of Physics-Condensed Matter **18**, 1079 (2006).

[117] R. Kubo and T. Toyabe, *Magnetic Resonance and Relaxation,* p. 810 (North-Holland, Amsterdam 1967).

[118] W. Low, *Progress in the Science and Technology of the Rare Earths,* Vol. 2, p. 55 (Pergamon Press, Oxford, 1966).

[119] L. J. Wu, H. J. Wiesmann, A. R. Moodenbaugh, R. F. Klie, Y. M. Zhu, D. O. Welch, and M. Suenaga, Physical Review B **69**, 125415 (2004).

[120] J. A. Fortner, E. C. Buck, A. J. G. Ellison, and J. K. Bates, Ultramicroscopy **67**, 77 (1997).

[121] J. Bentley, S. R. Gilliss, C. B. Carter, J. F. Al-Sharab, F. Cosandey, I. M. Anderson, and P. J. Kotula, Journal of Physics: Conference Series **26**, 69 (2006).

[122] L. A. J. Garvie and P. R. Buseck, Journal of Physics and Chemistry of Solids **60**, 1943 (1999).

[123] S. Tsunekawa, T. Fukuda, and A. Kasuya, Journal of Applied Physics **87**, 1318 (2000).

[124] L. Brus, Journal of Physical Chemistry **90**, 2555 (1986).

[125] S. Tsunekawa, J. T. Wang, Y. Kawazoe, and A. Kasuya, Journal of Applied Physics **94**, 3654 (2003).

[126] F. Zhang, Q. Jin, and S. W. Chan, Journal of Applied Physics **95**, 4319 (2004).

[127] S. Maensiri, C. Masingboon, P. Laokul, W. Jareonboon, V. Promarak, P. L. Anderson, and S. Seraphin, Crystal Growth & Design **7**, 950 (2007).

[128] J. C. Nie, Z. Y. Hua, R. F. Dou, and Q. Y. Tu, Journal of Applied Physics **103**, 054308 (2008).

[129] H. I. Chen and H. Y. Chang, Solid State Communications **133**, 593 (2005).

[130] C. W. Sun, H. Li, H. R. Zhang, Z. X. Wang, and L. Q. Chen, Nanotechnology **16**, 1454 (2005).

[131] Z. C. Orel and B. Orel, Physica Status Solidi B-Basic Research **186**, K33 (1994).

[132] L. X. Yin, Y. Q. Wang, G. S. Pang, Y. Koltypin, and A. Gedanken, Journal of Colloid and Interface Science **246**, 78 (2002).

[133] T. Masui, K. Fujiwara, K. Machida, G. Adachi, T. Sakata, and H. Mori, Chemistry of Materials **9**, 2197 (1997).

[134] H. Richter, Z. P. Wang, and L. Ley, Solid State Communications **39**, 625 (1981).

[135] J. E. Spanier, R. D. Robinson, F. Zheng, S. W. Chan, and I. P. Herman, Physical Review B **64**, 245407 (2001).

[136] W. H. Weber, K. C. Hass, and J. R. McBride, Physical Review B **48**, 178 (1993).

[137] I. Kosacki, T. Suzuki, H. U. Anderson, and P. Colomban, Solid State Ionics **149**, 99 (2002).

Chapter 5

MB_6 (M = Ca, Sr, Ba)

Experimental results for d^0 magnetism in the divalent alkaline-earth hexaborides, of chemical formula MB_6, where M = Ca, Sr, Ba, are presented in this chapter. The magnetic and structural properties of thin films grown by PLD are investigated. Following a brief introduction to this class of materials, an overview of the literature is presented, both experimental and theoretical, which is followed by the main experimental results and finally a summary of the results.

5.1. Introduction

Among boron compounds, the alkaline-earth hexaborides possess several useful properties such as high melting points, significant hardness, good chemical and thermal inertness, low electron work function and stable specific resistance. They are commonly used as high-temperature refractory materials, for surface protection, as wear-resistant materials and as neutron radiation absorbers in the nuclear industry. Since the alkaline-earth hexaboride nominally contain none of the unpaired *d* or *f* electrons normally associated with traditional magnetic order, these compounds are valid candidates for studying possible d^0 magnetic related phenomena pertaining to them. In terms of structure, the alkaline earth hexaboride series possess a cubic crystal structure (*Pm-3m* space group) with the divalent metal cation at each cube corner and an octahedral boron cage with a compensating negative charge at the body centre, as shown in Figure 5.1. Alternatively, one may visualize an equivalent structure where the cation lies at the body centre instead, with the octahedral cages located at each cube corner.

In the next section, the literature summary, the structural and electronic properties of the alkaline earth hexaboride series are comprehensively discussed in their relation to their magnetic properties. The nature of the bandstructure and electronic properties of these materials have been the subject of much debate, not to mention their magnetic properties.

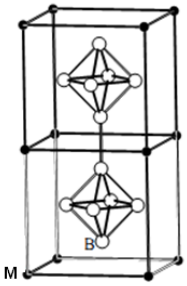

Figure 5.1. Crystal structure of the alkaline earth hexaboride series, MB_6, where M (black spheres) denotes the divalent metal cation, and B (open spheres) denotes the element boron.

5.2. Literature summary

Prior to presenting a literature summary of exotic high temperature magnetism in the alkaline-earth hexaborides, a brief overview of the divalent hexaboride EuB_6, a rare earth hexaboride which is structurally similar to the alkaline earth hexaborides, with Eu ions at the vertices and a boron octahedron at the centre of a cubic unit cell, is first presented. The reason that EuB_6 is first presented is in order to distinguish it from the alkaline-earth hexaborides in terms of its magnetic properties; EuB_6 may be regarded as a Heisenberg ferromagnet with predominantly ferromagnetic superexchange coupling between the $4f^7$ Eu^{2+} ions with S = 7/2, and is known to transform from a paramagnetic to a ferromagnetic phase upon cooling below 15 K, i.e. it is *a well established intrinsic ferromagnetic at low temperatures*. Strictly speaking there are actually two transitions, T_M at 15.3 K and at T_C at 12.5 K [1], where T_M is associated with a charge delocalization transition resulting from the overlap of magnetic polarons while T_C is the proper ferromagnetic transition. It has been calculated using DFT within the local density approximation (LDA) that there is a small overlap between the boron derived valence band with a primarily alkaline-earth derived conduction band at the *X* point of the Brillouin zone and semi-metallic properties for the ferromagnetic phase [2], in agreement with subsequent DFT calculations performed using the linear muffin-tin orbital (LMTO) framework [3] (which also calculate similar properties for the higher temperature paramagnetic phase) and quantum mechanical modeling [4]. Experimentally, EuB_6 single crystals grown by the Al-flux method have been found to have a magnetization of ~ 375 kA m^{-1} at 4.5 K [5], and it has been reported that ferromagnetic EuB_6 is an intrinsic semi-metal from magnetoresistance [6] and point contact Andreev reflection (PCAR) [7] measurements for example, in agreement with the aforementioned theoretical predictions. Pure EuB_6 single crystals are also measured to be semi-metallic below T_C and semiconducting above T_C with a bandgap of 0.05-0.1 eV [8], while the dominant magnetic interaction changes from ferromagnetic to antiferromagnetic with increasing carbon content [8,9,10]; the carbon-substituted EuB_6 has a metallic behaviour due to the donation of electrons to the conduction band by carbon atoms. ARPES measurements of single

crystals grown by the Al-flux method show a bandgap of ~1 eV at the *X* point for EuB_6 at 20-30 K [11,12] (hence for the paramagnetic semiconducting phase) and no semi-metallic properties. In contrast to the alkaline-earth hexaborides, *no evidence for RFTM* has been reported for EuB_6. For the similar rare earth hexaboride SmB_6, no RTFM has been reported either, with no ferromagnetism measured for polycrystalline SmB_6 (made by heating the elemental powders, 99.9% Sm and 99.999% B) from 300 K down to 0.35 K [13].

Now the attention is focused on the alkaline-earth hexaborides, also divalent hexaborides like the rare earth hexaborides EuB_6 and SmB_6 but with a completely different origin for the magnetism (the rare earth hexaboride YbB_6 is a different case to that of EuB_6 and SmB_6 as exotic high temperature magnetism *has* been measured in some cases for this compound, and is discussed later). The first experimental report for ferromagnetism in the alkaline-earth hexaborides was by Young *et al.* [14] in the year 1999 for La doped CaB_6 single crystals grown by the molten aluminium flux growth method, a common used method to grow single crystals of alkaline-earth hexaborides, in which a mixture of aluminium metal, the alkaline-earth metal (sometimes in the form of a common oxide or carbonate) and boron powder are heated under a flowing argon atmosphere at ~ 1500 °C. The authors measure a maximum magnetization of ~ 45 A m^{-1} (equivalent to a moment of ~ 0.07 μ_B/La) at 5 K for $Ca_{1-x}La_xB_6$ where x = 0.005, with a magnetic ordering temperature of about 600 K. A slightly smaller magnetization of ~ 30 A m^{-1} is also measured at both 30 K and 50 K for the same sample. Similar magnetization values with a maximum at x=0.005 are also measured for each of La, Ce and Sm doped SrB_6 crystals. The magnetism is almost anhysteretic (H_c of order mT) and only appears for a narrow range of La doping concentrations, approximately for x = 0.0025 - 0.01. For undoped MB_6 (M = Ca, Sr, Ba) crystals, the moments measured at 5 K were at least an order of magnitude smaller than that found for La doped samples, corresponding to magnetizations of about ≤ 5 A/m. Typical magnetization curves that were measured by Young *et al.* are shown in Figure 5.2 on the next page. Similar data is also published slightly later elsewhere by some of the same group of researchers [15]. Young *et al.* also measured ferromagnetic-like signals for Th doped CaB_6 at 5 K but the signals are smaller than those measured for La doping, with a maximum magnetization of ~ 30 A m^{-1} for x = 0.0025. The authors proposed that the magnetism may be attributed to defect states or the ferromagnetic polarization of the low density electron gas. In the low density electron gas model of ferromagnetism, as the density of an electron gas is lowered, a partially spin-polarized fluid state is stabilized before a transition to a Wigner crystal takes place, and the observed ferromagnetism may be ascribed to this partially spin-polarized state [16]. Other early proponents of the electron gas model included Ceperley [17], who (in the same volume of the journal *Nature* as Young *et al.* incidentally) from a theoretical consideration of the idealized homogeneous gas, suggested that a low density electron gas scenario may be applicable to the MB_6 series in general. Later, angle-resolved photoemission spectroscopy (ARPES) measurements of CaB_6 single crystals grown by the float zone method revealed a band gap of 1 eV at the *X* point at 30 K, and semiconducting characteristics, which the authors argued were also consistent with the ferromagnetic spin-polarized fluid state of the low density electron gas [18,19]. Specifically, it is reported that the estimated carrier number in the small Fermi surface at the *X* point lies in the region

where the spin polarization of electrons is predicted. In the former report a small room temperature magnetization of ~ 4 A m^{-1} is measured for the CaB_6 single crystal. The authors note the results unambiguously show that the band structure obtained by ARPES reflects the bulk property, even though the method is only surface sensitive, since the measured band dispersion periodicity matches well with that of the bulk Brillouin zone, and the carrier number estimated from ARPES shows a good quantitative agreement with their Hall resistivity measurements.

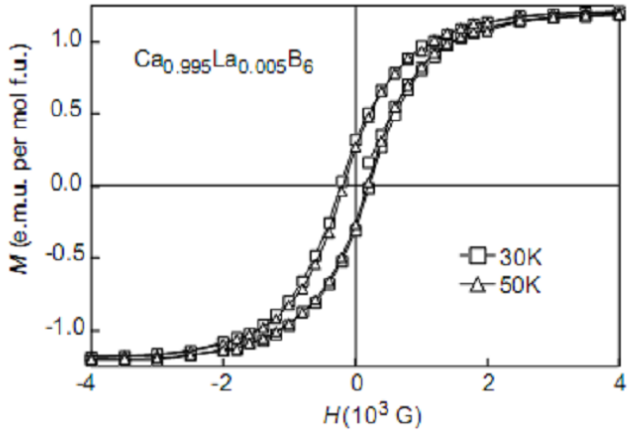

Figure 5.2. Magnetization curves published by Young *et al.* [14] for La-doped CaB_6 single crystals, which represents the first experimental report for ferromagnetism in the alkaline-earth hexaborides; $M_s \approx 30$ A m^{-1}, 10^3 G = 0.1 T.

Another early proposal was that the magnetism in $Ca_{1-x}La_xB_6$ (x=0.005) crystals grown by the flux growth and float zone methods, exhibiting metallic behaviour of electrical conduction, for which magnetizations of 180 A m^{-1} (5 K) and 20 A m^{-1} (300 K) were measured respectively, may be attributed to superparamagnetism, assuming that the ferromagnetic state is spatially inhomogeneous [20].

Alternatively to the dilute electron gas model proposed by Young *et al*, another early model for ferromagnetism in the hexaborides involved doping of an excitonic insulator, for which several reports were published, and which was first proposed by Zhitomirsky *et al*. [21,22] and applied to La-doped CaB_6. In the exciton model, a semimetal with a small band-overlap may be unstable against exciton (electron-hole pair) formation, and may thus enter a novel excitonic insulating state. Electrons doped into such a system are proposed to be distributed asymmetrically between two spin sub-bands, leading to ferromagnetism. It is argued that the unique electronic bandstructure of divalent hexaborides is favourable to the formation of the excitonic insulating state. The excitonic magnetism model may also be applied to hexaborides which possess a small band-gap (in addition to band overlap), and hence for semiconductors (in addition to semimetals). In the former of their reports [21], Zhitomirsky *et al*. calculate band gaps of -0.2 eV (overlap) and 0.15 eV by first principles calculations using LDA and LDA+U respectively, and a moment of ~ 0.14 μ_B per doped electron (La) for x=0.0035 in their latter report [22]. A subsequent theoretical report extended the exciton model to La doped SrB_6 [23] in addition to La doped CaB_6, which was followed by the

postulation of an excitonic insulator superstructure for La doped CaB_6 [24], which was calculated by band structure arguments to possess a moment of 1 μ_B/La, larger than that predicted previously (0.14 μ_B/La) by Zhitormirsky *et al* [22]. A later report by Zhitomirsky and Rice [25] using the random phase approximation and Hubbard scheme predicted an insulating dilute exciton gas with a small band overlap in *undoped* CaB_6, but also applicable to the alkaline earth hexaborides in general, with the formation of a dense electron-hole plasma upon further band overlap. Some of the authors of the seminal Young *et al.* paper note in their subsequent report [15] that excitonic ferromagnetism in the MB_6 compounds may be a plausible explanation. While another report measures and calculates by DFT (within the generalized gradient approximation, GGA) a small overlap between the conduction and valence bands at the *X* point and semi-metallic behaviour for SrB_6 down to at least 5 K, the authors argue that at high temperatures exciton formation is unlikely due to their energetic instability [26].

In further support of the excitonic model, by measuring the resistivity, a small gap of ~ 0.15 eV is measured at the *X* point for CaB_6 single crystals grown by the Al flux method, both undoped and La doped (x = 0.01, 0.005), and is attributed to the excitonic gap [27]. A magnetization of ~ 55 A m^{-1} (of similar magnitude to that measured by Young *et al.*) is measured at 30 K for the undoped Ca^{2+} vacancy-rich sample, whereas the undoped stoichiometric phase did not exhibit any ferromagnetism (at 2 K). While the authors report that CaB_6 is semiconducting and La doped CaB_6 is metallic, another resistivity study finds that CaB_6 single crystals grown by the float zone method are semi-metallic instead [28], which nevertheless still conforms to the requirements of the excitonic model. Another theoretical study (using electronic structure arguments) predicts excitonic magnetism in a Wigner crystal for the divalent hexaborides, pure and La doped, with a maximum moment for x = 0.005 La doping [29], similar to that found initially by Young *et al.*, while a semiconducting, multi-exciton bound state stabilized by charged impurities and assuming a finite gap is also predicted for similar doped and undoped divalent hexaborides using the effective mass approximation [30]. Further predictions for excitonic ferromagnetism in CaB_6 are deduced from quantum mechanical arguments for both the pure [31] and doped form [32,33], for which the latter report calculated a moment of 0.4 μ_B/carrier for x = 0.04 doping using mean field theory. Murakami *et al.* [34-36] calculate an excitonic ferromagnetic phase for $Ca_{1-x}La_xB_6$ using the Ginzberg-Landau theory for excitonic order parameters. Elsewhere, a slightly different scenario of a spin-1 Mott insulator was proposed for $Sr_{1-x}La_xB_6$ [37], possessing a spin gap of ~ 0.1 eV (as opposed to a charge or "band" gap) and a magnetic moment of 0.9 μ_B/f.u., as deduced from band structure calculations starting from the Hubbard model.

In terms of the electronic structure of the alkaline-earth hexaborides, there has been much debate over the size of the bandgap and whether they are insulators, semimetals or semiconductors. In order to properly treat the magnetic properties of the hexaborides, it is necessary to further discuss those reports relating to its electronic structure, as the two properties are likely correlated. For example, an early report in the 1950s suggested that the divalent hexaborides were insulating, but conducting and metallic when containing impurities, using band structure calculations [38]. In contrast, semiconducting behaviour was measured for alkaline-earth hexaborides in the 1960s [39]. A

later band structure calculation in the 1970s calculated band gaps of 2.11, 3.68. 2.64 and 2.4 eV for CaB_6, SrB_6, BaB_6 and LaB_6 respectively [40]. Closer to the present, a DFT calculation within the local spin density approximation (LSDA) in 1997 reported that hexaborides with divalent cations (specifically Ca, Sr, Eu) are semimetals, with a small direct overlap of a primarily boron-derived valence band with a primarily alkaline-earth derived conduction band at the *X*-point of the Brillouin zone [2]. A similar scenario was also later calculated for BaB_6 by some of the same authors [41]. This semi-metallic picture was later used my many proponents of the excitonic model for ferromagnetism [21, 22, 25-27, 30, 36], for which either a small bandgap or band overlap is compatible, corresponding to semiconducting or semi-metallic states respectively.

In contrast to the proposed semi-metallic scenario above, reports which refute the exciton model often base their arguments on the fact that the large bandgaps that they calculate/measure are incompatible with the exciton model, which some use to argue in favour of the dilute electron-gas model instead [18,19]. DFT-LMTO calculations calculate bandgaps at the *X* point of 1 eV for BaB_6 [42], ~ 0.1 and 0.02 eV for MgB_6 and CaB_6 respectively (both semiconducting) [43], and 0.48, 0.16 eV and 0.02 eV for CaB_6, SrB_6 and BaB_6 respectively (all semiconducting) [44]. In the latter report, the following moments are calculated (in a 10 T applied field): $Ba_{1-x}La_xB_6 \approx 2\times10^{-4}$ μ_B (x = 0.05), $YB_6 \sim 2.5\times10^{-4}$ μ_B, $LaB_6 \sim 3\times10^{-4}$ μ_B. In addition, doped MB_6 compounds are calculated to be semi-metallic, while similar results to those of the above report [44] are reported again slightly later by some of the same authors [3], but additionally including a calculated bandgap of 0.05 eV and semiconducting behaviour for YbB_6. Thus it is evident that even among reports using a similar DFT approach (LMTO), while semiconducting characteristics for the alkaline-earth hexaborides are most commonly found, the calculated bandgaps are not in close agreement.

For DFT calculations using the generalized gradient approximation (GGA) the bands are calculated to just touch at *X* point for CaB_6 [45], in agreement with another similar calculation for MB_6 (M = Ca, Sr, Ba) which also calculates no gap at E_F and semi-metallic behaviour [46]. The former report notes that for DFT calculations using the local density approximation (LDA), either a small (~ 0.3 eV) band overlap or gap is calculated depending on the lattice parameter used and that the band-gap is very sensitive to the special position parameter, while the latter notes that that GGA can only predict a semi-metallic bandstructure for the alkaline-earth hexaborides. For calculations using DFT within the GW approximation, in which the self-energy is the product of the single-particle Green function G and the screened interaction W, a semiconducting band gap of 0.8(0.1) eV is calculated for CaB_6 using GW based on the pseudopotential plane wave method [47]. In contrast, other GW calculations based on LDA-LMTO reveal a small overlap at the *X* point for CaB_6 with likely semi-metallic behaviour [48,49]. It is noted [48] that the discrepancy between this calculation and the previous one [47] may be due to the fact that the pseudopotential is adopted to calculate the valence energy levels and wavefunctions in the previous report [47], which cannot take into account contributions from core electrons (which are large in reality). In the GW method, quasiparticle energies are calculated including the effects of electron correlations beyond LDA. It is also noted [48,49] that while DFT-LDA is a widely used first-principles method and has had great success in predicting electronic structures, there exist some problems not only in materials with *d*

and *f* electrons but also those with *s* and *p* electrons, and that LDA has difficulty in describing excited states. Furthermore, typically the LDA underestimates band gaps in semiconductors and insulators, whereas the GW method takes account of electron correlations within the random phase approximation (RPA) to give band gaps in good agreement with experimental ones in many cases. However, in response to the above it is mentioned by one of the authors who used DFT-GGA [45] that while the GW method may be very accurate in describing the band structure, it cannot be used to calculate the *total* energy.

Another DFT approach uses the weighted density approximation (WDA), for which a band gap of 0.8 eV at the *X* point together with semiconducting behaviour is calculated for CaB_6 [50]. The authors note that WDA (and GGA) predict lattice parameters in excellent agreement with experiment, whereas for LDA the lattice parameter may be underestimated. In order to overcome the shortcomings of LDA in predicting excited states and lattice parameters, a so-called screened exchange (sX) LDA calculation, in which the effect of non-local electron-electron interactions are included, predicts a band gap > 1.2 eV at the *X* point and semiconducting characteristics for CaB_6 [51]. The authors note that conflicting results for the value of the bandgap at the *X* point indicate that the details of the band structure near E_F are clearly very sensitive to the way that the many-body correction is introduced. When the same authors [51] use LDA only, the calculations (incorrectly according to their arguments) present either a small band-gap (~ 0.1 eV) or band-overlap depending on the special positional parameter x used, in broad agreement with other LDA calculations.

It is now generally accepted that the alkaline-earth hexaborides are semiconductors (*not* semimetals) with band gaps of ~ 1 eV at the *X* point, which rules out the early excitonic explanation for the ferromagnetism, for which a small band overlap or gap (generally ≤ 0.3 eV for either) is required. ARPES measurements confirm the semiconducting behaviour, with Denlinger *et al.* measuring a band gap of 1.15 eV at 20-30 K for each of CaB_6, SrB_6 and EuB_6 single crystals grown by the Al flux method [11] and a band gap > 1 eV at the *X* point for CaB_6 (both stoichiometric and Ca rich) in another report [12]. The authors note that the gap magnitude is very sensitive to the conduction band occupation. Souma *et al.* [18,19] initially measured a bandgap of 1 eV at the *X* point at 30 K for semiconducting CaB_6 single crystals grown by the float zone method as mentioned previously, and later measured the same bandgap (at 20 K) for $Ca_{1-x}La_xB_6$ (x = 0.005) crystals grown by the same method [52], in which the authors noted that the surface sensitive ARPES results reflect the electronic structure of the bulk also.

Table 5.1 on the next page provides a summary of reports which calculate (the majority) or measure the bandstructure of MB_6, with further footnotes pertaining to the table given on the subsequent page. The electronic conductivity (metallic, semi-metallic, semiconducting or insulating) is also displayed where available. Note that from now on, "MB_6" will refer to the divalent alkaline-earth hexaborides in general, rather than the rare earth hexaborides (an exception is the rare earth hexaboride YbB_6, which is included in the discussion of the alkaline earth hexaborides as it is the only known rare earth hexaboride reported to exhibit room temperature ferromagnetism).

Table 5.1. Summary of reports which detail the bandstructure of MB_6

Method	System	Band gap and electronic structure at *X* point	Ref
Effective mass approx. for excitons	Divalent hexaborides (both pure and doped)	"finite" gap assumed (semiconducting)	30
Hubbard Model	$Sr_{1-x}La_xB_6$	*spin* gap ~ 0.1 eV [i]	37
Mean field approx. (extended Hubbard model)	CaB_6	single pair of semi-metallic bands necessary for FM in distorted tetragonal structure	53,54
Quantum Monte Carlo, Hartree-Fock + DFT	CaB_6	1.3±0.2 eV (semiconducting)	55
Resistivity measurements	$Ca_{1-x}La_xB_6$, x = 0, 0.01, 0.005 (single crystals, Al-flux grown)	0.168 eV for CaB_6 (semiconducting), $Ca_{1-x}La_xB_6$ metallic	27
Optical absorption measurements	CaB_6 single crystals (Al-flux grown)	1 eV (CaB_6, 99.999% purity B) 0.82 eV (CaB_6, 99.9% purity B) Both samples semiconducting	56,57
DFT-LDA	MB_6 (M = Ca, Sr, Eu)	band overlap (semimetallic)	2
DFT-LDA (+U)	$Ca_{1-x}La_xB_6$	band overlap (gap), -0.2 (0.15) eV	21
DFT-LDA	BaB_6	band overlap	41
DFT-LDA	CaB_6	band overlap	58
DFT-LDA	CaB_6	0.2 eV (band insulating)	59
DFT-LDA	CaB_6	0.2 eV (band insulating)	60
DFT-LMTO	BaB_6	1 eV	42
DFT-LMTO	MgB_6, CaB_6	~ 0.1, 0.02 for MgB_6, CaB_6 resp. (semiconducting)	43
DFT-LMTO	MB_6 (M = Ca, Sr, Ba, Yb, La), $Ba_{1-x}La_xB_6$ (x=0.05)	0.48, 0.16 eV for CaB_6, SrB_6 resp. (semiconducting), 0.02 eV for BaB_6 and doped MB_6 (both semi-metallic)	44
DFT- LMTO	MB_6 (M = Ca, Sr, Ba, Yb)	0.5, 0.2, 0.02, 0.05 eV for CaB_6, SrB_6, BaB_6, YbB_6 resp. (semiconducting)	3
DFT-GW [ii]	CaB_6	0.8±0.1 eV (semiconducting)	47
DFT-GW [iii]	CaB_6	band overlap (semimetallic)	48
DFT-GW [iii]	CaB_6	band overlap (semimetallic)	49
DFT-GGA	SrB_6	band overlap (semimetallic)	26
DFT-GGA [iv]	CaB_6	band overlap	45
DFT-GGA [v]	MB_6 (M = Ca, Sr, Ba)	band overlap (semimetallic)	46
DFT-GGA	CaB_6	band gap present (eV not given)	61
DFT-GGA [vi]	MgB_6	0.5 eV (semiconducting)	62
DFT-WDA [vii]	CaB_6	0.8 eV (semiconducting)	50
DFT-sX LDA [viii]	CaB_6	> 1.2 eV (semiconducting)	51
ARPES	CaB_6 (single crystal, Al-flux grown)	> 1 eV (semiconducting) at 20-30 K	11
ARPES [ix]	CaB_6, SrB_6, EuB_6 (single crystals, Al-flux grown)	1.15 eV (semiconducting) at 20-30 K [x]	12
ARPES	CaB_6 (single crystal, float zone growth)	1 eV (semiconducting) at 30 K	18
ARPES	$Ca_{1-x}La_xB_6$ (single crystal, Al-flux grown), x = 0.005	1 eV (semiconducting) at 20 K	52

- An early report [40] using LCAO (linear combination of atomic orbitals) to calculate the band structure revealed band gaps of 2.11, 3.68. 2.64 and 2.4 eV for CaB_6, SrB_6, BaB_6 and LaB_6 respectively

(Footnotes continued on next page →)

Footnotes to Table 5.1 (continued):

- Another report measures ^{11}B chemical shifts which are characteristic of *semiconductors* for MB_6 (M = Ca, Sr, Ba) 99.5% purity powders using an ^{11}B quadrupole spin-echo method [63], which is also supported by earlier electrical measurements [39]

[i] as opposed to the charge or "band" gap
[ii] based on the pseudopotential plane wave method
[iii] it is noted that LDA has difficulty in describing the excited states (typically underestimates band gaps in semiconductors and insulators) whereas the GW method takes account of electron correlations within the random phase approximation giving band gaps in closer agreement with experiment
[iv] It is note that while the GW method is very accurate in describing the band structure, it cannot be used to calculate the total energy; it is noted that LDA gives either a small (~0.3 eV max.) band overlap or gap depending on lattice parameter used and that the band-gap is very sensitive to the special position parameter
[v] it is noted that GGA can only predict a semimetallic bandstructure for the alkaline earth hexaborides
[vi] including atomic self-interaction corrections (no longer limited to a semimetallic prediction as per conventional GGA)
[vii] Weighted density approximation; it is noted that WDA predicts a lattice parameter in excellent agreement with experiment (LDA lattice parameter typically underestimated in contrast)
[viii] sX denotes screened exchange, in which the effect of non-local electron-electron interactions is included
[ix] + bulk sensitive k-resolved resonant inelastic X-ray scattering (RIXS)
[x] it is noted that the gap magnitude is very sensitive to the conduction band occupation

In contrast to the reports mentioned so far which attributed the magnetism of the alkaline-earth hexaborides to *intrinsic* ferromagnetism due to a dilute electron gas or an excitonic phase, some reports cast doubt on the whether the magnetism was intrinsic or not by suggesting that extrinsic ferromagnetic impurities may explain the magnetic signals. An early paper initially attributed the magnetic signals measured for CaB_6 *polycrystals*, grown by the borothermal reduction method (in contrast to the Al-flux growth method which produces *single* crystals such as those grown by Young *et al.* for example), which involves heating a mixture of CaO and boron powder (99.99% used) under an argon atmosphere, to Ca vacancies created upon heating at 1500 °C and the associated symmetry lowering (and not due to carrier doping) [64]. Magnetizations of ~ 5-50 A m^{-1} at room temperature (500 A m^{-1} at 90 K) were measured for samples containing Ca vacancies, while the stoichiometric phase (heated at 1200 °C) was diamagnetic. A boron nitride (BN) crucible was used in all of the borothermal reduction reactions. Subsequently however, some of the same group of authors retracted their above claim of intrinsic magnetism [65], attributing the magnetism in their CaB_6 (and LaB_6) polycrystals to iron impurities, and also cast doubt on the intrinsic nature of the magnetism proposed in the initial experimental report of Young *et al.* [14]. Magnetizations in the region 100 – 300 A m^{-1} at 300 K (measured in an applied field of 0.5 T) for CaB_6 polycrystals were now attributed to Fe-B phases, especially due to Fe coming from the ZrO_2 crucible (contains 17-46 ppm of Fe as measured by ICP-MS) used during the solid state reaction. Furthermore, M_s obtained at 300 K (and at 0.5 T) when using BN and MgO crucibles was ~ 0-50 A m^{-1} and ~ 730 A m^{-1} respectively, with the crucibles used containing 2-4 ppm and 160 ppm of Fe respectively. It was proposed that Fe may migrate from the crucible and concentrate in the polycrystals during their high temperature growth, since the authors find a correlation between the size of the measured magnetic signals and the level of iron impurity concentrations. Similar results

were subsequently published in more detail elsewhere [66], in which the ferromagnetism disappeared almost completely upon immersion of the polycrystals in hydrochloric acid (HCl), with a strong correlation between the magnitude of the reduced magnetization and the iron concentration in the acid. The magnetic signals were thus attributed to FeB or Fe_2B, which are mostly removed upon acid etching. Young *et al.* responded to these claims [65] (reply appended at the end of the article) by stating that while Fe may indeed be present in their crystals, it does not contribute to the magnetic signal directly but that strongly interacting defects in off-stoichiometric CaB_6 (comprising a few tenths of a per cent) that carry magnetic moments are responsible for the observed ferromagnetic properties. They further state that these defects may be iron atoms scavenged during the growth of CaB_6 crystals from boron-rich flux growths. By intentionally doping their crystals with iron, they conclude that the lack of dependence of the measured ordered moment on the iron concentration in the flux suggests that alien Fe–B phases, while possibly present, are not the source of ferromagnetism. In a subsequent paper by some of the authors associated with Young *et al.*, the measured magnetization, which reaches a maximum value of ~ 1200 A m^{-1} (measured at 0.1 T) at 25 K for 0.5 % La doping in semiconducting CaB_6 crystals grown by the Al flux method, *is attributed to defects* on the Ca and/or B sublattice [67]. No ferromagnetism is measured for pure CaB_6. For undoped SrB_6 single crystals, the magnetization measured at room temperature in an applied field (field value not given) is smaller, ~ 75 A m^{-1}.

Another report for $Ca_{1-x}La_xB_6$ single crystals grown by the Al-flux method using 99.999% nominal purity boron powder attributes the maximum M_s of ~ 70 A m^{-1} measured at 5 K for x = 0.01 to iron impurities detected by inductively-coupled plasma atomic emission spectroscopy (ICP-AES) analysis [68]; upon acid etching with nitric acid, M_s is reduced to ~ 20 A m^{-1}, while for x = 0.03 the small M_s of ~ 5 A m^{-1} measured at 5 K vanishes upon acid etching, from which the authors suggest that the acid treatment removes the iron impurities present in the crystals (~ 1000 ppm and ~ 50 ppm for x = 0.01 and x = 0.03 respectively as measured by ICP-AES) whose concentration levels may completely account for the magnitude of the measured magnetic signals. For an undoped CaB_6 crystal, the magnetization of ~ 80 A m^{-1} at 5 K may be accounted for by ~ 47 ppm of Fe (M_s of bulk Fe = 1.71 MA m^{-1}). In addition, no signature of an excitonic state is observed in the measured reflectivity spectra for any x (i.e. < 0.03). For $Ca_{1-x}La_xB_6$ single crystals of millimetre size, grown by the same method as above but in a HCl treated flux in order to help dissolve any iron impurities, the room temperature magnetization signals of ~ 50 A m^{-1} and 40 A m^{-1} for x = 0.0051 and x = 0.015 respectively are also attributed to Fe impurities by Otani and Mori [69,70] (the x = 0.015 sample is presented in the latter paper). For x = 0.0051, 0.015, the samples contain 100, 90 ppm Fe respectively (by ICP-MS analysis); the ferromagnetism vanishes upon subsequent acid washing of the crystals using more hydrochloric acid. In addition, no RTFM is reported for undoped CaB_6 single crystals grown in a HCl treated Al flux (≤ 10 ppm of Fe remains in the sample), but diamagnetism only with $\chi = -2.2 \times 10^{-7}$ emu/g [70], whereas for the same sample grown in the same way but *without* HCl treatment of the flux, the distinct RTFM signal of size ~ 115 A m^{-1} is attributed to 190 ppm of Fe impurities by ICP analysis [69]. This result confirms that growing the undoped crystals in a HCl flux removes most of the iron and the ferromagnetism. The following

argument is given for the presence of Fe impurities [69]; in the process of dissolving the aluminium flux by NaOH solution, the aluminium matrix acts as a cathode. The crystals which are held on the surface of the aluminium acts as an anode and iron ions are reduced to iron on the crystal surface. That is, the crystals are electrochemically plated with iron. Consequently, the crystals are covered with iron because iron is stable in the NaOH solution, which is then removed by HCl treatment because iron reacts with HCl solution. The authors further suggest that iron impurities are electrochemically plated onto the surface of $Ca_{1-x}La_xB_6$ crystals more readily than for undoped CaB_6, due to the lower resistivity of $Ca_{1-x}La_xB_6$ [70], which may explain why the HCl flux grown doped crystals exhibit larger magnetic signals than similarly grown undoped crystals. The same authors subsequently further elucidate the nature of the iron impurities in their undoped CaB_6 crystals (Al-flux grown, without HCl), measuring ~ 360 ppm of Fe present in the surface region to a depth of ~ 1 μm, as detected by ICP-AES, SEM-EDX and depth profiling with Auger electron spectroscopy (AES) [71]. After a initial rapid decrease in the oxygen Auger signal intensity as a function of sputtering time, the Fe and O Auger signals decrease in parallel, from which the authors infer that the iron is present as an oxide.

A later report attributes the average magnetization of ~ 125 A m^{-1} measured at 250 K for 14 undoped CaB_6 single crystals (maximum/minimum ~ 450/20 A m^{-1}) grown by the Al-flux method to iron and nickel located at the surfaces of their samples, especially at the edges of facets and at growth steps, as deduced from electron probe microscopy analyses [72]. For a crystal with an M_s of ~ 180 A m^{-1}, acid etching (using aqua regia) of 600 nm of the surface reduces M_s to ~ 90 A m^{-1}. M_s is not reduced any further for a 1200 nm surface acid-etch, from which the authors deduce that the etch is more effective at removing Fe and Ni contaminants on the surface than from the step and facet edges, to which the M_s of ~ 90 A m^{-1} may be ascribed for this crystal. Cao *et al.* [73] attribute the room temperature magnetization of ~ 75 A m^{-1} measured for their polycrystals synthesized by borothermal reduction (using 99.99% CaO and boron) to FeB, inferred by comparing the value of H_0, which is the field obtained by extrapolating the initial susceptibility to saturation, for the undoped sample to that measured for intentionally Fe doped $Ca_{1-x}Fe_xB_6$ samples, which show similar values of H_0 to the undoped sample. In addition, the undoped sample is found to contain ~ 100 ppm of iron impurities by ICP analysis. For the intentionally doped polycrystals, M_s ~ 245 A m^{-1} and ~ 19500 A m^{-1} for 100 ppm (x = 0.0001) and 10000 ppm (x = 0.01) Fe doping concentrations respectively, and the presence of FeB is revealed by XRD and electron probe microscopy analyses, which is found to be inhomogeneously distributed from the latter measurement. Furthermore, in a subsequent report, the same authors attribute the ferromagnetism measured for similarly grown $Ca_{1+\delta}B_6$ ($-0.05 < \delta < 0.05$) polycrystals to iron boride ($\delta < 0$) or iron oxide ($\delta > 0$) phases [74]. For stoichiometric CaB_6 at room temperature they measure M_s ~ 25 A m^{-1}, and the largest value (75 A m^{-1}) for Ca deficient $Ca_{1+\delta}B_6$ ($\delta = -0.01$). In addition, ~ 400 ppm of Fe is detected by ICP-MS in all of the samples. The authors state that since the magnetization of Fe–O phases is weaker than that of the Fe–B phases, this may explain why smaller magnetic signals are measured for the Ca rich ($\delta > 0$) samples compared to the Ca deficient ($\delta < 0$) ones. Elsewhere, it is reported that the Fe impurity content in CaB_6 powder (Kujundo Chemical Lab. Co.) is ~ 400 ppm,

and ~ 50 ppm in the single crystal grown by the Al-flux method from the powder, as deduced from both ICP-AES and Proton Induced X-ray Emission (PIXE) measurements [75]. A lower purity CaB_6 powder reveals ~ 2000 ppm of Fe (by PIXE), however the nominal powder purities are not given. In addition, a first principles calculation using Quantum Monte Carlo, Hartree-Fock and DFT calculations attributes the magnetism for La doped CaB_6 to magnetic impurities, and not to La or B [55]. The calculated semiconducting band gap of 1.3 ± 0.2 eV at the *X* point is in similar agreement with the current generally accepted DFT result for the electronic structure of the alkaline-earth hexaborides.

Tables 5.2 & 5.3, spread out for the sake of clarity on the following two pages, provide a summary of experimental reports which ascribe the magnetism of undoped and doped MB_6 samples respectively to ferromagnetic impurities. M_s is measured at room temperature unless stated otherwise, while the reagent purity is given where available.

Table 5.2. Experimental reports of magnetism attributed to ferromagnetic impurities for undoped MB_6; the first three listed samples are single-crystals, the rest are all polycrystals.

Sample	Growth method	M_s (A m^{-1})	Explanation proposed	Ref
CaB_6	Al-flux	125 (250 K)	Fe, Ni at surfaces [i]	72
CaB_6	Al-flux (99.999% boron)	80 (5 K)	Fe impurities [ii]	68
CaB_6	Al-flux	115	Fe impurities [iii]	69
CaB_6	BR (99.99% CaO, boron)	75	FeB [iv]	73
$Ca_{1+\delta}B_6$ ($\delta = 0$)	BR (99.99% CaO, boron)	25	iron boride ($\delta < 0$) or iron oxide ($\delta > 0$) phases [v]	74
$Ca_{1+\delta}B_6$ ($\delta = -0.01$)	BR (99.99% CaO, boron)	75	iron boride ($\delta < 0$) or iron oxide ($\delta > 0$) phases [v]	74
CaB_6	BR (99.99% boron)	~100 – 300 (at 0.5 T)	Fe-B phases [vi]	65
LaB_6	BR (99.99% boron)	~100 – 300 (at 0.5 T)	Fe-B phases [vi]	65
CaB_6	BR (99.99% CaO, boron) BN crucible used	30	FeB or Fe_2B [vii]	66
CaB_6	" " ZrO_2 crucible used	130	FeB or Fe_2B [vii]	66
CaB_6	" " MgO crucible used	730	FeB or Fe_2B [vii]	66

BR = Borothermal reduction

[i] Ferromagnetic impurities revealed by electron probe microscopy; the average M_s listed is for 14 undoped crystals (ranging from ~ 20-450 A m^{-1}) measured at 250 K. Upon acid etching 600 nm of the surface, M_s decreased by 47 % for a sample with an initial M_s of 180 A m^{-1}, with no further decrease in M_s for a 1200 nm etch

[ii] Fe impurities revealed by ICP-AES analysis; ferromagnetism vanishes upon acid-etching

[iii] 190 ppm of Fe impurities measured by ICP; a later report [71] for the same samples measures ~ 360 ppm of Fe by ICP-MS and provides further experimental evidence that the ferromagnetism is present in the surface region to a depth of ~ 1 μm from SEM-EDX and depth profiling with Auger electron spectroscopy

[iv] attributed to FeB by comparing H_0 for the undoped sample vs. Fe doped samples which both show similar values of H_0, and from ICP measurements

[v] ~ 400 ppm Fe detected by ICP-MS for the range $-0.05 < \delta < 0.05$

[vi] attributed to Fe-B phases, especially due to Fe coming from the ZrO_2 crucible (contains 17-46 ppm of Fe as measured by ICP-MS) used during solid state reaction

[vii] attributed to FeB or Fe_2B (as measured by ICP); the magnitude of the magnetism depends on the crucible used, and virtually disappears upon acid etching; the average M_s for 4 different BN crucibles is listed (ranging from 0 – 50 Am^{-1}) while the average M_s for 4 different ZrO_2 crucibles (0 – 360 Am^{-1}) is listed; only 1 MgO crucible was used

[70] report no ferromagnetism at 300 K (diamagnetism only; $\chi = -2.2 \times 10^{-7}$ emu/g) for CaB_6 single crystals grown in a HCl treated Al flux (HCl helps remove Fe, only ~ 10 ppm Fe remains) – hence it is concluded that any ferromagnetism must be due to Fe and is not intrinsic

[75] report that the Fe impurity content in CaB_6 powder (Kujundo Chemical Lab. Co., Ltd.) and the single crystal grown by the Al-flux method from the powder is ~ 400 ppm and ~ 50 ppm respectively (as measured by both ICP-AES and PIXE); a lower purity CaB_6 powder reveals ~ 2000 ppm of Fe by PIXE (nominal powder purities not given)

Table 5.3. Experimental reports of magnetism attributed to ferromagnetic impurities for doped MB_6; the Al-flux grown samples are single crystalline, the rest are polycrystalline.

Sample	Dopant	Growth method	M_s (A m^{-1})	Explanation proposed	Ref
$Ca_{1-x}La_xB_6$	La, x = 0.0051	Al-flux	50 [i]	Fe impurities	[70]
$Ca_{1-x}La_xB_6$	La, x = 0.015	Al-flux	40 [i]	Fe impurities	[70]
$Ca_{1-x}La_xB_6$	La, x = 0.01	" " (99.99% $CaCO_3$, 99.999% B)	70 (5 K) [ii]	Fe impurities	[68]
$Ca_{1-x}La_xB_6$	La, x = 0.03	" " (99.99% $CaCO_3$, 99.999% B)	~ 5 (5 K) [ii]	Fe impurities	[68]
$Ca_{1-x}Fe_xB_6$	Fe, x = 0.0001	BR (99.99% CaO, B)	245 [iii]	FeB	[73]
$Ca_{1-x}Fe_xB_6$	Fe, x = 0.01	BR (99.99% CaO, B)	19500 [iii]	FeB	[73]

BR = borothermal reduction

[i] for x = 0.0051, 0.015, samples contain 100, 90 ppm Fe respectively (as measured by ICP-MS) and the ferromagnetism vanishes upon acid etching; x = 0.0051 sample also presented in another report [69]
[ii] Fe impurities revealed by ICP-AES; upon acid etching, for x = 0.01, M_s is reduced to 20 A m^{-1}, whereas for x = 0.03 the ferromagnetism vanishes
[iii] attributed to FeB from XRD, ICP and electron probe microscopy measurements

In spite of the numerous reports attributing the ferromagnetism in MB_6 polycrystals and single crystals to iron impurities, most of which appeared shortly after the initial results of Young *et al.* [14], there are also many reports, including most of the recent ones, that propose that the magnetism is actually related to defects instead, as an alternative explanation to the earlier dilute electron-gas and excitonic ferromagnetism hypotheses; it should be emphasized that the latter proposal is now less plausible in light of the now generally accepted semiconducting properties of the MB_6 series. In fact, Young *et al.* in their initial report [14] do actually suggest that the magnetism may also possibly be due to defect states (in addition to their other suggestion of a dilute electron-gas scenario). In further support of defect magnetism, T. Jarlborg calculated a maximum moment of 0.24 μ_B/unit cell for x = 0.125 in $Sr_{1-x}La_xB_6$ using DFT within the LDA-LMTO approach for which a density of states (DOS) with an impurity-like La band was proposed [76]. The same author later reported magnetic moments of order 0.1 μ_B/La impurity for x = 0.125, 0.037 for the same system using the same DFT approach [77], in which it was calculated that while the undoped system has a vanishing DOS at E_F, for La-*d* band doping, E_F enters the band above the gap, while Al and In impurities result in the opposite effect. In a further report using the same approach the same author calculates a moment of ~ 2.1 μ_B/(3×3×3) supercell from 300 – 50 K for undoped SrB_6 [78]. The band results confirm that weak magnetism is possible either as standard Stoner magnetism around a B_6 vacancy or assisted by Coulomb energies near a La impurity, yet the author notes that it is difficult to understand the high T_C values from both of these mechanisms. However, as was mentioned previously, the LDA approach can have difficulty in accurately modelling excited states [49], hence the results of these calculations should be treated with circumspection.

DTF-LDA calculations for CaB_6 by Maiti *et al.* [59] show that impurities (~ 0.3%) in the boron sublattice, vacancies and/or La substitution dope low density charge carriers of 2*p* character which may mediate the magnetism. Both disorder in the boron sublattice and finite conduction electron density are proposed to be important to derive ferromagnetism in the hexaborides. Experimentally in the same report, a room temperature magnetization of ~ 90 A m^{-1} (200 A m^{-1} at 1.8 K) is measured for CaB_6 powders grown by arc-melting of the constituent elements (99.7% purity B used). The authors also calculate a band-gap of 0.2 eV and band insulating properties for CaB_6 in agreement with their high resolution photoemission spectra, although these results are at variance with earlier ARPES experiments which calculate larger semiconducting band gaps of ~ 1 eV for CaB_6 [11, 12, 18, 52]. In a subsequent report for the same system (CaB_6) the same authors calculate a magnetic moment of 0.018 μ_B/f.u. for 8.3% boron vacancies (V_B) using a similar calculation (DFT-LDA), while C and O impurities (expected as impurities in low purity boron) are found to play no significant role in the magnetic moment formation [60]. The introduction of a vacancy in the boron sublattice is proposed to lead to the formation of an impurity band near E_F, which may exhibit finite exchange splitting and a magnetic moment. In contrast to the above reports however, another DFT-LDA calculation finds that defects in CaB_6 (either Ca, B_6 or B vacancies) are not robustly spin-polarized enough to be stable at room temperature, and hence are not likely to mediate ferromagnetism [58]. It must be re-emphasized however that the LDA approach can have difficulty in describing excited states, and as such the results of DFT calculations performed within this framework must be treated with caution.

Elsewhere, a DFT calculation using the GW approximation attributes the magnetism of CaB_6 to a narrow impurity band, with a semiconducting band gap of 0.8 ± 0.1 eV calculated at the *X* point for this material [47]. For DFT-GGA calculations for CaB_6, the magnetism is attributed to boron vacancies [79], in which it is calculated that a neutral V_B carries a moment of 2.4 μ_B and which is further proposed to explain surface magnetism in the alkaline-earth hexaboride crystals, or to B defects and/or impurities [61] (such as C, N), with calculated moments in the range 0.8–1.2 μ_B/(3×3×3) supercell. In particular, for the last two reports mentioned [79,61], it is thought that the spin-splitting of the flat defect bands due to the strong exchange interactions in the B *p*-shell is responsible for the high temperature ferromagnetism, further to earlier susceptibility calculations of a wide range of a wide range of metallic elements [80]. Another DFT-GGA calculation for MgB_6, but including additional atomic self-interaction corrections, calculates that boron vacancies are responsible for magnetism in semiconducting MgB_6 (band gap = 0.5 eV), for which a moment of 0.5 μ_B/(2×2×2) supercell for 1 V_B is calculated [62]. In practice however, it is important to note however that the MgB_6 phase does *not* occur at equilibrium, and has only been observed as inclusions of a secondary phase during MgB_2 growth in high resolution TEM images [81].

Hotta *et al*. [53,54] attributed the magnetism of CaB_6 to surfaces/defects associated with the removal of cubic symmetry for the distorted tetragonal crystal structure, as deduced from molecular orbital theory (mean field approximation of the extended Hubbard model). In the latter paper however the authors also proposed that a single pair of semi-metallic (not semiconducting) bands is necessary for ferromagnetism, although they rule out the stability of an excitonic phase.

Edwards and Katsnelson [82] developed the idea of a narrow spin-split impurity band for CaB_6 (but applicable to carbon and boron systems in general), which could be formed from defect states and give rise to high-temperature Stoner ferromagnetism if the density of states of such a band is large enough near E_F. Such a band model may resolve the question of why both doped and undoped hexaboride samples have been found to be ferromagnetic, since it is the intrinsic defects themselves rather than any dopants which mediate the magnetism. In addition, the magnetism is independent of whether or not the defects responsible for the impurity band are ferromagnetic impurities.

Table 5.4 below provides an up to date summary of theoretical calculations which calculate magnetic moments for the divalent hexaborides.

Table 5.4. Summary of theoretical calculations which predict ferromagnetism in MB_6.

Method	System	Maximum moment calculated [i]	Ref
Deduced from band-structure arguments	$Ca_{1-x}La_xB_6$	~ 0.14 μ_B/doped electron (x = 0.0035)	22
" " " " "	$Ca_{1-x}La_xB_6$	~ 1 μ_B/La	24
" " " " "	Divalent hexaborides, both pure and La doped	Maximum moment for x = 0.005, magnitude not given	29
Mean field theory	Divalent hexaborides, pure and doped	0.4 μ_B/carrier (x = 0.04)	33
Hubbard Model	$Sr_{1-x}La_xB_6$	0.9 μ_B/f.u.	37
Stoner theory of Ferromagnetism	CaB_6	0.1 μ_B/B	82
DFT-LDA [ii]	CaB_6	0.018 μ_B/f.u. (for 8.3% V_B)	60
DFT-LMTO	$Sr_{1-x}La_xB_6$	0.24 μ_B/unit cell (x = 0.125) [iii]	76
DFT-LMTO	$Sr_{1-x}La_xB_6$	~ 0.1 μ_B/La impurity (for x = 0.125, 0.037)	77
DFT-LMTO	SrB_6	2.1 μ_B/(3×3×3) supercell (50 – 300 K) [iv]	78
DFT-LMTO	MB_6 (M = Ca, Sr, Ba, Yb, La), $Ba_{1-x}La_xB_6$ (x = 0.05)	At 10 T, $Ba_{1-x}La_xB_6$ (x = 0.05) ~ 2×10^{-4} μ_B, YB_6 ~ 2.5×10^{-4} μ_B, LaB_6 ~ 3×10^{-4} μ_B	44
DFT-GGA	CaB_6	neutral V_B carries a moment of 2.4 μ_B	79
DFT-GGA	CaB_6	0.8-1.2 μ_B/(3×3×3) supercell	61
DFT-GGA [v]	MgB_6	0.5 μ_B/(2×2×2) supercell for 1 V_B	62

[i] In comparison, Young *et al.*[14] measured 0.07 μ_B/La (x = 0.005) at 5 K for $Ca_{1-x}La_xB_6$ single crystals in the first experimental report for ferromagnetism in the divalent alkaline earth hexaborides
[ii] In contrast, another DFT-LDA calculation [58] reports that defects (Ca, B_6 or B vacancies) are not robustly spin-polarized enough to be stable at room temperature
[iii] > 50 % of moment on or near the La impurity
[iv] ~ 40 % of the total moment comes from the six B sites closest to the vacancy
[v] including atomic self-interaction corrections

Further to the (mostly) theoretical reports for defect magnetism mentioned just previously, some experimental reports also propose an intrinsic defect/impurity related magnetism from their measurements. As mentioned previously, in response to claims that the magnetism in hexaborides is due to iron contamination, some of the authors of the Young *et al.* [14] report responded by attributing the magnetism in semiconducting $Ca_{1-x}La_xB_6$ crystals grown by the Al-flux method to intrinsic defects on the Ca and/or B sublattice that form during crystal growth, some of which may bear a magnetic moment [67]. An electron spin resonance study of $Ca_{1-x}La_xB_6$ disks (x = 0.005) with (100) crystallographic orientation and cleaved from single crystals grown by the Al-flux method attributes the magnetism to surface layer spins of ~ 1.5 μm depth, and reports a very large M_s equivalent to 23.6 kA m^{-1} at 300 K [83]. However, several electron spin resonance studies conducted by Urbano *et al.* [84-87] for $Ca_{1-x}M_xB_6$ (M = Gd, Eu, $0.0001 \leq x \leq 0.3$) single crystals grown by the Al-flux method do not reveal any evidence of weak ferromagnetism in the spectra measured at 4-300 K, despite measuring magnetization values of 120, 60 and 55 A m^{-1} at 150 K for Gd doped samples where x = 0.0003, 0.003 and 0.01 respectively [84, 85]; it is suggested that the ferromagnetism may be isolated in clusters of defect-rich regions. In another report detailing the results of an NMR study of SrB_6 and $Ca_{1-x}La_xB_6$ crystals, the authors are unsure which mechanism is responsible for the magnetism, whether excitonic (band overlap/small gap at *X* point) or impurity related (large gap at *X* point), but suggest the latter from their low temperature (< 4 K) NMR data [88]. A low temperature (< 30 K) NMR study for SrB_6 tentatively attributed the weak itinerant ferromagnetism, estimated to be less than 10^{-2} μ_B/cell, to excitations of "small-moment ordering", but did not elaborate further [89].

Lofland *et al.* [90] attributed the magnetism of their CaB_6 powders, both purchased from Alfa Aesar and synthesized by solid state reaction, which both exhibited a room temperature magnetization of ~ 1 kA m^{-1} in a 1 T applied field, to either impurities or vacancies of B_6 clusters. For thermal magnetization measurements performed in an argon atmosphere, the magnetic signal was reduced by ~ 20 % compared to the measurements performed in air, from which it was proposed that heating in air (compared to argon) creates more defects and enhanced magnetism. In another experimental report, a room temperature magnetization of ~ 50 A m^{-1} is measured for CaB_6 polycrystals synthesized by heating "spectra-pure" CaO + B in argon (borothermal reduction) [45]; energy electron loss spectroscopy (EELS) measurements reveal features associated with B *p* orbitals hybridized with Ca *d* orbitals (i.e. band overlap). Another report attributes the magnetism of $Ca_{1-x}La_xB_6$ (x = 0.01) single crystals grown from a molten Al-flux using 99.9% purity (3N) boron, which exhibit a virtually temperature independent magnetization of ~ 210 A m^{-1} measured at both 5 K and 300 K , to boron-related defects which induce mid-gap states at about 0.2 eV below the conduction band and extra free charge carriers [56,57] (note that magnetization data is presented only in the earlier archived version of the paper [56]). Ferromagnetism is measured for a narrow range of La doping only, ~ 0.5 – 2.0 %. No ferromagnetism is measured for similarly grown crystals using a higher purity 99.9999% (6N) boron powder precursor; similar results were also published elsewhere [91] by the same authors, in which stoichiometric CaB_6 (3N) and boron rich $CaB_{6+\delta}$ (3N) crystals have room temperature magnetization values of ~ 10 A m^{-1} and ~ 15 A m^{-1} respectively, whereas no ferromagnetism was measured for boron deficient $CaB_{6-\delta}$ (3N) crystals. ARPES

measurements of MB_6 (M = Ca, Sr, Eu) single crystals revealed that the positioning of the bulk chemical potential in the conduction band and the resulting n-type carriers observed in nominally stoichiometric samples implicate the presence of boron vacancies, and that the physics of the divalent hexaborides is not that of an intrinsic semimetal, but that of a defect semiconductor, due to the bandgaps of ~ 1 eV measured [11, 12].

It has also been reported that CaB_6 and BaB_6 polycrystals prepared by solid state reaction using 99.995% boron do not exhibit ferromagnetism as a bulk property as measured by SQUID magnetometry, but show evidence of an enhanced muon relaxation rate correlated with enhanced short range magnetic moments of ~ 3.2×10^{-3} μ_B/B below 130 K and 110 K for CaB_6 and BaB_6 respectively, as measured by muon spin rotation spectroscopy by Kuroiwa *et al.* [92]. Meanwhile a report for CaB_6 single crystals synthesized under high pressure (1 GPa) and temperature (1050 °C) measured paramagnetism only at 300 K ($\chi = 5.45\times10^{-9}$ cm^3/g) with no trace of ferromagnetism for samples synthesized using either 99.99% or 99.9999% purity boron [93].

Tables 5.5 & 5.6, spread out over the next two pages for the sake of clarity, summarise experimental reports which ascribe the magnetism of undoped and doped MB_6 samples respectively to intrinsic magnetism (and not ferromagnetic impurities). M_s is measured at room temperature unless stated otherwise, while the reagent purity is given where available.

Table 5.5. Experimental reports of intrinsic magnetism for undoped MB_6.

Sample	Form	Growth method	M_s (A m^{-1})	Explanation proposed	Ref
CaB_6 [i]	SC	Al-flux	55 (30 K)	Excitonic magnetism	27
CaB_6	SC	Float zone	4	low density electron gas	18
CaB_6	SC	Al-flux (99.9% boron) [ii]	10	Boron related defects + extra free charge carriers	91
$CaB_{6+\delta}$	SC	Al-flux (99.9% boron) [ii]	15	" "	91
SrB_6	SC	Al-flux	75	defects on Ca and/or B sublattice	67
$YbB_{6-\delta}$ ($\delta \approx 0.3$)	SC	Al-flux (99.99% Yb, 99.9999% B)	15 [iii]	Surface defects/off-stoichiometry	94
YbB_6	SC	Not given	~ 230 (6 K) [iv]	Not given	95
CaB_6	PC	BR (99.99% CaO, B)	22 [v]	Ca vacancies + associated symmetry lowering	64
CaB_6	PC	BR ("spectra-pure" CaO, B)	50	EELS feature associated with hybridized B *p* and Ca *d* orbitals	45
YbB_6	PC	BR	8 (150 K) [vi]	surface defects	96
CaB_6	Powder	Purchased from Alfa A./solid state reaction	950 (in 1 T) [vii]	impurities or vacancies of B_6 clusters	90
CaB_6	Powder	Arc melting of elements (99.7% boron)	90 [viii]	impurities (~ 0.3%) and disorder in B sublattice + low conduction electron density at E_F	59

SC = single crystal, PC = polycrystal, BR = Borothermal reduction

Young *et al.* [14] report that for *undoped* MB_6 (M = Ca, Sr, Ba) single crystals grown by the Al-flux method, moments were at least an order of magnitude smaller than that found for La-doped samples at 5 K, corresponding to $M_s \leq 5$ A/m (at 5 K) – it was suggested that the magnetism may be attributed to defect states or to the ferromagnetic polarization of the low-density electron gas

[i] Contains Ca vacancies - stoichiometric phase did not exhibit any ferromagnetism (at 2 K)
[ii] no ferromagnetism measured when 99.9999% purity boron used; similar results also presented elsewhere [56,57]
[iii] magnetism vanishes upon acid etch; YbB_6 and $YbB_{6+\delta}$ crystals revealed diamagnetism and paramagnetism at 300 K respectively
[iv] Ferromagnetic signal of similar magnitude reported up to 300 K (hence $T_c >> 300$ K); a similar low temperature (< 30 K) NMR study for SrB_6 [89] single crystals tentatively attributes the weak itinerant ferromagnetism, estimated to be < 10^{-2} μ_B/cell, to excitations of "small-moment ordering"
[v] average M_s (ranging from 5-50 A m^{-1}) of 4 samples is given, which were heated at 1500 °C in boron nitride (BN) crucibles for durations of 3–24 h; M_s ~ 500 A m^{-1} at 90 K; the stoichiometric phase prepared at 1200 °C was diamagnetic – note that the claim of defect ferromagnetism was subsequently retracted in favour of extrinsic ferromagnetic impurity phases [65]
[vi] M_s = 1 A m^{-1} at 200 K
[vii] as measured in air; moment reduced by ~ 20 % in argon
[viii] M_s = 200 A m^{-1} at 1.8 K

Table 5.6. Experimental reports of intrinsic magnetism for doped MB_6; all single crystals unless stated otherwise.

Sample	Dopant	Growth method	M_s (A m^{-1})	Explanation proposed	Ref
$Ca_{1-x}La_xB_6$	La, x = 0.005	Al-flux	45 (5 K) [i]	low-density electron gas or defects	14
$Ca_{1-x}Th_xB_6$	Th, x = 0.0025	Al-flux	30 (5 K) [ii]	" "	14
$Ca_{1-x}La_xB_6$ [iii]	La, x = 0.005	Al-flux	28 (30, 50 K)	" "	15
$Ca_{1-x}La_xB_6$	La, x = 0.01	" " (99.9% boron [iv])	210	Boron related defects + extra free charge carriers	57
$Ca_{1-x}La_xB_6$	La, x = 0.01	" " (99.9% boron)	200 [v]	Boron related defects	91
$Ca_{1-x}La_xB_6$	La, x=0.005	Al-flux	1200 (25 K at 0.1 T) [vi]	defects on the Ca and/or B sublattice	67
$Ca_{1-x}La_xB_6$	La, x = 0.005	Al-flux	180 (5 K)	super-paramagnetism	20
$Ca_{1-x}La_xB_6$	La, x = 0.005	Float zone	20	super-paramagnetism	20
$Ca_{1-x}Gd_xB_6$	Gd, x = 0.0003	Al-flux	120 (150 K) [vii]	clusters of defect-rich regions	84
$Yb_{1-x}La_xB_6$ [viii]	La, x = 0.003	Borothermal reduction	8 (150 K) [ix]	surface defects	96

[i] Maximum M_s given; M_s ranges from 10-45 A m^{-1} (at 5 K) for x = 0.0023–0.01; Similar trend measured for $M_{1-x}La_xB_6$ (M = Sr, Ba) and $Sr_{1-x}M_xB_6$ (M = Ce, Sm) with maximum M_s measured at x = 0.005 (magnitude of M_s not given however)
[ii] Maximum M_s given; for x = 0.005, M_s = 5 A m^{-1} (at 5 K)
[iii] data from [14] also reported here
[iv] no ferromagnetism measured when 99.999% purity boron used
[v] Maximum M_s given; M_s = 14, 40 A m^{-1} for x = 0.005, 0.02 respectively
[vi] Maximum M_s given, for which M_s ~ 20 % smaller at 300 K in 0.1 T; M_s = 400 A m^{-1} (at 0.1 T) for x = 0.0075
[vii] Maximum M_s given; M_s = 60, 55 A m^{-1} (at 150 K) for x = 0.003, 0.01 respectively; same data also published elsewhere [85]
[viii] Polycrystal
[ix] M_s = 1 A m^{-1} at 200 K; similar signals measured for x = 0 – 0.006; for single crystals grown by the float-zone method, diamagnetism was measured for x ≤ 0.003 and paramagnetism for x = 0.005

Whereas most of the reports for RTFM in divalent hexaborides are for single crystals, polycrystals or powders, there are also a few reports for films, in which the magnetism is attributed to defects. For a 1.2 μm thick $Ca_{1-x}La_xB_6$ film grown by magnetron sputtering on Si(100) in argon, M_s ~ 5.5 kA m^{-1} at room temperature for x = 0.005 as reported by Sakuraba *et al.* [97]. The magnetism is attributed to defects from anisotropic lattice expansion (lowering of the lattice symmetry) associated with the introduction of argon gas, with the sample containing 0.35 at. % trapped argon exhibiting RTFM. In comparison, no RTFM was measured for a sample with much less (0.01 at. %) trapped argon; similar structural results are also presented elsewhere by the same authors [98]. For thin films grown by pulsed laser deposition in vacuum from 99.5% purity MB_6 (M = Ca, Sr) targets

by Dorneles *et al.* [99], even larger room temperature magnetization values were measured, for example, 10.9 kA m^{-1} and 9.5 kA m^{-1} for in-plane and out-of-plane measurements respectively for a 310 nm thick SrB_6 film grown on an MgO (100) substrate. For a 150 nm thick CaB_6 film grown on Al_2O_3 (0001), M_s ~ 30.2 kA m^{-1} for the out-of-plane measurement. Films grown on MgO (100) substrates were crystalline, whereas those grown on Al_2O_3 (0001) were amorphous. The magnetism, proposed to be located within a thin layer ~ 10 nm thick at the substrate/film interface, was attributed to a defect impurity band which mediates a long-range ferromagnetic interaction between the magnetic moments associated with molecular orbitals in the vicinity of the defects. Typical magnetization curves published in the above two reports by Sakuraba *et al.* [97] and Dorneles *et al.* [99] for alkaline-earth hexaboride films are shown in Figure 5.3 below, while a simple schematic of an interfacial defect layer structure proposed by Dorneles *et al.* to be applicable to thin film nanostructures is displayed in Figure 5.4. Dorneles *et al.* [99] measure a pronounced out-of-plane (perpendicular to film surface) demagnetizing effect for SrB_6 grown on MgO (100).

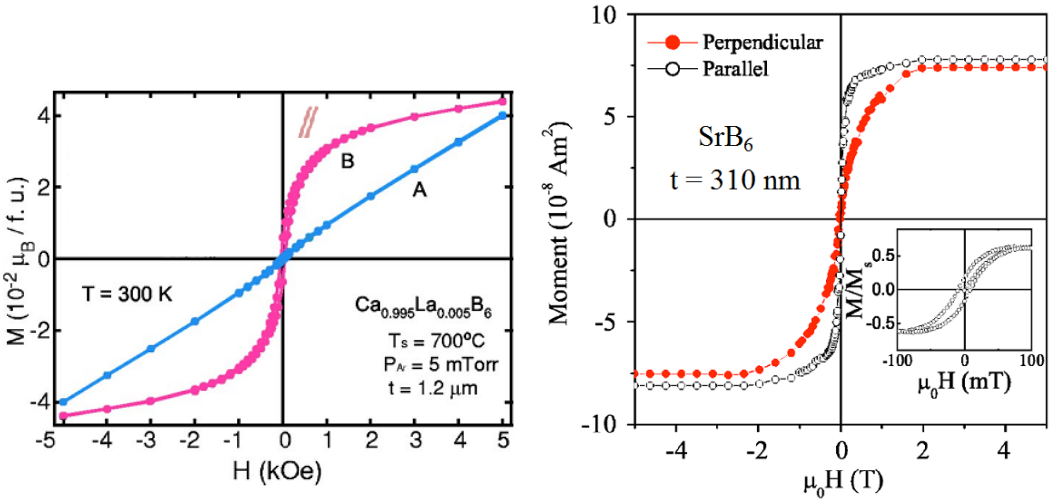

Figure 5.3. First two experimental reports for RTFM in alkaline-earth hexaboride films published by (left) Sakuraba *et al.* [97] who present typical in-plane magnetization curves (films A and B contain 0.01 and 0.35 at% Ar respectively) and by (right) Dorneles *et al.* [99] for in and out-of-plane measurements. Note that 1 kOe is equivalent to 0.1 T.

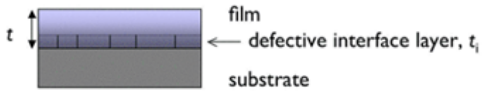

Figure 5.4. Simple schematic depicting a possible origin of RTFM in MB_6 thin film nanostructures due to an interfacial defect-rich layer residing at the thin film-substrate interface.

Table 5.7 summarizes experimental reports for RTFM in MB_6 films. M_s for in-plane (∥) and out-of-plane (⊥) measurements is denoted. Data published as part of this thesis by Ackland *et al.* [100,101] are also included, which are presented in the experimental results section (5.3).

Table 5.7. Experimental reports of RTFM for MB_6 films.

Sample	Thickness (nm)	M_s (kA m^{-1})	Ref
$Ca_{1-x}La_xB_6$ [i]	~ 14000	23.6 ∥	83
$Ca_{1-x}La_xB_6$ [ii]	1200	5.5 ∥	97
CaB_6 [iii]	150	30.2 ⊥	99
SrB_6 on MgO (100)	310	9.5 ⊥	99
SrB_6 on MgO (100)	310	10.9 ∥	99
BaB_6 [iv]	100	10.7 ∥	100
CaB_6	100	6.0 ∥	101
CaB_6	5	344 ∥	101
SrB_6	100	10.8 ∥	101
SrB_6	5	376 ∥	101
BaB_6	100	14.8 ∥	101
BaB_6	100	14.8 ⊥	101
BaB_6	5	120 ∥	101

[i] x = 0.005, disk cleaved from single crystal grown by Al-flux method – magnetism attributed to surface layer spins (~ 1.5 μm depth)
[ii] x = 0.005, film deposited by magnetron sputtering on Si(100) in argon – magnetism attributed to defects from anisotropic lattice expansion due to 0.35 at. % trapped Ar
[iii] (including all samples listed in rows below, unless stated otherwise) thin film grown by PLD on 5×5 mm Al_2O_3 (0001) crystalline substrate - magnetism attributed to a defect impurity band
[iv] maximum M_s listed for sample grown at 550 °C

For YbB_6, a divalent hexaboride which is structurally similar to the alkaline earth hexaborides but contains a rare earth cation (Yb^{2+}) instead of an alkaline earth cation, the magnetism of both pure and La doped (0.3 at. %, 0.6 at. %) polycrystals synthesized by borothermal reduction, for which small magnetizations of 8 A m^{-1} at 150 K (1 A m^{-1} at 200 K) were measured, was associated with the surface and proposed to be intrinsic [96]. The ferromagnetic polycrystals also exhibited increased internal fields upon cooling below 150 K by muon spectroscopy, suggesting that T_c ~ 150 K. The corresponding single crystals grown by the float zone method were diamagnetic, in agreement with earlier results for C doped YbB_6 crystals grown by the same method [9]. Conversely, other magnetization measurements of randomly orientated millimetre size single crystals (growth method not disclosed) revealed magnetizations of ~ 230 A m^{-1} at both 6 K and 300 K, providing evidence that T_c >> 300 K [95]; however, no explanation for the ferromagnetism was given. Elsewhere, for boron deficient $YbB_{6-\delta}$ (δ ~ 0.3) single crystals grown from the molten Al-flux using 99.9999 % purity boron, RTFM with a magnetization of ~ 15 A m^{-1} was measured [94]. The magnetism vanished upon acid etching (using HNO_3), while ferromagnetic impurities were ruled out as a source of the magnetism. Stoichiometric and boron rich ($YbB_{6+\delta}$) crystals were diamagnetic and paramagnetic respectively. The authors noted that while defects and off-stoichiometry in $YbB_{6-\delta}$ cause a carrier doping effect, they could not conclude what surface state created the magnetic signals. A summary of the above experimental results are included in Tables 5.5 & 5.6 shown previously. It is noted that none of the other rare earth hexaborides previously

discussed, namely EuB_6 and SmB_6, display any high temperature ferromagnetism.

Finally, it is mentioned that experimental reports of RFTM have also appeared for tetragonal CaB_2C_2, the first for a micropowder synthesized by heating the 99 % purity constituent elements in Ar [102]. M_s ~ 50 A m^{-1} at 5 K and ~ 30 A m^{-1} at 300 K. Using DFT-LDA calculations, the band overlap is calculated to be 0.64 eV for the simple tetragonal *P*4/*mbm* phase (semi-metal), and the band gap 0.43 eV for the body-centered tetragonal *I*4/*mcm* phase (semiconducting). The reason that this compound is mentioned is because it was argued on the basis of the above findings that the disputed threefold degeneracy specific to the cubic structure in the energy bands of divalent hexaborides is not essential for high-temperature ferromagnetism, and instead it was argued that the peculiar properties of the molecular orbitals near E_F appear to be crucial [102]. In contrast, for a subsequent experimental report that used 99.9% higher purity elements to synthesize the same compound, only diamagnetism was found in the range 300 – 2 K with $\chi = -2.6 \times 10^{-7}$ emu/g, and no trace of any ferromagnetic-like signal was measured [103]. The measured Fe content in the sample was < 10 ppm (as determined by ICP-AES analysis), and the authors proposed that the magnetism reported by [102] is likely due to ferromagnetic impurities. In a later theoretical paper using DFT-LMTO it was calculated [44] that the tetragonal phase of CaB_2C_2 possesses a small band overlap (semi-metallic, in agreement with [102]) and a moment of 2×10^{-4} μ_B in a 10 T applied field.

5.3. Experimental results

5.3.1 MB_6 powder synthesis and structural characterization (XRD, SEM)

MB_6 (M = Ca, Sr, Ba) powders were synthesized from high-purity elemental powders by solid state reaction at 1000 °C in evacuated sealed quartz tubes (10^{-5} mbar). The nominal purity of the Ca used was 99.5% while the Ba and Sr were of 99.9% nominal purity. The nominal purity of boron used was 99.7%. The resultant MB_6 powders were purple in colour, containing shiny specks visible to the eye, indicating the presence of large microcrystals. X-Ray powder diffraction (XRD) and subsequent Rietveld refinement together with scanning electron microscopy (SEM) confirmed that the hexaboride powders were microcrystalline cubic (*Pm-3m* space group), faceted, and single phase, as shown in Figure 5.5 on the following page. The lattice parameters for CaB_6 (4.1492 Å), SrB_6 (4.1965 Å) and BaB_6 (4.2671 Å) and were close (within ~ 0.1 %) to the respective reference values of 4.1535 Å, 4.1930 Å and 4.2624 Å found in the Powder Diffraction File (PDF) database.

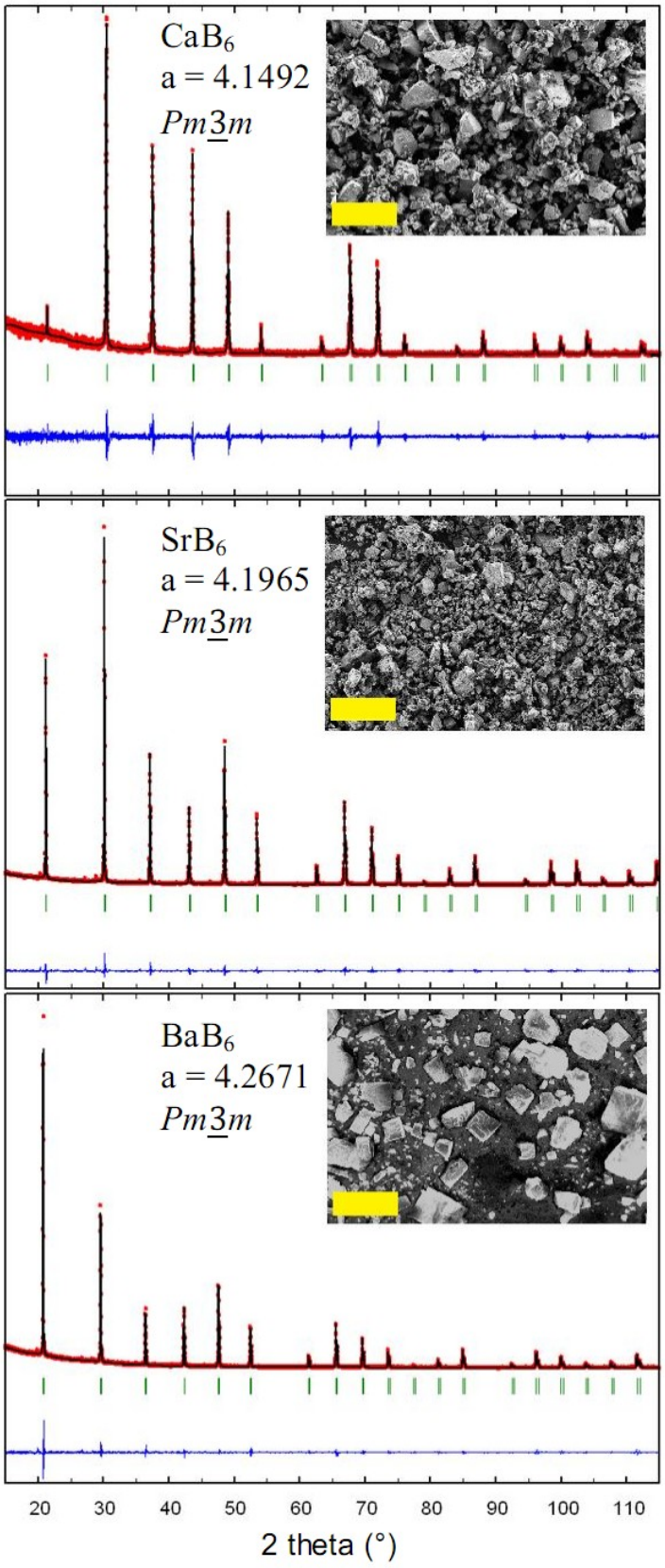

Figure 5.5. X-Ray powder diffraction profiles with Rietveld fits for crystalline MB_6 powders, with (insets) SEM images of powders (scalebar = 100 µm).

5.3.2 MB_6 thin film growth and initial structural characterization (XRD, XRR)

Thin films of MB_6 were grown by pulsed laser deposition (PLD) and initially characterized by both X-Ray diffraction (XRD) and X-Ray reflectivity (XRR).

As outlined in the experimental methods (Chapter 2, section 2.3), in order to fabricate targets for PLD, the synthesised hexaboride powders were ground, pressed in a 13 mm stainless steel die using a 10 ton press, and sintered under vacuum at 10^{-5} mbar for 12 hours at 950 °C. The target densities were typically ~ 60 % of the theoretical (maximum) values. Optical images of the targets are displayed in Figure 5.6. Upon closer inspection, shiny specks could be resolved on the target surfaces indicative of microcrystals, which were also previously resolved in the MB_6 powders by SEM.

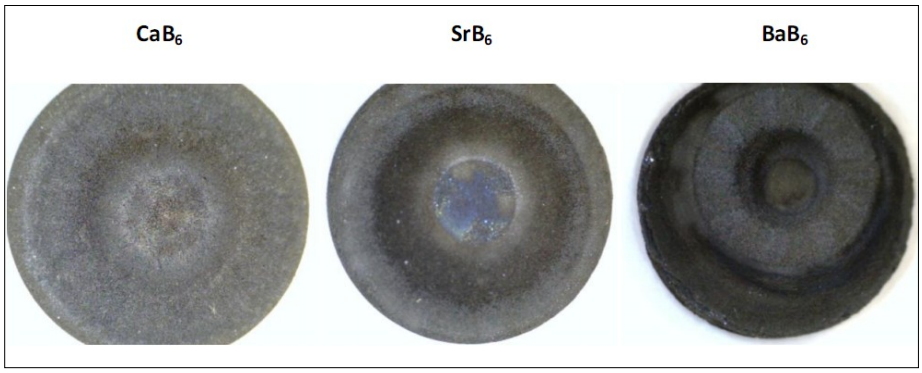

Figure 5.6. Optical images of MB_6 targets (ø = 13 mm). Pitting due to laser impingement upon the surface during PLD processing is visible.

Thin films were deposited by PLD using a 248 nm wavelength KrF excimer laser on (mostly) 5×5×0.5 mm^3 slices of high purity (> 99.99%) singe-crystal Al_2O_3 (0001) (c-cut) polished on one side, mounted on a non-magnetic ceramic substrate holder using Ag paint. Sapphire (Al_2O_3) substrates have a low impurity content and are quite chemically inert (compared to silicon for example), which means that chemical reactions between substrate and film, the formation of unwanted mixed phases at elevated temperatures and the formation of interfacial layers is minimized, in addition to allowing lower deposition temperatures to be used to obtain crystalline films (here the films grown are actually *amorphous* rather than crystalline – discussed more later). Films were deposited on the polished (shiny) side of the substrate, and hence the side on which the film was deposited could be easily distinguished from the rough (and dull) unpolished backside. Some films were also deposited on sapphire substrates of other crystal orientations including r-cut (1102) and m-cut (1010), as well as on 5×5×0.5 mm^3 slices of (100) MgO single-crystal (also > 99.99% purity), for which the typical

impurity concentration (ppm) is given by the supplier as Fe ≤ 50, Ca ≤ 40, Al ≤ 15, Si ≤ 10, C ≤ 10, Cr ≤ 10 and B ≤ 5. The lattice parameter mismatch is 10.4 % for BaB_6 (a = 4.262 Å) grown on Al_2O_3 substrates (a = 4.759 Å), with the film/substrate mismatch increasing slightly for SrB_6 (a = 4.193 Å) and CaB_6 (a = 4.153 Å). For MgO substrates (a = 4.217 Å), the lattice parameter is more similar to those of the MB_6 films. For low energy muon experiments, films were grown on Al_2O_3 (0001) substrates of larger area (10×10×0.5 mm^3) in order to improve the signal to noise ratio of the measurement. All substrates were purchased from MTI Corporation (mtixtl).

For PLD growth of the films, substrates were first heated in the PLD vacuum chamber to 800 °C in 0.3 mbar of O_2 for 15 minutes in order to outgas any impurities before film deposition. The targets were pre-ablated at the maximum laser repetition rate of 20 Hz for 3-5 minutes immediately prior to deposition in order to remove some of the surface of the target and thus present the pristine material beneath for ablation and film growth. Typical deposition parameters used were an energy density of 6 J cm^{-2} (well above the ablation threshold), a laser repetition rate of 6 Hz, and a deposition pressure of order 10^{-6} mbar in order to grow thermodynamically stable MB_6 films within the experimental range of substrate temperatures (300 – 850 °C) at which films were deposited [104]. The laser "spot" is actually rectangular in shape of area ~ 0.03 cm^2, while the laser energy used was typically 200 mJ. The target to substrate distance was fixed at 70 mm. Thicker films (of order 100 nm) had a greenish tinge after deposition; thinner films (of order 10 nm) were colourless. All films were transparent. The low densities of the targets combined with the high ablation energy densities used for deposition favours the formation of non-crystalline, defect-rich films.

XRD measurements of the deposited films indicated that they were almost amorphous when grown on Al_2O_3 (0001) since either no or very faint Bragg peaks due to the MB_6 crystal lattice were resolved. Figure 5.7 illustrates the similarity between the XRD data for a BaB_6 film and the Al_2O_3 (0001) susbtrate on which it was grown.

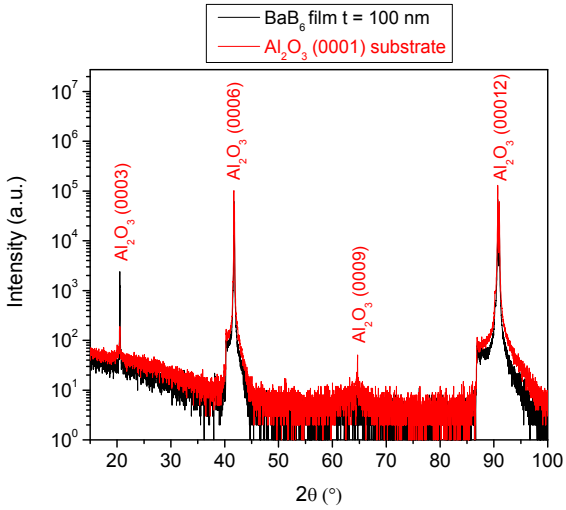

Figure 5.7. XRD data for a BaB_6 film grown by PLD compared to that for the blank Al_2O_3 (0001) substrate on which the film was grown.

The peak at 20.5° 2θ in Fig. 5.7 may be assigned to the Al_2O_3 (0003) reflection, whereas that for BaB_6 (100), although close to this value, falls at the slightly higher angle of 20.83°. For some substrates and films the Al_2O_3 (0003) reflection was not resolved, whereas the most intense Al_2O_3 (0006) and Al_2O_3 (0012) were always resolved. Possible higher angle (200), (300) and (400) reflections for BaB_6 would be hidden within those due to the Al_2O_3 substrate and hence they cannot be distinguished. No other reflections from other lattice planes of BaB_6 were resolved.

CaB_6 and SrB_6 films were also measured to be amorphous by XRD, as shown in Figure 5.8. The (100) reflection for CaB_6 and SrB_6, which was not resolved for either film, occurs at 21.38° and 21.13° respectively. These results are in agreement with previous XRD results of Dorneles *et al.* [99] which also found that films of CaB_6 and SrB_6 grown by PLD on Al_2O_3 (0001) substrates were amorphous. The reflection at 27-28° cannot be assigned to either of the films since no known reflection from either CaB_6 or SrB_6 falls within this range; this reflection is hence assigned to the substrate, and may correspond to the (0004) forbidden reflection of Al_2O_3, which was also resolved in some cases for blank Al_2O_3 (0001) substrates in addition to the more intense reflections of the same family of planes.

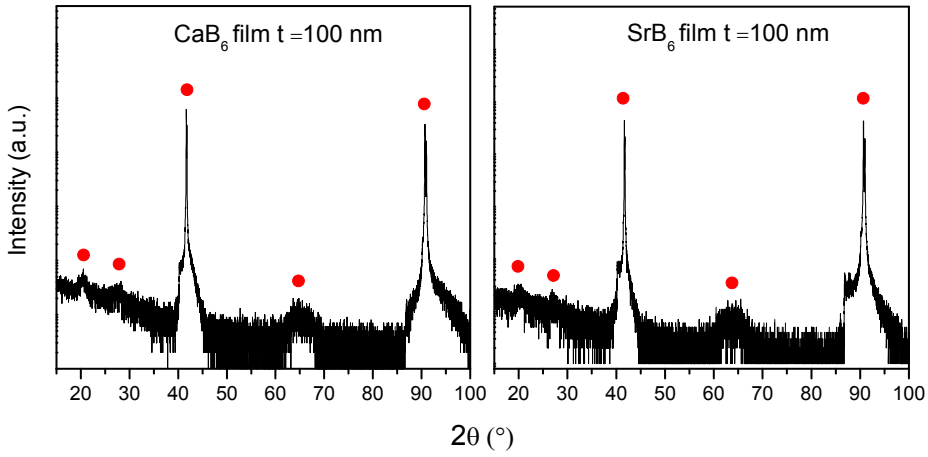

Figure 5.8. XRD data for CaB_6 and SrB_6 films grown by PLD grown on Al_2O_3 (0001) substrates – red dots denote the Al_2O_3 substrate reflections.

For BaB_6 films grown on MgO (100), no Bragg peaks due to the film may be resolved since the (100) family of planes for BaB_6 are all overlapped by the substrate reflections as shown in Figure 5.9, and hence it cannot be deduced conclusively from XRD whether the films are crystalline or amorphous.

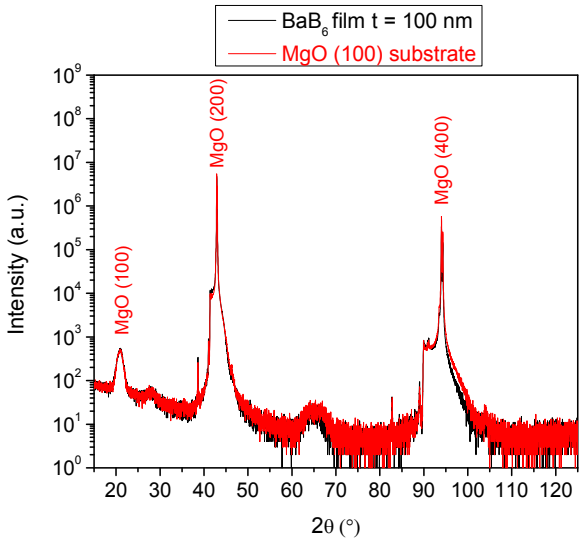

Figure 5.9. XRD data for a BaB_6 film grown by PLD compared to that for a blank MgO (100) substrate on which the film was grown.

For BaB_6 films grown on Al_2O_3 substrates, film thicknesses were estimated by either ellipsometry or by viewing FIB-SEM or TEM cross-sections, whereas for CaB_6 and SrB_6 films the thickness could be measured more directly by XRR. The thickness of BaB_6 films could not be measured by XRR since the densities of BaB_6 (4360 kg m^{-3}) and Al_2O_3 (3980 kg m^{-3}) are too similar, whereas those of CaB_6 (2400 kg m^{-3}) and SrB_6 (3390 kg m^{-3}) are dissimilar enough from the substrate to allow small angle interference fringes (oscillations) to be resolved; one of the prerequisites of the XRR technique is that the densities of film and substrate must differ. Representative XRR data for CaB_6 and SrB_6 films is shown in Figure 5.10. It is noted that the film densities are closer to the theoretical (maximum) values than the corresponding targets.

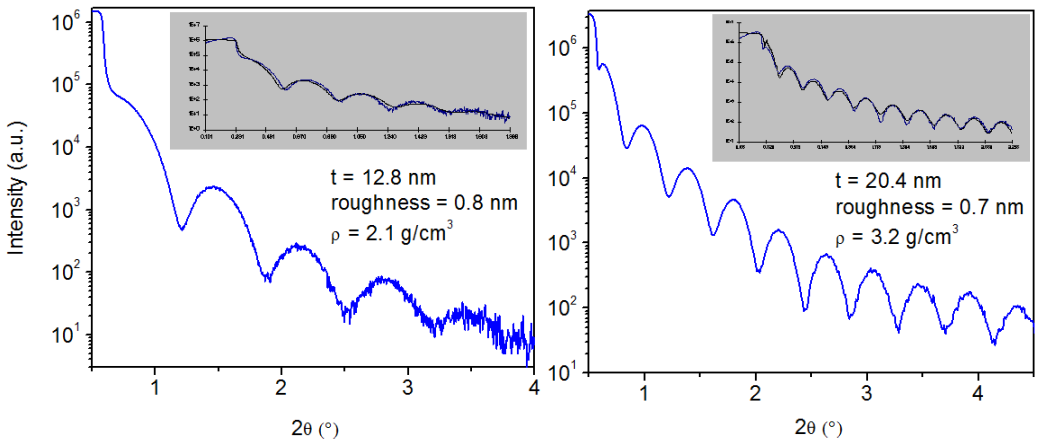

Figure 5.10. XRR data for CaB_6 (left) and SrB_6 (right) films grown by PLD on Al_2O_3 (0001) substrates; the insets show the experimental data fitted using the WinGixa XRR fitting software. The experimental data and fits are denoted by blue and black lines respectively.

5.3.3 Electrical properties - IV characterization

Electrical measurements of the amorphous magnetic MB_6 thin film samples (t ~ 100 nm) at room temperature using the four point probe method revealed that while BaB_6 was barely conducting, with a resistivity of order 50 Ω cm and exhibiting linear current-voltage dependence in the range ± 0.3 V, CaB_6 and SrB_6 were insulating. It is noted that Dorneles *et al.* [99] also measured their PLD-grown CaB_6 and SrB_6 films to be insulating, but upon subsequent in-situ annealing in the vacuum chamber after deposition, their CaB_6 and SrB_6 films exhibited a small resistivity of order 5 Ω cm and 50 Ω cm respectively. The BaB_6 films exhibited a decrease in conductivity with decreasing temperature, corresponding to semiconducting-like behaviour, as shown in Figure 5.11. The high temperature slope in Fig. 5.5 (b) may be used to estimate the bandgap (E_g), since the slope corresponds to E_g/2k for intrinsic semiconductivity, which yields E_g ~ 0.3 eV. In addition, the thin films did not exhibit any magnetoresistance in an applied field of ± 2 T at room temperature when measured (neither did CaB_6 or SrB_6 in a previous PLD study by Dorneles *et al.* [99]). It is noted that *crystalline* epitaxial films of BaB_6 (100) grown on MgO (001) substrates by molecular beam epitaxy (MBE) elsewhere were also measured to be semiconducting, with a smaller resistivity of 0.3 Ω cm measured at room temperature [105].

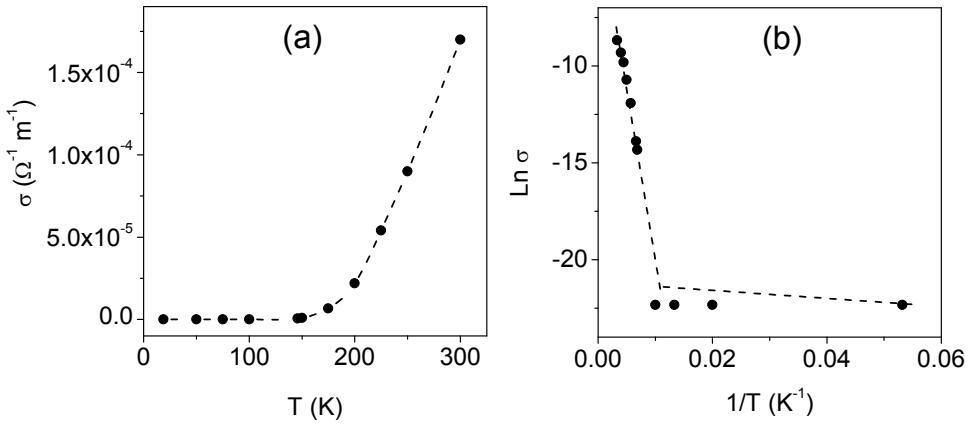

Figure 5.11. Thermal conductivity data measured for ~ 100 nm thick magnetic BaB_6 film grown on Al_2O_3 (0001). The dashed line in (b) shows the general trend expected for semiconducting behaviour.

5.3.4 Magnetization data

Firstly, a comprehensive magnetic and impurity analysis of the precursor materials was undertaken. This is particularly important since the magnetic signals measured for the thin films are often small and hence the contribution of ferromagnetic impurities or extrinsic contamination to the signal must be fully accounted for in order to be able to make a convincing claim that the magnetism is intrinsically defect-related. The magnetization of the 99.7% nominal purity boron powder precursor was analyzed to start with, since boron is sometimes extracted from borate ores which can contain iron (among other elements), hence some ferromagnetic iron may possibly be present in the boron. Both a thermal magnetization scan and a room temperature magnetization measurement as a function of applied field were measured. The magnetic properties of the barium precursor material (99.9% nominal purity) were also analyzed by a thermal magnetization scan. The results are shown in Figure 5.12.

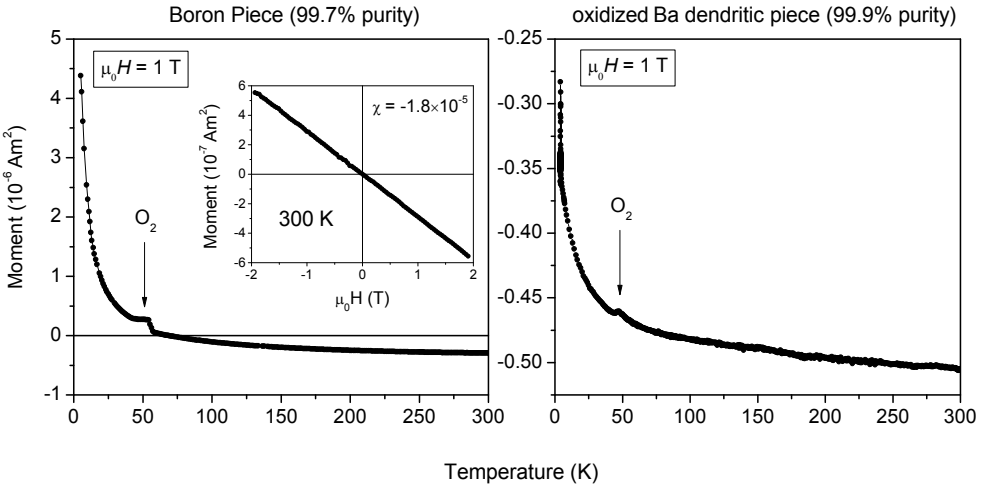

Figure 5.12. Thermal magnetization scans (measured in 1 T) for the boron and (oxidised) barium precursors. The marked cusps near 50 K are measurement artefacts (possibly due to trapped oxygen). The inset shows the room temperature magnetization data measured for boron. The mass of the boron sample was 47.7 mg, while that of (oxidized) barium was 70 mg.

From Fig. 5.12 above it is evident that the boron powder is diamagnetic at room temperature, and paramagnetic at low temperature (< 75 K); the cusp at around 50 K is a measurement artefact, and may possibly be due to molecular oxygen trapped in the SQUID vacuum chamber during the measurement. Molecular oxygen, which undergoes an antiferromagnetic transition at about 43 K, is strongly paramagnetic above this temperature. The SQUID system can

easily detect the presence of a small amount of condensed oxygen on the sample, which when in the sample chamber can interfere significantly with sensitive magnetic measurements. Oxygen contamination in the sample chamber is usually the result of leaks in the system due to faulty seals (other possible sources include improper operation of the airlock valve, outgassing from the sample, or cold samples being loaded). Apart from this artefact, there is no other evidence for the presence of ferromagnetic clusters (sharp upturns in the susceptibility), but the paramagnetic Curie upturn at low temperature can be accounted for by the presence of at most 0.06 wt % Fe^{3+} in the boron precursor (or equivalent to 0.02 wt % Fe^{3+} in the BaB_6 powder for example). For the barium precursor, the sample is diamagnetic from 300 – 5 K; however due to the high reactivity of barium with oxygen, the magnetic susceptibility of barium cannot be readily measured in metallic form, hence this measurement corresponds to the most common oxidised form of barium, BaO.

Thermal magnetization data for the MB_6 (M = Ca, Sr, Ba) targets, pressed from the MB_6 powders, is shown in Figure 5.13 on the next page, with the figure insets displaying the corresponding room temperature magnetization data. For ease of comparison, the thermal magnetization magnitudes are expressed in units of the specific mass magnetization σ ($Am^2\ kg^{-1}$). The samples are all paramagnetic at room temperature; for CaB_6, the mass magnetization σ (0.28 $Am^2\ kg^{-1}$) at 300 K is approximately three times larger than that of SrB_6, which in turn is about an order of magnitude higher than that of BaB_6. Meanwhile, the susceptibility measured at 300 K for CaB_6 ($\chi = 7.9\times10^{-4}$) is about an order of magnitude higher than that measured for the other two alkaline-earth hexaboride compounds. The paramagnetic susceptibility for each sample is almost temperature-independent, increasing by only ~ 5 % from 300 to 4 K. For SrB_6, an artefact in the thermal scan is marked, possibly due to molecular oxygen. There is no clear evidence for ferromagnetic clustering in any of the samples, which typically would be revealed by the presence of sharp upturns in the thermal magnetization data. The absence of such upturns may suggest that ferromagnetic (iron) impurities, if present, have formed small antiferromagnetically coupled clusters instead.

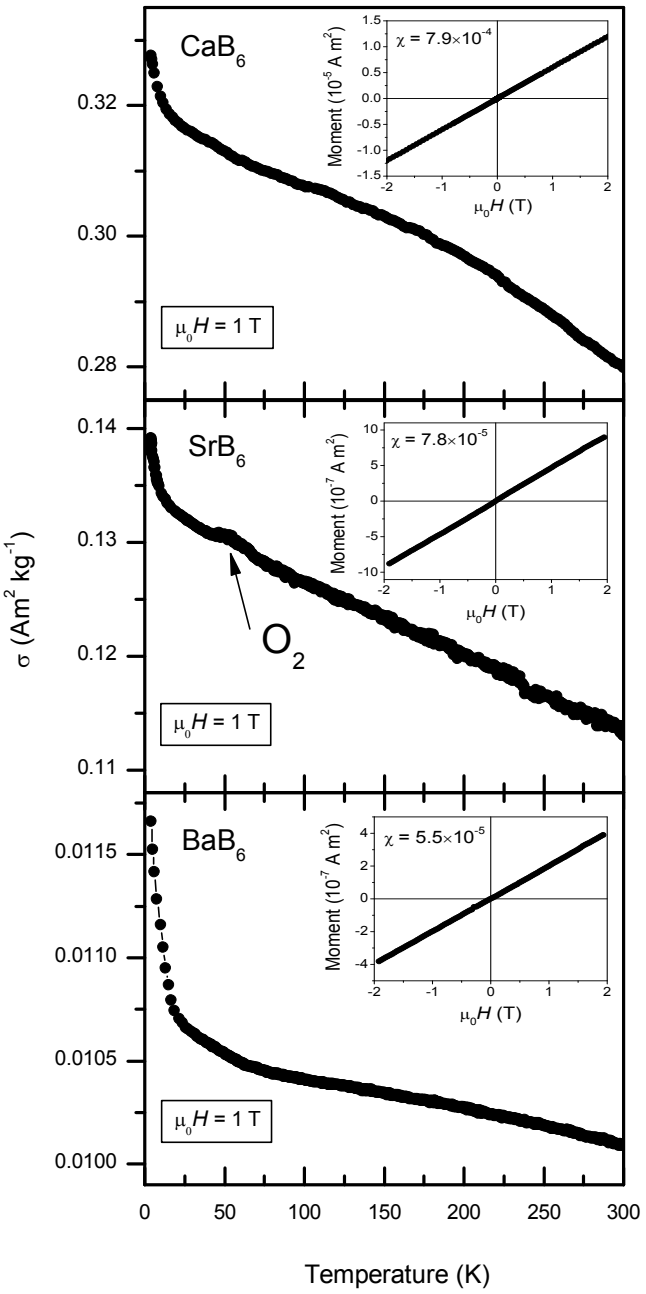

Figure 5.13. Thermal magnetization scans (measured in 1 T) for MB_6 (M = Ca, Sr, Ba) targets. The insets display the corresponding magnetization data measured at room temperature. The sample masses were 24.0 mg, 25.2 mg and 20.2 mg for CaB_6, SrB_6 and BaB_6 respectively.

Inductively-coupled plasma mass spectrometry (ICP-MS) analysis of the MB_6 targets was also performed in order to determine the impurity content of each (results included here rather than in a separate section for the sake of continuity). The quantity of Fe^{56}, the most abundant isotope of iron, was 0.288, 0.026 and 0.030 wt% in CaB_6, SrB_6 and BaB_6 respectively (0.1 wt% = 1000 ppm). It

is noted that the high temperature argon plasma (consisting of the neutral elements of the decomposed targets) first passes through a helium neutralizer before entering the mass spectrometer, so that the plasma and oxygen whose respective atomic masses of 39.94 (Ar) and 16.00 (O) sum to 55.94, cannot erroneously contribute to the result for the Fe^{56} content. The quantity of nickel or cobalt was less than 10 ppm in all of the samples. It is not clear why the iron abundance is an order of magnitude higher in CaB_6 compared to the other hexaborides, but it could due to a higher level of iron contamination during the powder synthesis from its elemental constituents and/or arising from handling. It was noted that the quantity of iron in the BaB_6 powder before die pressing was 0.02 wt%, suggesting that an additional 0.01 wt% or 100 ppm may be attributed to extrinsic contamination during the subsequent pressing and target processing since the target contains 0.03 wt% Fe. It is also noted that the quantity of iron in the BaB_6 powder (i.e. before pressing the target) measured by ICP-MS (0.02 wt%) is in agreement with that initially estimated from the paramagnetic Curie upturn at low temperature for the boron powder, from which the Fe content in BaB_6 powder (~ 0.02 wt%) was deduced by multiplying the result of the Fe content in boron (~ 0.06 wt%) by the mass ratio of B_6:BaB_6. Despite the fact that the ICP-MS results reveal that the targets contain iron, it is clear from the thermal magnetization data that the iron is not actually ferromagnetically ordered, but may be antiferromagnetically coupled. Lastly, some caution is advised concerning the interpretation of the ferromagnetic impurity content from ICP-MS, since the iron content of iron boride phases where the iron may be intercalated within a boron framework will not be detected as readily as “free” (non-intercalated) iron. The possibility of ferromagnetic impurities in the films is discussed later.

Room temperature magnetization curves for MB_6 films, with the field applied in-plane, corrected for the Al_2O_3 substrate signal (discussed further in the next paragraph) are shown in Figure 5.14 on the following page. The main plots are for thin films of thickness 5 nm, while the insets display magnetization curves measured for 100 nm thick films. All curves have been fitted to a tanh function of the form

$$M/M_s = \tanh(H/H_0) \quad (1)$$

where M_s is the saturation magnetization of the film and H_0 is the field obtained by extrapolating the initial susceptibility to saturation. It is interesting to note that the moments are not drastically different for the thinner films (5 nm) compared to the thicker ones (100 nm). Regarding substrates, larger signals were measured on average for films grown on Al_2O_3, either c-cut (0001) or r-cut (1102), than for MgO. For example, the moments for a 100 nm BaB_6 film grown under identical conditions at 500 °C on c-cut Al_2O_3, r-cut Al_2O_3 and (100) MgO were 3.8, 3.3 and 1.3 ($\times 10^{-8}$ Am^2) respectively. Since all of the films are amorphous, the effect of the substrate is expected to be less important than if the films were crystalline.

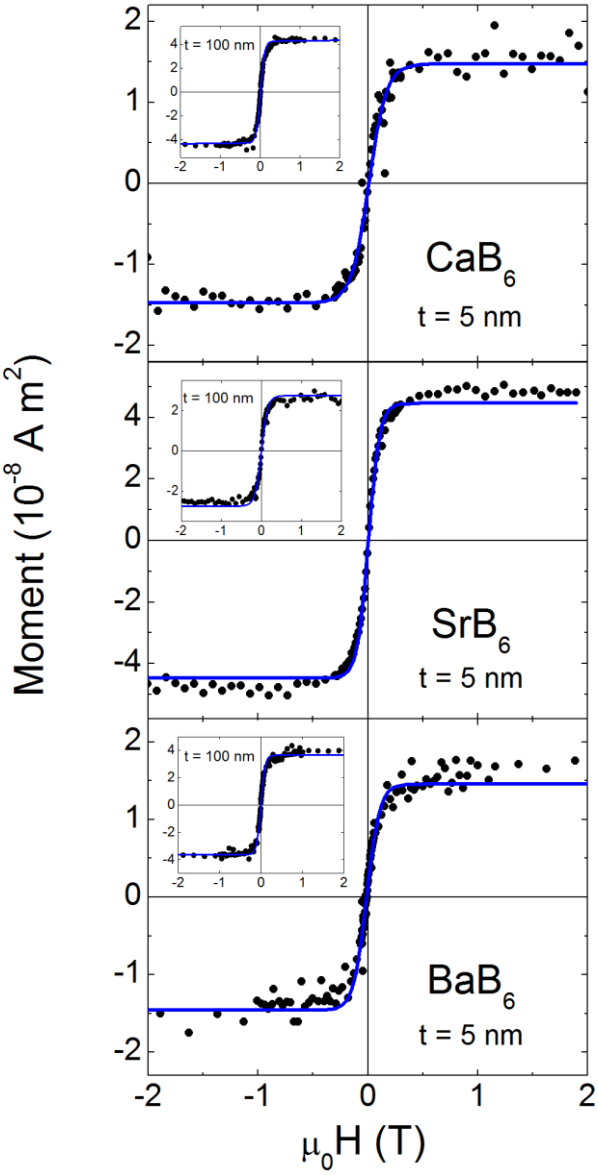

Figure 5.14. Selected room temperature magnetization curves for thin (5 nm) and (inset) thick (t ~ 100 nm) MB_6 films, fitted to tanh functions and corrected for the contribution due to the Al_2O_3 substrate (diamagnetic plus small ferromagnetic signal of at most 0.3×10^{-8} Am^2).

As a test, blank Al_2O_3 substrates were subjected to identical heating conditions used to deposit the MB_6 films; a small ferromagnetic signature was measured for some substrates, but it was never more than 0.3×10^{-8} Am^2, or about an order of magnitude smaller than that measured for many of the MB_6 films. Separate control films of ZnO and Al_2O_3 grown by ablation of targets made from 99.99 % nominal purity ZnO and Al_2O_3 powders respectively and deposited using similar conditions to those used for the MB_6 films that produced the larger moments exhibited maximum moments of no more than 0.2×10^{-8} Am^2 at room temperature. These controls indicate that ferromagnetic contamination from the deposition chamber is not the source of hexaborides' magnetic signals when

they exceed 0.3×10^{-8} Am^2. Furthermore, the silver paint used to affix the substrates to the substrate holder did not exhibit any ferromagnetic signature when measured at room temperature. The larger moments are also an order of magnitude greater than those reported elsewhere for blank sapphire substrates, one side polished (0.4×10^{-8} Am^2) [106,107], or for other common oxide substrates [108]. Artefacts arising from SQUID measurements of nanoscale samples are reported to give a maximum contribution to the signal of ~ 0.1×10^{-8} Am^2 [109]. Special care was taken throughout to minimise possible extrinsic sources of ferromagnetic contamination, including the use of plastic tools to handle samples and the use of a clean non-magnetic copper blade to detach the substrates from the ceramic holder after PLD growth, since the use of stainless steel tweezers or blades is known to cause contamination; for example, for silica glass intentionally pressed with iron tweezers, relatively large moments (for nanoscale magnetism) of up to 10×10^{-8} Am^2 are measured [109] (which actually exceeds the moments measured for the MB_6 films measured here), for MgO substrates cleaved with stainless steel blades smaller moments of up to 0.6×10^{-8} Am^2 are measured [110], while for HfO_2 thin films handled with stainless steel tweezers, intermediate moments of up to 1×10^{-8} Am^2 are measured [111].

The variation of moment with applied field direction and measurement temperature are shown in Figure 5.15 for a typical 100 nm thick film (BaB_6) grown on a Al_2O_3 (0001) single crystalline substrate, whose magnetization curves have been fitted to tanh functions.

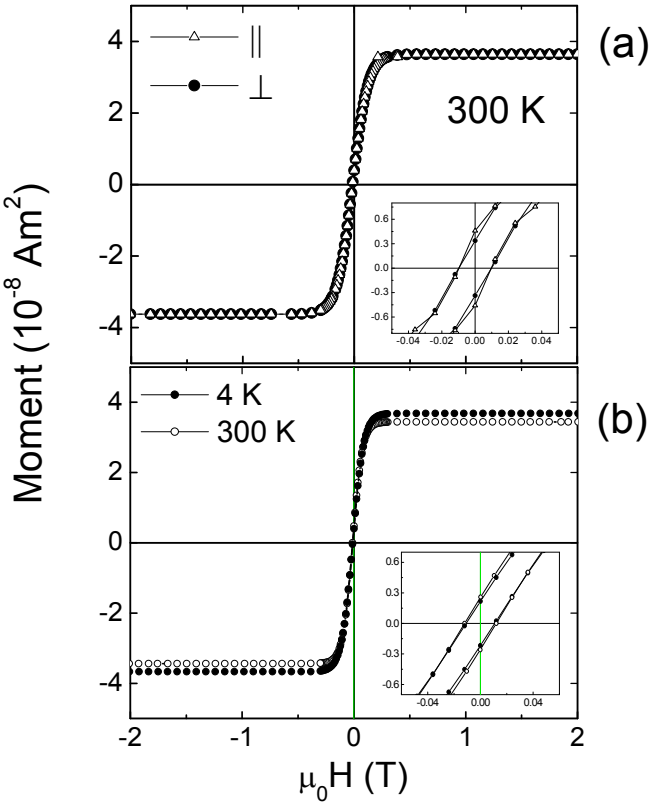

Figure 5.15. (a) Moment vs. applied field direction and (b) moment vs. measurement temperature for a typical 100 nm thick film (BaB_6) grown on a Al_2O_3 (0001) substrate. The insets show the region near the origin on a larger scale. Tanh fits of the data are displayed.

It is evident from the previous figure (Fig. 5.15) that the magnetism for amorphous 100 nm thick magnetic BaB_6 films is isotropic and virtually temperature independent from 4 - 300 K. The magnetic signals saturate easily ($\mu_0 H$ ~ 0.3 T) with applied field in either direction. The lack of temperature dependence of the magnetism indicates that secondary superparamagnetic impurity phases are not responsible for the magnetism and that dipole interactions rather than magnetocrystalline anisotropy governs the magnetization curve and the approach to saturation. The region of the curves around the origin (shown in the insets of Fig. 5.15) which displays the completed hysteresis loops indicates that the curves are essentially anhysteretic; measured coercivities were less than 10 kA m^{-1}. Typical magnetization curves for ~ 100 nm thick amorphous CaB_6 and SrB_6 films also grown on Al_2O_3 (0001) are shown below in Figure 5.16, this time on a larger applied field scale and showing both the raw data (circles) and tanh fits (lines). The characteristics of the magnetization curves are similar to those discussed for BaB_6. It is noted that the present films are grown on sapphire. In a previous report for amorphous MB_6 (M = Ca, Sr) films grown on sapphire and MgO at lower energy densities (1 J cm^{-2}) from targets obtained by pressing 99.5% nominal purity commercial hexaboride powders [99], for some of the crystalline films (grown on MgO) the parallel and perpendicular magnetization curves were clearly different (Fig. 5.3), with a marked magnetocrystalline anisotropy (demagnetizing effect for out-of-plane measurement). Here, for BaB_6 films grown on MgO (100) substrates, the characteristics of the magnetism were similar to those grown on Al_2O_3 (0001), namely isotropic magnetism with similar demagnetizing factors (slope at the origin), regardless of whether the magnetic field was applied parallel or perpendicular to the film surface. Thinner films grown on Al_2O_3 (0001), of order 10 nm thick, were also found to exhibit isotropic magnetism.

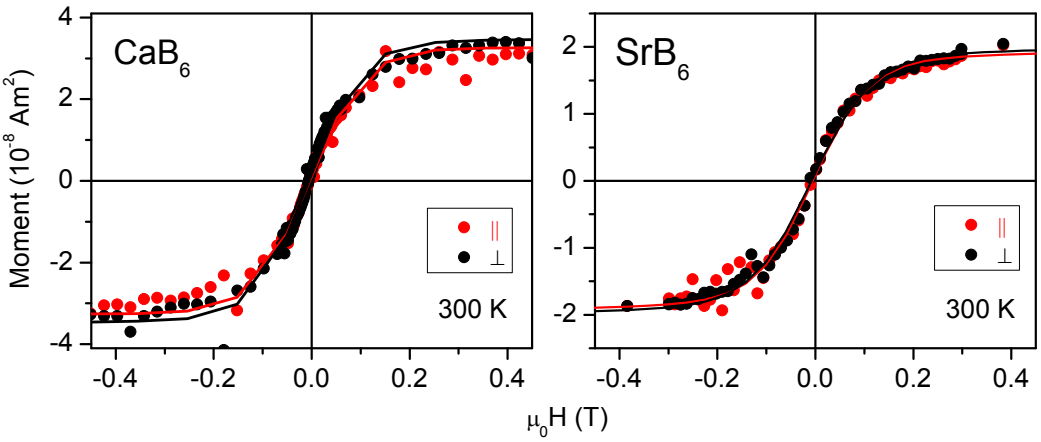

Figure 5.16. Moment vs. applied field for ~ 100 nm thick CaB_6 and SrB_6 magnetic films grown on Al_2O_3 (0001) substrates. The data has been fitted to tanh functions.

In terms of the stability of the magnetic signals measured for the thin films over time, Figure 5.17 displays some examples. For a BaB_6 magnetic film, ~ 100 nm thick, the magnitude of

the signal has decreased by about 33 % after 4 months, whereas for a SrB_6 film of similar thickness, the magnitude of the signal has decreased by about 25 % over the same duration. For a thinner BaB_6 film (15 nm), the magnitude of the magnetic signal has decreased by less (~ 15 %) over a longer interval (9 months). Thus it is evident that the magnetic signals are fairly robust over time, even more so for thinner films, and do not generally decay rapidly immediately after deposition, which is promising for potential applications.

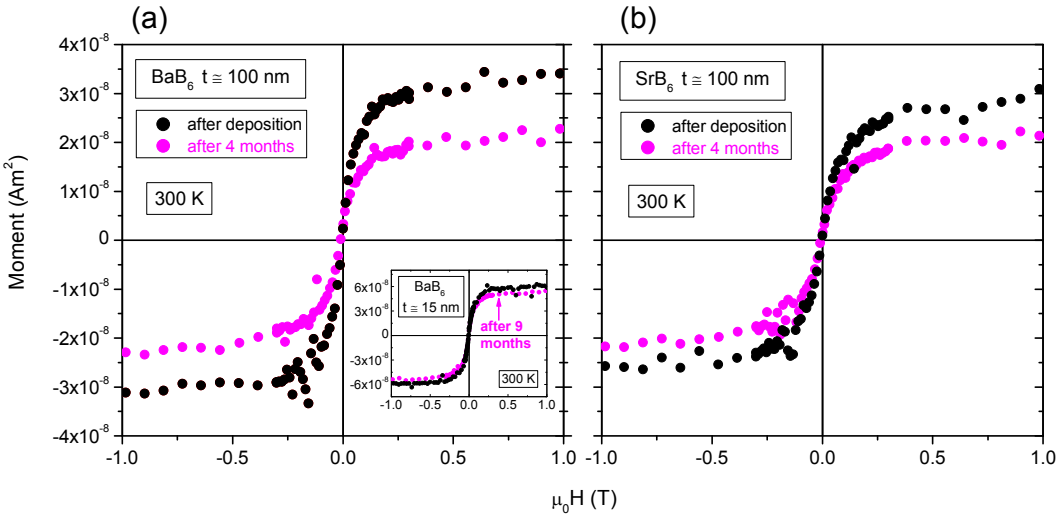

Figure 5.17. Room temperature magnetization curves for (a) BaB_6 (inset t = 15 nm) and (b) SrB_6 ~ 100 nm thick magnetic films grown on Al_2O_3 (0001) substrates, which show how the magnetic signals change over time.

Absolute magnetic moments measured for ~ 100 nm thick MB_6 films grown over a range of substrate temperatures are shown in Figure 5.18 on the next page.

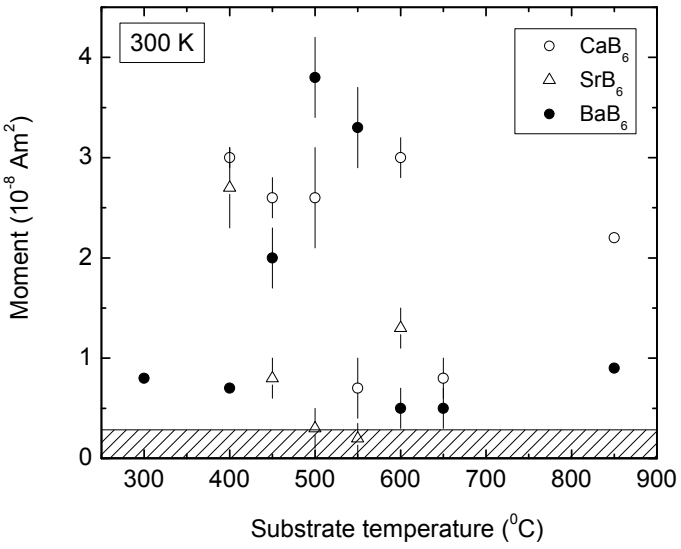

Figure 5.18. Average moment (measured at room temperature) vs. substrate deposition temperature for ~ 100 nm thick MB_6 films grown by PLD. Data points within the hatched region for SrB_6 and BaB_6 should be treated with circumspection because artefacts from the sapphire substrates are found to lie within this range. For CaB_6, the upper limit of the hatched region should be set at ~ 1.2×10^{-8} Am^2, because of the possible contribution of iron to the magnetic signal in these films.

Upon inspection of Figure 5.18 on the previous page, while the moment for BaB_6 appears to peak between 450°C and 600°C, the variation of moment with temperature is more erratic for the other two systems. The error bars indicate the range of experimental error for multiple films of same thickness grown at the same temperature. The variation may be due to local differences in defect concentrations, a parameter inherently prone to variability, or to some uncontrolled detail of the process. For the CaB_6 and BaB_6 targets in particular, it was noted that the intensity of the ablation plume degraded gradually after several depositions, necessitating re-polishing of the target surface, in order to remove the inscribed annular "groove" on the surface due to the impinging laser spot. For the SrB_6 target, the target integrity was slightly superior to that of the other hexaborides, enabling more depositions before re-polishing. It is also noted that a previous magnetic study of CaB_6 and SrB_6 films grown by PLD measured maximum moments at about 550 °C [99], but there the energy density was much lower (1 J cm^{-2}) than that used here (6 J cm^{-2}). What is clear from Fig. 5.18 however is that for films grown over a wide range of substrate temperatures, magnetic signals which cannot be accounted for by either the Al_2O_3 substrate contribution and/or ferromagnetic impurities are measured. For a BaB_6 film deposited at 500 °C and subsequently post-annealed in the PLD vacuum chamber for 16 hours at the same temperature and pressure used for deposition, the magnetic moment was found to actually *increase* to 4.5×10^{-8} Am^2, which is slightly higher than that typically measured (~$3.8 \pm 0.3 \times10^{-8}$ Am^2) after deposition (without any additional post treatment) from Fig. 5.18.

The possible contribution of iron to the magnetization, knowing its concentration in the target and assuming that it is completely ferromagnetically ordered in the film, may be calculated. For example, ICP-MS analysis of the CaB_6 target showed that it contained the most iron, 0.288 wt%. Assuming that the concentration of iron in the CaB_6 film is the same, and that it is ferromagnetically ordered, the maximum magnetization attributable to iron is about 4.8 kA m^{-1} (taking M_s of Fe = 1.71 MA m^{-1}), equivalent to a moment of 1.2×10^{-8} Am^2 for a 100 nm thick film, or 6×10^{-10} Am^2 for a 5 nm thick film. From Fig. 5.18, most of the CaB_6 films (100 nm thick) have moments of ~ $2\text{-}3\times10^{-8}$ Am^2, which is larger than the maximum amount possibly attributable to iron. Since the iron content measured by ICP-MS for the SrB_6 and BaB_6 targets are an order of magnitude smaller again than that measured for the CaB_6 target, the contribution of the iron to the magnetism would be much less significant in these films, ~ 0.1×10^{-8} Am^2 for a 100 nm thick film for example. SEM-EDX analysis of several regions of the films (discussed in more detail later in section 5.3.6) did not reveal any iron impurities or inclusions, similar to the analysis of the boron precursor.

Figure 5.19 displays the variation of magnetic moment with film thickness for some MB_6 films. There does not appear to be any marked correlation between moment and thickness, although it could be argued that there may be a slight increase in moments for films of order 10 nm thick.

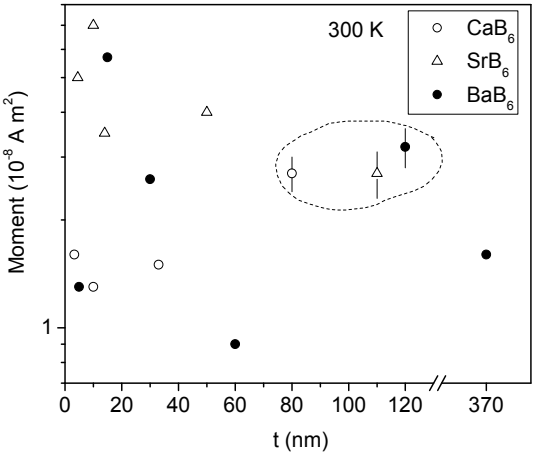

Figure 5.19. Moment vs. film thickness for some MB_6 films; the initial films which were grown are enclosed by the dashed circle, after which only the deposition time was changed in order to vary the thickness.

Figure 5.20 displays the variation of magnetization, defined as the ratio of film moment to film volume, with film thickness for a fixed deposition temperature, for various magnetic MB_6 films.

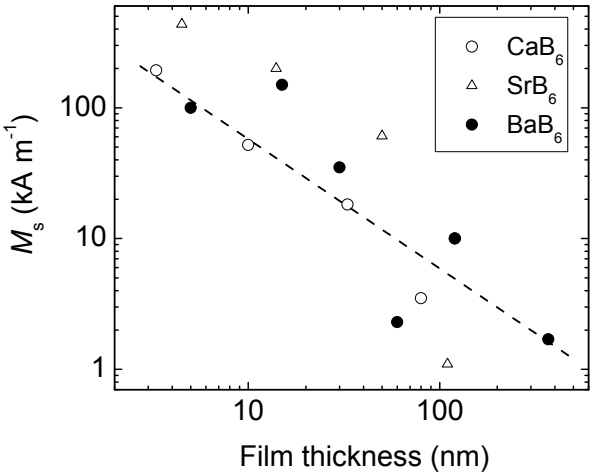

Figure 5.20. Magnetization vs. film thickness for magnetic MB_6 films. The dashed line with slope -1 is expected if the magnetic moment of the films is independent of thickness.

We had previously reported that for BaB_6 there was no systematic variation of the magnetization with thickness [100]. That particular report did not consider films less than ~ 120 nm thick however. In Fig. 5.20 a large increase in magnetization with decreasing film thickness from 100 to 5 nm is measured; for 100 nm thick films, M_s is of order 10 kA m^{-1}, which increases by almost an order of magnitude for films ~ 10 nm thick. The data in Fig. 5.20 loosely demonstrate that the moment is independent of film thickness by fitting with a slope of -1, from which it may be reasonably deduced that the magnetism is associated with the free film surface or the substrate-film interface. Since the numbers of defects in a film is independent of its thickness and the magnetism is found to be substrate-dependent, the enhanced magnetization for thinner films may be due to defects mostly localized near the interface between the film and the substrate (rather than at the free surface); an extrinsic ferromagnetic impurity explanation is simultaneously discredited since for this explanation the moment should actually *decrease* with decreasing film thickness (less volume = less ferromagnetic impurities); this is not the case from either Figs. 5.19 or 5.20 which both show that the moment does not exhibit any clear correlation with film thickness.

The ferromagnetic volume fraction of the sample f may be calculated as the ratio M_s/M_0 where M_s is the saturation magnetization of the film and M_0 is the magnetisation of the ferromagnetic regions [112]. The field H_0 obtained by extrapolating the initial susceptibility to saturation is related to M_0 by the effective demagnetising factor $\mathcal{N}$:

$$H_0 = \mathcal{N} M_0 \tag{2}$$

For films of order 100 nm thick, f ~ 5 %, which indicates that the magnetism is not a bulk effect and is instead inhomogeneously distributed. For these calculations a value of $\mathcal{N}$ = 1/3 has been used since the magnetism is isotropic. For thinner films of order 10 nm, f is much larger, hence a greater percentage of the sample volume is ferromagnetically ordered. Figure 5.21 shows that f

increases in almost direct proportion to the magnetization as expected (dashed line slope ~ 0.8), reaching values close to 100 % for the thinnest films (which also have the highest M_s values), where $\mathcal{N}$ = 1/3 has been adopted.

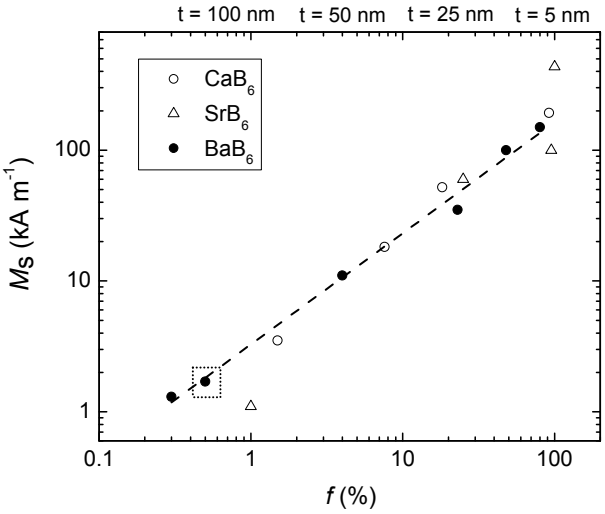

Figure 5.21. Room temperature saturation magnetization M_s vs. ferromagnetic volume fraction f for MB_6 films. Approximate film thickness is denoted above the plot, an exception to which is the data point enclosed within the dotted square (BaB_6) for which t ~ 60 nm. The dashed line is a linear fit to the data (slope ~ 0.8). A value of $\mathcal{N}$ = 1/3 was used to calculate f.

Determination of the depth profile of the magnetism within the films, such as by muon spin rotation spectroscopy [92,96], may help to elucidate the location of the magnetism, which has been previously proposed to reside in a thin layer, ~ 10 nm thick, at the interface with the substrate for CaB_6 and SrB_6 thin films [99]; some preliminary muon spectroscopy results for MB_6 powders and films are presented later in this chapter in section 5.3.7. A schematic of a ferromagnetic-like layer residing at the substrate-film interface is shown in Figure 5.22.

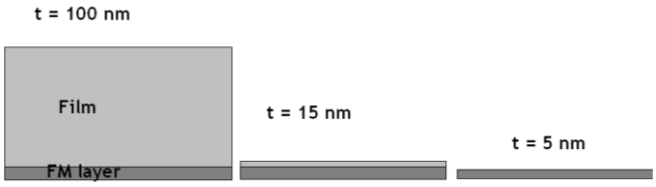

Figure 5.22. Schematic of a ferromagnetic (FM) layer which resides at the interface between the film and underlying substrate (latter not shown). The overall film thickness (including the FM layer) is depicted.

Figure 5.23 summarizes the variation of the room temperature saturation magnetization M_s with H_0 for the all of the alkaline hexaboride films synthesized by PLD during this study as well as for some iron and magnetite samples synthesized in our laboratory, similar to data presented

previously for dilute magnetic oxides [112]. H_0 is the field obtained by extrapolating the initial susceptibility to saturation. The three black lines show where the data for samples whose volumes are completely ferromagnetically ordered (f = 100 %) should lie, for three different values of the demagnetizing factor $\mathcal{N}$. The values $\mathcal{N}$ = 1, 1/3 and 1/6 represent scenarios where the magnetization is perpendicular to the plane of a thin film, isotropic (spherical approximation) or associated with grain boundaries respectively.

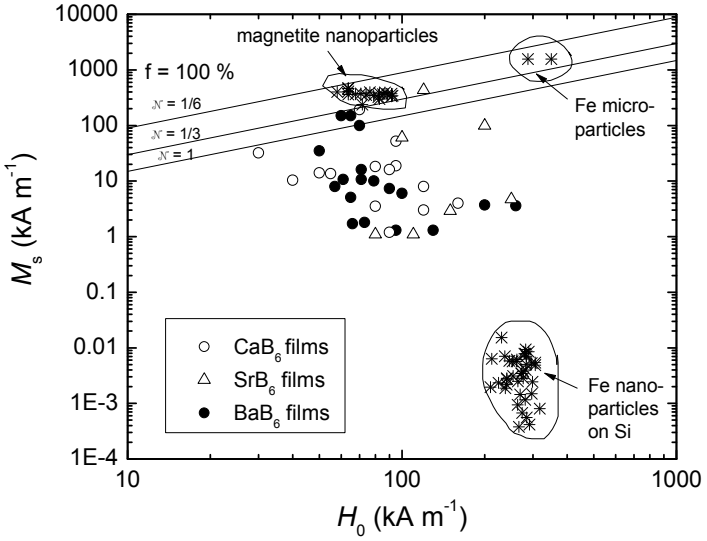

Figure 5.23. Room temperature M_s vs. H_0 (field obtained by extrapolating the initial susceptibility to saturation) values for MB_6 films synthesized by PLD during this study; data measured for some iron (metallic and oxide) samples are encircled for comparison.

Three key points can be taken from the M_s vs. H_0 plot shown in Fig. 5.23. Firstly, the values of H_0 for metallic iron samples, either micron or nano-sized, fall within a different region than those for MB_6 samples. Secondly, the values of M_s for the thinnest films of order 10 nm thick approach a 100 % ferromagnetic volume fraction f, possibly reflecting the enhanced role of defects and interfaces in the thinnest films, for which the magnetization reaches its highest values. The majority of the data points falling within the range M_s ~ 1-10 kA m^{-1} are for films ~ 100 nm thick grown over a range of deposition temperatures. Thirdly, the H_0 values for nanoparticles of magnetite do fall within the H_0 range measured for many of the MB_6 samples, unlike for metallic iron which typically has larger values of H_0. Hence it is possible that magnetite may be a magnetic impurity in the MB_6 films, and not metallic iron, although from inspection of Fig. 5.23, approximately 1 part out of 100 of the majority of the films at least (and even more for those films with higher M_s) would have to be magnetite impurities in order to account for the magnitude of the magnetic signals measured. Such quantities of magnetite are admittedly rather implausible in light of the impurity analyses performed.

It is useful at this juncture to discuss M_s and H_0 values measured for the alkaline earth hexaborides in the literature, by deducing M_s and H_0 from the magnetization curves where published, and to compare the data to the results measured here, as this may help to further understand the

results for our MB_6 thin films. First of all, data for undoped MB_6 samples for which room temperature magnetism is reported in the literature (and for which magnetization curves are presented) is displayed in Figure 5.24. The data has been differentiated between that to which intrinsic magnetism is attributed (black dots) and that to which the magnetic signals are attributed to iron impurities (blue circles). It is evident that the M_s values for thin films are several orders of magnitude higher than those for the bulk (powders or crystals), and that additionally the M_s values for the thinnest films (5 nm) are about an order of magnitude or more greater than those for thicker films (100 – 300 nm). The H_0 values for the majority of the samples are less than that of iron metal (i.e. < 200 kA m^{-1}), but similar to those of magnetite nanoparticles (~ 60 -100 kA m^{-1}, see previous figure, Fig. 5.23). For the samples for which the magnetism is attributed to iron impurities, H_0 is rather uniform with a value of ~ 200 kA m^{-1}, or similar to some of those measured for iron, with the exception of one distinct outlier at 50 kA m^{-1}.

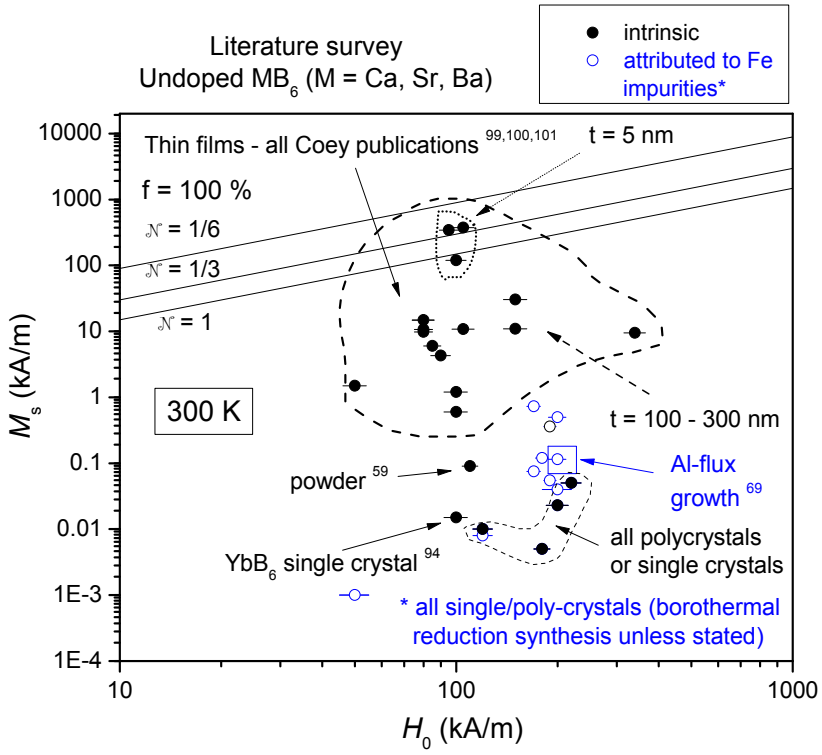

Figure 5.24. Room temperature M_s vs. H_0 values for undoped MB_6 samples (films, crystals and powders) from the literature.

M_s and H_0 data for *doped* MB_6 samples for which room temperature magnetism is reported in the literature (and for which magnetization curves are presented) is displayed in Figure 5.25. Most of the reports for room temperature magnetism are for La doped CaB_6 crystals. As per the previous figure, a distinction between the data points attributed to intrinsic magnetism and extrinsic ferromagnetic contamination/impurities has been made.

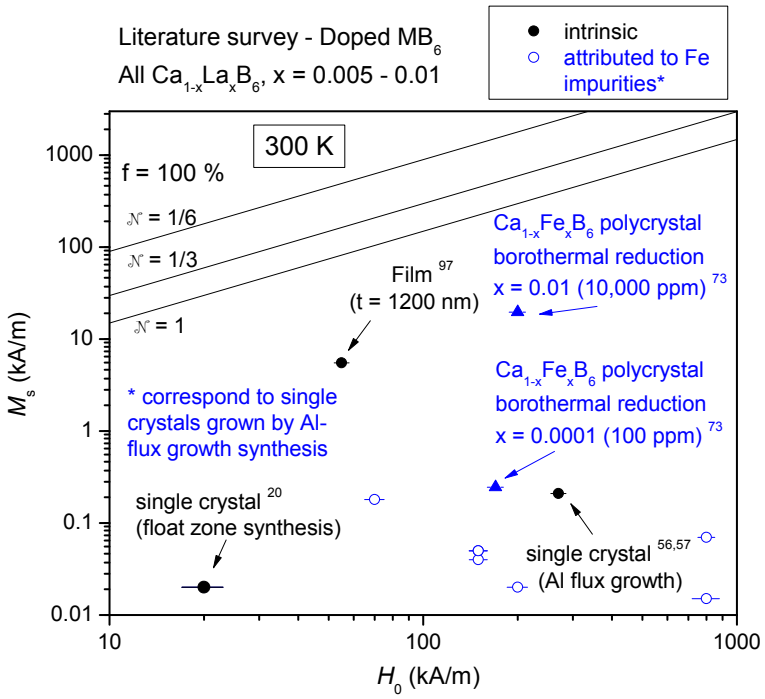

Figure 5.25. Room temperature M_s vs. H_0 values for doped MB_6 samples (films and crystals) from the literature.

Interpreting the M_s vs. H_0 data shown in Fig. 5.25 on the previous page, for the data attributed to intrinsic magnetism (black dots), the M_s values for films are several orders of magnitude larger than those for crystals, but H_0 values for the latter are rather variable. For the data attributed to iron impurities (blue circles), all of which are single crystals (Al-flux grown), the M_s values are similar in magnitude to those reported for intrinsic magnetism in this figure and also to those reported for undoped MB_6 (both intrinsic and due to Fe impurities) shown previously in Fig. 5.24. H_0 is again rather variable however. Data for CaB_6 polycrystals which were intentionally doped with two different quantities of iron are denoted by blue triangles [73]. M_s for a sample doped with 1 % iron (10,000 ppm) is ~ 20 kA m^{-1}, which is ~ 1 % of the value for pure bulk iron (1.71 M Am^{-1}). For a sample doped with 0.01 % iron (100 ppm), M_s is about two orders of magnitude less than for 1 % doping, as expected. H_0 for both samples lie in the range 180-210 kA m^{-1}, which is slightly less than that measured for metallic iron, although the authors attribute the magnetism to iron boride and not to metallic iron. In fact, the majority of authors who attribute the magnetism to ferromagnetic impurities attribute it to iron boride phases rather than metallic iron, possibly due to the tendency of any iron impurities to react with boron during the high temperature syntheses of MB_6 compounds.

Lastly for this particular analysis, M_s and H_0 data for MB_6 crystals from the literature, both doped and undoped, is grouped by method of synthesis and also by whether the magnetism is claimed to be intrinsic or not, since there is much debate concerning the possible correlation between synthesis route and ferromagnetic impurity content in these samples. The data is shown in Figure 5.26 on the next page. The two main methods of synthesis are Al-flux growth (dots) for single

crystals and borothermal reduction (triangles) for polycrystals, with the majority of doped crystals grown by the former method, and the majority of the undoped crystals grown by the latter method; intrinsic magnetism is denoted in black, ferromagnetic impurity magnetism in blue. M_s does not exceed 1 kA m^{-1} for any of the crystals, while H_0 for most of the samples is ~ 200 kA m^{-1}. It is noted again that for our samples presented in this thesis, a solid state reaction of the elemental powders in sealed quartz tubes (without a crucible) was used to synthesize MB_6 powders.

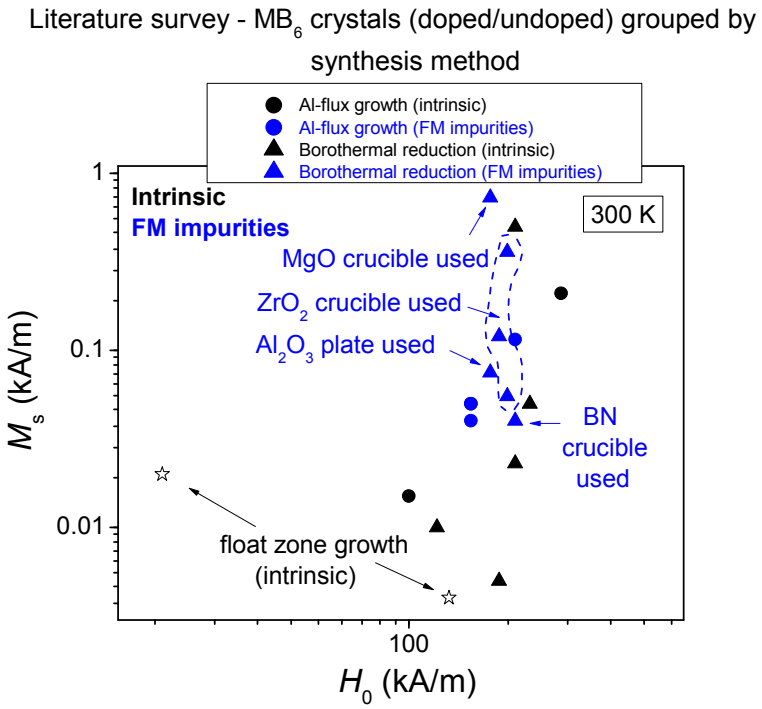

Figure 5.26. Room temperature M_s vs. H_0 values for MB_6 crystals only (both doped and undoped) from the literature, grouped by method of synthesis.

5.3.5 Electron microscopy analysis of thin films

Some representative SEM images of the surfaces of ~ 100 nm thick films are shown in Figure 5.27. The surface morphology of BaB_6 films grown at 500 °C and 650 °C with larger (3.8×10^{-8} Am^2) and smaller (0.7×10^{-8} Am^2) magnetic moments, denoted "strong" and "weak" magnetic respectively henceforth, are shown in panel (a) and (b) respectively. Laser ablation droplets due to subsurface boiling or ablation induced recoil pressure imposed by the high ablation energy densities used are clearly visible, although there is a contrast in morphology between the two films.

CaB_6 and SrB_6 magnetic films (possessing moments of order 3×10^{-8} Am^2) also contain numerous ablation droplets.

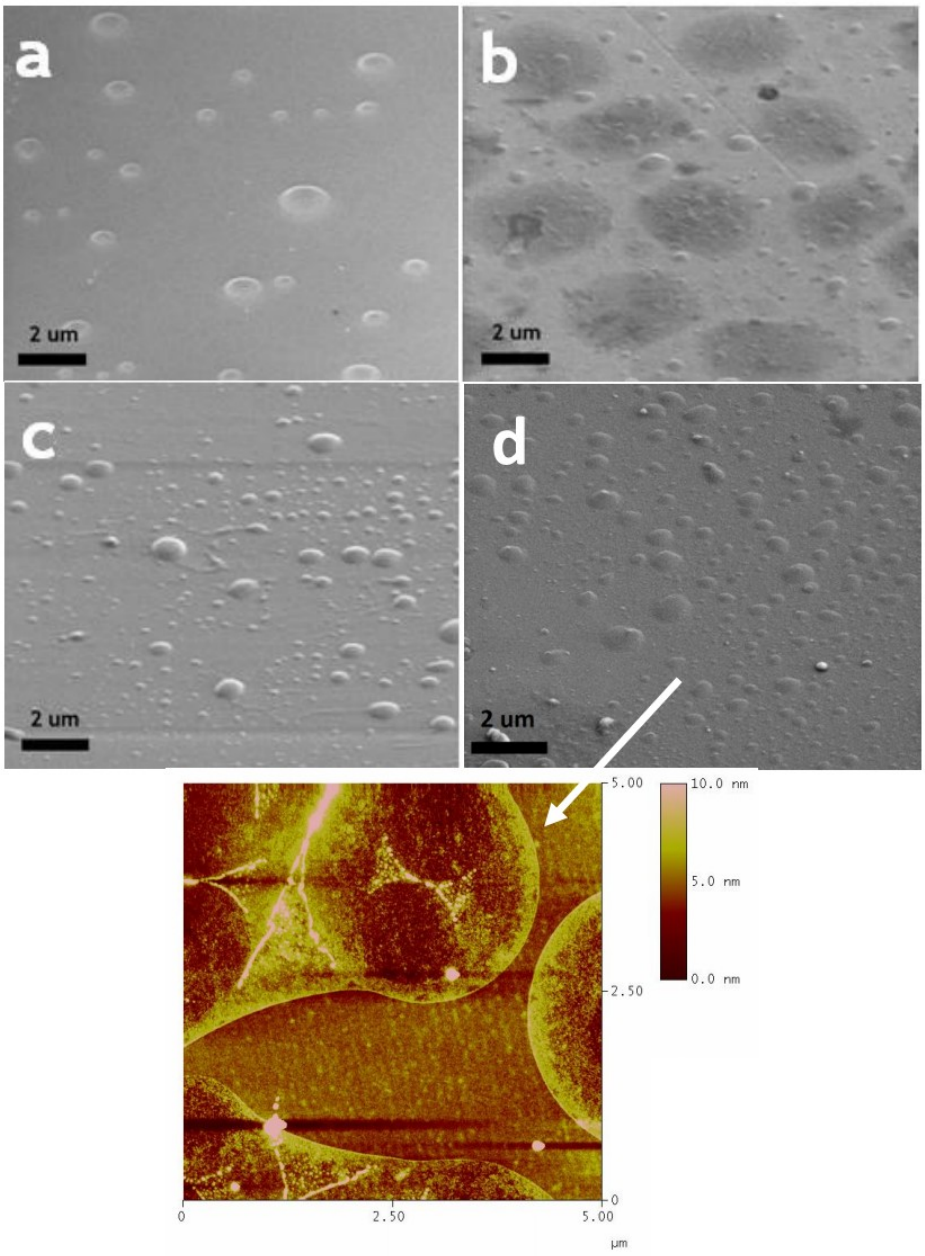

Figure 5.27. Representative SEM images (tilted at 52°) of the surfaces of (a) a "strong" magnetic BaB_6 film, (b) a "weak" magnetic BaB_6 film, (c) a magnetic CaB_6 film, and (d) a magnetic SrB_6 film with corresponding AFM image showing a larger ablation droplet (marked by the white arrow). All films are ~ 100 nm thick.

TEM cross-sections of films were imaged in order to reveal their nanostructure, in particular for BaB_6, for which data is presented here. A representative TEM cross-section of a ~ 100 nm thick BaB_6 film with a magnetic moment of 3.8×10^{-8} Am^2 ("strong" magnetic) is shown in Figure 5.28, at both low and high magnifications. Gold is deposited on top of the film to prevent charging during SEM imaging and to provide clear contrast with the underlying film, upon which platinum is subsequently deposited in order to protect the film during cross-sectioning by focused Ga^+ ions. An ablation droplet induced by the PLD process is visible.

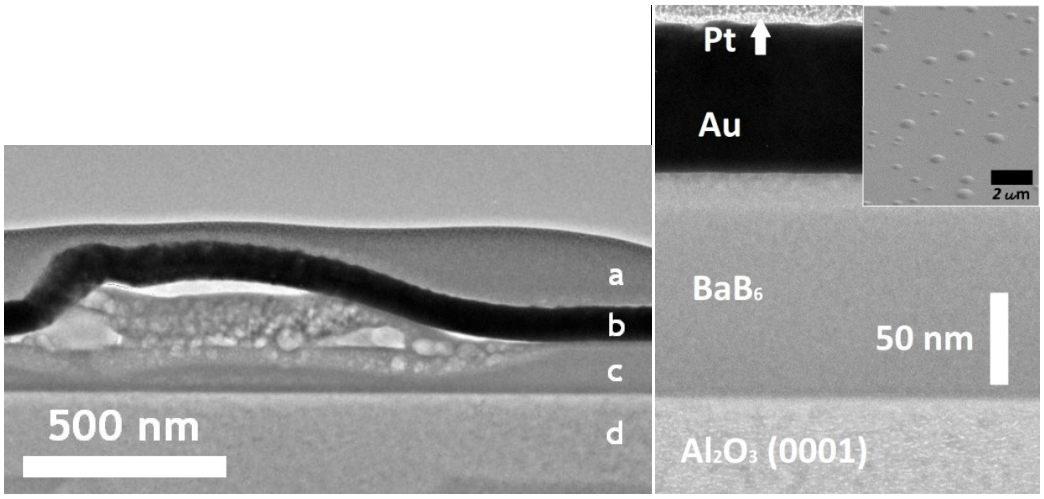

Figure 5.28. Left: Cross-section excised by FIB-SEM of a BaB_6 "strong" (3.8×10^{-8} Am^2) magnetic film together with a typical laser ablation droplet and imaged at low resolution in TEM; a = Pt overlayer, b = Au capping layer, c = BaB_6 film, d = Al_2O_3 substrate. A higher resolution image from a region without an ablation droplet is shown on the right (with corresponding SEM image of the film surface shown in the inset).

Higher resolution images of both "strong" and "weak" magnetic BaB_6 films are shown in Figure 5.29. That the MB_6 films are amorphous is confirmed since no crystalline structure can be resolved within the films, in contrast to the underlying single crystalline Al_2O_3 substrate, for which crystalline grains can be resolved. There appears to be a darker interfacial region between film and substrate for both films. The substrate-film interface is quite smooth, as highlighted in Figure 5.30, although the presence of a contrasting interface layer at the film-substrate interface is not so evident in these images.

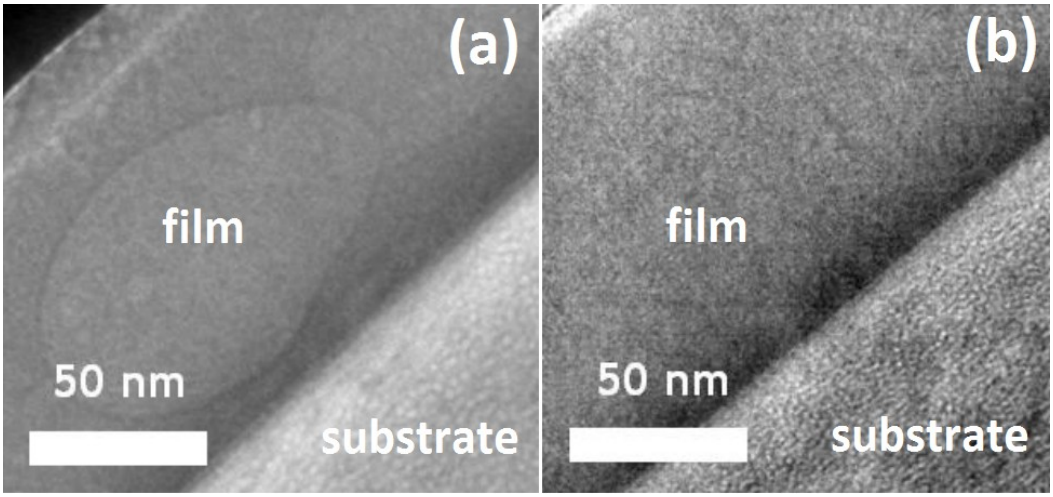

Figure 5.29. TEM cross-section images of (a) "strong" (3.8×10^{-8} Am^2) and (b) "weak" (0.7×10^{-8} Am^2) magnetic BaB_6 films respectively. The strong magnetic film was capped with gold, while the weak magnetic film was capped with copper. The substrate is Al_2O_3 (0001).

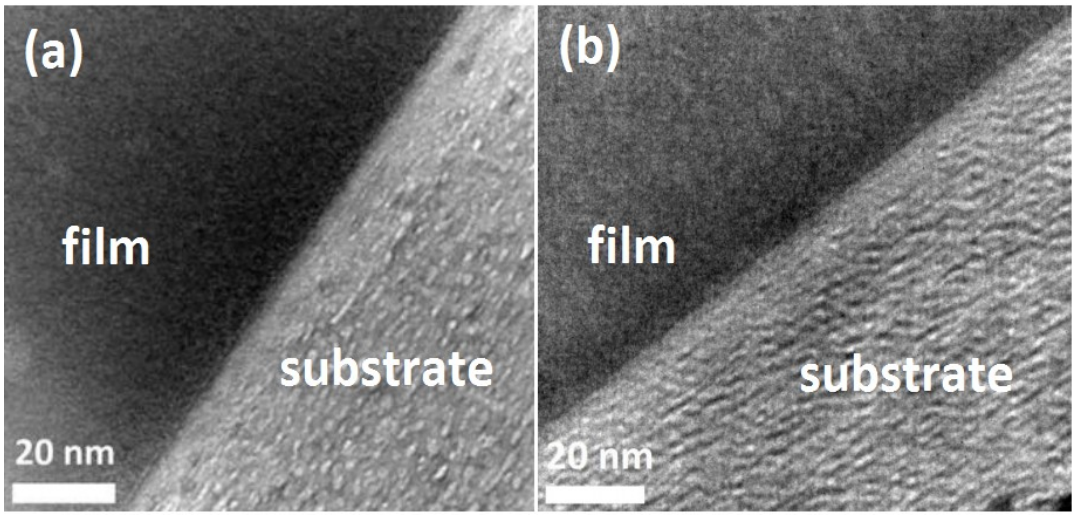

Figure 5.30. High resolution TEM cross-section images of the film-substrate interface of (a) "strong" (3.8×10^{-8} Am^2) and (b) "weak" (0.7×10^{-8} Am^2) magnetic BaB_6 films respectively.

5.3.6 SEM-EDX analysis of powders and thin films

SEM-EDX was performed in order to determine the elemental composition of films/powders while also searching for ferromagnetic impurities. If iron impurities are present, it is quite likely that they will form clusters and will not be completely homogeneously dispersed throughout the sample volume; hence although the detection limit of EDX is not so low (~ 0.2 wt %, or 2000 ppm), if even a small tendency towards clustering of ferromagnetic impurities occurs, EDX

should be able to detect this. This is the main argument for EDX as a useful tool for revealing the presence of ferromagnetic impurities, even if the absolute ferromagnetic impurity concentration is actually less than ~ 2000 ppm.

Firstly, a blank carbon sticky tab (upon which MB_6 powders were sprinkled) was imaged and an EDX spectrum acquired in order to deduce the background signal, the results for which are shown in Figure 5.31. In addition to carbon, the elements O, Na, S, and Si were also detected in order of decreasing abundance. No other elements were detected. For another area scan, similar wt. % values were measured to those for the area depicted in Fig. 5.31, with the values of the abundances of C and O measured to within 0.5% of the values obtained for the first area scan, and those of the other elements to within 0.1%. For an additional spot scan, the carbon wt. % increased to 83.4 %, while the oxygen wt. % decreased to 15.6 %; the wt. % of the other elements was similar to before.

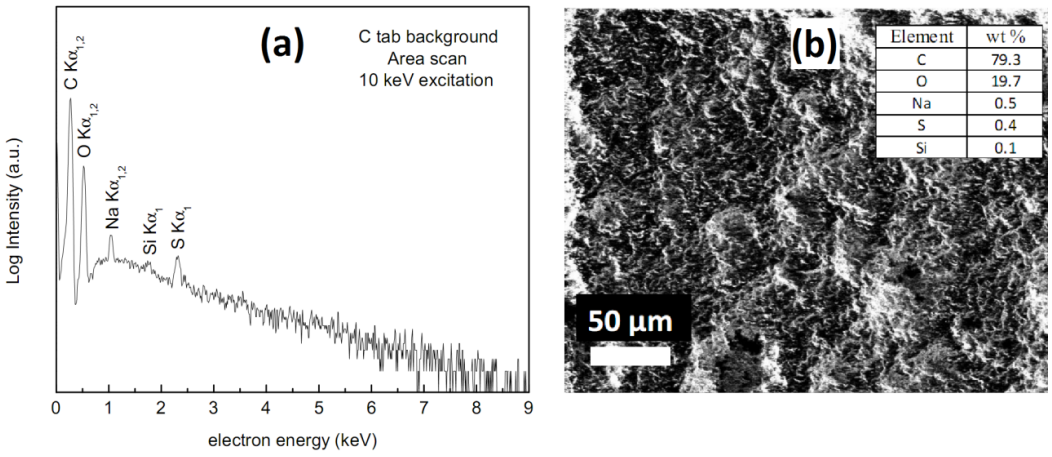

Figure 5.31. (a) EDX area spectrum acquired at 10 keV for a carbon sticky tab (b) Imaged area and measured elemental composition. The textured surface of carbon is evident.

After characterization of the carbon tab, SEM-EDX analysis of the 99.7% nominal purity boron powder precursor (Sigma Aldrich) used to synthesize the hexaborides was performed. The powder was ground as finely as possible in a pestle and mortar, of which < 1 mg was sprinkled directly onto a sticky carbon tab affixed to an SEM stub for analysis. EDX analysis of several regions of the boron imaged by SEM revealed no iron impurities/clusters. A spectrum acquired from a selected area of the sample is shown in Figure 5.32. The wt. % of boron is about 99 % with traces of oxygen and silicon also confirmed in the quantification. Note that a trace of carbon and nitrogen may be identified in the EDX spectrum, but were not detected by the quantification software (INCA). It is possible that the abundance of C and N is too low to be detected, and/or their X-Ray emission peak intensities are hidden within the more intense B and O peaks and are thus mis-identified by the quantification software. Another area scan gave very similar results (to within 0.1 wt %), while spot scans of boron pieces detected only B and O (no Si), with a wt. % of ~ 99.7% for

B and ~ 0.3 % for O. It is a little unexpected that the carbon wt % is so low considering that the powders were dispersed on carbon tabs; one possibility is that the boron powder has almost completely covered the tab (the dispersion was indeed rather compact) for the areas for which the EDX analyses was performed.

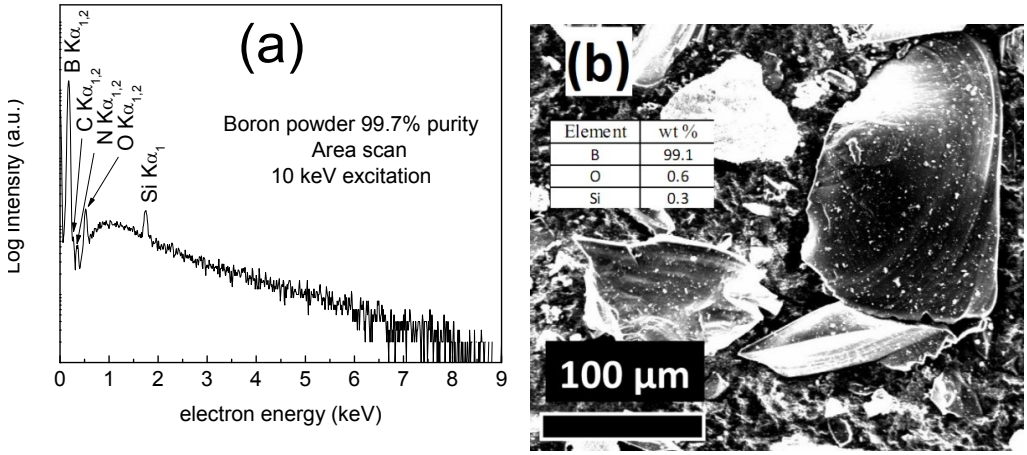

Figure 5.32. (a) EDX spectrum of boron powder, (b) corresponding image and elemental composition.

Results of the EDX analyses for MB_6 powders are now presented, in the order BaB_6, CaB_6, SrB_6. An EDX area spectrum and corresponding SEM image for the BaB_6 powder firstly is shown in Figure 5.33 (a) and (b) respectively. Ba was clearly resolved, as well as C, O, Al, Zn and Si. No boron was resolved (characteristic emission = Lα at 0.183 keV). No iron was detected either. The most intense X-Ray emission energy for iron metal is the $K\alpha_1$ line at 6.40 keV; at lower energy the less intense $L\alpha_{1,2}$ at 0.705 keV may also be used to identify the element. From ICP-MS analysis of the BaB_6 powder, the abundance of iron metal, which was the most abundant ferromagnetic impurity detected, should be 0.02 wt %, or 200 ppm. There is also no evidence for the presence of the other ferromagnetic elements Co and Ni (each present at < 10 ppm from ICP-MS measurements), for which the most intense $K\alpha_1$ X-Ray emissions occur at energies of 6.93 keV and 7.47 keV respectively, with less intense $L\alpha_{1,2}$ emissions at the lower energies of 0.77 keV and 0.85 keV respectively. In addition to the area scan, a spot scan focused on a crystal was also performed, whose SEM image is shown in Fig. 5.33 (c). Apart from an increase in the relative proportion of Ba (and a decrease in C, O and Al), no ferromagnetic elements were detected either. The carbon and silicon are likely due to the carbon tab background (the carbon tab also contains traces of Si). Carbon and oxygen are ubiquitous elements in the SEM vacuum chamber. Al and Zn (but no Si) were also detected by ICP-MS for the BaB_6 powder, with abundances of 0.025 wt% and 0.077 wt% respectively, which would explain their presence in the EDX spectrum of the BaB_6 powder.

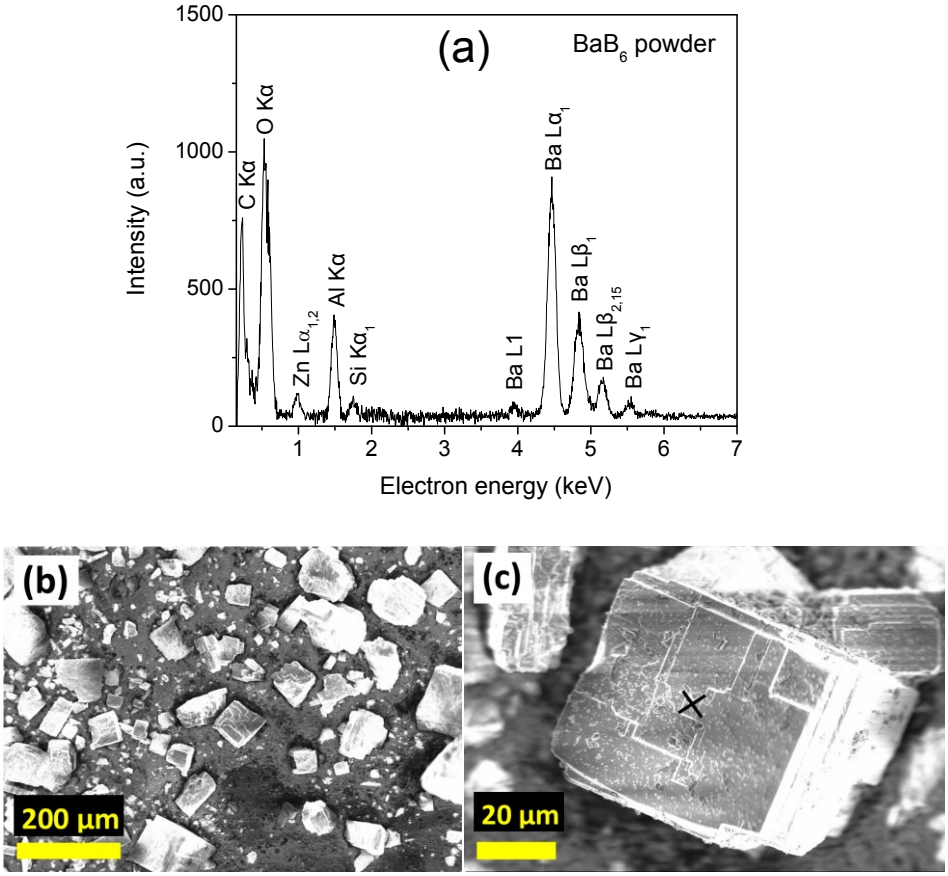

Figure 5.33. (a) SEM-EDX area spectrum for BaB_6 powder synthesized from its constituent elements by solid state reaction. The corresponding area imaged is shown in (b). A spot scan was also acquired at position x on the crystal shown in (c).

SEM-EDX analysis of the CaB_6 bulk powder was performed next. The analysis is of particular importance since the ICP-MS results reveal that the CaB_6 target pressed from the CaB_6 powder contains about an order of magnitude more iron impurities (0.288 wt %) than either the SrB_6 or BaB_6 targets. All EDX spectra were acquired using an excitation energy of 20 keV. Only the EDX peaks that were resolved are shown. Figure 5.34 (a) displays an EDX spectrum acquired from the large area (~ 120 µm × 90 µm) of the CaB_6 powder sprinkled onto a sticky carbon tab imaged in (b). No ferromagnetic impurities were detected. For a spot scan located on a large faceted CaB_6 crystal, an SEM image of which is displayed in (c), no ferromagnetic impurities were detected either (EDX spectrum not shown). For the spot scan, enhanced Ca, B and O content were measured relative to the area scan, while none of N, Na, P, S or Ti were resolved in contrast to the area scan (C, O, Na, S and Si may be due to the carbon tab background for the area scan). Similar results were obtained for spot scans of several other crystals, indicating that the individual crystals themselves seem to be free from ferromagnetic contamination.

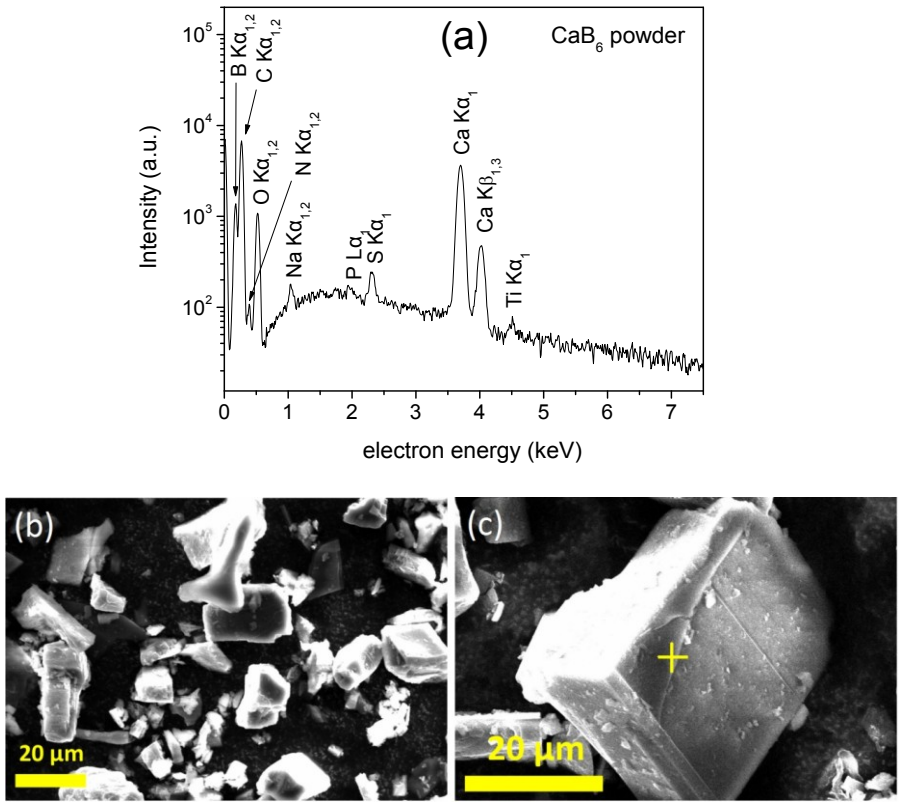

Figure 5.34. (a) SEM-EDX area spectrum for CaB_6 powder synthesized from its constituent elements by solid state reaction. The corresponding area imaged is shown in (b). A spot scan was also acquired at the position marked on the crystal in (c).

Upon further analysis of different regions of the CaB_6 powder sample however, some iron impurities were resolved, as shown in Figure 5.35 on the next page, in which an elemental map of the SEM image was acquired. The iron rich microparticle, which is located in the top middle of the secondary electron image, is clearly detected by the Fe elemental map. For the area imaged, of ~ 50 µm × 40 µm dimension, the iron concentration is 0.58 wt %, or 5800 ppm, or about double that measured by ICP-MS (0.288 wt %). For several other scans of same dimension within the same general region of the sample (< 500 µm distant), similar sized iron rich particles were detected in about 10 % of cases, while for multiple other regions > 500 µm distant, no iron was detected, similar to the result for the area imaged in Fig. 5.34 (b) above.

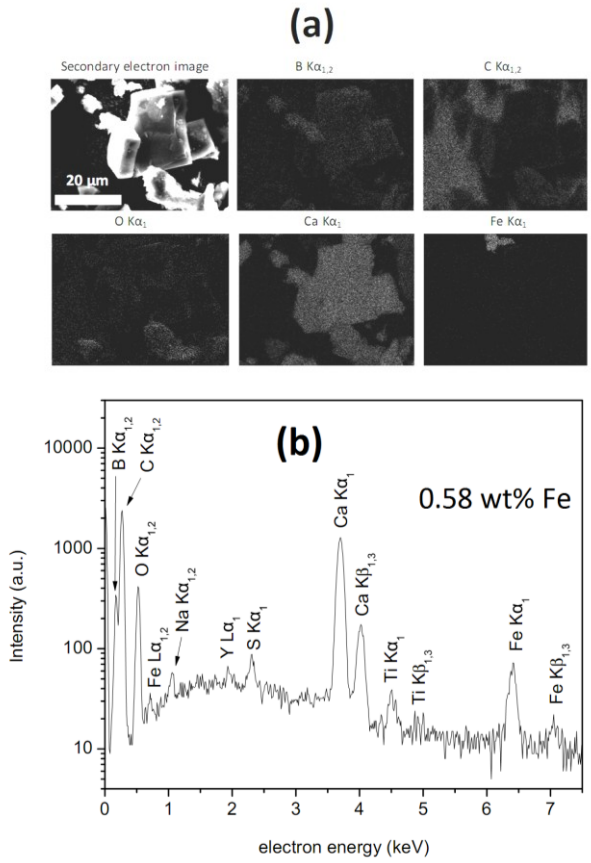

Figure 5.35. (a) SEM-EDX elemental map for a selected area (50 µm × 40 µm) of CaB_6 powder (b) Corresponding EDX spectrum.

In order to determine a more representative value for the overall iron impurity concentration in the region where the disperse iron impurities were found, a larger area of the sample surface, of ~ 800 µm × 900 µm dimension, was imaged and an EDX spectrum acquired. The result is shown in Figure 5.36. The iron impurity concentration is 0.06 wt % (or 600 ppm) for this area. In comparison, the value from ICP-MS is 0.288 wt %, which was for a 100 mg sample. The mass of powder analyzed by SEM-EDX here was of order 1 mg only. Hence it may be reasoned that while some localised EDX area scans may reveal iron impurity concentrations higher than that measured by ICP-MS, in the majority of regions no iron was detected, and the results can be broadly reconciled with those from ICP-MS. The iron-rich microparticles, when present, are in the form of isolated clusters; crucially however, the magnetization data show that the iron impurities in the bulk do not produce a ferromagnetic-like signal at room temperature.

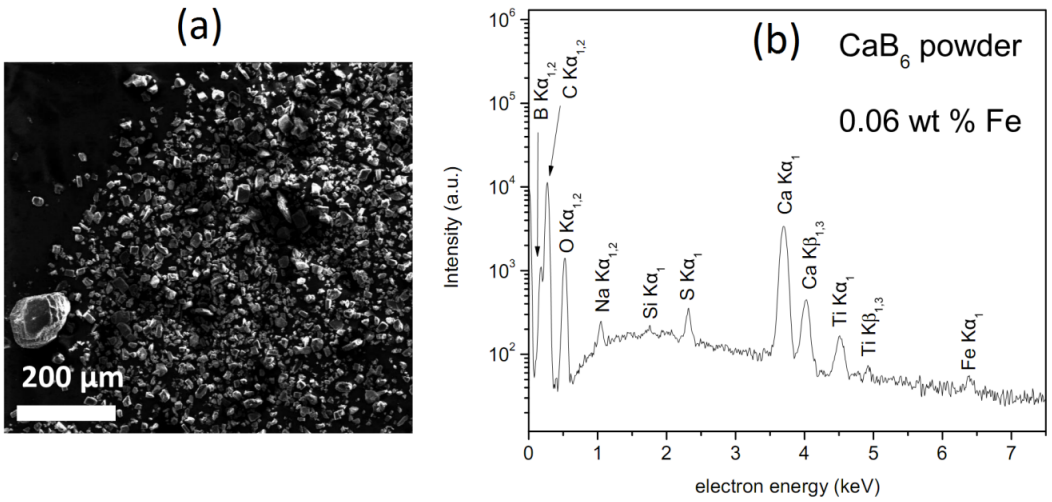

Figure 5.36. (a) SEM image of a large area (800 µm × 900 µm) of CaB_6 powder (b) Corresponding EDX spectrum.

An EDX area spectrum (acquired at 20 keV) and corresponding SEM image for the SrB_6 powder is shown in Figure 5.37 (a) and (b) respectively.

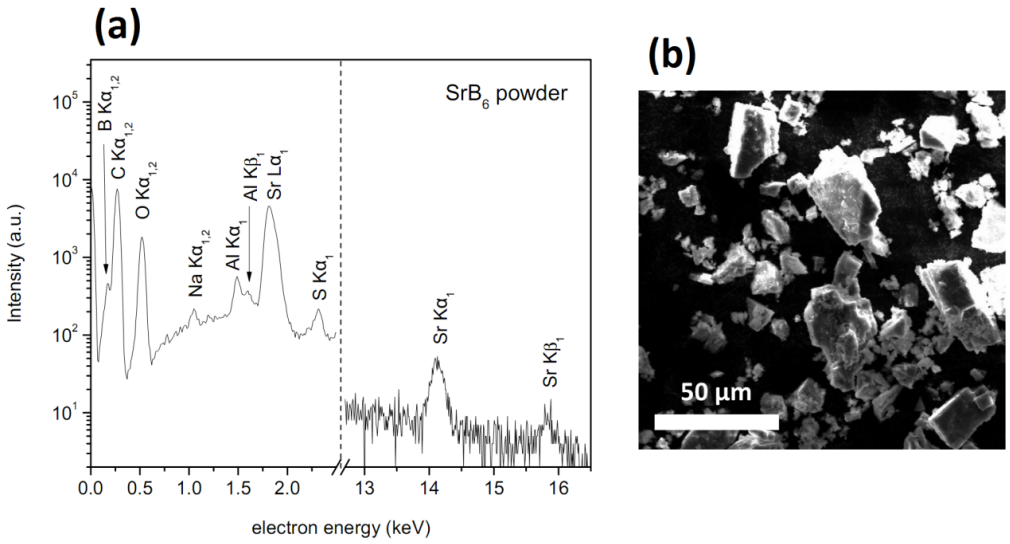

Figure 5.37. (a) SEM-EDX area spectrum for SrB_6 powder (b) SEM image of the corresponding area from which the spectrum was acquired.

For the EDX spectrum of SrB_6 powder shown in Fig. 5.37 above, only peaks which were resolved are displayed. In addition to Sr, B and other common elements (C, O, Na, S), some Al was also resolved (the latter for which 0.3 wt % was detected from the particular area shown in Fig. 5.37 (b), compared to 0.13 wt % as measured by ICP-MS). No iron impurities were detected. Similar results were obtained for other areas and regions of the sample, in none of which any ferromagnetic impurities were resolved. For localised spot scans of SrB_6 crystals, an increase in Sr and B

abundance compared to the area scans was detected, as expected. The iron impurity concentration is 0.026 wt % for the target pressed from the SrB_6 powder as revealed by ICP-MS. Hence it is likely that either the iron is too sparsely distributed to be detected by EDX, or (more likely) if aggregated in clusters the probability of locating one in an EDX area scan is quite low. It is noted that no ferromagnetic impurities were detected in BaB_6 powder either, which should have a similar level of Fe (0.02 wt %), whereas for CaB_6, which contains an order of magnitude more Fe, such impurities were more readily detected within some regions of the powder.

SEM-EDX spectra acquired for ~ 10 nm thick films grown on Al_2O_3 (0001) 5×5 mm substrates using an excitation energy of 14 keV and an imaging area of ~ 50×50 μm are shown in Figure 5.38 below. For 10 nm thick films, if ferromagnetic impurities are responsible for the magnitude of the magnetic signals measured, they should be readily detectable by EDX. Only the features that were resolved are shown; no features were measured at higher energies. No peaks characteristic of any of the ferromagnetic elements Fe, Co or Ni were resolved for similar area scans using a range of different excitation energies (5-20 keV) for any of the 10 nm thick MB_6 films. For CaB_6 and SrB_6 some Ca and Sr was resolved respectively, but for BaB_6 no Ba could be resolved, even at higher energies than shown (primary emission = $L\alpha_1$ at 4.46 keV). Al, O (both from the substrate) and C (mostly deposited during SEM imaging, also a ubiquitous element in the SEM vacuum chamber) are resolved for each system, in addition to some B for SrB_6. For the blank Al_2O_3 (0001) 5×5 mm substrate (also measured at 14 keV), Al and O are clearly resolved, together with some C, P and Ag (the latter of which is likely due to contamination from sample mounting with Ag paint). No ferromagnetic impurities were detected for the blank Al_2O_3 substrate.

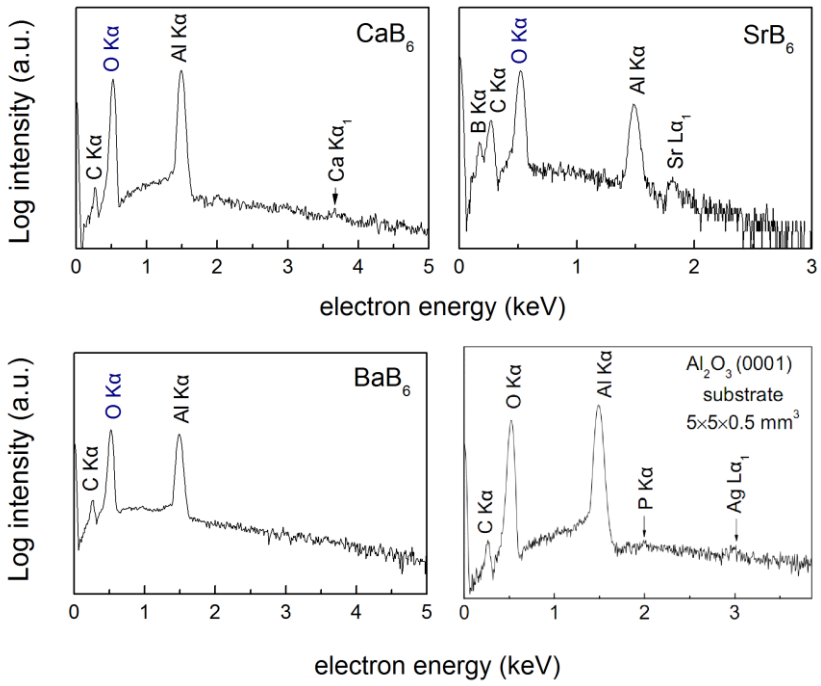

Figure 5.38. SEM-EDX spectra resolved for ~ 10 nm thick MB_6 films grown on (0001) Al_2O_3 substrates (excitation energy = 14 keV, area = 50×50 μm).

SEM-EDX spectra were also acquired for thicker (~ 100 nm) MB_6 films, the results of which are now presented in the order BaB_6, CaB_6, SrB_6. A spectrum/image for a ~ 100 nm thick "magnetic" (i.e. possessing a larger moment of ~ 3×10^{-8} Am^2) BaB_6 film firstly is shown in Figure 5.39; characteristic Ba emission peaks are resolved (unlike for the corresponding 10 nm thick film), and also some Na, Mg and Si in addition to C, O and Al. No ferromagnetic impurities are detected.

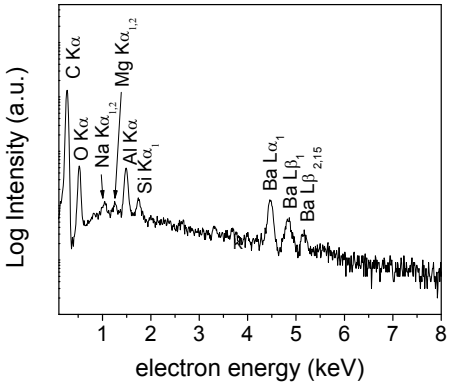

Figure 5.39. SEM-EDX spectra of a ~ 100 nm thick "magnetic" BaB_6 film (excitation energy = 14 keV, area = 50×50 μm).

An SEM-EDX spot spectrum and image of a microparticle on the surface of a 100 nm thick "magnetic" BaB_6 film are shown in Figure 5.40. The position where the spot scan was acquired is marked by a white x in the microparticle image. It is evident that the particle is mostly composed of O, C, Si and Mg, with additional small amounts of Ba (2 wt %), Al (1.1 wt %) and Fe (0.4 wt %). Thus small quantities of iron may be resolved for spot scans on some of the microparticles, which are not resolved in the area scans. However, such microparticles were found to be very scarce on the film surface, and some contained no measurable iron content; typically only one such microparticle of ~ 10 μm size (and volume ~ 5×10^{-16} m^3, approximating for a spherical-like morphology) was observed over large areas of about 300×300 μm, and compared to the volume of the 100 nm thick film over this area (9×10^{-15} m^3), represents a fractional volume of about 5 % only.

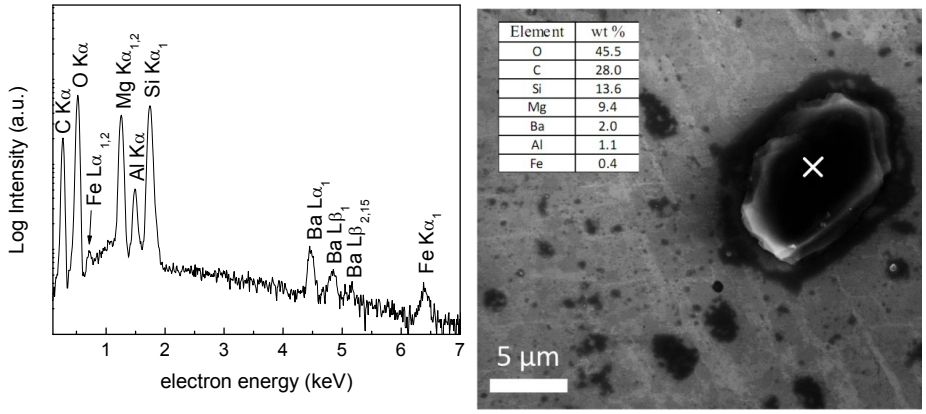

Figure 5.40. SEM-EDX spot spectrum and image of a microparticle at the surface of a ~ 100 nm thick "magnetic" BaB_6 film (excitation energy = 14 keV).

Another SEM-EDX image of a different microparticle on the surface of a 100 nm thick "magnetic" BaB_6 film is shown in Figure 5.41, from which a spot scan was acquired, its position marked with a black x. This particle is mostly composed of C and Ba. No Fe or B was detected. Such particles were very sparsely distributed (on average 1 per ~ 100 μm × 100 μm area) over the film surface however.

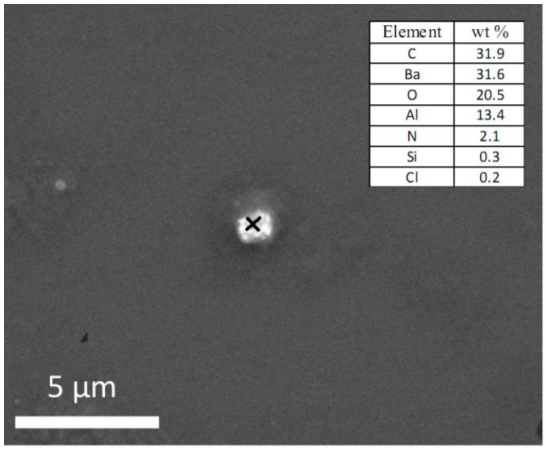

Figure 5.41. SEM image and EDX composition of particle at surface of ~ 100 nm thick "magnetic" BaB_6 film (excitation energy = 14 keV).

An SEM image of a 100 nm thick "magnetic" BaB_6 film acquired in back scattered detection mode is shown in Figure 5.42. This mode of detection provides visual contrast of elemental mass, with heavier elements appearing darker. From the image it can be seen that there are many dark spots apparently on the surface of the film. Spot and area scans of the surface however revealed the presence of mainly Al, O and a small quantity of Ba (≤ 3 %) (plus ubiquitous carbon), with no other heavy elements detected. Hence it is not probable that the dark regions are due to Ba clusters. One possibility is that the darker regions may be from the silver paste adhering to the backside of the substrate.

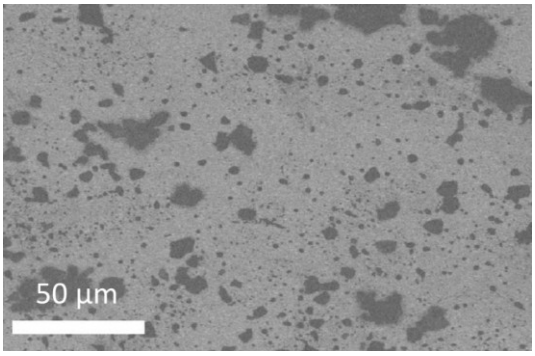

Figure 5.42. SEM image acquired in back-scattered detection mode of the surface of a ~ 100 nm thick "magnetic" MB_6 film.

An SEM-EDX area spectrum and image of a ~ 100 nm thick "magnetic" CaB_6 film are shown in Figure 5.43. Ca and B are resolved, in addition to Al and O from the substrate. Traces of Si are resolved also. No ferromagnetic impurities are detected, however. Spot scans of the particles circled in (b) revealed elevated levels of Si, of order 10 wt %, compared to that typically detected in area scans (of order 0.1 wt %), but no evidence of ferromagnetic elements. The "brightness" of some of the particles may be due to an increased amount of charging under the beam current compared to other areas. Similar scans of numerous other regions of the film, including areas not containing any visible particles on the surface, did not reveal the presence of any ferromagnetic contamination either. Hence it appears that the iron content resolved by EDX in the CaB_6 powder used to fabricate the target for PLD has not translated into the film.

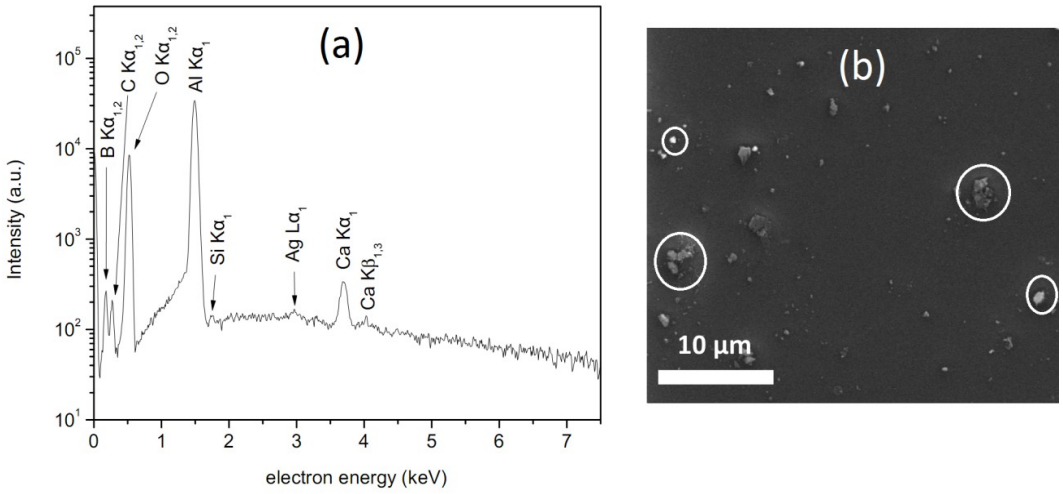

Figure 5.43. (a) EDX area spectrum of SEM image shown in (b) of a ~ 100 nm thick "magnetic" CaB_6 film. Spot scans were also acquired from the particles circled in (b).

Lastly in this section, an SEM-EDX area spectrum and image of a ~ 100 nm thick "magnetic" SrB_6 film are shown in Figure 5.44. Sr and B are resolved, in addition to Al and O from the substrate and the ubiquitous carbon. No traces of ferromagnetic impurities were resolved. A spot scan of the particle marked in (b) revealed an enhancement of carbon content from 16.1 wt % (area scan) to 68.0 wt %, indicating that it is mostly carbonaceous, with no evidence of any ferromagnetic impurities. No ferromagnetic impurities were detected for any other areas of the film or for other particles on the surface.

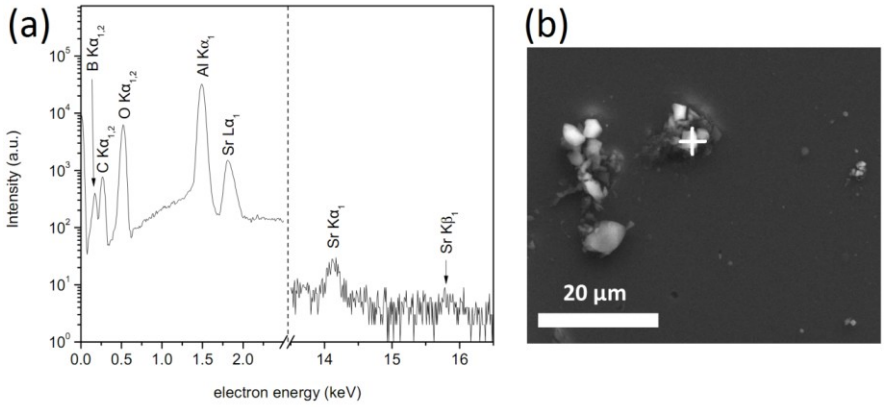

Figure 5.44. (a) EDX area spectrum of SEM image shown in (b) of a ~ 100 nm thick "magnetic" SrB_6 film. A spot scan was also acquired from the particle marked in (b).

5.3.7 Muon spin rotation spectroscopy

In order to further elucidate the local magnetic properties of MB_6 thin films, muon spin rotation (μSR) spectroscopy measurements were performed. Bulk MB_6 powders were also measured as a reference. To briefly re-cap the information provided in the experimental methods section (2.5.4), μSR involves the implantation of positively charged ~ 100 % spin-polarized muons in matter, which have S = 1/2, a magnetic moment of 3.18 μ_{proton} (sensitive to 10^{-3} – 10^{-4} μ_B) and a lifetime in vacuum of 2.197 μs. μSR is analogous to NMR (nuclear magnetic resonance) and EPR and measures the muon spin direction with time via the unique signature of the parity violating decay of the muon, in which its decay positron is emitted preferentially along the muon spin direction. The time evolution of the muon spin polarization depends sensitively both on the spatial distribution and dynamical fluctuations of the muons' magnetic environment. Magnetic and non-magnetic regions co-existing within the same specimen can result in distinct μSR signals whose amplitudes are proportional to the volume of the sample occupied by the particular phase, the frequency to the local field (magnitude of magnetic moments), and the damping to the inhomogeneity of the magnetic regions. Hence differences in the magnetic properties and local magnetic environment of strong/weak magnetic MB_6 films may be possible to elucidate in principle by analysis of the polarization decay signal of the muon ensemble in the films.

Some preliminary results from the muon beamtime are now presented. Firstly, the BaB_6 powder was measured; Figure 5.45 on the next page shows the muon asymmetry as a function of time measured at various temperatures in zero field, in which the data has been fitted to the zero-field Kubo-Tobaye (KT) function [113], whose general form is shown in Fig. 5.45, from which the magnetic field width, Δ_G, may be extracted. Magnetically ordered materials should produce a reduction in the muon asymmetry over time; from Fig. 5.45 it is evident that the damping increases

with decreasing temperature, indicative of enhanced magnetic order, especially below ~ 100 K. At 5.8 K for example, Δ_G is of order 0.5 T. The muon cannot easily distinguish between different types of long-range magnetic order however, hence it could be ferromagnetism (unlikely though from the room temperature magnetization analysis which shows an absence of ferromagnetism for the powder), antiferromagnetism, ferrimagnetism etc. A similar result is measured using muons by Kuroiwa *et al*. [92], who measure distinct magnetic order below 110 K for BaB_6 polycrystals.

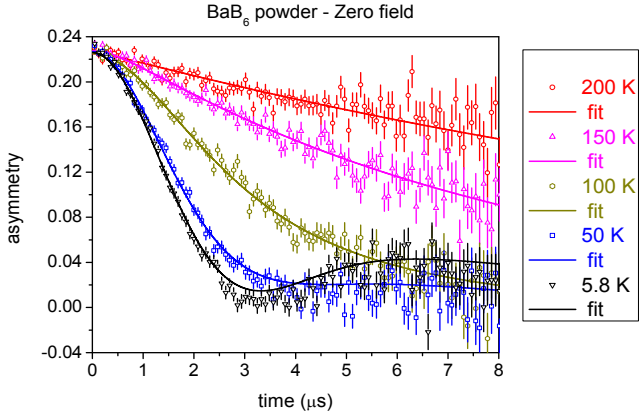

$$P_Z(t) = P_{KT}(t) = \frac{1}{3} + \frac{2}{3}(1 - \gamma_\mu^2 \Delta_G^2 t^2) \exp\left(-\frac{\gamma_\mu^2 \Delta_G^2 t^2}{2}\right) \qquad \omega_\mu = \gamma_\mu B_{ext}.$$

Figure 5.45. Temporal muon asymmetry measured for BaB_6 powder at various temperatures in zero applied magnetic field. The general form of the zero-field Kubo-Tobaye fit function is displayed below the graph.

Zero-field data measured for the CaB_6 powder fitted to the KT function are shown in Figure 5.46 (there was only beamtime for two temperature measurements). Here the CaB_6 powder *is* magnetically ordered at higher temperatures (unlike for BaB_6), with Δ_G ~ 0.4 T for example at 250 K. This result is different to that found by Kuroiwa *et al*. [92], who measure magnetic order for CaB_6 polycrystals below 130 K only (it is also noted that data were also measured here for SrB_6 powder, for which pronounced asymmetry damping is measured at 20 K, similar to the other powders at this temperature; the data collected at higher temperatures is still currently under analysis so is not included here).

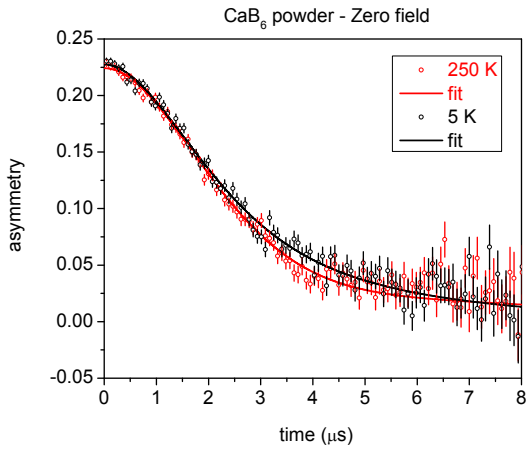

Figure 5.46. Temporal muon asymmetry measured for CaB_6 powder at two temperatures in zero applied magnetic field. The data is fitted to the zero-field Kubo-Tobaye function.

For MB_6 films the preliminary data is now summarized. Firstly, ~ no energy (depth) dependence of the magnetism in any of the MB_6 films was measured in zero field, i.e. the asymmetry vs. time data virtually superposes, with large damping indicative of inhomogenously distributed magnetic order. By varying the muon incident energy, and by using SRIM (Stopping and Range of Ions in Matter) calculations, for which the simulation package is freely available at www.srim.org, the depth at which muons penetrate into a material of particular density may be estimated. It was proposed previously that the magnetism in MB_6 (M = Ca, Sr) films may be concentrated at the film-substrate interface [99], but according to our preliminary muon results there is no difference between the magnetic order sensed by the muon (a) in regions where it stops near this interface and (b) in regions where it stops near the free film surface. Secondly, very little temperature dependence of the magnetism was measured, since the asymmetry vs. time data virtually superposes at 20 K and 200 K, in agreement with SQUID magnetometry measurements in which the measured magnetic signal is practically identical at 4 K and 300 K. Thirdly, little difference in the zero-field asymmetry vs. time data was measured between 100 nm thick "strong" and "weak" magnetic films (moments of ~ 3×10^{-8} Am^2 and ~ 0.5×10^{-8} Am^2 respectively as measured by SQUID magnetometry). As mentioned previously, the muon cannot distinguish between the different types of long-range magnetic order, so it could be the case that there is a significant antiferromagnetic component in *all* of the films, both "strong" and "weak" magnetic, for example. An additional complication towards interpretation of the muon data for the alkaline earth hexaborides is the presence of a quadrupolar level crossing resonance at about 7 mT, in which the muon and the nuclear spin levels can exchange energy, which can lead to muon spin-flipping and to a depolarization of the muon which may be confused with depolarization due to long-range magnetic order sensed by the muon; this question should be resolved by further measurements in longitudinally applied (rather than zero) field, which are currently being performed.

Finally for now, the values of the rates for the dipolar field width Δ and fluctuation frequency ν of the local field (due to muon diffusion) extracted from the zero-field KT fit function

to the data for BaB_6 and CaB_6 (SrB_6 is currently still under analysis), for both powders and thin films (t ~ 100 nm, "strong" magnetic, with the muon mostly probing approximately the bottom 50 nm portion of each film) measured in zero-field at various temperatures is presented in Figure 5.47. What is evident firstly is that the rates are almost temperature independent for both of the films. For the powders, for the dipolar field width Δ firstly, BaB_6 exhibits a decrease in dipolar field width (i.e. a decrease in magnetic order) with increasing temperature, whereas CaB_6 exhibits little variation of the dipolar field width with temperature, in agreement with the results of Figs. 5.45 & 5.46 respectively. The fluctuation rate ν of the local field (due to muon diffusion) decreases markedly below 150 K for BaB_6, which suggests that muon diffusion is present *above* 150 K. Muon diffusion (rather than hopping) can also produce a decay (in addition to long range magnetic order) in the muon asymmetry with time. For CaB_6 however, ν actually *increases* slightly with decreasing temperature; it is not clear why this is so since muon diffusion should result in a higher value for ν at higher temperatures where muon diffusion is more prominent. These questions and more should be resolved upon further detailed analysis of the data.

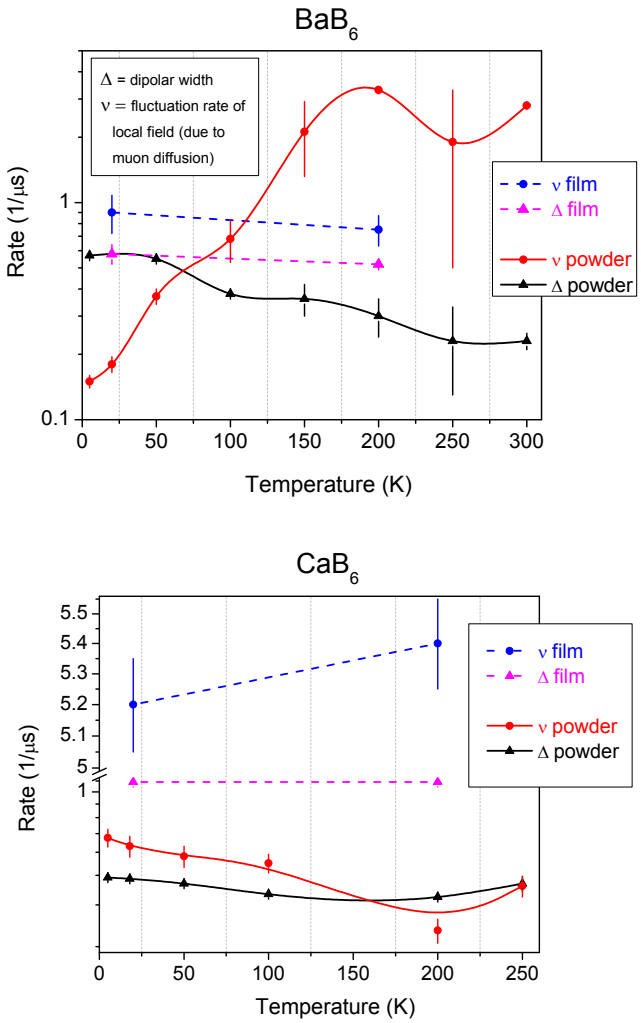

Figure 5.47. Rates for the dipolar field width and the fluctuation of the local field extracted from the zero-field Kubo-Tobaye fit function at various temperatures for zero-field measurements of both BaB_6 and CaB_6 powders and magnetic films (t ~ 100 nm).

5.3.8 Electron paramagnetic resonance spectroscopy

Electronic paramagnetic resonance (EPR) spectra measured for the bulk powders (corrected for their masses) at room temperature are shown in Figure 5.48 on the following page. Typically 3 – 4 mg of powder was measured. EPR measurements revealed asymmetric signals for each system, although the asymmetry is not so pronounced for CaB_6 compared to the other two systems; in addition, while for BaB_6 and SrB_6 there appears to be only a single distinct contribution to the EPR signal, for CaB_6 there appears to be *two* distinct contributions to the signal, one narrow and the other broad. The line asymmetries may possibly indicate the itinerant character of the spins. The powders were inferred to be somewhat conductive due to the partial reduction of the EPR signal magnitude of a MgO reference sample upon the additional insertion of the MB_6 powders inside the EPR cavity (the cavity having two apertures, one on top and one underneath), which indicates an increase in sample conductance associated with a reduction in the cavity Q factor. Specifically, upon insertion of MB_6 (M = Ca, Sr, Ba) powders, the EPR signal magnitude was reduced to 45 %, 57 % and 54 % respectively of its initial magnitude for the MgO calibration sample, when normalised for sample mass. No broad signals characteristic of ferromagnetic resonance with g values significantly different from the free electron value of 2.0023 were measured. The measured g_0 values (g value at EPR intensity 0) were 2.0024, 2.0065 and 1.9928 for CaB_6, SrB_6 and BaB_6 respectively, and the number of spins/gram were estimated (assuming S = 1/2) to be of order 10^{18} for CaB_6 and SrB_6 (equivalent to a paramagnetic concentration of 1000 ppm), and 10^{17} for BaB_6 (100 ppm). It is noted that the g_0 value measured for CaB_6 (2.0024) is the closest to that of the free electron value (2.0023). Similar signals have been measured at room temperature for single crystals of alkali (Li, Na) hexaborides [114], rare-earth (Eu) hexaborides [8] and pure CaB_6 crystals [115], the latter for which a g value of 2.005 was measured. For $Ca_{1-x}La_xB_6$ (x=0.005) discs cleaved from single crystals, *symmetric* EPR signals were measured [83], which the authors ascribed to surface spins within the microwave skin depth (1.5 μm) in a metallic sample. For $Ca_{1-x}M_xB_6$ (M = Gd, Eu, $0.0001 \leq x \leq 0.3$) single crystals, the lineshapes transform from Lorentzian to Dysonian as x increases, indicating a transition from an insulating to conducting environment [84-87]. It is noted that for MB_6 thin films grown from the MB_6 powder targets, no EPR signals were resolved after subtraction of the signal due to the Al_2O_3 substrate for any orientation of applied magnetic field with respect to the thin film surface. This result may not be surprising considering that the mass of a typical 100 nm thick MB_6 film is about 3 orders of magnitude smaller than that of the MB_6 powders measured, which would correspond to only $\sim 10^{14\text{-}15}$ spins/gram, which is not far above the absolute limit of the sensitivity of EPR ($\sim 10^{13}$ spins/gram).

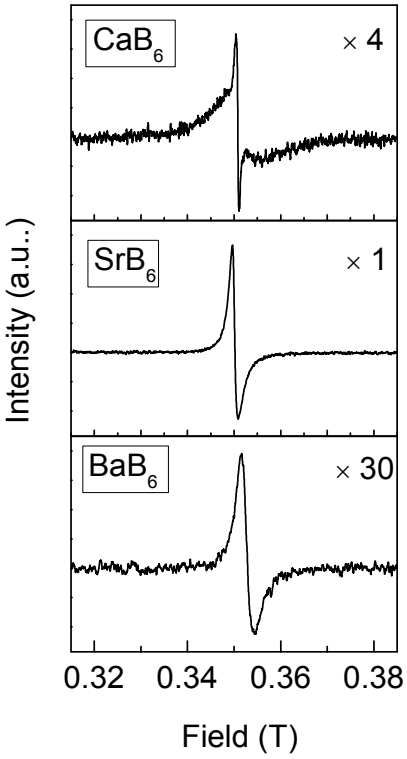

Figure 5.48. Room temperature EPR spectra measured for crystalline MB_6 powders.

5.3.9 Raman spectroscopy

Room temperature Raman spectra measured for the MB_6 powders are shown in Figure 5.49. The optical vibration modes of the cubic hexaborides at the Γ point are described by $\Gamma_{opt} = A_{1g} + E_g + F_{1g} + F_{2g} + 2F_{1u} + F_{2u}$, where A_{1g}, E_g, and F_{2g} are first-order Raman active scattering modes associated with the octahedral boron framework, which were measured for each powder sample; such first-order Raman active scattering modes have previously been measured for crystals of rare-earth (Eu, Gd) hexaborides [116], and for a host of divalent (Yb, Sr, Ca) and trivalent (Dy, Tb, Gd, Nd, La) hexaborides [117,118]. The Raman active modes of CaB_6 are among several hexaboride crystals measured by Ogita *et al.* [119-121], while Song *et al.* [122, 123] performed an in-depth Raman study of CaB_6 crystals alone. An additional mode (at ~ 1450 cm^{-1}) was measured here for SrB_6, which may be due to an impurity or defect which could trigger a local breaking of the B_6 octahedral symmetry. Shifts in Raman wavenumber of up to 20 cm^{-1} were found for different regions of the same powder, possibly as a result of intrinsic stoichiometric variations associated with different

defect vacancies. The origin of the asymmetry of the Raman signals is also likely defect related. For the corresponding thin films grown by PLD, the Raman modes were almost completely broadened out, indicative of their amorphous nature.

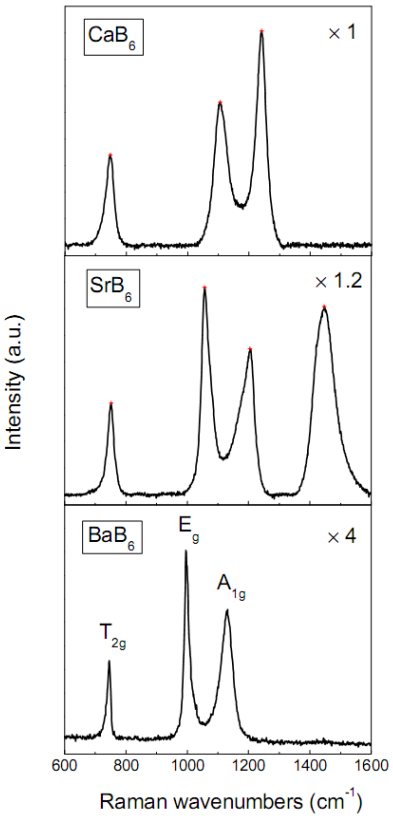

Figure 5.49. Raman spectra for crystalline MB_6 powders measured at room temperature.

5.4. Summary

Room temperature ferromagnetism is measured for many defect-rich amorphous MB_6 (M = Ca, Sr, Ba) films, when they are grown by PLD on Al_2O_3 substrates at 400 - 650°C. The magnetism is virtually anhysteretic, isotropic, temperature independent from 4−300 K and saturates quickly (< 0.3 T) in applied field. The magnetic signals correspond to average film magnetizations in the range 10−100 kA m^{-1}, but from analysis of the variation of the magnetic moment with film thickness, it is shown that the magnetism originates mainly near the interface with the substrate. It is shown using various characterization techniques (magnetization curve analysis, SEM-EDX, ICP-MS) that ferromagnetic impurities cannot account for the magnitude of the larger magnetic signals measured. The most plausible origin of the magnetism in the defect-rich amorphous thin films may be a defect-based impurity band, which can become spin-split and result in high temperature Stoner ferromagnetism when a localized density of states at the Fermi level is sufficiently large, according to the theoretical predictions of Edwards and Katsnelson [82], which could be confirmed by further measurements of the low temperature specific heat capacity and Pauli susceptibility for example.

5.5. References

[1] S. Sullow, et al., Physical Review B **57**, 5860 (1998).

[2] S. Massidda, A. Continenza, T. M. dePascale, and R. Monnier, Zeitschrift Fur Physik B-Condensed Matter **102**, 83 (1997).

[3] G. E. Grechnev, A. E. Baranovskiy, V. D. Fil, T. V. Ignatova, I. G. Kolobov, A. V. Logosha, N. Y. Shitsevalova, V. B. Filippov, and O. Eriksson, Low Temperature Physics **34**, 921 (2008).

[4] M. J. Calderon, L. G. L. Wegener, and P. B. Littlewood, Physical Review B **70**, 092408 (2004).

[5] R. G. Goodrich, N. Harrison, J. J. Vuillemin, A. Teklu, D. W. Hall, Z. Fisk, D. Young, and J. Sarrao, Physical Review B **58**, 14896 (1998).

[6] M. C. Aronson, J. L. Sarrao, Z. Fisk, M. Whitton, and B. L. Brandt, Physical Review B **59**, 4720 (1999).

[7] X. Zhang, S. von Molnar, Z. Fisk, and P. Xiong, Physical review letters **100**, 167001 (2008).

[8] J. M. Tarascon, J. Etourneau, J. M. Dance, P. Hagenmuller, R. Georges, S. Angelov, and S. Vonmolnar, Journal of the Less-Common Metals **82**, 277 (1981).

[9] J. M. Tarascon, J. Etourneau, P. Dordor, P. Hagenmuller, M. Kasaya, and J. M. D. Coey, Journal of Applied Physics **51**, 574 (1980).

[10] M. Kasaya, J. M. Tarascon, J. Etourneau, P. Hagenmuller, and J. M. D. Coey, Le Journal de Physique Colloques **40**, C5 (1979).

[11] J. Denlinger, J. Clack, J. Allen, G. H. Gweon, D. Poirier, C. Olson, J. Sarrao, A. Bianchi, and Z. Fisk, Physical Review Letters **89**, 157601 (2002).

[12] J. D. Denlinger, G.-H. Gweon, S.-K. Mo, J. W. Allen, J. L. Sarrao, A. D. Bianchi, and Z. Fisk, Journal of the Physical Society of Japan **71**, Suppl. pp. 1 (2002).

[13] A. Menth, E. Buehler, and T. Geballe, Physical Review Letters **22**, 295 (1969).

[14] D. P. Young, et al., Nature **397**, 412 (1999).

[15] H. R. Ott, J. L. Gavilano, B. Ambrosini, P. Vonlanthen, E. Felder, L. Degiorgi, D. P. Young, Z. Fisk, and R. Zysler, Physica B **281**, 423 (2000).

[16] G. Ortiz, M. Harris, and P. Ballone, Physical Review Letters **82**, 5317 (1999).

[17] D. Ceperley, Nature **397**, 386 (1999).

[18] S. Souma, H. Komatsu, T. Takahashi, R. Kaji, T. Sasaki, Y. Yokoo, and J. Akimitsu, Physical Review Letters **90**, 027202 (2003).

[19] S. Souma and T. Takahashi, Journal of Physics: Condensed Matter **19**, 355003 (2007).

[20] T. Terashima, C. Terakura, Y. Umeda, N. Kimura, H. Aoki, and S. Kunii, Journal of the Physical Society of Japan **69**, 2423 (2000).

[21] M. E. Zhitomirsky, T. M. Rice, and V. I. Anisimov, arXiv:cond-mat/9904330v1 [cond-mat.str-el] (1999).

[22] M. E. Zhitomirsky, T. M. Rice, and V. I. Anisimov, Nature **402**, 251 (1999).

[23] L. Balents and C. M. Varma, Physical Review Letters **84**, 1264 (2000).

[24] V. Barzykin and L. P. Gor'kov, Physical Review Letters **84**, 2207 (2000).

[25] M. E. Zhitomirsky and T. M. Rice, Physical Review B **62**, 1492 (2000).

[26] C. O. Rodriguez, R. Weht, and W. E. Pickett, Physical Review Letters **84**, 3903 (2000).

[27] P. Vonlanthen, E. Felder, L. Degiorgi, H. R. Ott, D. P. Young, A. D. Bianchi, and Z. Fisk, Physical Review B **62**, 10076 (2000).

[28] K. Yagasaki, Physica B: Condensed Matter **329-333**, 1259 (2003).

[29] T. Kasuya, Journal of Magnetism and Magnetic Materials **222**, 233 (2000).

[30] T. A. Gloor, M. E. Zhitomirsky, and T. M. Rice, The European Physical Journal B - Condensed Matter and Complex Systems **21**, 491 (2001).

[31] J. Li, N. Hao, and Y. Wang, arXiv:1006.1687v1 [cond-mat.dis-nn] (2010).

[32] T. Ichinomiya, Physical Review B **63**, 045113 (2001).

[33] M. Veillette and L. Balents, Physical Review B **65**, 014428 (2001).

[34] S. Murakami, R. Shindou, N. Nagaosa, and A. Mishchenko, Physical Review Letters **88**, 126404 (2002).

[35] S. Murakami, R. Shindou, N. Nagaosa, and A. S. Mishchenko, Journal of Physics and Chemistry of Solids **63**, 1285 (2002).

[36] S. Murakami, R. Shindou, N. Nagaosa, and A. S. Mishchenko, Physical Review B **66**, 184405 (2002).

[37] G. Baskaran, Physical Review B **65**, 212403 (2002).

[38] H. C. Longuet-Higgins and M. de V. Roberts, Proceedings of the Royal Society A: Mathematical, Physical and Engineering Sciences **224**, 336 (1954).

[39] R. W. Johnson and A. H. Daane, Journal of Chemical Physics **38**, 425 (1963).

[40] P. G. Perkins, D. R. Armstrong, and A. Breeze, Journal of Physics C-Solid State Physics **8**, 3558 (1975).

[41] S. Massidda, R. Monnier, and E. Stoll, European Physical Journal B **17**, 645 (2000).

[42] K. Schmitt, C. Stuckl, H. Ripplinger, and B. Albert, Solid State Sciences **3**, 321 (2001).

[43] S. V. Okatov, A. L. Ivanovskii, Y. E. Medvedeva, and N. I. Medvedeva, Physica Status Solidi B-Basic Research **225**, R3 (2001).

[44] A. E. Baranovskiy, G. E. Grechnev, A. V. Logosha, I. V. Svechkarev, V. B. Filippov, N. Y. Shitsevalova, O. J. Żogał, and O. Eriksson, physica status solidi (c) **3**, 229 (2006).

[45] S.-P. Gao, J. Jiang, M. Cao, J. Zhu, and J. Yuan, Physical Review B **69**, 214419 (2004).

[46] S. Shang, Y. Wang, and Z.-K. Liu, Physical Review B **75**, 024302 (2007).

[47] H. Tromp, P. van Gelderen, P. Kelly, G. Brocks, and P. Bobbert, Physical Review Letters **87**, 016401 (2001).

[48] H. Kino, F. Aryasetiawan, M. van Schilfgaarde, T. Kotani, T. Miyake, and K. Terakura, Journal of Physics and Chemistry of Solids **63**, 1595 (2002).

[49] H. Kino, F. Aryasetiawan, K. Terakura, and T. Miyake, Physical Review B **66**, 121103 (2002).

[50] Z. Wu, D. Singh, and R. Cohen, Physical Review B **69**, 193105 (2004).

[51] B. Lee and L.-W. Wang, Applied Physics Letters **87**, 262509 (2005).

[52] S. Souma, T. Takahashi, H. Komatsu, T. Sato, H. Matsui, N. Kimura, H. Aoki, S. Kunii, and J. Akimitsu, Physical Review B **70**, 073104 (2004).

[53] C. Hotta, M. Ogata, and H. Fukuyama, Journal of Physics and Chemistry of Solids **63**, 1505 (2002).

[54] C. Hotta, H. Fukuyama, and M. Ogata, Physical Review B **65**, 184421 (2002).

[55] Z. M. Helms, P. Sen, and L. Mitas, arXiv:cond-mat/0509363v1 [cond-mat.mtrl-sci] (2005).

[56] J.-S. Rhyee, B. H. Oh, B. K. Cho, M. H. Jung, H. C. Kim, Y. K. Yoon, J. H. Kim, and T. Ekino, arXiv:cond-mat/0310068v1 (2003).

[57] B. Cho, J.-S. Rhyee, B. Oh, M. Jung, H. Kim, Y. Yoon, J. Kim, and T. Ekino, Physical Review B **69**, 113202 (2004).

[58] I. J. Kang and C. H. Park, Journal of the Korean Physical Society **49**, S490 (2006).

[59] K. Maiti, V. Medicherla, S. Patil, and R. Singh, Physical Review Letters **99**, 266401 (2007).

[60] K. Maiti, Europhysics Letters **82**, 67006 (2008).

[61] J. Cao, Y. Zhu, Z. Yang, and R. Wu, Physical Review B **79**, 132404 (2009).

[62] I. Popov, N. Baadji, and S. Sanvito, Physical Review Letters **108**, 107205 (2012).

[63] R. E. J. Sears, Journal of Chemical Physics **76**, 5651 (1982).

[64] T. Moriwaka, T. Nishioka, and N. K. Sato, Journal of the Physical Society of Japan **70**, 341 (2001).

[65] K. Matsubayashi, M. Maki, T. Tsuzuki, T. Nishioka, and N. K. Sato, Nature **420**, 143 (2002).

[66] K. Matsubayashi, M. Maki, T. Moriwaka, T. Tsuzuki, T. Nishioka, C. H. Lee, A. Yamamoto, T. Ohta, and N. K. Sato, Journal of the Physical Society of Japan **72**, 2097 (2003).

[67] Z. Fisk, H. R. Ott, V. Barzykin, and L. P. Gor'kov, Physica B-Condensed Matter **312**, 808 (2002).

[68] K. Taniguchi, T. Katsufuji, F. Sakai, H. Ueda, K. Kitazawa, and H. Takagi, Physical Review B **66**, 064407 (2002).

[69] S. Otani and T. Mori, Journal of the Physics Society Japan **71**, 1791 (2002).

[70] T. Mori and S. Otani, Solid State Communications **123**, 287 (2002).

[71] C. Meegoda, M. Trenary, T. Mori, and S. Otani, Physical Review B **67**, 172410 (2003).

[72] M. Bennett, et al., Physical Review B **69**, 132407 (2004).

[73] M. Cao, J. Jiang, H. Liu, and J. Yuan, Physica B: Condensed Matter **364**, 150 (2005).

[74] M. Cao, J. Jiang, H. Liu, and J. Yuan, Physica B: Condensed Matter **369**, 39 (2005).

[75] M. Mihara, et al., International Journal of PIXE **15**, 85 (2005).

[76] T. Jarlborg, Physical Review Letters **85**, 186 (2000).

[77] T. Jarlborg, Physica B-Condensed Matter **307**, 291 (2001).

[78] T. Jarlborg, Journal of Physics-Condensed Matter **15**, L249 (2003).

[79] R. Monnier and B. Delley, Physical Review Letters **87**, 157204 (2001).

[80] J. Janak, Physical Review B **16**, 255 (1977).

[81] S. Li, O. Prabhakar, T. T. Tan, C. Q. Sun, X. L. Wang, S. Soltanian, J. Horvat, and S. X. Dou, Applied Physics Letters **81**, 874 (2002).

[82] D. M. Edwards and M. I. Katsnelson, Journal of Physics: Condensed Matter **18**, 7209 (2006).

[83] S. Kunii, Journal of the Physical Society of Japan **69**, 3789 (2000).

[84] R. R. Urbano, et al., Physica B-Condensed Matter **320**, 419 (2002).

[85] R. R. Urbano, et al., Physical Review B **65**, 180407 (2002).

[86] R. R. Urbano, P. G. Pagliuso, C. Rettori, P. Schlottmann, Z. Fisk, B. Chapler, and S. B. Oseroff, Physica Status Solidi a-Applications and Materials Science **203**, 1550 (2006).

[87] J. G. S. Duque, R. R. Urbano, P. G. Pagliuso, C. Rettori, P. Schlottmann, Z. Fisk, and S. B. Oseroff, Journal of Magnetism and Magnetic Materials **310**, 864 (2007).

[88] J. Gavilano, S. Mushkolaj, D. Rau, H. Ott, A. Bianchi, D. Young, and Z. Fisk, Physical Review B **63**, 140410 (2001).

[89] J. L. Gavilano, B. Ambrosini, H. R. Ott, D. P. Young, and Z. Fisk, Physica B **281**, 428 (2000).

[90] S. Lofland, B. Seaman, K. Ramanujachary, N. Hur, and S. Cheong, Physical Review B **67**, 020410 (2003).

[91] J.-S. Rhyee, Journal of Applied Physics **95**, 6675 (2004).

[92] S. Kuroiwa, H. Takagiwa, M. Yamazawa, J. Akimitsu, A. Koda, R. Kadono, K. Ohishi, W. Higemoto, and I. Watanabe, Science and Technology of Advanced Materials **7**, 12 (2006).

[93] S. Xin, S. Liu, Z. Zhao, J. Yang, B. Xu, Y. Tian, and D. Yu, Science China Physics, Mechanics and Astronomy **54**, 1791 (2011).

[94] J. Y. Kim, N. H. Sung, and B. K. Cho, Journal of Applied Physics **101**, 09D512 (2007).

[95] J. Gavilano, Physica B: Condensed Matter **329-333**, 570 (2003).

[96] F. Iga, Y. Ueda, T. Takabatake, T. Suzuki, W. Higemoto, K. Nishiyama, and H. Kawanaka, Physical Review B **65**, 220408(R) (2002).

[97] Y. Sakuraba, H. Kato, F. Sato, and T. Miyazaki, Physical Review B **69**, 140406(R) (2004).

[98] Y. Sakuraba, H. Kato, F. Sato, T. Miyazaki, N. Kimura, and H. Aoki, Journal of Magnetism and Magnetic Materials **272-276**, 1145 (2004).

[99] L. S. Dorneles, M. Venkatesan, M. Moliner, J. G. Lunney, and J. M. D. Coey, Applied Physics Letters **85**, 6377 (2004).

[100] K. Ackland, M. Venkatesan, and J. M. D. Coey, Journal of Applied Physics **111**, 07A322 (2012).

[101] K. Ackland, M. Venkatesan, and J. M. D. Coey, European Physical Journal B **86**, 104 (2013).

[102] J. Akimitsu, K. Takenawa, K. Suzuki, H. Harima, and Y. Kuramoto, Science **293**, 1125 (2001).

[103] T. Mori and S. Otani, Journal of the Physics Society Japan **71**, 1789 (2002).

[104] S. Shang and Z.-K. Liu, Applied Physics Letters **90**, 091914 (2007).

[105] Y. Kato, et al., Applied Surface Science **258**, 4000 (2012).

[106] R. Salzer, D. Spemann, P. Esquinazi, R. Höhne, A. Setzer, K. Schindler, H. Schmidt, and T. Butz, Journal of Magnetism and Magnetic Materials **317**, 53 (2007).

[107] S. M. M. Yee, D. A. Crandles, and L. V. Goncharova, Journal of Applied Physics **110**, 033906 (2011).

[108] M. Khalid, A. Setzer, M. Ziese, P. Esquinazi, D. Spemann, A. Pöppl, and E. Goering, Physical Review B **81**, 214414 (2010).

[109] M. A. Garcia, E. Fernandez Pinel, J. de la Venta, A. Quesada, V. Bouzas, J. F. Fernández, J. J. Romero, M. S. Martín González, and J. L. Costa-Krämer, Journal of Applied Physics **105**, 013925 (2009).

[110] L. M. C. Pereira, J. P. Araújo, M. J. Van Bael, K. Temst, and A. Vantomme, Journal of Physics D: Applied Physics **44**, 215001 (2011).

[111] D. W. Abraham, M. M. Frank, and S. Guha, Applied Physics Letters **87**, 252502 (2005).

[112] J. M. D. Coey, J. T. Mlack, M. Venkatesan, and P. Stamenov, IEEE Transactions on Magnetics **46**, 2501 (2010).

[113] R. Kubo and T. Toyabe, *Magnetic Resonance and Relaxation,* p. 810 (North-Holland, 1967).

[114] L. W. Rupp and D. J. Hodges, Journal of Physics and Chemistry of Solids **35**, 617 (1974).

[115] S. Angappan, M. Helan, A. Visuvasam, L. J. Berchmans, and V. Ananth, Ionics **17**, 527 (2011).

[116] M. Ishii, M. Aono, S. Muranaka, and S. Kawai, Solid State Communications **20**, 437 (1976).

[117] S. Turrell, Z. Yahia, J. P. Huvenne, B. Lacroix, and G. Turrell, Journal of Molecular Structure **174**, 455 (1988).

[118] Z. Yahia, S. Turrell, J. P. Mercurio, and G. Turrell, Journal of Raman Spectroscopy **24**, 207 (1993).

[119] N. Ogita, S. Nagai, N. Okamoto, F. Iga, S. Kunii, J. Akimitsu, and M. Udagawa, Physica B: Condensed Matter **328**, 131 (2003).

[120] N. Ogita, Physica B: Condensed Matter **329-333**, 661 (2003).

[121] N. Ogita, S. Nagai, N. Okamoto, F. Iga, S. Kunii, T. Akamtsu, J. Akimitsu, and M. Udagawa, Journal of Solid State Chemistry **177**, 461 (2004).

[122] M. Song, I.-S. Yang, J. Y. Kim, and B. K. Cho, Journal of the Korean Physical Society **49**, L1 (2006).

[123] M. Song, I.-S. Yang, J. Y. Kim, and B. K. Cho, Vibrational Spectroscopy **42**, 288 (2006).

Chapter 6

Discussion

In this chapter, a general discussion of the experimental results for d^0 magnetism in the three systems presented in this thesis, namely reduced HfO_2 micropowders, CeO_2 nanoparticles and MB_6 (M = Ca, Sr, Ba) alkaline-earth hexaboride thin films, is presented. Firstly, previous results for d^0 magnetism measured for other systems synthesized/grown in our laboratory are presented including a data mining exercise of M_s and H_0 values, and comparisons are drawn with the data from this thesis. Secondly, some models for d^0 magnetism are discussed together with which model best fits the experimental data for each system studied.

6.1. M_s and H_0 data mining

Plots of the saturation magnetization M_s versus the field H_0 obtained by extrapolating the initial susceptibility of the magnetization curve to saturation, as shown in previous chapters, are a useful way to graphically summarize large quantities of data for anhysteretic d^0 samples, since they allow a quick comparison of not only the M_s and H_0 values but also the ferromagnetic volume fraction f of large datasets.

Firstly, room temperature magnetization data for all of the d^0 or dilute magnetic oxide samples synthesized or grown in our laboratory since ~ 2004 was collected and compiled into a master plot of M_s and H_0 values, which is shown in Figure 6.1. Data for some other iron containing samples are also displayed for comparison, such as highly oriented pyrolytic graphite (HOPG), iron microparticles and nanoparticles, and data for the Canyon Diablo meteorite (mostly composed of magnetite and kamacite FeNi alloys) for example. The films possess M_s values several orders of magnitude higher than those measured for powder/bulk samples, while the majority of the samples have H_0 values of ~ 80 ± 30 kA m^{-1}, which is less than that of iron but similar to that of magnetite; since most of the films have M_s values of order 10 kA m^{-1} however, approximately 1 part in 30

would have to be magnetite impurities to account for the magnitudes of the magnetic signals measured. Such impurity levels are not typically measured for these films, hence it is rather implausible that the magnetic signals can be accounted for by ferromagnetic impurities alone. It is also evident that the ferromagnetic volume fraction for films is several orders of magnitude higher (generally 1 % or more) than those for the bulk (generally 10s or 100s of ppm only).

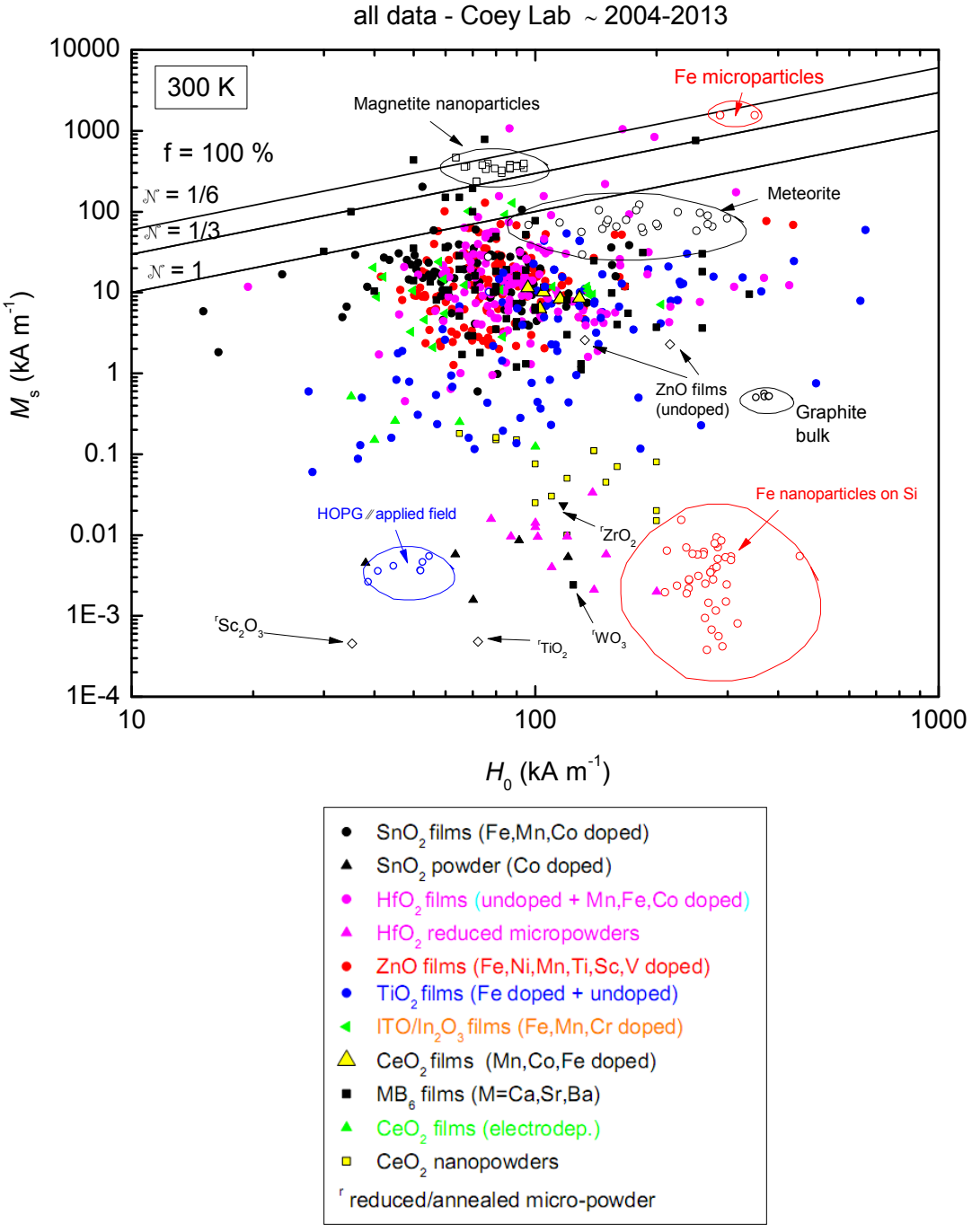

Figure 6.1. Room temperature M_s and H_0 values for all of the d^0 or dilute magnetic oxide samples synthesized/grown in our laboratory since ~ 2004. All films are grown by PLD unless stated otherwise.

In Figure 6.2, data for all of the films are compared only, differentiated by those that are doped and those that are undoped. The M_s values for the majority of the films, which are ~ 100-400 nm thick, are of order 10 kA m^{-1}, whereas those for thinner films, which are mostly undoped, are of order 100 kA m^{-1} or greater, and approach 100 % ferromagnetic volume fractions. The majority of the samples have H_0 values of ~ 80 ± 30 kA m^{-1}, regardless of whether they are doped or undoped. In fact, there is no clear difference between the data for undoped and doped samples, which may suggest that the magnetic phenomenon is similar for both datasets. In Figures 6.3 & 6.4 the data is broken down into that pertaining to undoped and doped films respectively.

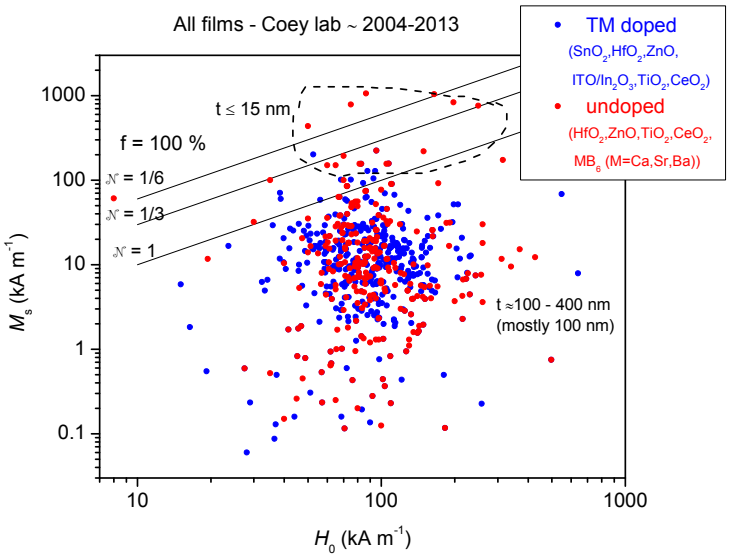

Figure 6.2. Comparison of room temperature M_s and H_0 values for doped and undoped films grown in our laboratory by PLD since ~ 2004.

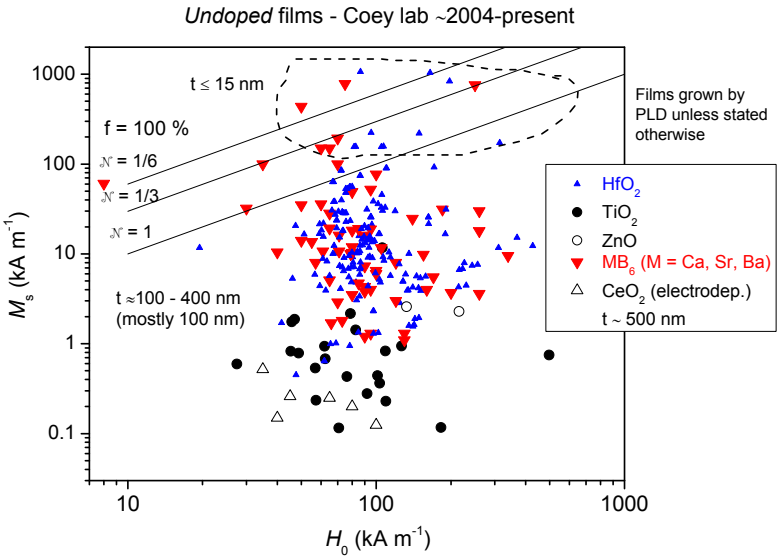

Figure 6.3. Room temperature M_s and H_0 values for *undoped* films grown in our laboratory since ~ 2004.

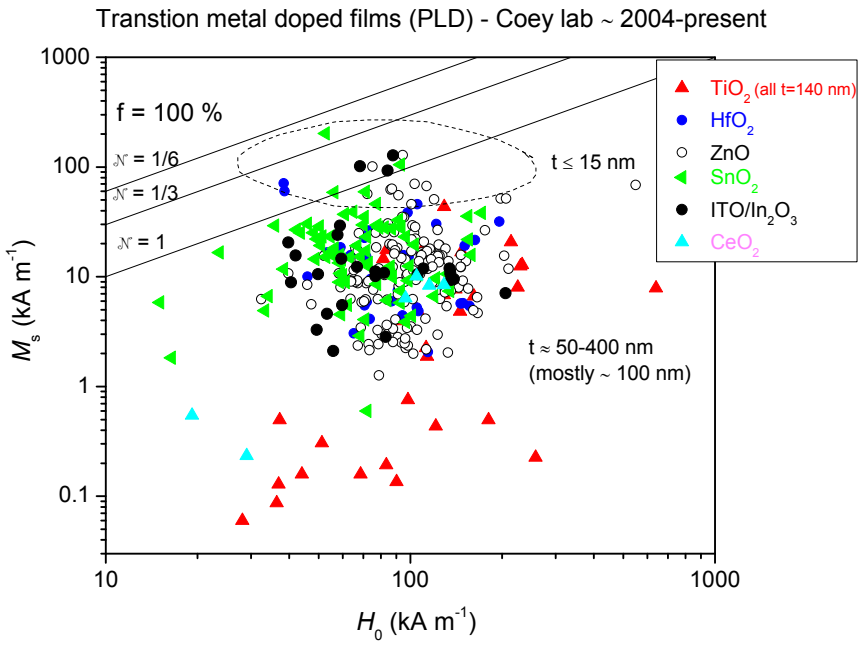

Figure 6.4. Room temperature M_s and H_0 values for *doped* films grown in our laboratory since ~ 2004.

Data for HfO_2 films only grown by PLD in our laboratory are shown next in Figure 6.5. The data highlights that M_s generally increases with decreasing film thickness, and that data for transition metal doped films generally fall within similar regions to those for undoped films. Similar data for ZnO, SnO_2 and TiO_2 films are also presented in Figures 6.6, 6.7 & 6.8 respectively.

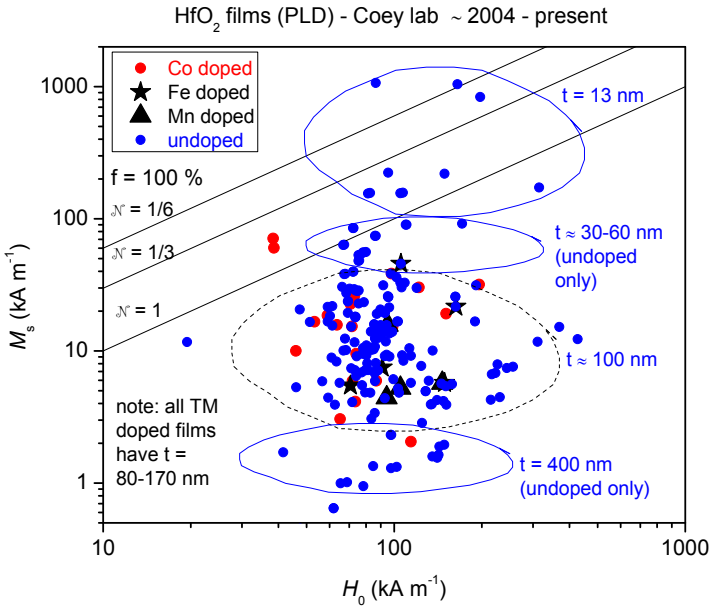

Figure 6.5. Room temperature M_s and H_0 values for HfO_2 films grown in our laboratory since ~ 2004.

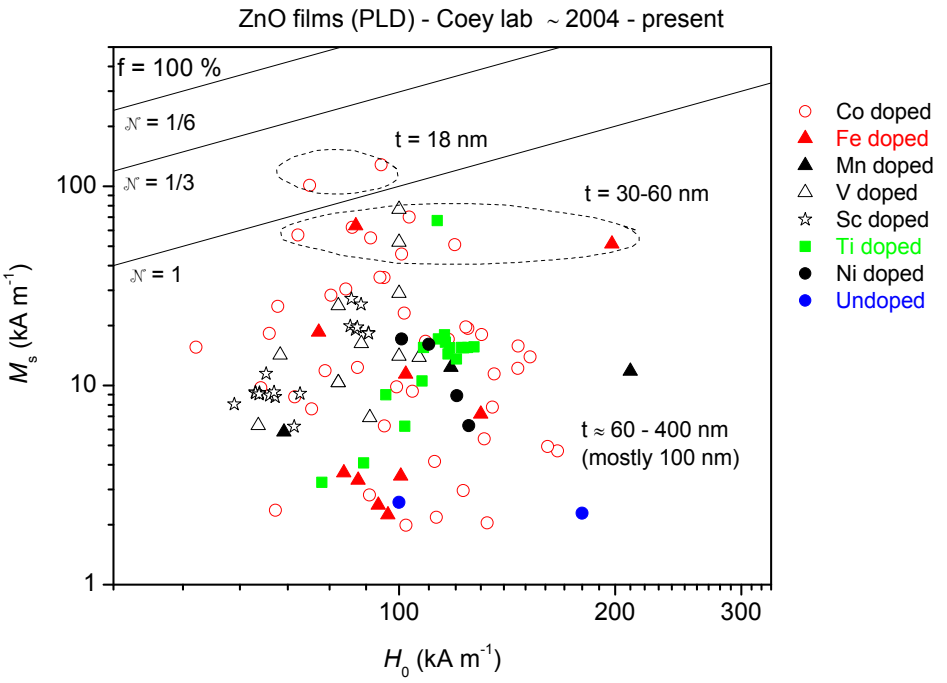

Figure 6.6. Room temperature M_s and H_0 values for ZnO films grown in our laboratory since ~ 2004.

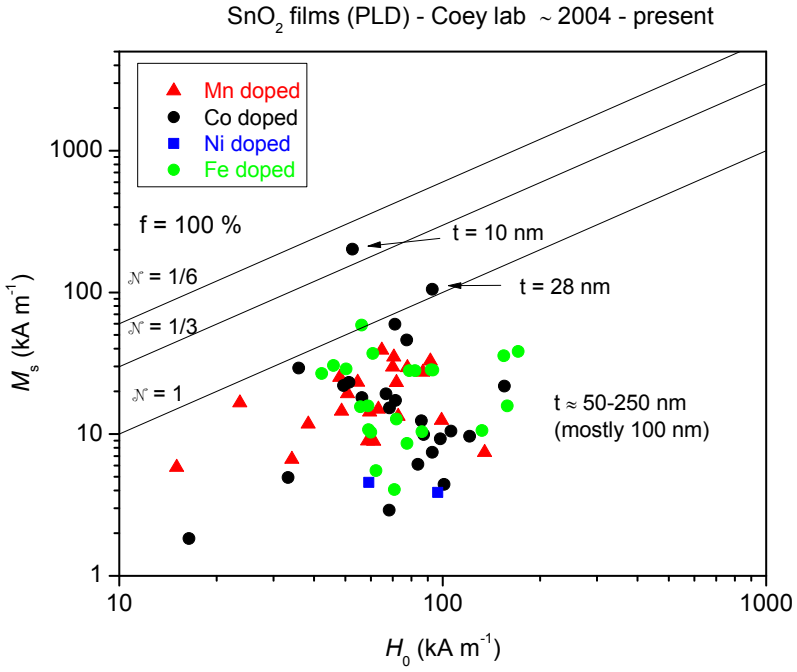

Figure 6.7. Room temperature M_s and H_0 values for SnO_2 films grown in our laboratory since ~ 2004.

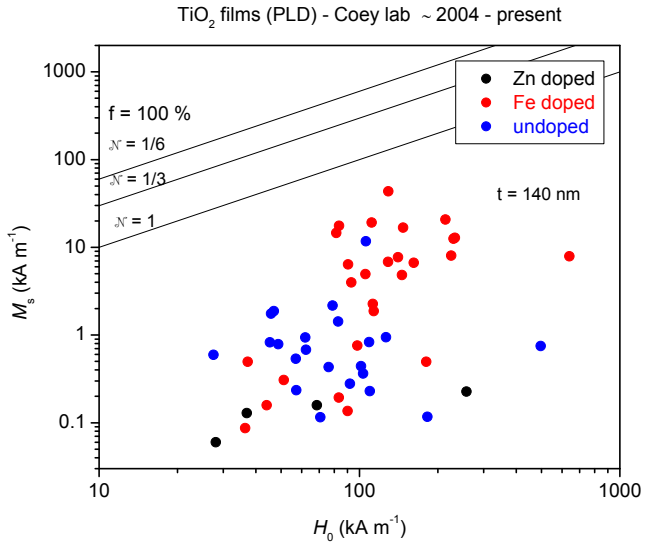

Figure 6.8. Room temperature M_s and H_0 values for TiO_2 films grown in our laboratory since ~ 2004.

To summarize, from the M_s vs H_0 data shown so far for d^0 oxide and MB_6 films grown by PLD, for the majority of films measured:

1. The magnetism is almost anhysteretic, and H_0 is markedly less than that due to metallic iron, but similar to that of magnetite nanoparticles
2. Typically the quantities of magnetite needed to account fully (or even partially in some cases) for the magnetic signals for the d^0 samples should be easily detected (such as by SEM-EDX, ICP-MS etc.), but rarely are, which suggests that magnetite or ferromagnetic impurities are not a general explanation
3. The ferromagnetic volume fraction f and saturation magnetization M_s of thinner films typically exceed those of thicker films; for films of order 10 nm thick f often approaches 100 %
4. There is no clear distinction between the regions where data points for transition metal doped films lie compared to those for undoped films on the M_s vs. H_0 scatter plots

Figure 6.9 summarizes the variation of M_s with film thickness for all of the above films; the data confirms that M_s does generally increase with decreasing film thickness, although the correlation is not particularly strong. Figure 6.10 summarizes the variation of the magnetic moment with film thickness; no general trend is evident, illustrating that the magnetic moment is typically independent of film thickness. The fact that the magnetic moment is independent of film thickness means that the magnetism is unlikely to be associated with the bulk of the film or due to ferromagnetic impurities, for which the moment should *increase* with film thickness (and hence volume) if that were the case. Instead it seems that interface or surface induced defects are

responsible for the magnetism, which may extend some distance, typically a few nm, into the film. Figure 6.11 displays the variation of magnetic moment *per unit area* with film thickness; there is little correlation between the moment per area and thickness, with moments per unit area of order 100 μ_B per nm^2 deduced for the majority of the films.

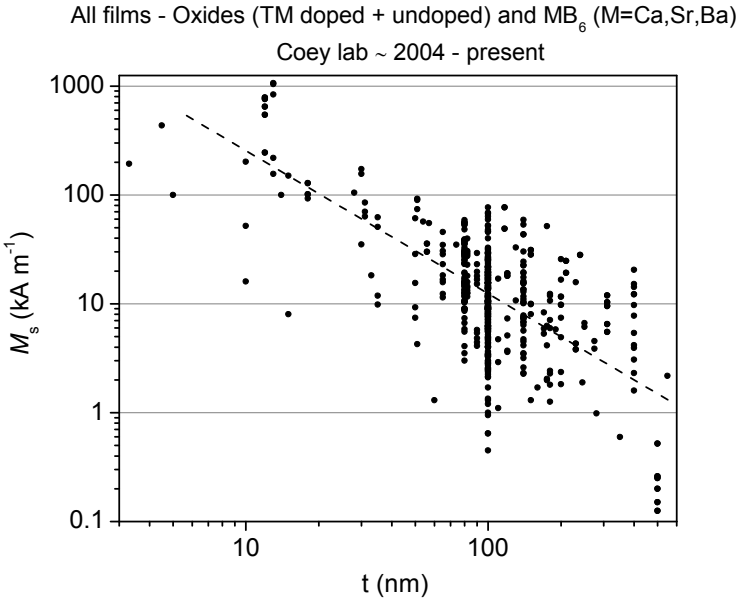

Figure 6.9. Variation of room temperature saturation magnetization M_s with film thickness for samples grown in our laboratory since ~ 2004. The dashed line indicates the best linear fit to the data, which yields a slope of -0.89 ± 0.09, indicative of a moment that is approximately independent of film thickness (furthermore see Fig. 6.10 below).

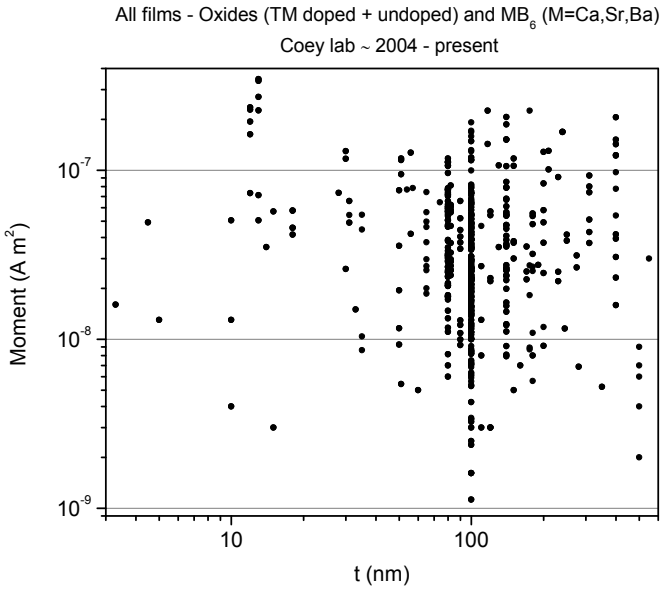

Figure 6.10. Variation of room temperature magnetic moment with film thickness for samples grown in our laboratory since ~ 2004. The moment is approximately independent of film thickness.

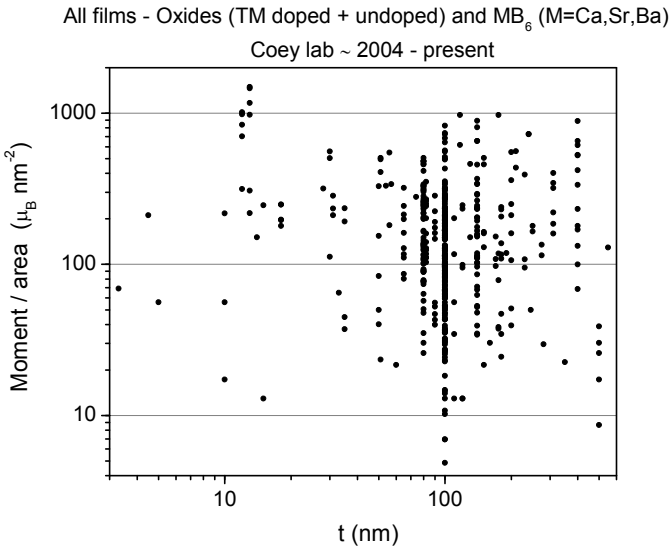

Figure 6.11. Variation of room temperature magnetic moment per unit area with film thickness for samples grown in our laboratory since ~ 2004.

Figure 6.12 shows M_s vs. H_0 data for bulk oxide micropowders (the exception is CeO_2 which is in nanopowder form and corresponds to the nanopowders synthesized in Chapter 4). It is evident that M_s is typically less than ~ 0.1 kA m^{-1} and that H_0 is ~ 100 kA m^{-1}. In addition, data for transition metal doped samples (black dots) fall within an approximately similar region to undoped samples. It is important to emphasize that none of the samples display any magnetism when in pristine bulk form, but only when doped, vacuum annealed or in nanopowder form. Hence all of the samples shown in Fig. 6.12 below are likely to be defect-rich, which may be correlated with their magnetic properties.

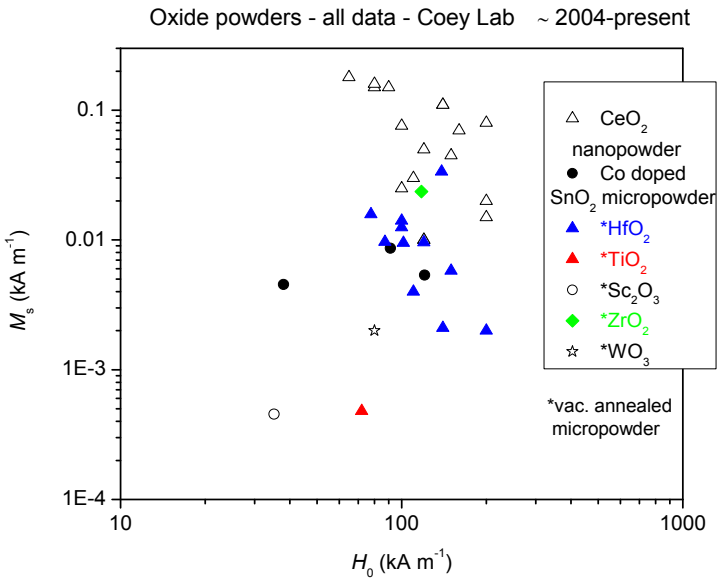

Figure 6.12. Room temperature M_s and H_0 values for oxide powders treated in our laboratory since ~ 2004.

Finally, M_s and H_0 data only for the three d^0 systems studied in this thesis are summarized in Figure 6.13 for comparison. The data serve to reinforce some of the conclusions deduced for other d^0 samples presented earlier in this chapter, namely that H_0 is less than that of Fe (metallic) but similar to that of magnetite, and that f and M_s for thin films > thick films >> bulk / powders.

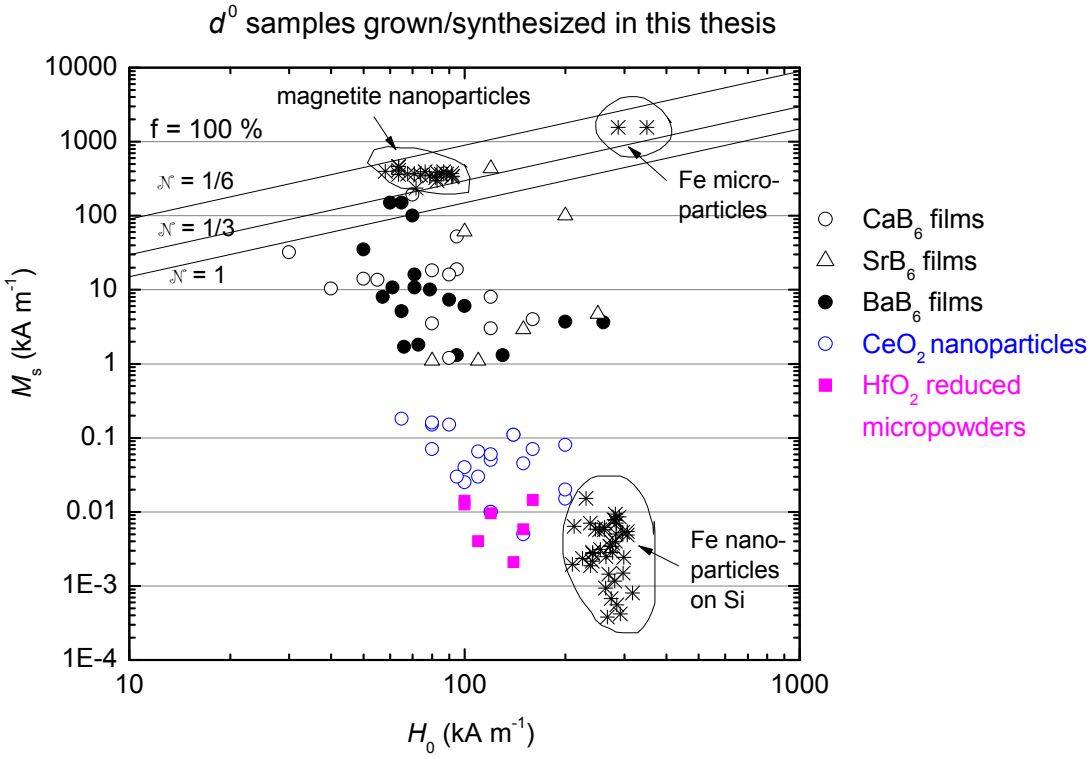

Figure 6.13. Room temperature M_s and H_0 values for the three d^0 systems studied in this thesis, namely MB_6 (M = Ca, Sr, Ba) thin films, CeO_2 nanoparticles and HfO_2 reduced powders.

The next section of this chapter suggests possible models for d^0 magnetism which may pertain to each of the three systems, HfO_2, CeO_2 and MB_6, shown in the above plot.

6.2. Models for d^0 magnetism

The three models for d^0 magnetism presented in this thesis are Stoner-type Charge Tranfer Ferromagnetism (CTF) [1,2], and two variants of Giant Orbital Paramagnetism (GOP) [3-5]. How they may pertain to each system studied in this thesis is now discussed. Models based on Zener or Heisenberg exchange coupling of defect-based localised moments *are not considered* because it seems that there is no way to obtain the necessary high Curie temperatures for defects with S = ½. Hence only band models involving delocalized moments (CTF and two variants of GOP) are considered.

Firstly, for magnetism in reduced HfO_2 micropowders, it is proposed that the magnetism is related to defects, primarily oxygen vacancies, induced by vacuum annealing. The CTF band model may best describe the appearance of RTFM signals for this system, including the anhysteresis and high T_c, in which delocalized electrons associated with defects occupy a defect-based impurity band which can become spin-split and may result in high temperature Stoner ferromagnetism if the density of states at the Fermi level is sufficiently high. The appearance of magnetism within a narrow range of annealing temperatures only suggests that there is an optimum concentration of oxygen vacancies for mediating the magnetism, which is also consistent with the CTF model.

For the magnetism of CeO_2 nanoparticles, the CTF model may also explain the magnetism, in which defects and/or non-magnetic dopants facilitate charge transfer with the impurity band. However, the model is unable to explain why separating the nanoparticles into clumps smaller than 100 nm should destroy the ferromagnetism The moment does not simply become thermally unstable (superparamagnetic), it actually disappears. The correct explanation may be Giant Orbital Paramagnetism, in which the broken symmetry associated with the surface of small (< 10 nm diameter) nanoparticles is proposed to create orbitals of large radius and giant moments. For nanoparticles of ceria it is widely known that the Ce^{3+} contribution due to the surface is enhanced as the particle size decreases. Yet it is noted that for ceria nanoparticles of ~ 6 nm diameter synthesized using 99.999% cerium nitrate, no RTFM was measured. This result suggests that for the ceria nanoparticles synthesized in this particular study, small size alone is not enough to create RTFM, but that dopants are also necessary, which may create the defects needed to produce the necessary surface conductivity. In effect, the theoretical predictions of both models, CTF and GOP, can account for the physical magnetic properties measured for nanoceria, such as the anhysteresis, temperature independent magnetization curves and high Curie temperatures, but only a variant of GOP can account for the fact that the RTFM may also depend on the mesoscale disposition of the ceria aggregates. Superparamagnetism is not a possible explanation because the magnetization curves show no sign of hysteresis at low temperature, and the magnetization curves superpose when plotted as a function of magnetic field, not magnetic field / temperature.

The closest analogy in the conventional paradigm to the size-dependence of the magnetization of CeO_2 aggregates is the stabilization of magnetic order in clusters of

superparamagnetic nanoparticles by dipole-dipole interactions [6]. The magnetite particle chains in magnetotactic bacteria are a nice example. Contiguous particles with a magnetization of order 0.5 MA m^{-1} and a moment of order 1000 μ_B are needed for the dipole interaction energy to exceed room temperature. The average moment of a CeO_2 nanoparticle is about three orders of magnitude less.

Our observation is not unprecedented. Radovanovich and Gamelin found that the moment of 6 nm nanoparticles of ZnO doped with 0.93% Ni only appeared in reaction-limited aggregates 400-500 nm in size [7], while Sundaresan *et al.* reported that the moment in 7 nm diameter CeO_2 nanopowders was modified upon sintering [8]. Those results establish that the magnetism is not an intrinsic property of the particles themselves. It does not just depend on atomic-scale defects within the particles. It appears that the extent and topology of the continuous particle surfaces may be the critical factor.

In the recent development of the model, a theoretical basis for collective d^0 magnetism has been proposed when quantum field theory is applied to conducting nanoparticles (work of Siddhartha Sen). An explanation for the collective magnetism is as follows; the magnetism is proposed to be due to giant orbital moments which form in coherent domains of clumps of nanoparticles, where the clump size is of order 100 nm, as shown schematically in Figure 6.14. When the clumps are broken up the coherent domains are no longer present and the magnetism is destroyed. Hence the magnetism depends critically on the *mesoscale disposition of the nanoparticles*. The theory is based on resonant fluctuations of the electromagnetic field (zero-point energy), similar to the theoretical idea advanced by Del Giudice *et al.* [9] in the context of water dipoles. These authors showed that if electromagnetic interactions due to zero-point fluctuations of the electromagnetic field are included in a model for water as a collection of rotating dipoles, then coherent domains where water is in an excited state emerge. A structured phase of water molecules and the electromagnetic field was predicted to coexist in these domains, whose size is determined by the excitation energies of the water molecules. However, the idea was that such coherent spontaneous structure formation could be a generic feature of many-body quantum systems, which naturally emerge when the methods of quantum field theory that give rise to the Casimir force are applied to study possible ground states of charged many-body systems interacting with electromagnetic radiation arising from zero-point fluctuations. When this theory, for which an succinct overview is presented in Appendix A.2, is applied to orbital magnetism, it predicts that the magnetic moment *m* should saturate as

$$m(H) = m(0)\, x/(1 + x^2)^{1/2} \qquad (6.1)$$

where $x = cH$, H is the magnetic field, and c is a constant which relates the energy scale to the length scale of the effect. In Chapter 4, section 4.3.13, experimental evidence for collective magnetism is supported by magnetization and electron microscopy measurements for CeO_2 nanoparticles dispersed with either 15 nm diameter γ-Al_2O_3 nanoparticles, icing sugar or latex beads, in which the magnetic signal appears to rapidly diminish when the clumps of CeO_2 are

broken up into ~ 100 nm sized aggregates; the reduction in the net magnetic signal is most marked for mixing CeO_2 with 15 nm diameter γ-Al_2O_3 nanoparticles.

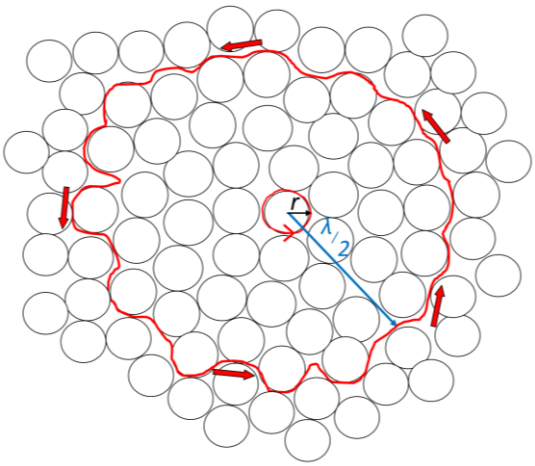

Figure 6.14. Schematic of collective magnetism due to the net orbital moment at the surface of a coherent domain (large clump of nanoparticles) > 100 nm size. *r* is the radius of the nanoparticles, *λ* is the coherence (wave)length, which is in effect the clump size. If the clump is broken up, so also are the coherent domains, and the magnetism disappears because the wavelength of the electromagnetic excitation can no longer be accommodated in the nanoparticle clump.

For the MB_6 (M = Ca, Sr, Ba) thin films grown by PLD, the magnetism also appears to be intimately related to defects. The films are amorphous and defect-rich due to the typically large lattice mismatch between film and substrate and due to the high laser fluences used to grow the films, with a large number of laser ablation droplets on the surfaces of the films resolved by AFM and electron microscopy analyses. Similar to the reduced HfO_2 powders, the magnetism appears within a certain range of annealing temperatures only, which suggests that the presence of defects alone is not a sufficient criterion to mediate the magnetism, but that there must also be an optimum concentration of defects, in agreement with the theoretical predictions of Edwards and Katsnelson [10] in which a narrow *sp* impurity band filled with itinerant electrons (with specific application to CaB_6) may become spin-split and mediate high temperature Stoner magnetism if a sufficiently large peak in the density of states coincides with the Fermi level energy, similar to that achieved more generally by electron transfer in the later CTF model.

It is probable that the quasi 2-dimensional structure of the thin films is related to the magnetism/defects; it is found that the magnetization is enhanced for thinner films and that the magnetism is likely to be located at the film-substrate interface rather than at the free surface of the film. It is probable that a spin-split impurity band is present here, but some direct measurement to establish a large density of states at the Fermi level would be needed to confirm the idea. Furthermore, the GOP model may also possibly be applicable here, in which the thin defect-rich film surface(s) provides the broken symmetry and large orbital radii necessary to induce giant orbital paramagnetism; in this case it is expected that the moment should depend on the direction of

the applied field relative to the film surface. This has been reported in some undoped thin film systems such as HfO_2 [11], ZnO [12] and TiO/TiO_2 [13] for example, but we did not find any such effect in the alkaline-earth hexaboride films grown by PLD presented in this thesis. A possible reason for the lack of anisotropy may be that the defect-rich films are not very uniform in texture. Further studies on thinner films are required.

6.3. References

[1] J. M. D. Coey, K. Wongsaprom, J. Alaria, and M. Venkatesan, Journal of Physics D: Applied Physics **41**, 134012 (2008).

[2] J. M. D. Coey, P. Stamenov, R. D. Gunning, M. Venkatesan, and K. Paul, New Journal of Physics **12**, 053025 (2010).

[3] A. Hernando, P. Crespo, and M. García, Physical Review Letters **96**, 057206 (2006).

[4] A. Hernando and M. A. García, Journal of Nanoparticle Research **13**, 5595 (2011).

[5] A. Hernando, P. Crespo, M. Angel Garcia, M. Coey, A. Ayuela, and P. Miguel Echenique, Physica Status Solidi B-Basic Solid State Physics **248**, 2352 (2011).

[6] S. Bedanta and W. Kleemann, Journal of Physics D-Applied Physics **42**, 013001 (2009).

[7] P. V. Radovanovic and D. R. Gamelin, Physical Review Letters **91**, 157202 (2003).

[8] A. Sundaresan and C. N. R. Rao, Nano Today **4**, 96 (2009).

[9] E. Delgiudice, G. Preparata, and G. Vitiello, Physical Review Letters **61**, 1085 (1988).

[10] D. M. Edwards and M. I. Katsnelson, Journal of Physics: Condensed Matter **18**, 7209 (2006).

[11] J. M. D. Coey, M. Venkatesan, P. Stamenov, C. Fitzgerald, and L. Dorneles, Physical Review B **72**, 024450 (2005).

[12] N. H. Hong, J. Sakai, and V. Brize, Journal of Physics-Condensed Matter **19**, 036219 (2007).

[13] X. H. Wei, R. Skomski, B. Balamurugan, Z. G. Sun, S. Ducharme, and D. J. Sellmyer, Journal of Applied Physics **105**, 07C517 (2009).

Chapter 7

Conclusions and future work

In this chapter some conclusions are drawn, together with some plans for future work. Some experimental results from a short vacuum annealing study of commercial WO_3 powders are given in the Appendix, followed by a theoretical basis for the collective magnetism model.

7.1. Conclusions

d^0 magnetism is still a relatively new field of research in magnetism, which is both a hot and often controversial topic, since there is no consensus as to the origin of this seemingly anomalous type of magnetic order, all of which warrants the need for further research in this field. It is still not widely accepted whether the magnetism is defect or size related (or perhaps both), or even a triviality arising from extrinsic ferromagnetic impurities and hence not a new magnetic phenomenon at all. Oxides and hexaborides, among other materials, may provide the evidence required to solve this puzzle. Aside from a purely theoretical interest, such materials could potentially be used in spin electronics devices, since they typically exhibit high Curie temperatures and virtually temperature independent magnetization values from liquid helium temperatures to several hundred kelvins above room temperature. The experimental picture is confused by the difficulty in reproducing many of the results, the often ephemeral nature and weakness of the ferromagnetic signal and the problem of characterizing defects. The poor reproducibility of the experimental data may be due to the difficulty in precisely recapturing the process conditions which lead to a specific defect distribution and density. The as-prepared samples are typically not in equilibrium and they often evolve with time and temperature, especially for nanoparticles synthesized by chemical methods, but also to some extent for thin films produced by PLD. The main conclusions for each of the three systems studied in this thesis, namely reduced HfO_2 micropowders, CeO_2 nanoparticles and MB_6 (M = Ca, Sr, Ba) thin films are now drawn.

Firstly, weak room temperature ferromagnetism with moments of order 10^{-8} Am^2 (M_s of order 10 Am^{-1}) was measured for high purity HfO_2 micropowders which were vacuum annealed at 650−750 °C. No ferromagnetism was measured for the virgin powders, while the magnetic signal for the ferromagnetic vacuum annealed powders was diminished upon re-annealing in air. The magnetism is virtually anhysteretic, and from analysis of the magnetization curve it may be estimated that only a small fraction (10s of ppm) of the samples is ferromagnetically ordered. Ferromagnetic contamination is ruled out as a source of the magnetic signals from ICP-MS and SEM-EDX analyses. It is hence proposed that the magnetism is likely related to defects, primarily oxygen vacancies, induced by vacuum annealing, which occupy a defect-based impurity band, which can become spin-split and can induce high temperature Stoner ferromagnetism when the density of states at the Fermi level is sufficiently high. The appearance of magnetism within a narrow range of annealing temperatures only suggests that there is an optimum concentration of oxygen vacancies for mediating the magnetism.

Secondly, reproducible room temperature magnetic signals were measured for polycrystalline CeO_{2-x} nanoparticles of ~ 4 nm diameter synthesized by homogeneous precipitation using a 99 % purity cerium nitrate cerium precursor. The magnetism is relatively weak (M_s typically ≤ 100 A m^{-1}), virtually anhysteretic and temperature independent from 300 – 4 K, with the magnetization curves superposing at both 4 K and 300 K, indicative of negligible magnetocrystalline anisotropy. It is shown that ferromagnetic impurities alone cannot account for the magnitude of the magnetic signals. No RTFM is measured for nanoparticles synthesized by homogeneous precipitation using a higher purity 99.999 % cerium nitrate precursor, but by doping these nanoparticles with small quantities of non-magnetic dopants (~ 1 wt %), a RTFM signal is once again obtained. A similar effect is measured for nanoporous films synthesized by electrodeposition. It is hence proposed that the magnetism may be related to structural defects, primarily Ce^{3+} and associated charge compensating oxygen vacancies, induced by intentionally doping pure nanometric ceria with non-ferromagnetic dopants; the main impurity in the 99 % purity cerium nitrate precursor is ~ 1 wt % La. It is shown from analysis of the magnetization curves that only a small fraction of the volume of the magnetic nanopowders are ferromagnetically ordered, < 0.1 %, consistent with inhomogeneous defect-related magnetism associated with grain boundaries or surfaces for example. Mixing of the CeO_2 nanoparticles with γ-Al_2O_3 nanopowder remarkably induces a marked reduction in magnetic signal and breaks the clumps of CeO_2 into < 100 nm sized aggregates, for which the magnitude of the reduction cannot be accounted for by the trivial loss of magnetic CeO_2 powder upon mixing. One possible origin of d^0 magnetism in nanometric ceria is the proposed existence of a defect impurity band which can become spin-split and result in high temperature Stoner ferromagnetism when the density of states at the Fermi level is sufficiently high. Another possible explanation is giant orbital paramagnetism due to surface currents associated with a 2-D electron gas at the surface of small (< 10 nm) spherical particles. A closely related third explanation which may account for the possible influence of the mesoscale disposition of the nanoparticles on the magnetic signal is that of collective magnetism, in which the magnetism is

proposed to be due to giant orbital moments which form in collective coherent domains of clumps (~ 100 nm) of nanoparticles, with a theoretical basis in the resonant fluctuations of the electromagnetic field (zero-point energy).

Thirdly, RTFM is measured for many amorphous MB_6 (M = Ca, Sr, Ba) films, when they are grown by PLD on Al_2O_3 substrates at 400−650°C. The magnetism is virtually anhysteretic, isotropic, temperature independent from 4−300 K and saturates quickly (< 0.3 T) with applied field. The magnetic signals correspond to average film magnetizations in the range 10−100 kA m^{-1}, but from analysis of the variation of the magnetic moment with film thickness, it is shown that the magnetism originates mainly near the interface with the substrate. It is shown by various methods (magnetization curve analysis, SEM-EDX, ICP-MS) that ferromagnetic impurities cannot account for the magnitude of the larger magnetic signals measured. The proposed origin of the magnetism is a defect-based impurity band following the theoretical predictions of Edwards and Katsnelson (and the later generic predictions of the Charge Transfer Ferromagnetism model) in which a narrow *sp* impurity band filled with itinerant electrons may become spin-split and mediate high temperature Stoner ferromagnetism if a sufficiently large peak in the density of states coincides with the Fermi level energy.

7.2. Future work

Firstly, for HfO_2, due partly to its potential widespread use as a replacement for the SiO_2 insulating gate oxide in future downscaled metal oxide semiconductor field effect transistors (MOSFETs), an understanding of its potential ferromagnetic-like properties is of the utmost importance, aside from a purely theoretical interest. Future research should focus on trying to better characterise the defects in HfO_2 in terms of their possible relation to the magnetic properties, for example by positron annihilation spectroscopy (PALS). Another useful study would be to investigate if mixing of the ferromagnetic micropowders with other non-magnetic powders (such as γ-Al_2O_3 nanopowder) has any effect on the magnetic signal, as it appears to do for ferromagnetic CeO_2 nanoparticles.

Secondly, for CeO_2 nanoparticles, the effect of further non-ferromagnetic (and possibly also ferromagnetic) dopants and doping concentrations on the magnetic properties warrants further investigation. The key goal is to try to controllably *tune* the magnetic moment, not only to gain a better understanding of the underlying magnetic phenomena, but more ambitiously in order to pave the way towards possible integration of these materials into spin electronics devices. This may be realised via electron injection/removal using different surfactants to chemically tune the magnetic moment of the nanoparticles for example, and/or via controlled defect creation using high energy irradiation such as PLD laser beams or synchrotron radiation. It is noted that the lattice parameters of bulk CeO_2 (5.411 Å) and silicon (5.431 Å) serendipitously match quite well, which is beneficial towards integration of CeO_2 with the existing silicon-based technology; furthermore, since nanometric CeO_2 undergoes lattice expansion compared to the bulk, the lattice mismatch for nanostructured CeO_2 on Si will be even less than that of bulk CeO_2 on Si. Other possible and closely related avenues of research include optical, thermal or electrical manipulation of the magnetism, which are also research goals applicable to most of the d^0 systems in general. It would also be interesting to try to modify the synthesis procedure used for producing CeO_2 nanoparticles in order to produce nanostructures of different *morphology* (which may be realised by suitable adjustment of the ratio of the reagent concentrations, in particular $[Ce^{3+}]$:$[OH^-]$) and size and to investigate their resultant magnetic properties. In addition, the effect of mixing (diluting) ferromagnetic CeO_2 nanoparticles with other ferromagnetic and non-ferromagnetic powders of various particle sizes, a brief study of which was initially conducted here, may help to elucidate the possible relation between the mesoscale aggregations and their magnetic properties (collective magnetism). In addition, how the magnetic signal of CeO_2 is affected by mixing with other powders with different *electronic properties* (insulators vs. metals for example), in addition to those of different size, warrants further investigation.

Thirdly, for MB_6 films, a suggested short term goal is the development of more *controllable* and *reproducible* methods of defect creation by high energy irradiation such as by FIB, laser beams or synchrotron radiation for example, since the magnetic properties measured for film grown by PLD here are rather variable. A more optimistic and long term goal would be the ultimate integration of MB_6 films into MTJ devices. This could be promising since thin films of d^0 materials have been shown to exhibit magnetic signals often several orders of magnitude greater than that of the bulk, which may be related to an enhanced concentration of defects within a thin interface layer. In consequence, another key challenge is to try to better characterise the defects present in these thin films, especially at the substrate-film interface, which may lead to a better understanding about how they may influence the magnetic properties. The proposal of a spin-split impurity band mediating the magnetism could be confirmed more immediately by measurements of the low temperature specific heat capacity and Pauli susceptibility for example. Another promising avenue of future experimental research is Mg doped MB_6 compounds, in which both *magnetic and ferroelectric* properties may be realisable, the magnetism arising intrinsically from MB_6, and Mg doping proposed to provide the net electric dipole moment and resultant ferroelectricity. The basic idea is that the small Mg atom can jitter around within the octahedral boron framework and can thus generate a net electric dipole moment, the theoretical basis for which has recently been advanced [1].

[1] I. Popov, N. Baadji, and S. Sanvito, Physical Review Letters **108**, 107205 (2012).

A Appendix

The first part of the Appendix, A.1, presents some experimental results for vacuum annealed WO_3 powders, while A.2 provides a brief overview of the mathematical basis of the collective magnetism model for d^0 magnetism, The final sections list publications, external dissemination (talks, conferences, posters) and summer schools/training courses attended/completed during the course of this thesis.

A.1 WO_3 powder vacuum annealing - experimental results

Like HfO_2, stoichiometric WO_3 is a wide band gap diamagnetic insulator, since the W^{6+} 5*d* band is empty, with an indirect band gap of ~ 2.6 eV at room temperature. Its main application is in electrochromic thin film devices, since it can change its optical properties, reversibly and persistently, by the application of an electrical voltage. About 200 mg of WO_3 powder (99.9% nominal purity, purchased from BDH chemicals) was heated in vacuum (10^{-5} mbar) at 600 °C for 1 hour at the maximum temperature using rapid (10 °C/minute) heating and cooling rates. The virgin powder had a greenish-yellow appearance, which transformed into a dark blue hue after vacuum annealing, which may indicate the formation of oxygen vacancies and other defects. The aim of the experiment was to investigate if vacuum annealing can induce ferromagnetic-like signals in pristine commercial WO_3 powder, similar to the results obtained for reduced HfO_2 micropowders in this thesis.

The most common crystal structure of WO_3 under ambient conditions is monoclinic, with the *P21*/*n* space group. Below 17 °C a transformation to a triclinic phase occurs. While all of the peaks for the vacuum annealed powder can be indexed to the monoclinic phase, for the pure virgin powder prior to annealing there are three extra unknown peaks at 27.2, 28.0 and 36.74° 2θ (which disappear upon vacuum annealing), as shown in Figure A.1 on the following page. These three extra peaks peaks do not correspond to any other tungsten oxide (or rhenium oxide or tantalum oxide for example) phases, nor to any tungsten metal phases.

Room temperature magnetization data for the powders are also shown on the next page in Figure A.2. The measured magnetic moments (magnetizations) are ~ 0.3×10^{-8} Am^2 (~ 0.4 A m^{-1}) and 0.6×10^{-8} Am^2 (1.7 A m^{-1}) for before and after vacuum annealing respectively, the former signal being very weak and rather indistinct, for which the sample masses were 55.9 mg and 25.6 mg respectively. The data is compared to a previous experiment conducted by another researcher in our laboratory (J. Mlack, unpublished results, 2009), who measured a similar magnetization of ~ 1.4

A m^{-1} for the same powder vacuum annealed at 600 °C, although the data is less noisy (possibly due to a larger mass of 78.1 mg used for measurement) and H_0 is smaller (~ 80 kA m^{-1}) compared to the latest measurement (~ 150 kA m^{-1}). No RFTM was measured by J. Mlack for powders which were vacuum annealed at either 700 °C or 800 °C, while the untreated powder did not exhibit a distinct ferromagnetic signal above the noise level, similar to the findings here.

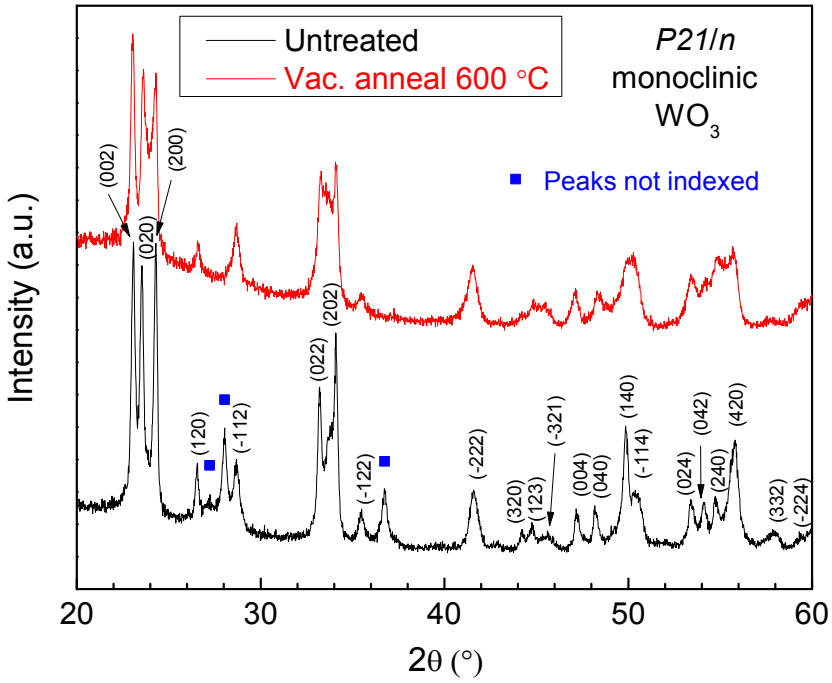

Figure A.1. XRD data for WO_3 powder before and after vacuum annealing at 600 °C.

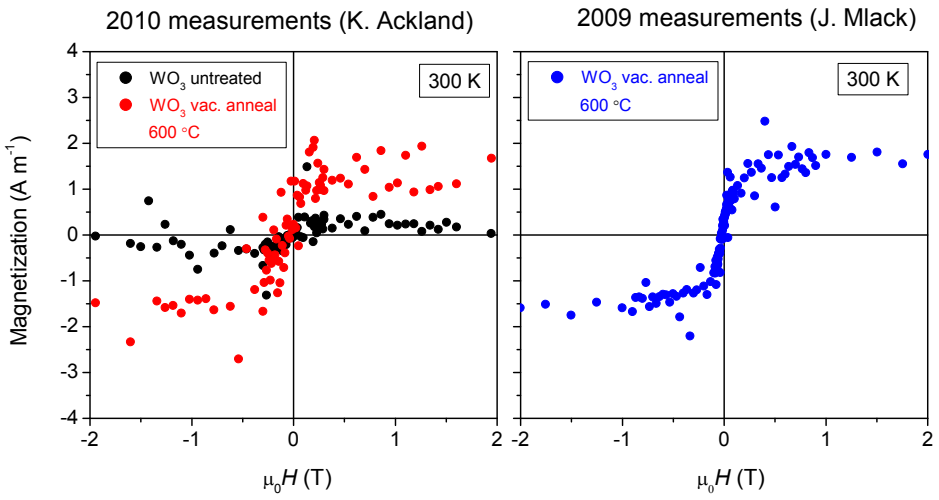

Figure A.2. Magnetization data for WO_3 powder before and after vacuum annealing at 600 °C is shown on the left. The data for the vacuum annealed powder is compared with a previous measurement shown on the right.

SEM images of the powder before and after vacuum annealing are shown in Figure A.3. The powder is in fact composed of large faceted microcrystals of ~ 20-80 μm size, with no noticeable difference in particle morphology or size between the virgin and vacuum annealed powders. EDX analysis of the powders indicated that while the virgin powder was actually slightly oxygen rich (the mass ratio of O:W = 0.28), the vacuum annealed powder was oxygen deficient (O:W = 0.20) as may be expected due to the creation of oxygen vacancies; for stoichiometric WO_3, the mass ratio of O:W = 0.26.

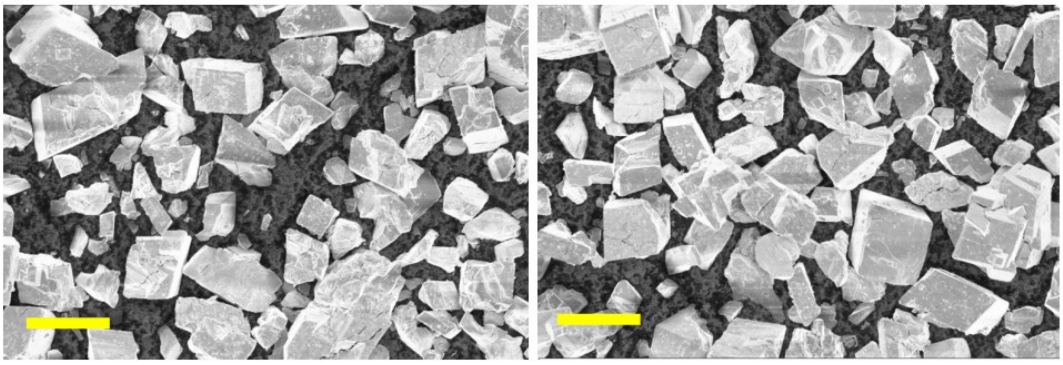

Figure A.3. SEM images for WO_3 powder before (left) and after (right) vacuum annealing at 600 °C; scalebar = 50 μm.

No EPR signal (after the background cavity plus empty EPR tube contribution was subtracted) was measured for either the pure or vacuum annealed powders at room temperature, despite using high gain values and optimization to ensure the best signal/noise values. The result indicates that no unpaired spins are detected down to ~ 10^{13} spins/gram, which is at about the detection limit; 1 mole of WO_3 has 2.6×10^{21} spins/gram in comparison. About 30 mg of powder was used for each measurement, and the powders may be inferred to be insulating since no loss of cavity Q value (which would be indicative of conduction) was measured upon sample insertion for measurement.

In summary, weak RTFM was measured for WO_3 commercial powders vacuum annealed at 600 °C, with a measured magnetization of 1.7 A m^{-1}, which confirms the results of a previous measurement (1.4 A m^{-1}). The magnitude of the magnetization measured is about an order of magnitude smaller than the largest values measured for a similar vacuum annealing study of HfO_2 commercial powder which was presented in this thesis. Whether the magnetism is associated with oxygen vacancies and/or is possibly due to ferromagnetic impurities is uncertain however, although the fact that no distinct RTFM is measured for either the untreated sample or for those previously annealed at either 700 °C or 800 °C helps to disprove the latter hypothesis. Finally, it is noted that *no RTFM* was measured for any vacuum annealed TiO_2, CeO_2 or ZrO_2 commercial micropowders, nor for any of the commercial oxide micopowders HfO_2, WO_3, TiO_2, CeO_2 or ZrO_2 which were annealed in an argon/hydrogen atmosphere.

A.2 Collective magnetism model – theoretical basis

In order to give a general succinct overview of some of the key mathematical equations on which the collective magnetism is based, the starting point is to consider electrons orbiting on the mesoscale, for which the Hamiltonian H may be represented as

$$H = \Sigma^{N}_{i=1} (L_i^2)/2mr^2 + e\boldsymbol{A}.\boldsymbol{J} \quad (A.1)$$

where L_i is the orbital angular momentum of an electron, r is its orbital radius, $\boldsymbol{A}$ is the vector potential of the part of the electromagnetic field due to zero-point fluctuations, and $\boldsymbol{J}$ represents persistent electron currents in coherent domains. Analysis in terms of path integrals leads to the emergence of coherent orbital moments on the nanoscale. We can calculate the expectation value of the orbital polarization $P = \mathbf{e}_m.\mathbf{e}_B$, where $\mathbf{e}_m$ and $\mathbf{e}_B$ are unit vectors in the direction of the orbital moment and the applied magnetic field respectively. The polarization is determined by using the fact that the applied field mixes the coherent state vectors by an angle α, for which the induced polarization P is

$$P = \kappa \sin 2\alpha \quad (A.2)$$

where κ is a constant which is fixed by the model, and $\tan \alpha = [1 + (1+x^2)^{1/2}]/x$, where $x = 2V/\hbar\omega = c\boldsymbol{B}$ is independent of temperature. Here V is the interaction of the electrons in a coherent domain of radius R with an external field $\boldsymbol{B}$ and ω is the excitation frequency associated with the electromagnetic field. The constant κ is of order 0.1 for a coherent configuration, and zero for an incoherent system. The magnetization curve is therefore

$$P = \kappa\, x/(1 + x^2)^{1/2} \quad (A.3)$$

This function differs only slightly from the empirical $P = \tanh y$ function often used to fit the magnetization curves, but it has a theoretical justification for d^0 magnetism.

The characteristic length scale of the coherent domains l_{coh} is related to the characteristic excitation frequency ω of CeO_2, which is resonant with the zero-point vacuum fluctuations. If we identify l_{coh} with the wavelength $\lambda = 2\pi c/\omega$, the magnetic interaction energy $V \sim \lambda^3 M\boldsymbol{B}$. Hence

$$\lambda^4 = \hbar c/2M \quad (A.4)$$

which gives $\lambda = 177$ nm. The corresponding photon energy is $\Delta = 7$ eV, which is tentatively associated with an allowed O $2p$ – Ce $5d$ transition in CeO_2. The magnetic moment of a coherent domain is $\lambda^3 M_s$; it contains $\sim 2\times10^8$ Ce atoms, or $\sim 2\times10^5$ nanoparticles.

The effect of the zero-point fluctuations is amplified by $\sqrt{N}$ in the coherent domain. Since there are ~ 0.3 electrons per Ce atom, $\sqrt{N}$ is of order 10^4. The frequency of the persistent orbital currents is given by the expression

$$\Omega_c = G\Gamma\omega \quad (A.5)$$

where the quantity $G\Gamma \approx 10^{-2}$. Hence Ω_c is $\approx 10^{14}$ s^{-1}, and the frequency of the currents circulating on a nanoparticle's surface is $(\lambda/2r_0)\Omega_c \approx 10^{16}$ s^{-1}.

A.3. Publications

A.3.1 Publications related to d^0 magnetism

I. J. M. D. Coey, K. Ackland, M. Venkatesan, and S. Sen, Collective magnetic response of CeO_2 nanoparticles, submitted for publication (2014).

II. K. Ackland, M. Venkatesan, and J. M. D. Coey, Room temperature magnetism in MB_6 (M = Ca, Sr, Ba) films grown by pulsed laser deposition, *European Physical Journal B* **86**, 104 (2013).

III. K. Ackland, M. Venkatesan, and J. M. D. Coey, Magnetism of BaB_6 thin films synthesized by pulsed laser deposition, *Journal of Applied Physics* **111**, 07A322 (2012).

IV. K. Ackland, L. M. A. Monzon, M. Venkatesan, and J. M. D. Coey, Magnetism of Nanostructured CeO_2, *IEEE Transactions on Magnetics* **47**, 3509 (2011).

A.3.2. Other publications published during thesis (2009-2013)

V. S. Mosivand, L. M. A. Monzon, K. Ackland, I. Kazeminezhad, and J. M. D. Coey, The effect of organics on the structure and magnetization of electro-synthesised magnetite nanoparticles, *Journal of Nanoparticle Research* **15**, 1795 (2013).

VI. L. M. A. Monzon, K. Ackland, S. Mosivand, M. Venkatesan, and J. M. D. Coey, The role of polyaniline in the formation of iron-containing nanocomposites, *Journal of Nanoparticle Research* **15**, 1533 (2013).

VII. C. Fowley, Z. Diao, C. C. Faulkner, J. Kally, K. Ackland, G. Behan, H. Z. Zhang, A. M. Deac, and J. M. D. Coey, Local modification of magnetic anisotropy and ion milling of Co/Pt multilayers using a He^+ ion beam microscope, *Journal of Physics D-Applied Physics* **46**, 195501 (2013).

VIII. M. Hakimi, M. Venkatesan, K. Rode, K. Ackland, J. M. D. Coey, The zero-magnetization Heusler ferrimagnet, *Journal of Applied Physics* **113**, 17B101 (2013)

IX. P. Dunne, R. Soucaille, K. Ackland, J. M. D. Coey, Structuring of electrodeposits with permanent magnet arrays, *Magnetohydrodynamics* **48**, 331 (2012).

X. J. F. Feng, K. Rode, K. Ackland, P. S. Stamenov, M. Venkatesan, and J. M. D. Coey, Ultrathin $(CoFe/Pt)_n$ multilayers with tuned magnetic properties, *Journal of Magnetism and Magnetic Materials* **324**, 2298 (2012).

XI. P. Dunne, R. Soucaille, K. Ackland, and J. M. D. Coey, Magnetic structuring of linear copper electrodeposits, *Journal of Applied Physics* **111**, 07B915 (2012).

A.4. External dissemination - Conferences, talks and posters

A.4.1 Conferences attended

I. Joint European Magnetic Symposia 2012 (Parma, Italy), September 2012.

II. 56th Magnetism and Magnetic Materials conference (Scottsdale, USA), November 2011.

III. Euromat 2011 conference (Montpellier, France), September 2011.

IV. IEEE Asia Intermagnetics conference (Taipei, Taiwan), April 2011.

A.4.2. External talks given

I. *"Magnetism of cerium dioxide nanoparticles"*, invited talk, Paul Scherrer Institute, Villigen, Switzerland, August 2013.

II. "*Room temperature magnetism in MB_6 (M = Ca, Sr, Ba) films grown by pulsed laser deposition"*, Joint European Magnetic Symposia 2012 oral presentation, Parma, Italy, September 2012.

III. "*Magnetism of nanostructured cerium dioxide*", invited talk, Glasgow University, Scotland, June 2011.

A.4.3 Posters presented

I. "*d^0 magnetism in nanoparticles and films*", Interfacing Oxides Summer School, Hesselberg, Germany, July 2012.

II. "*Magnetism of BaB_6 thin films synthesized by pulsed laser deposition*", 56th Magnetism and Magnetic Materials conference, Scottsdale, USA, November 2011.

III. "*Magnetism of Nano-Structured CeO_2"*, Euromat conference, Montpellier, France, September 2011.

IV. "*d^0 magnetism in oxides and hexaborides"*, IEEE Magnetics Society summer school, New Orleans, USA, May 2011.

V. "*Magnetism of nanostructured cerium oxide*", IEEE Asia Intermagnetics conference, Taipei, Taiwan, April 2011.

VI. *"d ^{0} ferromagnetism; Potential materials for spintronics"*, Globe Forum Conference (sponsored by the Irish Research Council for Science, Engineering and Technology), Dublin, Ireland, November 2011.

VII. *"Room-temperature ferromagnetism in CeO_2 nanopowders"*, HERCULES XX Symposium (Higher European Research Course for Users of Large Experimental Systems), Grenoble, France, March 2010.

A.5. External Summer Schools and training courses

I. Interfacing Oxides (IFOX) Summer School, Hesselberg, Germany, July 2012.

II. IEEE Magnetics Society Summer school, New Orleans, USA, May 2011.

III. HERCULES XX Symposium (Higher European Research Course for Users of Large Experimental Systems), Grenoble, France, March 2010.